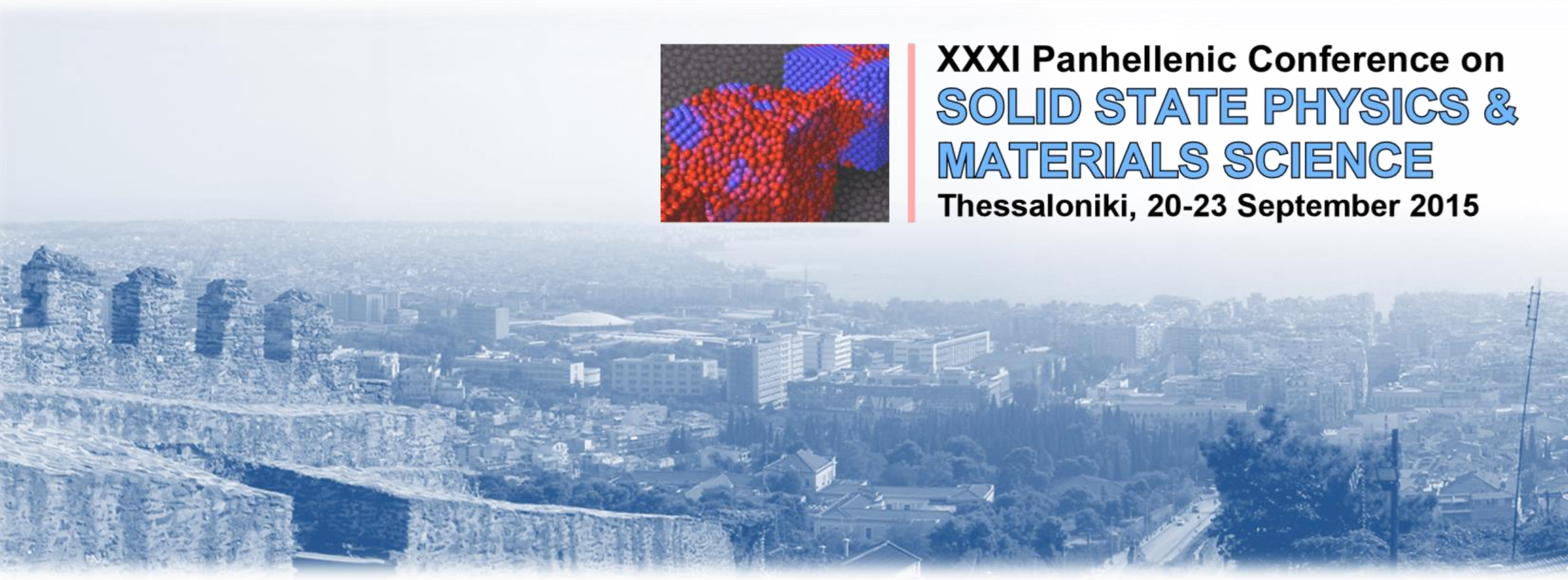

XXXI Panhellenic Conference on Solid State Physics and Materials Science

Book of Abstracts

20-23 September 2015
Thessaloniki, Greece

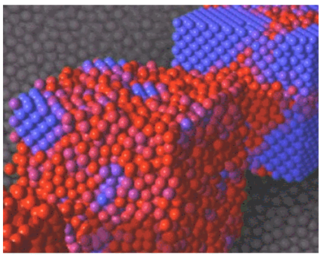

XXXI Panhellenic Conference on
SOLID STATE PHYSICS & MATERIALS SCIENCE
Thessaloniki, 20-23 September 2015

Conference Program

Organized by
Physics Department, AUTh

Location
Porto Palace Hotel, Thessaloniki

Under the auspices of

ARISTOTLE UNIVERSITY OF THESSALONIKI

SCHOOL OF PHYSICS (AUTH)

FACULTY OF SCIENCES (AUTH)

DEPARTMENT OF SOLID STATE PHYSICS
SCHOOL OF PHYSICS

POST-GRADUATE COURSE PROGRAM
“MATERIALS PHYSICS & TECHNOLOGY”

RESEARCH COMMITTEE (AUTH)

Sponsors

A.U.TH RESEARCH COMMITTEE

ANELIS
ANALYTICAL ENVIRONMENTAL
LIFE INDUSTRIAL SCIENCES

KLOTHAKIS ELEFTHERIOS
2, Plastira Sq, 11635 Athens-Greece
Τηλ: +30 210 7524444 Fax: +30 210 7560849
E-mail: eklot@tee.gr Website: www.anelis.gr

SPECS™

Rigaku

RENISHAW
apply innovation™

ITC
International Technology Corporation

VECTOR
TECHNOLOGIES

ASTERIADIS

ΑΝΑΛΥΤΙΚΕΣ ΣΥΣΚΕΥΕΣ Α.Ε.
Δρ Κ.Ι. ΒΑΜΒΑΚΑΣ - ΕΠΙΣΤΗΜΟΝΙΚΟΣ ΕΞΟΠΛΙΣΜΟΣ

Committees

Local Organizing Committee

Chair: Thomas Kehagias, Assoc. Prof.
Vice-Chair: M. Angelakeris (Assoc. Prof.)

Members

J. Arvanitidis (Assist. Prof.)
D. Christofilos (Assist. Prof)
G. Dimitrakopulos (Assoc. Prof.)
M. Gioti (Assist. Prof.)
M. Katsikini (Assist. Prof.)
J. Kioseoglou (Assist. Prof.)
G. Litsardakis (Prof.)
P. Patsalas (Assoc. Prof.)
K. Simeonidis (Dr.)
D. Tassis (Assist. Prof.)

Program Committee

C. Dimitriadis (AUTh)
N. Frangis (AUTh)
P. Komninou (AUTh)
E. Paloura (AUTh)

Advisory Committee

T. Bakas (Univ. Ioannina)
P. Kelires (Cyprus Univ. of Technol.)
S. Kennou (Univ. Patras)
S. Logothetidis (AUTh)
D. Niarchos (NCSR Demokritos)
C. Soukoulis (IESL/FORTH)
N. Stefanou (Univ. Athens)

Secretariat

K. Bazioti
E. Mirovali
A. Makridis
T. Koukoula
N. Florini
T. Pavloudis

Preface

The ***XXXI Panhellenic Conference on Solid State Physics & Materials Science*** is a historic event, started in Thessaloniki in 1982, that is held annually and constitutes a unique national forum bringing together all specialists working in different areas of Solid State Physics and Materials Science in Greece. Following the corresponding 2014 event in Herakleion, Crete, the XXXI Conference takes place in Thessaloniki, at the facilities of the Porto Palace hotel from 20th to 23rd of September 2015.

The Conference integrates fundamental and applied research, thereby merging cutting edge research with up-to-date and evolving applications. It strongly promotes an interdisciplinary approach to various issues related to the physical properties of solids. Emphasis is given to emerging nanostructured materials engineering for tailoring desired materials properties, as well as to the participation of graduate students, postdocs, and early career researchers, which represent the critical human resources for next generation science. The Conference is, therefore, dedicated to addressing the most recent advances and defining future directions in the field of Solid State Physics and Materials Science.

Under the consultancy of the Advisory and Program Committees, this Conference was specially designed to comprise high scientific interest topics, such as: *Photonics & optoelectronics*; *Structural, mechanical & optical properties of condensed matter*; *Electronic transport, semiconductors & devices*; *Magnetism, superconductivity & strongly correlated systems*; *Nanoscale, surface & interface science*; *Inhomogeneous materials, composite materials, polymers, biomaterials*; *Interdisciplinary solid state physics*.

A total of 182 abstracts were submitted, by almost all Greek Universities and Research Foundations, as well as Technical Institutes. Foreign contributors from the UK, USA, Germany, France and Poland set an international character for the Conference, which is also reflected upon the large number of collaborations among Greek and foreign scientists co-authoring the submitted abstracts. The scientific program consists of 62 oral (1 plenary, 2 keynote, 8 invited, and 51 contributed) and 120 poster presentations.

The Conference is organized by the Organizing Committee members, under the auspices of the Physics Department of the Aristotle University of Thessaloniki (AUTH) and sponsored by the AUTH Research Committee, ANELIS, ITC, Vector Technologies, N. Asteriadis S.A., and Analytical Instruments S.A.

Expecting a fruitful and enjoyable next event, it would be a pleasure to attend the 2016 event in Ioannina.

Assoc. Prof. Thomas Kehagias, Chairman

Introduction

The 31st Panhellenic Conference on Solid State Physics and Materials Science 20-23 September 2015, Thessaloniki, Greece is a four-day scientific meeting covering all areas of modern trends and applications of Materials Science and Technology. The conference is held on a rotational annual basis. The recent past conferences were held in Heraklion-Crete-2014, Athens-2013, Patras-2012, Limassol-Cyprus-2011, Ioannina-2010 and Thessaloniki-2009. Researchers and scientists from Universities, Research Institutions, State Organizations, and the Industry come together during the meeting to present and discuss the current state of the art in the area of physics, chemistry, materials science, and materials engineering.. At the same time, it provides the grounds for the graduate and post graduate students to present their projects, discuss scientific collaborations with other groups, as well as to explore employment opportunities. An exhibition of characterization instruments and accessories will be also organized in the conference place.

Topics

The topics that will be discussed include Photonics & optoelectronics, Structural, mechanical and optical properties of condensed matter, Electronic transport, semiconductors & devices, Magnetism, superconductivity and strongly correlated systems, Nanoscale, surface & interface science, Inhomogeneous materials, composite materials, polymers, biomaterials, Interdisciplinary solid state physics.

Venue

The conference will take place in the conference center of Porto Palace Hotel located in the west entrance of Thessaloniki. Its historical building is established at the New Port very close to the city center (as less as 5 minutes away), on the Avenue entering the Western Part of the City from Athens, Veroia, Kavala, Europe (FIX area), and very close to the Railway Station (OSE) and the Passenger Bus Station (KTEL). The hotel offers speedy Wi-Fi, free open parking with a capacity of 300 cars and direct access to Aristotelous Square served by a shuttle bus service.

City of Thessaloniki

Thessaloniki, the Capital City of the Greek North is world known for the Ancient Greek, Roman and Byzantine monuments, the charming shopping thoroughfares, the indulging local cuisine and exciting nightlife. Thessaloniki is Greece's second major economic, industrial, commercial and political centre, and a major transportation hub for the rest of southeastern Europe; its commercial port is also of great importance for Greece and the southeastern European hinterland. The largest city in the region of Macedonia was founded in the early years of the Hellenistic period, during Alexander the Great’s ecumenical empire. It was also dominated by the Romans and later experienced the glories of the Byzantine era as the “co-reigning city” before succumbing to the ottoman onslaught.

Thessaloniki has the distinction of being a city of uninterrupted urban activity for more than 2300 years. Over the centuries its strategic position has ensured that it has been one of the most important crossroads for the region as a whole. The city is developing rapidly and aims to continue to play a leading role in the Balkans. Built near the sea (at the back of the Thermaikos Gulf), it is a modern metropolis bearing the marks of its stormy history and its cosmopolitan character, which give it a special beauty and charm. The city is renowned for its festivals, events and vibrant cultural life in general, and is considered to be Greece's cultural capital. Events such as the Thessaloniki International Trade Fair and the Thessaloniki International Film Festival are held annually, while the city also hosts the largest bi-annual meeting of the Greek diaspora. The city's main university, Aristotle University, is the largest in Greece and the Balkans. The city was always associated with the White Tower, the Kamara and the Castles, St. Dimitrios’ church and the Rotonda.

Public transport in Thessaloniki is served by buses. The bus company operating in the city is the Thessaloniki Urban Transport Organization (OASTH) and is the only public means of transport in Thessaloniki at the moment. International and regional bus links are provided by KTEL at its Macedonia InterCity Bus Terminal, located to the west of the city centre. A public bus service is available 24 hours a day from the airport to the city centre, bus number 78 or 78N. These bus services operate from the airport approximately every 30 minutes. Tickets cost €2 one way. Taxi service in Thessaloniki is plentiful and economic. As a rough guide a taxi within the city will cost approximately 5 Euros, a taxi to the airport will cost between 20 –30 Euros. A double fare is applicable between midnight and 05:00 am.

Presentations

Scientific program will include plenary, invited and contributed lectures as well as poster presentations, which will provide an up-to-date presentation of modern trends Materials Science and related subjects of general interest. Plenary and Keynote speakers should plan on a 45 minutes long talk followed by 15 minutes of discussion while invited speakers should present a 25 min long talk followed by 5 minutes of discussion. Oral Presentations: presenting authors should plan on a 12 minutes long talk followed by 3 minutes of questions. Presentations should be in Microsoft PowerPoint format (ppt or pptx file) or Adobe Acrobat Reader format (pdf file). The file should be electronically handed by the speaker to the Registration Desk at least one session before his presentation. Contributed papers describing original research work will be also presented as posters in order to promote efficient discussion on new scientific ideas and results. The presenting authors should hang their posters in the morning, before 10 am, and remove them in the evening of the corresponding day. The preferable dimensions for posters should be A0 (~80 x 120 cm : width x height). All posters are required to conform to portrait orientation. Posters should be clear and easy to read. Type size should be sufficiently large to allow people to read from 2-3 meters.

All presentations should be in English.

Best presentation award

To encourage young students’ participation three awards have been defined for high quality work based on their posters or oral presentations. These awards will be given to recognize excellence in research and presentation. The winners will be announced during the Closing ceremony on 23th September at 13^{15}.

Exhibition

Suppliers of analytical instrumentation and laboratory equipment will exhibit their latest offerings during the Conference. The exhibition area is adjacent to the lecture area and within the poster, coffee break and lunch areas in the Conference Center of Hotel Porto Palace.

In memory of

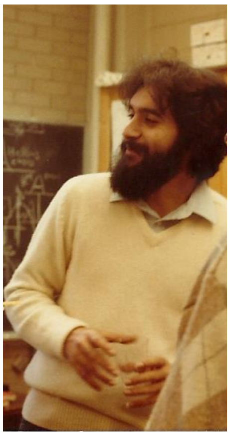

Nikos Flevaris, a physics professor in Physics Department of Aristotle University of Thessaloniki died on Saturday morning 25/04/2015 after fighting for 26 years with multiple sclerosis. Wishing him a peaceful journey, here are a few words about him:

Nikos Flevaris was born on July 11, 1953 in Achladokampos, a small mountain village in Argolis, Peloponnese, Greece After finishing high school at the nearby city of Argos, he was accepted (in 1971) at the Physics Department of Aristotle University of Thessaloniki where he graduated in 1975. His unceasing character and scientific curiosity led him to continue with MSc studies at University of Illinois at Chicago, USA, from September 1976 till 1978. Then he moved to Materials Science and Engineering Department of Northwestern University, Evanston, Illinois, USA where he completed his PhD in 1983. He was one of the pioneers of magnetic multilayers in his department and worldwide and many of the predictions drawn in his Thesis were subsequently proven right. After completion of PhD studies he decided to return to Greece and fulfill his military service. His academic career initiated by his election as lecturer in Physics Department of Aristotle University of Thessaloniki in 1985 and completed in 2013 as a full professor (1996-2013 full professor) when he had to retire due to health reasons. Since 1990 he set up a research group (http://multigr.physics.auth.gr) and with the aid of EU and regional financial support he managed to establish a magnetic multilayer laboratory still going on. His scientific interests included materials growth and characterization at the nanoscale level (structural, magnetic, electric, optic) focusing on compositionally modulated systems, thermodynamics of elastical-magnetic properties and phase transformations, electronic structure modeling via coherent-potential approximation. Last but not least, Nikos Flevaris as a supervisor was motivating his students and was providing them with intriguing problems of Physics and Materials Science enabling them to develop scientific open-minded thinking always mentioning his usual motto "*Expect the unexpected*".

ANELIS
ANALYTICAL ENVIRONMENTAL
LIFE INDUSTRIAL SCIENCES

SPECS™

Rigaku

RENISHAW
apply innovation™

The purpose of ANELIS operation is to provide integrated and best quality solutions in the field of scientific instruments and equipment, combined with full technical and scientific support.

The aim of ANELIS is to satisfy the high technology and recent research needs of public and private sector laboratories and to promote the sales of new technologies systems, with key applications in research, quality control, production process and life sciences.

SPECS leads the way in state-of-the-art technology, cutting-edge components and individually designed complex systems for surface analysis.

SPECS forms a team of scientists and engineers with more than 150 employees engaged in the design and production of instruments for nanotechnology, material science and surface science in general.

For now over 25 years, know-how, experience, intensive contact to scientists from all over the world, customer orientation and reliable quality control have been the keys to SPECS success.

Contact Info

Central Office: 14-16, Tydeos Str, 11635 Athens - Greece

Sales & Support: 14-16, Tydeos Str, 11635 Athens – Greece

Tel : +30 210 7524444 Fax : +30 210 7560849

Mob: +30 693 6794516

info@anelis.gr http://www.anelis.gr

International Technology Corporation was founded in 1977. Since 1978 we represent for Greece and Cyprus various companies like Agilent Technologies, SUSS MicroTec AG, AnnealSYS, Mantis Deposition Limited, Kemstream, Tristan Technologies, Silvaco. We provide a great variety of equipment like vacuum pumps, UHV chambers, Vacuum measuring units, Mask Aligners, Probers, Spin Coaters, Hot Plates.

Contact Info

International Technology Corporation

Filellinwn 22, 54645, Thessaloniki-Greece

Tel..: +30. 2310 856.585

Fax: +30. 2310 435.868

info@itc.com.gr

http://www.itc.com.gr

Vector Technologies LTD is a value added distributor of Test and Measurement Instruments and Operational Support systems in the Telecommunications, Educational and Public Sector market specializing in sales, marketing, technical support and after-sales service of hi-tech products.

It specializes also in the provision of troubleshooting, performance analysis and network consulting services of new technology networks.

Our strategic co-operations with leading international suppliers, together with the strong know-how of our people, provide a guarantee of the quality and the success of our solutions and services in every electronic application.

It is our company's policy to continuously seek for new ways to improve our processes and our modes of operation in order to maintain our competitive edge and achieve our targets.

Vector Technologies is offering a complete range of test & measurement products and systems and maintains partnership agreements with leading measurement systems manufacturers as follows: TEKTRONIX, KEITHLEY, AEROFLEX, AMETEK, Anite-NEMO, ACTIX, TTi, AARONIA, SPECTRACOM, AR, CAEN, AH Systems, etc

Contact Info

Vector Technologies LTD
Diogenous 40 Str. 152 34 Chalandri, Athens Greece
Tel.: +30 210 6858 008 Fax: +30 210 6858 118

info(@)vectortechnologies.gr

http://www.vectortechnologies.gr/

ASTERIADIS

N. Asteriadis S.A. operates: In the field of Equipment of Research and Development, Quality Control, Biomedicine and Biotechnology Laboratories, with complete solutions including the study and organization of laboratories. In the field of Electronic and Electrotechnical Industry, with equipment for the development of the production process and full supply of raw and other materials

Contact Info

4 Koukoufli Str., 546 22 Thessaloniki, Greece , P.O.BOX 50330, 540 13 Thessaloniki, Greece
Tel.: +30 2310 260 331, +30 2310 253 227, +30 2310 251 950, Fax: +30 2310 260 393

info@asteriadis.gr www.asteriadis.gr

ANALYTICAL INSTRUMENTS S.A.
DR C.J. VAMVACAS - SCIENTIFIC EQUIPMENT

ANALYTICAL INSTRUMENTS SA was established in 1962. It is committed to the support of the research, educational and health institutions, as well as the industrial sector in Greece. It provides complete solutions for:

- *chemical analyses and processes for research and development*
- *quality control and standardization in industrial production*

Acting as exclusive agents with long tradition and experience, we strive to protect and promote the interests of both our customers and our suppliers in the best possible way.

Contact Info

Athens: Tzavela 9, 152 31 Chalandri,
Tel. 210 67 48 973, Fax: 210 67 48 978

contact@analytical.gr www.analytical.gr

Detailed program

Monday 21 September 2015

8^{30}-9^{00} OPENING CEREMONY

(*Chair: T. Kehagias*)

9^{00}-11^{00} SESSION MO1

Nanoscale, Surface and Interface Science- 1

(*Chair: T. Karakostas, I. Zoumboulis*)

9^{00}-9^{30} **Phase-Field Modeling of irradiation induced microstructures**

Inv1 V. Pontikis (CEA/IRAMIS)

9^{30}-9^{45} **Evidence for Germanene formation on epitaxial hexagonal (h)-AlN(0001)/Ag(111)**

O01 E. Xenogiannopoulou (NCSR-Demokritos)

9^{45}-10^{00} **Molecular Beam Epitaxy of atomically thin 2D metal dichalcogenide Van der Waals semiconductor heterostructures**

O02 D. Tsoutsou (NCSR-Demokritos)

10^{00}-10^{15} **Superhard Protective Coatings Developed by Closed Field Unbalanced and Highly Ionized Magnetron Sputtering**

O03 S. Kassavetis (AUTh)

10^{15}-10^{30} **Alumina Supported Iridium Catalysts for N2O Abatement: Electron Microscopy Investigations of the Active Species**

O04 A. Delimitis (CPERI-CERTH)

10^{30}-10^{45} **Microscopical characterization of 2D-film selenide heterostructures grown on polar wurtzite AlN by molecular beam epitaxy**

O05 G. Dimitrakopulos (AUTh)

10^{45}-11^{00} **The effect of spatial confinement in the electron-phonon coupling constant studied with ultrafast electron diffraction**

O06 T. Vasileiadis (Fritz Haber Institute)

11^{00}-11^{30} ***Coffee Break***

11^{30}-13^{00} SESSION MO2

Photonics and Optoelectronics-1

(*Chair: J. Arvanitidis, M. Sigalas*)

11^{30}-12^{00} Ultra-low threshold GaN polariton lasing at room temperature

Inv2 N. Pelekanos (Univ. Crete)

12^{00}-12^{15} Engineering Giant Circular Dichroism in Silver-Coated Magnetodielectric Nanoparticles

O07 P. Varytis (Univ. Athens)

12^{15}-12^{30} Antenna-cavity mode hybridization in plasmonic nanocavities

O08 C. Tserkezis (CSIC-UPV/EHU)

12^{30}-12^{45} Microstructural evolution in high alloy content InGaN films grown by molecular beam epitaxy

O09 C. Bazioti (AUTh)

12^{45}-13^{00} Development and characterization of organic light emitting diodes on rigid and flexible substrates

O10 M. Gioti (AUTh)

13^{00}-13^{15} Modelling and design of graphene-based applications in sensing and photodetection

O11 E. Lidorikis (Univ. Ioannina)

13^{15}-13^{30} Laser Direct Writing of large area electronics on flexible substrates

O12 F. Zacharatos (NTUA)

13^{30}-14^{30} ***Lunch Break***

14^{30}-16^{30} SESSION MO3

Electronic transport, Semiconductors and Devices-1

Structural, mechanical and optical properties of condensed matter-1

(*Chair: C. Dimitriadis, E. Hristoforou*)

14^{30}-15^{00} Manipulating heat: Improved thermoelectrics and thermal/electrical clocking

Inv3 D. Niarchos (NCSR-Demokritos)

15^{00}-15^{15} Metal (Hydr)oxides for the removal of Cr(VI) from drinking water: a XAFS study

O13 F. Pinakidou (AUTh)

15^{15}-15^{30} Microstructure correlated thermoelectric properties of La1-xSrxCoO3 composites

O14 Z. Viskadourakis (Univ. Crete)

15^{30}-15^{45} High efficiency thermoelectric materials: a holistic approach from macro to nano- scale

O15 E. Stefanaki (AUTh)

15^{45}-16^{00} Efficient Si-based solar cell using aluminum induced crystallization and doping

O16 V. Gianneta (NCSR-Demokritos)

16^{00}-16^{15} InN bandgap determination in low electron concentration films

O17 A. Adikimenakis (IESL/FORTH)

16^{15}-16^{30} Porous Si thermal conductivity in the temperature range 5-350K

O18 K. Valalaki (NCSR-Demokritos)

16^{30}-17^{00} *Coffee Break*

17^{00}-19^{00} SESSION MO4

Magnetism and Superconductivity (*in memory of N.K. Flevaris*)

(*Chair: G. Litsardakis, D. Niarchos*)

17^{00}-17^{30} Tuning Magnetism in Nanostructures by Interface Design

Inv4 U. Wiedwald (Univ. Duisburg-Essen)

17^{30}-17^{45} Promising features of bimetallic magnetic nanoparticles allow tuning parameters in magnetic hyperthermia application

O19 A. Makridis (AUTh)

17^{45}-18^{00} Scaling laws analysis of magnetocaloric manganites

O20 G. Tonozlis (AUTh)

18^{00}-18^{30} Stress tensor distribution monitoring in steels using magnetic techniques

Inv5 E. Hristoforou (NTUA)

18^{30}-18^{45} Effect of pressure on the properties of iron oxypnictides: an ab initio study

O21 E. Gkogkosi (NTUA)

18^{45}-19^{00} Processing of anisotropic MnBi nanoparticles by surfactant assisted ball milling

O22 K. Kanari (AUTh)

19^{00}-20^{30} Poster Session 1

20^{30} ***Welcome Reception***

POSTER SESSION 1: Monday 21/09 19^{00}-20^{30}

(*Chair: M. Gioti, P.-I. Gouma, G. Kalosakas, J. Kioseoglou*)

Electronic transport, Semiconductors and Devices

P001 **Long-term stability and performance of photoelectrochromic devices for energy saving and power production**

G. Leftheriotis (NTUA)

P002 **Dopant-defect interactions in Ge and GeO_2: density functional theory calculations**

Y. Panayiotatos (TEI of Pireaus)

P003 **Electrical Conduction Mechanisms of ZnO sol-gel film**

T. Georgakopoulos (Univ. Patras)

P004 **Synthesis (structural characterization and complex conductivity study of $LiVO_3$**

H. Sarafidis (AUTh)

P005 **Modelling the multilevel resistive switching behaviour of forming free TiO_2-x memory devices**

P. Bousoulas (NTUA)

P006 **High performance MIS capacitors using silicon nanowires by metal-assisted chemical etching**

I. Leontis (NCSR ‘Demokritos’)

P007 **MOS pGe/GeO_2/HfO_2/Au structures: XPS and electrical analysis**

M. Mpotzakaki (Univ. Patras)

P008 **EIS studies of unconventional topological pseudo-insulator phases in incandescent lamps' tungsten wires**

I. Karagiannis (AUTh)

P009 **Effect of top barrier thickness on transistor performance in AlN/GaN/AlN HEMTs**

A. Adikimenakis (FORTH-ITE)

P010 **Galvanomagnetic Phenomena in Bi_2Te_3 and Bi_2Se_3 Thin Films**

K. Bidinakis (NTUA)

P011 **Non-Perturbative Approaches to Electron Transfer in Donor-Acceptor-Like Systems**

D. Psiachou

P012 **Gas sensing properties and electrical characterization of hot-wire porous metal oxides thin films**

G. Papadimitropoulos (NCSR 'Demokritos')

P122 **Simulation of nanoscale triple gate FinFETs, with TCAD tools – A comparative study**

A. Tsiara (AUTh)

Structural, mechanical and optical properties of condensed matter

P013 **Effective medium modelling of the interfacial roughness in multilayer coatings**

G. Leftheriotis (NTUA)

P014 **Structural and Spectroscopic Study of Two Isomeric Nitrato Complexes of Pt(II). Experimental and Computational Approach**

J. Arvanitidis (AUTh)

P015 **Coarse-grained Computer Simulations of Hexa-peri-hexabenzocoronene (HBC) and Hexa-n-dodecyl-hexa-peri-hexabenzocoronene (HBC-C12)**

G. Megariotis (NTUA)

P016 **Tuning the Localised Surface Plasmon Resonances (LSPR) of AuCu Nanocrystalline Epilayers via their Microstructure**

A. Delimitis (CERTH)

P017 **A Spectroscopical Study of the CiOi(SiI) Absorption Bands Upon Isothermal Annealing in Irradiated Silicon at Liquid Hellium Temperatures (L.H.T.)**

T. Angeletos (Univ. Athens)

P018 **Polarized Raman scattering and birefrigence studies of the orientational order in the nematic liquid crystal 4-n-pentyloxyphenyl 4-n-octyloxybenoate and its nanocomposite with semiconducting CdSe-ZnS quantum dots**

C. Kyrou (NTUA)

P019 **Simulation of the EXAFS and Raman spectra of InxGa1-xN enabling the equation of motion routine of FEFF8**

M. Katsikini (AUTh)

P020 **Structural and electronic properties of GaN/AlN and InN/GaN core /shell NWs**

Ph. Komninou (AUTh)

P021 **Small Angle Neutron Scattering investigation of thermal ageing effects in FeCr alloys**

Y. Katsandredakis (NCSR ‘Demokritos’)

P022 **Effect of welding process Parameters and filler metal types on microstructure and mechanical properties of dissimilar stainless steel welds**

N. Bensaid (NDT)

P023 **Effect of heat input and grain refining elements on microstructure and mechanical properties of Ferritic Stainless Steel welds parameters of X70 welds**

N. Bensaid (NDT)

P024 **NDT and Optimization of welding process**

M.F. Benlamnouar (NDT)

P025 **Characterization of TiO_2 nanoparticles by X-ray Absorption Fine Structure Spectroscopy**

S. Magkos (AUTh)

P026 **Filler metal composition and mechanical behavior of TIG disimilar joints**

M.F. Benlamnouar (NDT)

P027 **Molecular dynamics investigation of GaN nanocluster formation in SiO_2**

J. Karakostas (AUTh)

Magnetism, superconductivity and strongly correlated systems

P028 **Soft magnetic multilayered thin films for HF applications**

C. Serletis (NCSR ‘Demokritos’)

P029 **Finite Element Micromagnetic Simulation of μMag standard problems**

N. Ntallis (AUTh)

P030 **Micromagnetic modelling of superparamagnetic particles**

N. Ntallis (AUTh)

P031 **An alternate treatment of surface effects in micromagnetism. Theory and computations**

N. Ntallis (AUTh)

P032 **Optimization of magnetic hyperthermia via synthesis parameters of magnetic nanoparticles**

O. Patsia (AUTh)

P033 **The influence of nanoparticle arrays on magnetic hyperthermia**

E. Myrovali (AUTh)

P034 **Enhanced magnetic efficiency by nanoscale mixing and matching in ferrite-based nanoparticles**

S. Liébana-Vinas (Univ. Duisburg-Essen)

P035 **Reliable measurements and error-free data handling of magnetic particle hyperthermia parameters**

A. Terzopoulou (AUTh)

P036 **Orbital and spin order transitions in LaMn1-xCrxO3+δ (δ≈0) perovskite compounds**

K. Georgalas (Univ. Athens)

P037 **Thermomagnetic analysis and magnetic properties of RFe$_{6-x}$Si$_x$ (R= Y, Sm, Gd, Dy, Ho, Lu) alloys**

M. Gjoka (NCSR ‘Demokritos’)

P038 **Magnetic field modes for manipulation of magnetic nanoparticles**

N. Maniotis (AUTh)

P039 **Ferrite optimization for wireless powering**

C.A. Stergiou (CERTH)

P040 **High anisotropy induction into multilayer Fe-Co thin films, towards Rare Earth free permanent magnets applications**

G. Giannopoulos (NCSR ‘Demokritos’)

Inhomogeneous materials, composite materials, polymers, biomaterials

P041 **Nanomechanics of Magnetron Sputtered Ti-Nb Films**

D. Photiou (Cyprus Univ. of Technology)

P042 **Influence of structure and dynamics on the ionic conductivity of new solid polymer electrolytes**

A. Pipertzis (Univ. Ioannina)

P043 **Designing Molecules for Orgnanic Photovoltaics: The case of Hexasubstituted Benzenes carrying Ultrastrong Dipole Moments**

V. Margaritis (Univ. Ioannina)

P044 **Polymethacrylates with Polyhedral Oligomeric Silsesquioxane Moieties (POSS): The Influence of Spacer Length on Packing, Thermodynamics and dynamics**

G. Papamokos (Univ. Ioannina)

P045 Capillary Rise in Cylindrical Nanoconfinement of cis-1,4 Polyisoprene and Poly(methyl phenyl siloxane)

S. Alexandris (Univ. Ioannina)

P046 Dc conductivity measurements on PVDF composite samples of low graphene content

I. Stavrakas (TEI Athens)

P047 Transmission Electron Microscopy Studies of CoSi/Si3N4 Nanocomposite Materials

A. Delimitis (CERTH)

P048 Dielectric study of a lysozyme solution with molecular dynamics simulations: Non thermal effects of low alternating electric fields

S. Floros (AUTh)

P049 Microwave attenuation and dielectric properties of hybrid nanocomposites co-filled with organomodified graphene oxide

C.A. Stergiou (CERTH)

P050 Interactions of polyaspartic-b-poly(ethylene glycol) copolymer with magnetite nanoparticles

E. Rousalis (Univ. Patras)

P051 Structure-properties relationship of Barium Ferrite/Barium Titanate/Epoxy Resin Hybrid Nanocomposites

A. Kanapitsas (TEI Sterea Hellas)

P052 Conductivity analysis on epoxy resin/carbon nanotubes composites

G. Tomara (Univ. Patras)

P053 Low content ZnO/epoxy resin and BaTiO3/epoxy resin nanocomposites: Dielectric response

G. Tomara (Univ. Patras)

P054 Dielectric Properties of Ceramic Particles/Epoxy Resin Nanodielectrics

G.C. Psarras (Univ. Patras)

P055 Inorganic Filler-Polymer Matrix Nanocomposites as Bulk Energy Storing Devices

G.C. Psarras (Univ. Patras)

P056 Effect of different graphene nanoparticles on the structural, thermal and mechanical properties of high density polyethylene

E. Tarani (AUTh)

P057 Studying the Water Effect upon α-Relaxation in Thermoplastic Starch Biocomposites by means of Dielectric Spectroscopy

S. X. Drakopoulos (Univ. Patras)

P058 **Dielectric Characterization of Epoxy Resin - Strontium Ferrite Nanocomposites**

A. Sanida (Univ. Patras)

P059 **Thermomechanical characterization of hybrid epoxy composites with Carbon-based nanofillers**

A. Stimoniaris (Univ. Ioannina)

P060 **Selective removal of silver ions from synthetic mining effluents using Molecularly Imprinted Polymers (MIPs)**

G.Z. Kyzas (AUTh)

Tuesday 22 September 2015

9^{00}-11^{00} SESSION TU1

Structural, mechanical and optical properties of condensed matter-2

(*Chair: E. Lidorikis, N. Frangis*)

9^{00}-9^{30}	**Broadband Terahertz Generation from Metamaterials and Optical Metamaterials Resonances with High Quality Factor**
Inv6	C. Soukoulis (Univ. Crete)
9^{30}-9^{45}	**High-Pressure Phase Transition in $Y_3Fe_5O_{12}$**
O23	I. Zoumpoulis (NTUA)
9^{45}-10^{00}	**Amorphous Carbon Films For Protective and Solid Lubricant Applications**
O24	M. Constantinou (Cyprus Univ. of Technology)
10^{00}-10^{15}	**Metal vacancies in strained AlN/GaN interfaces: a first principles investigation**
O25	J. Kioseoglou (AUTh)
10^{15}-10^{30}	**Induced Raman scattering in multiferroic $EuTiO_3$**
O26	P. Pappas (NTUA)
10^{30}-10^{45}	**The effect of periodically arranged Stone – Walles defects in graphene on its mechanical properties: an ab-initio study**
O27	Z.G. Fthenakis (IESL/FORTH)
10^{45}-11^{00}	**Indentation Resistance Enhancement of Auxetic Materials: A Numerical Investigation**
O28	D. Photiou (Cyprus Univ. of Technology)

11^{00}-11^{30} *Coffee Break*

11^{30}-13^{00} SESSION TU2

Polymers, Biomaterials -1

(*Chair: E. Paloura, D. Vlachos*)

11^{30}-12^{30} Polymorphic Metal-Oxide based Sensors for the Diagnostic Breathalyzer

Key1 P.-I. Gouma (State Univ. of New York)

12^{30}-12^{45} Magnetic manipulation in a microfluidic system of hybrid composites made of MWCNTs functionalized with Fe_3O_4 nanoparticles for drug delivery applications

O29 J. Theodorakos (NTUA)

12^{45}-13^{00} Numerical simulations of drug release profiles

O30 G. Kalosakas (Univ. Patras)

13^{00}-13^{15} THz oscillations in small B-DNA segments

O31 K. Lambropoulos (Univ. Athens)

13^{15}-13^{30} Phase formation and stability in binary mixtures of cyanobiphenyl dimers

O32 E. Ramou (Univ. Patras)

13^{30}-14^{30} *Lunch Break*

14^{30}-16^{30} SESSION TU3

Inhomogeneous materials, Composite materials-1

(*Chair: Ph. Komninou, Ch.E. Lekka*)

14^{30}-15^{00} Carbon based composite structures and advanced tools for mechanical behaviour assessment

Inv7 C. Charitidis (NTUA)

15^{00}-15^{15} Molecular Simulation of Imidazolium-based Tricyanomethanide Ionic Liquids

O33 N. Vergadou (NSCR-Demokritos)

15^{15}-15^{30} Molecular dynamics simulation of highly confined ionic liquids

O34 G. Kritikos (NSCR-Demokritos)

15^{30}-15^{45} CoO octahedra with a Ferromagnetic Interface between two Antiferromagnets

O35 M. Spasova (Univ. Duisburg-Essen)

15^{45}-16^{00} The impact of grain size/interface at Boron Carbide/epoxy composites: dielectric properties and molecular dynamics

O36 E.C. Senis (Univ. Patras)

16^{00}-16^{15} Structural properties of thermally treated chromium containing waste

O37 S. Varitis (AUTh)

16^{15}-16^{30} Mesoscopic Simulations of the Viscoelastic Properties of Polymer Networks

O38 G. Megariotis (NTUA)

16^{30}-17^{00} *Coffee Break*

17^{00}-18^{30} SESSION TU4

Photonics and Optoelectronics-2

(*Chair: D. Christofilos, N. Pelekanos*)

17^{00}-17^{30} Photonic materials and devices for sensors and solar cells

Inv8 M. Sigalas (Univ. Patras)

17^{30}-17^{45} Enhancement of conversion efficiency of solar cells by down-conversion

O39 S. Gardelis (NCSR-Demokritos)

17^{45}-18^{00} Enhanced Light Emission in Extraordinary Optical Transmission Structures

O40 C.P. Mavidis (IESL/FORTH)

18^{00}-18^{15} Energy level alignment of PCBM interfaces with low work function substrates

O41 G. Skoulatakis (Univ. Patras)

18^{15}-18^{30} Frequency splitter based on the manipulation of surface modes in dielectric photonic crystals structures

O42 A.C. Tasolamprou (IESL/FORTH)

18^{30}-20^{00} Poster Session 2

PLENARY TALK

(*Chair: T. Kehagias*)

20^{00}-21^{00} Nitride Semiconductors: Physics and Applications

Ple1 T. Moustakas (Boston Univ.)

21^{00} *Conference Dinner*

POSTER SESSION 2: Tuesday 22/09 18^{30}-20^{00}

(*Chair: M. Gioti, P.-I. Gouma, G. Kalosakas, J. Kioseoglou*)

Inhomogeneous materials, composite materials, polymers, biomaterials

P061 **Development and Characterization of Epoxy Resin- Zinc Ferrite Nanocomposites**
S. Stavropoulos (Univ. Patras)

P062 **Thermal and Dielectric Properties of Graphene/poly Cyclic Butylene Terephtalate (pCBT) Nanocomposites**
S. Stavropoulos (Univ. Patras)

P063 **Dielectric and electrical properties of Fe_3O_4/CNT/PVDF Nanocomposites**
A. Speliotis (NCSR 'Demokritos')

P064 **Stabilization of Cr-rich tannery waste in fly-ash based cementitious materials**
Th. Karakostas (AUTh)

P065 **High pressure Raman study of L-phenylalanine crystals**
A. Zerfiridou (AUTh)

P066 **Composition and Characterization of Silicate Glasses Containing ZnO and CuO prepared through the Sol-Gel Process**
S.P. Petsi (AUTh)

P067 **On the consolidation of Bi2Te3 pellets: Taguchi optimization analysis**
K. Boutzi (AUTh)

P068 **Comparative study of natural fibre reinforced composite materials**
D. Patsiaoura (AUTh)

P069 **Synthesis and Characterization of Silicate Glasses Containing SrO through the Sol-Gel Process**
G. Theodorou (AUTh)

P070 **Strontium doped Mg-based ceramic: Characterization and bioactivity evaluation**
G. Theodorou (AUTh)

P071 **Effect of synthesis through foam replica technique method on the porosity and mechanical strength of Cu containing scaffolds**
G. Theodorou (AUTh)

P072 **Development and Characterization of Epoxy Resin- Barium Tungstate Composites**

S. Termine (Univ. Patras)

P073 **Synthesis, characterization and applications of copper based nanoparticles**

C. Gkanatsiou (AUTh)

P074 **Corrosion behaviour of dissimilar metal/metal joints including reinforcing additives**

C. Charitidis (NTUA)

P075 **Study of keratin tissues by means of Small Angle X – Ray Scattering (SAXS)**

C. Kamaraki (AUTh)

Photonics and Optoelectronics

P076 **Linear and Nonlinear Optical Properties of CdTe/ZnO Core/Shell Quantum Dots**

E. Paspalakis (Univ. Patras)

P077 **Optimization of out of plane optical coupling between optical/optoelectronic components and optical waveguides**

K. Vyrsokinos (AUTh)

P078 **Natural Dose Evaluation using Thermoluminescence and component resolved Optically Stimullated Luminescence analysis**

M. Karampiperi (AUTh)

P079 **Polysterene on 101 nm Nitride on Si**

A. Sotiropoulos (NCSR ‘Demokritos’)

P080 **Influence of nonolcality on fluorescence from a dipolar emitter coupled to a metallic nanoshell**

C. Tserkezis (CSIC/UPV-EHU)

P081 **Growth and optical characterization of GaAs-InGaAs core-shell piezoelectric nanowires on silicon substrates**

K. Moratis (Univ. Crete)

P082 **The Role of Intentional and Unintentional Nitridation of Si (111) in the Growth of GaN Nanowire by Plasma Assisted Molecular Beam Epitaxy**

S. Eftychis (Univ. Crete)

P083 **Optical Point spread function as a method for testing dynamic operation of CCDs**

V.E. Gavriil (NHRF)

P084 **Catalyst-free growth of GaN NWs on Si (111) and r- plane sapphire**

Ph. Komninou (AUTh)

P085 **Cobalt Ferrite Magnetic Nanoparticles as Anti-Inflammatory Drug Carriers**

V. Georgiadou (AUTh)

Nanoscale, Surface and Interface Science

P086 **Embedded Atom Method potentials for the simulation of Pt-Ni nanostructures fitted upon DFT calculations**

E. Symianakis (Imperial College London)

P087 **Phase investigation of PbTe +25%$PbSnS_2$ thermoelectric composite by electron crystallography**

C. Ioannidou (AUTh)

P088 **Monte Carlo study of the exchange bias effect in ferromagnetic/antiferromagnetic hybrid nanoparticles**

D. Kehrakos (ASPETE)

P089 **DNA hybridization on ultrasmall gold nanoparticles**

I. Michelakaki (NTUA)

P090 **Fabrication and characterization of free-standing porous silicon and alumina membranes**

M. Dimitropoulos (Univ. Patras)

P091 **Raman spectroscopy indications of the Verwey transition in epitaxial Fe_3O_4(111) films on Pt(111) and Ru(0001)**

N. Michalak (Polish Academy of Sciences)

P092 **Room temperature/ambient conditions study of the magnetic properties of few-nanometers-thick epitaxial Fe_3O_4(111) films on Pt(111) and Ru(0001)**

Z. Milosz (Poznan Univ. of Technology)

P093 **Plasmon sensors based on metallic bilayers**

P. Athanasiadis (Univ. Athens)

P094 **Nanoparticle Production and Surface Micromachining Through Femtosecond Laser Ablation**

G. Constantinides (Cyprus Univ. of Technology

P095 **Quantitative analysis of interfaces in multilayer structures grown on SiC**

A. Gκanatsiou (AUTh)

P096 **Structural models of defects in an Al-doped Si emitter of a p-n junction solar cell**

I. Katrantzis (AUTh)

P097 **Formation of Zn-Mg and Zn-Al alloyed coatings by hot dip galvanizing**

V. Syropoulos (AUTh)

P098 **Ab initio calculations of ionization and excitation energies of biologically important heterocyclic planar molecules**
M. Tassi (Univ. Athens)

P099 **L-glutamine on Cu-Fe surfaces by Density Functional Theory Calculations**
M.G. Bouri (Univ. Ioannina)

P100 **Density Functional Theory Calculations of H2O Adsorption on Cu(111)**
M. Zegkos (Univ. Ioannina)

P101 **Interaction of CVD graphene with femtosecond laser**
N. Chourdakis (FORTH-ITE)

P102 **The effect of confinement and coupling with the substrate in the electron-phonon coupling constant of magic Gold nanoclusters studied with ultrafast electron diffraction**
T. Vasileiadis (Max Planck Society)

P103 **Morphology, Structure, and Strain properties of Quantum Nanostructures**
N. Florini (AUTh)

P104 **Hydrogenated Zinc and Titanium Oxide Cathode Interfacial Layers For Efficient and Stable Inverted Organic Solar Cells**
E. Polydorou (NCSR ‘Demokritos’)

P105 **Tailoring Molybdenum Oxide Electronic Properties and Stoichiometry For Application as an Anode Interfacial Layer in Efficient and Stable Organic Solar Cells**
A. Soultati (NCSR ‘Demokritos’)

P106 **Stress-Strain Relation in (211)B-oriented InAs/GaAs Quantum Dot Superlattice**
T. Kehagias (AUTh)

P107 **Structural reconstructions, band gaps and bowing parameters of the ternary nitride alloys**
J. Kioseoglou (AUTh)

P108 **Strain and elastic constants in GaN and InN: a first principles study**
Ph. Komninou (AUTh)

P109 **Improved Hg^0 Removal from Flue Gases by Mn(IV) Feroxyhyte**
E. Kokkinos (AUTh)

Interdisciplinary Solid State Physics

P110 **Vitrification as a tool for sustainable solid waste management**
Th. Karakostas (AUTh)

P111 **Color fastness of green pigments in egg tempera technique under accelerated aging and weathering tests**
E. Lykartsi (AUTh)

P112 **Saint Demetrios Monastery of Stomion: Comparative analysis of plasters via TG-DSC and FTIR**
L. Malletzidou (AUTh

P113 **Comparative study of contemporary restoration mortars**
D. Papazoglou (AUTh)

P114 **Authenticity study of two German expressionism paintings using spectroscopic techniques**
K. Karatzia (AUTh)

P115 **Investigation of stiffness in micromagnetic simulations of spin valve sensors with OOMMF**
S. Mitropoulos (TEI Eastern Macedonia)

P116 **Anomalous fading in Durango apatite: comparison between grain sizes in the micro and the nano scale**
M. Niora (AUTh)

P117 **Research on anomalous fading of feldspars billion years old using thermoluminescence signal**
Z. Papari (AUTh)

P118 **Characterization of fossil remains using XRF, XPS and XAFS spectroscopies**
M. Katsikini (AUTh)

P119 **Study of archaeological and contemporary ceramic artifacts with physical-chemical techniques**
T. Kazakou (AUTh)

P120 **Study and characterization of an 18th century portable icon**
N. Kyriakou (AUTh)

P121 **Micro and conventional XAFS study of incinerated Cr-rich tannery wastes**
F. Pinakidou (AUTh)

Wednesday 23 September 2015

9^{30}-11^{00} SESSION WE1

Nanoscale, Surface and Interface Science- 2

(*Chair: S. Kennou, M. Katsikini*)

9^{30}-9^{45}	**Electrochemical Characterization and Quantified Surface Termination Obtained by LEIS and XPS of Orthorhombic and Rhombohedral $LaMnO_3$ Powders**
O43	E. Symianakis (Imperial College)
9^{45}-10^{00}	**Raman study of graphene irradiated with 350 eV N^+ ions**
O44	K. Filintoglou (AUTh)
10^{00}-10^{15}	**Multiscale approach to field-dependent energy barrier calculation of exchange biased nanoparticles**
O45	D. Kehrakos (ASPETE)
10^{15}-10^{30}	**Theoretical study on hydrogen evolution edge-site activity of MoS_2 and hybrid MoS_2/Graphene structures**
O46	A.E. Maniadaki (Univ. Crete)
10^{30}-10^{45}	**Adsorption of water on a cesium covered $SrTiO_3$ (100) surface**
O47	D. Vlachos (Univ. Ioannina)
10^{45}-11^{00}	**Effects of Macromolecular Architecture and Size on Polymer/Graphene Nanocomposites: Insight from Molecular Dynamics Simulations**
O48	K. Karatasos (AUTh)

11^{00}-11^{30} *Coffee Break*

11^{30}-13^{00} SESSION WE2

Electronic transport, Semiconductors and Devices-2

(*Chair: S. Gardelis, D. Tassis*)

11^{30}-12^{30} Low-Dimensional Charge-Transport Phenomena in Solution-Processed Metal Oxide Materials and Devices

Key2 T. D. Anthopoulos (Imperial College)

12^{30}-12^{45} Tungsten and tungsten-based alloy thin films as copper substitutes for microelectronics interconnects

O49 A. Kaidatzis (NCSR-Demokritos)

12^{45}-13^{00} Nanocrystalline TiO_2 Films Synthesized through a Simple Procedure for Dye-sensitized Solar Cells' Photoanodes

O50 D. Sygkridou (TEI of Western Greece)

13^{00}-13^{15} TiO_2 transport layer made with Pluronic P123 as template for efficient perovskite solar cells

O51 D. Karageorgopoulos (Univ. Patras)

13^{15}-14^{00} *Best Poster Awards - Closing Ceremony*

(*Chair: T. Kehagias*)

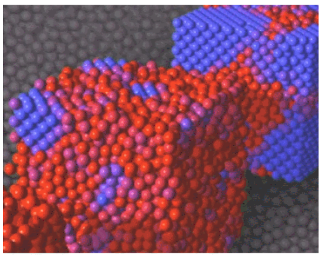

XXXI Panhellenic Conference on
SOLID STATE PHYSICS &
MATERIALS SCIENCE
Thessaloniki, 20-23 September 2015

Abstracts

Organized by

Physics Department, AUTh

Location

Porto Palace Hotel, Thessaloniki

SESSION MO1

NANOSCALE, SURFACE AND INTERFACE SCIENCE

Monday, 21 September 2015, 9^{00}-11^{00}

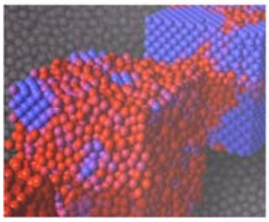

XXXI Panhellenic Conference on
SOLID STATE PHYSICS & MATERIALS SCIENCE
Thessaloniki, 20-23 September 2015

Phase-Field Modeling of irradiation induced microstructures

L. Luneville[1], G. Demange[2], V. Pontikis[2,3] and D. Simeone[2]

[1]DEN/DANS/DM2S/SERMA/LLPR/LRC-CARMEN, CEA Saclay, 91191 Gif-sur-Yvette, France
[2]DEN/DANS/DMN/SRMA/LA2M/LRC-CARMEN, CEA Saclay, 91191 Gif-sur-Yvette, France
[3]DSM/IRAMIS/LSI, CEA Saclay, 91191 Gif-sur-Yvette, France

E-mail: v.pontikis@cea.fr

MO1

INV1

In this work irradiation-induced phase separation and the resulting microstructures are obtained via the combination of Phase Field (PF) modeling with atomistic Monte Carlo simulations in the pseudo-grand canonical ensemble (GCMC). The last allow for calculating the equilibrium phase diagram of the silver-copper alloy, chosen as a model of binary systems with large miscibility gap and, for extracting the parameters of the excess free-energy PF functional. Relying on this methodology, the equilibrium phase diagram of the alloy is predicted in excellent agreement with the experiment (Fig. 1) whereas, under irradiation, the predicted microstructures are functions of the irradiation parameters. Different irradiation conditions result in various microstructures, which are conveniently represented as an out of equilibrium "phase diagram" in view to facilitate the comparison between modeling and experiment (Fig. 1).

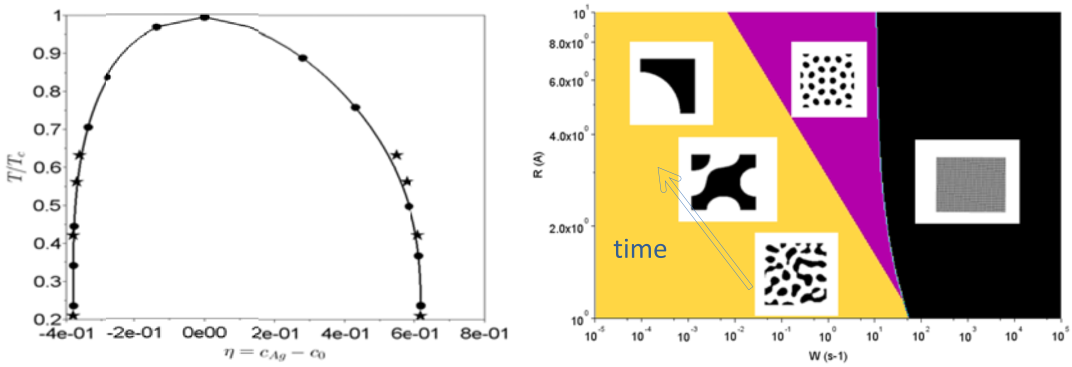

Figure 1: (a) Solubility limits, $\eta = c_{Ag} - c_{Cu}$, versus the temperature reduced by the value at the critical point, T_c=1423 K: experimental (stars), GCMC (full dots) and PF (full line). (b) Out of equilibrium phase diagram of a 50 at% AgCu alloy under irradiation at T=800 K: R is the atomic mean square displacement in cascades and W is proportional to the irradiation flux.

References

[1] L. Luneville, G. Demange, V. Pontikis and D. Simeone, Mater. Res. Soc. Symp. Proc. 1743 (2015), DOI: 10.1557/opl.2015.360

Evidence for Germanene formation on epitaxial hexagonal (h)-AlN(0001)/Ag(111)

E. Xenogiannopoulou[1], **P. Tsipas**[1], **J. Marquez Velasco**[1, 3], **D. Tsoutsou**[1], **F. d'Acapito**[2], **S. Torrengo**[2] **and A. Dimoulas**[1]

[1]Institute of Nanoscience and Nanotechnology, National Center for Scientific Research
'DEMOKRITOS', GR-15310, Athens, Greece.
[2]CNR-IOM-OGG c/o European Synchrotron Radiation Facility,
71 Avenue des Martyrs, F-38043 Grenoble, France.
[3]National Technical University of Athens, Department of Physics, 15784 Athens, Greece.

E-mail: e.xenogiannopoulou@inn.demokritos.gr

Early theoretical studies [1] predicted that free standing silicene and germanene, the silicon and germanium 2D analogues to graphene, can be stable in the low buckled (LB) configuration, preserving the Dirac cone at K-points of Brillouin zone (BZ). Just like silicene [2], the growth of germanene on metals is challenging. First studies showed that Ge, at 1/3 ML coverage, interacts strongly with Ag(111) forming an ordered Ag_2Ge surface alloy [3]. Since then, there is a lot of progress showing evidence that germanene can be grown on metal (e.g. Al(111) [4]) substrates. Nevertheless, the growth of metal-supported silicene and germanene is not suitable for field effect devices and for this reason germanene on non-metallic substrates [2] is preferred. Theoretically, it has been shown that germanene can stably attach through weak van der Waals interactions on another 2D graphite-like material, such as hexagonal (h-) boron nitride (BN) [5]. Alternatively, 2D h- AlN can be used, which is a metastable phase favoured at small thickness compared to w-AlN phase which is stable at large thickness or bulk [6].

In this work we first review our results [7] which show that 2D ultrathin hexagonal AlN layers can be prepared epitaxially on Ag(111) substrates by plasma assisted MBE. Then, we present our newest data on the growth of Ge layers by molecular beam epitaxy (MBE) on h-AlN nanosheets on Ag(111) [8]. The RHEED spectra (Fig.1) present a (4×4) Ge superstructure with respect to (1×1) h-AlN, or a (3×3) superstructure with respect to (1×1) germanene. Additionally, the structural analysis of Ge/h-AlN/Ag(111) layers have been investigated by X-ray Absorption Spectroscopy (XAS) at the Ge-K edge and compared with model samples of Ge directly deposited on Ag(111) (Fig. 2). The Ge-Ge bond in the Ge/ h-AlN is found to be shorter than that of bulk Ge and Ge/Ag sample (Fig. 2), with a length of 2.38 Å (Tab.1). Such a reduced value is compatible only with an sp^2 hybridization of Ge valence orbitals and it agrees (Fig. 3) with DFT calculations for free-standing germanene [1] as well as with our first principles calculations [8] in the Ge/h-AlN/Ag(111) system (Fig. 3) with a buckling of 0.7 A. We then present evidence, by a direct structural method, that symmetrically buckled germanene, similar to free-standing Germanene, can be grown epitaxially on h-AlN/Ag(111) substrates.

Acknowledgements: NCSR Demokritos acknowledges financial support from the 2D-NANOLATTICES Grant No.270749 of the EU FP7-FET program. The X-ray Absorption Spectroscopy experiment was supported by ESRF under the code MA-1983. GILDA is a project jointly financed by CNR and INFN.

References

[1] S. Cahangirov, M. Topsakal, E. Akturk, H. Sahin and S. Ciraci, Phys. Rev. Lett. 102 (2009) 236804.

[2] For a recent review see e.g. A. Dimoulas, Microelectron. Eng. 131 (2015) 68–78.

[3] E. Golias, E. Xenogiannopoulou. D. Tsoutsou, P. Tsipas, S. A. Giamini and A. Dimoulas, Phys. Rev. B 88 (2013) 075403.

[4] M. Derivaz, D. Dentel , R. Stephan , M.-C. Hanf, A. Mehdaoui, P. Sonnet and C. Pirri, Nano Lett. 15 (2015) 2510-2516.

[5] L. Li and M. Zhao, Phys. Chem. Chem. Phys. 15 (2013) 16853.

[6] C.L. Freeman, F. Claeyssens and N.L. Allan, Phys. Rev. Lett. 96 (2006) 066102.

[7] P. Tsipas, S. Kassavetis, D. Tsoutsou, E. Xenogiannopoulou, E. Golias, S. A. Giamini, C. Grazianetti, D. Chiappe, A. Molle, M. Fanciulli and A. Dimoulas, Appl. Phys. Lett. 103 (2013) 251605.

[8] F. d'Acapito, S. Torrengo, E. Xenogiannopoulou, P. Tsipas, J. Marquez Velasco, D. Tsoutsou and A. Dimoulas, submitted (2015), *under review.*

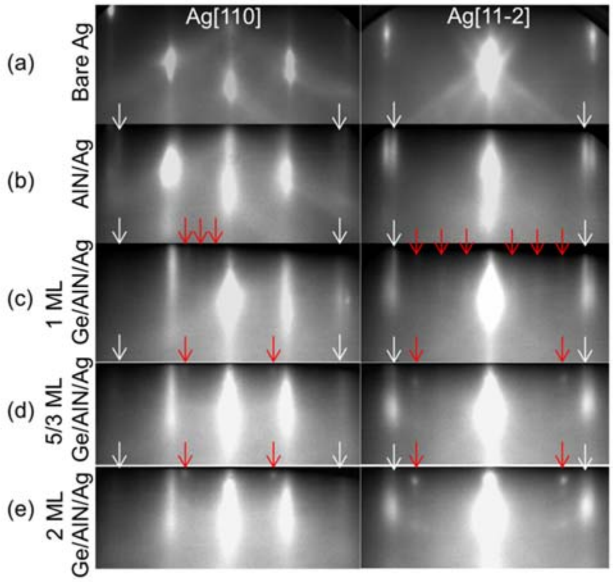

Figure 1: RHEED patterns of: (a) Ag(111), (b) epitaxial AlN buffer layer on Ag(111) and (c-e) 1ML, 5/3 ML and 2 ML Ge deposited on epitaxial AlN/Ag(111) template, along [110] (left) and [11-2] (right) azimuths of silver respectively. The white and red arrows indicate the AlN and Ge diffraction streaks, respectively. In (b) the (1x1) h-AlN reconstruction is shown while in (c) the (4x4) Ge reconstruction with respect to (1x1) hexagonal-AlN is observed. In (d-e) the (4x4) reconstruction faints out and the streaks at distance of 3/4 of h-AlN streaks are observed.

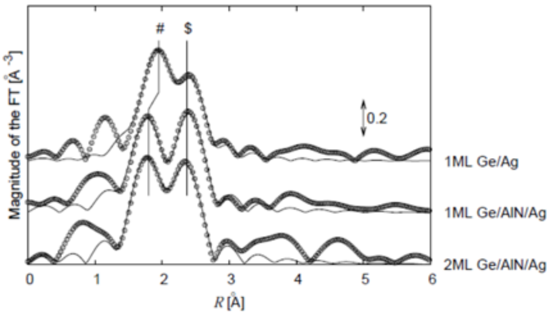

Figure 2: FFT of the EXAFS spectra experimental data: open dots, best fit curves: lines. # marks the position of the Ge-Ge peak whereas $ marks the position of the Ge-Ag peak.

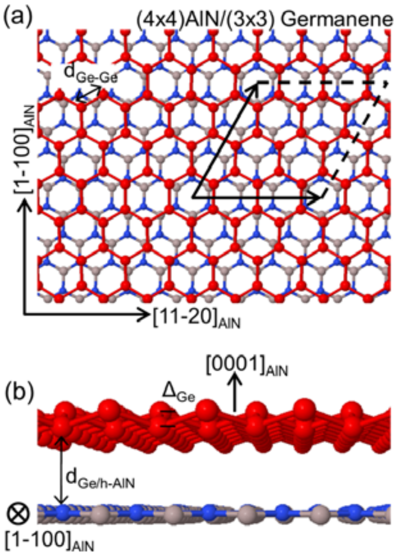

Figure 3: Atomic configuration of the DFT optimized Germanene on h-AlN structure. Red, green, blue and grey spheres represent the Ge, Al, N and Ag atoms, respectively. (a) In top view the (4x4) Germanene unit cell with respect to (1x1) h-AlN unit cell is depicted with Germanene lattice constant of a ≈ 3.928 Å. Also the Ge-Ge interatomic distance $d_{Ge\text{-}Ge} \approx 2.372$ Å is indicated (b) lateral view indicating the Germanene layer buckling $\Delta_{Ge} \approx 0.705$ Å and the Germanene/h-AlN planes distance $d_{Ge/h\text{-}AlN} \approx 3.83$ Å.

Table 1: Quantitative results of the EXAFS data analysis. R is the atom-atom distance and N is the amplitude.

Sample	**Ge-Ge**		**Ge-Ag**	
	N	R(Å)	N	R(Å)
Ge bulk	4.0	2.45		
1ML Ge/Ag	2.6(9)	2.44(2)	1.8	2.65(2)
1ML Ge/AlN/Ag	1.6(2)	2.38(2)	2.6	2.62(2)
1ML Ge/AlN/Ag	1.3(2)	2.39(2)	3.0	2.63(2)

Molecular Beam Epitaxy of atomically thin 2D metal dichalcogenide Van der Waals semiconductor heterostructures

MO1

O02

K. E. Aretouli[1,2], P. Tsipas[1], E. Xenogiannopoulou[1], D. Tsoutsou[1], J. Marquez-Velasco[1,3], S.A. Giamini[1,2], N. Kelaidis[1], C. Bazioti[4], G.P. Dimitrakopulos[4], Ph. Komninou[4], G. Kordas[1] and A. Dimoulas[1]

[1]Institute of Nanoscience and Nanotechnology, National Center for Scientific Research
"DEMOKRITOS", 15310, Athens, Greece
[2]University of Athens, Department of Physics, Section of Solid State Physics, 15684 Athens, Greece
[3]National Technical University of Athens, Department of Physics, 15780 Athens, Greece
[4]Physics Department, Aristotle University of Thessaloniki, 54124 Thessaloniki, Greece

E-mail: k.aretouli@inn.demokritos.gr

The advent of stable 2D atomically thin transition metal dichalcogenide semiconductors offers exciting possibilities for nanoelectronic device scaling and extends our options to a number of low power versatile applications. Group IVB ((Zr,Hf)X$_2$) can be combined with group VIB [(Mo,W)X$_2$] materials to form van der Waals [1] heterostructures with sharp, defect–free heterointerfaces and type-II or III band alignments [2] showing prospect for applications in novel vertical staggered or broken gap 2D Tunneling Field Effect Transistors (TFETs).

In this work, we show that using molecular beam epitaxy (MBE) it is possible to grow good crystalline quality MoSe$_2$/HfSe$_2$ (ZrSe$_2$) heterostructures on large area (up to 2 inch) w-AlN(0001)/Si(111) technologically important substrates. All materials require a two step growth: deposition at the optimum temperature followed by in-situ UHV annealing at higher temperature. Epitaxy can start either with MoSe$_2$ [3] in direct contact with AlN substrate followed by HfSe$_2$ [4, 5] or ZrSe$_2$ [6] or with the reverse order. RHEED patterns and HRTEM (Fig. 1a) indicate that the 2D heterostructures, despite the relatively large lattice mismatch, are epitaxially grown on AlN such that the [11-20] in-plane crystallographic direction of all materials are aligned, indicative of v.d.W epitaxy. The surfaces of the epilayers are investigated *in-situ* by room temperature UHV-STM revealing a rms roughness of 0.3 nm over an area 1x1μm^2. A high resolution STM image of 1ML HfSe$_2$ (Fig.1b) indicates a Se adlayer which is correlated with a reduction of HfSe$_2$ work function estimated from the low energy cut-off in our UPS spectra. The Raman spectra for layered HfSe$_2$ and ZrSe$_2$ (Fig. 2a) is in agreement with reference crystals exfoliated from bulk. Mapping over large areas on the wafers show little or no variation of the Raman peaks with respect to Raman shift, indicating uniform and continuous films. The electronic valence band structures of a few layers of HfSe$_2$ (Fig. 2b) and ZrSe$_2$ are imaged by in-situ HeI-ARPES and found to be consistent with our DFT calculations. Using in-situ XPS, the films are found to be very close to the ideal stoichiometry, with no signs of intermixing neither with the AlN substrate nor with MoSe$_2$. Using Kraut's method, the valence band offsets are calculated to be VBO~0.58eV and VBO~0.13eV for MoSe$_2$/ZrSe$_2$ and HfSe$_2$/MoSe$_2$ (Fig.2c) respectively, indicating a type II band alignment which shows prospect for the fabrication of tunneling FETs.

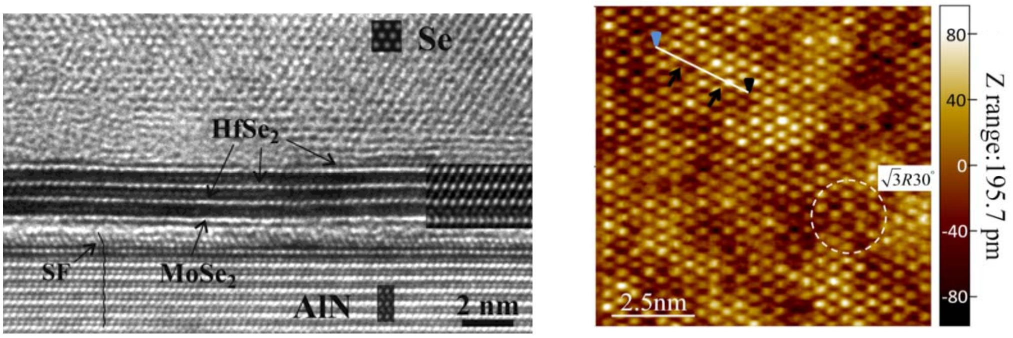

Figure1: (a) High magnification TEM micrograph of HfSe/MoSe/AlN structure. (b) Room temperature high resolution UHV-STM image of 1ML $HfSe_2$ on AlN(0001).

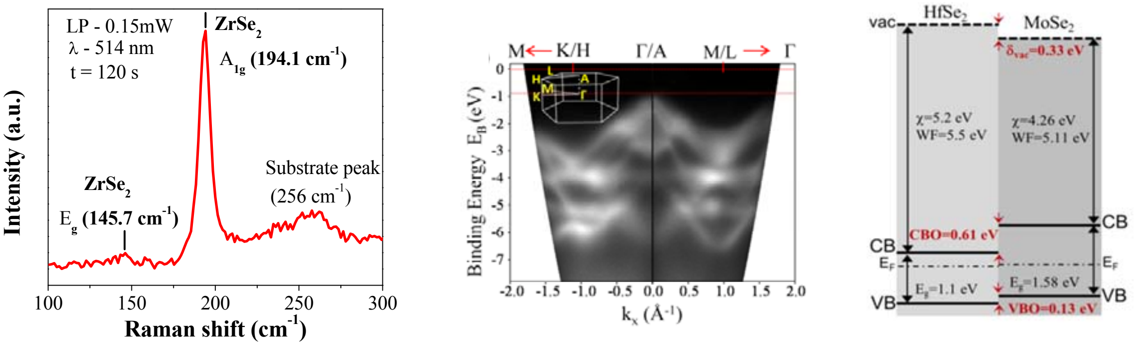

Figure 2: (a) Raman spectra of a 10ML $ZrSe_2$ film (b) ARPES valence band imaging along the high symmetry directions K/H-Γ/A-M/L of the Brillouin zone for a 6 ML $HfSe_2$/AlN smple (b) schematic of the $MoSe_2$/$HfSe_2$ band offsets.

Acknowledgements: The project is financially supported by the ERC Advanced Grant 291260 and the Greek program of excellence (ARISTEIA I) TOP ELECTRONICS-745

References

[1] A. Koma and K. Yoshimura, Surf, Sci. 174 (1986) 556.

[2] C. Gong, H. Zhang, W. Wang, L. Colombo, R. M. Wallace, and K. Cho, Appl. Phys. Lett., 103 (2013) 053513.

[3] E. Xenogiannopoulou, P. Tsipas, K. E. Aretouli, D. Tsoutsou, S. A. Giamini, C. Bazioti, G. P. Dimitrakopulos, Ph. Komninou, S. Brems, C. Huyghebaert, I. P. Radu, and A. Dimoulas, Nanoscale 7 (2015) 7896-7905.

[4] R. Yue, A. T. Barton, H. Zhu, A. Azcatl, L. F. Pena, J. Wang, X. Peng, N. Lu, L. Cheng, R. Addou, S. McDonnell, L. Colombo, J. W. P. Hsu, J. Kim, M. J. Kim, R. M. Wallace, and C. L. Hinkle, ACS Nano 9 (2015) 474.

[5] K. E. Aretouli, P. Tsipas, D. Tsoutsou, J. M. Velasco, E. Xenogiannopoulou, S. A. Giamini, E. Vassalou, N. P. Kelaidis, A. Dimoulas, Appl. Phys. Lett.106 (2015) 143105.

[6] P. Tsipas, D. Tsoutsou, J. Marquez-Velasco, K.E. Aretouli, E. Xenogiannopoulou, E. Vassalou, G. Kordas, A. Dimoulas, Microelectronic Engineering 147 (2015) 269-272.

MO1

O03

Superhard Protective Coatings Developed by Closed Field Unbalanced and Highly Ionized Magnetron Sputtering

S. Kassavetis, A. Spiliotis, S. Karamanidis and S. Logothetidis

Lab of Thin Films - Nanosystems& Nanometrology (LTFN), Physics Department,
Aristotle University of Thessaloniki, Thessaloniki, Kentriki Makedonia, GR-54124, Greece

E-mail: skasa@physics.auth.gr

Growth and accurate characterization of nanostructured protective coatings properties is particularly complicated, but it is crucial since these nanomaterials attract the interest of the scientific community and meet the needs of various industrial sectors.
In this paper, we focus on the growth and nanomechanical characterization of superhard protective coatings using depth-sensing nanoindentation, scratch test and atomic force microscopy (AFM). The coatings where developed using High Power Impulse Magnetron Sputtering and Closed-field Unbalanced Magnetron Sputtering. The goal is to study in details the effect of the different growth technique to the nanomechanical performance of the nanostructured protective coatings.

The nanoindentation testing was performed using two Berkovich (triangular-pyramid) type diamond indenters with different tip roundness (nominal tip roundness 20 nm and 50 nm), while the AFM was used to image the nanoindentation imprints and to study the difference in the deformation induced to the coatings by the two different Berkovich diamond tips. The analysis of the nanoindentation load-displacement curves showed that hardness values over 35 GPa.

Finally, the mechanical properties were correlated with the protective coatings structure coming from the X-rays diffraction (XRD), reflection (XRR).

Acknowledgments: Hellenic National Strategic Reference Framework 2007–2013, contract no. 11ΣΥΝ-5-1280, Project ‘Nano-Hybrid’, within the Program ‘Competitiveness and Entrepreneurship’.

Alumina Supported Iridium Catalysts for N_2O Abatement: Electron Microscopy Investigations of the Active Species

A. Delimitis[1], **E. Pahatouridou**[1,2], **E. Papista**[3], **G. E. Marnellos**[1,3], **M. Konsolakis**[2],
I. V. Yentekakis[4] **and E. F. Iliopoulou**[1]

[1] Chemical Process & Energy Resources Institute (CPERI), Centre for Research & Technology Hellas
(CERTH), 57001 Thermi, Thessaloniki, Greece
[2] School of Production Engineering and Management, Technical University of Crete,
73100 Chania, Crete, Greece
[3] Department of Mechanical Engineering, University of Western Macedonia,
Bakola & Sialvera, 50100 Kozani, Greece
[4] School of Environmental Engineering, Technical University of Crete, 73100 Chania, Crete, Greece

E-mail: andel@cperi.certh.gr

Nitrous oxide (N_2O) has been recently recognized as a harmful greenhouse gas exhibiting 300 times higher Global Warming Potential compared to CO_2, as well as a stratospheric ozone layer depletion contributor. One of its major sources is combustion of fossil and biomass fuels and, as a consequence, several technologies have been developed towards its end-of-pipe control or abatement. Catalytic decomposition represents the most promising method, due to lower energy requirements and cost. Currently, noble metal (Pt, Pd, Ir) catalysts exhibit satisfactory activity at low temperatures, with Ir-based composites to show a promising behavior [1]. Enhancement of the active catalytic phase's intrinsic features usually takes place via support-mediated promotional effects and/or surface doping. In the present study, the nanostructural characteristics of Ir catalysts supported either on pure Al_2O_3 or CeO_2-modified Al_2O_3 (AlCe), or surface promoted with K ions are explored applying electron microscopy (TEM, HRTEM, STEM) techniques. Their structural features are correlated with their catalytic performance in order to define the most active species for N_2O decomposition.

The morphology of the unmodified 0.5 wt% Ir/Al_2O_3 sample is depicted in Fig. 1(a). IrO_2 catalyst adopts two diverse particle morphologies: a medium-size (up to 70 nm), crystalline rectangular one, as evidenced by the selected area diffraction (SAD) pattern (inset I) and a smaller size one (inset II), with disordered particles that are densely aggregated on top of Al_2O_3. Supporting Ir on AlCe results in the almost exclusive formation of larger size, highly crystalline IrO_2 particles, as illustrated in Fig. 2(a), although the Ir loading is identical in both catalysts. The particles' mean size is up to 500 nm in Ir/AlCe. However, in line with previous literature studies, the presence of Ir in highly dispersed species has been further confirmed by high angle annular dark field (HAADF) experiments, as shown in Fig. 1(b) and 2(b) for the Ir/Al_2O_3 and Ir/AlCe, respectively. An improved dispersion is observed in Ir/AlCe, whereas cluster formation predominately takes place in Ir/Al_2O_3, with sizes up to 1.8 nm. The exact phase and chemical identity of these species has been thoroughly investigated using advanced electron microscopy methods and will be exploited.

The superior structural quality of Ir catalysts was reflected in their remarkable ~100% N_2O conversion at 600 °C, under O_2 deficient conditions. In addition, the effect of structural promotion by the AlCe support becomes more evident at O_2 excess conditions, where the Ir/AlCe catalyst showed a 95% N_2O conversion at 600 °C, compared to 66% for the pure Ir/Al_2O_3 material. This is most probably a result of the trend of oxygen ad-atoms, formed by N_2O dissociative adsorption, to desorb and regenerate the active sites for further reaction more easily from the highly crystalline, clear IrO_2 surfaces [2] rather than from defected cites, mainly present in the smaller disordered particles. On the other hand, the isolated Ir species evidenced by HAADF experiments may account for the efficient activation of N_2O, indicating that, in order to develop an improved catalyst, a certain $Ir^{\delta+}/Ir^0$ ratio is required [3,4].

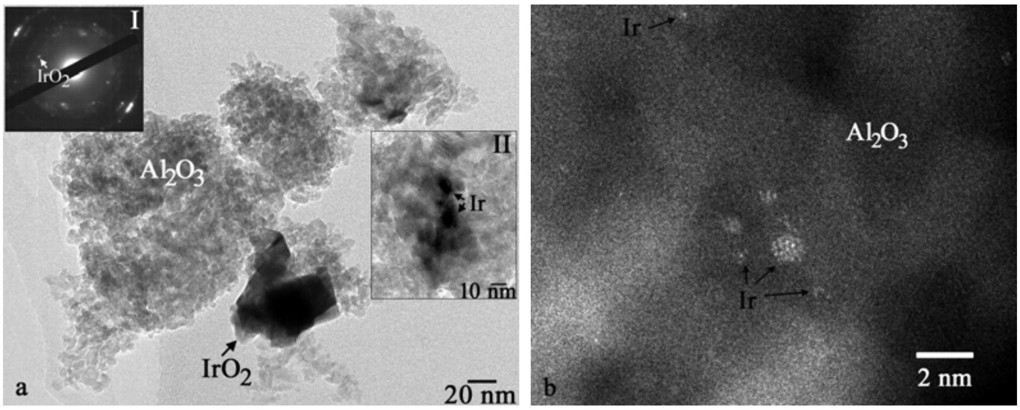

Figure 1: Electron microscopy results of the 0.5Ir/Al_2O_3 catalyst (a) TEM images showing the IrO_2 discrete particles morphology and (b) HAADF STEM image, where the Ir metallic species are denoted with black arrows.

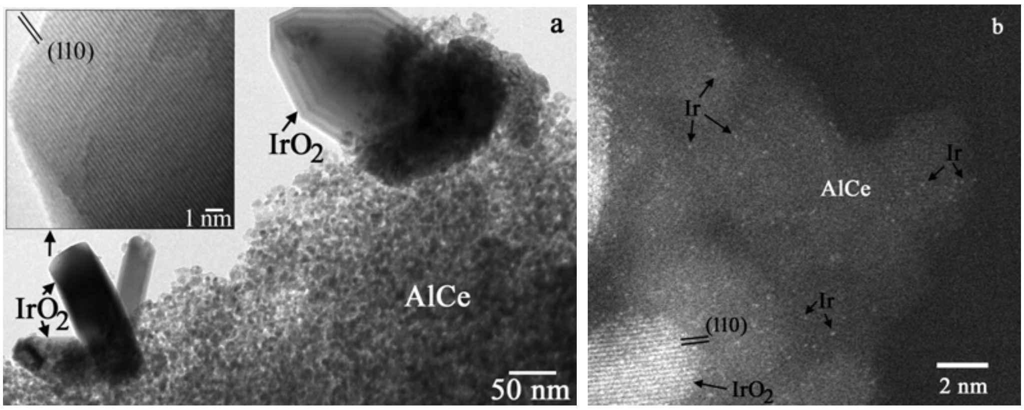

Figure 2: Electron microscopy characterization of the 0.5Ir/AlCe catalyst (a) TEM/HRTEM images revealing the larger IrO_2 particles and (b) HAADF STEM image illustrating the isolated Ir metallic species (black arrowed), widely dispersed on top of the AlCe support and on IrO_2 particles, too.

References

[1] E. Pachatouridou, E. Papista, E.F. Iliopoulou, A. Delimitis, G. Goula, I.V. Yentekakis, G.E. Marnellos and M. Konsolakis, J. Env. Chem. Eng. 3 (2015) 815-821.

[2] M.D. Amiridis, C. Mihut, M. Maciejewski and A. Baiker, Topics Catal. 28(1-4) (2004) 141-150.

[3] Financial support by the program "*THALES*" (MIS 375643), co-financed by the Greek Ministry of Education and Religious Affairs and the European Social Fund is acknowledged.

[4] The research leading to these results has received funding from the European Union Seventh Framework Programme under Grant Agreement 312483 - ESTEEM2 (Integrated Infrastructure Initiative–I3).

Microscopical characterization of 2D-film selenide heterostructures grown on polar wurtzite AlN by molecular beam epitaxy

Ph. Komninou[1], C. Bazioti[1], G.P. Dimitrakopulos[1], K. E. Aretouli[2,3], P. Tsipas[2], E. Xenogiannopoulou[2], D. Tsoutsou[2], J. Marquez-Velasco[2,4], S.A. Giamini[2,3], N. Kelaidis[2], G. Kordas[2], A. Dimoulas[2]

[1]Physics Department, Aristotle University of Thessaloniki, 54124 Thessaloniki, Greece
[2]Institute of Nanoscience and Nanotechnology, National Center for Scientific Research "DEMOKRITOS", 15310, Athens, Greece
[3]University of Athens, Department of Physics, Section of Solid State Physics, 15684 Athens, Greece
[4]National Technical University of Athens, Department of Physics, 15780 Athens, Greece

E-mail: gdim@auth.gr

In this work, we present the structural and interfacial properties of MBE-grown selenide heterostructures that have been studied by high resolution transmission electron microscopy (HRTEM). In particular, the growth of the topological insulator (TI) Bi_2Se_3, which is promising for novel spintronics and quantum computing, can be greatly benefited by using (0001) AlN/(111)Si templates instead of silicon wafers. The HRTEM results revealed an almost perfect registry between Bi_2Se_3 and AlN, with no chemical reaction and interdiffusion at the interface. This high-quality epitaxial one-step growth of Bi_2Se_3, in single crystal form is facilitated by a 3:4 plane matching with the substrate, leading to excellent scaling of the film down to a thickness of three quintuple layers (QLs). Only vertical and in-plane 180° rotational domain boundaries were observed. A vertical twin boundary is illustrated in Figure 1. A similar interfacial quality was not achievable when Bi_2Se_3 was deposited directly on silicon.

Additionally, 2D films comprising a few monolayers (MLs) of $MoSe_2$ and/or $HfSe_2$ semiconductors, that are promising for novel nanoelectronic devices, can be achieved by deposition on (0001) AlN. Using Bi_2Se_3 as a buffer layer helps retaining very low growth temperatures, which is advantageous for large scale manufacturing. Cross sectional HRTEM observations revealed perfect epitaxial orientations and high crystalline quality, with lack of defects over an extended scale, despite the large mismatch and the low growth temperature. HRTEM image simulations were employed in order to characterize and verify the structure of interfaces between dissimilar materials. Strain measurements were performed by geometrical phase analysis in order to determine variations in lattice spacings. This high structural quality of 2D semiconductor/TI heterostructures, allows epitaxial growth of multilayers, offering advanced device possibilities, mediated by the van der Waals bonding and by exploiting the non-trivial TI properties. Such heterostructure is illustrated in Figure 2. The structural observations were consistent with angle-resolved photoelectron spectroscopy measurements.

Acknowledgements: The project is financially supported by the ERC Advanced Grant 291260 and the Greek program of excellence (ARISTEIA I) TOP ELECTRONICS-745.

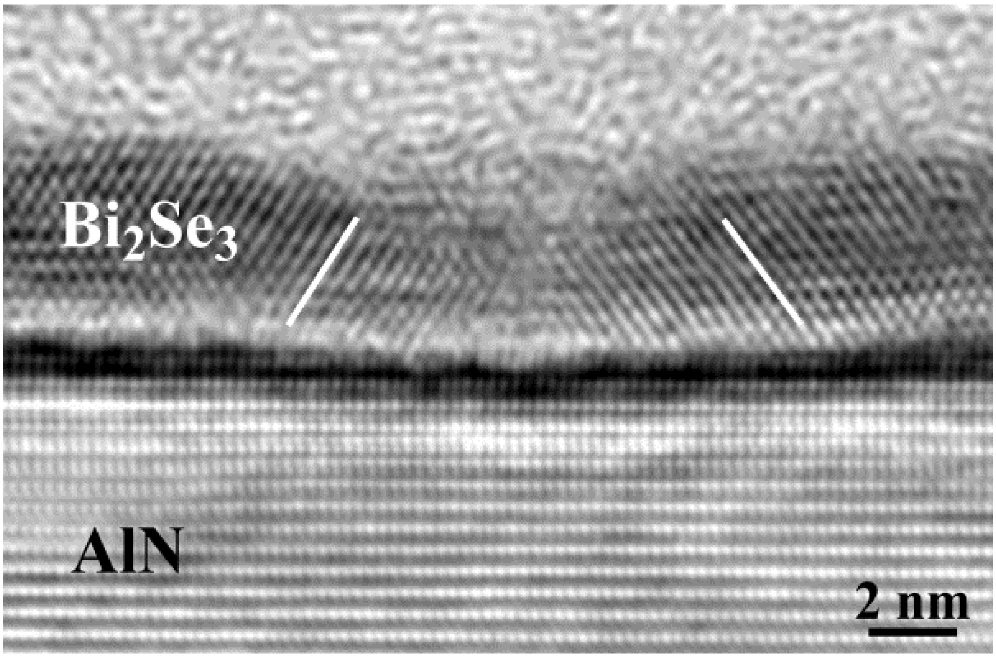

Figure 1: Cross sectional HRTEM image obtained along the $[11\bar{2}0]_{AlN}$ zone axis, showing good registry of a three Bi_2Se_3 QL thin film on (0001) AlN template. A vertical rotational twin boundary is visible.

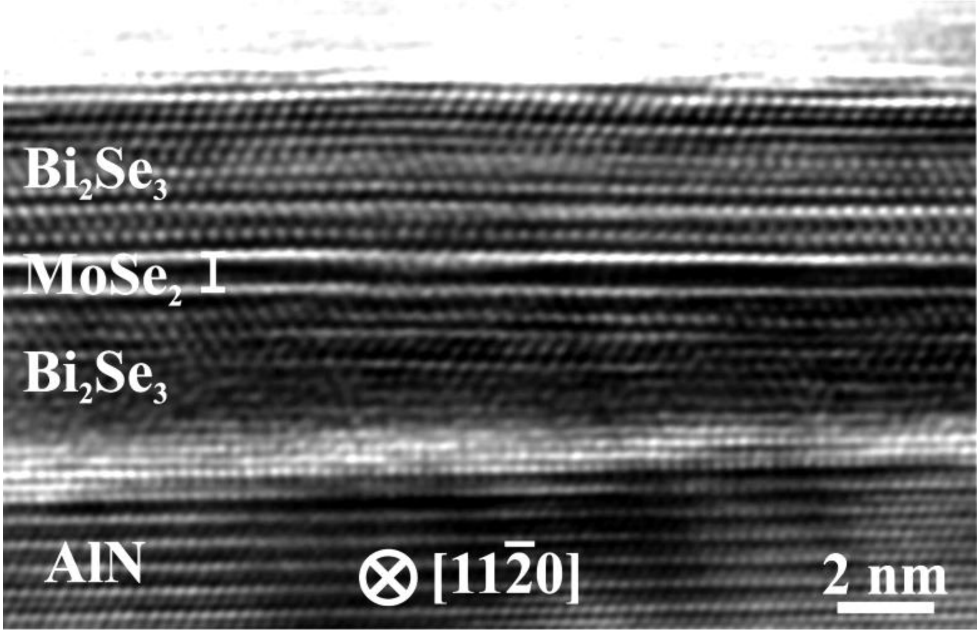

Figure 2: Cross sectional HRTEM image along the $[11\bar{2}0]_{AlN}$ zone axis showing a $Bi_2Se_3/MoSe_2/Bi_2Se_3$ heterostructure grown on AlN.

The effect of spatial confinement in the electron-phonon coupling constant studied with ultrafast electron diffraction

T. Vasileiadis[1], **L.Waldecker**[1], **R. Bertoni**[1], **D. Wells**[2],
R. Palmer[2] **and R. Ernstorfer**[1].

[1]Physical Chemistry Department, Fritz Haber Institute, Faradayweg 4-6, 14195 Berlin, Germany.
[2]Nanoscale Physics Research Laboratory, University of Birmingham, Edgbaston Birmingham
B15 2TT, UK.

E-mail: vasileiadis@fhi-berlin.mpg.de

Time-resolved diffraction is a novel technique for the investigation of ultrafast phenomena associated with electron-lattice interactions [1]. Electron diffraction, especially, is an ideal tool for nanostructures because of the much higher scattering cross-section in comparison with X-rays. The electronic subsystem of the crystal is excited by a femtosecond laser pulse, while subsequent energy transfer to the lattice subsystem is probed by ultrashort electron pulses at certain time delays. The evolution of the lattice temperature is probed by the decrease of intensity of the diffraction peaks due to the Debye-Waller effect. From the position of diffraction peaks ultrafast expansion of nanostructures can be measured with subpicometer resolution. The exact mechanism of coupling between the electronic and the lattice subsystems is of particular interest in spatially confined systems. When the crystalline symmetry spans over few unit cells both electronic and vibrational excitations acquire more molecular-like characteristics [2]. In this study we performed time-resolved diffraction of size-selected Au nanoclusters to determine the electron-phonon coupling constant in various degrees of confinement. Size selection is based on the increased stability of the so-called magic clusters that are characterized by very precise shape and number of atoms, and can be understood from both geometrical and electronic considerations [3]. Our first measurements are focused on Au clusters with 923 atoms that are located at the borders of bulk and nano regimes based on ultrafast optical measurements [4]. In addition to the above, interesting effects are expected to arise due to coupling of the nanoclusters to the substrate. For this reason different substrates have been used; thin films of a-C (0D on 3D structure) and few-layer Graphene (0D on 2D structure).

References

[1] R. J. D. Miller *et al.* , Acta Crystallographica A 66 (2010) 137.
[2] M. Walter *et al.* PNAS 105 (2008) 9157.
[3] P. Pyykkö, Nature Nanotechnology 2 (2007) 273.
[4] S. H. Yau *et al.***,** Acc. Chem. Res., 46 (2013) 1506.

SESSION MO2

PHOTONICS AND OPTOELECTRONICS

Monday, 21 September 2015, 11^{30}-13^{30}

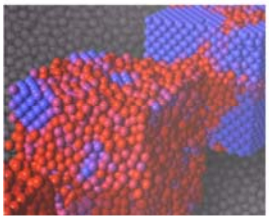

XXXI Panhellenic Conference on
SOLID STATE PHYSICS &
MATERIALS SCIENCE
Thessaloniki, 20-23 September 2015

Ultra-low threshold GaN polariton lasing at room temperature

R. Jayaprakash[1, 2], F. G. Kalaitzakis[2], E. Amargianitakis[3], G. Christmann[2], K. Tsagaraki[2], M. Hocevar[4, 5], B. Gayral[4, 5], E. Monroy[4, 5] and N. T. Pelekanos[1, 2]

[1]Department of Materials Science and Technology, University of Crete, 71003 Heraklion, Greece.
[2]Microelectronics Research Group, IESL-FORTH 71110 Heraklion, Greece.
[3]Department of Physics, University of Crete, 71003 Heraklion, Greece
[4]Université Grenoble-Alps, 38000 Grenoble, France
[5]CEA, INAC-SP2M, 17 av. des Martyrs, 38000 Grenoble, France

E-mail: pelekano@materials.uoc.gr

The possibility of having low-threshold, inversion-less lasers, making use of the macroscopic occupation, of the low density of states, at the bottom of the lower polariton branch, has intensified polariton research in the last two decades. State of the art devices based on this admixed quasiparticle have already been realized using GaAs and CdTe active layers, although the accomplishment of room temperature lasers has been limited by their relatively weak binding energy. The high binding energy and oscillator strength, as well as the advantageous relaxation dynamics of wide bandgap semiconductors, such as GaN, are well suited for room temperature polariton operation. The current prevailing demonstrations of GaN based polariton lasers rely on bulk GaN, GaN quantum wells, and GaN nanowires as the active layer. In the latter approach, individual nanowires are positioned in a microcavity showing remarkable polariton characteristics, but questions remain on the scalability of the approach, as well as on how to turn these nanowire-based structures into real electrically-injected devices. The former two cases are technologically viable, but are currently limited by the relatively poor quality of the active region, due to the structural disorder introduced by the bottom GaN based DBR mirrors.

Our approach is to use a very straightforward processing technique using photo-electrochemical etching, to etch away an InGaN sacrificial layer, creating ultra-smooth membranes containing optimal quality GaN/AlGaN QW's, which are then embedded between high quality dielectric DBR's. A temperature dependent study unveils the strong coupling regime in the produced structure, exhibiting a robust Rabi splitting as large as 61meV at room temperature. The non-linear properties are investigated under non-resonant quasi-continuous excitation, with polariton lasing demonstrated at an ultra-low threshold of 4W/cm^2, the lowest ever reported for a 2D GaN based system, accompanied by a spectacular condensation pattern in k-space. The latter is attributed to a site-specific polariton trapping mechanism, where polaritons accumulate in discrete levels within the trapping potential, helping to escalate the polariton density locally. This, along with the high optical quality of the all-dielectric microcavity, explains the obtained ultra-low threshold. It should be noted that the use of ultra-smooth GaN membranes in microcavities is fully compatible with the realization of electrically injected GaN polariton devices.

Acknowledgments: This work is supported by the European Social Fund and National resources through the THALES program "NANOPHOS", and the PROENYL research project, Action KRIPIS, project MIS-448305 funded by the General Secretariat for Research and Technology, Ministry of Education, Greece and the European Regional Development Fund (Sectoral Operational Programme: Competitiveness and Entrepreneurship, NSRF 2007-2013)/European Commission.

Engineering Giant Circular Dichroism in Silver-Coated Magnetodielectric Nanoparticles

P. Varytis[1], **N. Stefanou**[1], **A. Christofi**[2] **and N. Papanikolaou**[2]

[1]Department of Solid State Physics, National and Kapodistrian University of Athens,
University Campus, GR-157 84 Athens, Greece
[2]Institute of Nanosciense and Nanotechnology, NCSR "Demokritos," GR-153 10 Athens, Greece

E-mail: parisvarytis@phys.uoa.gr

Composite magnetoplasmonic nanoparticles with core-shell morphology exhibit intriguing optical properties and offer impressive opportunities for tailoring in a controllable manner the light-matter interaction at subwavelength dimensions. These properties are usually analyzed in the framework of the quasistatic approximation which, however, is often inadequate and thus a full electrodynamic treatment is required. In this respect, we developed a rigorous method for an accurate description of electromagnetic scattering by a gyrotropic sphere coated with a nongyrotropic concentric spherical shell, based on the full multipole expansion of the wave field [1], and employed this method for studying circular dichroism in silver-coated magnetodielectric (garnet) nanospheres using the dielectric functions of the constituent materials from the literature [2,3]. In such particles, there are two dielectric-metal interfaces and thus both cavity- and particle-like plasmon modes are formed at the inner and outer surfaces of the shell, respectively. These modes interact with each other and give rise to hybrid plasmon modes, by analogy to the formation of bonding and antibonding electron states of a molecule by symmetric and antisymmetric linear combination of the atomic orbitals, respectively [4]. Here, we shall be concerned only with dipole plasmon modes since higher-order plasmons have a long lifetime and are washed out by dissipation. For a high-refractive-index core, like e.g. a garnet material, the eigenfrequency of the cavity-like plasmon is below that of the particle-like plasmon. For a relatively thick silver shell, cavity- and particle-like plasmons interact weakly with each other. Therefore, both the low-frequency bonding hybrid plasmon and the corresponding high-frequency antibonding plasmon have a considerable dipole moment and couple efficiently with external radiation giving rise to pronounced resonances in the absorption (and scattering) cross sections. By reducing the shell thickness, the bonding and antibonding hybrid plasmons are red and blue shifted, respectively, because of their stronger interaction which, at the same time, increases the dipole moment of the bonding plasmon leading to a more pronounced resonance in the absorption cross section and reduces the dipole moment of the antibonding plasmon rendering it gradually inactive (see Fig. 1). When the garnet core is magnetized, e.g. along the direction of incidence, the resonance peaks for left- and right- circular polarized light are split giving rise to circular dichroism, which is defined as the difference between the corresponding absorption cross sections $\Delta\sigma_{abs} = \sigma_{abs}^{(L)} - \sigma_{abs}^{(R)}$. While for a thick shell both bonding and antibonding hybrid plasmons yield similar resonance peaks in the absorption spectrum in the absence of gyrotropy, the relative shift of these peaks when the core is magnetized is about an order of magnitude larger for the low-frequency bonding resonant mode than for the high-frequency antibonding one, because of the larger concentration of the former in the active magnetic region. As a result, we obtain very strong circular

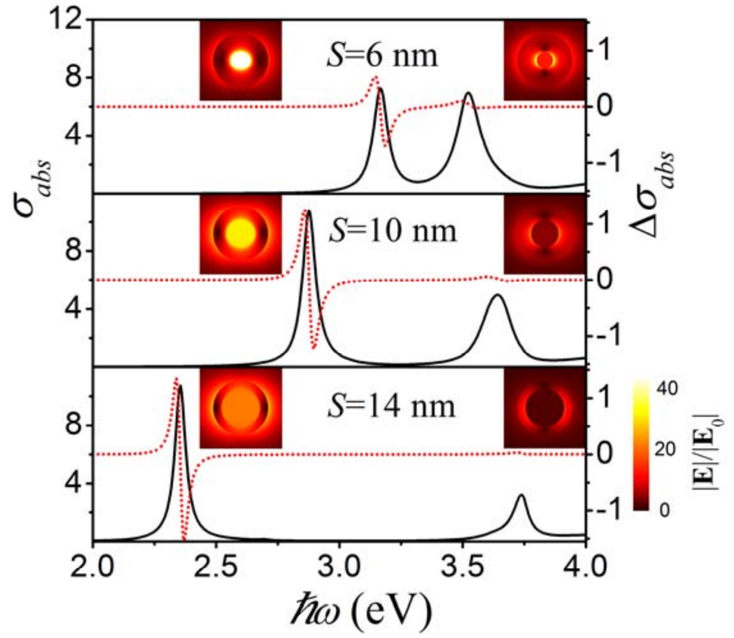

Figure 1: Absorption cross section spectra normalized to the geometric cross section (solid lines) of an unmagnetized garnet sphere of radius S coated with a concentric spherical silver shell of thickness D (S+D=20 nm), in air, and field distribution in the plane of polarization at the different resonances. The corresponding circular dichroism if the garnet core is magnetized along the propagation direction of the incident light is displayed by dotted lines.

dichroism signal in the frequency region of the bonding hybrid plasmon, and weak signal in the region of the antibonding hybrid (see Fig. 1). With increasing the size of the magnetic core, the separation between circular polarization modes increases for the bonding hybrid plasmon, which extends considerably in the active magnetic region, due to the stronger magneto-optic interaction. This result, in conjunction with the fact that the corresponding absorption resonances become gradually sharper explains the increasing circular dichroism at lower frequencies with reducing the shell thickness. On the contrary, for the antibonding hybrid plasmon which extends gradually less and less in the core region, the separation between the weak resonances for the two circular polarization modes becomes progressively smaller and the circular dichroism signal gradually vanishes. In conclusion, silver-coated magnetic garnet nanoparticles exhibit a giant circular dichroism, which largely exceeds that of homogeneous noble-metal nanoparticles in an external magnetic field [5] and can be tuned by varying the shell thickness.

References

[1] A. Christofi and N. Stefanou, Int. J. Mod. Phys. B 28 (2014) 1441012.
[2] P. B. Johnson and R. W. Christy, Phys. Rev. B 6 (1972) 4370-4379.
[3] K. Fang, Z. Yu, V. Liu and S. Fan, Opt. Lett. 36 (2011) 4254-4256.
[4] E. Prodan, C. Radloff, N. J. Halas and P. Nordlander, Science 302 (2003) 419-422.
[5] F. Pineider, G. Campo, V. Bonanni, C. de Julián Fernández, G. Mattei, A. Caneschi, D. Gatteschi, and C. Sangregorio, Nano Lett. 13 (2013) 4785-4789.

MO2

O08

Antenna-cavity mode hybridization in plasmonic nanocavities

C. Tserkezis[1], **R. Esteban**[1], **D. O. Sigle**[2], **J. Mertens**[2], **L. O. Herrmann**[2], **J. J. Baumberg**[2] **and J. Aizpurua**[1]

[1]Donostia International Physics Center and Centro de Física de Materiales CSIC-UPV/EHU, Paseo Manuel de Lardizabal 4, Donostia-San Sebastián, 20018, Spain
[2]Nanophotonic Centre, Cavendish Laboratory, Department of Physics, JJ Thomson Avenue, University of Cambridge, Cambridge, CB3 OHE, United Kingdom

E-mail: christos_tserkezis001@ehu.es

Plasmonic nanocavities formed by two metallic components in close proximity are a subject of increasing interest, owing to the enhanced interactions between plasmonic modes and the numerous applications that rely on them. Particularly attractive is the nanoparticle-on-mirror (NPoM) architecture, where metallic nanoparticles (NPs) couple to their mirror image in an underlying metallic film, forming reproducible narrow plasmonic cavities [1]. Different materials, such as organic monolayers [2] or two-dimensional semiconductors [3] can be used as spacers to prevent conductive contact between the NP and the film, and provide templates for enhancing the electromagnetic field [1], studying quantum and nonolocal effects [4], or tracing NP morphological changes on the atomistic scale through optics [3]. In the latter case, much attention is required, since the NP shape can be crucial to define the exact optical response. For spherical NPs, longitudinal antenna modes equivalent to the bonding dimer plasmons in NP dimers are excited [1-3]. Cubic NPs on the other hand are dominated by transverse cavity modes reminiscent of those encountered in opti-cal patch antennas [5]. Here we show that faceted spherical NPs combine the characteristics of both geometries, with antenna and cavity modes concurrently excited. The interaction and hybridization of these modes is explained through numerical simulations and symmetry arguments.

The NPoM cavity under consideration consists of a 100-nm spherical Au NP separated from a Au film by a 0.6-nm-thick spacer described by a dielectric constant equal to 1.63. The extinction spectra of such a system are characterized by longitudinal antenna modes which depend strongly on spacer thickness [1]. The spectral positions of the first two modes of this type, ℓ_1 and ℓ_2, are shown by open circles at the bottom of Fig. 1. In order to examine how NP restructuring affects optics, we remove spherical cups off the bottom of the NP and create circular facets of diameter w. Then, due to the resulting increase in NP-film interaction, the ℓ modes initially redshif, until, for larger w, they start blueshifting because of NP height reduction. At the same time, for facet diameters larger than about 15 nm, a concurrent excitation of new modes with almost linear dependence on w is observed. These are transverse cavity modes, whose wavelength, λ, can be expressed as a function of w through a Fabry-Perot model, $\lambda_{mn} = \pi\, w\, n_{eff} / (a_{mn} - \beta)$ [6], where n_{eff} is the effective refractive index of the cavity, a_{mn} is the n-th root of the Bessel function J_m, and β an appropriate reflection angle. The first four physically meaningful solutions, s_{mn} with mn = 11, 02, 12, 03, are depicted in Fig. 1 with black lines and reproduce the calculated extinction peaks for each w. What becomes immediately clear is that while the s_{1n} cavity modes can cross the antenna ℓ modes without interaction, the s_{0n} modes interact with the ℓ modes, resulting in anticrossings and formation of hybrid ℓ-s modes. This interaction can be explained by the charge distributions along the plasmonic cavity, as shown in the schematics of Fig. 1. The induced charges of s_{1n} and ℓ cancel each other out, leading to zero interaction. On the other hand, s_{0n} and ℓ have similar symmetry and their interaction results in hybridization of the two modes. These schematic charge distributions are verified by electric field contour plots inside the cavity (in a plane parallel to the substrate), as shown in the rightmost part of Fig. 1 for the first two cavity modes (s_{11} and s_{02}), for a facet with $w = 75$ nm.

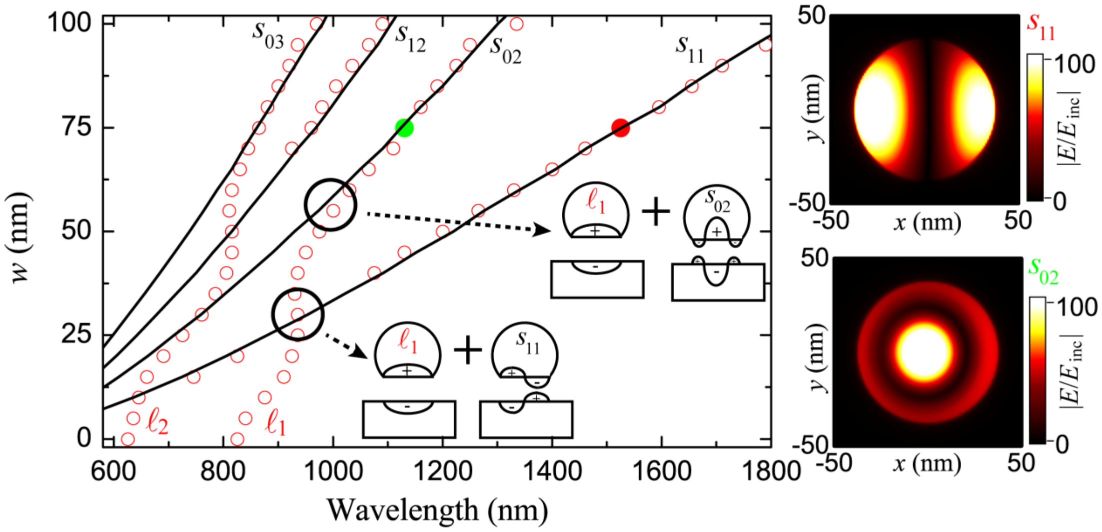

Figure 1: Extinction peaks (open circles) as a function of facet diameter, w, for a 100-nm Au NP separated from a Au film by a 0.6-nm-thick spacer. Black lines depict the solutions of the Fabry-Perot model for the first four cavity (s_{mn}) modes. The interaction of antenna (ℓ) and cavity modes is schematically described in the insets for the ℓ_1, s_{11}, and s_{02} modes. Electric field contours inside the cavity ($w = 75$ nm) for s_{11} ($\lambda = 1525$ nm,) and s_{02} ($\lambda = 1130$ nm) (red and green solid dots in the spectra, respectively) are shown on the right-hand side.

In conclusion, we have shown that both longitudinal antenna modes and transverse cavity modes can be excited in plasmonic cavities formed by faceted spherical NPs on a metallic film, and analyzed their interaction in terms of modal symmetry. The evolution and interplay between these NPoM modes can serve as a fingerprint of complex atomistic processes in photochemistry and optoelectronics.

References

[1] J. Mertens, A. L. Eiden, D. O. Sigle, F. Huang, A. Lombardo, Z. Sun, R. S. Sundaram, A. Colli, C. Tserkezis, J. Aizpurua, S. Milana, A. C. Ferrari and J. J. Baumberg, Nano Lett. 13 (2013) 5033-5038.

[2] F. Benz, C. Tserkezis, L. O. Herrmann, B. de Nijs, A. Sanders, D. O. Sigle, L. Pukenas, S. D. Evans, J. Aizpurua and J. J. Baumberg, Nano Lett. 15 (2015) 669-674.

[3] D. O. Sigle, J. Mertens, L. O. Herrmann, R. W. Bowman, S. Ithurria, B. Dubertret, Y. Shi, H. Y. Yang, C. Tserkezis, J. Aizpurua and J. J. Baumberg, ACS Nano 9 (2015) 825-830.

[4] C. Ciracì, R. T. Hill, J. J. Mock, Y. Urzhumov, A. I. Fernández-Dominguez, S. A. Maier, J. B. Pendry, A. Chilkot and D. R. Smith, Science 337 (2012) 1072-1074.

[5] J. B. Lassiter, F. McGuire, J. J. Mock, C. Ciracì, R. T. Hill. B. J. Wiley, A. Chilkoti and D. R. Smith, Nano Lett. 13 (2013) 5866-5872.

[6] C. Tserkezis, R. Esteban, D. O. Sigle, J. Mertens, L. O. Herrmann, J. J. Baumberg and J. Aizpurua, Phys. Rev. Lett., *submitted*.

Microstructural evolution in high alloy content InGaN films grown by molecular beam epitaxy

C. Bazioti[1], E. Papadomanolaki[2], Th. Kehagias[1], T. Walther[3], J. Smalc-Koziorowska[4], E. Pavlidou[1], Ph. Komninou[1], Th. Karakostas[1], E. Iliopoulos[2] and G. P. Dimitrakopulos[1*]

[1] Physics Department, Aristotle University of Thessaloniki, GR 541 24, Thessaloniki, Greece
[2]Microelectronics Research Group (MRG), IESL, FORTH, P.O. Box 1385, 71110 Heraklion Crete, Greece; and Physics department, University of Crete, Heraklion Crete, Greece
[3]Department of Electronic & Electrical Engineering, University of Sheffield, Sheffield S1 3JD, UK
[4] Institute of High Pressure Physics, Polish Academy of Sciences, Sokolowska 29/37, 01-142 Warsaw, Poland

E-mail: kbazio@physics.auth.gr

InGaN alloy thin films with high indium content set a realistic perspective for high efficiency photovoltaic as well as for large-wavelength optoelectronics applications. However, due to their intense metastability, chemically-induced phenomena take place, resulting in a complex microstructural behavior that is sensitive to the growth conditions. In this work, a systematic study was performed on samples deposited by plasma-assisted molecular beam epitaxy (PAMBE) on (0001) GaN/Al_2O_3 and AlN/Al_2O_3 templates, utilizing low temperature growth regimes. Transmission electron microscopy (TEM) techniques were used for the structural and chemical characterization of the films, including high resolution TEM (HRTEM), geometrical phase analysis (GPA), scanning TEM (STEM) and energy-dispersive x-ray spectroscopy (EDXS), together with high resolution X-ray diffraction (HRXRD) results.

Distinct strain relaxation mechanisms come into play depending on the growth conditions. These depend sensitively on the indium adlayer coverage and adatom mobility, leading to distinct growth modes, indium concentrations, film thicknesses, and surface morphologies. At higher growth temperatures, strain relaxation takes place by the opening up of V-defects that are connected to **c**-component threading dislocations arriving from the substrate. By lowering the temperature, a change of relaxation mode takes place, with **a**-type threading dislocations (TDs) becoming the dominant structural defect. Their emanation commenced above a self-formed strained InGaN interfacial layer, as shown in Fig. 1. The TD introduction was promoted by the introduction of multiple basal plane stacking faults (BSFs) as illustrated in Fig. 2. A nanomechanism permitting lattice TD generation from BSFs is proposed. EDXS and GPA measurements revealed a gradually increasing indium concentration with film thickness. The interfacial layer is gradually suppressed with further lowering of the growth temperature due to the early saturation of the surface with indium adatoms.

Acknowledgement: This research has been co-financed by the European Union (European Social Fund – ESF) and Greek national funds through the Operational Program "Education and Lifelong Learning" of the National Strategic Reference Framework (NSRF) - Research Funding Program: THALES.

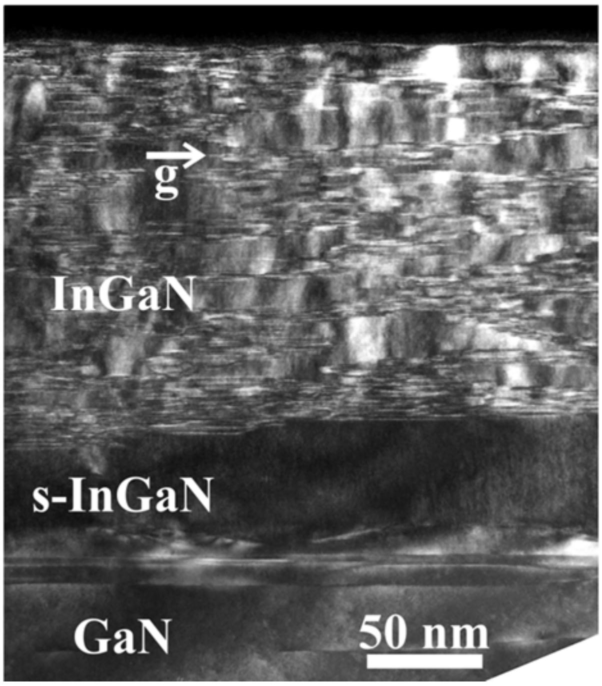

Figure 1: Cross sectional dark field TEM image obtained near the $[11\bar{2}0]$ zone axis with $g1\bar{1}00$, showing the self-formed strained InGaN interfacial layer (s-InGaN). Multiple BSFs and TDs are visible after the s-InGaN interface.

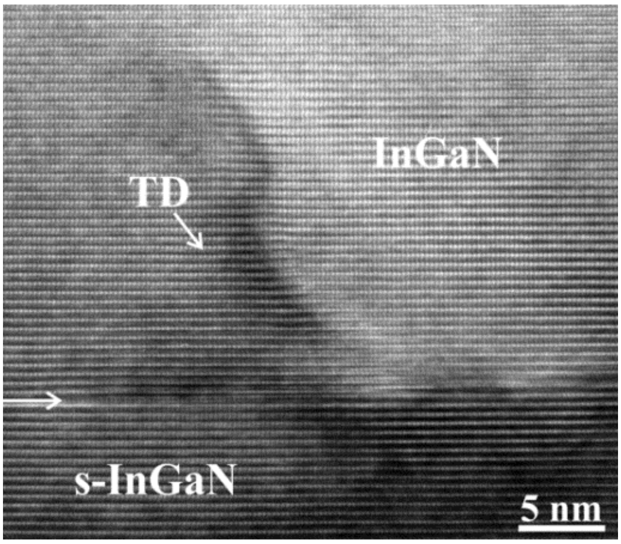

Figure 2: Cross sectional HRTEM image along the $[11\bar{2}0]$ zone axis showing the emanation of a TD from a BSF at the InGaN/s-InGaN interface (white arrow).

MO2

O010

Development and characterization of organic light emitting diodes on rigid and flexible substrates

M. Gioti[1], C. Chaidou[1], C. Polyzoidis[1], D. Kokkinos[1], C. Pitsalidis[1], C. Kapnopoulos[1], A.K. Andreopoulou[2,3], E. Mparmpoutsis[2], J.K. Kallitsis[2,3] and S. Logothetidis[1]

[1]Laboratory for Thin Films-Nanosystems and Nanometrology (LTFN), Physics Department, Aristotle University of Thessaloniki, GR-54124 Thessaloniki, Greece
[2]Department of Chemistry, University of Patras, University Campus, Rio-Patras GR26504, Greece
[3]Foundation for Research and Technology Hellas, Institute of Chemical Engineering Sciences (FORTH/ICE-HT), Platani Str., Patras GR26504, Greece

E-mail: mgiot@physics.auth.gr

Organic light-emitting diodes based on light-emitting polymers (PLEDs) are an attractive type of electrical devices due to the possibility of ease processing and manufacturing because the conjugated polymers are soluble. They have many advantages over existing emissive type technologies, because they are lightweight, battery operated, highly visible and have low turn-on voltages [1]. PLEDs can be deposited on a substrate from solution by simple processing techniques such as spin-coating or printing. They also can be fabricated on flexible substrates such as indium–tin oxide (ITO) coated polyethylene terephtalate (PET), which are quite durable, light, and thin. Therefore, they are very promising for applications where low-cost fabrication or large-area devices are desired.

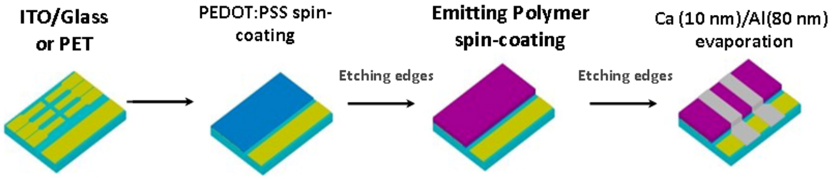

Figure 1: The process and the architecture of the PLED devices.

In this work, commercially available polymers such as polyfluorenes (PFO:F8BT) and polyphenylene vinylenes (MEH-PPV) were applied as emitting materials in PLED devices in green and red characteristic emission wavelengths, respectively. These materials were used as reference active materials for PLED applications. Additionally, new synthesized anthracene-based and carbazole-based polymers were also applied as promising, alternative materials providing the potentiality to tailor their properties depending on their preparation conditions. Spin coating processes were used for the fabrication of the polymer thin films and the final produced devices were either in rigid or flexible form. For the rigid and flexible PLED devices patterned ITO covered glass and PET were used as substrates, respectively. The interface between the polymer and the metal electrode that is used to pass the electrical current through the active polymer layer is very important. Thus, in order to improve the performance of PLEDs, the introduction of conducting polymers between the ITO and light-emitting polymer such as poly(ethylene-dioxy)thiophene mixed with poly(stylene sulphonic acid) (PEDOT:PSS) is used. This leads to a more efficient transport of the carriers since the PEDOT:PSS layer with a higher work function (5.0 eV) than that (~4.8 eV) of ITO allows holes to be injected easily into the luminescent layer. Fig. 1 represents the process used for the fabrication of PLEDs and the final architecture of our devices

The photoluminescence (PL) of the polymeric films were evaluated by Fluorescence Spectroscopy revealing the characteristic emission of each material. The optical properties of the polymers were investigated by NIR-Vis-far UV Spectroscopic Ellipsometry. The accurate determination of the thickness and the optical constants (refractive index, dielectric function and absorption coefficient as a function of wavelength) were derived. Representative PL and absorption coefficient results derived from the produced samples are depicted in Figs. 2 (a) and (b). Furthermore, quantum yield measurements, brightness, chromaticity and current density–voltage characteristics of the devices were obtained. A strong correlation between the optical properties, the thickness and the devices' performance was established since external quantum efficiency of electroluminescence also depends on the optical interference of the beams of emitted light multiply reflected from the layer interfaces. This provides substantial insights into the final design of the optimum final multi-layer structure of the OLEDs whereas the potentiality for the development of flexible OLEDs with bigger active area devices is demonstrated.

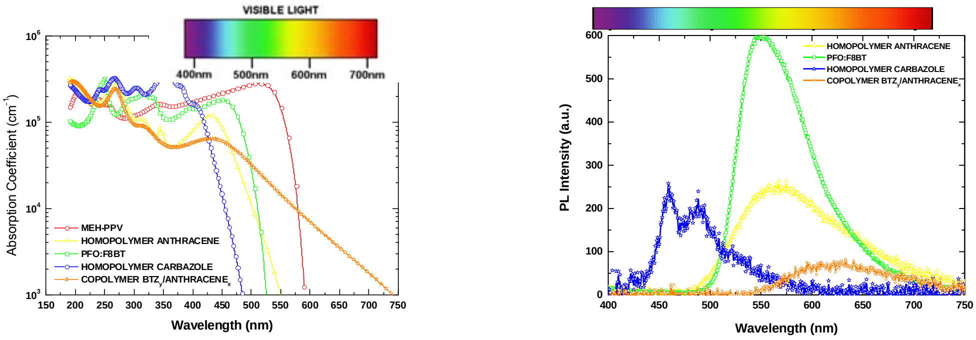

(a) (b)

Figure 2: The absorption coefficient (a) and the PL spectra (b) of the light-emitting polymers films.

Figure 3: Photos of the produced PLED devices on glass and PET substrates emitting in green, red and yellow.

Acknowledgements: This work has been supported by the National Strategic Reference Framework (NSRF) 2007-2013 under the Project GR-Light (11-SYN_5_573).

MO2

O11

Modelling and design of graphene-based applications in sensing and photodetection

A. Dagkli, S. Evangelou, N. Myoung and E. Lidorikis

Department of Materials Science and Engineering, University of Ioannina, 45110 Ioannina, Greece

E-mail: elidorik@cc.uoi.gr

Graphene has unique properties, such as high carrier mobility and constant optical absorption from visible to IR. When these are combined with the ease of Fermi level tuning by chemical doping or electrical gating, they open up great opportunities in electronics, optoelectronics and sensing [1]. There are still, however, limitations that need to be overcome. For example, the lack of strong conductance modulation in graphene due to Klein tunnelling, or the poor light absorption of 2.3%. In this talk we discuss different design approaches to alleviate the aforementioned drawbacks, such as the combined use of electric and magnetic barrier arrays for increasing the conductance modulation depth, or the use of plasmonics and interference effects to increase the Vis-midIR absorption (e.g. see Fig. 1), targeting applications in graphene-based sensing and photodetection.

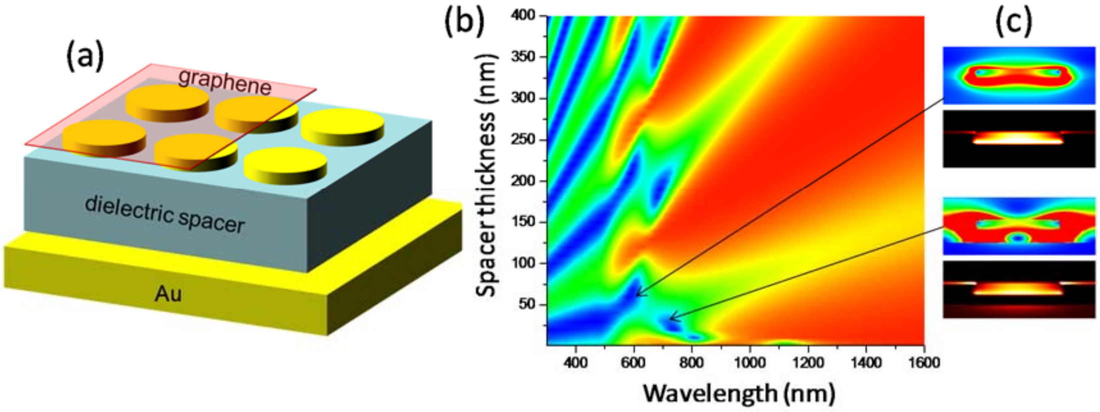

Figure 1. (a) Schematic of a graphene photodetector design based on a plasmonic perfect absorber. (b) Reflectivity of the system vs wavelength and spacer thickness. Points of zero reflection are found. (c) Field intensity and absorption distribution for two zero-reflection points emerging from the anti-crossing of a localized surface plasmon resonance with the Fabry-Perot resonances of the cavity. They show light absorption switching between the metal elements and graphene. Graphene absorption is found to reach up to an overall 50% for optimized devices.

Acknowledgement: This work was funded by the EC Graphene Flagship (contract no.604391)

References

[1] A.C. Ferrari et al., Science and technology roadmap for graphene, related two-dimensional crystals, and hybrid systems, Nanoscale 7 (2015) 4598-4810.

Laser Direct Writing of large area electronics on flexible substrates

F. Zacharatos, M. Makrygianni, S. Papazoglou and I. Zergioti

National Technical University of Athens, Physics Department, Zografou Campus Greece, 15780

*E-mail: zergioti@central.ntua.gr

To date, Laser Direct Write (LDW) techniques, such as Laser Induced Forward Transfer (LIFT), Selective Laser Ablation and Selective Laser Sintering (SLS) of metallic nanoparticle (NP) ink layers are receiving growing attention for the printing of uniform and well-defined conductive patterns with resolution down to 10μm [1]. For flexible substrates in particular, LDW of such NP patterns has been widely applied, as a low temperature and high resolution process compatible with organic electronics. The all laser fabrication of conductive interconnects with $\rho<10\mu\Omega$.cm [2] and fully functional chemical and biological sensors with high sensitivity have been reported [3]. In this work, LDW of Ag and Cu NP inks has been carried out on polyimide (PI) and polyethylene-naphthalate (PEN) substrates to achieve low electrical resistivity electrodes. In more detail, short pulsed (picosecond and nanosecond) Nd:YAG lasers operating at 532 and 256nm, were used for the printing (LIFT) of the metal NP inks. As a result, uniform and continuous patterns with lateral sizes tunable from 50μm up to 1mm have been accomplished. In order to achieve high fabrication quality and low line edge roughness, it is essential to have a well-defined geometry with high precision of all the critical dimensions, and to maintain very accurate control of the laser fluence over a large irradiation area. To accomplish that, we employed flat top optics, incorporating a refractive beam homogenizing system in the experimental laser set-up: the default output of the Nd:YAG ns pulsed laser is a Gaussian shape beam. Although a mechanical mask may be used to shape roughly the Gaussian beam and achieve patterns with moderate precision, a more sophisticated way of laser processing is to replace the static, fixed mask with a real-time reconfigurable mask, by using a spatial light modulator: beam shaping experiments were carried out with a commercial refractive beam homogenizer resulting in a top-hat profile. Next, the printed patterns were laser sintered with ns pulses at 532nm over a wide laser fluence window, resulting in an electrical resistivity of 10μOhm.cm. Spatial beam shaping experiments were carried out to achieve a top-hat laser intensity profile and employ selective laser ablation of thin films (thickness on the order of 100nm), so as to produce silver micro-electrodes with resolution on the order of 10μm and low line edge roughness. Laser sintering was combined with laser ablation to constitute a fully autonomous micro-patterning technique of metallic micro-features, with a 10μm resolution and geometrical characteristics tuned for interdigitated electrodes for sensor applications and for transmission lines. The structural properties of the all-laser fabricated electrodes were characterized by optical microscopy, SEM and AFM (Fig. 1). Moreover, the dynamics of the LIFT process were investigated by time resolved imaging, in a time scale ranging from 0.1 μs to a few μs (Fig. 2). Jetting behavior of Cu NP ink was observed during the ejection of the ink. It was found that titanium DRL assisted LIFT resulted in smooth and low velocity (20-50 m/s) jetting behavior, for a wide process window (180-300 mJ/cm^2), indicating therefore, a great potential for a high quality direct printing process. These laser printed electrodes' width may range from 50 up to 500μm and their thickness from 200nm up to a few micrometers. Therefore, their design is flexible and can be tuned according to the desired application, e.g. flexible electronics and sensors.

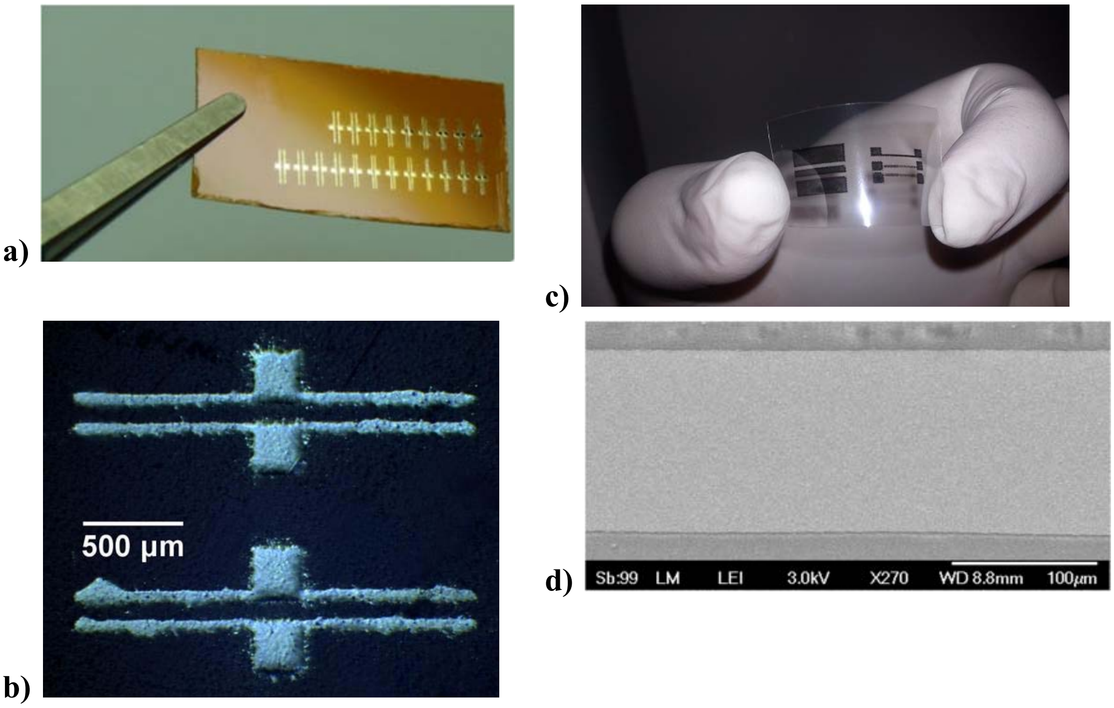

Figure 1: Example structures fabricated by LDW: Interdigitated electrodes on PI (a) and optical microscope picture (b). Transmission lines on PEN (c) and SEM micrograph (d) showing the high fabrication precision after employing flat top optics.

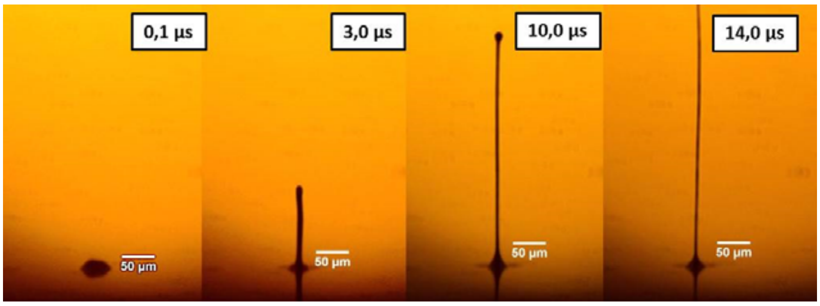

Figure 2: Sequence of pictures taken for the Cu NP ink ejection by using Ti/quartz donor substrates at 240 mJ/cm^2 at 240 mJ/cm^2. The time delays are indicated on the frames.

References

[1] M. Makrygianni, S. Papazoglou, I. Zergioti “Direct Laser Printing for Organic Electronics", Wiley Encyclopedia of Electrical and Electronics Engineering, accepted for publication (2014).
[2] I. Theodorakos, F. Zacharatos, R. Geremia, D. Karnakis and I. Zergioti, ‘Selective laser sintering of Ag NPs ink for applications in flexible electronics’, Appl. Surf. Sci. 336 (2015) 157-162.
[3] E. Touloupakis, M. Chatzipetrou, C. Boutopoulos, A. Gkouzou, I. Zergioti,, “A polyphenol biosensor realized by laser printing technology”, Sensors and Actuators B: Chemical 193 (2014) 301–305.

SESSION MO3

ELECTRONIC TRANSPORT, SEMICONDUCTORS AND DEVICES
&
STRUCTURAL, MECHANICAL AND OPTICAL PROPERTIES OF CONDENSED MATTER

Monday, 21 September 2015, 14^{30}-16^{30}

Manipulating heat: Improved thermoelectrics and thermal/electrical cloaking

D. Niarchos and R. Tarkhanyan

Institute of Nanosciences and Nanotechnology, NCSR Demokritos, Athens, Greece

E-mail: d.niarchos@inn.demokritos.gr

One of the principal advantages of thermoelectric devices is their ability to convert heat into electricity and vice versa without any moving parts. Thermoelectric power generation is based on the Seebeck effect, the phenomenon that develops a voltage when a conductor is under temperature gradient. In last two decades, a great effort has been made to enhance the range of high-performance thermoelectric materials for industrial applications [1-3]. There is a critical need for new materials and processes to enable more efficient and economical conversion, transportation, storage and use of thermal energy. On the other hand there is a great interest in heat manipulation research which may soon become new fundamental science and device technology [4-6].

We propose the development of physical theory and mathematical concepts- transformation thermodynamics [7]- for an investigation of novel opportunities for heat management and conversion of thermal energy in multilayer structures- a novel type of thermal metamaterials (TMM) for heat management- based on bulk and porous semiconducting materials. The combination of these materials with various magnetic and plasmonic nanoinclusions will allow elaboration of a new material platform for the design of next generation thermoelectric devices carrying out direct conversion of waste heat into electricity. Based on the results above a simultaneous thermal and electrical cloaking will be presented.

References

[1] M. Dresselhaus, G. Chen, M. Tang, R. Yang, H. Lee, D. Wang, Z. Ren, J. Fleurial, and P. Gogna, Advanced Materials 19 (2007) 1043.
[2] J.F. Li, W.S. Liu, L.D. Zhao, and M. Zhou, Nature Asia Mater. 2 (2010) 152.
[3] H. Lee, D. Vashaee, D. Wang, M. Dresselhaus, Z. Ren, and G. Chen, J. Appl. Phys. 107 (2010) 094308.
[4] S. Narayana and Y. Sato, Phys Rev. Lett. 108 (2012) 214303.
[5] M. Maldovan, Nature 503 (2013) 209-217.
[6] M. Moccia,G. Castaldi, S. Savo,Y. Sato, and V. Galdi, Phys. Rev. X 4 (2014) 021025.
[7] R. Schittny, M. Kadic, S. Guenneau and M. Wegener, Phys. Rev. Lett, 110 (2013) 195901; also Appl. Phys. Lett. 106 (2015) 143904.

Metal (Hydr)oxides for the removal of Cr(VI) from drinking water: a XAFS study

F. Pinakidou[1], **E. Kaprara**[2], **M. Katsikini**[1], **E. C. Paloura**[1],
K. Simeonidis[1] **and M. Mitrakas**[2]

MO3

O13

[1]Aristotle University of Thessaloniki, School of Physics, Department of Solid State Physics, 54124, Thessaloniki, Greece
[2]Aristotle University of Thessaloniki, School of Chemical Engineering, Analytical Chemistry Laboratory, 54124, Thessaloniki, Greece

E-mail: fpina@physics.auth.gr

Chromium is a naturally occurring element, commonly present in the environment in two forms, trivalent Cr(III), and hexavalent Cr(VI). Cr(III) is a nutritionally essential element in humans, while Cr(VI) is well-established as a carcinogen.[1] Cr(VI) can enter groundwater from both anthropogenic (industrial by-products) and natural sources (contact of water with ultramafic rocks).[2] Considering the severe health effects of Cr(VI) and its verified natural occurrence in groundwater it becomes crucial to develop technologies that can both reliably reduce Cr(VI) in water, to concentrations of low ppb and also allow scaling up to full-scale treatment. Among the several methods developed to remove Cr(VI) from water, the use of materials that can combine reductive and adsorptive capacity became a very promising solution. Sn(II)-(hydr)oxides are efficient Cr(VI) adsorbents, since the presence of Sn^{2+} ions in (hydr)oxides' surface combines Cr(VI) reduction followed by Cr(III) adsorption on the material.

The understanding of chromium adsorption under realistic water treatment can promote the design of optimum adsorbents in respect to their efficiency and the environmental impact after their disposal. Therefore, this study attempts to explain the reduction and adsorption behavior of Cr(VI) by means of Extended X-ray Absorption Fine Structure (EXAFS) and X-ray Absorption Near Edge Structure (XANES) spectroscopies. The studied Sn-(hydr)oxides were prepared at the kilogram-scale by the hydrolysis of $SnCl_2 \cdot 2H_2O$ in a two-stage continuous flow reactor. Drops of NaOH (30 % w/w) were added to control the pH in both stages. The collected out-flowing solid suspension was thickened for 24 h in an Imhoff tank and then the obtained sludge was washed, centrifuged, dried at 100 °C, ground and sieved to obtain either a fine powder form (<45 μm) used for batch adsorption experiments or granules (0.25-0.50 mm) for column tests.

The oxidation state of Cr in a series of Sn-adsorbents with different Cr-loading was investigated using XANES spectroscopy at the Cr-*K*-edge. As in all 3d-trasistion metals, a pre-edge absorption occurs in the Cr-*K*-XANES spectra, the characteristics of which are modulated by the Cr-valence: a prominent pre-edge peak due to a 1s→3d transition occurs when Cr(VI) is present. This transition is forbidden for octahedral Cr(III) while it becomes allowed in non-centrosymmetrical tetrahedral $Cr(VI)O_4$ molecules. Nevertheless, a weak pre-edge peak is present in the spectra of octahedral Cr(III) due to 1s transition to $3d(t_{2g})$ and $3d(e_g)$ electronic states, respectively.[3] In the XANES spectra of all studied samples, shown in Fig. 1, a weak pre-edge absorption is detected. The characteristics of the pre-edge peak (intensity and energy position) are identical to the respective in reference $Cr(OH)_3$, a finding that verifies the presence of Cr(III) in octahedral sites. Thus, the successful reduction of Cr(VI) to Cr(III) is revealed: independently of the different synthesis conditions and Cr-loading, only Cr(III) species are detected.

During chromium adsorption, the Cr(III) species and Cr(VI)-oxyanions form complexes with the Sn-polyhedra and are retained onto the surface of the adsorbent through various physical or chemical mechanisms. Cr(VI) forms outer sphere complexes when adsorbed in soils, while Cr(III) adsorption occurs mainly by the formation of bitentate inner-sphere surface complexes in the binuclear (^{2}C) and mononuclear (^{2}E) geometries.[4] Since the XANES results indicate the presence only of Cr(III) species, the Cr-*K*-EXAFS spectra were fitted assuming ^{2}C and ^{2}E contributions of the Cr oxycations: in the former case, the CrO_6 octahedron shares two corners with oxygen atoms of the Sn-(hydr)oxides while in the latter, the CrO_6 polyhedron and the Sn_6O_8 structural groups share a common edge.

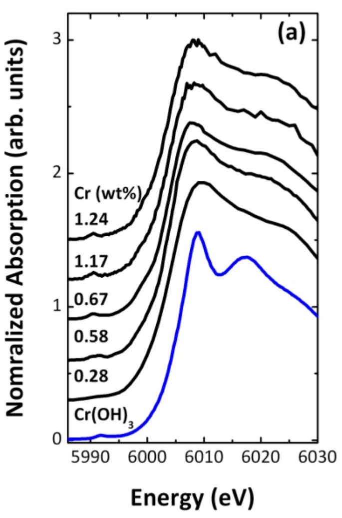

Figure 1: (a) Cr-*K*-XANES spectra and (b) Fourier Transforms (FT) of the $k^2*\chi(k)$ Cr-*K*-EXAFS spectra of the studied samples and reference Cr(OH)$_3$.

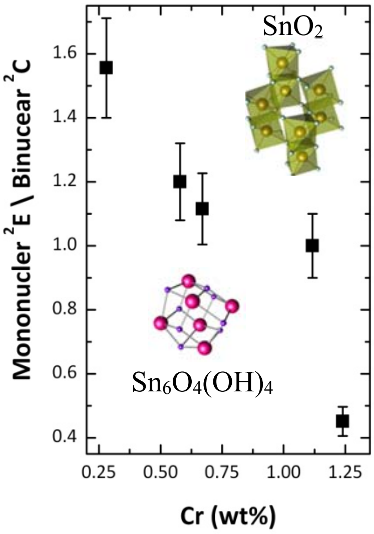

Figure 2: The ratio of bidentate ^{2}E *vs.* ^{2}C complexes, as a function of Cr loading.

The EXAFS analysis results reveal that the weight percentage of Cr uptake yields the formation of different Cr(III)-complexes during sorption. More specifically, as shown in Fig. 2, in the low Cr-loading regions, the bidentate mononuclear (^{2}E) complexes are favoured while as the Cr-uptake increases, the bidentate binuclear (^{2}C) complexes is more prevalent. The sorption mechanism of Cr(III) is not effected by neither the different syntehis pH nor sorption pH. Thus, it can be proposed that chromate retention onto Sn-(hydr)oxides is mainly modulated by the surface coverage of Cr: inner sphere complexes involving both ^{2}E and ^{2}C are formed, however ^{2}C bidentate bridging complexes are in greater proportion in the highest surface coverages.

References

[1] M. Costa, Toxicol. Appl. Pharm., 188 (2003) 1-5.
[2] E. Kaprara *et al.* J. Hazard. Mater., 281 (2015) 2-11.
[3] F. Farges, Phys. Chem. Minerals, 36 (2009) 463–481.
[4] F. Fendorf *et al.*, Environ. Sci. Technol. 31 (1997) 315-320.

MO3

O14

Microstructure correlated thermoelectric properties of $La_{1-x}Sr_xCoO_3$ composites

Z. Viskadourakis[1], **G. I. Athanasopoulos**[2, 3], **E. Kasotakis**[4] **and I. Giapintzakis**[2, 3]

[1] Crete Center for Quantum Complexity and Nanotechnology, University of Crete
P.O. Box 2208, GR-71003 Heraklion, Greece
[2]Department of Mechanical and Manufacturing Engineering, University of Cyprus,
75 Kallipoleos Avenue, P.O. Box 20537, 1678 Nicosia, Cyprus
[3]Nanotechnology Research Unit, School of Engineering, University of Cyprus,
75 Kallipoleos Avenue, P.O. Box 20537, 1678 Nicosia, Cyprus
[4]Materials Science and Technology Department, University of Crete
P.O. Box 2208, GR-71003 Heraklion, Greece

E-mail: zach@iesl.forth.gr

Thermoelectric performance of the $La_{1-x}Sr_xCoO_3$ solid solution with respect to Sr doping as well as its microstructure, is investigated. In particular two $La_{1-x}Sr_xCoO_3$ sample series were produced using the same chemical technique. Microstructure differs between the two sample series; the first sample series exhibits a microstructure consisting of inhomogeneously mixed large and small grains, while the other series includes highly porous samples consisting of almost identical sized grains. Electrical transport, thermal conductivity and Seebeck coefficient, measured for both sample series, reveal distinct thermoelectric behaviour between them. Detailed experimental data analysis show that such dissimilar thermoelectric performance can be correlated to the different microstructure among samples. It can be concluded that fine manipulation of coarse/fine grain ratio along with the high porosity could lead to enhanced thermoelectric performance of the $La_{1-x}Sr_xCoO_3$ solid solution.

High efficiency thermoelectric materials: a holistic approach from macro to nano- scale

E. C. Stefanaki[1], **E. Hatzikraniotis**[1], **Th. Kyratsi**[2] **and K.M. Paraskevopoulos**[1]

[1] Solid State Physics Section, Physics Department, Aristotle University of Thessaloniki, Greece
[2]Dept. of Mechanical & Manufacturing Engineering, University of Cyprus,1678 Nicosia, Cyprus

E-mail: elste@physics.auth.gr

The environmental impact of climate change due to the combustion of fossil fuels is becoming increasingly alarming. So the need for sustainable and eco-friendly energy conversion technology, such as thermoelectric generators (TEGs), for waste heat harvesting becomes crucial. The efficiency of a thermoelectric (TE) material depends on the figure of merit $ZT=S^2\sigma T/(k_e+k_L)$ where T, S, σ, k_e, k_L are the temperature, Seebeck coefficient, electrical conductivity and the electronic and lattice components of thermal conductivity respectively.

The state of the art efforts towards higher performing bulk thermoelectrics can be classified into two routes a) reduction of lattice thermal conductivity (k_L) through nanostructures and hetero-structures [1] and b) band engineering to achieve higher S and σ [2]. These two trends were combined together in an all-scale hierarchical approach [3]. Recently, a combination of synergistic approaches including all-scale hierarchical architectures, intra-matrix band engineering and matrix/inclusion band engineering was also, presented [4]. The standard characterization procedure of TE materials is the measurement of S, σ, k with temperature and the definition of the optimum operation temperature that is designated by the peak of T-ZT curve.
In this work is developed an analytical characterization procedure, beyond the limits of the typical one described above, and as an example, a high performing (ZT=1.4 @ 800K) TE material, Bi-doped $Mg_2Si_{0.55}Sn_{0.4}Ge_{0.05}$, studied across all length –scales, from macro-scale to atomic-scale (Fig.1) will be extensively discussed. The techniques applied include X-ray Diffraction (XRD), Scanning Electron Microscopy with Electron Diffraction Spectroscopy (SEM/EDS), Fourier Transform Infrared spectroscopy (FTIR) and micro-FTIR, Scanning hot probe Seebeck (SHP), conductivity and Hall-effect measurements, Transmission Electron Microscopy (TEM) and High Resolution TEM (HR/TEM) [5]. All results support the existence of both nano-structure and hetero-structure in this high ZT material, with a phase separation in four groups of different composition: the major phase-matrix, Sn-rich, Si-rich and Ge-rich phase [6].

TE materials are heavily doped semiconductors, where unintentional phase and dopant separations that create local variations and in-homogeneities in the composition and the TE parameters may occur during the synthesis process. An innovative process towards tracing in-homogeneities in TE materials using as a probe the mapping of plasmon frequency (ω_p) (Fig.2a), SEM/EDS and Scanning Hot Probe measurements is also presented (*S*) (Fig.2b) [7]. A better understanding of the band structure of a TE material can be revealed through a Pisarenko plot (Seebeck coefficient vs carrier concentration) and the theoretical curve that best describes the experimental data based on a specific model (single parabolic, non parabolic or multiple band model). Such a plot and analysis is also presented towards the deeper understanding of the band structure of TE materials and the calculation of the effective mass (m^*_s) (Fig.3).

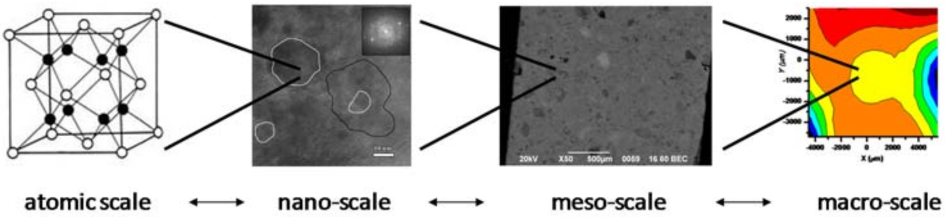

Figure 1: Structure & properties from macro to atomic scale.

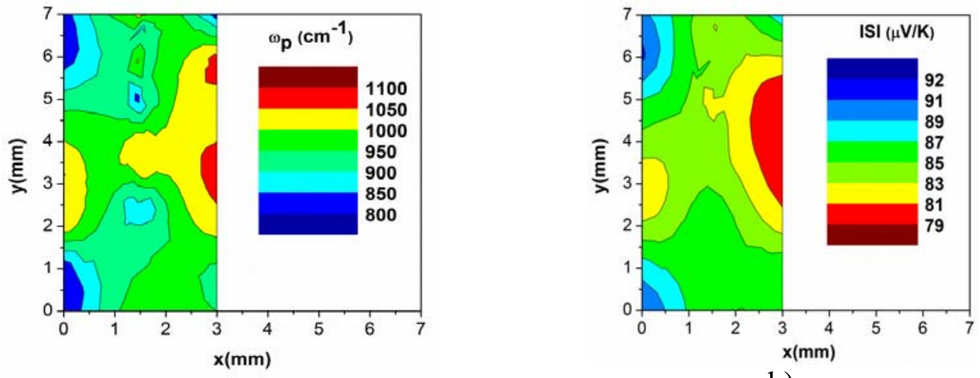

a)

b)

Figure 2: Tracing in-homogeneities in TE materials with a) plasmon frequency (ω_p) and b) Seebeck coefficient, providing the same trend; higher ω_p lower Seebeck coefficient S (in absolute values).

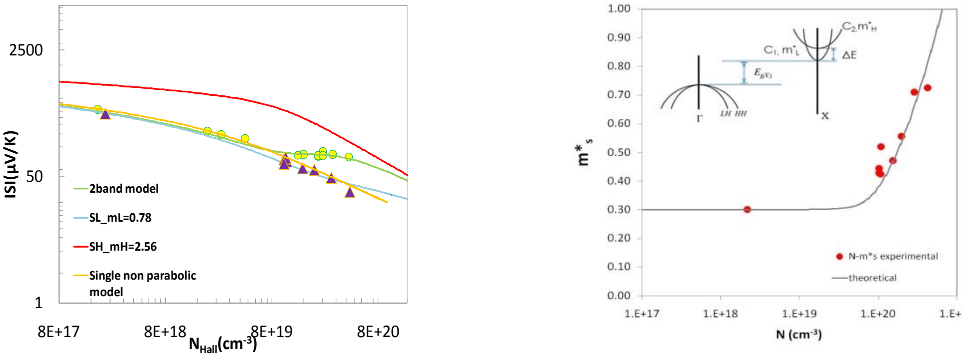

a)

b)

Figure 3: a) Fitting of Pisarenko plot of $Mg_2Si_{1-x}(Bi,Sb)_x$ (triangles) and $Mg\text{-}Si_{1-x-y}Sn_xGe_y$ $(Bi,Sb)_z$ with a two band model and a single non parabolic model. b) Susceptibility effective mass (m^*_s) versus carrier concentration. The inset shows a schematic of the band structure of $Mg_2Si_{1-x}Sn_x$ solid solutions.

References

[1] K. Biswas, J. He, Q. Zhang, G. Wang, C. Uher, V.P. Dravid and M.G. Kanatzidis, Nat. Chem. 3 (2011) 160-166.

[2] Y. Pei, X. Shi , A. LaLonde, H. Wang, L. Chen and J. Snyder, Nature 473 (2011) 66-69.

[3] K. Biswas, J. He, I. D. Blum, C. I. Wu, T. P. Hogan, D. N. Seidman, V. P. Dravid, and M.G. Kanatzidis, Nature 489 (2012) 414-418.

[4] L. D. Zhao, V. P. Dravid and M. G. Kanatzidis, Energy Environ. Sci. 7 (2014) 251-268.

[5] G. S. Polymeris, N. Vlachos, A. U. Khan, E. Hatzikraniotis, Ch. B. Lioutas, A. Delimitis, E. Pavlidou, K. M. Paraskevopoulos and Th. Kyratsi, Acta Mater. 83 (2015) 285-293.

[6] A. U. Khan, N. V. Vlachos, E. Hatzikraniotis, G. S. Polymeris, Ch. B. Lioutas, E. C. Stefanaki, K. M. Paraskevopoulos, I. Giapintzakis and Th. Kyratsi, Acta Mater. 77 (2014) 43-53.

[7] E. C. Stefanaki, G. S. Polymeris, P. M. Nikolic, Ch. Papageorgiou, E. Pavlidou, E. Hatzikraniotis, Th. Kyratsi, and K. M. Paraskevopoulos, J. Electron. Mater. 43 (2014) 3785-3791.

Efficient Si-based solar cell using aluminum induced crystallization and doping

V. Gianneta[1], A. G. Nassiopoulou[1], C. Gkanatsiou[2] and N. Vourountzis[2]

[1]NCSR Demokritos, INN, Patriarchou Grigoriou & Neapoleos 15310, AghiaParaskevi, Attiki, Athens, Greece
[2] Department of Physics, Aristotle University of Thessaloniki, University Campus, 54124 Thessaloniki, Greece
E-mail: v.gianneta@inn.demokritos.gr

Third generation Si-based thin film solar cells constitute an interesting solution towards lowering cost of a solar cell without significantly lowering device efficiency. An interesting solution towards this goal is Al-induced crystallization (AIC) and simultaneous doping of a thin amorphous Si layer [1]. The resulting p-doped polycrystalline Si layer can be used as the absorber of a thin film solar cell. The substrate may be either Si or a different, lower cost, substrate, e.g. quartz. By using an n-type Si substrate, after the AIC process a p^+n junction is directly formed.
In this work, we fabricated AIC layers on an n-type Si wafer starting from the deposition of a 20 nm thick amorphous Si layer, deposited by sputtering, and following with a 10 nm thick Al layer, deposited by electron gun evaporation. Extended annealing at 430°C for 4h, followed by a second step at 500°C for 2h, resulted in a highly-doped p-type layer. The doping level of the p^+ layer was measured to be: 2.45E-18cm^{-3}. This value derived from capacitance-voltage (C-V) measurements.

Transmission electron microscopy was used to investigate the structure of the AIC layers. This analysis revealed the high crystallographic quality of the layers, composed of large crystals in the x-y plane, grown preferentially in the (111) Si crystallographic orientation. Fig. 1 shows an example of cross sectional high resolution transmission electron microscopy (HR SEM) image of the AIC film. The as-grown amorphous Si film was partially crystallized, with the top layer composed of large crystals in the x-y plane with sizes from 100 nm up to 1.3μm, their growth following the (111) crystallographic orientation. Underneath this layer there is an amorphous layer with some embedded nanocrystals at the interface with Si, with sizes smaller than those of the top layer, following in that case the (100) crystallographic orientation of the Si substrate.

Starting from the above AIC layer as absorber, we fabricated Si-based solar cells using a simple architecture, in which the 1 cm^2 solar cell area was confined within a 100 nm thick field oxide. An Al grid was used as gate metal and an ohmic contact was formed on the backside of the wafer. Electrical and photoelectric measurements were performed in order to characterize the solar cells. An example of current-voltage characteristics is shown in Fig. 2. Good performance of the solar cell was achieved, with a short current density at 33.05 mA, Voc = 0.440 V and fill factor FF=61%. The above characteristics were obtained without any additional antireflective coating, the AIC layer providing itself such antireflection.

The solar cell efficiency was 8.9%, which is higher that the best reported so far in the literature using the above technique and much more complicated process steps [2].

The obtained results are very promising if we take into account the simple process used and the low cost of fabrication, involving only low temperature processing.

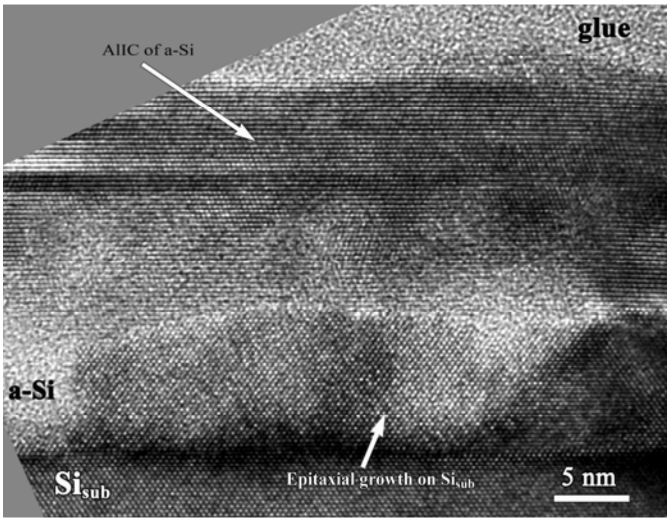

Figure 1: Cross sectional TEM images of the 20 nm thick α-Si layer crystallized by inverse AIC-Si. It is clearly shown that the AIC film is composed of a two-layer structure, with the top crystallized layer showing (111) preferred orientation and the bottom layer being amorphous, and containing small Si crystals at the interface with Si, following the (100) crystallographic orientation of the substrate.

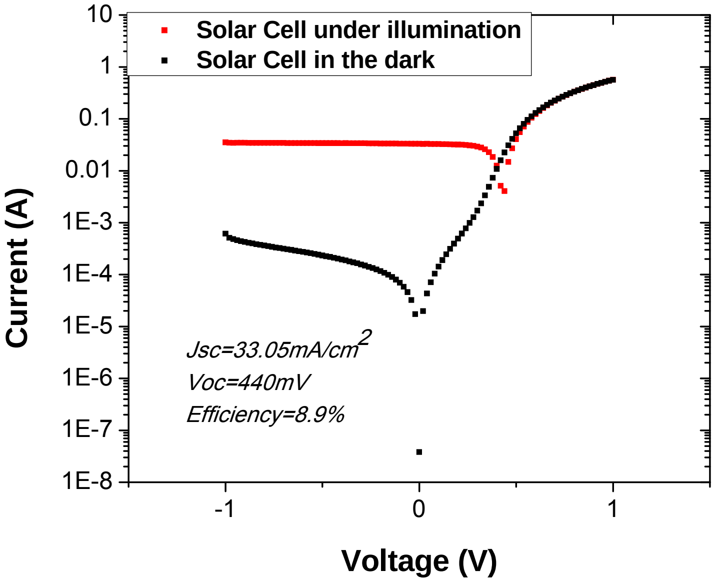

Figure 2: I-V curves in the dark (black curve) and under illumination (red curve) of the solar cell.

References

[1] S. Gardelis, A. G. Nassiopoulou, P. Manousiadis, N. Vouroutzis, and N. Frangis, Appl. Phys. Lett., 103 (2013) 241114.

[2] Y. Qiu, O. Kunz, S. Venkatachalam, D. Van Gestel, R. Egan, I. Gordon, J. Poortmans, presented at EU PVSEC, Valencia Spain, 6-10 September, 2010.

InN bandgap determination in low electron concentration films

A. Adikimenakis[1], M. Androulidaki[1], K. Tsagaraki[1], S.A. Kazazis[2], E. Iliopoulos[1,2], A. Bairamis[1,2],N.T. Pelekanos[1,3] and A. Georgakilas[1,2]

[1]Microelectronics Research Group, IESL/FORTH, P.O. Box 1385, 71110 Heraklion, Greece
[2]Physics Department, University of Crete, P.O. Box 2208, 71003 Heraklion, Greece
[3]Materials Science and Tech. Department, University of Crete, P.O. Box 2208, 71003 Heraklion, Greece

E-mail: alexandr@physics.uoc.gr

The present paper focuses on the bandgap determination of undoped InN films with low electron concentration. Sufficiently thick InN (0001) thin films were grown by plasma assisted MBE (PAMBE) and were investigated by optical spectroscopies for an improved determination of the actual InN bandgap.

More specifically, 5.0 - 5.7 μm-thick InN films (as determined by cross section SEM measurements) have been grown on c-plane sapphire substrates, using a thin AlN nucleation layer, followed by a thin GaN buffer layer. The InN films were, then, grown at ~400 °C, under stoichiometric growth conditions (Indium/Nitrogen flux ratio = 1). Throughout the entire growth time, special care was taken to maintain this growth condition, in order to avoid indium accumulation on the surface.

SEM and AFM scans revealed smooth InN surfaces with low surface roughness, but some shallow pits were evident on the surface. Single magnetic field Hall effect measurements, at room temperature, indicate an electron concentration of $9.6\text{x}10^{17}$ cm^{-3} with mobility of 1516 cm^2/Vs, if the electrons are homogenously distributed within the entire InN film. Relatively narrow HR-XRD curves were recorded, with a FWHM of 698 arcsec for the (0002) reflection. The c and a lattice constants of the InN film were determined using the extended Bond method, and they were found to be c=5.7035Å, and a=3.537Å, respectively. These values suggest that the InN film is unstrained.

The fundamental band gap and the optical properties of the InN films where studied by transmittance (T), reflectance (R), photoluminescence (PL) and spectroscopic ellipsometry (SE) measurements. First, the absorption coefficient (α) was calculated from T and R measurements, following the Swanepoel model, as well as by SE measurements. The band edge was extrapolated from the plot $(\alpha E)^2$ vs E , and it was found to be 0.636 eV. PL emission could not be recorded at room temperature. The 20K PL spectra were dominated by two peaks, with energies of 0.681 and 0.668 eV, and FWHM of 11 and 24 meV, respectively.

The results suggest that the room temperature InN bandgap is ~0.636 eV or less, depending on the actual bulk electron concentration and the resulting Burstein-Moss shift. Additional experimental work is planned to further analyze the electronic and optical properties of the InN layers.

Acknowledgement: This work has been supported by the ESPA ARISTEIA program, project "NITROHEMT"

Porous Si thermal conductivity in the temperature range 5-350K

K. Valalaki and **A.G. Nassiopoulou**

NCSR "Demokritos", Institute of Nanoscience and Nanotechnology (INN), Terma Patriarchou Grigoriou, Aghia Paraskevi, 15310, Athens, Greece

E-mail: k.valalaki@inn.demorkitos.gr

Highly porous Si (pSi) is a material composed of interconnected Si nanowires and nanocrystals separated by voids. Due to its structure and morphology, it shows much lower thermal conductivity than that of bulk crystalline Si, which is even below the amorphous limit at porosities exceeding 60%. The low thermal conductivity of Psi makes it a promising material for on-chip thermal isolation with many reported applications [1,2].

We measured temperature the dependence of thermal conductivity of porous Si (pSi) with porosities 63% and 72% prepared by electrochemical etching of bulk c-Si. PSi layers with different morphologies (Fig. 1) were measured in the temperature range 5-350K using two different methods – the 3ω method and the DC method with consequent FEM analysis.

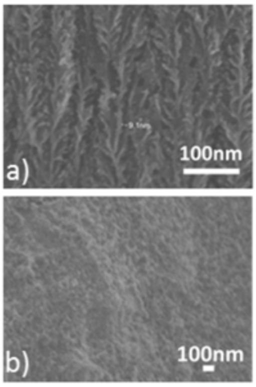

Figure 1: SEM cross sectional image of an anisotropic pSi layer with 72% porosity and vertical dendritic-like pores (a) and an isotropic pSi layer with 63% porosity and sponge like structure.

The test structure for our measurements is shown schematically in Fig.2. Our experimental results for pSi thermal conductivity of anisotropic layer with dendritic-like pores and 72% porosity are summarized in Fig. 3 for two layer thicknesses (40μm and 100μm). As it can be seen, there is very good agreement between the results from the two studied methods. Moreover, there is a monotonic increase of pSi thermal conductivity with temperature, in the temperature range 20-350K, while below 20K the thermal conductivity tends to reach a constant value. This behavior is common to amorphous solids and disordered materials and it results from the pSi structure approaching that of an amorphous material (composed of a skeleton of interconnected nanocrystals and nanowires, covered by a native oxide shell and separated by voids).

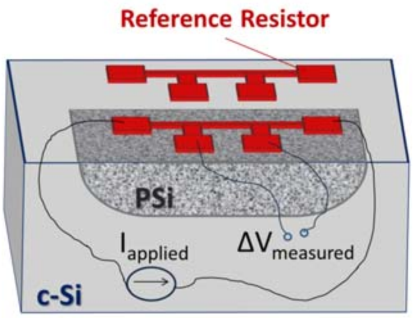

Figure 2: 3D representation of the test structure to measure thermal conductivity with both methods used.

The second pSi layer measured was more homogenous and isotropic than the above, having a sponge-like morphology and 63% porosity (see Fig. 1). The measured thermal conductivity values of this layer are presented in Fig. 4, in comparison to the above studied layer. It is clearly deduced from Fig. 4 that the temperature dependence of thermal conductivity of this sample is similar to that of the 72% porosity sample, with a plateau at ~0.04W/m.K below 20K [3] and a monotonic increase above this temperature [4]. This sample showed lower thermal conductivity than the previous one in the whole temperature range studied. This is attributed to its structure and morphology, which is more close to an amorphous phase. In the case of the anisotropic sample, its cross plane thermal conductivity (due to the existence of heat conductive paths) is much larger than its in-plane one. As a result, the temperature increase measured on its surface is lower than that of the isotropic sample. This was also confirmed with FEM analysis simulations.

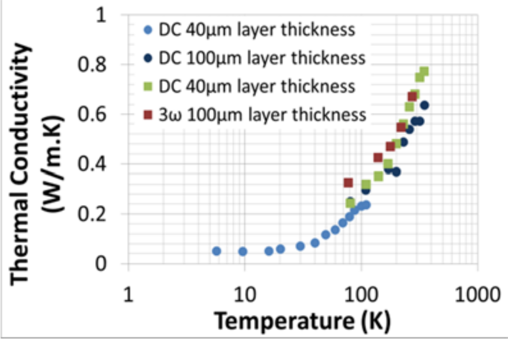

Figure 3: Temperature dependence of thermal conductivity of anisotropic pSi layers measured with both DC and 3ω methods.

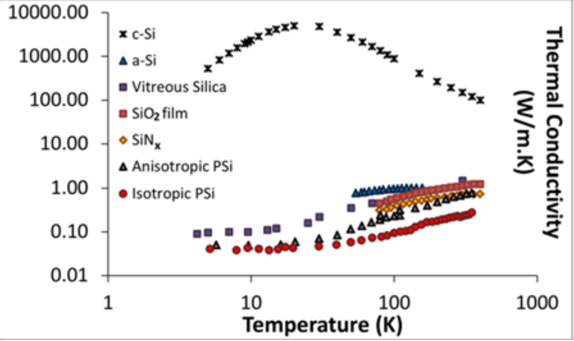

Figure 4: Thermal conductivity of the pSi layers studied compared to that of c-Si, a-Si, SiO_2 and SiN_χ layers, taken from the literature (see refs. 3, 4).

Fig 4 shows a comparison of the thermal conductivity of the two pSi layers studied with that of c-Si, a-Si, SiO_2 and SiN_χ layers, taken from the literature. Both pSi layers have much lower thermal conductivity than that of bulk c-Si and this difference exceeds four orders of magnitude at low temperatures. Their thermal conductivity is also lower than the other Si-technology-compatible materials of Fig. 4 (most commonly used thermal insulators). The extremely low values of pSi thermal conductivity are attributed to four basic factors: the presence of air inside the pores, the dioxide covering the nanostructures of the porous Si skeleton, phonon confinement in Si nanostructures composing porous Si due to their small size and phonon-wall scattering.

To summarize, we measured the thermal conductivity of two different pSi samples by two different measurement methods. Our results show that pSi thermal conductivity is lower than or comparable to that of the majority of known low thermal conductivity Si-technology-compatible materials in the literature. This is valid in the whole temperature range 5-350K. From the above, it is clear that pSi is an excellent choice for use as a local substrate on the Si wafer for local thermal isolation and thermal device integration.

References

[1] E. Hourdakis and A.G. Nassiopoulou, Sensors (Basel) 13 (2013) 13596 .
[2] E. Hourdakis, P. Sarafis, and A.G. Nassiopoulou, Sensors (Basel) 12 (2012) 14838.
[3] K. Valalaki and A.G. Nassiopoulou, Nanoscale Res. Lett. 9 (2014) 318.
[4] K. Valalaki and a G. Nassiopoulou, J. Phys. D. Appl. Phys. 46 (2013) 295101.

SESSION MO4

MAGNETISM AND SUPERCONDUCTIVITY

Monday, 21 September 2015, 17^{00}-19^{00}

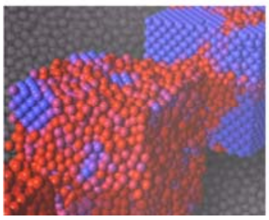

XXXI Panhellenic Conference on
SOLID STATE PHYSICS &
MATERIALS SCIENCE
Thessaloniki, 20-23 September 2015

Tuning Magnetism in Nanostructures by Interface Design

U. Wiedwald[1], S. Liébana-Viñas[1,2], M. Spasova[1], R. Salikhov[1], A. Elsukova[1], J. Perl[1], B. Zingsem[1], A. S. Semisalova[1,3], B. Arvan[1], X. Yao[1], M. Farle[1] V. Salgueiriño[2], C. Bran[4], E. M. Palmero[4], M. Vazquez[4], P. Toson[5] and J. Fidler[5]

[1]Faculty of Physics and Center for Nanointegration (CENIDE), University of Duisburg-Essen, 47057 Duisburg, Germany
[2]Departamento de Física Aplicada, Universidade de Vigo, 36310, Vigo, Spain
[3]Helmholtz-Zentrum Dresden-Rossendorf, Bautzner Landstr. 400, 01328 Dresden, Germany
[4]Institute of Materials Science of Madrid, CSIC, 28049 Madrid, Spain
[5]Institute of Solid State Physics, Vienna University of Technology, 1040 Vienna, Austria

E-mail: ulf.wiedwald@uni-due.de

Magnetic nanorods and nanowires based on 3d transition metal alloys might be suitable candidates for alternative rare-earth free permanent magnets. Exploiting the alignment magnetocrystalline and shape anisotropy axes in conjunction with exchange bias is one strategy for maximized hysteretic energy products.

In this contribution we report on $Co_{80}Ni_{20}$ nanorods (length 52.5 nm, diameter 6.5 nm) prepared by a polyol reduction [1]. Structural, morphological, and chemical investigations revealed surface oxidized nanorods consisting of a metallic hcp CoNi core (single crystalline) and a Co-rich oxide shell with a thickness of about 2 nm (polycrystalline). The magnetic easy axis is the <0001> crystallographic direction and points parallel to the nanorods axis [2]. A Co-rich oxide shell has been formed by natural oxidation around the core with a defined crystallographic orientation, i.e. $\langle 0001\rangle_{hcp} \parallel \langle 001\rangle_{fcc}$. The magnetic characterization shows strong unidirectional anisotropy at low temperatures after field cooling while the exchange bias vanishes above T = 175 K. Interestingly, the coercive field rises by almost a factor of 2 in the temperature range 175 K < T < 250 K, before it starts decreasing again [2]. This effect is discussed within a three regime model considering superparamagnetic fluctuations of antiferromagnetic grains in the Co-rich oxide shell.

In a second example we focus on the magnetic hardening of $Fe_{30}Co_{70}$ nanowires by means of magnetic pinning at the tips of the nanowires. We observe that 3 nm FeCo oxide layers increase the coercive field by 20%, indicating that domain wall nucleation starts at the tips. Micromagnetic simulations support our experimental findings showing that the increase of the coercive field can be achieved by controlling domain wall nucleation using antiferromagnetic capping [3]. The results offer a guideline on tailoring exchange anisotropies in nanoscale systems for the enhancement of magnetic hardness.

Financial support from the Seventh Framework Programme under grant agreement no. 280670 (REFREEPERMAG), the Xunta de Galicia (Regional Government, Spain) and University Duisburg-Essen is acknowledged.

References

[1] Y. Soumare, J. Y. Piquemal, T. Maurer, et al., J. Mater. Chem. 18 (2008) 5696-5702.
[2] S. Liébana-Viñas, U. Wiedwald, A. Elsukova, et al., Chemistry of Materials 27 (2015) 4015-4022.
[3] S. Liébana-Viñas, R. Salikhov, C. Bran *et al.*, submitted

Promising features of bimetallic magnetic nanoparticles allow tuning parameters in magnetic hyperthermia application.

A. Makridis[1], **K. Simeonidis**[1], **E. Myrovali**[1], **T. Samaras**[1], **O. Kalogirou**[1],
M. Angelakeris[1], **S Liébana Viñas**[2], **Zi-An Li**[2], **U. Wiedwald**[2], **M. Spasova**[2],
M. Farle[2], **M. Tziomaki**[3], **K. Topouridou**[3], **M. P. Yavropoulou**[3] **and J. G. Yovos**[3]

[1]Department of Physics, Aristotle University of Thessaloniki, 54124 Thessaloniki, Greece
[2]Fakultät für Physik and Center for Nanointegration Duisburg-Essen (CeNIDE), Universität Duisburg-Essen, 47048,Germany
[3]Division of Molecular Endocrinology, AHEPA University Hospital, Aristotle University of Thessaloniki, 54124 Thessaloniki, Greece

E-mail: anmakrid@physics.auth.gr

Magnetic particle hyperthermia represents a least-invasive modality in cancer treatment in good synergy with standard schemes, currently under clinical trials. Heat dissipation can be exploited from magnetic nanoparticles (MNPs) under an AC magnetic field in specific tumor sites, resulting to a therapeutic outcome and driving malignant cells to destruction. In magnetic particle hyperthermia magnetic nanoparticles should possess diverse eligibility criteria. First of all, the good response to AC field variations constitutes the key issue for such biomedical applications. Up to date, various MNPs have been tested such as superparamagnetic, ferrimagnetic or even ferromagnetic in effort to optimize hyperthermia's outcome.[1] Among metal oxides ferrites, with the general formula MFe_2O_4 where M=Fe, Ni, Mn, Co, have been of particular interest as magnetization can be fine-tuned. Ferrites have always been a subject of great interest from magnetic applicability point of view due to their facile fabrication, chemical stability and more recently due to their great perspectives in biomedical applications.[2] Although issues of biocompatibility and toxicity limit the choice of materials, the use of proper coatings successfully addresses this issue.

In this study we combine manganese or cobalt ferrites with magnetite in a bimetallic nanoparticle form and cover them with citric acid in an effort to tune their magnetic profile while achieving enhanced biotolerance. The synthesis is based on the aqueous co-precipitation of proper salts, a facile, low-cost, environmentally friendly and high yield synthetic approach. Detailed structural and magnetic characterization is performed to unravel the connection of magnetic particle hyperthermia efficiency with structural and magnetic features.

The quantifiable measure of hyperthermia, i.e. the Specific Loss Power (SLP), appears strongly enhanced when two magnetic phases are combined, either Mn-ferrite or Co-ferrite with magnetite as compared to their single-phase counterparts.[3] Additionally, the SLP strongly depends on the colloidal properties (dispersion medium, concentration) and the magnetic field parameters (frequency, amplitude). After optimizing the SLP, magnetic nanoparticles of optimum efficiency undergo in-vitro testing in three cell samples: one cancer cell line and two reference healthy cell lines in order to check their performance in-vitro as shown for the representative case of cancer cell line Saos-2 in Figure 1. Figures 1a and 1b show the hyperthermia curves for in-vitro (Saos-2) samples as recorded for the 1st and 2nd run where for both nanoparticle systems, the heating curves easily enter the desirable hyperthermia region (shaded band). Figure 1d depicts room temperature hysteresis loops of bimetallic Mn and Co ferrite nanoparticles combined with magnetite where the magnetic feature enhancement due to combination of two magnetic phases in nanoparticle formulation is evidenced. Figures 1e and 1f depict the multi-pulse hyperthermia runs where again in both cases the desirable hyperthermia region (41-45°C) is achieved. Magnetic nanoparticles are incorporated in the incubation assay of the cell lines. Both bimetallic systems appear to be internalized and well tolerated by the cells lines while a versatile hyperthermia protocol (multiple pulse) seems to selectively harm the cancer cells as shown in Figures 1c and 1g where the cell viability for single-pulse hyperthermia (Fig.1c) and multiple-pulse hyperthermia cycles (Fig. 1g).

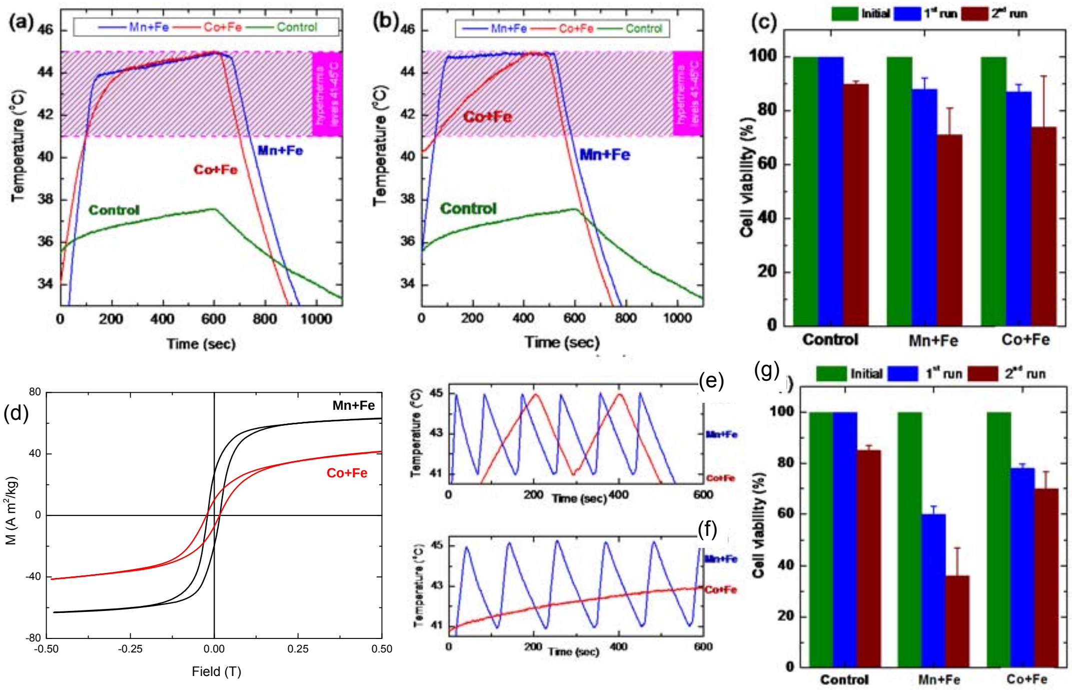

Figure 1: Saos-2 in-vitro hyperthermia sequences performed in two runs with a 48 h interval in-between: Blue/Red curves refer to cell samples incubated with bimetallic Mn+Fe/Co+Fe ferrite nanoparticles, respectively, while green curves correspond to the cell control samples. Single-pulse hyperthermia: (a) 1st run (b) 2nd run (c) cell viability assay. (d) Both bimetallic systems exhibit distinct collective magnetic features which are particularly significant for magnetic hyperthermia. Multiple-pulse hyperthermia: (e) 1st run (f) 2nd run (g) cell viability assay.

Consequently, manganese or cobalt ferrite nanoparticles combined with magnetite and covered by citric acid synthesized by a facile, high-yield, scalable approach show a great potential as magnetic particle hyperthermia agents. By fine-tuning their magnetic and structural profiles, enhanced hyperthermia features are exhibited while their low inherent toxicity as dictated by magnetite and citric acid allows them to be well internalized and mediate their cargo (heat) selectively at the malignant cellular level.

References

[1] A. Chalkidou *et al.* J. Magn. Magn. Mater. 323 (2011) 775–780.
[2] A. Makridis *et al.* J. Mater. Chem. B 2 (2014) 8390.
[3] M. Angelakeris *et al.* J. Magn. Magn. Mater. 381 (2015) 179–187.

Scaling laws analysis of magnetocaloric manganites

G. Tonozlis[*]**and G. Litsardakis**

Laboratory of Materials for Electrotechnics,
Dept. of Electrical & Computer Engineering, AUTh, Greece

E-mail: gtonozlis@sch.gr

MO4

O20

The magnetocaloric effect (MCE) consists in the temperature change of a material when it is subject to a magnetic field change. It has been used to achieve very low temperatures below 0,3 K (cooling by adiabatic demagnetization). Recently, magnetic refrigerators based on the room-temperature magnetocaloric materials have been proposed as an environmentally friendly alternative option to conventional cooling devices [1].

The temperature change in adiabatic conditions ΔT_{ad} is due to, and is proportional to the magnetic entropy change ΔS_M, which is commonly used to quantify the MCE

$$\Delta S_M(T, \Delta H) = \int_{H_i}^{H_f} \left(\frac{\partial M(T,H)}{\partial T}\right)_H dH$$

as obtained by integration of the Maxwell relation

$$\left(\frac{\partial S_M(T,H)}{\partial H}\right)_T = -\left(\frac{\partial M(T,H)}{\partial T}\right)_H$$

Since the magnetocaloric effect peaks when $\Delta M/\Delta T$ takes its maximum value, it is of great importance to study the nature of magnetic transitions in magnetocaloric materials. In terms of performance of magnetocaloric materials, it is of great importance the order of the magnetic transition, whether it is a first order magnetic transition (FOMT) or a second order one (SOMT) ; the order type is determined by the order of the derivative that is discontinuous at the transition. Numerous research groups investigate the magnetothermal phenomena in intermetallic, ceramic or even amorphous materials, belonging to one of the above mentioned categories. Although the values of magnetocaloric effect are larger for FOMT materials, the existence of hysteresis phenomena is a negative factor which limits the usefulness of a material's MCE.

Most manganites of the type $RE_{1-x}AE_xMnO_3$ display moderate size MCE values which can be attributed to second order phase transition. In this work we examine the effect of the applied field H and absolute temperature T on magnetic entropy change ΔS_M of $(La_{0.9}RE_{0.1})_{0.7}Ba_{0.3}MnO_3$ (where RE = Pr, Nd, Gd, Dy). The field dependence near the transition point was analyzed assuming a power- law relation of the type $\Delta S \sim H^n$. The exponent n depends on the magnetic state of the compound and it was locally calculated [2]. In this way a map of $n\ (T,H)$ was obtained for every compound. In figure 1 the results for the case of $(La_{0.9}Pr_{0.1})_{0.7}Ba_{0.3}MnO_3$ are presented. The exponent is roughly field independent and approaches approximate values of 2 and 1, far above and below the Curie temperature respectively.

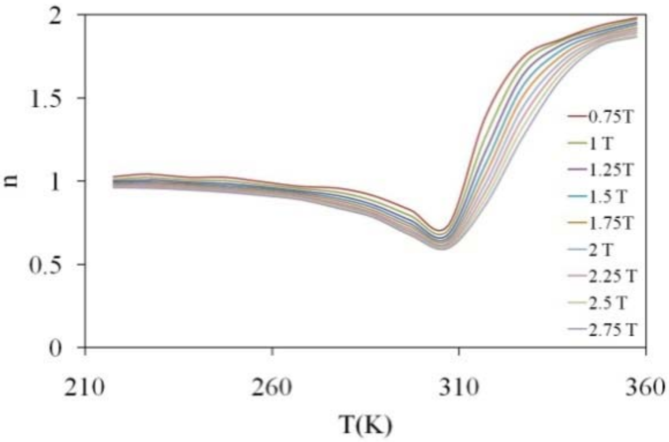

Figure 1: Field and Temperature dependence of n.

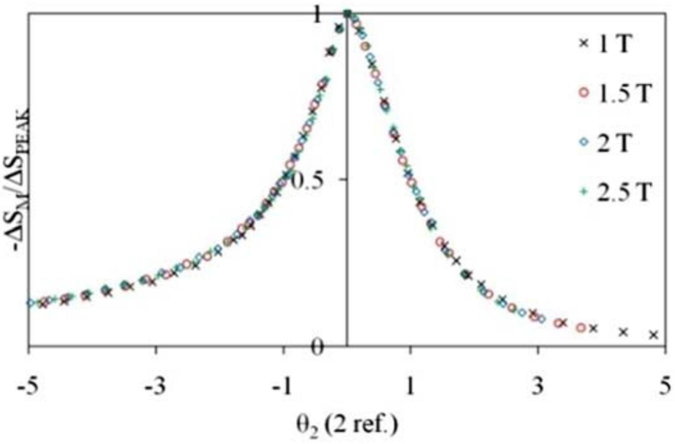

Figure 2: Universal curve for $(La_{0.9}Pr_{0.1})_{0.7}Ba_{0.3}MnO_3$

A universal curve relating ΔS_M to H and T has been proposed for materials with second order phase transitions [2]. This can be achieved by normalizing all the $\Delta S_M(T)$ curves for various field values H to their respective maximum value and rescaling the temperature axis above and below the Curie temperature setting zero at T_C [3]. In figure 2 it can be seen the collapse of magnetic entropy change data for $(La_{0.9}Pr_{0.1})_{0.7}Ba_{0.3}MnO_3$ at fields H=1, 1.5, 2, 2,5 T onto a single curve verifying the second order type of the transition.

References

[1] A. M. Tishin, I. Spichkin, The Magnetocaloric Effect and Its Applications (Bristol, IOP, 2003).
[2] V. Franco, A. Conde, Int. J. Refrigerant 33 (2010) 465 – 473.
[3] G. Tonozlis and G. Litsardakis, IEEE Transactions on Magnetics 50 (11), 6971492

MO4

INV5

Stress tensor distribution monitoring in steels using magnetic techniques

E. V. Hristoforou

National Technical University of Athens, Greece

E-mail: eh@metal.ntua.gr

A magnetic method for the monitoring of the stress tensor distribution in steels is presented in this paper. Our method is based on the controlled development of stresses using no-additive welding techniques. Implementing either plasma or TIG or electron beam welding, we can introduce residual stresses up to the positive and negative yield point of the under test steel. The monitoring of the residual stress tensor in the welded area, the heat affected zone and the base material, is obtained by the XRD Bragg-Brentano and the neutron diffraction methods for surface and bulk stresses respectively. At the points where the stress tensor is measured, the surface and/or bulk magnetic permeability tensors are also determined. The correlation of the permeability and stress tensors results in a monotonic calibration curve, unique for the different types of steels. The normalization of this curve with the gradient of magnetostriction and the yield point respectively, results in a sigmoid curve, universal for all tested steels, allowing for the development of a new physical law in magnetism and physical metallurgy. We currently investigate stresses in the atomic level by correlating the permeability tensor with dislocations and dislocation density, using the electron back scattering diffraction technique. The method is currently under standardization and has been industrially implemented in the Corinth Pipe Works, boat hulls and marine shafts, automobile steels, oil & gas etc.

Effect of pressure on the properties of iron oxypnictides: an ab initio study

E. Gkogkosi and **L. Tsetseris**

Department of Physics, National Technical University of Athens

E-mail: e.gkogkosi@gmail.com

Iron-based superconductors have drawn intense interest since their discovery in 2008 [1], as their parent or defective compounds may exhibit critical temperatures (T_c) up to 56 K [2] correlated with structural/ magnetic transitions along their phase diagram [3]. Using extensive quantum-mechanical ab initio calculations we investigate the effect of pressure on the electronic properties (and, concomitantly, on phase transitions) in the ReOFeAs compounds (Re stands for Sm, Nd or Ce). The calculations were performed within density functional theory (DFT), employing the Perdew-Burke-Ernzerhof (PBE) exchange-correlation functional and ultrasoft pseudo-potentials [4, 5], as implemented in the Quantum Espresso code [6]. Plane wave basis cutoff and kpoint-grid were set at 60 Ry and 20x10x10 Monkhorst pack grid respectively, on the grounds of convergence control. The cell parameters and ionic positions were relaxed and found within 2% deviation from reported values in the literature [7]. Density of States (DOS) calculations were verified against the extensively studied LaOFeAs compound (Fig.1).

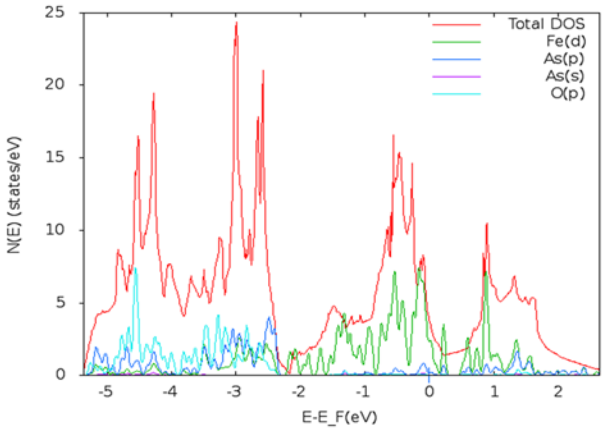

Figure 2: Total & local projected DOS for the LaOFeAs.

DOS and band structure calculations were performed for the stress-free and hydrostatically compressed unit cell. In the DOS diagram for SmOFeAs, peaks start shifting towards the Fermi level at 4 GPa and become intense at 8 GPa (Fig. 2a). The effect of pressure on band structure is even more distinct (Fig. 2c). According to Raman spectroscopy studies [3, 8] small deviation from linearity in vibrations lies at 4.5 GPa (due to second order contributions to the stronger Sm mode) and a possible lattice anomaly at pressure higher than 6 GPa (where the compound may become superconducting). Similarly, electronic profile of CeOFeAs is altered when 8 GPa are reached (Fig. 2b). As reported in the literature, Ce-containing compounds undergo structural transition at the pressure of 13.9 GPa [9].

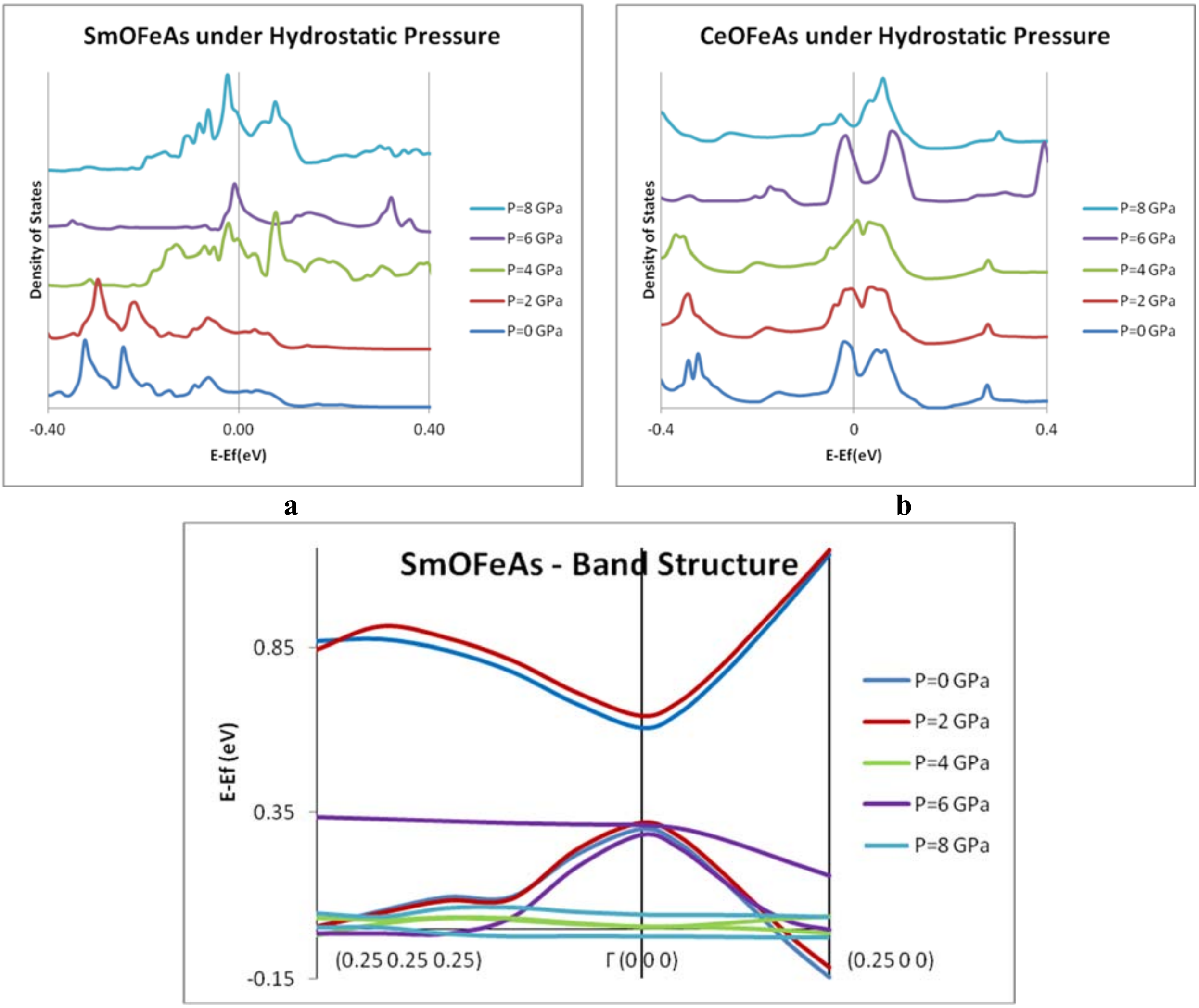

a b

c

Figure 3: Effect of hydrostatic pressure on DOS/Bands of SmOFeAs (a,c) and CeOFeAs (b).

Concluding, with the application of increasing hydrostatic pressure, alterations in electronic properties precede those of structural nature and may therefore trigger the phase transitions encountered among these compounds.

References

[1] Y. Kamihara, T. Watanabe, M. Hirano, and H. Hosono, J. Am. Chem. Soc. 130 (2008) 3296.
[2] R. Pöttgen, and D. Johrendt, Z. Naturforsch. B 63 (2008) 1135.
[3] E. Liarokapis, A. Antonakos *et al.*, J. Supercond. Nov. Magn. 26 (2013) 1325-1330.
[4] D. Vanderbilt, Phys. Rev. B, 41 (1990) 7892(R).
[5] A. M. Rappe, K. M. Rabe, E. Kaxiras, and J. D. Joannopoulos, Phys. Rev. B 41 (1990) 1227(R).
[6] http://www.quantum-espresso.org/
[7] P. Quebe, L. J. Terbuchte, W. Jeitschko, J. Alloys Compd. 70 (2000) 302.
[8] E. Liarokapis *et al.*, J. Phys. Chem. Solids, 74 (2013) 1465–1469.
[9] J. Zhao, H. Liu *et al.*, Inorg. Chem. 52 (2013) 8067−8073.

Processing of anisotropic MnBi nanoparticles by surfactant assisted ball milling

K. Kanari[1], C. Sarafidis[1], M. Gjoka[2], D. Niarchos[2] and O. Kalogirou[1]

[1]Dept. of Physics, Aristotle University of Thessaloniki, 54006 Thessaloniki, Greece
[2] INN, NCSR Demokritos, Athens 15310, Greece

E-mail: hsara@physics.auth.gr

Nowadays, the field of magnetic applications is dominated by high performance permanent magnets based on rare-earth metals, due to their high values in maximum energy product, as high as 56 MGOe [1]. However, the high cost along with the limited supplies of rare-earth elements resulted in research trying to find potential substitutions, free of any rare-earth magnets. Unfortunately, the rare-earth-free permanent magnets have exhibit low energy products, a key characteristic for advanced applications, that is necessary to improve [2].

The intermetallic compound MnBi is a rare-earth-free, promising permanent magnetic material, with unique structure and temperature-dependent magnetic properties that recently has attracted a lot of interest. The low temperature phase (LTP) has a large magnetocrystalline anisotropy ($K \approx 10^7$ erg cm^{-3}) [2] due to its hexagonal NiAs crystal structure and a positive temperature coefficient of coercivity H_C [3], which makes it an excellent candidate for high temperature applications. The unique temperature dependent behavior of MnBi is a result of the variation of the crystal lattice ratio of c/a with temperature [1].

Due to the peritectic reaction of Mn with Bi, which leads Bi to segregate from MnBi below the temperature of 446 ºC [3], it is a rather challenging task to prepare single-phase particles of MnBi. A lot of conventional methods have been used, such as arc-melting, rapid solidification and sintering, with the best results, more than 90% of the LTP MnBi coming from melt-spinnin.[4] In our research we are following a mechanochemical approach, with surfactant assisted ball milling using Fritsch Pulverisette mill. First, MnBi ingots were arc-melted under Ar atmosphere and they were subsequently annealed, to optimize the dispersion of Mn and Bi inside the ingots. Then, they were grinned, until the particles were smaller than 50 μm. The MnBi powder was mechanically milled along with oleic acid, as the surfactant and hexane as the dispersant. The BPR was 10:1 and the time of milling varied, from 30 to 170 minutes. The particles of each sample were left to dry in air and then were characterized. The crystal structure of the as-milled samples as well as the initial MnBi, were examined by X-ray powder diffraction (XRD) and the total chemical composition was measured with EDS. Microstructural characterization was carried out using scanning electron microscopy (SEM) and magnetic hysteresis loops were measured using a vibrating sample magnetometer (VSM).

The results of the research were encouraging. We began with MnBi particles (Fig. 1) and size smaller than 50 μm. Samples were extracted from the mill in t= 10, 20, 25, 35, 50, 80, 170 min. It was observed that starting at 0.175 T, the coercivity of the samples is increased reaching 1.14 T at 35 min, and decreases till it becomes almost zero. In a similar tone, MnBi has magnetic remanence (M_r) of 18.05 Am^2/kg at the beginning, reaching 20.35 Am^2/kg at 20 min. As for the spontaneous magnetization, our samples have a starting value of 36.55 Am^2/kg and reach the maximum value of 37.73 Am^2/kg at 20 min. After 170 min of ball milling it was observed that the MnBi magnetization almost vanishes.

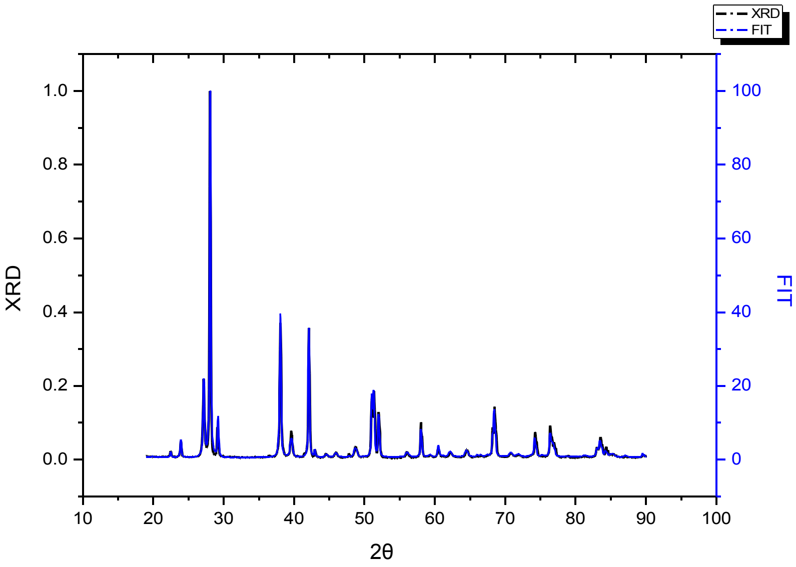

Figure 1: XRD analysis of initial MnBi powder.

This work has shown that MnBi is a very brittle material and needs only 20-35 minutes to reach its optimum magnetic properties. However, it should be noted that even with the surfactant protection, MnBi still oxidizes when left in air, which ultimately alters its magnetic properties. Compared to literature, no significant differences in the magnetic properties were found that could be attributed to the surfactant.

References

[1] Jian Shen, Huizhong Cui *et al.*, RCS Adv. 5 (2015) 5567-5570.

[2] N.V. Rama Rao, A.M. Gabay, X. Hu and G.C. Hadjipanayis, J. Alloys Compds. 586 (2014) 349-352.

[3] Y. B. Yang *et al.*, J. Appl. Phys. 111 (2012) 07E312.

[4] N.V. Rama Rao, A.M. Gabay, and G.C. Hadjipanayis, J. Phys. D: Appl. Phys. 46 (2013) 062001-062004.

POSTER SESSION

ELECTRONIC TRANSPORT, SEMICONDUCTOR AND DEVICES

Monday, 21 September 2015, 19^{00}-20^{30}

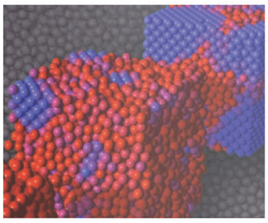

XXXI Panhellenic Conference on
SOLID STATE PHYSICS &
MATERIALS SCIENCE
Thessaloniki, 20-23 September 2015

Long-term stability and performance of photoelectrochromic devices for energy saving and power production

G. Leftheriotis, G. Syrrokostas and P. Yianoulis

Renewable Energy and Environment Lab, Physics Department,
University of Patras, Rion, 26500, Greece

E-mail: glefther@physics.upatras.gr

In recent years a considerable research effort has been directed towards materials and devices intended for the dynamic solar control of buildings (often referred to as "smart windows") [1]. Photoelectrochromic (PEC) devices are hybrids of dye-sensitized (DSSC) solar cells and electrochromics (EC), developed to combine solar energy production and dynamic windows [2]. The performance of PEC devices involves many elementary processes such as electron injection, diffusion and recombination within the dye-sensitized TiO_2 film, Li ion diffusion into the EC WO_3 film, catalysis of the I^{3-} reduction on the Pt counter electrode, regeneration of the light absorbing N719 dye, and others, as shown in Fig. 1a.

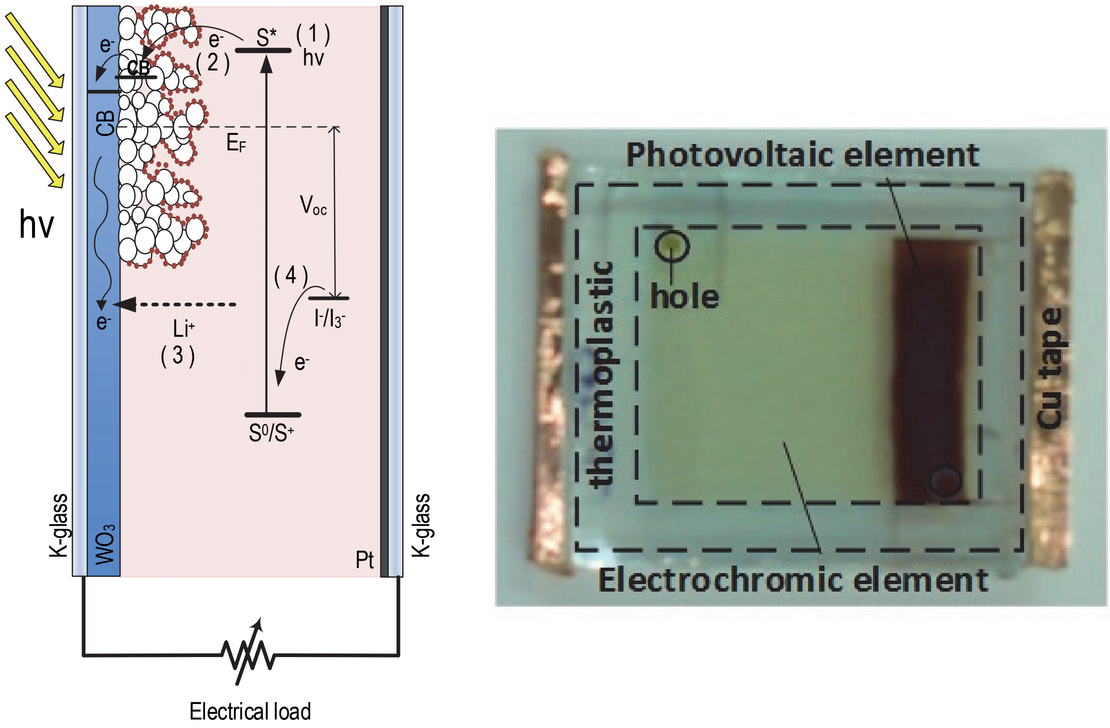

Figure 1: a) Sketch of a PEC device and the processes involved (shown in parentheses): absorption of photons by the dye (1), injection of photoelectrons in TiO_2 and electron diffusion into WO_3 (2), intercalation of Li^+ into the WO_3 layer for charge equilibration (3), causing coloration of the WO_3 film, regeneration of dye molecules by iodide ions (4), b) Picture of a fabricated PEC device.

These combine to give the overall device performance, which also depends on "macroscopic" factors, such as the efficiency of the DSSC element, the thickness and morphology of the electrochromic film, the relative area of DSSC and EC parts, and many others.

In this work, a systematic experimental study is presented, carried out to determine the influence of each of the above factors. For the characterization of materials and devices, various electrochemical techniques have been used, such as cyclic voltammetry, galvanostatic intermittent titration, (GITT), chornoamperometry, etc, in conjunction with electrical and optical methods. Thus, optimum device architectures were developed. Furthermore, the long term stability of the devices was investigated by prolonged exposure and cycling, in order to reveal possible degradation mechanisms.

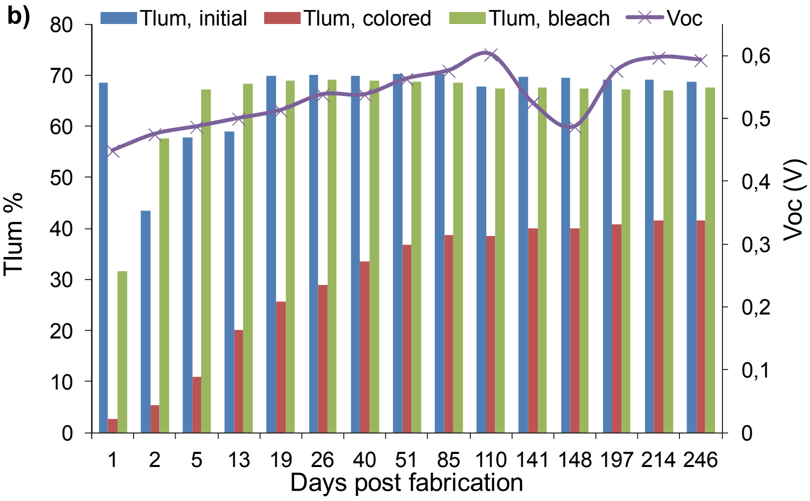

Figure 2: Luminous transmittance (T_{lum}) and open circuit voltage (V_{oc}) *vs.* days post fabrication of a device with K-glass/WO_3/TiO_2 anode annealed at 100 °C and the 0.5 M LiI/0.005 M I_2/0.5 M 4-TBP/ACN.

This process has led to reversible devices with shelf life exceeding 8 months, as shown in Fig. 2. The best materials combination thus far is a K-glass/WO_3/TiO_2 anode annealed at 100 °C and an electrolyte consisting of 0.5 M LiI/0.005 M I_2/0.5 M 4-TBP/ACN [3]. Electrolytes specifically designed for PEC devices need to be developed for optimum operation.

Acknowledgments: Financial support by the “ARISTEIA-I” Action of the “Operational Programme Education and Lifelong Learning” co-funded by the European Social Fund (ESF-EU) and National Resources (Greece), through the project ′′COOL-NANO′′ No 733, is gratefully acknowledged.

References

[1] C.G. Granqvist, Thin Solid Films 564 (2014) 1–38.
[2] G. Leftheriotis, G. Syrrokostas, P. Yianoulis, Sol. Energy Mater. Sol. Cells 96 (2012) 86–92.
[3] G. Syrrokostas G. Leftheriotis P. Yianoulis, Solid State Ionics 277 (2015) 11–22.

Dopant-defect interactions in Ge and GeO_2: density functional theory calculations

A.Chroneos[1,2] and Y. Panayiotatos[3]

[1]Department of Materials, Imperial College London, London SW7 2BP, United Kingdom
[2]Faculty of Engineering and Computing, Coventry University, Priory Street, Coventry CV1 5FB, United Kingdom
[3]Department of Mechanical Engineering, TEI of Piraeus, P.O. Box 41046, Athens 12201, Greece

E-mail: gpana@teipir.gr

Germanium (Ge) is being actively considered by the semiconductors community as a mainstream material for nanoelectronics applications. This is driven by its advantageous materials properties, however, the defect processes in Ge are not as well understood as compared to other materials such as silicon. Recent developments in the study of impurities including dopant-defect interactions, diffusion and point defect engineering are considered. The focus is on technologically important *p*-type, *n*-type dopants but also important impurities such as oxygen (O) are also discussed.

The improvement of the electron mobility of devices (for example the Ge-metal-oxide-semiconductor field-effect transistor) necessitates the formation of good Ge/dielectric interfaces. Germanium dioxide (GeO_2) is reconsidered as a passivation layer for Ge, however, its O vacancies (V) need to be controlled as they have a deleterious impact on its properties. Here, we employ density functional theory calculations to investigate the introduction of trivalent ions such as aluminium (Al), yttrium (Y) and lanthanum (La) in α-quartz GeO_2. The densities of states calculations reveal that the oxygen vacancy dangling bonds introduce states in the gap. The binding energies of the AlV, YV and LaV pairs reveal that the introduction of dopants may control V in α-quartz GeO_2 and reduce the dangling bonds. It is shown in the present study that the introduction of Al will limit the concentration of oxygen vacancies at low Fermi energy.

Electrical Conduction Mechanisms of ZnO sol-gel film

T. Georgakopoulos[1], **V.Lionas**[1], **D. Karageorgopoulos**[2],
A. Apostolopoulou[2], **K. Pomoni**[1] **and E. Stathatos**[2]

[1]Department of Physics, University of Patras, 26500 Patras Greece
[2]Department of Electrical Engineering, Technological-Educational Institute of Western Greece, 26334 Patras, Greece

E-mail: tgeorgakop@upatras.gr

Abstract: The electrical conductivity of sol-gel ZnO films was investigated at temperatures from 10 to 300 K. The electrical conductivity behavior versus the inverse of temperature suggests that several conduction mechanisms act at different temperature regimes. It shows that the conduction mechanism is well described by Small Polaron Hopping (SPH) and Grain Boundary Model (GB) at the high temperature regime while Variable Range Hopping (VRH) dominates at low temperatures.

Transparent oxides thin films have been widely investigated for their interesting structural, optical and electrical performances. ZnO has attracted much attention as a promising material in recent years due to its unique properties such as a direct wide band gap on the order of 3.3 eV, for short wavelength optoelectronic devices, such as emitting diodes and laser diodes, especially as TCO in solar cells, gas sensors and acoustic devices [1].

0.183 g of Zinc chloride were dissolved in 6 ml of isopropanol (i-prOH) for the preparation of ZnO films. Then, poly(propylene glycol) bis(2-aminopropyl) ether oligomer was added under vigorous steering in a molar ratio [BAPPG]:[ZnCl2]=1/5. The mixture was heated at 80 ^{o}C and after naturally cooling down at room temperature; films were formed on borosilicate glass substrates with dip-coating from the above solution. They were finally calcined up to 500^{0}C for 15 min.

A proposed mechanism for particle formation and the role of the oligomer is presented in Fig. 1. The XRD spectra are presented in Fig. 2.

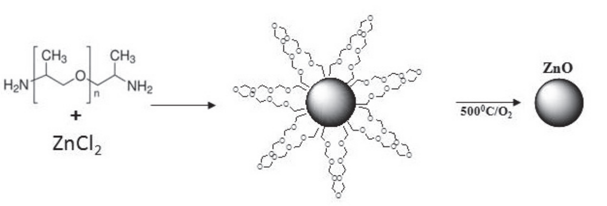

Figure 1: Scheme of the preparation procedure.

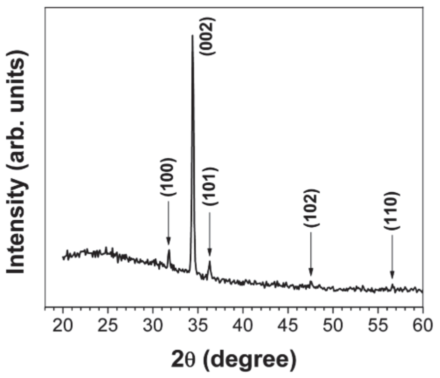

Figure 2: XRD image of the prepared ZnO film.

A highly intense peak occurs at 2θ=34.5° corresponding to the (002) reflection. The temperature dependence of the conductivity for the sample, plotted as ln(σ) versus $10^3/T$, in vacuum, is given in Fig. 3. More than one conductivity mechanisms are shown, acting at different temperature domains [2]. In the low temperature regime 45-95 K, the electrical conduction is well explained with VRH (Variable Range Hopping), illustrated in Fig. 4. The calculated values of the characteristic temperature coefficient and the density of states near EF are $T_o = 2.82\times10^4$ K and $N(E_F) = 1.41\times10^{28}\,m^{-3}eV^{-1}$, respectively. In Fig. 5, the temperature dependence of $\ln\sigma T^{3/2}$ versus $10^3/T$ suggests the SPH non-adiabatic conduction mechanism in the temperature regime 95-195 K, with an activation energy $W = 48.2$ meV. At high temperatures (200-300 K), the best linear fit was achieved using GB model (Fig. 6), indicating that grains are fully depleted of charge carriers, with an activation energy 70meV.

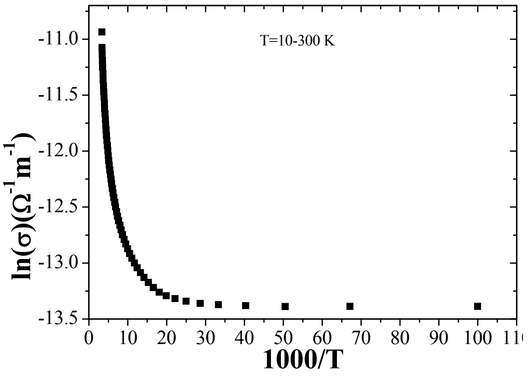

re dependence of the
ty plotted as ln(σ)
m, in the temperature

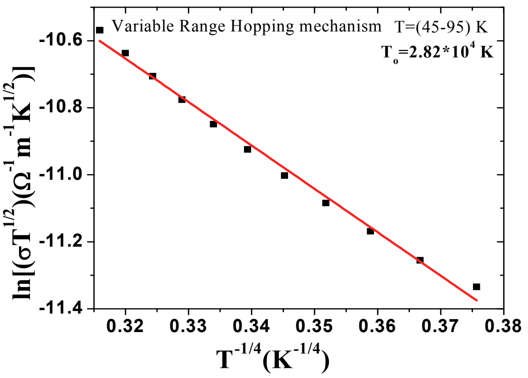

Figure 4: Temperature dependence of $\ln(\sigma T^{1/2})$ versus $T^{-1/4}$, in vacuum in the temperature range 45-95 K. Solid lines are the best fit lines.

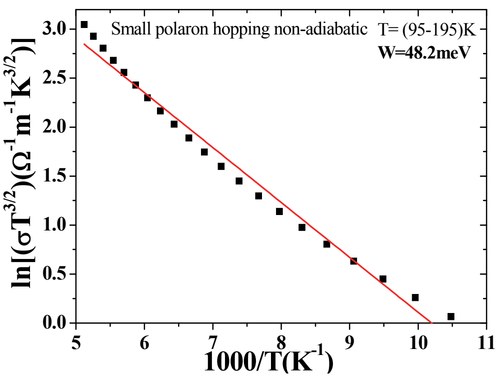

Figure 5: Temperature dependence of $\ln(\sigma T^{1/2})$ versus $10^3/T$, in vacuum, in temperature range 95-195 K. Solid lines are the best fit lines.

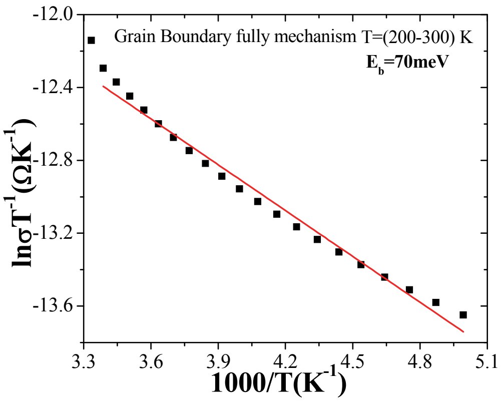

Figure 6: Temperature dependence of $\ln(\sigma T^{-1})$ versus $10^3/T$, in vacuum, in temperature range 200-300 K. Solid lines are the best fit lines.

References

[1] A. Janotti and C. G Van de Walle, Rep. Prog. Phys. 72 (2009) 126501.
[2] T. Georgakopoulos, M.V. Sofianou, K. Pomoni, and C. Trapalis, J. Alloys Comp. 586 (2014) 52–58.

Synthesis, structural characterization and complex conductivity study of $LiVO_3$

G. Alexandridis[1], C. Sarafidis[1], A. Kazakopoulos[2] and O. Kalogirou[1]

[1]Department of Physics, Aristotle University of Thessaloniki, Thessaloniki, Greece
[2]Department of Electronics, Technological Educational Institute of Thessaloniki, Thessaloniki, Greece

E-mail: hsara@physics.auth.gr

In this study pure polycrystalline $LiVO_3$ was synthesized via a solid state reaction. Impedance data of the sample were obtained for frequencies in the range 42 Hz - 1 MHz and temperatures up to 480° C during both the heating and cooling cycles and the equivalent electrical circuit was simulated for every temperature level. The elements of the equivalent circuit were assigned to relaxation phenomena either in the grains or through the grain boundaries and the corresponding activation energies were calculated.

The Li-V-O system gained a lot of scientific attention as a promising material for fuel cells and lithium ion batteries [1-2] or humidity sensors [3]. $LiVO_3$ synthesized via a solid state route has been proposed as a possible cathode material in lithium batteries [4]. In this work, conductivity mechanisms of $LiVO_3$ are studied thoroughly for the first time at temperature levels from room temperature to 480° C.

Polycrystalline $LiVO_3$ was synthesized via a solid state reaction between Li_2CO_3 and V_2O_5 at 600° C for 8 h. X-Ray diffraction data of the powdered sample were obtained using CuKa radiation and the morphology of the sample was determined by scanning electron microscopy (SEM). Impedance data were collected on cylindrical pellets made of pressurized powder using a HIOKI 3531 impedance analyzer, for 90 frequency values in the range 42 Hz - 1 MHz, at different temperature levels during both the heating and cooling cycles between RT and 480° C.

XRD diffraction pattern of the compound was indexed to pure monoclinic $LiVO_3$ phase with C2/c space group and no impurity was detected. SEM images of the sample were used to measure the average grain size which was determined to be about 50 μm within a good approximation. The impedance data were fitted using the Equivcrt program [5] and an equivalent circuit was drawn, which models the electrical behavior of the sample at each temperature (Fig.1). The equivalent circuit is in general comprised of three (R||Q) elements in series, each of which represents a unique conductivity process, specifically, relaxation phenomena of dipoles either in the bulk of the grains or through the grain boundaries or at the electrodes interface. Using the impedance data, the conductivity $\sigma(f)$ was calculated and $\sigma(f)$-f plots were drawn for each temperature level, which show that the behavior of $\sigma(f)$ obeys to the universal relaxation law proposed by A.K. Jonscher [6], which is typical to most ionic conductors. Finally, the Arrhenius plots of the conductivity mechanisms obtained by the equivalent circuits were drawn and the activation energies of the corresponding processes were calculated. As for the heating cycle, the activation energy of the bulk conductivity was found to be 0.89 eV, while the activation energy of the conductivity through the grain boundaries was calculated equal to 0.18 eV for temperatures up to 300° C, and 1.58 eV for temperatures above 300° C. Similar results were obtained during the cooling cycle except for the activation energy of the conductivity through the grain boundaries for temperatures above 300° C, which was found to be 1.25 eV.

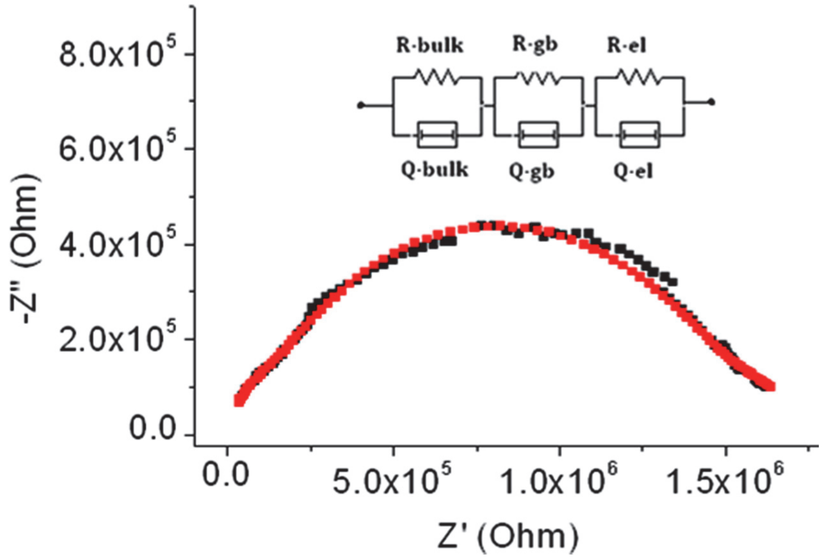

Figure 1: Impedance data at 340° C (black dots), simulation (red line) and the equivalent circuit.

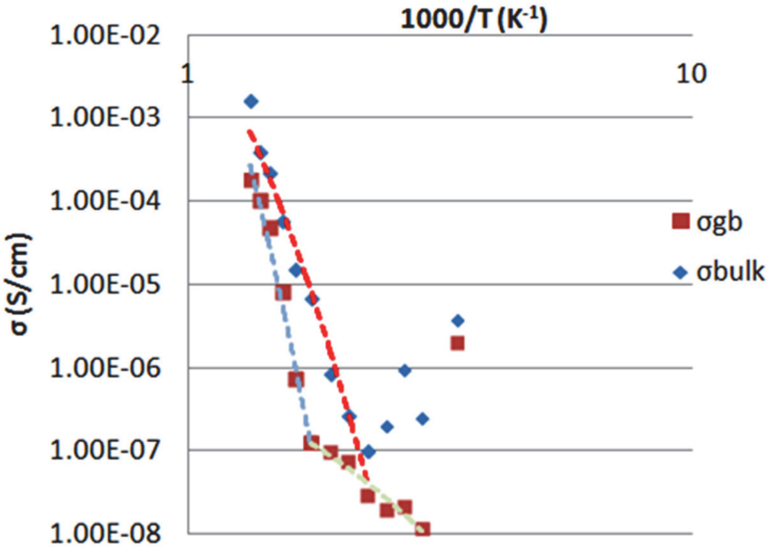

Figure 2: Arrhenius plots of the bulk conductivity (blue dots) and the conductivity through the grain boundaries (red dots).

References

[1] G.T. Fey, D. Huang, Electrochim. Acta 45 (1999) 295-314.
[2] Ch. Muller, J.-C. Valmalette, J.-L. Soubeyroux, F. Bouree, J.-R. Gavarri, J. Sol. State Chem., 156 (2001) 379-389.
[3] A. Kazakopoulos, C. Sarafidis, O. Kalogirou, Ionics 19 (2013) 1085-1090.
[4] X.M. Jian, J.P. Tu, Y.Q. Qiao, Y. Lu, X.L. Wang, C.D. Gu, J. Power Sources, 236 (2013) 33-38.
[5] Bernard A. Boukamp, Equivalent Circuit, University of Twente (1989).
[6] A. K. Jonscher, J. Phys. D: Appl. Phys., 32 (1999) R57.

MOP

P005

Modelling the multilevel resistive switching behaviour of forming free TiO_{2-x} memory devices

P. Bousoulas[1], **I. Giannopoulos**[1], **P. Asenov**[2], **I. Karageorgiou**[1] **and D. Tsoukalas**[2]

[1] School of Applied Sciences, National Technical University of Athens, Heroon Polytechniou 9, 15773 Athens, Greece
[2] School of Electrical and Computer Engineering, National Technical University of Athens, Heroon Polytechniou 9, 15773 Athens, Greece

E-mail: panbous@mail.ntua.gr

The incessant desire for device scaling has pushed both academia and industry into alternative concepts in order to meet the future information storage needs. Among the potential non-volatile memory candidates, Resistance Random Access Memories (RRAM) based on metal oxides seem to gain significant ground in the non-volatile memory race, mainly due to their simple structure and high integration density. The central notion of this type of memory is to manipulate a high-resistance-state (HRS) and a low-resistance-state (LRS) by external electrical inputs in order to store the information data “0” or “1”.

In this work we report high multilevel resistance switching at room temperature deposited TiO_{2-x} thin films, which operate without an electroforming process and exhibit self-rectifying characteristics. At least five-level resistance states have been achieved by either increasing the amplitude of the voltage pulse or controlling the compliance current (I_{cc}). The origin of the gradual transition can be found in the high number of oxygen vacancies within the dielectric matrix and a detailed description of their impact on the switching effect, can divulge valuable information of the physical underlying mechanisms that take place. Also, the Ti TE impact on the enhanced resistive switching performance is highlighted by simulation results, based on the temperature and field accelerated migration of oxygen ions, which provide a microscopic interpretation of the conducting filaments shape (Fig. 1).

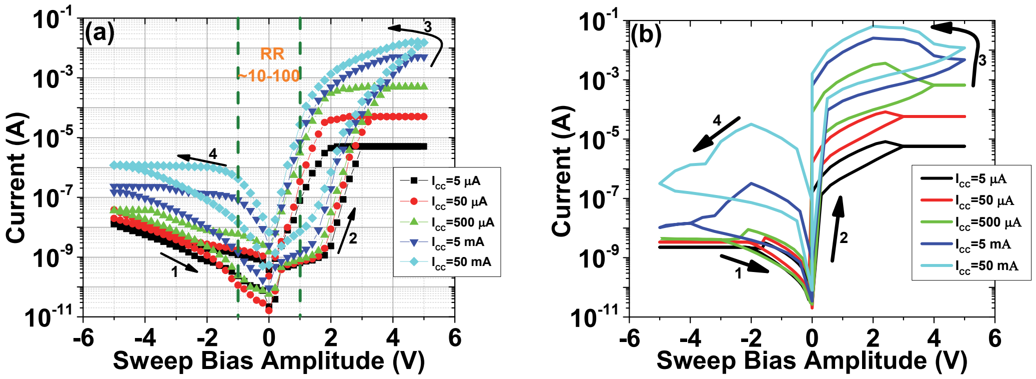

Figure 1: (a) Measured and (b) calculated I-V forward and backward sweeps, under different compliance currents, revealing the continuous transition between the HRS (forward sweep) and LRS (backward sweep). The arrows in the graph indicate the switching direction. Also rectification ratios (RR) for the LRS are presented (sweep rate 1V/s).

In order to get a better insight into the origins of the enhanced multilevel switching capability of our devices, we quantitatively investigate the ionic component of the resistive switching effect (oxygen ion migration). The transport of oxygen ions is predicted by the ion transport, carrier continuity and Joule heating equations, which were solved consistently with a numerical solver (COMSOL):

$$\frac{\partial n_D}{\partial t} = \nabla \cdot (D \nabla n_D - v \cdot n_D) + G \quad (1)$$

$$\nabla \cdot \sigma \nabla \psi = 0 \quad (2)$$

$$-\nabla \cdot k_{th} \nabla T = J \cdot E \quad (3)$$

where n_D is the concentration of defects, $D = \frac{1}{2} \cdot a^2 \cdot v_0 \cdot \exp(-\frac{E_a}{k_B T})$ the diffusivity, a the effective hopping distance (0.05 nm), v_0 the attempt-to-escape frequency (10^{13} Hz), k_B the Boltzmann constant, T the temperature, ψ the electric potential, E_a the diffusion barrier for ion migration $E_a = E_a^{formation} + E_a^{migration} = 0.3 + 1.2 = 1.5$ eV, $v = a \cdot v_0 \cdot \exp(-\frac{E_a}{k_B T}) \cdot \sinh(\frac{QEa}{2k_B T})$ the drift velocity of ions, E is the electric field and Q is the ion charge (2q for oxygen ions). In order to solve the set of equations self-consistently, inputs for electrical conductivity (σ) and thermal conductivity (k_{th}) are needed. A detailed description of the used models can be found in ref. [1], [2]. Fig. 2 presents the distribution of oxygen vacancies under the application of 5 V on the TE. Due to the oxygen gettering ability of Ti ($n_G^{Ti} > n_G^{Au}$), a larger number of oxygen vacancies is created which increases the filaments diameter. During the simulations we assume that when an oxygen ion leaves its position an oxygen vacancy is created, contributing thus to the local enhancement of the electrical conductivity. In the case of Ti TE, the conducting filaments which are created are bigger and stronger due to the higher density of oxygen vacancies. As a result, they permit more precise control of their thickness by adjusting the values of I_{cc} and pulse amplitude.

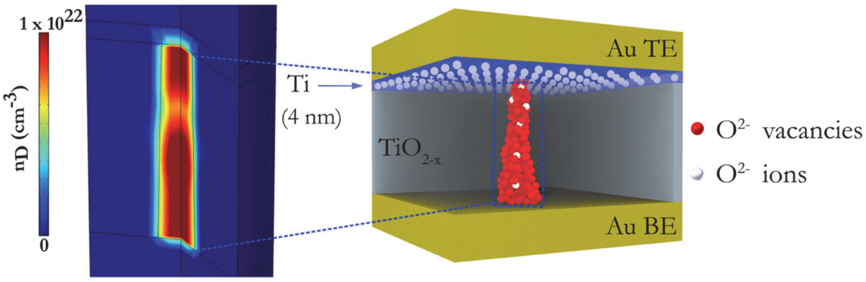

Figure 2: Calculated map of the oxygen vacancy density for Ti TE and representation of the conducting filament formation, under the application of a positive voltage bias (+5 V) at the TE.

References

[1] S. Larentis, F. Nardi, S. Balatti, D. C. Gilmer, and D. Ielmini, IEEE Trans. on Elec. Dev., 59 (2012) 2468-2475.

[2] S. Kim, S.-J. Kim, K. M. Kim, S. R. Lee, M. Chang, E. Cho, Y.-B. Kim, C. J. Kim, U. -I. Chung & I.-K. Yoo, Nat. Sci. Rep. 3 (2013) 1680.

High performance MIS capacitors using silicon nanowires by metal-assisted chemical etching

I. Leontis[1,*], **M. Botzakaki**[2], **S. Georga**[2] **and A. G. Nassiopoulou**[1]

[1] NCSR Demokritos, INN, Terma Patriarchou Grigoriou, Aghia Paraskevi, 153 10 Athens Greece.
[2]Department of Physics, University of Patras, Greece

E-mail: i.leontis@inn.demokritos.gr

An effective way to increase the capacitance density of Metal-insulator-semiconductor (MIS) capacitors is by three-dimensional (3D) structuring of the capacitor surface area. Si nanowires (SiNWs) formed on Si by metal-assisted-chemical etching (MACE) constitute a promising solution towards this goal. There are some references in the literature reporting on MIS capacitors using Si nanowires by MACE [1], however their obtained performance is questionable.

In this work, we used Si nanowires by MACE [2] formed on p-type silicon with resistivity in the range of 1-2 Ω.cm in order to fabricate high capacitance density MIS capacitors with improved characteristics. The length of the Si nanowires was 1.3 μm. In order to reduce their surface roughness, which is at the origin of the large density of interface states at the Si nanowire/dielectric interface, we applied different chemical treatments of the samples before dielectric deposition. More specifically, the samples were subjected to successive piranha/HF treatments, which act as follows: piranha chemical cleaning oxidizes the Si nanowire surface, while HF removes the formed oxide. In this way, the nano-roughness at the Si nanowire surface is smoothed out, thus reducing the density of interface states. The dielectric used in the MIS capacitor was aluminum oxide (Al_2O_3) deposited by atomic layer deposition (ALD) [2]. Its nominal thickness was 10 nm. For the MIS capacitor fabrication, a 500 nm thick field oxide was used, in which windows were opened using lithography and chemical etching for defining the device area (50x50, 100x100 and 300x300 μm^2). The nanowires were then formed within the SiO_2 windows, using a resist as mask for protecting the SiO_2 field oxide. After chemical cleaning of the nanowires as described above, the ALD alumina layer was deposited, followed by Al deposition and patterning in order to form the gate metal. A back ohmic contact was also formed. Fig. 1 (a) shows a cross sectional schematic representation of the Si nanowire MIS capacitor, while Fig. 1 (b) is a cross sectional scanning electron microscopy (SEM) image of the Si NWs after chemical cleaning, dielectric and Al deposition. The Al crystals of the metallization layer are depicted on the SiNW surface, covering in a conformal way all the NW surface, with, however, more material accumulated at their tops.

A comparative study between MIS capacitors with as-grown Si nanowires and nanowires with one or two cycles of piranha/HF chemical cleaning was performed. The Si nanowire devices were also compared to a planar reference MIS capacitor without nanowires. Capacitance-voltage (C-V), current-voltage (I-V) and conductance-voltage measurements were performed in order to characterize the devices. The major results from this study are as follows: In all fabricated devices, the leakage current at -2 V remained below 10^{-8} A/cm^2. After the two-step chemical treatment, almost no frequency dispersion was observed at accumulation, indicative of the reduction of the leakage current and the density of interface states. This is achieved by reducing the surface roughness on the nanowire surface. After the single piranha/HF treatment, a small frequency dispersion was observed. Compared to the reference sample without Si nanowires, a significant increase in the capacitance density was observed in the presence of the nanowires (from 0.6μF/cm^2 in the reference sample to 2.6μF/cm^2 in the SiNW capacitor after the two-step chemical cleaning). A slightly lower value was obtained after the single step cleaning, which will be discussed. From conductance measurements we deduced the density of interface states, which was relatively low in the case of the two-step chemical treatment. Surprisingly, the nature of states involved in the case of the single step treatment was different from that in the case of the two-step chemical cleaning. This will be discussed. An electrical model was used to determine the density of interface states of the SiNW MIS capacitors.

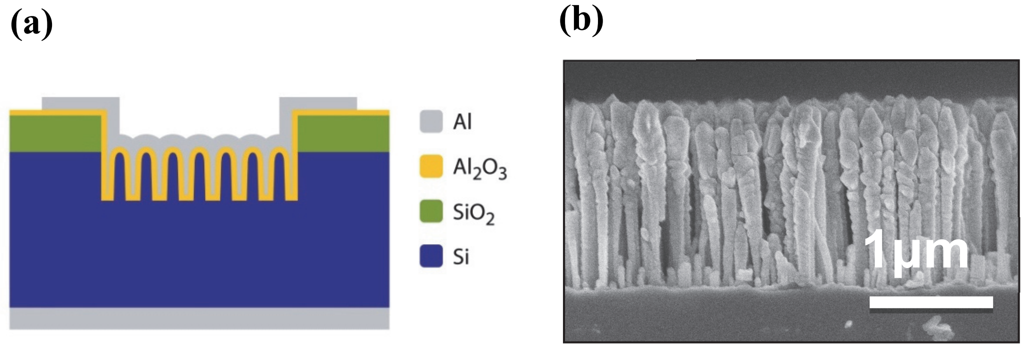

Figure 1: **(a)** Schematic illustration of the fabricated SiNWs 3d capacitors, and **(b)** characteristic cross section SEM image of the 1.3μm formed SiNWs MIS structures

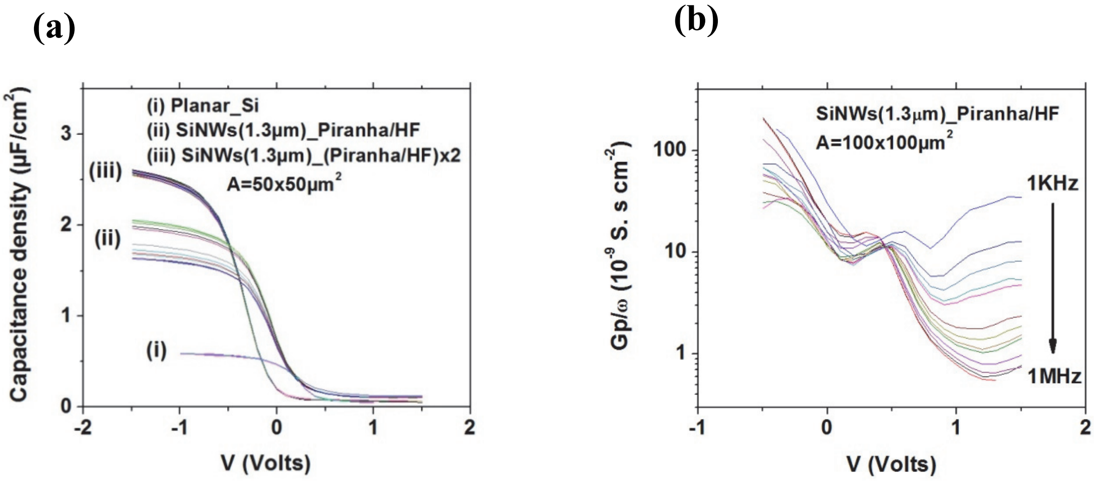

Figure 2: (a) C-V and (b) (Gp/ω)-V characteristics of the MIS capacitors studied.

References

[1] S. Chang, J. Oh, S. T. Boles and C. V. Thompson, Appl. Phys. Lett. 96 (2010) 153108.

[2] I. Leontis, A. Othonos and A. G. Nassiopoulou Nanoscale Research Letters 8 (2013) 383.

[3] M. Botzakaki, A. Kerasidou, N. Xanthopoulos, D. Skarlatos, S. Kennou, S. Ladas, S.N. Georga and C.A. Krontiras, Phys. Status Solidi C 10 (2013) 137-140.

MOS pGe/GeO$_2$/HfO$_2$/Au structures: XPS and electrical analysis

**M. A. Botzakaki[1], G. Skoulatakis[2], P. Svarnas[3], S. Kennou[2], S. Ladas[2],
C.Tsamis[4], S.N. Georga[1] and C.A. Krontiras[1]**

[1]Dept. of Physics, University of Patras, 26504, Patras, Greece
[2] Dept. of Chemical Engineering, University of Patras, 26504, Patras, Greece
[3]Dept. of Electrical and Computer Engineering, High Voltage Laboratory, University of Patras, 26504 Rion-Patras, Greece
[4] NCSR “Demokritos”, Inst. of Advanced Materials, Physicochemical processes, Nanotechnology & Microsystems, GR 15310 Aghia Paraskevi, Athens, Greece

E-mail: mpotzakaki@physics.upatras.gr

Silicon based semiconductor technology approaches the limits of traditional Si- based MOS scaling, mainly due to the degeneration of SiO$_2$ for thicknesses less than 1nm. The introduction of novel and alternative materials in combination with innovative device structures are required for future and faster MOS devices. In order to achieve higher drive currents in MOSFET devices, substrates having inherently higher carrier mobility (like Ge, strained-Si, GaAs etc.) are considered as possible substitutes of Si. Germanium, has become of great interest as a semiconductor, mostly because of its high hole and electron mobility. Furthermore, trying to replace SiO$_2$, other materials with higher permittivity values (high-k dielectrics) are also studied [1,2].
However, the concurrent replacement of both substrate and dielectric film requires several critical issues to be addressed. One of them is the quality of the interface between the dielectric film and the semiconductor, which affects the electrical response and the efficient operation of the structure. It is found that the interface between high-k dielectrics and Ge substrate are in general “defect sources”. In order to reduce the interface traps, improving thus the electrical response of the structures, many studies concerning the growth of a thin passivation layer (La$_2$O$_3$, GeO$_2$ etc.) [3-5] have been performed.

In this work, pGe/GeO$_2$/HfO$_2$/Au MOS structures were grown and characterized through XPS and electrical measurements. 1.7nm stable plasma-grown thin GeO$_2$ film is developed as passivation layer onto pGe substrates. For the plasma oxidation, a simple single frequency Reactive Ion Etcher (RIE) at low power was used [5]. During the oxidation, Ge substrate, was maintained close to ambient temperature. Using Atomic Layer Deposition (ALD) technique, 3nm HfO$_2$ film was deposited onto 1.7nm GeO$_2$ film at 200°C. Tetrakis(dimethylamido)Hafnium and water were used as precursor and co-reactant respectively. The stoichiometry and thicknesses of both developed dielectric films (GeO$_2$ and HfO$_2$) as well as the interfaces Ge/GeO$_2$ and GeO$_2$/HfO$_2$ were investigated through XPS analysis. For the electrical characterization, Au gate electrodes were deposited through photolithography and lift off methods resulting in pGe/GeO$_2$/HfO$_2$/Au structures.

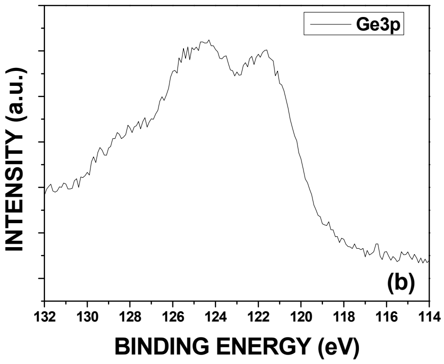

Figure 1: Ge3p XPS spectrum of $Ge/GeO_2/HfO_2$ structure.

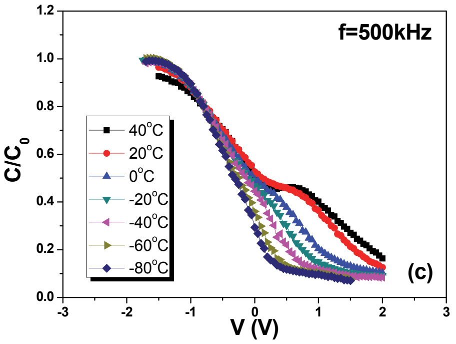

Figure 2: Normalized C-V characteristics for $pGe/1.7nm\ GeO_2/3nm\ HfO_2/Au$ structure with temperature as a parameter at 500kHz

Figure 1 depicts the Ge3p XPS spectrum of $Ge/GeO_2/HfO_2$ structure. The thicknesses of the oxidized Ge (1.7nm) and HfO_2 (~3nm – in very good agreement with ALD nominal thickness) layers were obtained from the measured intensity ratio Ge(0)3d/Ge(ox)3d and Hf4f/Ge(0)3d respectively, using the appropriate equations and X-ray source database [1]. C-V, C-f and J-V measurements were conducted in the temperature range from -80°C to 40°C. Figure 2 represents the normalized C/C_0 versus voltage characteristics of the $pGe/1.7nm\ GeO_2/3nm\ HfO_2/Au$ structure in the temperature range from -80^{0}C to 40^{0}C at 500kHz. It is obvious that with decreasing temperature, the stretching out effect of C-V characteristics is shrinking leading to improved electrical response of the structures [2]. Taking into account the evaluated by XPS thicknesses of GeO_2 and HfO_2 and the capacitance at accumulation the dielectric constant of HfO_2 was calculated to be ~18. D_{its} were also calculated and found one order of magnitude lower compared to reference samples ($pGe/7nm\ HfO_2/Au$). J-V performed measurements reveal lower leakage currents compared to those measured on reference structures.

Acknowledgments

This research has been co-financed by the European Union (European Social Fund – ESF) and Greek national funds through the Operational Program "Education and Lifelong Learning" of the National Strategic Reference Framework (NSRF) – Research Program: Heracleitus II. Investing in knowledge society through the European Social Fund.

References

[1] M. Botzakaki, A. Kerasidou, L. Sygellou, V. Ioannou-Sougleridis, N.Xanthopoulos, S. Kennou, S. Ladas, N.Z. Vouroutzis, Th. Speliotis, D. Skarlatos, ECS Solid State Lett. 1 (2) (2012) 32–34.

[2] M. Botzakaki, A. Kerasidou, N. Xanthopoulos, D. Skarlatos, S Kennou, S Ladas, S.N. Georga, C.A Krontiras, Phys. Status Solidi C, 10 (1) (2013) 137–140.

[3] D. Tsoutsou, Y. Panayiotatos, S. Galata, A. Sotiropoulos, G. Mavrou, E. Golias, A. Dimoulas, Microelectron. Eng. 88 (2011) 407–410.

[4] Q. Xie, S. Deng, M. Schaekers, D. Lin, M. Caymax, A. Delabie, X.-P. Qu, Y.-L. Jiang, D. Deduytsche and C. Detavernier, Semicond. Sci. Technol. 27 (2012) 074012

[5] M.A. Botzakaki, G. Skoulatakis, P. Svarnas, S. Kennou, S. Ladas, C.Tsamis, V. Karoutsos, S.N. Georga and C.A. Krontiras, "Stable plasma-grown GeO2 passivation layer on $Ge/GeO_2/HfO_2/Au$ MOS structures", INFOS 2015.

EIS studies of unconventional topological pseudo-insulator phases in incandescent lamps' tungsten wires

I. Karagiannis and **I.Samaras**

Solid State Physics Section, Physics Department, Aristotle University, Thessaloniki, Greece

E-mail : iokar@physics.auth.gr

Tungsten wires in incandescent lamps are one of the oldest bulk nanomachined metals in nanotechnology. Using severe plastic deformation (SPD) techniques, an application driven thermo-mechanical technology of tungsten wires morphology solved many problems of the devices (incandescent lamps). In this work, we investigate the semiconducting properties of some thin tungsten wires in incandescent lamps. The optimum solution for recent wires was found for highly elongated clusters of W-grains, and nano-vacancies using different morphological topologies. Today, the fine control of the size and morphology of the impurities in these wires has not only solved most of the problems but it may result in the beginning of a new scientific era. The "magic" audio oscillator HP200A (1942) was the model to support the start-up company HP (1950s) [2].

Today, similar phenomena may open an interesting era in the field of new scattering modes of carriers from static or dynamic nanostructures [3]. The recent W-wires can be considered as a synthetic metal of W-grains clusters separated by impurities of K (potassium) nano-vacancies in the order of 100nm. The synthetic metal forms a percolation system of a W-metal and a dielectric K-nanobubbles. The fine control of insulating nanobubbles' volume percentage due to the DC electrical heating and the AC electrical measurement of the complex impedance Z (= Zr + jZi). This technique is known also as **EIS** (Electrochemical Impedance Spectroscopy) where the DC part is used as parameter to scan different energy levels. Upon initial heating (with the DC part), the real component Zr of the complex impedance Z represents both the Joule effect and an abrupt-additional increase due to a virtual decrease in metallic tungsten wires' diameter. Also, the imaginary component Zi of Z represents the abrupt increase in nanobubbles' diameter d_N of insulating phase, following the volume percentage V_N % increase.

The heating evolution versus electrical power P, of the calculated lumped parameters (R_1//R_2C) in an equivalent circuit (Fig.1). Using normalized (%) electrical parameters Hp, Hv and Hi (Hp for power P, Hv for voltage V, and Hi for current i), almost all devices present universal electrical behavior. A percolation regime for common wires is found from 0 to 1% of power P having a percolation threshold at 1% (LogHp=0, in Fig.2), just before visual light appears at 2 to 3%. In this percolation regime some wires present unconventional topological insulator phases if the lamps are in a dewar with liquid Nitrogen (77.3K). These phases show a 2 to 3-orders increase in Za (Z-amplitude). However this increase is only at the sub-hertz frequency ranges, while at high frequencies (f>100Hz), we observe a rather common metallic character. So, we name these partial insulators as pseudo-insulators. The topological property results from the conducting character of the stationary nodes based on the dielectric K-nanobubbles that are changing their phenomenological character from a metallic to insulating one [4]. We shall discuss more this character change that is taking place only in a small percentage of commercial lamps.

References

[1] P. Schade, ,Int. J. Refract. Met. Hard Mater, 16 (1998) 77-87.
[2] Patent US20140093782 (2014)
http://www.hp.com/hpinfo/abouthp/histnfacts/museum/earlyinstruments/0002/0002history.html
[3] M. Zebarjadi, B. L. Liao, K. Esfarjani, M. S. Dresselhaus and G. Chen, 25 (2013) 1577.
[4] Liang Fu and C. L. Kane, Phys. Rev. Lett., 102 (2009) 216403.

Effect of top barrier thickness on transistor performance in AlN/GaN/AlN HEMTs

Ch. Zervos[1,2], A. Adikimenakis[1], A. Bairamis[1,2], A. Kostopoulos[1], M. Kayambaki[1], K. Tsagaraki[1], G. Doundoulakis[1,2], G. Konstantinidis[1] and A. Georgakilas[1,2]

[1]Microelectronics Research Group, IESL/FORTH, P.O. Box 1385, 71110 Heraklion, Greece
[2]Physics Department, University of Crete, P.O. Box 2208, 71003 Heraklion, Greece

E-mail: alexandr@physics.uoc.gr

In the present work, AlN/GaN/AlN double barrier heterostructures, with different AlN top barrier thicknesses, have been directly grown on sapphire substrates by plasma-assisted molecular beam epitaxy. High electron mobility transistors (HEMTs) were fabricated, with photolithography, in order to assess the effect of AlN top barrier thicknesses on device performance. The total epilayer thickness on sapphire was only 0.5 μm. The structures were capped by 1 nm GaN and non-passivated HEMT devices were processed with gate width of W_g= 50 μm and gate length L_g= 1 μm.

The transistor threshold voltage changed linearly from +0.2 V to -2.7 V by varying the AlN top barrier thickness from 1.5 nm to 4.5 nm, respectively. The on-resistance of the devices ranged from 3.9 to 4.8 Ohm·mm, for AlN thicknesses between 3.0 - 4.5 nm. Dc I-V measurements exhibited a maximum drain current of 1.1 A/mm for intermediate AlN barrier thicknesses, while the maximum transconductance was 320 mS/mm. Higher currents were obtained from pulsed I-V characteristics due to the elimination of thermal effects (1.4 A/mm for 3.7 nm AlN barrier thickness). The measured gate and drain lag, for 500 ns pulse-width, varied between 6-12% and 10-18%, respectively for the entire drain-source voltage range. A small increase in the threshold voltage was observed for 3, 3.7 and 4.5 nm AlN thickness. The off-state breakdown voltage obtained at I_{ds}=1 mA/mm was V_{br} = 70 V, for drain-source spacing of 3.6 μm. The results suggest that the double barrier AlN/GaN/AlN heterostructure design may offer significant advantages for the breakdown and current stability characteristics of high current HEMTs, due to improved confinement of the electrons in the GaN channel.

Galvanomagnetic Phenomena in Bi_2Te_3 and Bi_2Se_3 Thin Films

K. Bidinakis[1], **N-C. K. Papaioannou** [1], **C. Charitidis**[2],
D. Niarchos[1] **and Th. Speliotis**[1]

[1]Institute of Nanoscience and Nanotechnology, NCSR “Demokritos” Aghia Paraskevi 15310 Greece.
[2]School of Chemical Engineering, NTUA, Zographos, Athens, 15773 Greece.

E-mail: kbidinakis@gmail.com

MOP

P010

Bi_2Te_3 and Bi_2Se_3 are two compounds commonly used for thermoelectric applications that both have been experimentally confirmed to have topological insulator properties. Thermoelectric materials have thermal, electrical, and semiconducting properties that allow them to be used to convert waste heat into electricity or electrical power into cooling and heating [1]. Topological insulators are electronic materials with a bulk band gap like an ordinary insulator and protected conducting states on their surface. These states exist because of spin orbit interactions and time reversal symmetry [2].

Bi_2Te_3 and Bi_2Se_3 thermoelectric thin films were prepared on Si(100)/SiN_x and MgO substrates by DC magnetron sputtering with thickness values ranging from 50nm to 500nm at a low deposition rate. The base pressure was approximately $5x10^{-8}$Torr. The Argon deposition pressure was fixed at 3 mTorr and all the depositions were performed at ambient temperatures.

The films were analyzed in terms of their crystalline structure using X-Ray diffraction measurements and their surface morphology using Field Emission Scanning Electron Microscopy and Atomic Force Microscopy. Transport properties were measured using a Quantum Design Physical Property Measurement System (PPMS) from 5 to 300K using the van der Pauw configuration. The FESEM images were used for a statistical analysis on the distribution of the grain sizes of the films, depending on their thickness and their substrate. Finally, certain samples were treated to an annealing process in order to indicate variations in their properties.

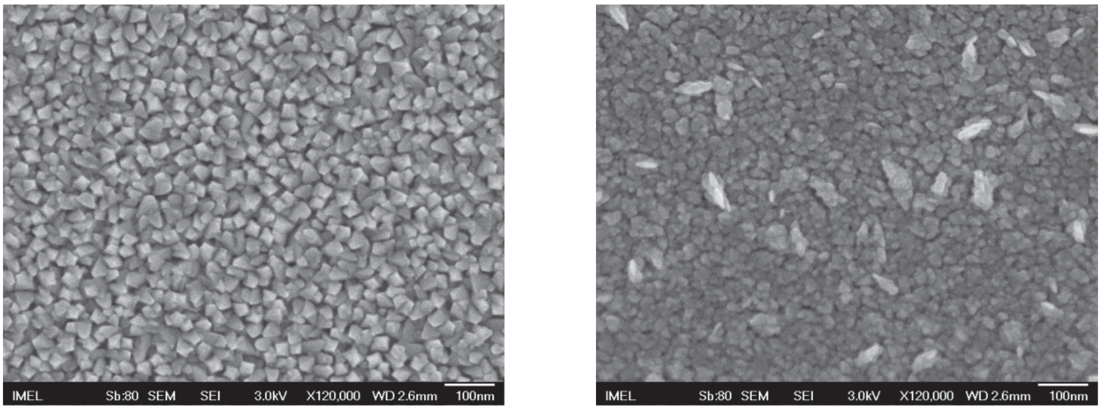

Figure 1: FESEM Images from Bi_2Te_3 (155 nm) and Bi_2Se_3 (143nm) thin films respectively.

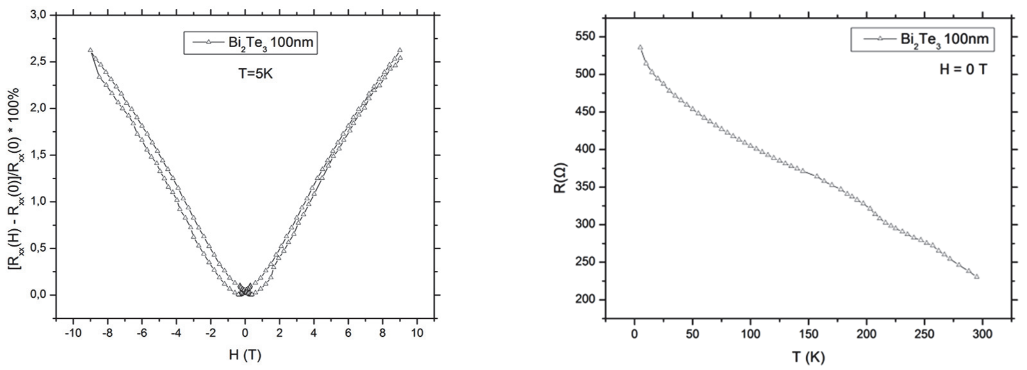

Figure 2: Magnetic Field and Temperature dependence of Resistance for Bi_2Te_3 thin films.

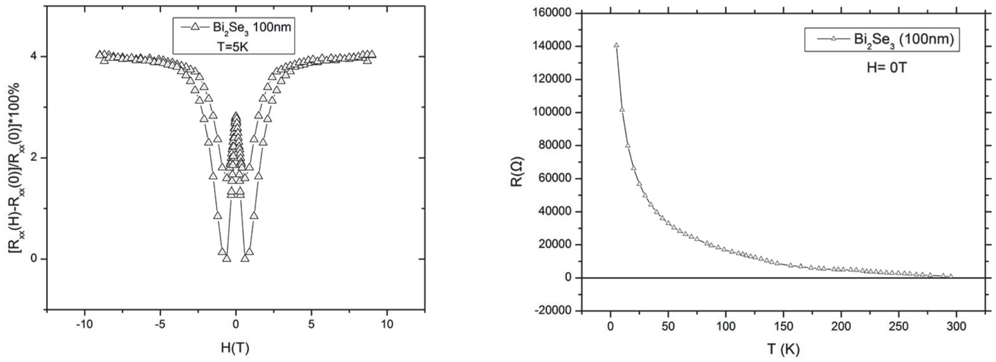

Figure 3: Magnetic Field and Temperature dependence of Resistance for Bi_2Se_3 thin films.

References

[1] Y2uan Deng, Hui-min Liang, Yao Wang, Zhi-wei Zhang, Ming Tan, and Jiao-lin Cui, Journal of Alloys and Compounds, 509 (2011) 5683.
[2] M. Z. Hasan, C. L. Kane, Rev. Mod. Phys., 82 (2010) 3045.

Non-Perturbative Approaches to Electron Transfer in Donor-Bridge-Acceptor Like Systems

D. Psiachos

E-mail: dpsiachos@gmail.com

Using a mixed classical-quantum electron-ion dynamics model, and exact diagonalization, electron transfer in a donor-bridge-acceptor-like molecular junction system based on polyacetylene is studied [1]. Figure 1 (top) shows a schematic of the general system structure and energy scales for a donor-bridge-acceptor. An electron at a donor site at time t=0 transfers through the system while Rabi oscillations of electron density are observed (Fig. 1, bottom) in the system. Two qualitatively-different transfer regimes are identified: hopping, where discrete hops are made along all sites in the bridge and tunnelling, where the transfer to the acceptor occurs without occupying the bridge. The conditions for achieving each regime, as well as the criteria for minimizing inelastic scattering and decoherence arising from the coupling to the ions are determined. Connections are made to quantities derived from electron dynamics in simpler, three-state model systems.

In order to make connections with experiments, we compute effective electron transfer rates as well as the current, which accounts for the overall amount of electron transfer, in addition to the rate. The quantities obtained using non-perturbative approaches [2] are shown to differ qualitatively from those obtained using perturbative (scattering-based) methods; for example for certain arrangements of the bridge molecules, destructive interferences (a zero charge transfer rate) are predicted in the perturbative but not in the non-perturbative approaches (Figure 2).

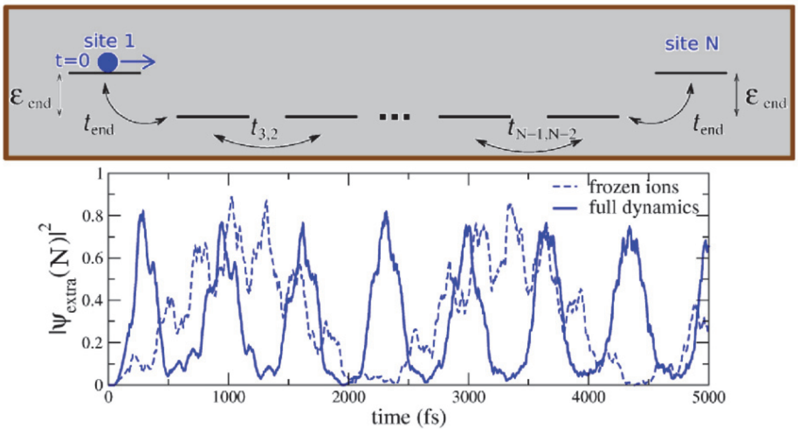

Figure 1: (Top) Schematic of electron transfer in a Donor-Bridge-Acceptor like system: polyacetylene chain with nearest-neighbour hoppings $t_{i,i-1}$ coupled to molecular levels offset by an energy ε_{end} at ends. (Bottom) Population of the acceptor site N as a function of time for t_{end}=0.4 eV and ε_{end}=0.7 eV with frozen ions ($t_{i,i-1}$ fixed at 2.0 eV) or with electron-ion dynamics ($t_{i,i-1}$ varying).

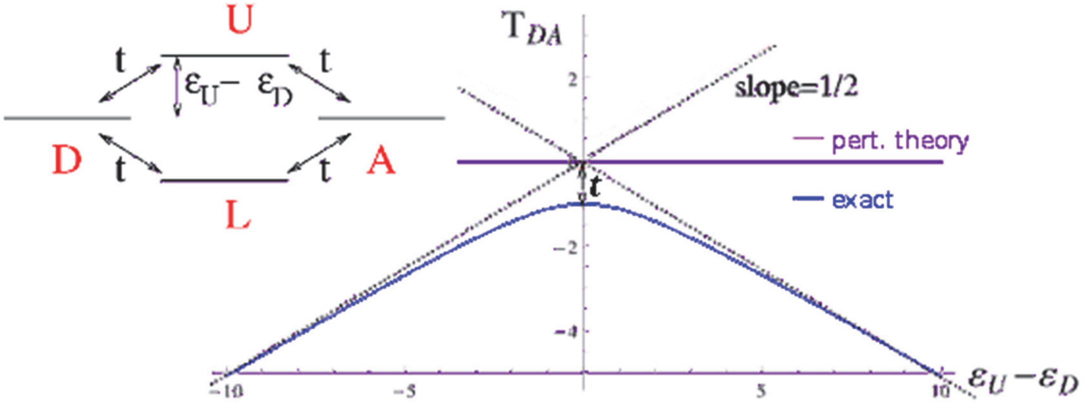

Figure 2: Schematic of a Donor (D) - Acceptor (A) system with two bridges - upper (U) and lower (L) and energies ε in the symmetric case (ε_L=-ε_U). The transfer-matrix element T_{DA} (corresponding to the charge-transfer rate) as a function of the bridge energy is shown for both the perturbative and exact solution.

References

[1] D. Psiachos, Chemical Physics, 436-437 (2014) 8-16.
[2] D. Psiachos, Annals of Physics, 360 (2015) 33-43.

MOP

P122

Simulation of nanoscale triple gate FinFETs, with TCAD tools – A comparative study.

A. Tsiara, D. Tassis and C. Dimitriadis

Physics Department, Aristotle University of Thessaloniki, GR-54124 Thessaloniki, Greece

E-mail: artsiara@physics.auth.gr

A comprehensive study has been conducted in the simulation of nanoscale triple gate FinFETs (Fig. 1). The importance of the simulation parameters has been stressed out as well as assumptions - approximation of the underlying physical models used. The comparison comprised devices with different meshes (from crude to very fine) as well as different numerical methods and accuracy used to solve the electrostatics as well as transport phenomena. The methods can affect not only the efficiency but also the convergence to a solution, and even the computer run-time, by orders of magnitude.

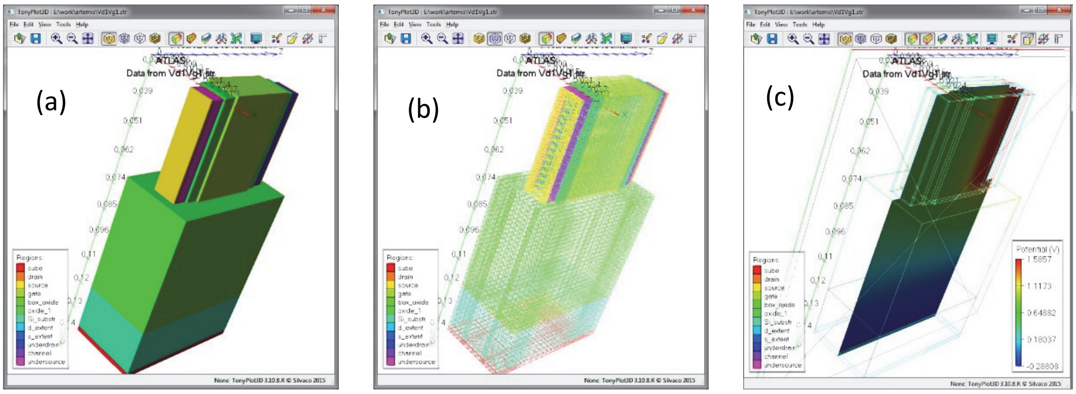

Figure 1. 3D view of the FinFET, showing the regions used for the simulation (a), a typical mesh (b) and a cut plane along the channel showing the potential in an instance with $V_D = V_G = 1$ V (c).

Also, two commercial TCAD tools (from Silvaco and Sentaurus) have been compared in terms of capabilities, ease of use, learning curve and reusability of the code.

Acknowledgements

This work was supported by ARISTEIA II (project 4154) of the Greek General Secretariat for Research and Technology, co-funded by the European Social Fund and national funds.

Gas sensing properties and electrical characterization of hot-wire porous metal oxides thin films

G. Papadimitropoulos and D. Davazoglou

NCSR Demokritos, Institute of Nanoscience and Nanotechnology, Terma Patriarchou Grigoriou and Neapoleos, 15310, Aghia Paraskevi, Greece

E-mail: g.papadimitropoulos@inn.demokritos.gr

The suitability of a material to be used in the fabrication of chemical sensors depends on its ability to return its resistance to its initial state upon removal of the cause that induced the change of its properties. Many materials have been used up to now for the formation of chemical sensors. Among them are a lot of metal oxides like WO_3, Ta_2O_5 and MoO_3 [1,7]. The above oxides are of great interest and have been investigated extensively owning to their promising physical and chemical properties [2-3]. Many techniques are being used for the fabrication of metal oxides thin films, including thermal evaporation [4], chemical vapor deposition [5] and sputtering [6].

The aim of our research is to examine hot-wire metal oxides (hwMO) thin films as sensory materials in chemical sensors [7] and to investigate their electrical properties. These films are deposited very easily compared to other methods by a heated metallic filament under vacuum. This deposition method can be applied for all metallic oxides having higher vapor pressure than the corresponding metal. The deposited oxides are porous [8] and exhibit reversible resistance changes stimulated by their environment; render them suitable for gas sensing applications.

The resistance variations of these configurations caused by changes in their environment were monitored. Reversible changes of resistance, of the order of several KOhms and MOhms, were observed in these metal oxides films caused by the presence or upon removal of gases (H_2 and CO). The magnitude of these changes, related to the sensitivity, was found to depend on hydrogen and carbon monoxide concentration and temperature of measurement (150 ^oC - 450 ^oC). The time needed (response time) for the resistance to drop or to rise after gas exposure was found comparable to that needed to recover to its initial value after gas removal. Response times of the order of a few seconds were measured on hwMO films, much shorter than those measured on metal oxides samples deposited by other methods, like chemical vapor deposition [5].

Acknowledgment: Dr. G. Papadimitropoulos acknowledges financial support by IKY FELLOWSHIPS OF EXCELLENCE FOR POSTGRADUATE STUDIES IN GREECE-SIEMENS.

References

[1] C.Wang, L. Yin, L. Zhang and D. Xiang, R. Gao, Sensors, 10 (2010) 2088-2106.
[2] C. Sanrato, M. Odziemkowski, M. Ulmann, and J. Augustynski, Am. Chem. Soc, 123 (2001) 0639-10649.
[3] G. C. Granqvist, Sol. Energy Mater. Sol. Cells, 60 (2000) 201-262.
[4] M. W. Qu and W. Wlodarski, Sens. Actuators, B 64 (2000) 42-48.
[5] D. Davazoglou, A. Moutsakis, V. Valamontes, V. Psycharis, and D. Tsamakis, J. Electrochem. Soc, 144 (1997) 595-599.

[6] M. Bendahan, R. Boulmani, L. J. Seguin, and K. Aguir, Sens. Actuators B, 100 (2004) 320-324.
[7] G. Papadimitropoulos, I. Kostis, R. Triantafyllopoulou, V. Tsouti, M. Vasilopoulou, and D. Davazoglou, Miroelectronic Eng., 90 (2012) 51-54.
[8] G. Papadimitropoulos, N. Vourdas, K. Giannakopoulos, M. Vasilopoulou, and D. Davazoglou, Journal of Applied Physics, 109 (2011) 103527-7.

Effective medium modelling of the interfacial roughness in multilayer coatings

G. Leftheriotis, **S. Tsakanikas and E. Koubli**

Renewable Energy and Environment Lab, Physics Department,
University of Patras, Rion, 26500, Greece

E-mail: glefther@physics.upatras.gr

Effective medium theory (EMT thereafter) in its most general form attempts to approximate the complex optical behavior of a system of aberrations, typically randomly distributed, inside an otherwise homogeneous material, by a simpler description which should nevertheless give a good representation of reality. Thus the effective medium can be applied to systems of dielectrics that incorporate metallic nanoparticles or to inhomogeneities inside a film (voids or holes) or even to model the rough surface of a film [1,2]. Previous work [2] has shown that the use of EMTs such as that of Bruggeman, Maxwell Garnett, as well as extensions of them, can provide a satisfying prediction of the general optical behavior of rough or discontinuous surfaces.

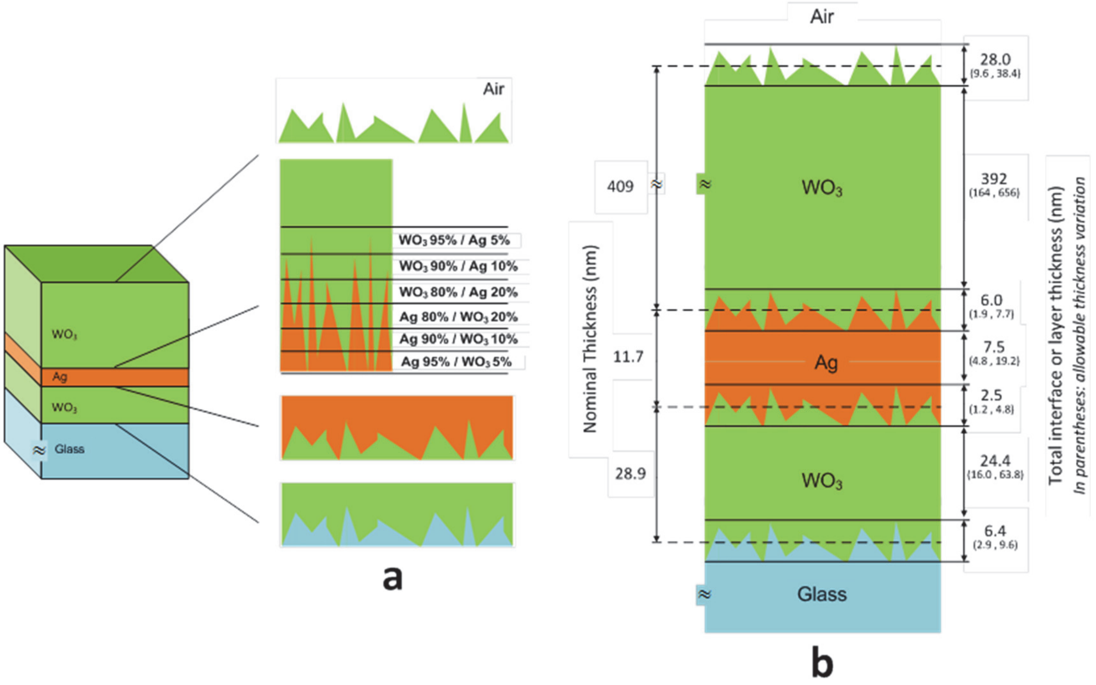

Figure 1: a) Graphical representation of the EMT extension on the characteristic matrix model to account for surface roughness. b) Graphical representation of the Glass/WO_3/Ag/WO_3 coating nominal and total interface thicknesses in nm, obtained by the Bruggeman model. In parentheses the thickness variation range allowed by the Monte Carlo routine.

In this work, a previously developed design algorithm based on the Characteristic Matrix- Monte Carlo method (to be called "Bulk" model hereafter) [3], was enhanced by a Bruggeman EMT code in order to predict the surface roughness effect on the optical properties (e.g. transmittance, *T* and reflectance *R*) of multilayer coatings, as shown in Fig. 2.

The method was applied to Glass/WO_3/Ag/WO_3 stacks, intended for use in low emittance and electrochromic applications. As a result, a 12% and a 39% correction of T and R curves with respect to experimental data was achieved, revealing that through the exploitation of Bruggeman theory and the use of the EMT enhanced Matrix method, a mitigation of the divergence between experimental and theoretical data is possible.

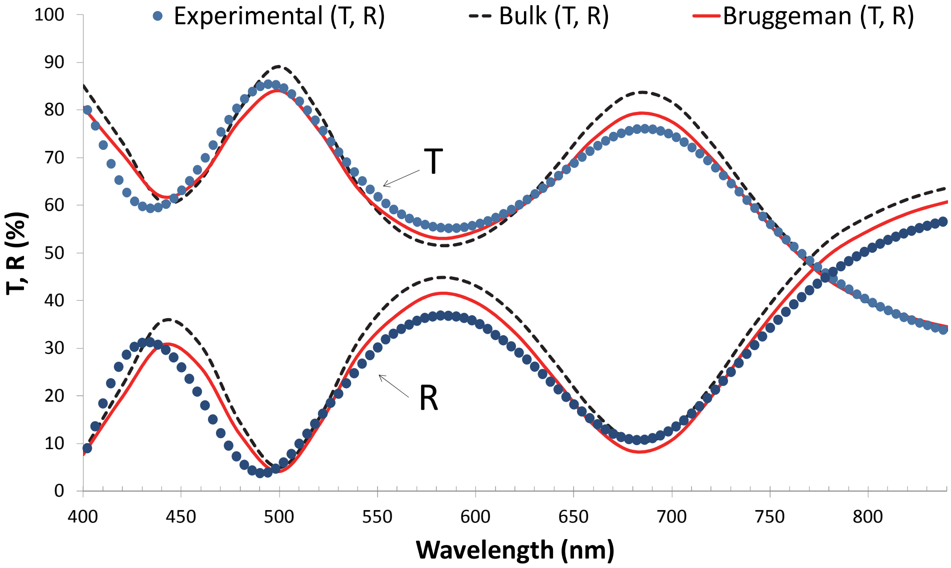

Figure 2: Transmittance and reflectance spectra of a Glass/WO_3/Ag/WO_3 coating: Measured spectra and predictions of the "Bulk" and "Bruggeman" models.

In order to evaluate the credibility of the total interface thickness between consecutive materials as well as the total coating thickness, obtained by the suggested model, SEM, XRR and AFM measurements were carried out for the specific coating. It was found that despite the large "freedom" imposed (60%) on thickness variability (see Fig. 1b), the model's outputs for the thickness of both interfaces and homogeneous films achieve a very good match to the experimental data [4].

This proves the reliability of the applied model in improving the simple characteristic matrix results, while maintaining a truthful representation of the individual films and their interfaces.

References

[1] D. Rönnow, S.K. Anderson and G.A Niklasson, Optical Materials 4 (1995) 815–821.
[2] A. N. Ranade *et al.*, Thin Solid Films 519 (2010) 1490–1494.
[3] G. Leftheriotis, E. Koubli, and P. Yianoulis, SOLMAT, 116 (2013) 110–119.
[4] E. Koubli *et al.*, Solid State Ionics 272 (2015) 30–38.

Structural and Spectroscopic Study of Two Isomeric Nitrato Complexes of Pt(II). Experimental and Computational Approach

N. I. Dodoff[1], **N. G. Vassilev**[2], **R. P. Nikolova**[3], **V. Miletić**[4], **M. Lalia-Kantouri**[5], **O. E. Petrov**[3], **D. Christofilos**[6] **and J. Arvanitidis**[7]

[1]Roumen Tsanev Institute of Molecular Biology, Bulgarian Academy of Sciences, 1113 Sofia, Bulagria.
[2]Institute of Organic Chemistry with Centre of Phytochemistry, Bulgarian Academy of Sciences, 1113 Sofia, Bulgaria.
[3]Ivan Kostov Institute of Mineralogy and Crystallography, Bulgarian Academy of Sciences, 1113 Sofia, Bulgaria.
[4]Institute of Chemistry, Faculty of Science, University of Kragujevac, 34000 Kragujevac, Serbia.
[5]Department of Chemistry, Faculty of Sciences, Aristotle University of Thessaloniki, P.O. Box 135, 54124 Thessaloniki, Greece.
[6]Chemical Engineering Department, Aristotle University of Thessaloniki, 54124 Thessaloniki, Greece
[7]Physics Department, Aristotle University of Thessaloniki, 54124 Thessaloniki, Greece.

E-mail: dodoff@obzor.bio21.bas.bg

In the last decade we undertook a systematic study on the platinum complexes of *N*-3-pyridinylmethanesulfonamide (PMSA) [1-3]. Such type of compounds is of special interest for the experimental cancer chemotherapy [4], and we have indeed found some of them to exhibit cytotoxic activity [5]. In continuation of these studies, here we report the experimental and computational structural and spectroscopic results on two newly synthesized isomeric Pt(II) complexes: *cis*-$[Pt(PMSA)_2(NO_3)_2]$ (**1**) and *trans*-$[Pt(PMSA)_2(NO_3)_2]$ (**2**). The structure of complex **1** has been solved by single crystal X-ray diffraction [6,7] as orthorhombic; *Pbca*; a = 19.8017(6), b = 9.8042(3), c = 24.0279(8); $Z = 8$; $R_{\text{int}} = 0.044$); Figures 1 and 2.

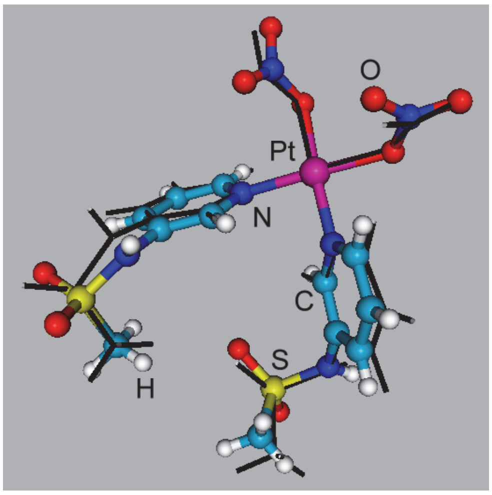

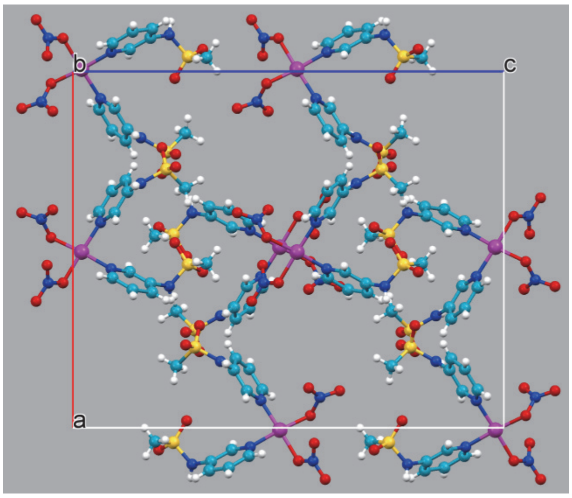

Figure 1: (Left) Superposition of the experimental molecular structure of **1** found by X-ray crystallography and the HF *ab initio* calculated one (the black stick diagram). The starting geometry for the optimization was taken from the X-ray structure. **Figure 2:** (Right) The unit cell of **1** viewed along the *b* axis.

Both **1** and **2** have been characterized by powder X-ray diffraction [8]. The experimental powder diffraction pattern and the unit cell parameters for **1** are in excellent agreement with those found by the single crystal analysis. This confirms that the particular single crystal and the bulk material of **1** have the same crystal structure. The analysis of the X-ray powder pattern of **2** revealed the following unit cell parameters: triclinic; $P\bar{1}$; $a = 16.149(6)$, $b = 19.744(7)$, $c = 7.486(4)$, $\alpha = 96.00(4)$, $\beta = 94.66(2)$, $\gamma = 93.55(9)$; $Z = 2$. Quantum mechanical optimization (HF *ab initio* level with 6-31++G(d,p)/LANL08-ECP basis sets [9,10]) of the molecular geometry followed by vibrational analysis has been performed for **1** and **2**. The results for **1** are in good agreement with the experimental crystallographic data (Figure 1). The HF optimized molecular structure of **2** is depicted in Figure 3.

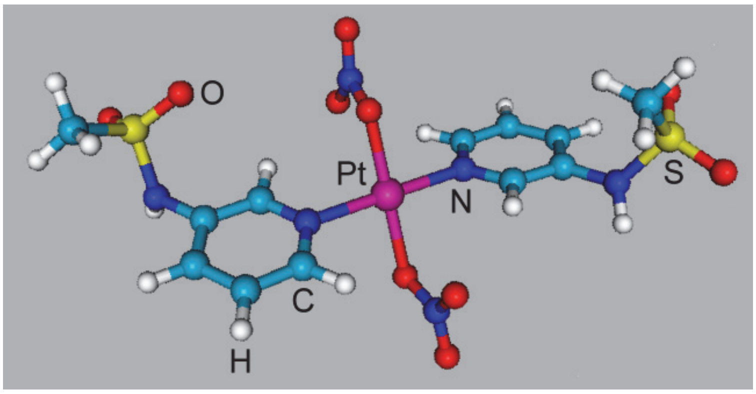

Figure 3: HF *ab initio* optimized structure of the molecule of **2**. The starting torsion angles were set as in the X-ray crystallographic structure of **1**.

The complexes have been characterized by 1D and 2D NMR spectroscopy of the ^{1}H, ^{13}C and ^{195}Pt nuclides in solution and the spin coupling constants have been calculated. The IR spectra of the compounds in the solid state have also been recorded and interpreted in the light of the computational vibrational analysis.

Acknowledgement

The work is part of the bilateral cooperation between the Aristotle University and the Bulgarian Academy of Sciences (2015-17).

References

[1] N. I. Dodoff, R. Varga and D. Kovala-Demertzi, Z. Natutforsch., B 59 (2004) 1070-76.

[2] N. I. Dodoff, M. Lalia-Kantouri, M. Gdaniec, A. Czapik, N. G. Vassilev, L. S. Markova and M. D. Apostolova, J. Coord. Chem. 65 (2012) 688-704.

[3] N. I. Dodoff, B. L. Shivachev, R. P. Nikolova. M. Lalia-Kantouri, V. Miletic, T. I. Pajpanova, Chin. J. Struct. Chem. 31 (2012) 1476-82.

[4] M.S. Aris and P.N. Farrell, Eur. J. Inorg. Chem. (2009) 1293-1302.

[5] N. I. Dodoff, I. Iordanov, I. Tsoneva, K. Grancharov, R. Detcheva, T. Pajpanova and M. R. Berger, Z. Naturforsch., C 64 (2009) 179-85.

[6] CrysAlisPro, Version 1.171.33, Oxford Diffraction Ltd., Yarnton, Oxfordshire, UK (2009).

[7] G. M. Sheldrick. Acta Cryst., A, 64 (2008) 112-22.

[8] Rex.Cell, Version 0.1.3, Powder Diffraction Data Indexing [http://www.rexpd.com/rexcell]; M. Bortolotti and I. Lonardelli, J. Appl. Cryst. 46 (2013) 259-61.

[9] GAMESS, Version 25 March, 2010, from Iowa State University; M. W. Schmidt, K. K. Baldridge, J. A. Boatz, S. T. Elbert, M. S. Gordon, J. H. Jensen, S. Koseki, N. Matsunaga, K. A. Nguyen, S. Su, T. L. Windus, M. Dupuis and J. A. Montgomery, Jr., J. Comput. Chem. 14 (1993) 1347-63.

[10] EMSL Basis Set Exchange Library, Version 1.1.2 [http://bse.pnl.gov/bse/portal]; K. L. Schuchardt, B. T. Didier, T. Elsethagen, L Sun, V. Gurumoorthi, J. Chase, J. Li, J. and T. L. Windus, J. Chem. Inf. Model. 47 (2007) 1045-52.

Coarse-grained Computer Simulations of Hexa-*peri*-hexabenzocoronene (HBC) and Hexa-*n*-dodecyl-hexa-*peri*-hexabenzocoronene (HBC-C12)

G. Megariotis, O. G. Ziogos and D. N. Theodorou

School of Chemical Engineering, National Technical University of Athens, 9 Heroon Polytechniou,
Zografou Campus, Athens 15780, Greece

E-mail: gmegariotis@yahoo.gr

Derivatives of hexa-*peri*-hexabenzocoronene (HBC) are investigated today in the crystalline and liquid crystalline states for organic electronics applications. Computer simulation is a promising avenue for molecular engineering design based on these systems. Although atomistic simulations have become a valuable tool for the study of molecular systems, they are limited to rather small time and length scales and hence cannot address a number of important self-organization phenomena. The idea of gathering groups of atoms into larger entities and thus reducing the number of degrees of freedom used for the description of each molecule is termed *coarse-graining* and may be based on either systematic or non-systematic methods. In the former category, a number of methods have been developed, such as Iterative Boltzmann Inversion (IBI), Force Matching, and inverse Monte Carlo ([1-4]). All these methods fall in the category of *bottom-up* (as opposed to *top-down*) coarse-graining. Atomistic and coarse-grained representations of HBC-C12 and HBC molecules are depicted in Figs. 1(a) and 1(b), respectively. The former molecule is simulated at the atomistic level as a collection of 124 atoms with all alkyl tails being modeled in the united-atom representation. Its coarse-grained representation entails 36 superatoms; 6 of them represent the core of the thirteen aromatic rings (type AR1), whereas the rest are equally shared among the 6 peripheral alkyl tails (type AL1). On the other hand, HBC is simulated using 60 atoms at the atomistic level but only 6 superatoms (type AR1) in the coarse-grained representation; the superatoms are placed at the same positions as in the polyaromatic core of HBC-C12. Both coarse-grained models have been developed by applying the IBI method ([1], [4]). In this study, HBC and HBC-C12 molecules are simulated in the crystalline phase at a temperature of 300K. In the crystal these molecules form stacks, each stack containing equidistant rows of two molecules. Our analysis of structure is based on the Saupe ordering tensor (**Q**), which is widely used in the study of liquid-crystalline phases [4]. The analysis begins with defining a unit vector $\hat{\mathbf{u}}_i$ perpendicular to each mesoscopic hexagonal ring *i*. The Saupe ordering tensor is defined by the following equation:

$$\mathbf{Q} = \frac{1}{N}\sum_{i=1}^{N}\left\{\frac{3}{2}\hat{\mathbf{u}}_i\hat{\mathbf{u}}_i - \frac{1}{2}\mathbf{1}\right\} \tag{1}$$

The sum above is taken over all molecules (*N*) of the system. HBC-C12 possesses two superatom-types (AR1, AL1); therefore, 3 radial distribution functions (rdfs) are needed for reproducing its structure at the coarse-grained level of description. In particular, the intermolecular rdfs for the pairs AR1-AR1, AR1-AL1 and AL1-AL1 are reproduced by applying IBI. In addition, 8 intramolecular distributions are used in developing the coarse-grained model. In the case of HBC molecule, the number of rdfs being optimized is smaller, due to its simpler structure. Only one rdf (AR1-AR1) and 3 intramolecular distributions need to be taken into account. Figure 2 depicts two of the three aforementioned rdfs (pairs AR1-AR1 and AR1-AL1) after eleven IBI iterations (red coloured curves). These rdfs are plotted along with the corresponding atomistic ones (black coloured curves), to visualize convergence. The multi-peaked appearance of these distribution functions reflects the complex crystalline structure adopted by the molecules.

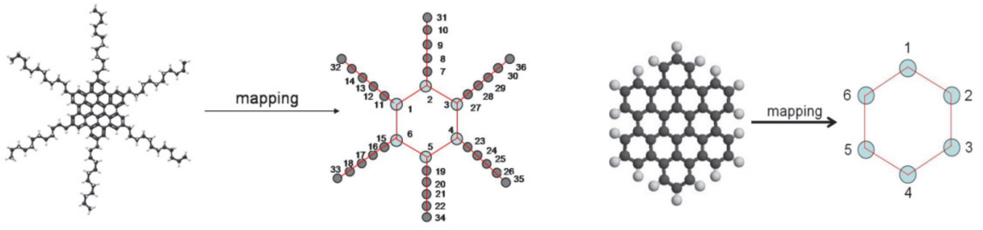

(a) (b)

Figure 1: Atomistic and mesoscopic representations of (a) HBC-C12 and (b) HBC molecules.

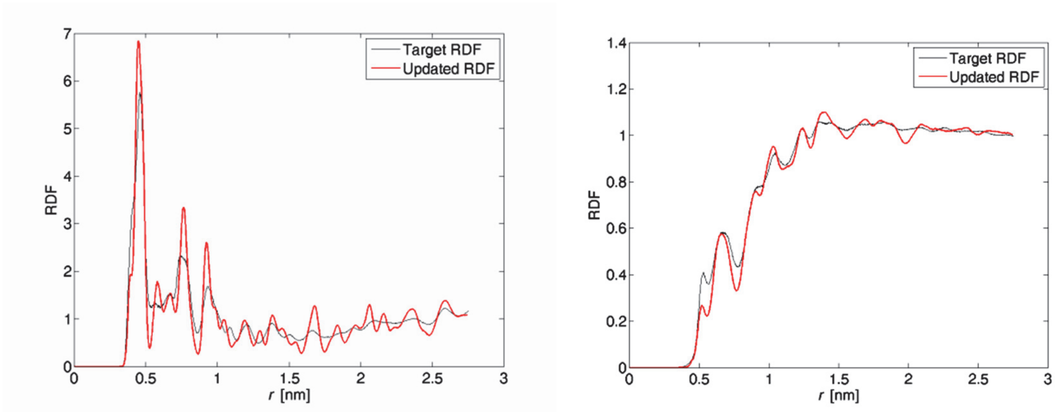

Figure 2: Comparison of atomistic and coarse-grained rdfs after the implementation of IBI method. (a) rdf AR1-AR1 and (b) AR1-AL1 of the HBC-C12 molecule.

Acknowledgments: This research has been co-financed by the European Union (European Social Fund-ESF) and Greek national funds through the Operational Programme 'Education and Lifelong Learning' of the National Strategic Reference Framework (NSRF)-Research Funding Programme: THALIS. Investing in knowledge society through the European social fund [grant number MIS 379436] and by the IKY Fellowships of Excellence for Postgraduate Studies in Greece-Siemens Programme [award number 11126/13a].

References

[1] F. Müller-Plathe, Chem. Phys. Chem. 3 (2002) 754-769.
[2] A. P. Lyubartsev and A. Laaksonen, Phys. Rev. E. 52 (1995) 3730-3737.
[3] S. Izvekon and G. A. Voth, J. Phys. Chem. B 109 (2005) 2469-2473.
[4] G. Megariotis, A. Vyrkou, A. Leygue and D. N. Theodorou, Ind. Eng. Chem. Res. 50 (2011) 546-556.

Tuning the Localised Surface Plasmon Resonances (LSPR) of AuCu Nanocrystalline Epilayers via their Microstructure

A. Delimitis[1], **A. Sousanis**[2,3] **S. Grammatikopoulos**[4],
V. Dracopoulos[4] **and P. Poulopoulos**[2,3]

[1] Chemical Process & Energy Resources Institute (CPERI), Centre for Research & Technology Hellas (CERTH), 57001 Thermi, Thessaloniki, Greece
[2] Laboratory of High-Tech Materials, School of Engineering, University of Patras, 26504 Patras, Greece
[3] Materials Science Department, University of Patras, 26504 Patras, Greece
[4] Institute of Chemical Engineering Sciences (ICE-HT), Foundation for Research & Technology, Hellas (FORTH), 26504 Patras, Greece

E-mail: andel@cperi.certh.gr

Metal nanoparticles (NPs) display strong and unique optical resonances in the near ultraviolet-visible and near-infrared spectrum region due to the resonant response of free electrons to the electric field of light [1]. Such resonances of charge density oscillations confined to metallic NPs embedded in colloidal suspensions or in solid dielectric matrices are defined as localized surface plasmon resonances (LSPR). The optical absorption spectra of Au NPs in the visible light are dominated by LSPR, which strongly depend on their size, shape, and dielectric environment [1,2]. It is not only fascinating for fundamental physics, but also materials of noble metal NPs with LSPR find advanced technological applications, such in biological and chemical nanosensors, enhanced efficiency solar cells and negative index metamaterials. As a result, there is a large effort to efficiently fabricate plasmonic materials with well-defined structure and controllable tuning of the position and intensity of LSPR.

In this study, we report on the structure and LSPR optical properties of a prototype system: Au NPs self-organized in a CuO dielectric matrix, after selective oxidation of nanocrystalline AuCu solid solution thin films. AuCu thin films with Au in the range of 4-12 at.% were prepared with radio frequency magnetron sputtering. After annealing at 430 ^{o}C, even for short times, Cu was fully oxidized while Au remained pure metallic. As transmission electron microscopy (TEM) showed (Fig. 1 & 2), the phase separation resulted in Au NPs located at the Si substrate interface.

The morphology of the AuCu films grown on top of Si(100) and subsequently annealed for 30 min and 16 h are depicted in Fig. 1 and 2, respectively. The average film thicknesses after oxidation are at the 36-40 nm range. The root mean square roughness (R_{rms}) is relatively large (5.61 and 4.8 nm, respectively), attributed to the oxidation mechanism of metallic copper in air. In such a case, cations diffuse outwards and react with oxygen to form new oxide at the oxide/gas interface [3]. The process of bringing fresh Cu upwards on the surface increases the film thickness and roughness and results in an effective sinking of Au nanocrystallites at the interface, whereas CuO remains on the top of the epilayer. Interestingly, the shape of Au nanocrystals is platelet-like at the AuCu film annealed for 30 min. Their average diameter is ~28 nm and their height is 14 nm. On the other hand, Au crystallites do not show tendency for a platelet-like shape at the AuCu film annealed for 16 h. They appear almost spherical, often with octahedral-like shape and they have similar height and width sizes, in the 23-30 nm range. This spherical-like octahedral shape marks the achievement of final shape of small metallic crystals under thermodynamic equilibrium as predicted by the theory of Wulff [4]. High resolution TEM (HRTEM) confirmed the solely metallic character of Au grains. Au crystallites often expose {111}-type lattice planes, whose spacing is d_{111}=0.235 nm. On the other hand, CuO crystallites do not have a specific shape and morphology. Their sizes are within the 10 nm range and their orientation with respect to the substrate is random.

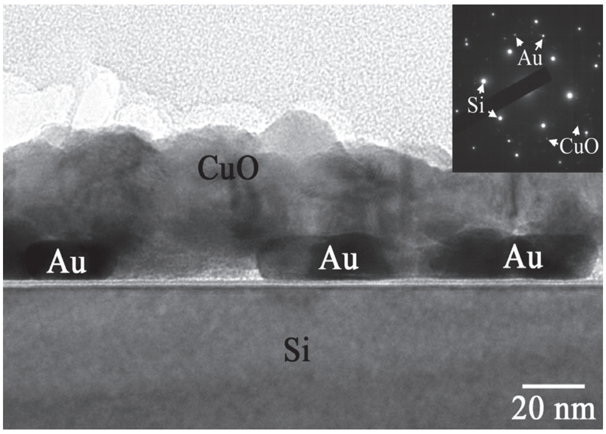

Figure 1: TEM image of a short-time annealed AuCu film on Si(100). The SAD pattern, shown as inset in the image, reveals the metallic character of Au grains. On the contrary, no metallic Cu was left after this short time oxidation.

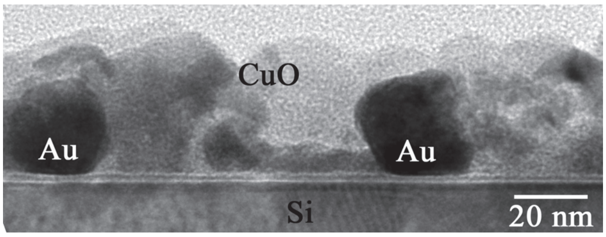

Figure 2: TEM image of a long-time annealed AuCu film on Si(100). The morphological differences of the Au NPs are outlined.

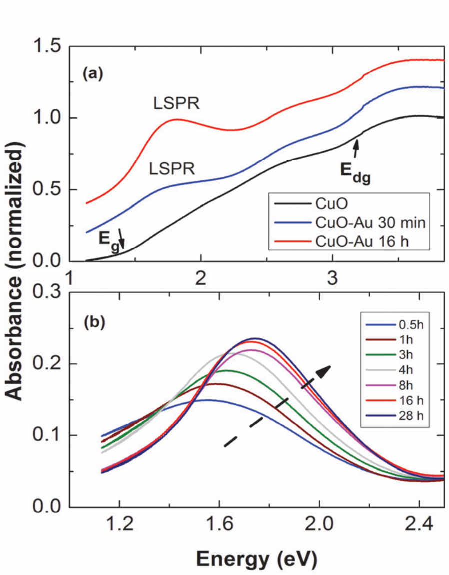

Figure 3: (a) Normalized absorbance for 30 nm CuO and AuCu films after 30 min and 16 hours of annealing. The films were deposited on Corning glass. The spectra have been vertically shifted for clarity of presentation. (b) After correcting for the background of CuO the LSPR experimental data curves appear as Gaussians.

The films readily exhibited LSPR, as shown in Fig. 3, due to the existence of isolated Au nanoparticles in the dielectric matrix. The amplitude of the LSPR increases and they show a blue shift with annealing time. This behavior is justified via TEM, which revealed the distinct modifications in the shape of Au NPs with time. We show that the amplitude of LSPRs can be controlled with Au concentration and time of annealing, while the LSPR position can be effectively controlled by annealing time. Such systems can be interesting for a series of modern applications related to LSPRs.

References

[1] S. Link and M.A. El-Sayed, J. Phys. Chem. B 103 (1999) 4212-4217.
[2] S. Grammatikopoulos, S. D. Pappas, V. Dracopoulos, P. Poulopoulos, P. Fumagalli, M. J. Velgakis and C. Politis, J. Nanopart. Res., 15 (2013) 1446.
[3] W. Brückner and S. Baunack, Thin Solid Films, 355-356 (1999) 316-321.
[4] A. Zangwill, Physics at Surfaces, Cambridge University Press, Cambridge (1988).

A spectroscopical study of the $C_iO_i(Si_I)$ absorption bands upon isothermal annealing in irradiated silicon at liquid helium temperatures (L.H.T.)

T. Angeletos and **C. A. Londos**

Solid State Section, Physics Department, University of Athens,
Panepistimiopolis. Zografos, 157 84 Athens, Greece

E-mail: angelet@phys.uoa.gr

The vast majority of modern electronic devices, is made by semiconducting materials such as crystalline Si. The wide-range of its applications makes it one of the most important semiconducting materials used in electronics industry and technology in general. The properties and behavior of silicon under varying conditions are studied ceaselessly the last 50 years in order to optimize the performance of devices based on this. Lattice defects created either by design or by different processes, influence the thermal, electrical, optical and other properties of Si. The most common method to induce defects in Czochralski Si (Cz-Si) controllably, is to irradiate it with electrons. The immediate products of the irradiation are vacancies (V) and self-interstitial atoms (Si_I) which react with other impurities to product complex defects. Carbon and oxygen are the main unintentionally added impurities in Si during growth. During irradiation or processing give rise to electrically active complex defects. Upon annealing oxygen acts as a trap [1] for carbon atoms to form the C_iO_i defect, which can trap [2] Si_I atoms to form the $C_iO_i(Si_I)$. This defect gives rise two main bands located at low temperatures at about 940 and 1024 cm^{-1}[3].

The aim of this work is to study via Infrared Spectroscopy, the thermal evolution of the $C_iO_i(Si_I)$ defect by measurements at liquid helium temperature (LHT). To this goal, a group of Cz-Si samples ($[O_i]_o=6.2\times10^{17}$ cm^{-3}, $[C_s]_o=1.2\times10^{17}$ cm^{-3}) was irradiated with 2 MeV electrons at a dose of $5\text{x}10^{17}$ e^-/cm^2, at a temperature ~90 °C. After irradiation, the corresponding values of oxygen and carbon concentration were 5.2×10^{17} and 0.62×10^{17} cm^{-3}, respectively. Then, the samples were subjected to isothermal annealing at 150, 220, 280 and 315 °C, in steps of $\Delta t=60$ min. After each annealing step, IR absorption spectra were recorded by means of FTIR spectrometer (FTIR 470 plus) at LHT.

Fig.1 and Fig. 2 show segments of IR absorption spectra measurements and the evolution of the 1024 and 939 cm^{-1} absorption bands of the $C_iO_i(Si_I)$ defect, respectively. Upon annealing at 150°C, the above two bands decay and three new bands at 973, 952 and 724.5 cm^{-1} emerge. These three bands in turn, upon annealing at 220°C, are transformed into other three bands at 969, 951 and 977 cm^{-1}which are eliminated after 6 hours annealing at 280 °C. Remarkably, the decay of this last group of bands is accompanied by the emergence of another two bands, at 1024 and 973 cm^{-1}.It is important to note that when the measurements are carried out at room temperature [4], the second group of band (at 973, 952 and 724.5 cm^{-1}) is not present in the spectra. Furthermore, from the three bands of the third group only two, that is 947 and 967 cm^{-1}, make their appearance [4].

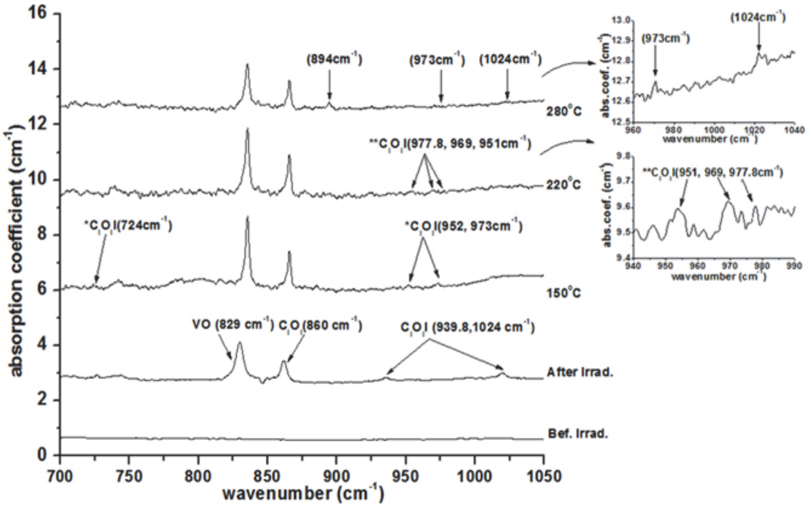

Figure 1: Segments of the IR absorption spectra in the range of 700-1050 cm^{-1} before and after irradiation as well as on thermal anneals at 150, 220 and 280 °C temperatures, for measurements at L.H.T.

Murin *et al.* [3] have proposed that the three groups of the bands correspond to different atomic configurations of $C_iO_i(Si_I)$ defects. In contrast to that, theoretical calculations predicted that the two later groups may originate from $C_iO_i(Si_I)_n$ complexes with $n>1$ [5]. Apart from that, in neutron irradiated silicon the 947 and the 967 cm^{-1} bands have been attributed to $C_iC_s(Si_I)_2$ defects [6] because they appear in IR spectra simultaneously with the disappearance of the 987 993 cm^{-1} bands attributed to the $C_iC_s(Si_I)$ complex. Now, concerning the 1024 and 973 cm^{-1} bands, previous studies [4] have been proposed that the first band may correlate with the decay of 546 cm^{-1} band belonging to C_iC_s. In any case, the picture is not clear and any positive identification of the identity of these bands needs further investigation.

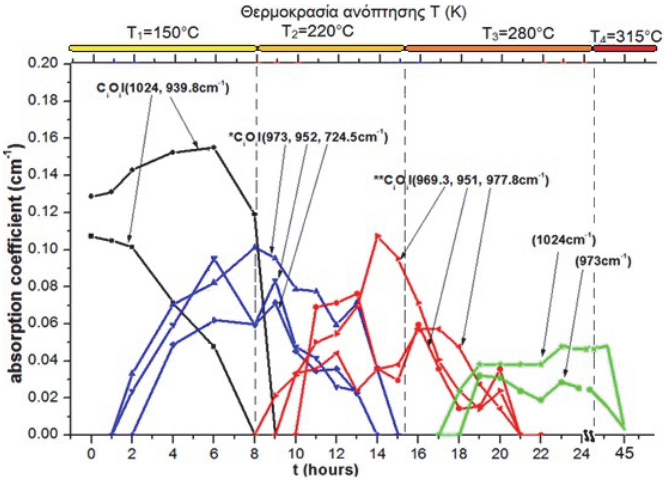

Figure 2: The evolution of $C_iO_i(Si_I)$ bands *vs*. annealing time, at 150, 220, 280 and 315°C temperatures.

References

[1] G. Davies, A. S. Oates, R. C. Newman, R.A. Woolley, E. C. Lightwlers, M. H. Binns, and J. G. Wilkes, J. Phys. C, 19 (1986) 841.

[2] V. P. Chappell and R. C. Newman, Semicond. Sci. Technol., 2 (1987) 691.

[3] L. I. Murin, J. L. Lindstrom, G. Davies, and V. P. Markevich, Nucl. Instrum. Meth. B, 253 (2006) 210-213.

[4] C. A. Londos, E. N. Sgourou, A. Andrianakis, A. Misiuk, V. V. Emtsev, and H. Ohyama, Solid State Phenomena, 178-179 (2011) 147-153.

[5] B. J. Backlund and S.K. Estreicher, Phys. Rev. B, 77 (2008) 205205-8.

[6] M. S. Potsidi and C.A. Londos, J. Appl. Phys. 100 (2006) 033523-4.

MOP

P018

Polarized Raman scattering and birefrigence studies of the orientational order in the nematic liquid crystal 4-n-pentyloxyphenyl 4-n-octyloxybenoate and its nanocomposite with semiconducting CdSe-ZnS quantum dots.

C. Kyrou[1], M. Panagopoulou[1], Y. S. Raptis[1] and I. Lelidis[2]

[1] School of Applied Mathematical & Physical Sciences, National Technical University of Athens, GR 157 80 Athens, Greece
[2] Solid State Section, Department of Physics, University of Athens, Panepistimiopolis, Zografos, Athens, GR 157 84, Greece

E-mail: marpanag@mail.ntua.gr

Orientational order is one of the most significant properties that characterizes the liquid crystalline phases and correlates with the anisotropic behaviour of these substances. We report measurements of the temperature dependence of the optical birefringence (Figs. 1, 2) and of the vibrational Raman depolarization ratios (Fig. 3) in the Isotropic, Nematic, Smectic-A and Smectic-C phases of the pure nematic liquid crystal 4-n pentyloxyphenyl 4-n-octyloxybenoate made of rod-like molecules, in order to evaluate the order parameters as a function of temperature.

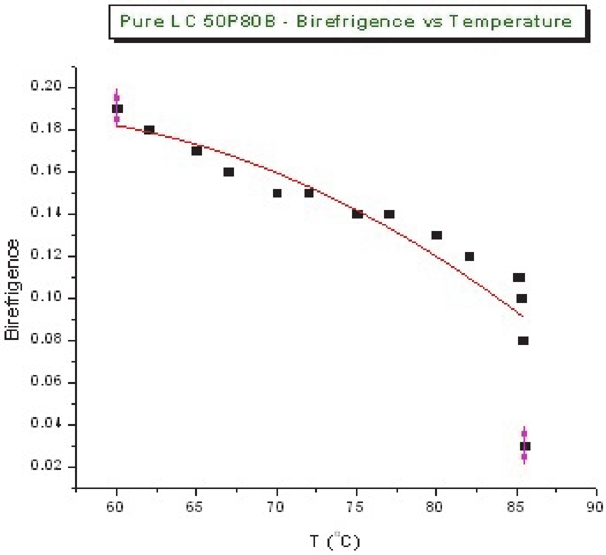

Figure 1: Birefrigence of the pure liquid crystal 4-n-pentyloxyphenyl 4-n-octyloxybenzoate versus temperature.

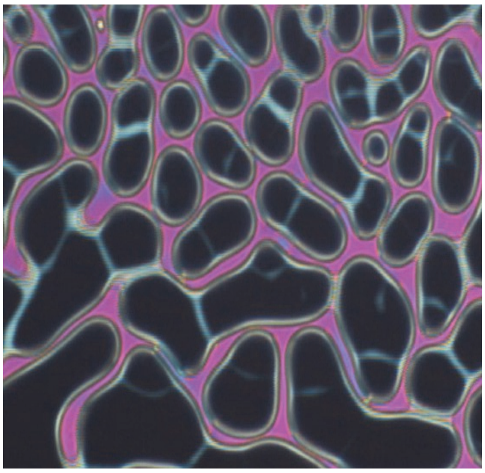

Figure 2: Polarized-light microscopy image about the phase transition Isotropic-Nematic of the pure liquid crystal 4-n-pentyloxyphenyl 4-n-octyloxybenzoat.

The Raman depolarization study was based on the formalism proposed by Jen et al. [1]. The analysis and the evaluation of our data, in combination with semiempirical methods, also enabled us to determine the molecular polarizability and the anisotropy of polarizability of the liquid crystalline substance.

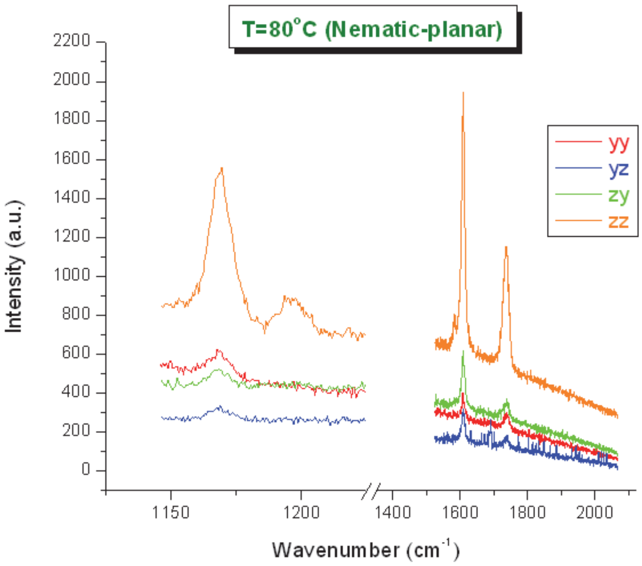

Figure 3: Polarized Raman spectra of the pure liquid crystal 4-n-pentyloxyphenyl 4-n-octyloxybenzoate with planar geometry in nematic phase.

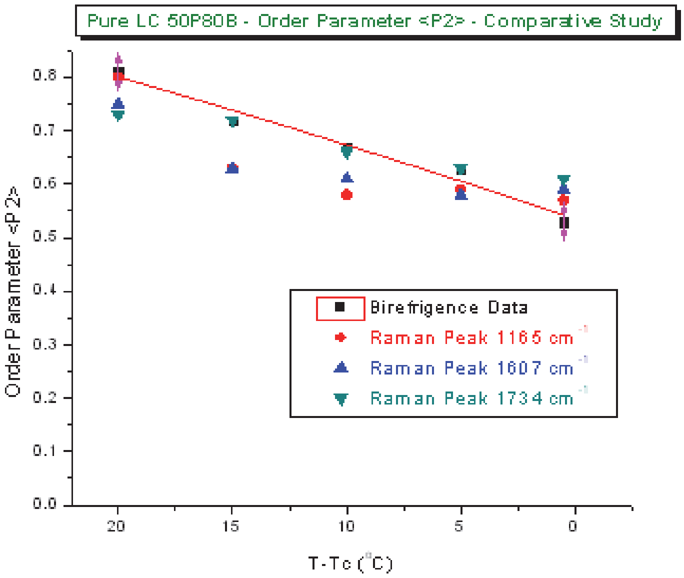

Figure 4: Order parameter of the pure liquid crystal 4-n-pentyloxyphenyl 4-n-octyloxybenzoate by polarized Raman spectroscopy and birefrigence data.

The temperature dependence of the Order-Parameter obtained by the two independent (Birefrigence and micro-Raman) methods are compared (Fig. 4) and discussed. These results are also compared with those of a mixture of the liquid crystalline compound with semiconducting quantum-dots nanoparticles CdSe-ZnS of 1,44 % concentration in weight, that were treated to be hydrophobic, in order to determine the impact of the nanoparticles on the orientational order and the microstructure of the sample.

References

[1] S. Jen, N. A. Clark, P. S. Pershon, and E. B. Priestley, J. Chem. Phys., 66 (1977) 4635-4661.

Simulation of the EXAFS and Raman spectra of $In_xGa_{1-x}N$ enabling the equation of motion routine of FEFF8

M. Katsikini[1], **F. Pinakidou**[1], **E. C. Paloura**[1], **J. Arvanitidis**[1], **S. Ves**[1], **U. Reinholz**[2], **E. Papadomanolaki**[3] **and E. Iliopoulos**[3]

[1]Aristotle University of Thessaloniki, School of Physics, Thessaloniki, Greece
[2]BAM Federal Institute for Materials Research and Testing, Berlin, Germany
[3]University of Crete, Department of Physics and IESL-FORTH, Heraklion, Greece

E-mail: katsiki@auth.gr

$In_xGa_{1-x}N$ alloys have direct band-gaps that take values in the spectral region from NIR (0.7 eV) to UV (3.3 eV). In-rich alloys have potential applications in the fabrication of solar cells. In semiconductor ternary alloys it is commonly observed that, in the local nearest bonding configuration of the absorbing atom, the virtual crystal approximation breaks down. As a result, although the nearest neighbor distances are expected to depend on x, which affects the lattice parameters of $In_xGa_{1-x}N$ according to Vegard's law, deviations are observed. Such a behavior has been verified in a number of semiconductor alloy systems, with the degree of deviation depending on the bond polarization. In this work, $In_xGa_{1-x}N$ alloys with varying In/Ga ratio are studied by means of EXAFS spectroscopy at the Ga- and In-K-edge. In addition to the common analysis procedure with a shell-by-shell fitting, the $\chi(k)$ spectra are also simulated using the FEFF8 code. The Debye-Waller factors are obtained using the equation of motion method that also provides the vibrational density of states (V-DOS) that is compared with the Raman spectra of the samples. As an outcome, the force constants of atom pairs are also obtained.

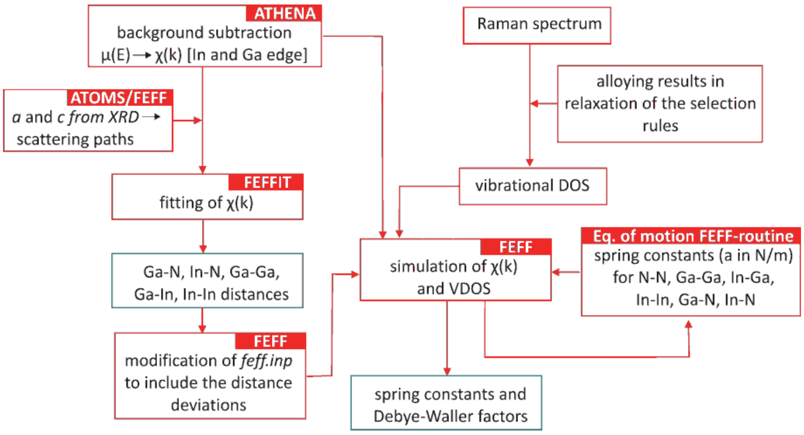

Figure 1: Analysis procedure

The $In_xGa_{1-x}N$ layers with x ranging from ~0.3 to ~0.5 were grown by plasma-assisted molecular beam epitaxy on Al_2O_3 (0001) substrates using AlN buffer layers. The Ga- and In-K-edge EXAFS spectra were recorded at the KMC-II and BAMLine beamlines, respectively, of the BESSY-II storage ring at the Helmholtz Zentrum, Berlin. The Raman spectra were recorded in the backscattering geometry using a micro-Raman system equipped with a liquid nitrogen cooled charge coupled device detector. The 457.9 nm blue line of an Ar+ laser was used for the excitation of the Raman spectra.

The analysis procedure is summarized in Fig. 1. The nearest neighbor distances are determined by shell-by-shell fitting. In the sample with x=0.48, the Ga-N, In-N, Ga-Ga, Ga-In and In-In distances were found equal to 1.96, 2.14, 3.29, 3.35 and 3.39 Å, respectively. The *feff.inp* file is then modified to take into account such distortions in the 1st and 2nd nearest neighboring shells. Next, the Ga- and In-K-edge $\chi(k)$ spectra are simulated and the Debye-Waller factors are calculated with the Equation of Motion method that also provides the stretching force constants for various types of atom pairs (Ga-N, In-Ga, Ga-Ga etc.). Best force constant values are obtained by comparing the calculated partial vibrational DOS with the Raman spectrum. Due to alloying, considerable fluctuations in the crystal potential take place leading to phonon confinement and consequently to the relaxation of the selection rules. As a result, the Raman spectrum resembles to the V-DOS. Simulation of the $\chi(k)$ spectra (in the k- and R-space) recorded at the Ga- and In-K-edges along with the Raman spectrum of the $In_{0.48}Ga_{0.52}N$ sample and the calculated contribution of atom-pairs in the V-DOS are shown in Fig. 2 and 3, respectively. Therefore, information on both the structure and the dynamics of the lattice can be obtained. Furthermore, due to the more accurate determination of the Debye-Waller factors, the uncertainty in the determination of the nearest neighbor distances can be considerably reduced.

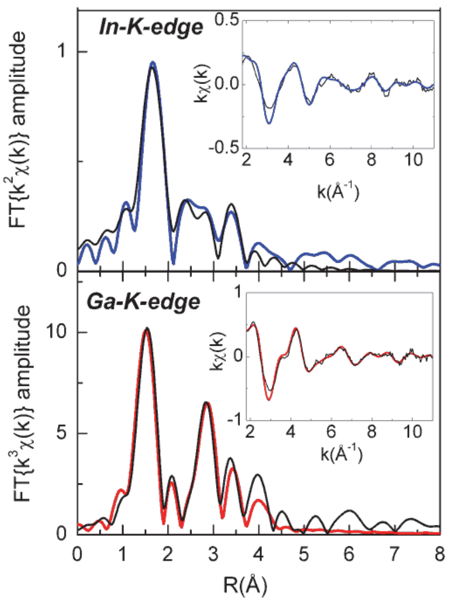

Figure 2; Simulation of the In- and Ga-K-edge $\chi(k)$ spectra and the corresponding Fourier transforms of the $In_{0.48}Ga_{0.52}N$ layer. The experimental curves are shown in black and the simulations by color lines.

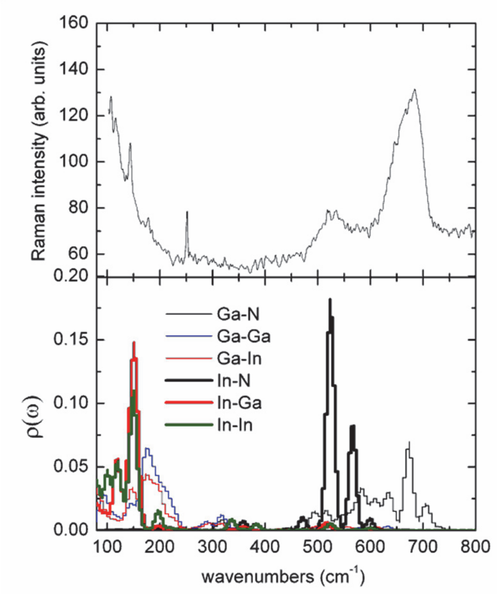

Figure 3; (Top) Raman spectrum of the $In_{0.48}Ga_{0.52}N$ layer, (Bottom) Partial contribution of the considered atom-pair scattering paths to the total V-DOS.

Acknowledgements: This work is supported by the European Union (European Social Fund – ESF) and Greek national funds through the Operational Program "Education and Lifelong Learning" of the National Strategic Reference Framework (NSRF)-Research Funding Program: THALES, project NitPhoto. The measurements at BESSY were funded from the European Community's Seventh Framework Programme (FP7/2007-2013) under grant agreement no.312284.

Structural and electronic properties of GaN/AlN and InN/GaN core /shell NWs

T. Pavloudis[1], Ph. Komninou[1], P.R. Briddon[2] and J. Kioseoglou[1]

[1]Physics Department, Aristotle University of Thessaloniki, GR-54124 Thessaloniki, Greece
[2]School of Electrical and Electronic Engineering, University of Newcastle upon Tyne

E-mail: corresponding-sifisl@auth.gr

III-nitride core/shell nanowires (NWs) grown along the polar direction comprise defect free non-polar interfaces, even for greatly lattice mismatched materials, offering significant improvements in the light-extraction efficiency compared with their planar counterparts. In this work GaN/AlN and InN/GaN core/shell NWs are investigated with the LAMMPS Molecular Dynamics and the AIMPRO DFT codes. Structural models of several thousands of atoms with multiple shell-to-NW rations are examined. The variations of the a lattice constants along [10-10] though the middle and through the edge and [11-20] are calculated and the results show an variation which is dependent on the direction. The a lattice constant remains unchanged through the core but it decreases with the shell-to-NW ratio, leading to a conclusion that as the shell gets thicker the core is increasingly compressed. The average stress calculations along [11-20] and [10-10] show that the shells are under tensile stress at the sides and the inner edges while being almost relaxed at the outer edges (Figure 1). The cores are under compressive stress, which is larger at the edges, and are almost relaxed in the center. The density of states is examined for each case and the bandgaps of the core/shell NWs are found to be free of deep states. The bandgaps increase exponentially with the shell-to-NW ratio and reach a maximum value for approximately 0.5.

.

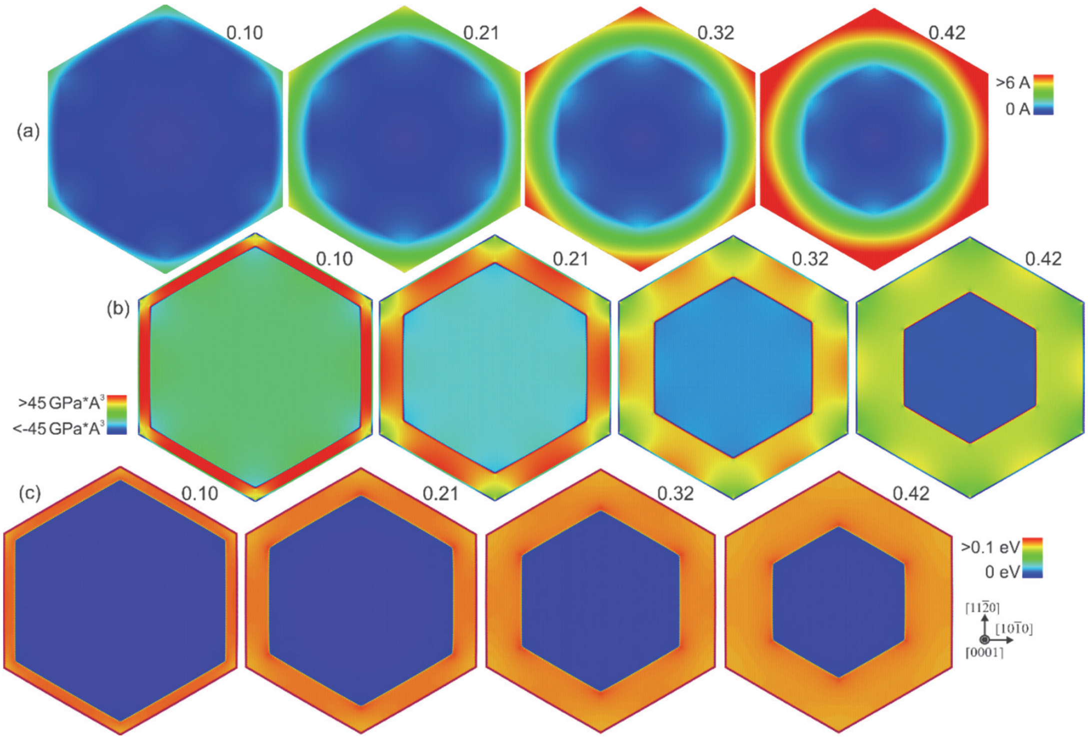

Figure 1: (a) Displacement magnitude compared to the relaxed GaN nanowire for the various shell-to-NW examined. (b) The average stress along the [11-20] and [10-10] directions for the various shell-to-NW ratios examined. (c) The excess energy per atom for the various shell-to-NW examined. In all the cases the atoms are pigmented according to the individual parameter that is calculated by the IP and following the corresponding color bar.

Acknowledgements: This research is supported by the European Union (European Social Fund – ESF) and Greece through the Operational Program "Education and Lifelong Learning" of the National Strategic Reference Framework (NSRF) and the Research Funding Program THALES: "Reinforcement of the interdisciplinary and/or inter-institutional research and innovation, project "NanoWire". The computations were supported by the LinkSCEEM-2 project, funded by the European Commission under the 7th Framework Program through Capacities Research Infrastructure, INFRA-2010-1.2.3 Virtua Research Communities, Combination of Collaborative Project and Coordination and Support Actions (CP-CSA) under grant agreement no RI-261600.

Small Angle Neutron Scattering investigation of thermal ageing effects in FeCr alloys

Y. Katsandredakis[1], **K. Mergia**[1], **S. Messoloras**[1],
U. Keiderling[2] **and A. Radulescu**[3]

[1] National Centre for Scientific Research Demokritos, Aghia Paraskevi, Athens 15310, Greece
[2] Helmholtz-Zentrum Berlin für Materialien und Energie GmbH, 12489 Berlin, Germany
[3] Jülich Centre for Neutron Science JCNS-1, Forschungszentrum Jülich GmbH, 52425 Jülich, Germany

E-mail: katsandredakis@ipta.demokritos.gr

The binary body centered cubic (bcc) Fe-Cr alloy is the base of many important industrial steels, especially in the nuclear industry. Ferritic martensitic steels are prime candidate structural materials for future fusion power plants and advanced nuclear applications. FeCr alloys with Cr concentrations in the range 6-15wt% are known to be highly resistant to radiation effects.

The equilibrium phase diagram for the Fe-Cr system indicates the presence of the miscibility gap for the alloy concentration above 10at% Cr at room temperature where a Cr-rich bcc a'-phase with up to 85 at% Cr is precipitated [1]. For lower concentrations of Cr the alloy is fully miscible and, moreover, diffuse neutron scattering experiments show a dramatic change of the ordering tendency towards the short-range order for these alloys [2]. Olsson et al. [1] showed that the bcc FeCr alloy exhibits an anomalous stability for compositions around 6-9at% Cr. The stability is apparent in the mixing enthalpy which is negative in this region but not for higher content.

In the current work model FeCr having Cr content between 0 and 14 wt%, with a low dislocation density and very low impurity level specially fabricated, were studied after isochronal thermal ageing Small-Angle Neutron Scattering (SANS) measurements. SANS is an important method for determining clustering phenomena or short range order. Samples of these alloys were isochronally thermally aged for 2 and 9 days at temperatures ranging from 400 to 700 ^{o}C. The application of a magnetic field during SANS measurements allows the separation of the magnetic correlations from the structural ones.

Acknowledgment: “The authors acknowledge funding from the Greek General Secretariat for Research and Technology and the European Regional Development Fund under the Action “Development Grants For Research Institutions–KRIPIS” of OPCE II.”

References

[1] P. Olsson *et al.*, Phys. Rev. B, 73 (2006) 104416.
[2] I. Mirebeau *et al.*, Phys Rev. Lett., 53 (1984) 687.

Effect of welding process Parameters and filler metal types on microstructure and mechanical properties of dissimilar stainless steel welds

N. Bensaid[*], A. Boutagane, M. F. Benlamnouar and M. Gousmine

Welding and NDT Research Centre (CSC), BP 64, Road of Dely Brahim, Chéraga, Algiers, Algeria.

E-mail: nblbensaid@gmail.com

Dissimilar weldments have been widely used in the industry and there are many applications in which weldments are made from metals of different compositions, because of economic benefits. However dissimilar is often more difficult than joining the same metals, due to the differences in the physical, mechanical, and metallurgical properties of the metals to be joined.

In this work the effect of welding process parameters and filler metal types such as 308L, 309L and 2205 on microstructure and mechanical properties of dissimilar stainless steel welds joints are studied. Microstructure, microhardness and tensile strength of the welds joints have been evaluated and the results are compared. The fracture surfaces of the tensile specimen were examined by scanning electron microscopy (SEM). From this investigation it is observed that we can use austenitic and duplex filler if the welding process parameters are optimized.

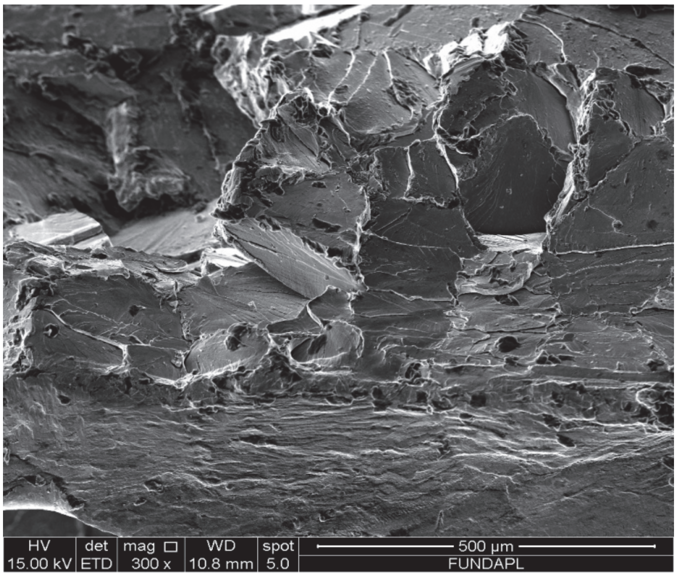

Figure 1: SEM fractographs of tensile specimens

References

[1] J. C. Lippold and D.J. Kotecki, Welding Metallurgy and Weldability of Stainless Steels, Wiley, Hoboken, NJ, 2005
[2] V. Satyanarayana, G. M. Reddy, and T. Mohandas, Journal of Materials Processing Technology, 160 (2005) 128–137.
[3] C. Silva, H. Miranda, H B. de Sant' Ana, and J. P. Farias. Materials and Design, 47 (2013) 1–8.

Effect of heat input and grain refining elements on microstructure and mechanical properties of Ferritic Stainless Steel welds

N. Bensaid[*], R. Badji, N. Tala Ighil, M. Hadji and M. F. Benlamnouar

Welding and NDT Research Centre (CSC), BP 64, Road of Dely Brahim, Chéraga, Algiers, Algeria.

E-mail: nblbensaid@gmail.com

Ferritic stainless steels are classified as such because the predominant metallurgical phase present is ferrite. These steels are characterized by good resistance to stress corrosion cracking (SCC), pitting corrosion, crevice corrosion (particularly in chloride environments), higher thermal conductivity, low coefficient of heat dilation and lower cost, when compared to austenitic stainless steels. The combination of low cost and good properties has made ferritic stainless steel more and more attractive in various application fields, such as, heat exchangers, petroleum refining equipment, storage vessels, protection tubes, solar water heaters, and exhaust manifold applications.

However, ferritic stainless steel steels are associated with many problems during the welding process. These problems are the martensite formation and grain growth, causing a reduction of ductility and toughness. For these reasons, until recently, the application of this group steels is limited in welded structures.

The aim of the present study is to investigate the influence of the Ti and Al on the microstructure and mechanical properties of AISI 430 ferritic stainless steel welds produced by GTA welding. The details of tensile tests, optical microscopic observations, microhardness, and Scanning electron microscopy (SEM) fractography, are discussed.

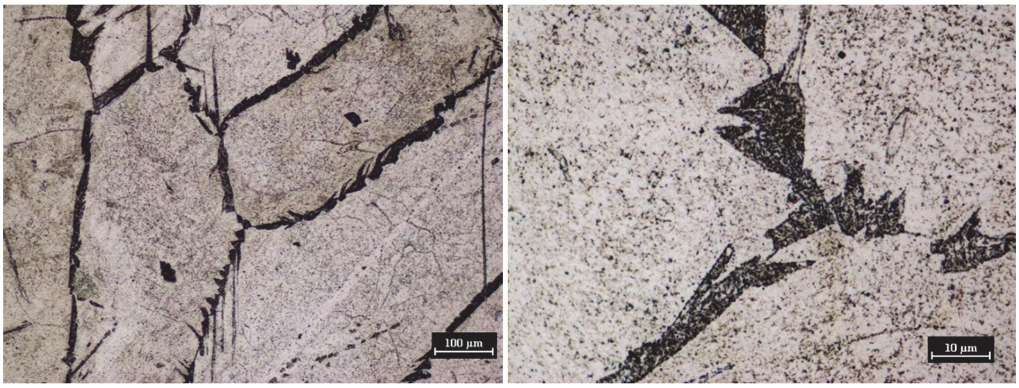

Figure 1: Martensite formation and grain growth in fusion zone of AISI 430 ferritic stainless steel weld

References

[1] M. Amuda and S. Mridha, Mat. Des., 35 (2012) 609-618.
[2] V. Villaret *et al.*, J. Mat. Res. Tech., 213 (2013) 1538-1547.
[3] M. Gurram, K. Adepu, R. Pinninti, M. R. Gankidi, J. Mat. Res. Tech., 2 (2013) 238-249.

MOP

P024

NDT and Optimization of welding process parameters of X70 welds

M. F. Benlamnouar, R. Badji, M. Hadji, N.Bensaid and M. Temmar

Welding and NDT Research Center (CSC), PB 64, Chéraga Algiers, Algeria

E-mail: csc.farid@yahoo.dz

Despite having extensive reference of tungsten arc welding process, publications number which describes relationships between different TIG welding parameters is very low. In This paper, we presents a new approach to optimize of TIG welding parameters by non destructive testing system in order to determine a total number of weld defects for each weld parameter. Radiographic image processing and ultrasonic techniques are used for evaluation of two parameters TIG welding of API X70 High Strength Low Alloy (HSLA). Increasing welding current from 75 to 150A and welding frequency from 2 to 6 Hz causes radical changes in the nature and number of welding defects. A better combination between welding current and welding frequency is obtained for 120 A and 4 Hz.

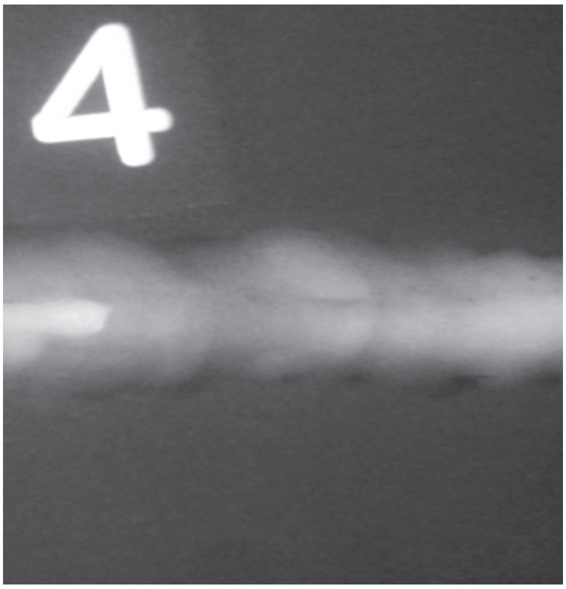

Figure 1: Radiographic image of sample (120A)

References

[1] Gang Wang and T. Warren Liao, NDT&E International, 35 (2002) 519–528.
[2] T. Saravanana and B. B. Lahiria, Procedia Engineering 86 (2014) 469– 475.
[3] Dong Hu, Qiang Wang, Kun Xiao, and Yehao Ma, Procedia Engineering, Volume 43 (2012) 459–463.

MOP

P025

Characterization of TiO_2 nanoparticles by X-ray Absorption Fine Structure Spectroscopy

S. Magkos[1], **F. Boscherini**[2], **L. Pasquini**[2], **and Z. El Koura**[3]

[1]Aristotle University of Thessaloniki, School of Physics, Thessaloniki, Greece
[2] University of Bologna, Department of Physics and Astronomy, Bologna, Italy
[3] University of Trento, Department of Physics, Trento, Italy

E-mail: smagkos@physics.auth.gr

Titanium dioxide (TiO_2) is a material used as a photocatalyst. It finds numerous applications in various fields such as water treatment, air pollution reduction, self-cleaning surfaces and photoelectrolysis of water. It is the only naturally occurring oxide of titanium at atmospheric pressure and it crystallizes in three polymorphs, with rutile and anatase being the only ones playing any role in its applications. Their unit shells are shown in Fig. 1. In this work, X-Ray Absorption Fine Structure (XAFS) spectroscopy has been used to study the local structure of TiO_2 nanoparticle samples.

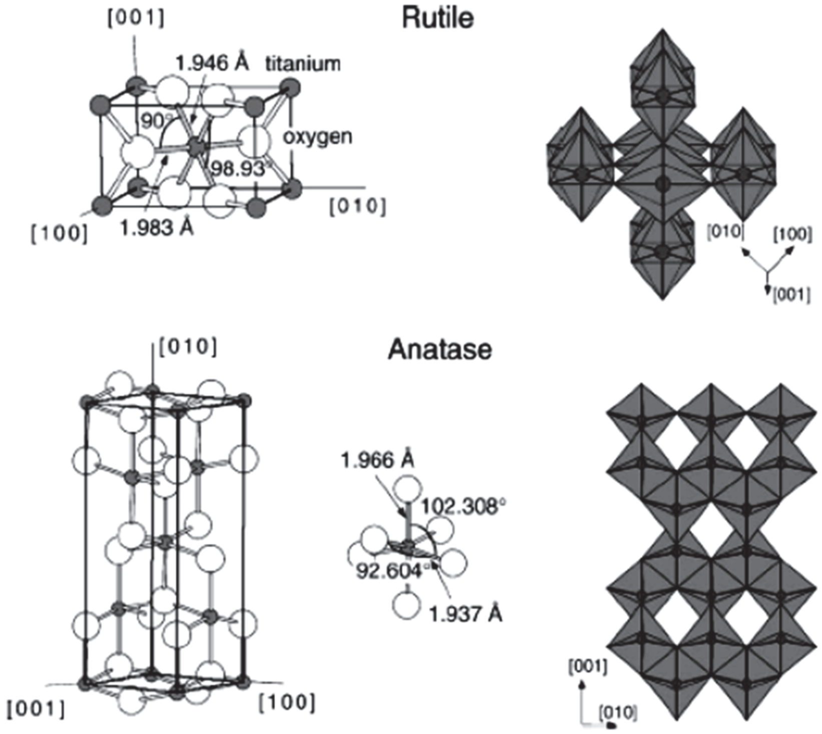

Figure 1: The unit cells of rutile and anatase [1]

The TiO_2 samples were grown on a silicon substrate. Their XAFS spectra were recorded at ELETTRA in Trieste and at the ESRF in Grenoble, performing either Direct Transmission or Fluorescence measurements.

The spectra obtained for all the samples were analysed with the same procedure being followed. The nearest neighbour distances are determined by shell-by-shell fitting. As shown in Fig. 2, multiple scattering paths have also been taken into consideration. Conclusions about the crystallization of the nanoparticles were reached and their structure was identified as that of either rutile or anatase or, when this was not possible due to a lack of a long-range order, it was deemed amorphous.

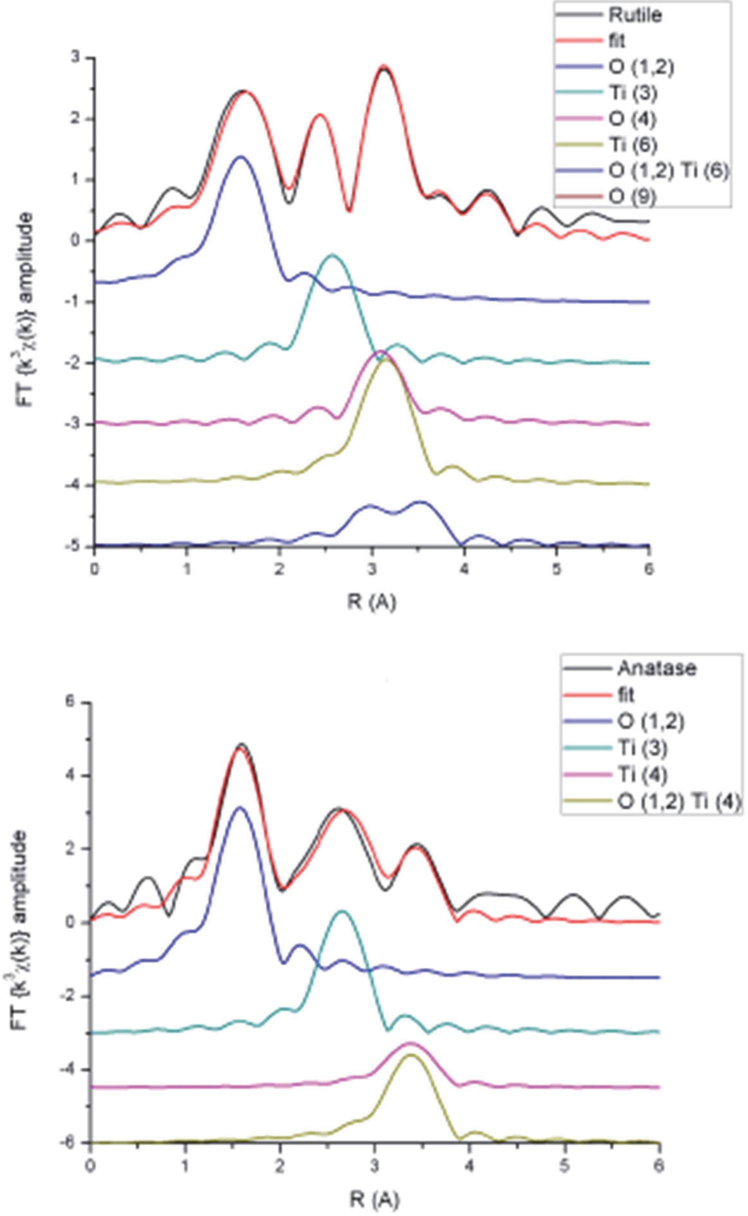

Figure 2: Magnitude of the Fourier transform, fit and contributions of individual paths for rutile and anatase. The numbers in brackets refer to the coordination shell that the corresponding atoms belong to.

References

[1] U. Diebold, Surface Science Reports, 48 (2003) 53-229.

Filler metal composition and mechanical behavior of TIG dissimilar joints

M. F. Benlamnouar, M.Gousmine, N. Bensaid andA. Boutaghane

Welding and NDT Research Center (CSC), PB 64, Chéraga Algiers, Algeria

E-mail: csc.farid@yahoo.dz

Bimetallic weld techniques have progressed a great deal in the last decade. In this work, the effect of the filler metal composition on microstructure and mechanical behavior of dissimilar HSLA-X70/304L stainless steels weld joint is investigated.
The dissimilar weld joints are fabricated using austenitic, duplex and low Carbone filler metal. The mechanical behavior is investigated through microhardness, charpy impact and tensile test.

The results show that, the weld metal composition has a great influence on mechanical properties and microstructure of weldments, in particular the grain size and phases nature, changes with filler metal composition. In addition presence of Martensitic lattes in the FZ when using the low Carbone filler metal, detailed microstructure examination is carried out and related to the mechanical behavior of the dissimilar joints.

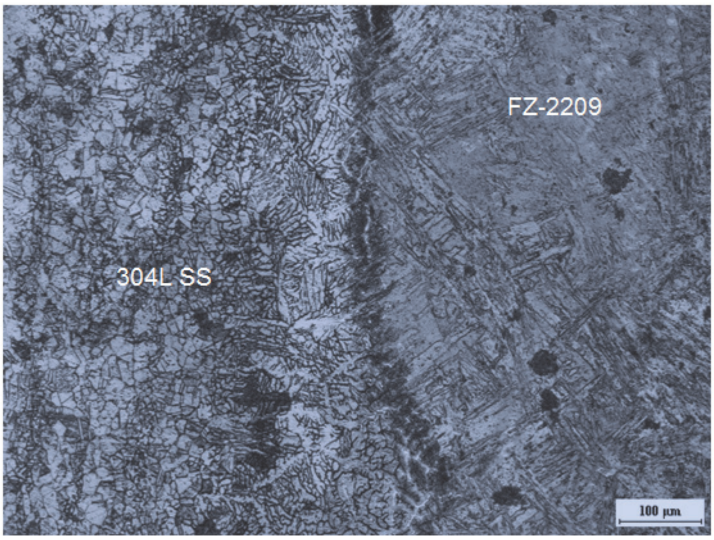

Figure 1: Micrographic of dissimilar joint 304L SS with 2209 DSS filler metal

References

[1] S. Jana, Journal of Materials Processing Technology, 33 (1992) 247-261.
[2] S. Wang, Q. Ma and Y. Li, Materials and Design, 32 (2011) 831–837.

Molecular dynamics investigation of GaN nanocluster formation in SiO_2

J. Karakostas[1], M. Katsikini[1], K. Termentzidis[2], E. Paloura[1] and J. Kioseoglou[1]

[1]Physics Department, Aristotle University of Thessaloniki, GR-54124 Thessaloniki, Greece
[2]Université de Lorraine, LEMTA UMR 7563, CNRS F-54506 Vandoeuvre Les Nancy, France

E-mail: sifisl@auth.gr

MOP

P027

Gallium and Nitrogen implantation in amorphous SiO_2 substrates and subsequent annealing lead to the formation of GaN nanocrystals with a broad dispersion in size that results in broadening of their emission spectra. In order to understand the growth and kinetic mechanisms involved in the GaN nanocluster formation in SiO_2, Molecular Dynamics simulations are implemented. By the use of atomistic modelling and taking into account all the necessary interatomic interactions, the in-depth analysis of the structural as well as of the physical properties of the related phenomena are analysed.

Initially all the possible crystalline structures of Si-O are analysed. A variety of interatomic potentials are tested on the various crystalline structures and the Tersoff [1,2] interatomic potential is concluded as the most suitable in order to describe accurately not only the Si-O interactions[3] but also the Ga-N, Ga-Ga[4] and the N-O, Ga-O, Si-N[5] and Ga-Si interactions. The a-quartz crystal structure of the SiO_2 is found the energetically favourable configuration, and the amorphization procedure is based on this structure. Several alternative procedures are used in order to tailor the parameters of the atomistic modelling of the amorphous SiO_2. Two experimentally identified characteristics of the amorphous SiO_2 are used in order to parametrize sufficiently the amorphization procedure of the atomistic modelling; the density of the amorphous phase and the pair correlation function. Both characteristics are accurately reproduced by the concluded amorphization procedure. In figure 1 the simulated amorphous phase of SiO_2 is presented as well as the corresponding pair correlation function (PCF) in agreement with the accompanied PCF of the crystalline structure.

Subsequently, the physical properties such as annealing temperature, Gallium and Nitrogen concentrations as well as the initial bonding environment of the implanted species in SiO_2 are established in order to tailor the growth of the GaN nanoclusters.

References

[1] J. Tersoff, Phys. Rev. B, 39 (1989) 5566–5568.
[2] D. W. Brenner, Phys. Rev. Lett., 63 (1989) 1022–1022.
[3] S. Munetoh, T. Motooka, K. Moriguchi, and A. Shintani, Comp. Mat. Science, 39 (2007) 334-339.
[4] J. Nord, K Albe, P. Erhart and K. Nordlund, J. Phys.: Condens. Matter, 15 (2003) 5649.
[5] Onyekwelu U. Okekea and J. E. Lowther, Physica B 404 (2009) 3577-3581.

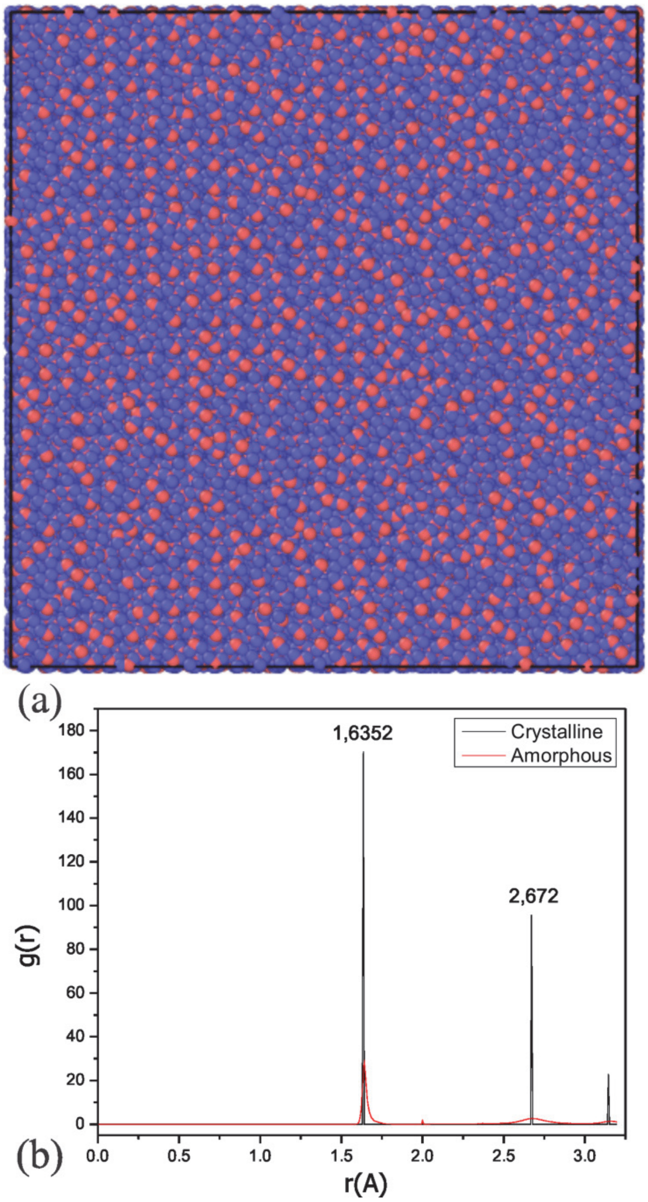

Figure 1: Atomistic model of the amorphous SiO_2(a) and the corresponding pair correlation function (b) which is found in agreement with the experimental one published in the literature [3].

Soft magnetic multilayered thin films for HF applications

**C. Serletis[1], G. Giannopoulos[1], G. Loizos[1], T. Maity[2], S. Roy[2], N. Lupu[3],
H. Kijima[4], M. Yamaguchi[5] and D. Niarchos[1]**

[1] Institute of Nanoscience and Nanotechnology, NCSR "Demokritos", Athens, Greece
[2]Micropower-Nanomagnetics Group, Tyndall National Institute,
University College Cork, Cork, Ireland
[3]National Institute of R&D for Technical Physics, Iasi, Romania
[4]Frontier Research Institute for Interdisciplinary Sciences, Tohoku University
[5]Dept. Of Electrical Engineering, Tohoku University

E-mail: cserleti@yahoo.gr

The recent surge in demand for miniaturization of power transformers and inductors requires magnetic core materials with low energy loss, high flux density, high permeability and high operating frequency. Furthermore, recent developments in magnetic materials such as CoZrO granular films, polymer bonded materials and CoNiFe alloy thin films, have been evaluated for the next generation integrated devices for high frequency applications [1]. Although there is an intensive activity in this area, it is still difficult to develop a high-power, high-frequency converter that uses inductors or transformers with integrated magnetic cores, particularly due to the lack of availability of high performance integratable high frequency magnetic materials [2].

In this work, several commercial amorphous materials (Metglas® 2605HB1M, Permalloy alloys, and Co/Zr alloy) with well known high flux density and low loss properties at lower frequencies are used to produce multilayered thin films by sputtering with very promising properties at higher frequencies.

Multilayered films were prepared using an Edwards 2-inch magnetron sputtering system, with a base pressure of $4\text{x}10^{-7}$Torr. Films were prepared from the following materials: Permalloy79 (79% Ni/16% Fe/5% Mo), Permalloy81 (81% Ni/17% Fe/2% Mo), and Co/Zr amorphous alloy (85% Co/15% Zr). In the case of Metglas® 2605HB1M (or in short HB1), a composite 2-inch diameter target made from amorphous ribbon was used (simply a stack of several round thin discs of 50 mm diameter cut out from the amorphous ribbon reel).

All the depositions were performed on SiO_2 substrates at 4mTorr Ar pressure. A 50nm Cr buffer was deposited on the substrate, in order to increase the adhesion of the magnetic layer. Aluminum oxide was used as an insulator. The DC power on the magnetic targets was 40 W, while the Al_2O_3 layer was deposited using 50 W of RF power.

X-ray diffraction patterns were obtained with a Rigaku Ultima+ diffractometer, using CuKa radiation. All samples exhibit an amorphous behavior, with no peaks indicating any crystalline traces.

AC hysteresis loops measurements were performed by B-H Loop Tracer at 50Hz. Table 1 summarizes the results for comparisons.

Table 1: Main magnetic properties of manufactured films

Sample	J_s (T)	H_c (Oe)
HB1	1,65	1,1
Permalloy79	0,8	0,5
Permalloy81	0,7	0,37
Co/Zr	0,99	11,85

The best results come from the HB1 sample, which possesses low coercivity combined with high saturation magnetization. The Permalloy samples have even lower coercivity, but their saturation magnetization does not exceed that of the bulk material, while the Co/Zr sample has a relatively high coercivity, which leads to higher AC magnetic losses. This is probably due to the presence of a secondary magnetic phase, evident in the hysteresis loop.

High-frequency complex permeability measurements up to 9 GHz were performed on the second batch samples in a PMM-9G1 permeameter from Ryowa Electronics, with a bias field of 10Oe. The results show no obvious correlation between samples. Still, some conclusions can be drawn: all samples retain their permeability up to 600MHz. The HB1 sample shows the best behavior so far, having a constant μ' greater than 800, up to 900MHz, with relatively low initial μ''. Both Permalloy samples have μ' greater than 800, but their μ'' is also large, and the cutoff frequency is low (<600MHz). The Co/Zr sample shows a behavior similar to that of HB1, with higher initial μ'' and the same performance vs. frequency, but a significantly lower μ' (≈300).

Multilayer thin films were fabricated on SiO2 substrates by sputtering. The films' microstructure has been investigated by SEM, TEM and XRD measurements. The multilayered films show the following soft magnetic properties: low Hc of 1-10Oe; Js of 0.7-1.6T; initial permeability greater than 300 in all samples, which remains constant up to nearly 900MHz in the best case. The very good soft magnetic properties of the multilayer films are associated with the reproducibility of the original amorphous material by sputtering and the multilayer concept itself. Our multilayer thin film properties in combination with their easy, fast and reproducible fabrication demonstrate that they may have applications as materials used under high frequency in the megahertz range for integrated inductive components.

References

[1] Q. Li, M. Lim, J. Sun, A. Ball, Y. Ying, F. C. Lee, and K. D. T. Ngo, Proc. IEEE 6th Int. Power Electron. Motion Control Conf. (2009) 1–8.

[2] C. O΄ Mathuna, N. Wang, S. Kulkarni, S. Roy, IEEE Trans. Power Elec. 27 (2012) 4799-4816.

Finite Element Micromagnetic Simulation of μMag standard problems

N. Ntallis and K.G. Efthimiadis

Department of Physics, Aristotle University, 54124 Thessaloniki, Greece

E-mail: kge@auth.gr

MOP

P029

In this work the finite elements method is used to study the μMag standard problems 1, 2 and 3 of National Institute of Standards and Technology [1]. A dynamic micromagnetic model is presented, where the evolution of the magnetization vector is not described by the trivial approach of the Landau-Lifshitz-Gilbert equation. The derivation of the partial differential equations (PDE) is based on a Lagrangian approach, assuming that the rotation of the magnetization vector in an elementary volume can be described by that of a rigid current loop.

Simulation model: Assuming a local magnetic moment as a current loop of constant dimensions and current intensity, the equations of motion can be obtained through Lagrangian mechanics. In order to take dissipation into account, a Rayleigh function is added, which describes a homogenous and isotropic dissipation with respect to the time gradient of the system. The PDE of magnetization $\vec{M}$ takes the form:

$$\left[\frac{\partial^2\vec{M}}{\partial t^2}-\left(\frac{\vec{M}}{M_s^2}\cdot\frac{\partial^2\vec{M}}{\partial t^2}\right)\vec{M}\right]+\frac{1}{\tau}\frac{\partial\vec{M}}{\partial t}=\frac{\upsilon}{2I}\left(\vec{M}\times\mu_0\vec{\mathcal{H}}\right)\times\vec{M}$$

where I is the moment of inertia of the loop about a symmetry axis lying on its plane, υ is the volume associated with the magnetic moment of the loop, M_s is the saturation magnetization and τ is the relaxation time of the system. The effective field $\vec{\mathcal{H}}$ can be defined by the variational derivative of the free micromagnetic energy. The main contributions to the micromagnetic energy arise from exchange, magnetocrystalline, magnetostatic and Zeeman energy. In this context, assuming a uniaxial anisotropy:

$$\vec{\mathcal{H}}=\ell^2\nabla^2\vec{M}+\kappa^2\left(\hat{u}\cdot\vec{M}\right)\hat{u}+\vec{H}_d+\vec{H}$$

where $\ell=\sqrt{\frac{2A}{\mu_0M_s^2}}$ is the exchange length, $\kappa=\sqrt{\frac{2K_1}{\mu_0M_s^2}}$ is the hardness parameter with K_1 the first order anisotropy constant and $\hat{u}$ the direction of the easy axis. In the absence of conducting media, the demagnetizing field $\vec{H}_d$ can be calculated from the gradient of a magnetic scalar potential φ, which obeys the Poisson equation $\nabla^2\varphi=-\nabla\vec{M}$. Finally, $\vec{H}$ is the external applied field.

The three PDE for magnetization components and the one for magnetic scalar potential are solved simultaneously through the finite element method by directly applying the weak form. Magnetization is interpolated using 3rd order Lagrange elements in the domain of a magnetic particle. The mesh consists of simplex tetrahedra and the mean mesh size was kept smaller than the width of a Bloch wall. For the magnetic potential

2^{nd} order Lagrange elements have been used, both on the magnetic particle domain and on the surrounding outer domain.

Simulation results

µMag Standard Problem No.1

Calculation of the magnetization loop in a permalloy film of length 2µm, width 1µm, thickness 20nm, exchange stiffness 1.3 10^{-11} J/m, saturation magnetization 8.0 10^5 A/m and uniaxial magnetocrystalline anisotropy of 5.0 10^2 J/m^3 with easy axis parallel to the long edge. External field is applied parallel to (a) the long side and (b) the short side of the film.

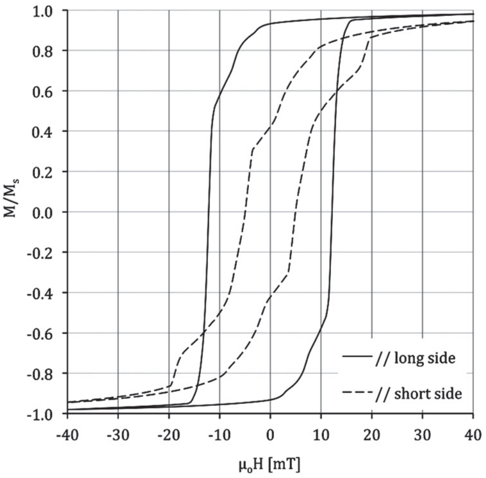

µMag Standard Problem No.2

Calculation of coercivity and remanence in a thin film of thickness *t*, width d and length *L*, as a function of *d/ℓ* with aspect ratios held constant at *t/d*=0.1 and *L/d*=5.0. Crystalline anisotropy is neglected and external field is applied in [111] direction.

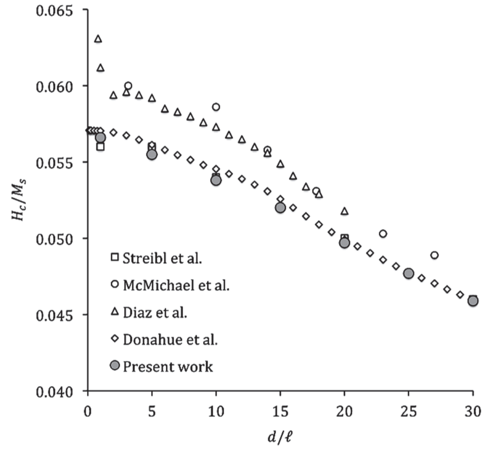

µMag Standard Problem No.3

Calculation of the single domain limit of a cubic ferromagnetic particle, i.e. the critical size *L/ℓ* of equal energy for the so-called flower state and the curling state. The particle has uniaxial anisotropy with hardness parameter κ=0.1 and with the easy axis directed parallel to a principal axis of the cube.

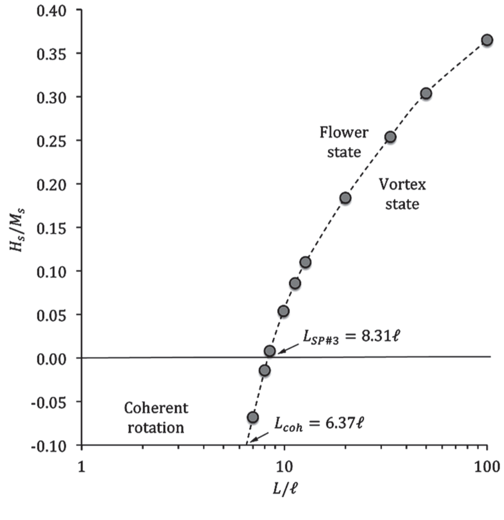

References

[1] http://www.ctcms.nist.gov/~rdm/mumag.org.html

Micromagnetic modelling of superparamagnetic particles

N. Ntallis and K.G. Efthimiadis

Department of Physics, Aristotle University, 54124 Thessaloniki, Greece

E-mail: kge@auth.gr

MOP

P030

In modern applications the size of magnetic particles extends to the range of a few nanometers. At this range superparamagnetic effects play an important role [1]. An increase in temperature leads to fluctuations of their magnetic moment, i.e. flipping it between the energy minima of the system. Brown's theory [2] states that the relaxation time of such a system τ can be described by an Arrhenius type law

$$\tau = \tau_0 e^{E/kT}$$

where τ_0 describes the time interval between attempts, E the energy barrier height and T the temperature.

In this work, we present a micromagnetic model for uniaxial spherical superparamagnetic nanoparticles. The evolution of the magnetization vector $\vec{M}$ is described by a partial differential equation (PDE) under the influence of an effective magnetic field arising from the exchange interactions, the magnetic anisotropy, the Zeeman energy and the dipole energy [3]. In a continuum approach the PDE takes the form

$$\tau \frac{d\vec{M}}{dt} = -\frac{1}{M_s^2} \vec{M} \times \left[\vec{M} \times \left(\vec{H}_{eff} + \vec{H}_{th}\right)\right],$$

where τ is a relaxation time of the system, $\vec{H}_{eff}$ is the effective magnetic field and M_s is the saturation magnetization [3]. For an isotropic and homogeneous material, the exchange field component of the $\vec{H}_{eff}$ is written as $\vec{H}_{ex} = \ell_x^2 \nabla^2 \vec{M}$, where $\ell_x = \sqrt{2A/\mu_o M_s^2}$ is the exchange length and A is the exchange stiffness. $\vec{H}_{th}$ is a thermal field that simulates thermal agitation and is considered as a Gaussian random process in space and time. The PDE are solved with the finite element method. The simulations begin with the particle at the saturated state, and the demagnetizing curve is calculated by reducing the external field, until negative saturation is reached.

In figure 1, the calculated demagnetization curves vs the amplitude of the thermal field are shown. From these curves, it is derived that the increase of thermal agitation leads to a reduction of the coercive field.

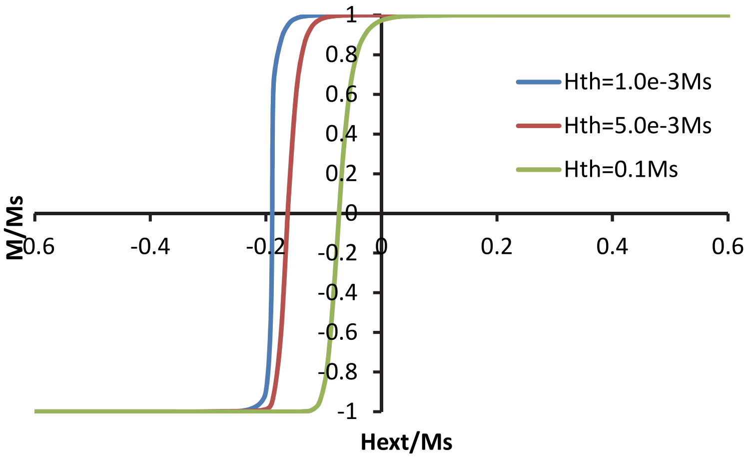

Figure 1: Demagnetization curves with respect to H_{th}. $H_k = 0.2M_s$

In figure 2, the calculated reversal time for zero magnetization with different degrees of freedom vs the amplitude of the thermal field is shown.

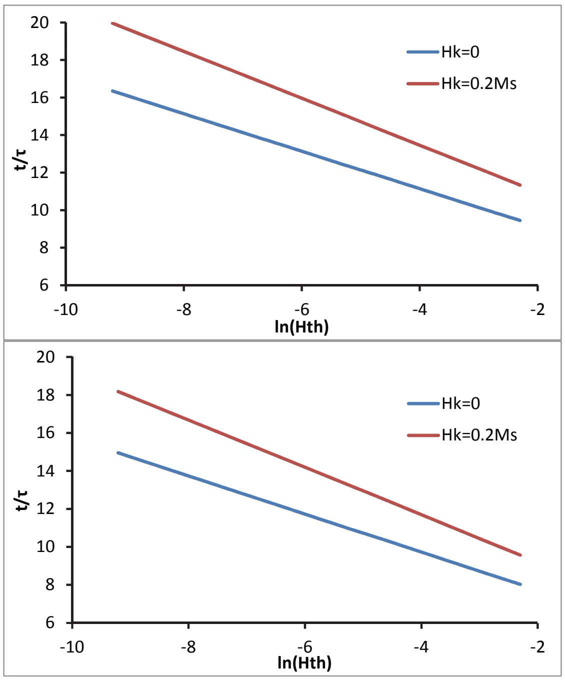

Figure 2: Reversal time versus the thermal field. for a) 6931 and b) 43812 degrees of freedom

The reversal time obeys a relation of the form

$$\frac{t}{\tau} = aln(H_{th}) + b$$

Both a, b depend on the anisotropy constant. Calculations show that the b coefficient shows a weak dependence from the degrees of freedom.

References

[1] J. M. D. Coey, Magnetism and Magnetic Materials, Cambridge University Press (2009)
[2] W.F. Brown Jr., Phys. Rev., 130 (1963) 1677.
[3] N. Ntallis, K.G. Eftimiadis, J. Magn. Magn. Mater. 363 (2014) 152.

An alternate treatment of surface effects in micromagnetism. Theory and computations

N. Ntallis[1], **K. N. Trohidou**[2] **and K. G. Efthimiadis**[1]

[1]Department of Physics, Aristotle University, 54124 Thessaloniki, Greece
[2]Institute of Nanoscience and Nanotechnology, NCSR Demokritos, Aghia Paraskevi, Attiki, Greece

E-mail: kge@auth.gr

The low temperature magnetic properties of magnetic nanoparticles as the size decreases are governed by surface effects [1]. Surface effects on magnetic nanoparticles have already been studied by means of atomistic Monte Carlo (MC) [1] and continuum micromagnetic approach using core-shell type morphology [2]. Here a micromagnetic model is presented for ferromagnetic nanoparticles, where the surface is treated as an effective artificial layer. The model consists of two coupled magnetization vectors for the volume and boundary respectively. The evolution of each one is described by a partial differential equation (PDE) under the influence of an effective magnetic field arising from the exchange interactions, the magnetic anisotropy, the Zeeman and dipole energy [3]. In a continuum approach the evolution of the magnetization vector $\vec{M}$ is described by an equation of the form [3]

$$\tau\frac{d\vec{M}}{dt} = -\frac{1}{M_s^2}\vec{M}\times\left(\vec{M}\times\vec{H}_{eff}\right),$$

where τ is a relaxation time of the system, $\vec{H}_{eff}$ is an effective magnetic field and M_s the saturation magnetization. Main contributions to the effective field arise from exchange interactions, anisotropy, dipole and Zeeman energy. For an isotropic and homogeneous material, the exchange field is written as $\vec{H}_{ex} = \ell_x^2\nabla^2\vec{M}$, where $\ell_x = \sqrt{2A/\mu_o M_s^2}$ is the exchange length and A is the exchange stiffness. The PDE are solved by means of a finite element method (FEM). The surface atoms, are subject to forces arising from the reduced number of neighbors leading to reduction of ℓ_x. Assuming an isotropic distribution on the surface the number of neighbors drops to half, thus $\ell_{xI} = \ell_x/\sqrt{2}$. The anisotropy can be directly defined by changing the magnitude and direction. Thus the equations to be solved are

$$\tau\frac{d\vec{M}}{dt} = -\frac{1}{M_s^2}\vec{M}\times\left(\vec{M}\times\left(\vec{H}+\ell_x^2\nabla^2\vec{M}\right)\right) \qquad \text{for the volume and}$$

$$\tau\frac{d\vec{M}}{dt} = -\frac{1}{M_s^2}\vec{M}\times\left(\vec{M}\times\left(\vec{H}_I+\ell_{xI}^2\nabla_T^2\vec{M}\right)\right)+\frac{\ell_x^2}{a}\frac{\partial\vec{M}}{\partial n} \qquad \text{for the surface nodes.}$$

∇_T^2 represents the tangent Laplacian on the boundary. In the above equations $\vec{H}$ and $\vec{H}_I$ in the core and the surface respectively represent the components of the effective field, not including the exchange. The last term represents the flux interchange between the core and the surface layer of the particle. For a more comprehensive study FEM simulations for core-shell type and atomistic MC simulations also took place for the same magnetic parameters.

In all of the simulations the particle is initially at the saturated state, and the demagnetizing curve is measured by reducing the external field, until negative saturation is reached. All methods indicate that H_s, the field where the departure for saturation takes place, has dependence analogous to $1/D$, where D is the diameter of the particle. Due to uncompensated surface spins there is a clear difference for small particles, because of the fact that the latter effects are not taken into account in the continuum approximation, showing that the continuum approach is valid over a physical size of the particle In the case of higher surface anisotropy convergence with MC is reached for smaller radii indicating the fact the higher anisotropy constant may wipe out more easily the effect of uncompensated spins.

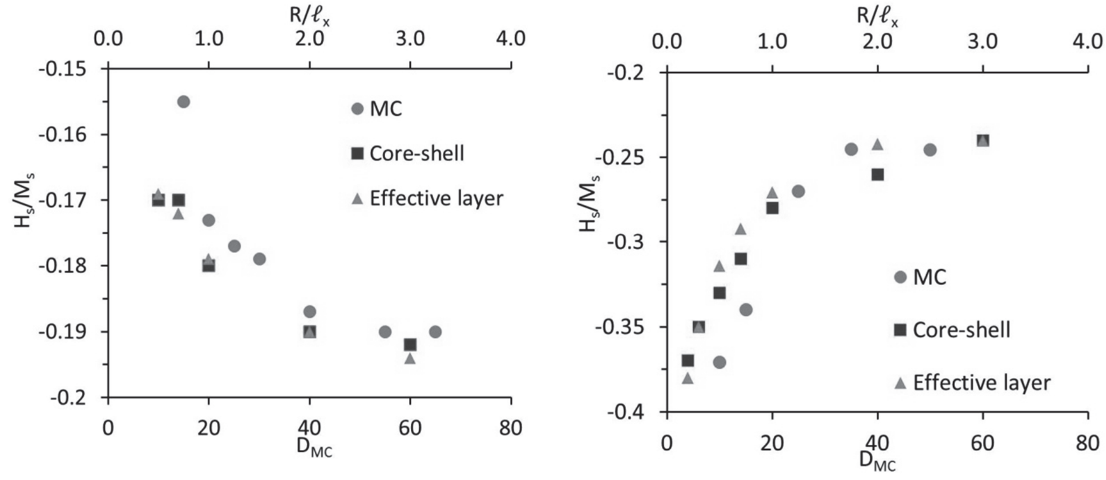

(a)

(b)

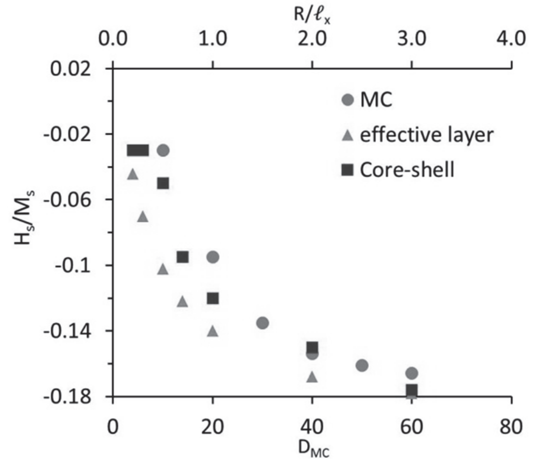

(c)

Figure 1: H_s vs R/ℓ_x for $a/\ell_x = 0.1$. Core has uniaxial anisotropy with $K_V = 0.1\mu_o M_s^2$ and surface has (a) uniaxial anisotropy with $K_S = 0.05\mu_o M_s^2$, (b) uniaxial anisotropy with $K_S = 0.25\mu_o M_s^2$, (c) normal anisotropy with $K_S = 0.1\mu_o M_s^2$. D_{MC} represents the diameter of the particle, in atomistic units, for MC simulations.

References

[1] K. N. Trohidou, "Monte Carlo studies on surface and interface effects of magnetic nanoparticles" in "Surface Effects in Magnetic Nanoparticles", Ed. D. Fiorani, Springer (2005).
[2] W. Scholz, D. Suess, T. Schrefl, and J. Fidler, J. App. Phys., 95 (2004) 6807.
[3] N. Ntallis and K.G. Eftimiadis, J. Magn. Magn. Mater., 363 (2014) 152.

Optimization of magnetic hyperthermia *via* synthesis parameters of magnetic nanoparticles

O. Patsia, E. Myrovali, A. Makridis, K. Simeonidis, I. Tsiaousis,
D. Sakellari and M. Angelakeris

Department of Physics, Aristotle University, 54124 Thessaloniki, Greece

E-mail: opatsia@physics.auth.gr

Magnetic hyperthermia has been recently described as a supplementary or even an alternative method to improve the therapy of cancer. This therapy involves the targeted administration of magnetic nanoparticles (MNPs) into the human body, their accumulation at cancer sites, and their local heating when an external AC magnetic field is applied. This heating can lead to cellular degradation and ultimately induce cancer cell apoptosis.

Iron oxide nanoparticles are the most widely studied materials for magnetic hyperthermia due to their biocompatibility and chemical stability. Another magnetic phase which is described as the sulfur equivalent of magnetite is the thiospinel greigite (Fe_3S_4), appears as a byproduct during magnetite biomineralization into magnetotactic bacteria. Greigite nanoparticles have recently attracted some interest in biomedical applications owing to their relative ease of surface functionalization, low toxicity and minimum effect to normal cells during magnetic hyperthermia.

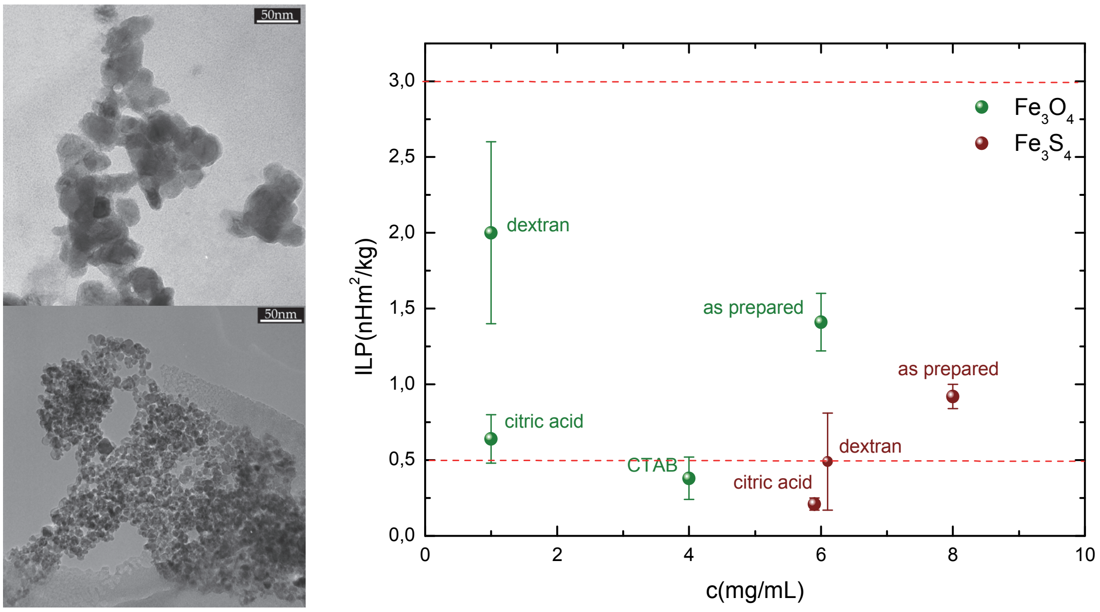

Figure 1: Left column: TEM imaging of greigite (top) and magnetite (bottom) nanoparticles. Right column: Maximum ILP values for each sample versus concentration. Each bar represents the width of ILP values as calculated for the field amplitudes under study (20, 25, 30mT) under frequency 765 kHz. The dotted horizontal lines denote current commercial hyperthermia ILP region.

The objective of this work constitutes the study of magnetite and greigite MNPs synthesized by co-precipitation of various bivalent iron salts using various surfactants (citric acid, CTAB, dextran) in an attempt to optimize the colloidal stability, the properties and heating efficiency under high frequency of AC magnetic field.

X-Ray Diffraction and Transmission Electron Microscopy indicate their single-phase and good crystallization (Left column in Fig.1). In terms of the magnetic features, their ferrimagnetic behavior is proved through Vibrating Sample Magnetometry hysteresis loops. For their thermal response, measurements of magnetic hyperthermia were made in different concentrations and fields of fixed frequency (765KHz) and variable amplitude (20, 25, 30 mT). The heating efficiency of MNPs is expressed by Intrinsic Loss Power (ILP) index which represents the heat amount released per particle mass, normalized against the field amplitude and frequency, so it is possible to directly compare experimental results performed in different laboratories and under different AC field conditions (Figure 1 Left). Thus, the horizontal dotted lines correspond to minimum and maximum ILP values of commercial ferrofluids from literature [1-2].

Eventually, our work reveals the role of surfactants in colloidal stability without sparing magnetic and heating efficiency features. Moreover, the greigite nanoparticles are introduced as novel materials with possible development in biomedical applications, achieve high thermal efficiency values comparable to those of magnetite and the biocompatible coatings such as citric acid and dextran can contribute to optimization of heating efficiency in lower concentrations and field amplitudes. Such milder hyperthermia conditions are desirable and exploitable for further application of magnetic hyperthermia in clinical practice.

References

[1] M. Kallumadil, M. Tada, T. Nakagawa, M. Abe, P. Southern, and Q. A. Pankhurst, Journal of Magnetism and Magnetic Materials, 321 (2009) 1509-1513.

[2] D. Sakellari, S. Mathioudaki, Z. Kalpaxidou, K. Simeonidis, and M. Angelakeris, Journal of Magnetism and Magnetic Materials, 380 (2014) 360–364.

The influence of nanoparticle arrays on magnetic hyperthermia

E. Myrovali[1], V. Ntoumpougidis[1], N. Maniotis[1], A. Terzopoulou[1], D. Sakellari[1], K. Simeonidis[1], U. Wiedwald[2], M. Farle[2], T. Samaras[1], O. Kalogirou[1] and M. Angelakeris[1]

[1] Physics Department, Aristotle University of Thessaloniki, 54124 Thessaloniki, Greece
[2] Faculty of Physics and Center for Nanointegration Duisburg-Essen (CENIDE), Universität Duisburg-Essen, 47048, Duisburg, Germany

E-mail: emiroval@physics.auth.gr

Hyperthermia is one of the many clinical protocols used as coadjutant therapy for cancer treatment. It has demonstrated a clear synergistic effect when combined with radiotherapy, as well as enhancing effects with numerous cytotoxic drugs. Magnetic hyperthermia uses a combination of alternating magnetic fields (AMF) and magnetic nanoparticles (MNPs) as heating agents. Materials' research for magnetic hyperthermia agents, up to date, focuses on iron oxide nanoparticles because they are biocompatible, and may be exploited at multifunctional aspects (i.e. MRI contrast agents, drug-carriers). The goal of this approach is to heat specifically and exclusively the local tumor region by means of the magnetic losses of magnetic nanoparticles in an external, alternating magnetic field, without damaging the surrounding healthy tissues. The heating efficiency of MNPs is quantified by the specific loss power (SLP) is determined of the power absorption per unit mass of magnetic material (W/g).The thermal response of MNPs depends on a large number of parameters, such as the intrinsic properties of nanoparticle (e.g. size, magnetization), the medium parameters (e.g. viscosity, stability) of the solution and the field features (amplitude, frequency). Depending on conditions (e.g. pH variations, medium viscosity) MNPs may be arranged in a controllable way to form stable arrays, (e.g. spheres or lines) in which magnetic interactions (exchange and/or dipolar) may beneficiary combine resulting to enhanced SLP values [1].

In this work, we investigate the possibility to arrange magnetite nanoparticles into arrays and study the effect of such formations in their magnetic hyperthermia efficiency. Two magnetite nanoparticle systems consisting of smaller ~10 nm and bigger ~40 nm MNPs were prepared following an aqueous co-precipitation synthetic route. To achieve their arrangement, MNPs were dispersed in an agar solution (0.5-50 mg/mL) under a static magnetic field to form the oriented arrays and left to cool down, to fix these designations within an agarose gel matrix. In each case, two array specimens were prepared under a field of 40 mT applied for 30 min either parallel ($\theta=0^o$) or perpendicular ($\theta=90^o$) with respect to hyperthermia field direction (Figure 1e) while a reference sample with random MNPs (Figures 1a and 1b) was left to cool down without magnetic field. Structural and morphological characterization was performed by X-ray Diffraction and Scanning (SEM) and Transmission Electron Microscopy (TEM). Static magnetometry hysteresis loops at room temperature were recorded for all samples and finally AC hyperthermia cycles were recorded in two different applied frequencies (210, 765 kHz) and field 30 mT.

As the SEM images of Figures 1c and 1d depict, the MNPs are forming (linear arrays) following the guidance of the external magnetic field while agar's structure maintains their blocking to this direction after field removal. Therefore, arrays' length is determined by the agar's concentration. The array formation is readily expressed at the shape of hysteresis loops and seems to have a positive (depending on field configurations depicted in Figure. 1e) influence on magnetic hyperthermia efficiency as expressed by SLP values shown in Figure 1f. In order to unravel how the array formation affects AC hyperthermia response, the heat transfer within the colloid was simulated under realistic experimental conditions including field parameters (field amplitude and spatial uniformity) and colloidal features (solution viscosity, agar content, MNPs concentration).

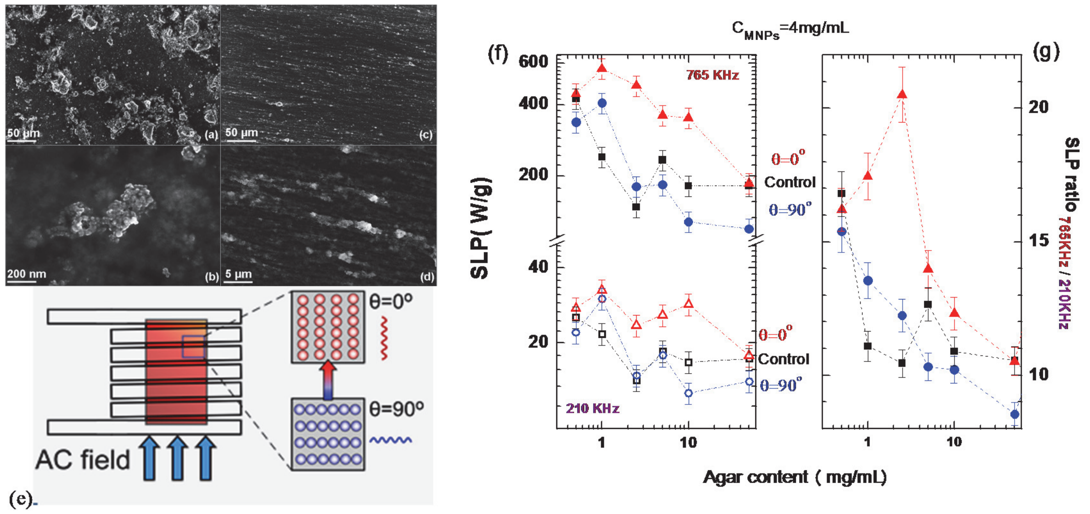

Figure 1: Magnetite MNPs (~40 nm, 4 mg/mL): SEM images of 1 mg/mL agar-content aqueous dilution, without magnetic field (a), (b), under static magnetic field (c), (d). Schematics of the hyperthermia coil with the sample inserted, where the two array configurations (θ=0, 90°) with respect to AC field are also shown (e). The effect of varying agar content for the three different configurations (control: random MNPs, θ=0°, and θ=90°) (f) frequency ratio influence (g).

This work deals with the formation of nanoparticle arrays, when the samples are subjected to the magnetic field, and reveal the improvement of heating efficiency. The latter is attributed to the effect of solution viscosity tuned by the agar concentration to the formation of the line arrays together with the dipolar interactions governing array formations and their stability.

The oriented arrangement of magnetic nanoparticles is recognized as an important pathway in the magnetic-hyperthermia material roadmap. By arranging at the nanoscale, enhanced heating efficiency occurs in correlation with collective magnetic features. This knowledge opens new perspectives for improved manipulation of magnetic hyperthermia agents, a facile, alternative option to conventional material oriented schemes.

References

[1] D. Serantes, K. Simeonidis, M. Angelakeris, O. Chubykalo-Fesenko, M. Marciello, M. del Puerto Morales, D. Baldomir and C. Martinez-Boubeta, J. Phys. Chem. C, 118 (2014) 5927–5934.

MOP

P034

Enhanced Magnetic Heating Efficiency By Nanoscale Mixing And Matching In Ferrite-Based Nanoparticles

S. Liébana Viñas[1,3], K. Simeonidis[2], Zi-An Li[1], E. Myrovali[2], A. Makridis[2], D. Sakellari[2], M. Angelakeris[2], U. Wiedwald[1], M. Spasova[1] and M. Farle[1]

[1]Fakultät für Physik and Center for Nanointegration Duisburg-Essen (CeNIDE), Universität Duisburg-Essen, Lotharstr. 1, Duisburg 47048, Germany
[2]Department of Physics, Aristotle University of Thessaloniki, 54124, Greece
[3]Departamento de Física Aplicada, Universidade de Vigo, Vigo, Spain

E-mail: sara.liebana-vinas@uni-due.de

Magnetic Particle hyperthermia (MPH) is an anti-cancer therapeutical scheme able to deliver severe thermal shocks to targeted cancer sites. In an external AC magnetic field magnetic nanoparticles (MNPs) produce heat via mechanisms strongly interconnected with their morphological, structural and magnetic profile. In addition to the established usage of iron oxide magnetic nanoparticles (MNPs) in biomedicine spinel ferrites are nowadays proposed as alternatives for MPH mediators, MRI contrast agents or drug carriers [1].

In an attempt to combine hard with soft magnetic features and simultaneously introduce biocompatibility, two alternative synthetic procedures were followed, each one comprised of two stages. The first synthetic procedure initiated by Co-ferrite or Mn-ferrite nanoparticles followed a typical thermal decomposition route in an organic environment resulting in typical sizes < 10 nm. At a second stage, magnetite synthesis was attempted, using Co-ferrite or Mn-ferrite as seeds, resulting in MNPs of < 15 nm in diameter. The goal was to form a Fe_3O_4 shell around the intrinsically toxic ferrite nanoparticles, providing internal nanoscale magnetic interfaces and suitable biocompatible coverage as well. A second independent synthetic procedure based on the aqueous co-precipitation of proper salts was also attempted to obtain similar mixed ferrite systems with an additional biocompatible shell of citric acid.

Structural and morphological features were revealed by XRD and TEM studies while EDX mapping unraveled the stoichiometry of the nanoparticle. SQUID magnetometry indicated that mixed ferrite systems have significant coercivity and high magnetization values, appearing as the result of the exchange interaction between a magnetically "harder" with a magnetically "softer" phase at the *intra*-particle interface. These features are readily seen also in magnetic particle hyperthermia experiments where the superior behavior of mixed ferrite systems may be directly exploited.

Acknowledgements: Financial Support from the European Community´s Seventh Framework Program (FP7-NMP) under grant agreement no. 280670 (REFREEPERMAG) and the University Duisburg Essen is acknowledged. Complementary support of the "DAAD" from a bilateral German-Greek collaboration under IKYDIA project is also acknowledged.

References

[1] M. Angelakeris *et al.*, J. Magn. Magn. Mater., 381 (2015) 179.

Reliable measurements and error-free data handling of magnetic particle hyperthermia parameters

A. Terzopoulou, N. Varveris, A. Makridis, E.Myrovali, K. Simeonidis,
T. Samaras, O. Kalogirou and M. Angelakeris

Department of Physics, Aristotle University of Thessaloniki, 54124 Thessaloniki, Greece

E-mail: anterzop@physics.auth.gr

MOP

P035

In magnetic particle hyperthermia (MPH), the heat generated by magnetic nanoparticles (MNPs) in an alternating magnetic field is used to achieve a temperature increase in the surrounding environment. It is known that cancer cells are more vulnerable in mild temperature increases (41ºC-45ºC) than healthy ones. That is the reason why magnetic hyperthermia is nowadays regarded as an alternative least-invasive technique against cancer tumors. The heating ability of MNPs is quantified by Specific Loss Power (SLP) index expressed in (W/g), which refers to the amount of energy converted into heat (J) per time (s) and per mass (g) of the magnetic material (m_{MNNPs}) as follows:

$$SLP = C_p \frac{m_f}{m_{MNPs}} \frac{\Delta \mathrm{T}}{\Delta \mathrm{t}}$$

where C_p is the specific heat of the solution, m_f is the solution mass and $\Delta T/\Delta t$ the initial slope of the heating curve under magnetic field extracted from experimental data.

A wide variety of magnetic nanoparticles have been developed for use in MPH, focusing initially on the facile preparation, expected biocompatibility and chemical stability of a wide spectrum of MNPs and eventually on nanomagnetism tuning to further increase heating efficiency. For example, increase of the saturation magnetization, control of magnetic anisotropy through the crystallinity, shape, exchange and interparticle interactions of MNPs are also alternative approaches currently being examined to maximize heating efficiency.

Despite the intrinsic nature of heating efficiency described above, another important issue is related to the magnitude of reported SLP values that appear to vary considerably for similar materials. Such discrepancy is usually related to the experimental parameters and protocols followed by studies performed in different labs. This originates from the use of diverse commercial or custom-made devices working under different conditions and, as a consequence, the absence of a universal protocol to give reliable, comparable results [1,2]. Accordingly, any kind of comparison should not be performed by just considering the SLP index, but only after evaluating a series of parameters and ensuring the highest resemblance in experimental conditions. Left image of figure 1 depicts an experimental hyperthermia setup indicating the parameters interfering in SLP estimation. Beside the intrinsic property due to magnetic fluid dispersion, AC generator (field frequency and amplitude), thermal insulation, thermometer and induction coil setup (turns, diameter) also influence significantly the SLP estimation. In this work, we propose an experimental protocol, together with a calculation sequence, providing more reliable SLP values, avoiding overestimations and misinterpretations. To start with, modeling of experimental setups has indicated that important errors may be introduced because of heating losses to the environment, insufficient or exaggerated cooling of the coil and formation of temperature gradients within the sample volume (in Fig. 1, right top figures depict potential temperature gradients due to coil, vessel and thermometer position).

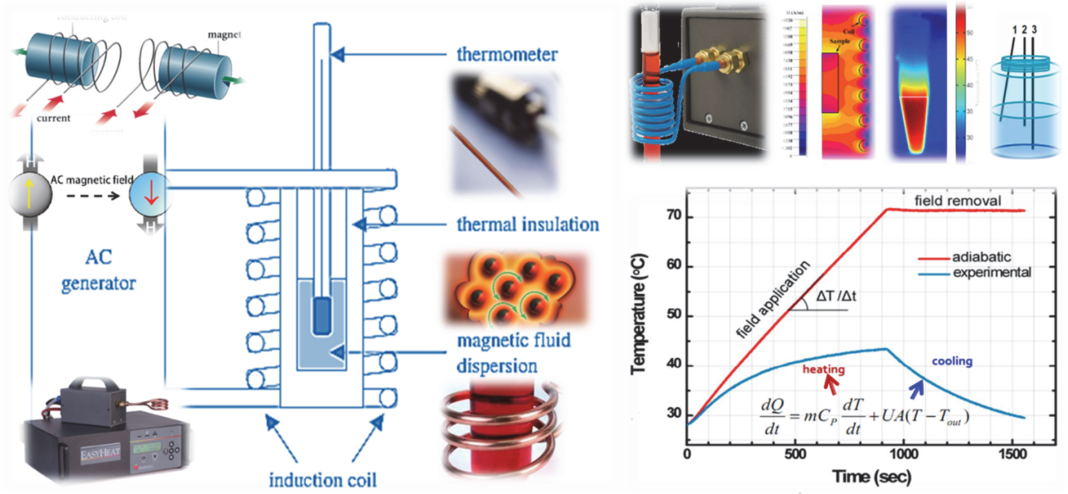

Figure 1: Left: Schematic of a magnetic hyperthermia experimental setup showing the various components affecting SLP index: (magnetic fluid dispersion, AC generator: frequency, amplitude, thermometer, induction coil, thermal isolation). Right: Top image: temperature distribution study due to coil setup, vessel material, shape and insulation, thermometer position. Bottom diagram: Experimental heating curve (blue) and adiabatic one (red) after data treatment to isolate magnetic nanoparticle heating effect.

In addition, we experimentally examine the measurement setup parameters (such as various thermal insulations, different vessel materials and shapes, variable thermometer positions and coil setups varying in turns, diameter, frequency and amplitude of AC field) that may affect the SLP estimation by changing dramatically the experimentally observed temperature variations. Reliable calculation of SLP from the experimental MPH curve (blue curve in bottom right diagram of Fig. 1) has two stages: (a) Coil heating effect and (b) Environmental losses. Initially, a background signal measured for pure solvent under similar conditions is subtracted to eliminate any contribution to sample temperature from coil heating. To exclude the environmental losses, we follow the modified law of cooling, [3] an ideal heating curve is extracted based on exponential fitting of the cooling stage of experimental curve (denoted as adiabatic curve (blue) also shown in bottom right diagram of Fig. 1). Ultimately, this ideal heating curve provides the actual temperature rise caused solely by the magnetic field of the nanoparticles, to provide reliable and accurate SLP estimation by excluding all non-magnetic origin heating contributions.

References

[1] S. Huang, S.-Y.Wang, A. Gupta, D.-A. Borca-Tasciuc, and S. Salon, Measur. Sci. Technol., 23 (2012) 035701.
[2] R. Wildeboer, P. Southern, and Q. Pankhurst, J. Phys. D: Appl. Phys., 47 (2014) 495003.
[3] K. Simeonidis, C. Martinez-Boubeta, Ll. Balcells, C. Monty, G. Stavropoulos, M. Mitrakas, A. Matsakidou, G. Vourlias and M. Angelakeris, J. Appl. Phys., 114-10 (2013) 103904.

Orbital and spin order transitions in $LaMn_{1-x}Cr_xO_{3+\delta}$ ($\delta \approx 0$) perovskite compounds.

K. Georgalas, E. Syskakis and A. Samartzis

Department of Solid State Physics, School of Physics, University of Athens,
Panepistimiopolis, GR-15784 Zografos, Athens.

E-mail: kogeorg@phys.uoa.gr

In the present work the effect of Cr substitution for Mn on the orbital order-disorder (Jahn-Teller) transition in $LaMn_{1-x}Cr_xO_3$ (x=0.00-0.35) has been investigated. The literature has mainly focused on their magnetic-structural properties in order to investigate the nature of the magnetic interactions in Mn^{3+}-Cr^{3+} (double exchange (DE) or super exchange interactions (SE))[1, 2]. The influence of Cr-doping on the Jahn-Teller distortion has not been investigated up to present times. Cr^{3+}, with an ionic radius (0.615Å) almost similar with Mn^{3+} (0.645Å) is not expected to cause appreciable lattice distortion. However, as the Cr^{3+} has the same electronic configuration with Mn^{+4} (t_{2g}^3 e_g^0) which is non-Jahn-Teller ion, non-distorted $Cr^{3+}O_6$ octahedra should be randomly distributed at spatially fixed Mn^{3+} sites in the perovskite lattice.

The powders of $LaMn_{1-x}Cr_xO_{3+\delta}$ ($\delta>0$) compounds have been prepared (using high purity La_2O_3, $Cr(NO_3)_3 \cdot H_2O$ and MnO_2) by solid state reaction in air. Pressed samples of different Cr concentrations were simultaneously treated at $T=1300^0C/t=5h$ under $P_{O2} \approx 9 \cdot 10^{-11}$ bar in order to achieve negligible excess of oxygen ($\delta \approx 0$). Electrical resistivity $\rho(T)$ (T=300-1100K), heat capacity $C_P(T)$ (T=300-820K) and $\chi_{ac}(T)$ (T=80-300K) measurements were carried out to investigate the effect of Cr-doping on the cooperative Jahn-Teller distortion, as well as the magnetic ordering in $LaMn_{1-x}Cr_xO_3$ specimen. Measurements of heat capacity, $C_P(T)$ were carried out by a home-made calorimeter using the relaxation method. XRPD patterns confirmed that the specimen are single phased with Orthorhombic symmetry (Pnma) at T=300 K. An abrupt decrease of $\rho(T)$, observed at 650-750K, fig. 1, is recognized as the signature of orbital order-disorder Jahn-Teller transition. Upon increasing Cr content, the drop of $\rho(T)$ becomes progressively smeared and is not observed for $x \geq 0.20$. The transition temperature, T_{J-T}, shifts almost linearly to lower values for x<0.20.

According to the $C_P(T)$ measurements, single peaks are observed at T≈400-750K, reflecting the Jahn-Teller phase transitions (fig 2). The peak temperatures of $C_P(T)$ decrease with increasing Cr content and they are very close to the corresponding T_{J-T} for each x. The peak which is observed for the sample with x=0.20 seems to be very broad. The gradual broadening of the peaks and their height decrease with x, clearly indicates that the lattice deformation is diminished. The entropy and enthalpy changes estimated from the data of fig. 2, associated with the $C_P(T)$-peaks, decrease monotonously with x.

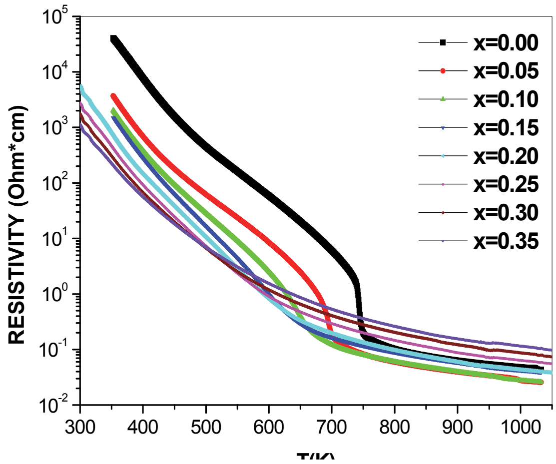

Figure 1: Resistivity of $LaMn_{1-x}Cr_xO_3$ (x=0.00-0.35)

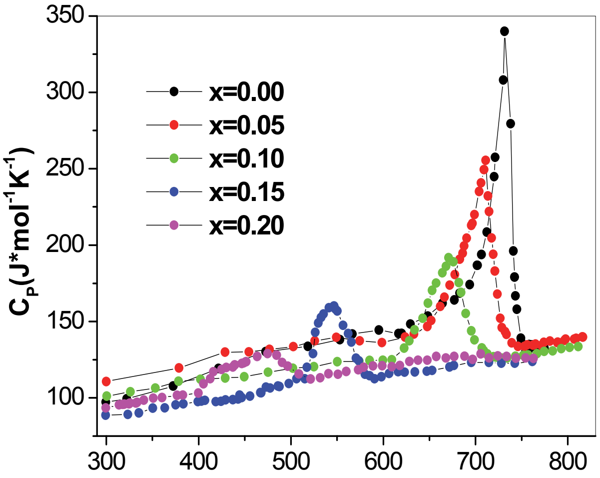

Figure 2: Heat Capacity of $LaMn_{1-x}Cr_xO_3$ (x=0.00-0.20)

The $C_P(T)$ of the non-doped sample is in good agreement with literature [3]. However, in other work [4], the $C_p(T)$ of $LaMnO_3$ sample displays a narrower and a slightly higher peak at the same T. Our results clearly show that Cr substitution for Mn in $LaMn_{1-x}Cr_xO_3$ suppresses the cooperative J-T distortion and weakens the orbital order-disorder transition. It should, however, be remarked that the results of ρ(T) and $C_P(T)$ comes unambiguously in sharp contrast to the conclusions in ref. [5].

The $\chi_{ac}(T)$ of undoped sample shows an A-type AFM transition at $T_N \approx 135$ K. The spontaneous susceptibility increases drastically with Cr content, reflecting the FM alignment of Cr with the neighbor magnetic ions [6]. The peaks of Cr-doped samples are attributed to Canted-AFM transitions. For the Cr-doped specimen the T_{CA} decrease with x, while going through a shallow minimum for x=0.15-0.25 due to the development of strong FM-AFM competition between Cr^{3+} and Mn^{3+} ions.

References

[1] Y. Sun *et al.*, Phys. Rev. B, 63 (2001) 174438.
[2] L. Morales *et al.*, Phys. Rev. B, 72 (2005) 132413.
[3] K. T. Jakob and M. Attaluri, J. Mater. Chem., 13 (2003)
[4] H. Satoh *et al.*, Thermochim. Acta, 299 (1997) 123-126.
[5] Aline Y. Ramos *et al.*, Phys. Rev. B, 87 (2013) 220404(R).
[6] L. Morales *et al.*, J. of Alloys and Compounds, 369 (2004)

Thermomagnetic analysis and magnetic properties of $RFe_{6-x}Si_x$ (R= Y, Sm, Gd, Dy, Ho, Lu) alloys.

M. Gjoka, V. Psycharis and D. Niarchos

INN, NCSR “Demokritos”, Athens, Greece

E-mail: m.gjokas@inn.demokritos.gr

In this work is reported the research on the possible new intermetalics $RFe_{4.48}Si_{1.52}$ (R=Y, Sm, Gd, Ho, Lu), and $DyFe_{6-x}Si_x$ (x=1, 1.2, 1.4). All studied samples contain different phases in variable composition like the silicon doped $Re(Fe,Si)_{17}$, (Rhombohedral Th_2Zn_{12} structure type), the RFe_4Si_2, ($ZrFe_4Si_2$ structure type), the RFeSi (PbClF structure type) and the RFe_2Si_2 (CeAl2Ga2 structure type). Some samples show one magnetic transition, the other two or three magnetic transition.
The intermetallic compounds containing rare-earth atoms form a numerous class, is well studied for many years in both fundamental and applied research. Ternaries occur in most cases in R-T-X systems, where R is a rare-earth, T is a transition metal, and X is a post-transition element. A compilation of crystal data and a discussion of the crystal chemistry of ternary rare-earth intermetallics were made by Parthé and Chabot [1]. An updating of ternary phase equilibria and crystal chemistry in ternary rare-earth systems was reported by Gladyshevskii et al. (1990) [2] etc. The total number of known ternary phases increases every year.

The research on iron–based intermetallic compounds as possible candidates for permanent magnets still remains attractive. There have been many efforts for the improvement of these materials. Most have to do with the partial replacement of Nd by another rare earth or the partial substitution of Fe atoms by the magnetic Co or even by non magnetic atoms, like a post-transition metal Ga and Bi or a metalloid like Si and the partial substitution of B by carbon atoms. In this work we report our research on the possible new intermetallics with starting composition $R(FeSi)_6$.
R-Fe-Si ingots were prepared by arc-melting elemental constituents of high purity (99.9%), with the starting composition $RFe_{4.48}Si_{1.52}$ (R =Y, Sm, Gd, Ho, Lu), and $DyFe_{6-x}Si_x$ (x=1, 1.2, 1.4) subsequently followed by annealing (wrapped in tantalum foil) in vacuum at 973 K for thirty days and then fast quenching in water. X-ray diffraction (XRD) data of powder samples were obtained using Cu–Kα radiation. The TMA measurements were carried out by applying a magnetic field of 150 Oe, using a heating rate of 5 ^{o}C/min under Ar flow. Magnetization isothermal measurements at 10 and 300 K were recorded by VSM and SQUID magnetometer.
In the Table 1 are given the Curie temperatures and the magnetization values for allstudied samples at 10 K and at 300 K (RT).

The room temperature magnetization of samples increases from 29.5 for Dy to 55.9 Am^2/kg for Y-sample, while the magnetization at 10 K reach a value of 70.03 Am^2/kg for Y. The Ho samples have a coercive field H_c of 3.2 kOe at 10 K. Demagnetization curves measured at 10 K and at RT are shown for Gd and Ho.

Analysis of XRD diffraction patterns shows that the system is a complicated one, no one of the studied samples is a single phase one (Table 2). All studied samples contain different phases in variable composition. These phases are: the silicon doped $R(Fe,Si)_{17}$, (Rhombohedral Th_2Zn_{12} structure sype), the RFe_4Si_2 , ($ZrFe_4Si_2$ structure type), the RFeSi , (PbClF structure type) and the RFe_2Si_2($CeAl_2Ga_2$ structure type).

Table 1: Curie temperatures and the magnetization values for all studied samples at 10 K and at 300 K (RT)

Sample	**Curie Temperature (K)**	**Magnetization (Am^2/kg)**	
		10 K	**300 K**
$SmFe_{4.48}Si_{1.52}$	T_{c1}=516 (5), T_{c2}=1024	-	-
$GdFe_{4.48}Si_{1.52}$	T_{c1}=139, T_{c2}=544.8 (5)	59.7	45.8
$DyFe_5Si_1$	T_c=483(5)	51.8	29.5
$DyFe_{4.8}Si_{1.2}$	T_c=485 (5)	52.9	44.3
$DyFe_{4.6}Si_{1.4}$	T_c=487 (5)	52.87	35.2
$HoFe_{4.52}Si_{1.48}$	T_c=475 (5)	49.96 H_c=3.1 kOe	34.1
$LuFe_{4.52}Si_{1.48}$	T_c=304, T_{c2} =440 (5)	44.1	33.3
$YFe_{4.48}Si_{1.52}$	T_c=458(5)	70.03	55.9

Table 2: Crystallographic data, a, b, c (Å) and the volume cell V (Å^3) of samples according the Rietveld analysis. *Samples with Sm contain also other phases which have not been identified yet.

Sample	**Structure type-Crystal structure parameters-composition**	**S.G.**
$SmFe_{4.48}Si_{1.52}$	RFe_4Si_2 a=7.2211(9) c=3.7535(3) V=195.7(1), *	P 42/m n m
$GdFe_{4.48}Si_{1.52}$	2:17 a=8.4767(5) c=12.4260(8) V=773.23(8) 65% RFe_2Si_2 a=3.9331(3) c=9.9930(9) V=154.58(2) 30% RFeSi a=4.0008(5) c=6.843(2) V=109.53(3) 5%	R -3 m I 4/m m m P 4/n m m
$DyFe_5Si_1$	2:17 a=8.4443(4) c=12.3677(8) V=763.75(7) 38% RFe4Si2 a=7.1751(3) c=3.7852(2) V=194.87(1) 56% RFeSi a=3.9639(5) c=6.752(2) V=106.10(3) 6%	R -3 m P 42/m n m P 4/n m m

References

[1] E. Parthé., B. Chabot, Handbook on the Physics and Chemistry of Rare Earths, vol. 6, Ch. 48, p. 113 (1984).

[2] R. E. Gladyshevskii, K. Cenzual and E. Parthé, J. Alloys Compd., 189 (1992) 221.

Magnetic field modes for manipulation of magnetic nanoparticles

N. Maniotis, A. Makridis, E. Myrovali, T. Samaras and M. Angelakeris

Department of Physics, Aristotle University of Thessaloniki, 54124 Thessaloniki, Greece

E-mail: nimaniot@physics.auth.gr

In this work we theoretically examine how a DC or AC magnetic field affects magnetic nanoparticles (MNPs) in a suspension. This project is guided from our experimental results on (a) MNPs array formation under static magnetic field guidance (b) magnetomechanical effects experienced by in-vitro cell cultures due to MNPs inside a rotating magnetic field, and (c) magnetic particle hyperthermia of MNPs inside AC magnetic fields. Despite the distinct differences in magnetic field modes in these experiments, magnetic field mapping in two and three dimensions is a prerequisite to unravel the connection of magnetic field distribution properties (intensity and uniformity) with the desirable outcome.

To start with, two polymer matrices were manufactured by a 3D printer (Fig. 1a) to support various types of commercial magnets. Such a magnet assembly in which the flux density may be altered by simple variations in block magnet configurations is significantly faster and versatile in operation than conventional electromagnets. These magnetomechanical plates may be placed on a rotating motor in order to examine also rotating magnetic fields. Magnetic flux density calculations of magnetic fields in each different combination of block magnets (see Fig.1b for a representative case Fig.1a) were performed using COMSOL Multiphysics, which is a finite element based software for modeling and simulation of any physics-based system. Theoretical estimations were compared and found in good agreement (Fig.1c) with experimental measurements obtained using an analytical method based on the generated magnetic flux density in a sample volume.

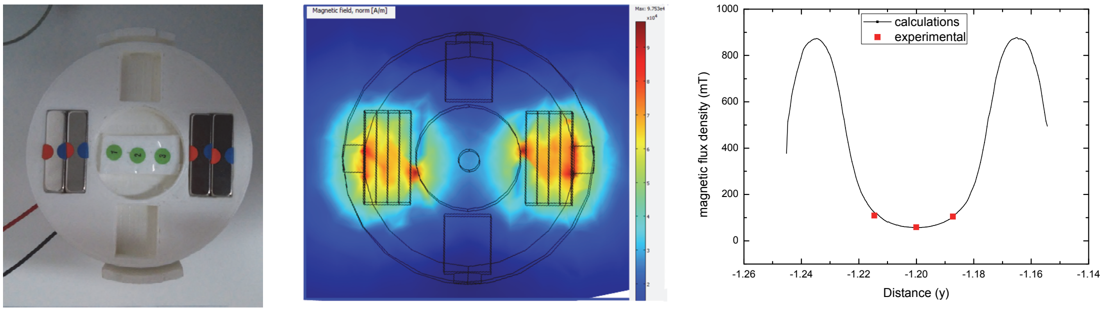

(a) *(b)* *(c)*

Figure 1: (a) 3D polymer matrix to support arrays of commercial block magnets (b) 2D magnetic field color mapping using COMSOL (c) Comparison of 3 experimental points as indicated in Fig.1a with calculated magnetic flux intensity.

Examples of different DC and AC magnetic field modes will also be discussed and magnetic field intensity will be correlated with MNPs chain formation (DC field) while the field uniformity and existence of magnetic gradients inside a magnetic hyperthermia induction coil and how these affect MNPs heating efficiency will be the topic of AC magnetic field application.

Ferrite optimization for wireless powering

C.A. Stergiou[1] and V.Zaspalis[2]

[1]Lab. of Inorganic Materials, Centre for Research and Technology-Hellas, 57001 Thermi, Thessaloniki, Greece
[2]Lab. of Materials Technology, Dept. of Chemical Engineering, Aristotle University, 54124 Thessaloniki, Greece

E-mail: stergiou@cperi.certh.gr

In typical Inductive Power Transfer (IPT) applications, magnetic materials are employed as low reluctance paths in order to improve the inductive coupling and support the manipulation of any leakage magnetic fields. Taking into account their critical role in system's performance, our goal is to investigate the impact of magnetic material properties on the basic features of low-power wireless powering systems.

To this end, two cubic ferrite compositions, $Ni_{0.4}Zn_{0.6}Fe_2O_4$ and $Ni_{0.3}Cu_{0.1}Zn_{0.6}Fe_2O_4$, were prepared with the conventional solid-state reactions route. This process includes mixing of the precursor oxides, prefiring at 800°C, ball milling and roll granulation with the addition of plasticizer. The granulated powders were pressed to form disc and ring specimens at the constant density of 2.90gr/cm^3, which were subsequently sintered at different top temperatures between 1000°C and 1300°C in air. Through the variation of composition and sintering temperature the material properties are controlled in an attempt to derive their influence on the overall performance.

Therefore, the ring-shaped samples were initially characterized with regard to saturation magnetization B_{sat}, complex permeability μ^* and power loss density P_v in various frequency regions of the 10kHz to 1GHz range. The observed trends and variations of these properties are mainly explained on the basis of the presented microstructural characteristics of the materials. Finally, we have studied the impact of various topologies involving the ferrite disc substrates on the link and shielding effectiveness during wireless power transfer. These topologies were designed to simulate realistic operation features, thus they include the operation under a dc bias or in the vicinity of a conducting object. The measurements were performed on the power transfer established between two near-field loop probes, with emphasis on the 100-300 kHz frequency range. By that means, the correlation between the fundamental ferrite properties and critical system's aspects are highlighted.

Acknowledgement: This work was supported by the IKY fellowships of excellence for postgraduate studies in Greece - Siemens program.

High anisotropy induction into multilayer Fe-Co thin films, towards Rare Earth free permanent magnets applications

G. Giannopoulos[1], R. Salikhov[2], L. Reichel[3,4], A. Markou[5], I. Panagiotopoulos[5], M. Farle[2], S. Fähler[3], V. Psycharis[1] and D. Niarchos[1]

[1]INN, NCSR Demokritos, Athens 15310, Greece
[2] Fakultät für Physik and Center for Nanointegration (CeNIDE),
Universität Duisburg-Essen, 47057 Duisburg, Germany
[3]IFW Dresden, PO Box 270116, 01171 Dresden, Germany
[4]TU Dresden, Institute for Materials Science, 01062 Dresden, Germany
[5]Department of Materials Science and Engineering, University of Ioannina, Ioannina 45110, Greece

E-mail: g.giannopoulos@inn.demokrtitos.gr

Fe-Co is among possible candidate alloys for permanent magnet applications due to its high magnetic moment. In this work we present sputtered thin Fe-Co multilayer films doped with Carbon, in order to stabilize metastable tetragonal phases, by straining the unit cell and thus inducing magnetocrystalline anisotropy in the system [1]. According to theoretical calculations, by adding Carbon we can stabilize the strain and increase the magnetocrystalline anisotropy of the system [2]. In order to maintain the strain in the magnetic Fe-Co thin films, preventing the partial strain relaxation which we have observed as film thickness increases [3], we followed two multilayer approaches. At first we deposited ultrathin Fe and Co layers on AuCu buffer doped with carbon up to 10% at. As a result we produced $[Fe/Co]_n$, $[FeC/Co]_n$ or $[Fe/CoC]_n$ structures. In our second Fe-Co/ Au-Cu approach, variable thickness Fe-Co (1-3nm) and Au-Cu(1-3nm) layers were deposited on MgO (100) substrate at 300°C. By employing this structure, strain is induced from both sides.

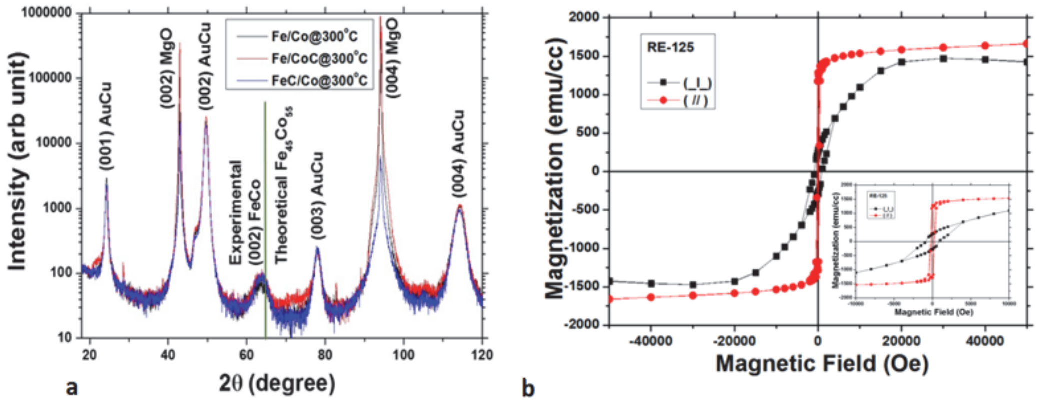

Figure 3: a. X-rays diffraction of Fe/Co, FeC/Co and Fe/CoC thin films, b. In and out of plane magnetic hysteresis loops for $[AuCu/FeCo]_{12}$ multilayer sample.

Concerning the Fe/CoC & FeC/Co multilayers approach a strong Fe-Co diffraction peak along (002) direction is observed for all Fe/Co, FeC/Co and Fe/CoC samples in the diffraction pattern (Fig. 1a). This indicates epitaxial growth of Fe-Co systems on the $Au_{50}Cu_{50}$ buffer, preserving the underlayer orientation. Moreover the FeCo (002) XRD peak is shifted towards smaller angles compared to the theoretical expected $Fe_{45}Co_{55}$ (002) reflection. The shift ratio of Δa/a spacing is in the order of ~ 1 %. We also report large perpendicular anisotropy in our thin magnetic films, in the excess of $1 MJ/m^3$, confirmed by FMR measurements [4].

In $[Fe_{45}Co_{55}$(1-3 nm)/$Au_{30}Cu_{70}$ (1-3 nm)$]_{12}$ multilayers approach, the easy axis of magnetization is in plane for all the samples. A Magnetocrystalline Anisotropy Energy of about $0.4 MJ/m^3$ is found in $[Fe_{45}Co_{55}$(3 nm)/$Au_{30}Cu_{70}$ (1 nm)$]_{12}$ system. Thus, our multilayer approach supports significantly the thickness scaling up of Fe-Co films, preserving large perpendicular magnetocrystalline anisotropy. Furthermore a coercivity of about 850 Oe was observed (Fig. 1b), which is a step forward towards rare earth free permanent magnets applications.

References

[1] T. Burkert, L. Nordström, O. Eriksson, and O. Heinonen, Phys. Rev. Lett., 93 (2004) 027203.
[2] E. K. Delczeg-Czirjak, A. Edstrom, M. Werwinski, J. Rusz, N. V. Skorodumova, L. Vitos, and O. Eriksson, Phys. Rev. B, 89 (2014) 144403.
[3] L. Reichel, G. Giannopoulos, S. Kauffmann-Weiss, M. Hoffmann, D. Pohl, A. Edstrom, S. Oswald, D. Niarchos, J. Rusz, L. Schultz, and S. Faehler, J. Appl. Phys., 116 (2014) 213901.
[4] G. Giannopoulos, R. Salikhov, B. Zingsem, A. Markou, I. Panagiotopoulos, V. Psycharis, M. Farle, and D. Niarchos, APL Materials 3 (2015) 041103.

Nanomechanics of Magnetron Sputtered Ti-Nb Films

**D. Photiou[1], N.T. Panagiotopoulos[2], L. Koutsokeras[1],
G.A. Evangelakis[3] and G. Constantinides[1]**

[1]Research Unit for Nanostructured Materials Systems,
Department of Mechanical Engineering and Materials Science and Engineering,
Cyprus University of Technology, Lemesos, CY
[2]SIMAP-CNRS, Institut Polytechnique de Grenoble, FR
[3]Department of Physics, University of Ioannina, Ioannina, 45110, GR

E-mail: g.constantinides@cut.ac.cy

Titanium and its alloys are considered excellent candidate materials for the human implants sector, as they outperform other materials due to their lightweight, high strength to weight ratio, excellent corrosion resistance, low elastic modulus and excellent biocompatibility. Nevertheless, these alloys still possess high elastic moduli compared to the hosting matrix, the bone, which can lead to premature failures. In fact, when high stiffness materials are used, the implant carries a significant portion of the body loading, which ‘shields’ the bone from the necessary loading required to maintain its density and as a consequence strength and healthy microstructure (stress–shielding effect). In this study, we report an experimental based methodology in search of the optimum Ti–Nb composition, based on a systematic understanding of the structure–property relations. Various sub-micron Ti–Nb films with compositions covering the whole possible alloy span, from pure Ti to pure Nb films, have been deposited using magnetron sputtering. The resulting porous films have been tested for their thicknesses (Profilometry), densities (X-Ray Reflectivity), composition (X-Ray Diffraction), microstructure (Scanning Electron Microscope) and nanomechanical response (nanoindentation). It is shown that the β-stabilizer, niobium, induces enhanced hardness and creep performance compared to the pure titanium counterparts, while their elastic response can be reduced depending on the composition. These structure-property relationships could be used for developing optimum Ti-alloy films for biomedical applications.

Aknowledgements: The authors would like to acknowledge the financial support from the Strategic Infrastructure Project NEW INFRASTRUCTURE/STRATE/0308/04 of DESMI 2008, which is co-financed by the European Regional Development Fund, the European Social Fund, the Cohesion Fund, and the Research Promotion Foundation of the Republic of Cyprus.

Influence of structure and dynamics on the ionic conductivity of new solid polymer electrolytes

G. Zardalidis[1], A. Pipertzis[1], S. Pispas[2] and G. Floudas[1]

[1]Department of Physics, University of Ioannina, P.O. Box 1186, 451 10 Ioannina, Greece
[2]Theoretical and Physical Chemistry Institute, National Hellenic Research Foundation,
116 35 Athens, Greece

E-mail: apipertzis@cc.uoi.gr

Replacing the currently used liquid electrolytes by solid ones recently received considerable attention due to improved safety, wider potential of electrochemical stability and ability for thin film processing. Hence, solid polymer electrolytes (SPE) emerged as promising materials for technological applications including batteries, fuel cells, super capacitors as well as electrochemical devices [1-4]. In particular, the design of SPE from block copolymers with appropriate compositions offers opportunities for such purposes. Such advantages rely on the mechanical strength and propensity for phase separation at the nanoscale [5]. In this respect, the soft nanophase can be employed as an ion conductor, whereas the hard nanophase offers the required mechanical strength. Poly(ethylene oxide) (PEO) has been employed as one of the blocks because of its flexible backbone and a great ability for solvating salts. Early reports [6,7] on the phase diagram and conductivity[8] behavior of the archetypal PEO-LiX electrolytes ($X = CF^3SO^{3\,-}$, ClO^{4-}, AsF^{6-}) revealed that below 313 K (the melting point of PEO) these systems are mixtures of different phases. They include a crystalline phase of PEO and a crystalline stoichiometric compound of PEO with the salt (called “complex”), both embedded in amorphous PEO regions. Recently, it was shown[8] that ionic conduction in PEO/LiTf electrolytes takes place both within the stoichiometric complex and in the amorphous phase that is continuously enriched with LiTf ions, with the latter having the major contribution. In addition, ion transport was found to be coupled to the local segmental motion of the polymer chains.

Herein we propose a new SPE that is based on densely grafted PEO chains on a PHOS backbone as well as on the diblock copolymer with polystyrene (PS) PS-b-(PHOS-g-PEO). We employ differential scanning calorimetry (DSC) for the thermodynamic state, polarizing optical microscopy (POM) for characterizing the complex crystal and PEO crystal growth rates, wide angle and small angle x-ray scattering for characterizing the complex crystal unit cell and block copolymer nanostructure respectively, dielectric spectroscopy (DS) for the ionic conductivity and rhelogy for characterizing the viscoelastic properties of the complex crystal. From DSC, POM and WAXS we obtain the phase diagram of the PHOS-g-PEO/LiTf system comprising the complex melting and PEO crystal melting temperatures. From DS, we obtain a non-Arrhenius temperature dependence with a maximum conductivity for the 12:1 [EO]:[Li^+] ratio. Furthermore the measured dc-conductivity is high and comparable to the archetypal PEO/LiTf electrolyte. However in the present care, the shear modulus of the system can have values in the range from 10^4 Pa to ~10^9 Pa at ~323 K with a nearly elastic behavior, suitable for applications as SPEs.

References

[1] J. M. Tarascon and M. Armand, Nature 414 (2001) 359−367.
[2] T. P. Lodge, Science 321 (2008) 50−51.
[3] M. Armand, J.-M. Tarascon, Nature 451 (2008) 652−657.
[4] R. C. Agrawal and G. P. J Pandey, Phys. D.: Appl. Phys. 41 (2008) 223001.
[5] (a) Hamley, I. A. In The Physics of Block Copolymers; Oxford University Press: Oxford, U.K., 1998. (b) N. Hadjichristidis, S. Pispas, G. Floudas, In Block Copolymers: Synthetic Strategies, Physical Properties and Applications; Wiley-Interscience: New York, 2002.
[6] C. D. Robitaille and D. J. Fauteux, J. Electrochem. Soc. 133 (1986) 315−325.
[7] P. Lightfoot, M. A. Mehta, and P. G. Bruce, Science 262 (1993) 883−885.
[8] G. Zardalidis, E. Ioannou, S. Pispas, and G. Floudas, Macromolecules 46 (2013) 2705−2714.

Designing Molecules for Orgnanic Photovoltaics: The case of Hexasubstituted Benzenes carrying Ultrastrong Dipole Moments

V. Margaritis[1], J. Wudarczyk[2], K. Muellen[2], G. Papamokos[1] and G. Floudas

[1]Department of Physics, University of Ioannina, 45110 Ioannina, Greece
[2]Max-Planck Institute for Polymer Research, 55128 Mainz, Germany

E-mail: vamarg92@gmail.com

The design of high-performance organic materials with applications in photovoltaics requires the reduction of exciton binding energy through the increase of dielectric permittivity. If active materials with higher dielectric permittivity could be synthesized, solar cells with an efficiency comparable to that of the inorganic counterpart could be manufactured. [1,2] In this context new hexasubstituted benzenes have been synthesized starting from 4,5-diamino-3,6-dibromophthalonitirile which subsequently has been converted into novel tetracyano-structures with high dielectric constants and dipole moments as well as strong acceptors. Further transformation to 4,7-dibromobenzo [c][1,2,5]thiadiazole-5,6-dicarbonitrile coupled with various thiophenes yielded donor-acceptor compounds potentially applicable to organic electronics.[3] Dipole moments were measured by dielectric spectroscopy at dilute solutions in solvents of medium polarity (THF, chloroform). In addition, DFT calculations of the dipole moments and HOMO-LUMO energy values of the molecules were performed. As a result, molecules with tuneable dielectric permittivities could be designed.

References

[1] N. Camaioni and R. Po, J. Phys. Chem. Lett., 4 (2013) 1821-1828.
[2] S. Y. Leblebici *et al.*, ACS Appl. Mater. Interfaces, 5 (2013) 10105-10110.
[3] J. Wudarczyk, V. Margaritis, G. Papamokos, G. Floudas, and K. Muellen. *In preparation*

Polymethacrylates with Polyhedral Oligomeric Silsesquioxane Moieties (POSS): The Influence of Spacer Length on Packing, Thermodynamics and dynamics

S. Alexandris[1], A. Franczyk[2,3], G. Papamokos[1], B. Marciniec[3], K. Matyjaszewski[2], K. Koynov[4], M. Mezger[4] and G. Floudas[1]

[1]Department of Physics, University of Ioannina, 45110 Ioannina, Greece
[2]Department of Chemistry, Carnegie Mellon University, 4400 Fifth Avenue, Pittsburg, Pennsylvania 15213, United Sates
[3]Center for Advanced Technologies, Adam Mickiewicz University in Poznan, Umultowska 89c, 61-614 Poznan, Poland
[4]Max-Planck Institute for Polymer Research, 55128 Mainz, Germany

E-mail: gpapamokos@seas.harvard.edu

Polymethacrylates with polyhedral oligomeric silsequioxane (POSS) moieties (poly(POSS-MA)s) with flexible spacers between the POSS cages and the methacrylate group [1,2] have distinctly different properties from their linear counterpart, i.e., PMMA. POSS cages modify interchain correlations and result in multiple dynamic processes that reflect the cooperative relaxations of both the pendant POSS units and ester dipoles and the polymer backbone. As a result the freezing of the backbone dynamics is shifted to lower temperatures and the nanocomposites appear softer than in linear PMMA chains of similar degrees of polymerization. POSS cages can be employed as nanometer size blocks that, depending on the polymer backbone and the spacer, can impart mobility and control over the mechanical properties of nanocomposites.

References

[1] A. Franczyk, H. He, J. Burdynska, C. M. Hui, K. Matyjaszewski, and B. Martiniec, ACS Macro Lett., 3 (2014) 799-802.
[2] S. Alexandris, A. Franczyk, G. Papamokos, B. Marciniec, K. Matyjaszewski, K. Koynov, M. Mezger, and G. Floudas, Macromolecules, 48 (2015) 3376-3385.

Capillary Rise in Cylindrical Nanoconfinement of cis-1,4 Polyisoprene and Poly(methyl phenyl siloxane)

S. Alexandris[1], **G. Sakellariou**[2], **M. Steinhart**[3], **A. Avgeropoulos**[4] **and G. Floudas**[1]

[1]Department of Physics, University of Ioannina, 45110 Ioannina, Greece
[2]Department of Chemistry, University of Athens, 15771 Athens, Greece
[3]Institut für Chemie neuer Materialien, Universität Osnabrück, 49074 Osnabrück, Germany
[4]Department of Material Science Engineering, University of Ioannina, 45110 Ioannina, Greece

E-mail: salexan@cc.uoi.gr

Understanding fluid flow in nanoconfined geometries is crucial for a broad range of scientific problems relevant to the behavior of porous materials in nanotechnology. When a capillary is inserted into a liquid, the liquid will rapidly flow into it. This phenomenon is studied for 2 different amorphous and unentangled polymers: cis-1,4 polyisoprene with molecular weights in the range from 0.8×10^3 to 5.0×10^3 g/mol and poly(methyl phenyl siloxane) with molecular weights of 2.1×10^3 and 6.0×10^3 g/mol. As a capillary, self-ordered nanaporous alumina membranes (AAO) with well-defined cylindrical pores of 400 and 65 nm diameters were employed. Capillary rise was investigated via SEM. A linear relationship between the length of the capillary flow and the square root of the flow time was observed. This is in agreement with the Washburn theory of the capillary flow: $L(t) = (\gamma R\cos\theta/2\eta)^{1/2}t^{1/2}$, $L(t)$ being the flow distance, R the pore radius, γ the interfacial tension, $\cos\theta$ the contact angle, η the polymer viscosity and t the flow time. Although the predicted $L(t)\sim t^{1/2}$ dependence was found experimentally, the slope strongly deviates from the Washburn theory. These deviations are discussed in terms of (i) a dynamic contact angle, (ii) wall slip and (iii) an effective viscosity.

References

[1] E. Washburn, Phys. Rev., 17 (1921) 273-283.
[2] T. P. Russell, Nature Materials, 6 (2007) 961-965.
[3] K. I. Winey, Macromolecules, 48 (2015) 2324-2332.
[4] K. Binder, Phys. Rev. Lett., 99 (2007) 054501.

MOP

P046

Dc conductivity measurements on PVDF composite samples of low graphene content

G.T. Malliaros, I. Stavrakas, P. Photopoulos and D.Triantis

Laboratory Electronics Device and the Materials, Department of Electronics Engineering,
Technological Educational Institute of Athens, 12210 Athens Greece.

E-mail: ilias@ee.teiath.gr

In recent years there is a great interest on graphene based composite materials in polymeric matrices since they constitute high permittivity materials and are widely used to develop high-performance electronic devices [1]. In this work Isothermal Polarization/Depolarization Current (IPC/IDC) and dc conductivity measurements were conducted on polyvinylidene fluoride (PVDF) as host polymeric matrix and graphene inclusion additives ranging from 0 up to 1wt%. Specifically, five sets of samples were prepared with the graphene content ranging from 0.1wt% up to 1wt%. Additionally a set of pure polyvinylidene fluoride (PVDF) was prepared in order to be used as reference. The conductivity was calculated through the slope of the J-E curves obtained thought I-V test in a vacuum chamber using a sensitive electrometer (Keithley 6517A), while the applied eclectic field varied up to 1kV/cm. The dc conductivity was also calculated using the IPC/IDC curves via [2,3]:

$$\sigma \approx \frac{\varepsilon_0 \cdot \left(I_p - I_d\right)}{C_0 \cdot U_0} \qquad (1)$$

where ε_0 is the vacuum permittivity, C_0 denotes the measured geometric capacitance (2.2pF), U_0 is the polarizing step voltage value and I_p and I_d are the polarization and depolarization at times of slow IPC/IDC processes.

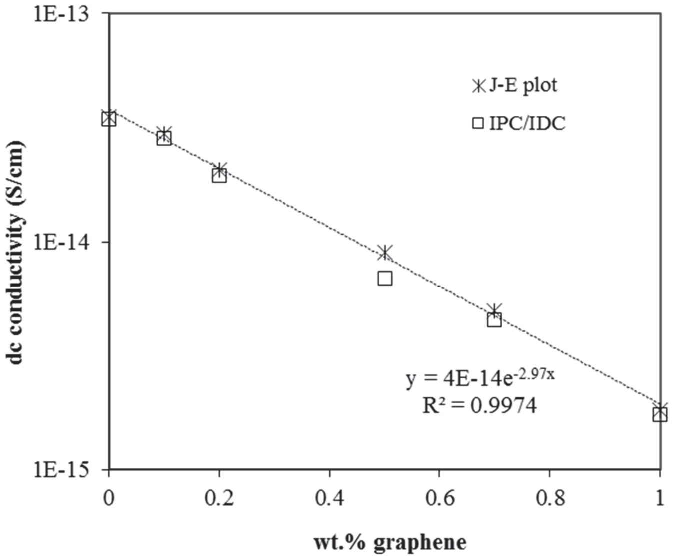

Figure 1: dc conductivity as a function of grapheme for the tested PVDF composite specimens.

The values of the dc conductivity, as calculated through the J-E characteristics and the IPC/IDC tests, are in the good agreement for all the tested samples (see fig.1). This observation clearly shows the validity of the IPC/IDC method for calculating the dc conductivity. The behavior of the dc conductivity with respect to the %wt content of the graphene composites, shows that an exponential decay of the dc conductivity with respect to the %wt of graphene exists.

Acknowledgements: This research has been co-financed by the European Union (European Social Fund – ESF) and Greek national funds through the Operational Program "Education and Lifelong Learning" of the National Strategic Reference Framework (NSRF)- Research Funding Program: THALES. Investing in knowledge society through the European Social Fund.

References

[1] J. Yu, X.Huang, C.Wu and P. Jiang, IEEETrans. Dielect. Elect. Insulation, 18 (2011) 478.
[2] T. K. Saha, P. Purkait, IEEE T. Dielect. El. In., 11 (2004) 144.
[3] I. Stavrakas, D. Triantis, G. Hloupis, K. Moutzouris, Central European Journal of Physics, 12 (2014) 286-291.

Transmission Electron Microscopy Studies of CoSi/Si_3N_4 Nanocomposite Materials

A. Delimitis[1], **M. Ioannou**[2] **and Th. Kyratsi**[2]

[1]Chemical Process & Energy Resources Institute (CPERI), Centre for Research & Technology Hellas (CERTH), 57001 Thermi, Thessaloniki, Greece
[2]Department of Mechanical and Manufacturing Engineering and Nanotechnology Research Unit, University of Cyprus, 1678 Nicosia, Cyprus

E-mail: andel@cperi.certh.gr

In recent years, significant progress has been made in the development of thermoelectric (TE) materials for energy conversion devices [1], especially via the use of the nanocomposite approach. TE nanocomposites produced by adding inclusions or mixing particles of the same or different phases have been reported as sources of increased phonon scattering and reduction of thermal conductivity [2]. CoSi has been a promising candidate for advanced TE applications due to its quite large Seebeck coefficient at room temperature [3], although it lacks in thermal conductivity. In this work, the structural amendments induced by Si_3N_4 inclusions in CoSi, aiming to lattice thermal conductivity reduction, are investigated using transmission electron microscopy methods.

The CoSi compound was prepared by solid state synthesis and Si_3N_4 nanoparticles, with different concentrations, were introduced as a secondary phase in the matrix to produce TE nanocomposites. The materials were structurally studied using transmission electron microscopy (TEM, HRTEM) and energy dispersive X-ray spectroscopy (EDS). The characterization results are correlated with the thermal conductivity of CoSi and the effect of nanostructuring is exploited.

The grainy morphology of the CoSi/xSi_3N_4 nanocomposites was elucidated by TEM observations, as shown in Fig. 1 from the sample with 2.5% Si_3N_4. The main phase, CoSi consists of large grains with typical sizes 400-900 nm. They are highly crystalline, as shown by the selected area diffraction (SAD) pattern inset in Fig. 1, where the main CoSi reflections are indexed. Along with CoSi, the existence of SiO_2 phase is also observed, agglomerated with the parent grains. The SiO_2 is entirely amorphous and, hence, its particles have no specific morphology or size. Its presence was confirmed by EDS analysis and a typical spectrum is illustrated as an inset in the same image. Based on the TEM observations, the SiO_2 phase comprises of not more than 10% in the samples studied.

Formation of Si_3N_4 nanoparticles (nano-Si_3N_4) took place inside the CoSi matrix, as presented in both Fig. 1 (black arrowed) and the HRTEM image of Fig. 2. The particle has almost spherical shape with a diameter of 20 nm and is coherently embedded with CoSi, as proved by the Moiré fringe pattern superimposed on the two crystals, CoSi and Si_3N_4. The lattice fringes resolved are attributed to the $(20\bar{2}1)$, $(11\bar{2}0)$ and (110) crystal planes of hexagonal Si_3N_4 and cubic CoSi, respectively. Apart from the nano-Si_3N_4 embedded inside CoSi, the formation of single crystalline Si_3N_4 grains, up to 300 nm, was also detected by TEM and EDS. The random aggregation of the CoSi, Si_3N_4 and SiO_2 phases resulted in a significant amount of porosity in the samples.

The lattice thermal conductivity of all samples showed a strong dependence on x values and decreased monotonously with nano-Si_3N_4, as presented in Fig. 3. This is attributed to the incorporation of nano-Si_3N_4 phase in the matrix, the agglomerated micro- and nano-SiO_2 and Si_3N_4 phases that enhanced phonon scattering as well as the apparent porosity. Consequently, the nanocomposite approach provides a cost-effective way to obtain high ZT bulk materials, which can have significant advantages in mass production, device construction and operation.

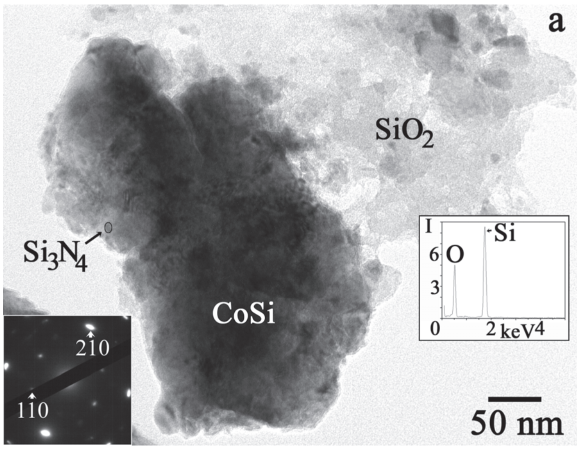

Figure 1: TEM image of the main CoSi phase and agglomerated SiO_2 particles. The SAD pattern and EDS spectrum from CoSi and SiO_2, respectively, are shown as insets.

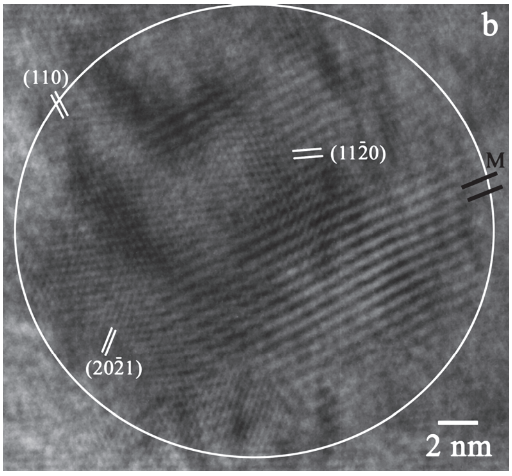

Figure 2: HRTEM image of a characteristic Si_3N_4 nanoparticle inside the CoSi matrix

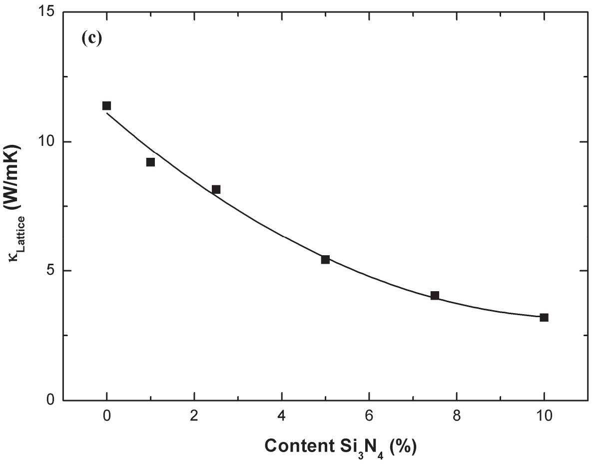

Figure 3: Room temperature thermal conductivity of the hot-pressed CoSi/xSi_3N_4 nanocomposites pellets as a function of the Si_3N_4 content.

References

[1] D. M. Rowe, CRC Handbook of Thermoelectrics, CRC Press, (1995).
[2] J. Lan, Y.H. Lin, Y. Liu, S. Xu and C. W. Nan, J. Am. Ceram. Soc., 95 (2012) 2465–2469.
[3] W.L. Ren, C.C. Li, L.T. Zhang, K. Ito and J. S. Wu, J. Alloys Compd., 392 (2005) 50-54.

MOP

P048

Dielectric study of a lysozyme solution with molecular dynamics simulations: Non thermal effects of low alternating electric fields

S. Floros[1], **M. Liakopoulou-Kyriakides**[1],
K. Karatasos[1] **and G. E. Papadopoulos**[2]

[1]Faculty of Chemical Engineering, Department of Chemistry,
Aristotle University of Thessaloniki, Thessaloniki 54124, Greece
[2]Department of Biochemistry and Biotechnology, University of Thessaly,
Ploutonos 26 & Aeolou, Larisa 41221, Greece

E-mail: florosstylianos@gmail.com

In this work frequency depended structural changes of lysozyme at relative low electric field intensities in the microwave region are reported. Analysis of molecular dynamics simulation data of a lysozyme solution at different frequencies reproduced the experimentally observed dielectric behavior as well that from simulations according to the Fröhlich-Kirkwood approach. Structural changes in the protein have been observed only at frequencies near its absorption maximum indicating non thermal biological effects of microwaves. The average number of protein-water hydrogen bonds is drastically affected in the frequency region of β- and δ1-process.

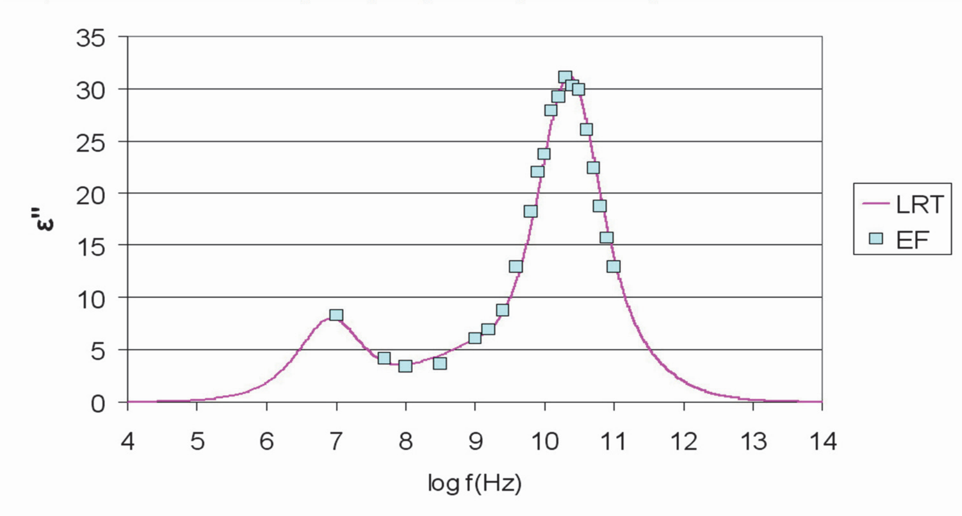

References

[1] Gerald Loeffler, Hellfried Schreiber and Othmar Steinhauser, J. Phys. Biol., 270 (1997) 520-534.
[2] Knocks, H. Weingärtner, Chem. B, 105 (2001) 3635-3638.
[3] Niall J. English, Gleb Y. Solomentsev, and Paul O'Brien, The Journal of Chemical Physics, 131 (2009) 035 106-1-10.

Microwave attenuation and dielectric properties of hybrid nanocomposites co-filled with organomodified graphene oxide

C. A. Stergiou[1,2], **A. Z. Stimoniaris**[3] **and C. G. Delides**[3]

[1]Lab. of Materials for Electrotechnics, Dept. of Electrical and Computer Engineering,
Aristotle University, 54124 Thessaloniki, Greece
[2]Lab. of Inorganic Materials, Centre for Research and Technology-Hellas,
57001 Thermi, Thessaloniki, Greece
[3]Dept. of Pollution Control Technologies, Technological Education Institute of
Western Macedonia, 50100 Kila, Kozani, Greece

E-mail: stergiou@cperi.certh.gr

With a view to the critical need for shielding of electronic/telecommunication systems or sensitive civil infrastructure against plane electromagnetic waves, we have studied the microwave electromagnetic performance of novel nanocomposite materials doped with the promising graphene oxide (GO).

In composites technology, GO is basically used as a precursor of highly conductive graphene filler, which is finally formed through in-situ thermal or chemical reduction [1,2]. However, insulating GO sheets can effectively improve the dispersion of carbon nanotubes in polymer matrices [3]. Actually, nanocomposites comprising GO were recently found to exhibit high permittivity and low dielectric losses in the frequency range below 1 MHz, with excellent potential for energy storage applications [4,5]. Despite this advancement, there is a lack of research reports on the microwave dielectric properties of graphene oxide-filled nanocomposites, especially with regard to its synergy with other carbonaceous fillers.

To this end, we have prepared hybrid epoxy nanocomposite samples containing organomodified graphene oxide up to 0.5wt%, in combination with carbon black nanoparticles (CB) up to 2wt% or with multiwalled carbon nanotubes (MWCNT) up to 0.5wt%. The preparation procedure is similar to that described in [6]. Properly machined ring samples were characterized in terms of their complex electromagnetic parameters in the range 2-18 GHz, by means of a vector network analyzer. The dielectric measurement technique is outlined in [7]. The extracted complex permittivity $\varepsilon^{*}=\varepsilon'$-j$\varepsilon''$ indicates the enhancement of dielectric polarization with the incorporation of modified GO, mainly in the MWCNT set of samples. Additionally, we have investigated the impact of GO addition on the return losses of the two nanocomposite systems epoxy/MWCNT and epoxy/CB. The recorded experimental results highlight the potential of GO-doping in enhancing the microwave properties of the nanocomposites under study.

References

[1] F. Liu, R. Huo, X. Huang and P. Jiang, 2013 IEEE International Conference on Solid Dielectrics, (2013) 919-922.
[2] J-M. Thomassin, M. Trifkovic, W. Alkarmo, C. Detrembleur, C. Jerome and C. Macosko, Macromolecules, 47 (2014) 2149-2455.
[3] C. Wu, X. Huang, X. Wu, L. Xie, K. Yang and P. Jiang, Nanoscale, 5 (2013) 3847-3855.
[4] K. S. Kumar, S. Pittala, S. Sanyadanam and P. Paik, RCS Advances, 5 (2015) 14768.
[5] S. Biswas, G. P. Kar, D. Arora, and S. Bose, RCS Advances, 5 (2015) 24132.
[6] Th. V. Kosmidou, A. S. Vatalis, C. G. Delides, E. Logakis, P. Pissis, and G. C. Papanicolaou, eXPRESS Polym. Lett., 2(5) (2008)364-372.
[7] C. A. Stergiou, A. Z. Stimoniaris and C. G. Delides, IEEE Trans. on EMC 57 (2015) 470-476.

Interactions of polyaspartic-b-poly(ethylene glycol) copolymer with magnetite nanoparticles

I. Rousalis[1], **A. Bakandritsos**[1], **G. Mountrichas**[2] **and S Pispas**[2]

[1]University of Patras, Department of Materials Science, Patras, 26504, Greece,
[2]Theoretical and Physical Chemistry Institute N.H.R.F., Athens, Greece

E-mail: hrousalis@hotmail.gr

MOP

P050

Surface engineering of magnetite nanoparticles (MNPs) is a key aspect of their effective application as therapeutic and diagnostic systems.[1] The coating should impart high colloidal stability, bio-repellent properties for stealth behavior and drug loading ability. The block copolymer of polyaspartic-b-poly(ethylene glycol) (pAsp-b-pEG), with the free caraboxylates is considered appropriate for coordination on the surface Fe atoms of the MNPs, while its PEG block secures the high steric stability and low protein bonding (stealthiness).

In this study a pAsp block of 8 monomers and PEG (Mw of 5kDa) was added during or after the synthesis of MNPs. Alkaline precipitation with a single FeII or FeII-FeIII precursors were studied and several synthetic conditions were varied, such as the type and amount of base, metal salt and polymer concentrations. The products were evaluated with colloidal stability assays in neat H_2O and high ionic strength aqueous solutions. A few pAsp-b-pEG derivatized magnetic nanoparticles were identified to be stable for several months in neat H_2O, with hydrodynamic diameters in the range of 100-50 nm. Nevertheless the systems were destabilized after two successive washing and redispersion steps and in high ionic strength aqueous solutions.

Therefore, an alternative pathway was explored by first synthesizing cationically charged magnetite colloids and following their interaction with the anionic carboxylates of pAsp-b-pEG was studied. In order to impart cationic charges to MNPs D,L carnitine hydrochloride and O-Phosphorylethanolamine were used. The nanoparticles produced were purified by isolation with centrifugation, and addition of new amount of d. H_2O twice. The D_h values of the obtained MION-polymer complexes varied in the region between 60 and 100 nm, and were indefinitely stable, even after three successive washings steps. These MNPs displayed colloidal stability in high-ionic strength media,. The products only precipitated at ~60 ^oC in presence of 2M NaCl, a finding that underpins their successful dense PEGylation and steric stabilization.[2]. The effective PEGylation was also confirmed through protein binding experiments.

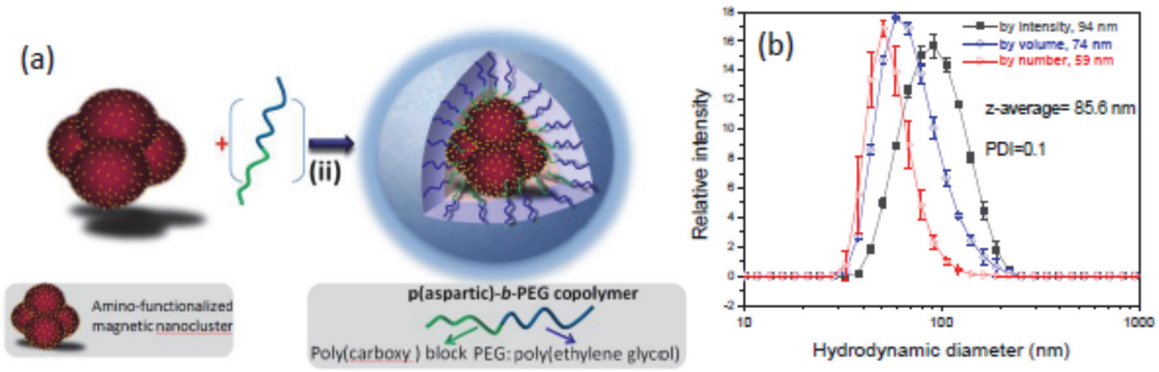

Figure 1: (a) Schematic illustration of the probable interaction between cationic magnetic nanoparticles and the anionic block of poly(aspartic-b-ehtylene glycol) copolymer, and (b) the respective dynamic light scattering results of the assemblies.

References

[1] D. Ling and T. Hyeon, Small, 9 (2013) 1450.
[2] S. Honda, T. Yamamoto, Y. Tezuka, Nat. Commun., 4 (2013) 1574.

MOP

P051

Structure-properties relationship of Barium Ferrite/Barium Titanate/Epoxy Resin Hybrid Nanocomposites.

A. Kanapitsas[1], C. Tsonos[1], G. Psarras[2], Th. Speliotis[3] and D. Triantis[4]

[1]Electronics Engineering Department, TEI of Sterea Ellada, 35100 Lamia, Greece,
[2]Department of Materials Science, University of Patras, Patras, 26504, Greece
[3]Institute of Advanced Materials, Physicochemical Processes, Nanotechnology and Microsystems, NCSR "Demokritos" Aghia Paraskevi, 15310 Athens, Greece,
[4]Department of Electronic Engineering,TEI of Athens, 12243 Athens, Greece.

E-mail: kanapitsas@teilam.gr

The purpose of this work is to investigate the molecular dynamics of epoxy resin hybrid nanocomposites. In this study $BaFe_{12}O_{19}$/$BaTiO_3$/epoxy hybrid nanocomposites were prepared and tested, varying the amount of the filler. Specimen's morphology was studied by means of scanning electron microscopy and x-ray diffraction spectra, while their dielectric response, and functionality was investigated via broadband dielectric spectroscopy. Obtained results are compared and discussed with respect to those of $BaFe_{12}O_{19}$/epoxy and $BaTiO_3$/epoxy nanocomposites. The relaxation phenomena recorded include contributions from both the polymeric matrix and the reinforcing phase [1-3].

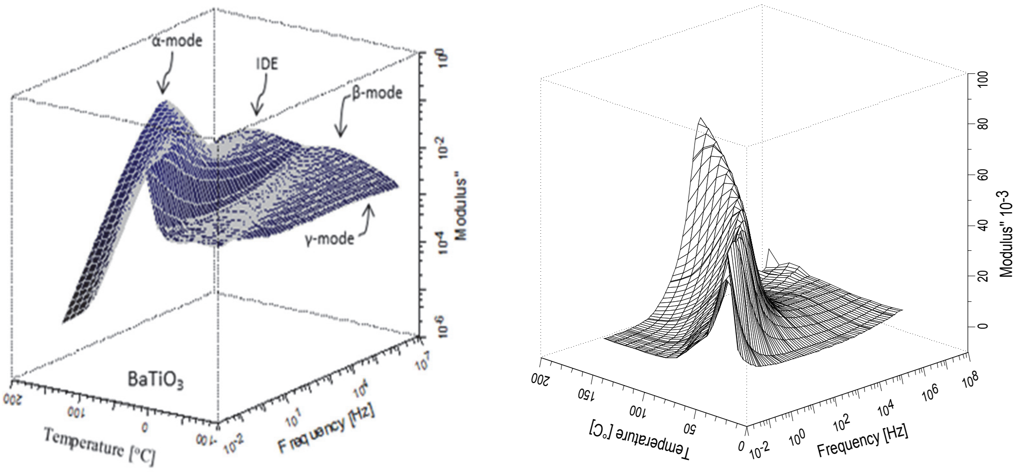

Figure 1: 3D graph of the imaginary part of electric modulus versus frequency and temperature for the samples with 5 phr in $BaTiO_3$/epoxy and 5 phr in $BaFe_{12}O_{19}$/epoxy respectively.

A relaxation observed in the high temperature region (α-mode) is related to the glass to rubber transition of the polymer matrix [Fig. 1]. Two secondary relaxations arise from the restricted local motions of the polymer chains (β-, γ-modes). Another relaxation, lying between the fast and the slow processes is observed, connected to the presence of the filler.

The slowest recorded process is attributed to interfacial phenomena. The influence of environmental conditions upon the dielectric response of the system was also examined and discussed. Finally, the energy storing efficiency of the nanocomposites is examined varying the temperature, frequency, type and the amount of the filler [4, 5].

This research has been co-financed by the European Union (European Social Fund – ESF) and Greek national funds through the Operational Program "Education and Lifelong Learning" of the National Strategic Reference Framework (NSRF) - Research Funding Program: THALES (MIS 379346). Investing in knowledge society through the European Social Fund.

References

[1] V. Toner, G. Polizos, E. Manias, and C. Randall, J. Appl. Phys.. 108 (2010) 074116.
[2] A. Patsidis, K. Kalaitzidou and G. Psarras, J. Therm. Anal. Calorim., 116 (2014) 41.
[3] A. Patsidis, K. Kalaitzidou and G. C. Psarras, Mater. Chem. Phys., 135 (2012) 798.
[4] C. Tsonos, A. Kanapitsas, G. Psarras, and Th. Speliotis, Sci. Adv. Mater., 7 (2015) 588.
[5] A. Patsidis and G. Psarras, Smart Materials and Structures, 22 (2013) 115006.

Conductivity analysis on epoxy resin/carbon nanotubes composites

G. N. Tomara[1], N-C.K. Papaioannou[1], P.S. Antonakopoulou[1], E.E. Zavvou[1], A. Christoulaki[1], P. Athanasiadis[1], N. Spiliopoulos[1], Th.K. Karachalios[2] and P. K. Karahaliou[1]

[1] Department of Physics, University of Patras, 26504, Patras, Greece
[2] Nanothinx S.A., Stadiou Street, Platani, GR-26504 Rio-Patras, Greece

E-mail: tomgeo@physics.upatras.gr

In recent years allotropic forms of carbon, such as carbon nanotubes (CNTs), attract significant scientific attention due to the combination of outstanding properties. Their unique atomic structure, the high aspect ratio and the remarkable mechanical strength and flexibility render CNTs an ideal reinforcing phase in nanocomposites [1, 2]. In particular, epoxy resin/CNTs composites are highly promising materials for technological applications and therefore they are extensively investigated.

In the present work epoxy resin/MWCNTs nanocomposites were prepared, in various filler concentrations ranging from 0.05 up to 3 % [3]. During the preparation procedure, great care was taken in order to achieve a homogeneous dispersion of nanotubes into the polymer matrix. The dispersion of nanotubes is hindered by their tendency to agglomerate due to intermolecular van der Waals interactions [4, 5]. In order to form a MIM structure Au electrodes were deposited on the samples by spattering.

All samples were characterised via Broadband Dielectric Spectroscopy (BDS) in the frequency range from 0.1 Hz to 1 MHz. Isothermal frequency scans were performed for each of the examined specimens in the temperature range from -100°C to 100°C in steps of 10°C between successive frequency sweeps.

The dielectric response of all samples is analysed via the conductivity (σ') representation. Figures 1 and 2 are representative graphs of the conductivity dependence upon frequency and temperature for the sample with 0.5% and 2% in MWCNTS, respectively. The plateau formation of conductivity, observed in both figures, is characteristic of the DC conductivity (σ_{DC}). From the temperature dependence of σ_{DC} at 0.1HZ the activation energy is calculated. The effect of the filler concentration on the dielectric response of the nanocomposites is also investigated. Finally σ_{DC} is further analysed with regard to the percolation threshold, meaning the critical concentration of CNTs above which they are interconnected forming a conductive path for electrons to flow through the sample [1, 2].

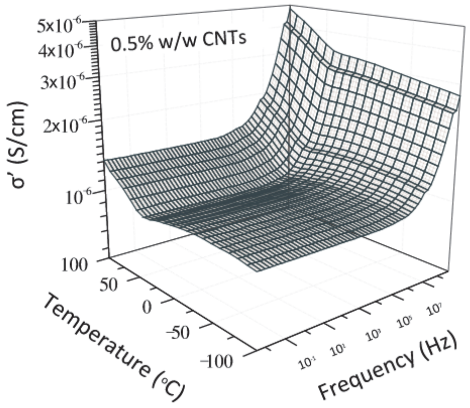

Figure 1: 3D graph of the dielectric conductivity versus frequency and temperature for the composite with 0.5% w/w in CNTs.

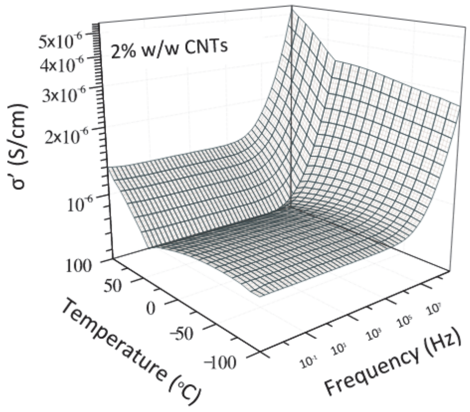

Figure 2: 3D graph of the dielectric conductivity versus frequency and temperature for the composite with 2% w/w in CNTs.

References

[1] Z. Špitalský, C.A. Krontiras, S.N. Georga and C. Galiotis, Composites Part A: Applied Science and Manufacturing, 40 (2009) 778-783.
[2] Z. Špitalský, S.N. Georga, C.A. Krontiras and C. Galiotis, Advanced Composite Letters, 19 (2010) 179-189.
[3] S.F. Nitodas and T.K. Karachalios, International Journal of Nanomanufacturing, 6 (2010) 111-124.
[4] J-H. Du, J. Bai, H-M. Cheng, eXPRESS Polymer Letters, 1 (2007) 253–273.
[5] K. Guru, S.B. Mishra, and K.K. Shukla, Applied Surface Science, 349 (2015) 59-65.

Low content ZnO/epoxy resin and $BaTiO_3$/epoxy resin nanocomposites: Dielectric response.

G. Tomara[1], E. Grigoriadi[1], A. Giannouli[1], A. Patsidis[2], P. Karahaliou[1], G. Psarras[2], S. Georga[1] and C. Krontiras[1]

[1] Department of Physics, University of Patras, 26504, Patras, Greece
[2] Department of Materials Science, University of Patras, 26504, Patras, Greece

E-mail: tomgeo@physics.upatras.gr

The ongoing progress in electronic devices requires materials with enhanced dielectric permittivity combining at the same time, suitable dielectric properties, mechanical strength and ease of processing. Polymer nanocomposites, formed by homogenously distributed, ferroelectric and/or piezoelectric particles in an amorphous matrix, constitute a new highly promising class of materials able to address the engineering demands [1].

Polymers are suitable matrices for nanocomposite materials due to their ease processing, light weight, resistance to corrosive environments and good adhesion with the reinforcing phase. Thus, in the present work, epoxy resin was used as matrix where, zinc oxide (ZnO) and barium titanate ($BaTiO_3$) nanoparticles were incorporated as the reinforcing phase.

ZnO crystallizes in two main structures, hexagonal and cubic. It is a wide-bandgap semiconductor with high piezoelectric tensor. This property renders it to a technologically important material for many piezoelectric applications, which require a large electromechanical coupling [2]. $BaTiO_3$ is another ceramic material, with ferroelectric and piezoelectric properties. It is an inorganic compound that crystallizes in different phases depending on temperature. All phases, with the exception of the cubic one, exhibit ferroelectric behaviour. Thus, $BaTiO_3$ is widely used as dielectric in capacitors and other electronic devises [3, 4].

In the present work epoxy resin – ZnO and epoxy resin – $BaTiO_3$ nanocomposites were prepared, in various filler concentrations ranging from 3 up to 12 phr (parts per hundred resin) and they were tested via Broadband Dielectric Spectroscopy (BDS) over a wide temperature (from -100 °C to 150 °C) and frequency (from10^{-1} Hz to 10^6 Hz) range. The dielectric relaxation phenomena recorded, include contributions from both the polymeric matrix and the reinforcing phase. They are denoted, with increasing temperature, as: γ-mode assigned to the re-orientation of small segments of the polymer chain, β-mode attributed to the rearrangement of polar side groups of the polymer chains [5, 6], IDE (Intermediate Dipolar Effect) located intermediate in the dielectric spectra and attributed to relaxation phenomena related to the filler [2, 6], α-mode attributed to the glass to rubber transition of the polymer matrix [4, 6] and IP (Interfacial Polarization), taking place in the interfaces of the polymer matrix and the filler [4, 6], as a result of the electrical heterogeneity of the systems (Fig.1 and Fig.2).

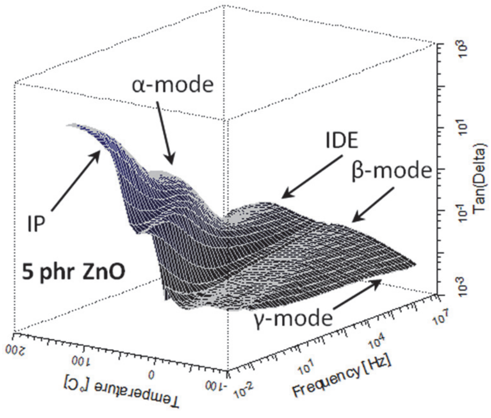

Figure 1: 3D graph of the loss factor versus frequency and temperature for the specimen with 5 phr in ZnO.

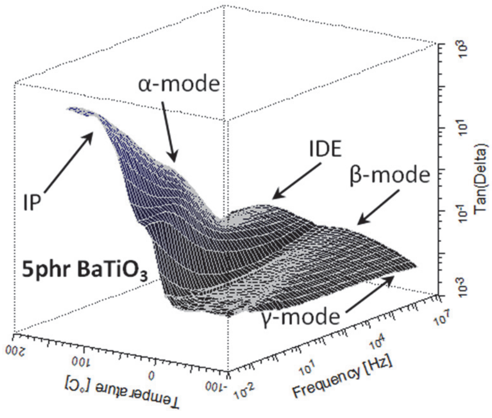

Figure 2: 3D graph of the loss factor versus frequency and temperature for the specimen with 5 phr in $BaTiO_3$.

The dielectric response is analysed via the loss factor ($\tan\delta$) (Fig.1 and Fig.2), the electric modulus (M) and the real part of the electrical conductivity (σ') representations. The temperature dependence of the relaxations is examined and the activation energies are calculated. In addition, the effect of the filler on the dielectric response of the nanocomposites is investigated through a comparison between systems with varying filler concentration. Finally, the energy storage efficiency of all composites is examined.

Acknowledgements: This research has been co-financed by the European Union (European Social Fund – ESF) and Greek national funds through the Operational Program "Education and Lifelong Learning" of the National Strategic Reference Framework (NSRF)-Research Funding Program: THALES. Investing in knowledge society through the European Social Fund, MIS 379346.

References

[1] H. Hammami, M. Arous, M. Lagache, and A. Kallel, Composites Part A: Applied Science and Manufacturing, 37 (2006) 1-8.
[2] A. Soulintzis, G. Kontos, P. K. Karahaliou, G. C. Psarras, S. N. Georga, and C. A. Krontiras, Journal of Polymer Science Part B: Polymer Physics Journal 47 (2009) 445-454.
[3] A. Patsidis, S. N. Georga, C. A. Krontiras, G. C. Psarras, A. Kanapitsas, and C. Tsonos, Macromol. Symp., 331-332 (2013) 189–196.
[4] A. Patsidis and G. C. Psarras, eXPRESS Polymer Letters, 2 (2008) 718–726.
[5] G. A. Kontos, A. L. Soulintzis, P. K. Karahaliou, G. C. Psarras, S. N. Georga, C. A. Krontiras, and M. N. Pisanias, eXPRESS Polymer Letters, 1 (2007) 781–789.
[6] G. N. Tomara, A. P. Kerasidou, A. C. Patsidis, P. K. Karahaliou, G. C. Psarras, S. N. Georga, and C. A. Krontiras, Composites Part A: Applied Science and Manufacturing, 71 (2015) 204-211.

Dielectric Properties of Ceramic Particles/Epoxy Resin Nanodielectrics

G. C. Psarras[1], **A. Kanapitsas**[2] **and C. Tsonos**[2]

[1]Department of Materials Science, University of Patras, Patras 26504, Greece
[2]Electronics Engineering Department, TEO of Sterea Ellada, Lamia 35100, Greece

E-mail: G.C.Psarras@upatras.gr

MOP

P054

Nanodielectrics consisted of a polymer matrix and ceramic nanoparticles as reinforcing phase are currently widely investigated, because of their ability to tune dielectric response and energy storage efficiency [1-3]. Nanodielectrics are able not only to replace conventional dielectric materials, but also to be exploited in applications such stationary power systems, cellular phones, wireless personal digital assistants and hybrid electric vehicles. The presence of polar oxides within a polymer matrix adds functionality to the overall performance of the nanocomposite due to the variable polarization, temperature dependence of conductivity and energy storage [2-5].

In this study series of ZnO/TiO_2/epoxy and $ZnO/BaTiO_3$/epoxy hybrid nanocomposites were prepared and studied, varying the fillers content. All contents are expressed in parts per hundred resin per weight (phr). Morphology and dielectric response are investigated by means of scanning electron microscopy and broadband dielectric spectroscopy, respectively. Obtained results are compared and discussed taking into account the performance of epoxy binary systems containing ZnO, TiO_2 and $BaTiO_3$. Data analysis is focused in realizing the optimum type and amount of reinforcing phase with respect to dielectric behavior, functionality and energy storage efficiency.

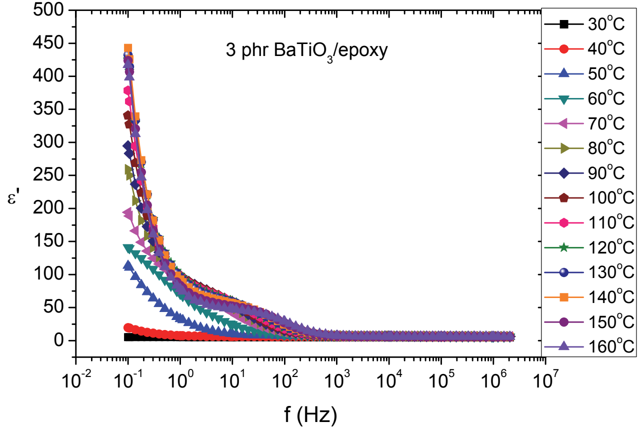

Figure 1: Variation of the real part of dielectric permittivity with frequency, at various temperatures, for the 3 phr $BaTiO_3$ nanoparticles /epoxy specimen.

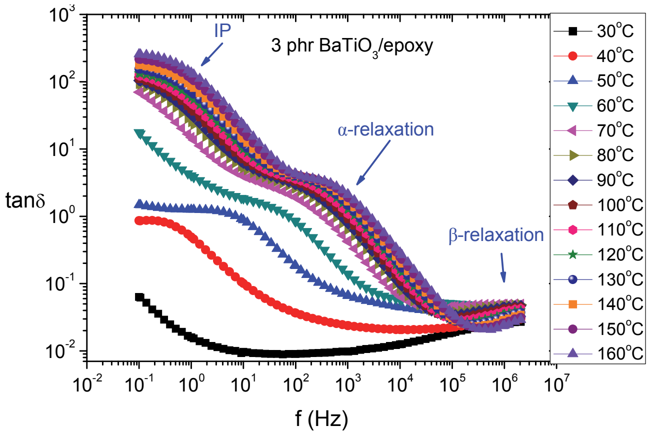

Figure 2: Variation of the loss tangent with frequency, at various temperatures, for the 3 phr $BaTiO_3$ nanoparticles /epoxy specimen.

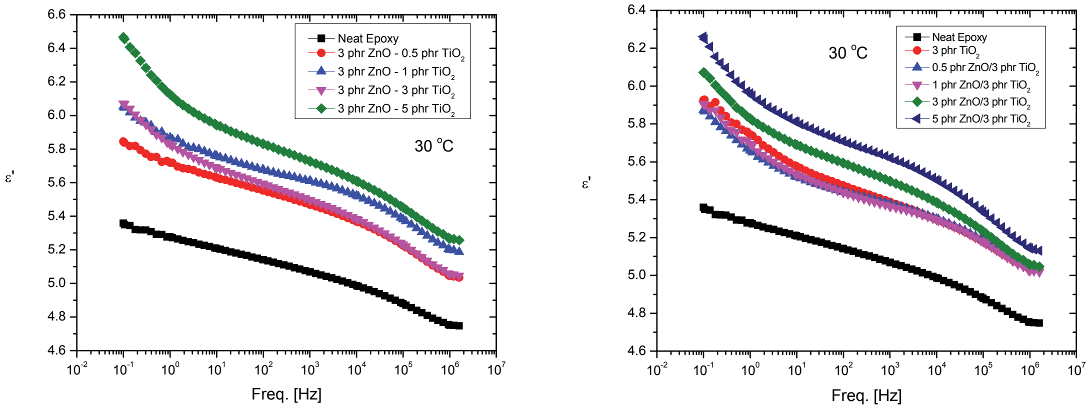

Figure 3: Variation of the real part of dielectric permittivity with frequency, at 30°C, for the ZnO/TiO_2/epoxy hybrid system, at constant ZnO content (left), and constant TiO_2 content (right).

It is evident that permittivity increases, in general, with filler content, since the ceramic particles have higher values of ε′ with respect to the polymer matrix. Additionally permittivity increases with decreasing frequency, because dipoles attain sufficient time to align themselves parallel to the field. The recorded relaxation processes are attributed to interfacial polarization, glass to rubber transition of the matrix (α-process), and re-orientation of polar side groups (β-process).

Acknowledgments: This research has been co-financed by the European Union (European Social Fund – ESF) and Greek national funds through the Operational Program "Education and Lifelong Learning" of the National Strategic Reference Framework (NSRF)-Research Funding Program: THALES. Investing in knowledge society through the European Social Fund, MIS 379346.

References

[1] V. Toner, G. Polizos, E. Manias, and C.A. Randall, J. Appl. Phys., 108 (2010) 074116.
[2] A. C. Patsidis, K. Kalaitzidou and G. C. Psarras, Mater. Chem. Phys., 135 (2012) 798-805.
[3] A. C. Patsidis and G. C. Psarras, Smart Materials and Structures, 22 (2013) 115006.
[4] G. N. Tomara, A. P. Kerasidou, A. C. Patsidis, P. K. Karahaliou, G. C. Psarras, S. N. Georga, and C. A. Krontiras, Comp. Pt. A-Apll. Sci. Manuf., 71 (2015) 204-211.

Inorganic Filler-Polymer Matrix Nanocomposites as Bulk Energy Storing Devices

D. A. Karolidis[1], **N. Mourtasagas**[2] **and G. C. Psarras**[3]

[1]Department of Energy Technology Engineering,
Technological Educational Institute (T.E.I.) of Athens, Aegaleo 12210, Greece,
[2]Thetiko Educational Centre, I. Dragoumi 2, Kavala 65302, Greece,
[3]Department of Materials Science, University of Patras, Patras 26504, Greece,

E-mail: G.C.Psarras@upatras.gr

Polymer nanocomposites reinforced with inorganic particles represent a novel class of engineering materials. Polymer matrix nanocomposites exhibit a number of advantages, such as easy processing, thermo-mechanical stability, resistance to corrosive environments etc. Moreover their dielectric behaviour can be tailored by simply controlling the type and the amount of the employed nanofiller [1-3]. Thus, it is expected to replace conventional insulating materials in a variety of applications. Current applications of inorganic-polymer nanocomposites, include packaging, electromagnetic radiation shielding, circuit board, interlayer dielectrics, leakage current controllers, self-current regulators, passive protection etc.

Insulating polymer matrices incorporating nanoinclusions are also referred as nanodielectrics [4]. Nanoinclusions could be able to service as an inherent network of nanocapacitors. Charging and discharging under control the, embedded in a matrix, nanocapacitors defines an energy storing procedure at the nanoscale level. The latter could be exploited in bulk energy storing devices suitable for emerging technological applications such as cellular phones, wireless personal digital assistants, acoustic emission sensors, stationary power systems and hybrid electric vehicles.

In this work the ability of inorganic particles/polymer matrix nanocomposites for electrical energy storage is investigated by means of energy density function. Energy density is defined via Equation (1) being a function of dielectric permittivity and field's intensity:

$$U = \int E \cdot dD \Rightarrow U = \frac{1}{2}\varepsilon_0 \varepsilon' E^2 \qquad (1)$$

where E is the field's intensity, D the dielectric displacement, ε' dielectric permittivity, and ε_0 permittivity of free space. It is well known that ε' is a material property being a function of the frequency of the applied field and temperature. Indicative results of two polymer nanocomposite systems are shown in Figures 1 and 2. The first system is consisted of an amorphous polymer (epoxy resin) as matrix and various amounts of TiC nanoparticles as filler, while the second one is consisted of a semi-crystalline rubber reinforced by alumina nanoparticles of various dimensions. All contents are expressed in parts per hundred resin per weight (phr). Figure 1a presents the variation of energy density with frequency, at 30°C, for the TiC/epoxy system. U_{rel} is a normalized quantity of the composite's energy density upon the energy density of the neat matrix. Figure 1b depicts results of U_{rel} of the TiC/epoxy system, as a function of temperature at 0.1 Hz.

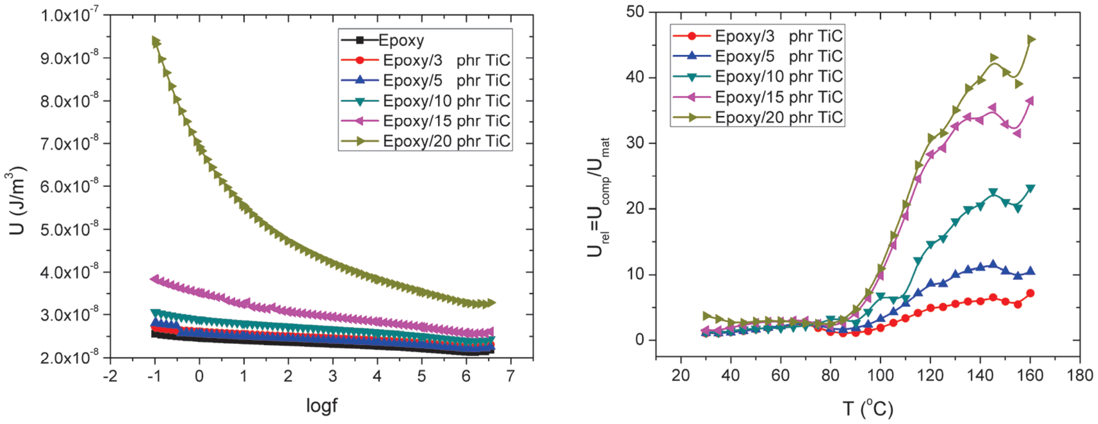

Figure 1: Variation of energy density with frequency, at 30°C (left), and U_{rel} as a function of temperature, at 0.1 Hz (right), for the TiC/epoxy system.

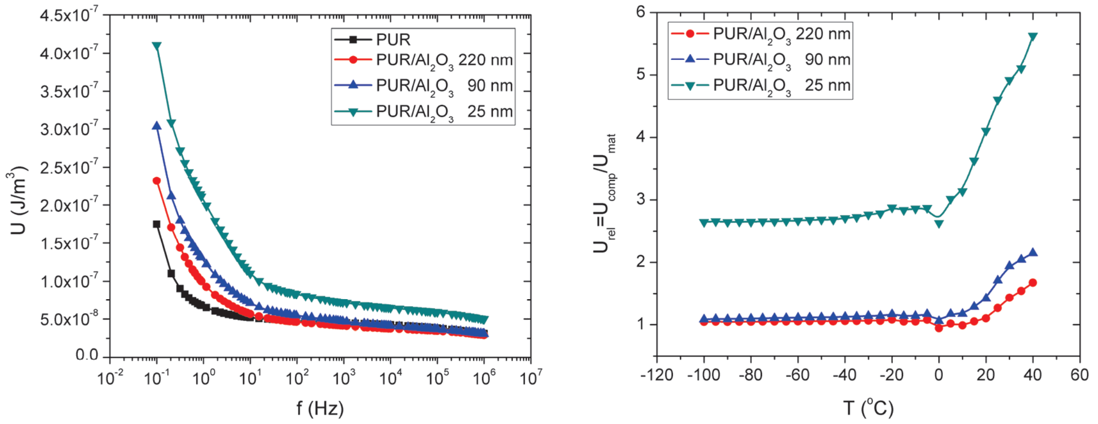

Figure 2: Variation of energy density with frequency, at 50°C (left), and U_{rel} as a function of temperature, at 0.1 Hz (right), for the Al_2O_3/PUR system. Alumina content is constant at 10 phr.

In the case of the TiC reinforced system energy storing efficiency is enhanced up to 45 times, while in the alumina reinforced polymer the energy storing capability of the specimens' increases with decreasing of the size of the employed filler.

References

[1] A. C. Patsidis and, G. C. Psarras, Smart Materials and Structures, 22 (2013) 115006.
[2] A. C. Patsidis, K. Kalaitzidou and G. C. Psarras, Materials Chemistry and Physics, 135 (2012) 798-805.
[3] G. C. Psarras, Conductivity and dielectric characterization of polymer nanocomposites, in "Polymer nanocomposites: Physical properties and applications", edited by S. C. Tjong and Y.-M. Mai, Woodhead Publishing Limited, Cambridge, (2010) 31-69.
[4] G. C. Psarras, Express Polymer Letters, 2 (2008) 460.

Effect of different graphene nanoparticles on the structural, thermal and mechanical properties of high density polyethylene

E. Tarani[1], **Z. Terzopoulou**[2], **D. N. Bikiaris**[2], **E. Pavlidou**[1], **G.Vourlias**[1] **and K. Crissafis**[1]

[1]Physics Department, Solid State Physics Section, Aristotle University of Thessaloniki, 54124 Greece
[2]Department of Chemistry, Laboratory of Polymer Chemistry and Technology, Aristotle University of Thessaloniki, 54124 Greece

E-mail: etarani@physics.auth.gr

High Density Polyethylene (HDPE) is one of the most important commodity polymers. It has grown most rapidly due to the good balance between rigidity and strength, and more flexible processing. As well as modifying the chain structure, mechanical and thermal properties of HDPE can be improved by reinforcing with rigid nanoparticles [1]. Graphene, a monolayer of sp^2-hybridized carbon atoms arranged in a two-dimensional lattice, has been intensively studied as the next generation reinforcing material for polymers due to its large aspect ratio, high strength and stiffness, and sublime mechanical and thermal properties [2]. Melt processing is a typical method for the preparation of thermoplastic polymer nanocomposites. It is a practical, environmentally friendly, cheap and suitable method for mass production in industrial applications [3].

The main objective of our study is to synthesize via melt mixing and investigate the effect of various concentrations and particle sizes of graphene filler on the thermal and mechanical properties of HDPE. For this purpose, HDPE/ graphene nanocomposites with five different weight percents of graphene nanoparticles (GNPs) have been prepared. The GNPs used in this research were of three different sizes. All the nanocomposites were prepared using melt rheo-mixing while a physical pre-mixing was performed using solid state high energy ball milling in order to improve the dispersion of graphene nanoparticles into polymer matrix.

X-ray diffraction is used to determine the interlayer spacing of the filler in the intercalated nanocomposites and demonstrate the spatial distribution of GNPs on structural homogeneities in nanocomposites. Fourier transform infrared spectroscopy (FTIR) measurements were performed to evaluate the functionalization effect. Differential scanning calorimetry (DSC) and thermogravimetric analysis (TGA) were used to analyze the effect of the introduction of nanofillers into a polymer matrix on the thermal stability of the polymer. Gas chromatography-Mass spectrometric (GC-MS analysis) analysis was used to separate and identify the products of decomposition. Finally, mechanical properties testings were performed on an Instron 3344 dynamometer, in accordance with ASTM D638. The values of Young’s modulus, tensile strength at yield and at break point and elongation at break were determined.

From XRD patterns and the average crystallite size calculations, it is clear that the composites with filler content have larger crystallite size than neat HDPE. Meanwhile, the typical absorption of GNPs in FTIR spectra is not detected because it is either too weak or overlaps with the absorption peak of HDPE. The peak melting temperatures in the nanocomposites were only slightly higher than the pure polymer indicating the impact of graphene nanoparticles on polymer morphology. The filler serves as a nucleating agent to induce crystallization at a higher temperature. The collected fragments are the same as in neat HDPE and no modification in the decomposition products can be seen through pyrolysis, confirming the thermal analysis finding that the main difference between the decomposition of HDPE and HDPE/GNPs is in the initial decomposition reactions. Also, it is confirmed that the enhanced thermal stability comes from the more thermally stable graphene as well as the tortuosity effect of the GNPs hampering the diffusion of oxygen and volatile products throughout the composite materials during thermal decomposition. Finally, the improvement of mechanical properties can be attributed to a large aspect ratio and high intrinsic mechanical characteristics of GNPs as well as the relatively strong interfacial interaction between GNPs and HDPE, leading to a better interfacial stress transfer efficiency, which restricts the movement of the polymer chains.

References

[1] A. H. Tullo, C& E News, 88 (2010) 10-16.
[2] A. K. Geim and K. S. Novoselov, Nat. Mater., 6 (2007) 183-191.
[3] H. Kim, A. A. Abdala and C. W. Macosko, Macromolecules, 43 (2010) 6515-6530.

Studying the Water Effect upon α-Relaxation in Thermoplastic Starch Biocomposites by means of Dielectric Spectroscopy

S. Drakopoulos[1], G. Psarras[1], L. Lendvai[2] , Á. Kmetty[2,3]and J. Karger-Kocsis[2,3]

[1]Department of Materials Science, University of Patras, Patras 26504, Greece,
[2]Department of Polymer Engineering, Faculty of Mechanical Engineering, Budapest University of Technology and Economics, Műegyetem rkp. 3., H-1111 Budapest, Hungary,
[3]MTA–BME Research Group for Composite Science and Technology, Műegyetem rkp. 3., H-1111 Budapest, Hungary

E-mail: msci1347@upnet.gr

Thermoplastic starch “green” composites attracted the scientific interest because of their abundance in nature and their potential applications in packaging industry due to their biodegradability. In the present study, the electrical behaviour of thermoplastic starch composites reinforced with microcellulose or latex particles is investigated. Molecular dynamic simulations have been conducted following the Vogel-Fulcher-Tammann (VFT) equation. The specimens were prepared via twin-screw extruder, internal mixer and compression molder, varying the filler concentration. Dielectric properties and related relaxation phenomena were studied via Broadband Dielectric Spectroscopy in a wide frequency and temperature range.

Nowadays there is a great interest on the amount of waste from petrochemicals plastics mostly in packaging industry. Up to date, research has been focused to biodegradable polymers from renewable resources known as ‘’green’’ polymers. Thermoplastic starch is considered as the most promising biopolymer for such applications mostly because of its abundance in nature and its biodegradability [1-3].

The dielectric properties of biocomposites and ‘’green’’ polymers have attracted a lot of research interest the last decade. Latex has been categorized from electrically insulating to fully conductive [4,5]. The dielectric properties of thermoplastic starch, though, have not been explored as yet.The dynamics of α-relaxation is a non-linear process and is described by Vogel -Fulcher-Tammann equation. This process is directly connected to the mechanism of glass to rubber transition [6].

In the present study, the influence of humidity in α-mode in thermoplastic starch composites reinforced with microcellulose B600 or Latex particles is investigated.

The specimens were prepared with commercially available raw materials, via extrusion. In the present study, starch powder (Brenntag Hungaria Ltd, type: Hungramid F) with the plasticizer, Glycerol, (Variachem Ltd, type: Glicerine, Hungary Budapest) in a 4:1 w/w ratio and B600 cellulose microfiber (60μm length, 20μm thickness) were supplied by J.RETTENMAIER & SÖHNE GMBH +CO. The Latex nanoparticles (Natur Latex dry content 60%) were supplied by Varicham Ltd, Hungary. The dielectric characterization was conducted by means of broadband dielectric spectroscopy, using Alpha-N Frequency Response Analyzer and the 1200 BDS dielectric cell, while the temperature control was achieved with the Novotherm system, all provided by Novocontrol Technologies.

The composites have been separately immersed into seven different mixtures varying filler content (5, 10, 20% w/w) with B600 cellulose and latex as reinforcement, and the reference material.

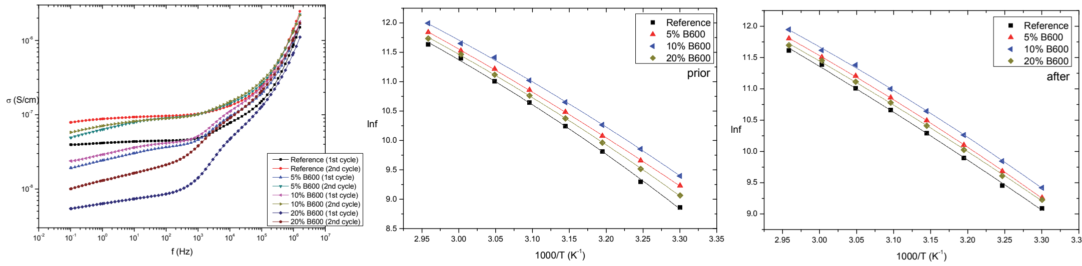

Figure 1: The real part of conductivity as a function of frequency for all TPS B600 specimens prior and after water evaporation (left), temperature dependence of the loss peak maxima for α-relaxation prior (middle) and after (right) water evaporation.

An overall of 7 specimens have been prepared, including the reference sample. The water evaporation affects the glass to rubber transition of the composites, as it can be seen after the VFT analysis. This change is more intense in low temperatures, below 45 ^{o}C. It also affects the measure of activation energy of α-relaxation. The real part of conductivity plot shows that TPS cellulose composites are more conductive than TPS latex composites, prior or after water evaporation. It is also observed that after the evaporation of any existing humidity inside the composites, conductivity increases.

References

[1] J. Karger-Kocsis, Á. Kmetty, L. Lendvai, S. X. Drakopoulos, and T. Bárány, Materials, 8 (2015) 72-95.

[2] L. Lendvai, J. Karger-Kocsis, Á. Kmetty, and S. X. Drakopoulos, Journal of Applied Polymer Science, 132 (2015) 42397.

[3] Y. L. Chung, S. Ansari, L. Estevez, S. Hayrapetyan, E. P. Giannelis, and H. Lai, Carbohydrate Polymers, 79 (2010) 391-396.

[4] P. Ortiz-Serna, M. Carsí, B. Redondo-Foj, and M. J. Sanchis, Journal of Non-Crystalline Solids, 405 (2014) 180-187

[5] G. C. Psarras, S. Siengchin, P. K. Karahaliou, S. N. Georga, C. A. Krontiras, and J. Karger-Kocsis, Polymer International, 60 (2011) 1715-1721.

[6] F. Stickel, E. W. Fischer and R. Richert, The Journal of Chemical Physics, 102 (1995) 6251-6257.

Dielectric Characterization of Epoxy Resin - Strontium Ferrite Nanocomposites

A. Sanida, S. Stavropoulos, E. Senis , O. Vryonis and G. Psarras

Department of Materials Science, University of Patras, Patras 26504, Greece

E-mail: ksanida@upatras.gr

MOP

P058

Polymer based nanocomposites is a subject of considerable research due to their ability to combine the advantages of both polymers and filler components. There are several applications of polymeric nanocomposites based on their optical, electrical, mechanical and magnetic properties. Current applications of inorganic semiconducting filler/polymer matrix nanocomposites include packaging, electromagnetic radiation shielding, circuit board, and interlayer dielectrics [1-3].
In the present study a set of specimens of commercially available epoxy resin and ceramic $SrFe_{12}O_{19}$ (strontium ferrite) nanoparticles with mean diameter less than 100 nanometers, have been prepared varying the concentration of the inclusions. Strontium ferrite is an important ferromagnetic oxide. Due to its remarkable properties these materials can be used as permanent magnets, and as a component in microwave and high frequency devices, in small electric motors, microwave devices, recording media, magneto-optic media, telecommunication and electronic industry [4].

The dielectric response of the nanocomposites was studied by means of Broadband Dielectric Spectroscopy (BDS) in the frequency range 10^{-1}-10^{7} Hz and temperature interval from 30ºC to 150ºC. BDS has been proved to be a powerful tool for the investigation of molecular mobility, phase changes, conductivity mechanisms and interfacial effects in nanocomposite systems [1].

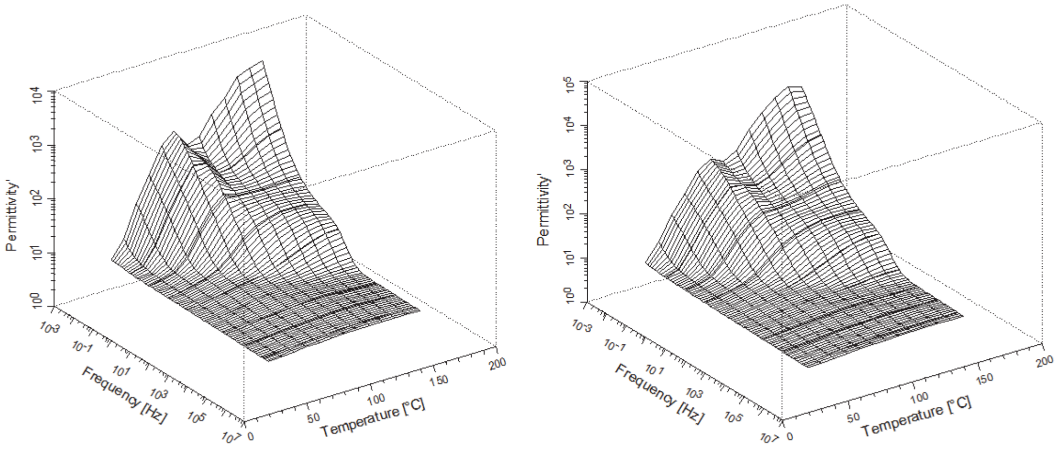

Figure 1: 3-D plots of the real part of dielectric permittivity of the specimens with 3 phr (left) and 10 phr (right) strontium ferrite content as a function of frequency and temperature.

Experimental results demonstrate an increase in the real part of dielectric permittivity with the filler concentration. Three different relaxation mechanisms were observed: Interfacial polarization (also known as Maxwell-Wagner-Sillars phenomenon) is observed at low frequencies, α-relaxation (glass to rubber transition) at intermediate frequencies and β-relaxation (re-orientation of small polar side groups) at high frequencies.

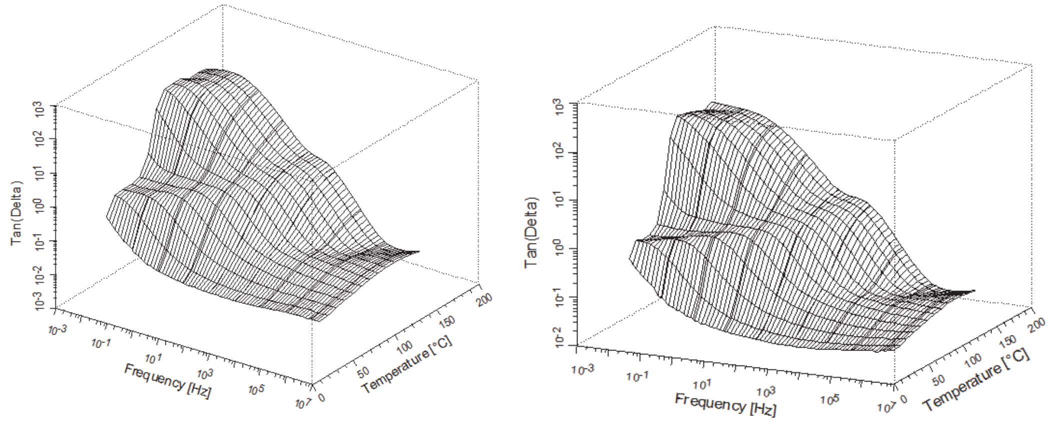

Figure 2: 3-D plots of loss tangent of the specimens with 3 phr (left) and 10 phr (right) strontium ferrite content as a function of frequency and temperature.

References

[1] G. Psarras, Physical Properties and Applications of Polymer Nanocomposites, Ed. S,C Tjong and Y.W Mai, Woodhead Publishing in Materials (2010).

[2] G. Psarras, E. Manolakaki and G. Tsangaris, Journal of Composites A 33 (2002) 375-384.

[3] N. Bouropoulos, G. Psarras, N. Moustakas, A. Chrissanthopoulos, and S. Baskoutas, phys. stat. sol., 205 (2008) 2033 – 2037.

[4] M. Soloman, P. Kurian, M. Anantharaman, and P. Joy, Journal of Elastomers and Plastics, 37 (2005) 109.

Thermomechanical characterization of hybrid epoxy composites with Carbon-based nanofillers

A. Z. Stimoniaris[1,4], **C. A. Stergiou**[2,3], **M. A. Karakassides**[4],
D. Gournis[4] **and C. G. Delides**[1]

[1]Dept. of Environmental Engineering, Technological Education Institute of Western Macedonia,
50100 Kila, Kozani, Greece
[2]Lab. of Inorganic Materials, Centre for Research and Technology-Hellas,
57001 Thermi, Thessaloniki, Greece
[3]Lab. of Materials for Electrotechnics, Dept. of Electrical and Computer Engineering,
Aristotle University of Thessaloniki, 54124 Thessaloniki, Greece
[4]Department of Materials Science and Engineering, University of Ioannina, 45110 Ioannina, Greece

E-mail: adamstimoniaris@gmail.com

Epoxy nanocomposites with a variety of fillers are used in a wide range of applications due to their outstanding performance, processability and low cost [1,2]. Carbon nanofillers are among the most suitable fillers for improving the mechanical and electrical properties of the epoxy composites [3,4]. The properties of nanocomposite materials depend not only on the filler content, but also on the filler morphology and interfacial characteristics. Geometrical factors such as the shape, the particle's structure and geometry, the surface area for a given volume and the chemical functionalization of the filler play a dominant role controlling the physicochemical properties of the composite [5,6].

The materials used for sample preparation are: diglycidyl ether of bisphenol A (DGEBA) as matrix, triethylenetetramine (TETA) as hardener and carbon nanofillers (carbon black (CB), amine-modified multi-walled carbon nanotubes (MWCNTs) and organomodified graphene oxide (OMGO)]. The sample preparation conditions have been presented in details previously [7]. Dynamic mechanical Analysis (DMA) measurements were performed in wide range of temperature.

Typical DMA spectra for the epoxy hybrid nanocomposites are shown in Figures 1 and 2. The results show that the DMA spectra of the composites are strongly affected by the filler shape and the structure of the nanoparticles. There are differences either at α-relaxation and/or at β-relaxation regions. The glass transition temperatures (T_g), calculated from the maximum value of tan δ (Figures 1 and 2), present a complicate dependence on the fillers content and their combination. This may be attributed to extra constrain affecting the long scale segmental motions [2, 5] in the case of CB and MWCNTs and to the presence of the short flexible carbon chains surrounding the OMGO particles, acting in some way as plasticizer [8]. The storage modulus (E′) increases with filler content for samples with CB and MWCNTs and decreases with OMGO. When two fillers (OMGO and MWCNTs) are used the net result of the two competitive effects (constrains of carbon nanotubes and plasticization of OMGO), affecting either the E′ and/or the Tg, is observed (Figure 2).

Concerning the β-relaxation, the peak is sifted to higher temperature as the filler content increases in the case of CB. On the other hand, for the composites with carbon nanotubes and OMGO this shifting is much lower, duo probably to their interphasial presence produced by the modification additives, which affects the crankshaft rotation of hydroxyl ether group responsible for the β-relaxation [7].

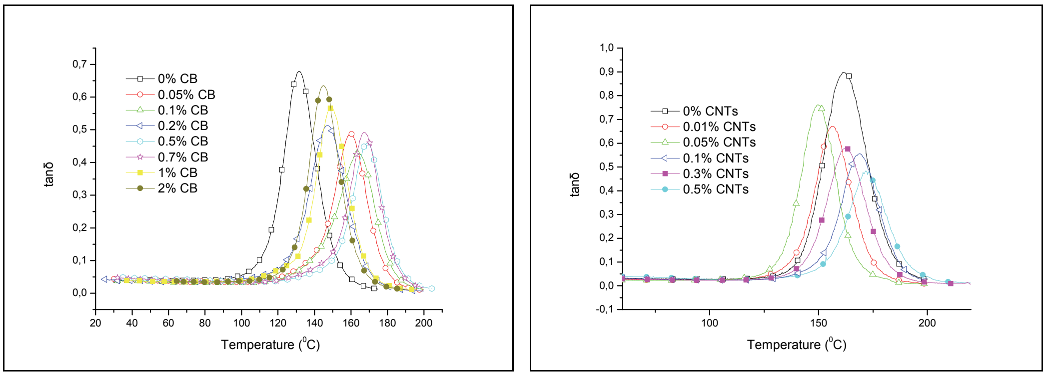

Figure 1: Tan δ DMA spectra for epoxy/TETA/CB and epoxy/TETA/MWCNTs composites as a function of filler content.

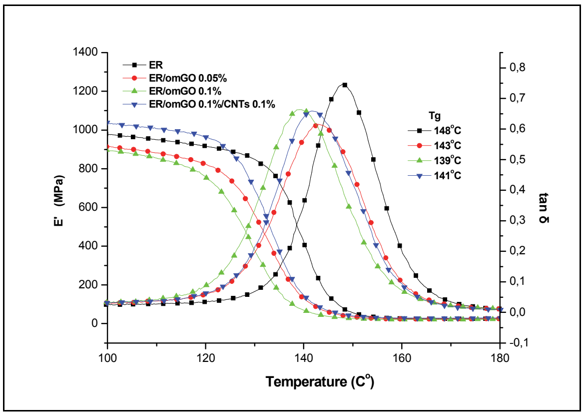

Figure 2: DMA spectra for epoxy/TETA/OMGO/MWCNTs hybrid composites (synergy of nanofillers).

References

[1] W. Li. D. He, Z. Dang and J. Bai, Composites Science and Technology, 99 (2014) 8-14.

[2] Qinghong Liu, Xufeng Zhou, Xinyu Fan, Chunyang Zhu, Xiayin Yao and Zhaoping Liu, Polymer-Plastics Technology and Engineering, 51 (2012) 251-256.

[3] D. Vennerberg, Z. Rouger and M. R. Kessler, Polymer, 55 (2014) 1854-1865.

[4] Mehdi Barikani and Iraj Hasanzadeh, Polymer-Plastics Technology and Engineering, 52 (2013) 869-876.

[5] Yan-Jun Wan, Long-Cheng Tang, Li-Xiu Gong, Dong Yan, Yi-Bao Li, Lian-Bin Wu, Jian-Xiong Jiang, and Guo-Qiao Lai, Carbon, 69 (2014) 467–480.

[6] H. J. Kim and D. W. Seo, International Journal of Fatique, 28 (2006) 1307-1314.

[7] Th.V. Kosmidou, A.S. Vatalis, C.G. Delides, E. Logakis, P. Pissis and G. C. Papanicolaou, eXPRESS Polymer Letters, 2 (2008) 364-372.

[8] Constantinos G. Delides, 6th Conference THERMA, 26-28 September, Larisa, Greece (2014).

Selective removal of silver ions from synthetic mining effluents using Molecularly Imprinted Polymers (MIPs)

G. Z. Kyzas and D. N. Bikiaris

Laboratory of Organic Chemical Technology, Department of Chemistry, Aristotle University of Thessaloniki, GR-541 24 Thessaloniki, Greece

E-mail: georgekyzas@gmail.com

Silver is a precious metal used since the ancient times to make money coins and high values objects. In its native form this precious metal occurs alloyed with Gold, Copper(II). Lead(II), or combined with other chemical elements in ores such as horn silver (AgCl), Argentite (Ag_2S). Nowadays it is used in numerous fields of applications that include: photographic and electronic, porcelain, mirroring, electroplating, ink formulation, dentistry, medical equipments, chemical and jewellery industries etc., Despite its wealth of applications, silver remain a scare metal with very limited natural sources. Most of the metal used is recovered from bearing silver wastes such as photographic films, scraps from jewellery and electroplating wastewater. In most cases silver ions are present at very low concentration in solution and their enrichment and separation prior to their recovery is necessary. Conventional techniques which have been applied to the extraction of soluble silver metal from its solutions include solvent extraction, precipitation, ion exchange and electrodeposition. Hence there is still need to develop more efficient technologies for the separation and recovery of silver ions. In the last decade significant research effort have been directed towards techniques improving the selective extraction of silver ions; and ion imprinted polymeric materials with different functional groups have been frequently used. In this work, two Ag(I) imprinted polymers (IIPs) were prepared by a precipitation polymerization method using two functional monomers, 4-vinyl pyridine (4-VP) and 1-vinyl imidazole (1-VID), with N,N-ethylene bisacrylamide (EBAm) as the cross linker. Characterization of the polymeric materials, optimization of variables affecting the extraction efficiency of Ag(I) ion from aqueous media as well as their selectivity for Ag(I) ion were investigated.

The synthesis of beads imprinted polymers was performed by precipitation polymerization, using the molar ratio 1:2:8 (template: functional monomer:cross linker). The functional monomers (in 20 mL ethanol) were added to $AgNO_3$ solution (prepared by dissolving 0.1698 g $AgNO_3$ in 30 mL deionized water) with continuous stirring at pH around 7.0 until formation of the template Ag(I)/monomer complex. It was then polymerized with cross linking monomer N,N-ethylene bisacrylamide (EBAm) using 2,20-azobis(2-methylpropionamidine) dihydrochloride (AMP) as initiator with constant stirring at 70 °C for 24 h. At the end of the reaction, the Ag(I) containing polymer beads were washed with the mixture of a methanol: water (1:1) several times and dried in oven at 60 °C for 24 h.

SEM showed that the surface of IIPs was not smooth but it had many channels and cavities.

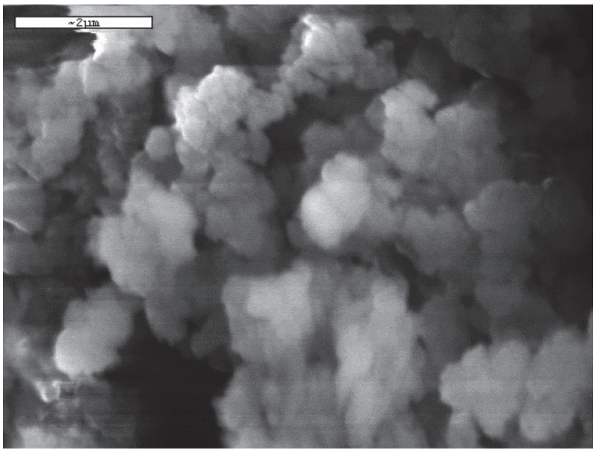

Figure 1: SEM photos of IIP.

The experiments for the pH effect showed that the optimum value was at alkaline conditions for all IIPs. Comparing the suitability of isotherms in fitting the adsorption data, both Langmuir and Langmuir-Freundlich adsorption isotherm seem to provide better fitting for both imprinted polymer (R^2 is above 0.96). However, the values of the correlation coefficient (R^2 for 4-VP-EBAm and 1-VID-EBAm imprinted polymers are 0.990 and 0.995 respectively) showed that the Langmuir equation gave a better fit to the adsorption isotherm. Furthermore, the theoretical values of maximum adsorption capacity (74 and 76 mg/g) obtained from the Langmuir equation for 1-VP-EBAm and 1-VID-EBAm imprinted polymers were very close to the experimental values 73 and 77 mg/g, respectively.

Competitive adsorption of Ag(I) ion in the presence of Cd(II), Pb(II) and Cu(II) was investigated in an equilibration/adsorption batch system. The selected ions often co-exist with precious metals in the scrape or ore exhibiting certain interference properties in aqueous environment. Additionally, all of the competing ions have similar ionic radii and they are soft or borderline metal ions in the Pearson's classification. The obtained results indicate that, except for Cu(II) the highest (b) values were obtained for Ag(I), and the more remarkable differences were observed for Cd(II) and Pb(II) ions. The highest selectivity (68.01) was recorded for Ag^+/Cd^{2+} with 4-VP-EBAm polymer, while the lowest selectivity (2.04 and 1.85) were recorded for Ag^+/Cu^{2+} with both polymers. This could be explained by the fact that Cu^{2+} has the smallest ionic radius [Cu^{2+} 71 pm] when compared to the other competing ions, and also has a strong affinity for this type of ligands. These results strongly suggest that prepared imprinted polymers have a high selectivity for Ag(I) ions. This could be attributed to molecular geometry since the polymers were prepared in the presence of Ag(I) as target ion.

Acknowledgment: The support for this study was received from the State Scholarships Foundation (IKY) of Greek Ministry of Education and Religious Affairs (in the framework of the Hellenic Republic - Siemens Settlement Agreement) through the research program "IKY Fellowships of Excellence for Postgraduate Studies in Greece - Siemens Program" under the title "Advanced Molecularly Imprinted Polymers (MIPs) as materials for the selective binding and recovery of various high-added value environmental targets with application to industrial-scale adsorption columns", which is gratefully appreciated.

SESSION TU1

STRUCTURAL, MECHANICAL & OPTICAL PROPERTIES OF CONDENSED MATTER-2

Tuesday, 22 September 2015, 9^{00}-11^{00}

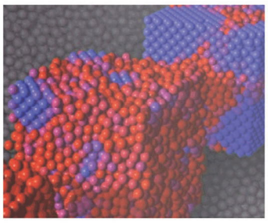

XXXI Panhellenic Conference on
SOLID STATE PHYSICS &
MATERIALS SCIENCE
Thessaloniki, 20-23 September 2015

Broadband Terahertz Generation from Metamaterials and Optical Metamaterials Resonances with High Quality Factor

Costas. M. Soukoulis[1,2]

[1]*Ames Laboratory, and Dept. of Physics and Astronomy, Iowa State University, Ames, Iowa*
[2]*Institute of Electronic Structure and Laser (IESL), FORTH, Heraklion, Crete, Greece*
soukoulis@ameslab.gov

Most metamaterials (MMs) to date are made with metallic constituents, resulting in significant dissipation loss in the optical domain. Therefore, we need to find other ways to create high-quality resonators with less dissipative loss for the meta-atoms. One innovative approach we plan is to reduce dissipative losses by making use of dielectrics rather than metals for building the EM resonators. This avoids resonant loss in the metals and we indeed demonstrate electric and magnetic dielectric metamaterial resonators with very large quality factors. The resulting structures can be straightforwardly scaled at optical frequencies to create low-loss MMs with a wide range of properties. We experimentally demonstrate efficient broadband THz generation, ranging from 0.1 - 4 THz, from a thin layer of SRRs with few tens of nanometers thickness by pumping at tele-communications wavelength of 1.5 microns (200 THz).

The terahertz spectral range of the electromagnetic spectrum—from about 100 GHz to 15 THz—has long been a challenging region in between the successful realms of electronics and photonics, because of the lack of efficient and compact sources and detectors for terahertz radiation. In the past few decades, however, the development of technologies like quantum-cascade lasers, terahertz wave generation through nonlinear crystals and terahertz time-domain spectroscopy has enabled the exploration of terahertz science and the rapid rise of terahertz imaging and spectroscopy for, amongst others, biomedical and security applications [1-3]. Likewise, electronic devices are pushing their boundaries to the THz regime from below, where many potential applications exist in different disciplines. The strategic emphasis of our research has been to merge two prominent research themes of current focus, namely femtosecond nonlinear technology [1] and metamaterials [4]. *One key challenge is to develop ultrafast few-cycle THz pulses with extraordinary stability and a gapless spectrum covering the entire THz region.*

Earlier this year, we have developed [5] an approach based on meta-atoms called split-ring resonators (SRRs). By tailoring their size, these can exhibit a strong magnetic response to any desired frequency in the THz to infrared spectrum. Ames Lab/Iowa State Univ. and Karlsruhe Institute of Technology demonstrated [5] efficient single-cycle broadband THz generation, ranging from about 0.1–4 THz from a thin layer of split-ring resonators by pumping at the telecommunication wavelength of 1.5 microns (200 THz). The team's SRR metamaterial THz emitters measured only 40 nm and performed as well as traditional emitters (ZnTe) that are thousands of times thicker (0.2 mm or 1 mm). The terahertz emission arises from exciting the magnetic-dipole resonance of the split-ring resonators and quickly decreases under off-resonance pumping. This, together with pump polarization dependence and power scaling of the terahertz emission, identifies the role of optically induced nonlinear currents in split-ring resonators. By comparison with theory, we have shown [5] a giant sheet nonlinear susceptibility that far exceeds known thin films and bulk inorganic materials such as ZnTe. Our approach provides a potential solution to bridge the "*THz technology gap*" by solving the four key challenges in the THz emitter technology: *efficiency*; *broadband spectrum*; *compact size* and *tunability*. Optical metamaterials resonances with high quality factor [6].

In summary, we have shown that a single nanometer-scale layer of SRRs merges nonlinear metamaterials and THz science/technology, representing a new platform for exploring artificial magnetism induced nonlinear THz generation. This leads to broadband THz emission from deep-subwavelength meta-atoms.

References

[1] M. Tonouchi, Nature Photon. 1 (2007) 97.
[2] W. J. Padilla et al., Phys. Rev. Lett. 96 (2006) 107401.
[3] G. Scalari et al., Laser Photon. Rev. 3 (2009) 45.
[4] C. M. Soukoulis et al., Nature Photon. 5 (2011) 523.
[5] L. Luo et al., Nature Commun. 5 (2014) 3055.
[6] A. Jain et al. Phys. Rev. Lett. 112 (2014) 117403.

High-Pressure Phase Transition in $Y_3Fe_5O_{12}$

Camelia V. Stan[1], Jue Wang[2], Ilias S. Zouboulis[3],
Vitali Prakapenka[4], and Thomas S. Duffy[2]

[1]Department of Chemistry, Princeton University, Princeton, NJ 08544, USA
[2]Department of Geosciences, Princeton University, Princeton, NJ 08544, USA
[3]Department of Physics, National Technical University of Athens, Athens, Greece
[4]GeoSoilEnviroCARS, University of Chicago, Argonne National Lab, Argonne, IL 60439, USA

E-mail:isz@princeton.edu, zoubisig@central.ntua.gr

The behavior of yttrium iron garnet (YIG, $Y_3Fe_5O_{12}$) was examined up to 74 GPa and 1800 K using synchrotron x-ray diffraction in a diamond anvil cell.. At room temperature, YIG remained stable in the garnet phase until abrupt amorphization occurred at 51 GPa, consistent with earlier studies. Upon laser heating to up to 1800 K, the material transformed to a single-phase A-site disordered orthorhombic $GdFeO_3$-type perovskite of composition $(Y_{0.75}Fe_{0.25})FeO_3$. No evidence of decomposition of the sample was observed. Both the room-temperature amorphization and high-temperature transformation to the perovskite structure are both consistent with the behavior of other rare earth oxide garnets. The perovskite sample was compressed from 28- 74 GPa with annealing to ~1500 K every 3-5 GPa. Between 46 and 50 GPa, an 6.8% volume discontinuity is observed without any accompanying change in the number and type of diffraction peaks. This is indicative of a high spin to low spin transition in Fe^{3+}, likely in the octahedrally coordinated B-site of the perovskite. The properties of the inferred spin transition are generally consistent with those observed in other rare earth ferric iron perovskites at high pressures.

Amorphous Carbon Films For Protective and Solid Lubricant Applications

M. Constantinou[1], **M. Pervolaraki**[2], **L. Koutsokeras**[1], **P. C. Kelires**[1], **P. Patsalas**[3], **J. Giapintzakis**[2], **G. Constantinides**[1]

[1]Research Unit for Nanostructured Materials Systems and Department of Mechanical Engineering and Materials Science and Engineering, Cyprus University of Technology, Limassol, Cyprus
[2]Nanotechnology Research Center and Department of Mechanical and Manufacturing Engineering, University of Cyprus, Nicosia, Cyprus
[3]Department of Physics, Aristotle University of Thessaloniki, Thessaloniki, Greece

E-mail: g.constantinides@cut.ac.cy

Amorphous Carbon (a-C) films have been the subject of extensive research in diverse fields of science. This relates to their wide variety of interesting properties covering high hardness (≥10GPa), low friction coefficient (≤0.3), excellent biocompatibility, antibacterial properties, etc. [1, 2]. Nevertheless, they still possess some disadvantages which limit their extent of exploitation in applications such as protective and solid lubricant coatings, where scratch resistance and mechanical toughness are required to increase the performance of the films under tribological and abrasive conditions. In this work, we investigate the effect of silver incorporation in a-C networks on the a-C:Ag nanocomposite film's hardness and scratch resistance with the aim to quantitatively record any change in the tribological response. Additionally, the influence of temperature during and after the growth of a-C:Ag films on the mechanical properties is studied. Two deposition techniques were used to grow a-C:Ag nanocomposite films: (a) Pulsed Laser Deposition (PLD) and (b) a custom-made hybrid Plasma Enhanced Chemical Vapour Deposition/Physical Vapour Deposition (PECVD/PVD). The mechanical behavior and structural bonds of a-C:Ag films were investigated using nanoindentation and XPS techniques. It is found that the silver content decreases the percentage of C-C sp3 bonds in the matrix with subsequent reductions in hardness but an increase in ductility, leading to a material with enhanced tribological characteristics. The ability to tailor the microstructure of a-C:Me films which includes the control on the carbon bonds (sp^3, sp^2 or sp^1), the hydrogen content, and the type and content of metallic nanoparticles opens new avenues for a broad range of applications were mechanical, physical and/or optical properties are required [3, 4].

References

[1] Erdemir, A. & Donnet, C. (2006), J Phys D Appl Phys, vol. 39, no. 18, pp. R311-R327.
[2] Hauert, R. (2003), Diam Relat Mat, vol. 12, no. 3-7, pp. 583-589.
[3] Robertson, J. (2002), Materials Science and Engineering: R: Reports, vol. 37, no. 4-6.
[4] Zoubos, H. et al. (2013), Sol Energ Mat Sol C, vol. 117, pp. 350-356.

Aknowledgements

The authors would like to acknowledge the financial support from the Strategic Infrastructure Project NEW INFRASTRUCTURE/STRATE/0308/04 of DESMI 2008, which is co-financed by the European Regional Development Fund, the European Social Fund, the Cohesion Fund, and the Research Promotion Foundation of the Republic of Cyprus.

Metal vacancies in strained AlN/GaN interfaces: a first principles investigation

Th. Pavloudis[1], V. Pontikis[2], Ph. Komninou[1],
J. Chen[3], Th. Karakostas[1], and J. Kioseoglou[1]

[1]Physics Department, Aristotle University of Thessaloniki, GR-54124 Thessaloniki, Greece
[2]Commissariat à l'Energie Atomique (CEA), Institut Rayonnement Matière de Saclay (IRAMIS), Laboratoire des Solides Irradiés (LSI), 91191 Gif-sur-Yvette Cedex, France
[3]Laboratoire de Recherche sur les Propriétés des Matériaux Nouveaux, Université de Caen, IUT d'Alençon, 61250 Damigny, France

E-mail: corresponding-sifisl@auth.gr

AlN/GaN heterostructures have been studied using density-functional pseudopotential calculations yielding the formation energies of metal vacancies under the influence of local interfacial strains, the associated charge distribution and the energies of vacancy-induced electronic states. Interfaces are built normal to the polar <0001> direction of the wurtzite structure by joining two single crystals of AlN and GaN that are a few atomic layers thick; thus, periodic boundary conditions generate two distinct heterophase interfaces (Figure 1). We show that the formation energy of vacancies is a function of their distance from the interfaces: the vacancy-interface interaction is found repulsive or attractive depending the type of the interface. When the interaction is attractive, the vacancy formation energy decreases with increasing the associated electric charge, and hence the equilibrium vacancy concentration at the interface is greater. This finding can reveal the well-known morphological differences existing between the two types of investigated interfaces. Moreover, we found that the electric charge is strongly localized around the Ga vacancy, while in case of Al vacancies is almost uniformly distributed throughout the AlN/GaN heterostructure. Crucially, for the applications of heterostructures, metal vacancies introduce deep states in the calculated band gap at energy levels from 0.5 to 1 eV above the valence band maximum (VBM). It is, therefore, predicted that vacancies could initiate "green luminescence" i.e. light emission in the energy range of 2.5 eV stemming from electronic transitions between these extra levels, and the conduction band, or energy levels, due to shallow donors.

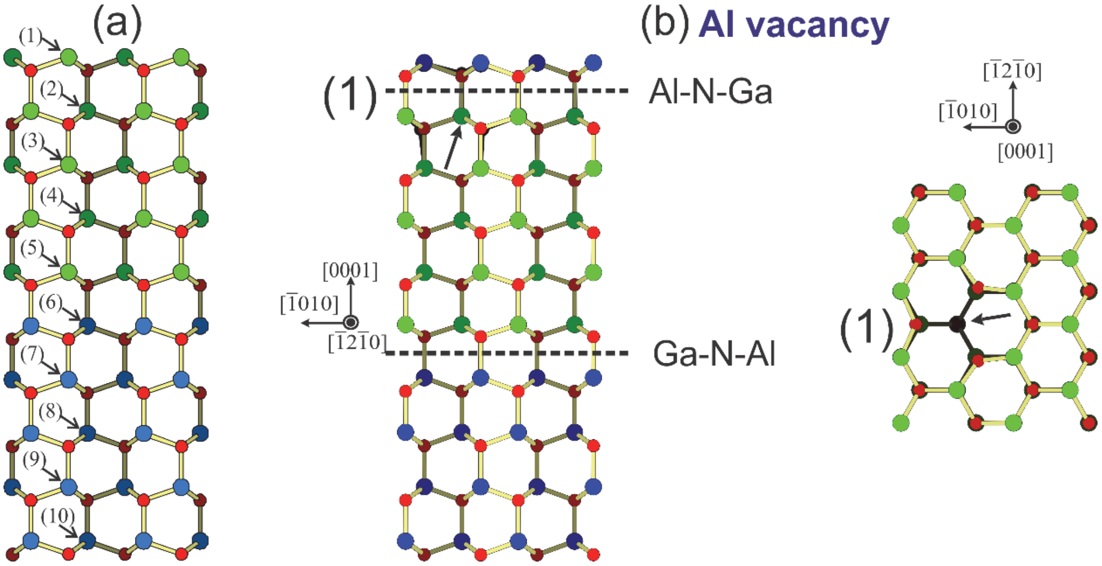

Figure 1. (a) The optimized supercell and the positions where the vacancies were inserted. (b) The relaxed atomistic configuration where an Al vacancy was inserted at the position (1).

Acknowledgements

This research is supported by the European Union (European Social Fund – ESF) and Greece through the Operational Program “Education and Lifelong Learning” of the National Strategic Reference Framework (NSRF) and the Research Funding Program THALES: “Reinforcement of the interdisciplinary and/or inter-institutional research and innovation, project “NanoWire”. The calculations have been performed at “CRIHAN”, Centre de Ressources Informatiques de HAute Normandie (http://www.crihan.fr).

Induced Raman scattering in multiferroic $EuTiO_3$

P.Pappas[1], E.Liarokapis [1], J. Köhler[2], and A. Bussmann-Holder[2]

[1]Department of Physics, National Technical University of Athens, GR15780, Athens, Greece
[2]Max-Planck-Institut für Festkörperforschung, Heisenbergstr. 1, 70569 Stuttgart, Germany

E-mail: panospappas192@gmail.com

$EuTiO_3$ (ETO) is a multiferroic compound where its paraelectricity is associated with the Ti^{4+} ions in the TiO_6 octahedra and coupled with the magnetic degrees of freedom from the Eu^{2+} ions. ETO shares similar properties with $SrTiO_3$ (STO) and crystallizes in the cubic structure (Pm-3m) with almost the same lattice constants (a=3.9Å [1] for STO and a=3.904Å for ETO [1]). Since Eu has comparable ionic radius to Sr, one expects similarity between the two compounds in their structural modifications [2], [3]. But, the presence of the magnetic Eu ions leads to the appearance in ETO of an antiferromagnetic phase transition at T_N=5.5K and an anomaly in the dielectric constant at T_N that indicates magnetoelectric coupling. In the cubic structure there are three IR-active F_{1u} modes and none Raman active. Several experimental results have shown an antiferrodistortive structural phase transition to tetragonal phase in ETO at high temperatures (T_s≈285K), while in STO T_s=110K [1],[4],[5]. A double well potential has been proposed for both compounds, which for STO is wide and shallow while in ETO is expected to be deep and narrow [2]. Since there is a disagreement between the T_s value obtained by the specific heat measurements and xrd data, we have investigated the phase transition with Raman spectroscopy. In spite the fact that several modes are expected to be Raman active by symmetry in the tetragonal phase and such modes have already been observed for the homologous STO compound, we could not detect any spectral modification across T_s (Fig.1). This surprising result that cannot be explained from lattice symmetry has triggered us to investigate other means of activating modes in Raman scattering. Therefore, we have applied an external electric field either by direct contacts or in a capacitor set-up hoping to break the inversion symmetry and activate IR modes in Raman scattering. The first method did not induce any peaks, but setting the sample under a strong dc electric field could activate the modes in Raman scattering. By applying the external voltage we could observe the samples to rotate trying to align with the external electric field. After the alignment, the re-application of the field did not induce any further realignment of the samples. Without any external effect, the Raman spectra were structureless with a strong continuum scattering. As a result of the field, the spectra have been considerably modified showing peaks that varied in intensity with the amount of applied voltage. Peaks appeared at 268, 323, 480, 532cm^{-1} and two weaker and wider ones at 190cm^{-1} and 420cm^{-1} (Fig.2). By removing the field the peak intensities of the spectra were gradually decreased, but with a considerable time delay (Fig.2). In a cycle of applying voltage and letting the compound to relax, a hysteresis and aging effects have been observed with the modified spectrum remaining for several days (Fig.3). All data indicate that we have broken the inversion symmetry activating Raman scattering in the paraelectric phase of this compound. The strong hysteresis and aging effects that we have detected are absent or very weak in STO. The reason of this difference is not clear yet, though we suspect that there is an effect that originates from the different double well potential [3] of the two compounds.

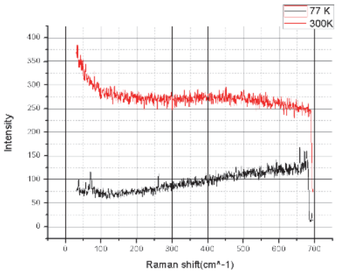

Fig.1 Raman spectra of ETO at RT (top) and 77K (bottom).

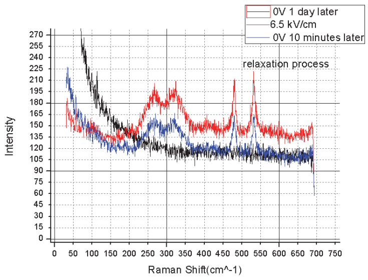

Fig.2 Raman spectra of ETO under a field of 6.5kV/cm (red), 10min after (blue) and after a day (black).

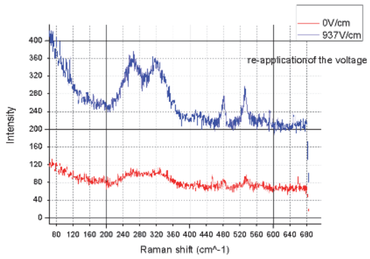

Fig. 3 Raman spectra at zero electric field after many days (bottom) and upon re-aplication of a field of 937V/cm (top).

References

[1] J.LSpalek, Ph.D. thesis, “Emergent phenomena near selected phase transitions”, Cambridge University (2008).

[2] A.Bussmann-Holder *et al*,arxiv: 1105.6029 (2011).

[3] Jerry L.Bettis *et al*, Physical Review Letters B 84 (2011) 184114.

[4] V.Goian *et al,*Physical Review Letters B 86 2012) 054112.

[5] Konstantin Z.Rushchanskii *et al*, Physical Review Letters B **85** (2012) 104109

The effect of periodically arranged Stone – Walles defects in graphene on its mechanical properties: an *ab-initio* study

Z. G. Fthenakis[1,2] **and N. N. Lathiotakis**[3,4]

[1]Physics and Astronomy Dept., Michigan State University East Lansing, Michigan 48824, USA
[2]Institute of Electronic Structure and Laser, FORTH, P.O. Box 1527, 71110 Heraklio, Crete, Greece
[3]Theoretical and Physical Chemistry Institute, NHRF, V. Constantinou 48, GR-11635 Athens, Greece
[4]Max-Planck-Institut für Mikrostrukturphysik, Weinberg 2, D-06120 Halle (Saale), Germany

E-mail: fthenak@iesl.forth.gr, lathiot@eie.gr

In the present work we investigate how the mechanical properties of graphene are affected by introducing periodically arranged Stone – Walles defects (SWDs) all over the hexagonal graphene lattice [1]. (A SWD [2] is the rotation of a C-C bond around its center by 90°, resulting (in the case of graphene) to the transformation of the surrounding hexagons to two pentagons and two heptagons). Obviously, there are infinitely many different ways that SWDs can be periodically arranged in the graphene lattice, leading to an infinite number of graphene allotropes (i.e. two dimensional structures with three-fold coordinated Carbon atoms). Since it is impossible to study all of them, we select three representative ones, which transform graphene to two pentaheptites (PeHe-A and PeHe-B) and octagraphene (OcGr). Pentaheptites [3,4] are graphene allotropes, which are built entirely of pentagonal and heptagonal rings, while OcGr [5] is another graphene allotrope, which is built entirely of square and octagonal rings. The equilibrium PeHe-A, PeHe-B, OcGr and graphene structures are shown in Fig. 1. It is worth noting that OcGr can be obtained either from PeHe-A or PeHe-B (see Fig. 1) by introducing selected SWDs of the pentaheptite structure, which transform pentagons and heptagons to squares and octagons [1].

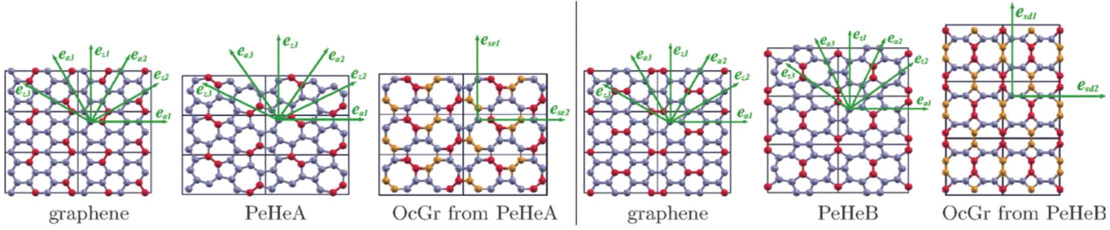

graphene PeHeA OcGr from PeHeA graphene PeHeB OcGr from PeHeB

Fig. 1. Periodically arranged SWDs. The rotated bonds are shown in red (for the conversion of graphene to PeHe-A and PeHe-B) and orange (for the further conversion of PeHe-A and PeHe-B to OcGr).

For the purpose of our investigation we apply tensile strain along high symmetry directions and we study the mechanical response of these structures. For graphene, PeHe-A and PeHe-B these directions were selected to be the directions along the arm-chair and the zig-zag chains of the initial graphene structure. The directions are shown in Fig. 1 and they are denoted by e_{a1}, e_{a2} and e_{a3} (arm-chair directions) and e_{z1}, e_{z2} and e_{z3} (zig-zag directions). Obviously, for graphene, all arm-chair chain directions (as

well as zig-zag chain directions) are equivalent with each other. However, for PeHe-

A and PeHe-B only e_{a1}, e_{a2} and e_{z1}, e_{z2} are different. On the other hand, for OcGr both e_{a1} and e_{z1} are equivalent with each other. Depending on the selected SWDs which lead to OcGr, e_{a1} and e_{z1} may coincide either with the e_{se} (along square edges) or e_{sd} (along square diameters) direction, as shown in Fig. 1.

For the above described structures and the selected strain directions, we study their response to tensile strain up to their fracture. We calculate the Young's modulus, Poisson ratio, speed of sound, ultimate tensile stress (UTS) σ_u and the corresponding strain ε_u. We also study strain as an assisting factor for the conversion of graphene to these allotropes.

For our calculations we used the DFT method at the GGA/PBE level as implemented by the Quantum Espresso DFT code [6]. For all structures a 16 atom unit cell was adopted, which in most of the cases was selected to be rectangular. We used an ultra soft pseudopotential for C, a 6x12 k-point mesh, and cutoffs of 50 and 500 Ry for the wave functions and the charge density, respectively. Calculations were performed under constant strain, while the structure was fully optimized (i.e. atomic positions and the vertical to the strain unit cell dimensions were both optimized).

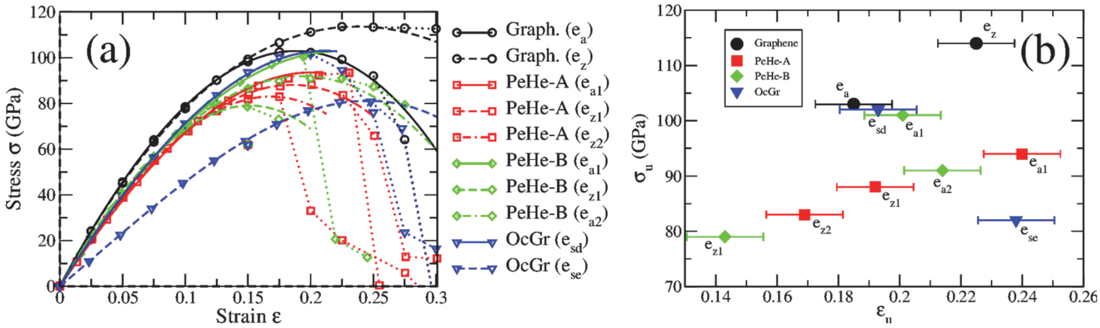

Fig. 2 (a) Stress - Strain curves and (b) UTS σ_u vs the corresponding strain value ε_u for all cases and strain directions.

According to our results [1], graphene exhibits the highest Young's modulus value (≈1020 GPa) followed by PeHe-B (≈840 – 940 GPa), PeHe-A (≈825 -865 GPa) and OcGr. PeHe-A and PeHe-B are quite isotropic, while OcGr is highly anisotropic, with Young's modulus values along e_{sd} and e_{se} directions ≈865 and ≈460 GPa, respectively. These results were obtained from the stress – strain curves, which are shown in Fig. 1(a). We also find that the corresponding Poisson's ratio values (from the lower to the higher) are 0.175 for graphene, 0.21 - 0.25 for PeHe-B, 0.25 - 0.26 for PeHe-A and 0.17 and 0.56 for OcGr for strain along e_{sd} and e_{se} directions, respectively. In Fig. 2(b) we show the Ultimate Tensile Strength (UTS) as a function of the corresponding strain values for all those structures and strain directions. As we can see, periodic SWDs may lower the high UTS values of graphene up to ≈30%, depending on the set of SWDs and strain direction.

References

[1] Z. G. Fthenakis and N. N. Lathiotakis, Phys. Chem. Chem. Phys. 17 (2015) 16418 – 16427.

[2] S. J. Stone and D. J. Wales, Chem. Phys. Lett. 128 (1986) 128.

[3] V.H.Crespi, L.X.Benedict, M.L.Cohen and S.G.Louie, Phys. Rev. B 53 (1996) R13303–R13305.

[4] H. Terrones, M. Terrones, et al., Phys. Rev. Lett. 84 (2000) 1716–1719.

[5] X.-L. Sheng, H.-J. Cui, et al, J. Appl. Phys. 112 (2012) 074315.

[6] P. Giannozzi, S. Baroni et al, J. Phys.: Condens. Matter 21 (2009) 395502.

Indentation Resistance Enhancement of Auxetic Materials: A Numerical Investigation

D. Photiou[1], N. Prastiti[1], E. Sarris[1] and G. Constantinides[1]

[1]Research Unit for Nanostructured Materials Systems, Department of Mechanical Engineering and Materials Science and Engineering, Cyprus University of Technology, 3041 Lemesos, Cyprus

E-mail: g.constantinides@cut.ac.cy

The thermodynamic constrains on a material's elastic properties allow for its Poisson's ratio to move into the negative domain, more specifically in the range of -1≤v≤0.5. This leads to the counter-intuitive behavior, in which materials tend to expand in the lateral dimension in response to stretching. This geometrically/kinematically-driven response to loading leads to several interesting material characteristics, among of which is an enhanced resistance to indentation. Within this study the finite element method is employed to investigate indentation resistance of auxetic materials. Both conical and spherical indenter geometries are used and the results are contrasted to analytical solutions and experimental data [1]. The stress profiles and contact details are systematically analyzed and the increase in resistance is traced to the shear stiffening and the reduction of contact area compared to conventional materials. Furthermore, it is shown that the analytical linear elastic solution deviates from the numerical results and correction factors for the whole ν range are therefore proposed. The effects of contact-friction and indenter cone-angle are also studied and quantified.

References

[1] Alderson, K.L., Pickles, A.P., Neale, P.J., Evans, K.E., 1994. Acta Metall. Mater. 42 (1994) 2261–2266.

Aknowledgements

The authors would like to acknowledge the financial support from the Strategic Infrastructure Project NEW INFRASTRUCTURE/STRATE/0308/04 of DESMI 2008, which is co-financed by the European Regional Development Fund, the European Social Fund, the Cohesion Fund, and the Research Promotion Foundation of the Republic of Cyprus. GC and ES would also like to acknowledge the financial support from Cyprus University of Technology start-up grant.

SESSION TU2

POLYMERS, BIOMATERIALS-1

Tuesday, 22 September 2015, 11^{30}-13^{30}

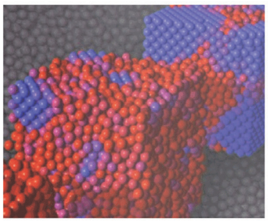

XXXI Panhellenic Conference on
SOLID STATE PHYSICS &
MATERIALS SCIENCE
Thessaloniki, 20-23 September 2015

Polymorphic Metal-Oxide based Sensors for the Diagnostic Breathalyzer

Pelagia-Irene (Perena) Gouma[1]

[1]State University of New York at Stony Brook

Functional metal oxides, such as titania and tungsten trioxide, are known to exist as several distinct phases-polymorphs, depending on the processing method used to synthesize them and their relative grain size. Each of these polymorphs typically has distinct properties, such as affinity to a specific chemical or a class of chemical compounds. Thus, a single binary oxide system provides a “toolbox” of phases to use to develop highly selective resistive gas sensors. This presentation reviews some of the nanoscale processes used by our research group to synthesize nanostructures of a variety of metal oxides, including □-MoO_3, h-MoO_3, □-WO_3, □-WO_3, spanning sol-gel processing, electrospinning, flame spray pyrolysis, and even electron lithography in the TEM. These nanostructures were used as sensing elements to detect signaling metabolites-i.e. gases/vapors released in a single human breath exhaled. It is discussed how the onset of nanotechnology and the ability to control the structure and morphology of metal oxides at the nanoscale has enabled us to develop highly reliable and inexpensive gas-sensing elements with high sensitivity, low detection threshold, high selectivity, and fast response and recovery to the chemical analyte/gas of interest. Handheld, portable, battery-operated, breathalyzer device prototypes have also been developed by our group, which aiming to detect from the onset of an asthma attack to the monitoring metabolic diseases and malfunctions, such as diabetes. Thus, materials and sensor nanotechnology impacts nanomedicine and advances personalized medicine through the availability of these diagnostic breathalyzer tools.

TU2

O29

Magnetic manipulation in a microfluidic system of hybrid composites made of MWCNTs functionalized with Fe_3O_4 nanoparticles for drug delivery applications

L. Agiotis[1], I. Theodorakos[1], S. Papazoglou[1], M. Makrygianni[1], A. Ntziouni[2], M. Patitsa[3], G. Vertsioti[4], D. Stamopoulos[4], K. Kordatos[2], A. Klinakis[3], Y.S. Raptis[1], I. Zergioti[1]

[1]National Technical University of Athens, Physics Department, Heroon Polytehneiou 9,
15780, Zografou, Greece
[2]National Technical University of Athens, Chemical Engineering Department,
Heroon Polytehneiou 9, 15780, Zografou, Greece
[3]Biomedical Research Foundation Academy of Athens, 4 Soranou Ephessiou St.,
115 27, Athens, Greece
[4]Institute of Advanced Materials, Physicochemical Processes, Nanotechnology and Microsystems,
NCSR Demokritos, Aghia Paraskevi, 15310, Athens, Greece

E-mail: zergioti@central.ntua.gr

In recent years, drug delivery, biomedical imaging and especially targeted delivery of anti-cancer drugs i.e. doxorubicin, cyclodextrin etc., have been under intense study, due to the high potential health impact that they present. In particular, carbon nanotubes (CNTs) have been widely studied for their potential applications in nanobiotechnology and biomedical applications such as drug delivery systems. In this context, iron oxide nanoparticles originating from magnetite (Fe_3O_4), were attached on the multi-walled carbon nanotube's (MWCNTs) outer core, aiming to form a magnetically controlled nano-platform. All the nanocomposite materials have been characterized both structurally (XRD, SQUID characterization) and morphologically (SEM), (Figure 3), so as to achieve a homogeneous distribution of iron oxide nanoparticles across the nanotube surface and minimize their aggregation in larger agglomerates, which could lead to the formation of thrombus, thus blocking the blood flow. In a later study, a magnetically-navigated drug delivery system will also be equipped with an anti- cancer drug and fluorescent molecules for the visualization of the nanocomposite movement in a microfluidic channel.

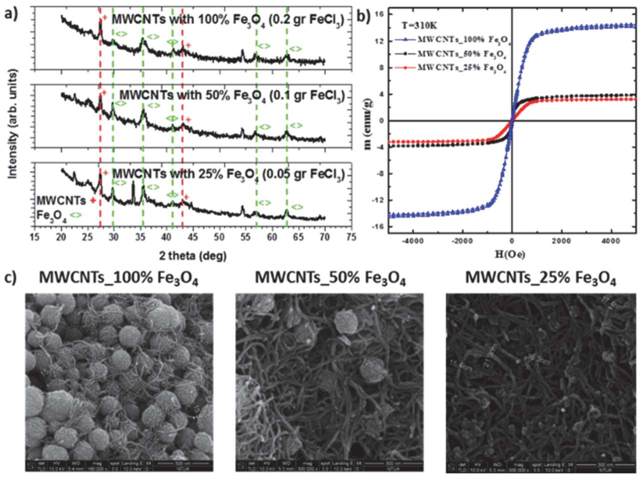

Figure 3: Characterization results of MWCNTs which have been functionalized with magnete (Fe_3O_4) nanoparticles through an 'autoclave' procedure. a) XRD, b) SQUID and c) SEM results for three different amounts of $FeCl_3$ solution inserted into the autoclave chamber and end up to three different concentrations and ratios of magnetite nanoparticles.

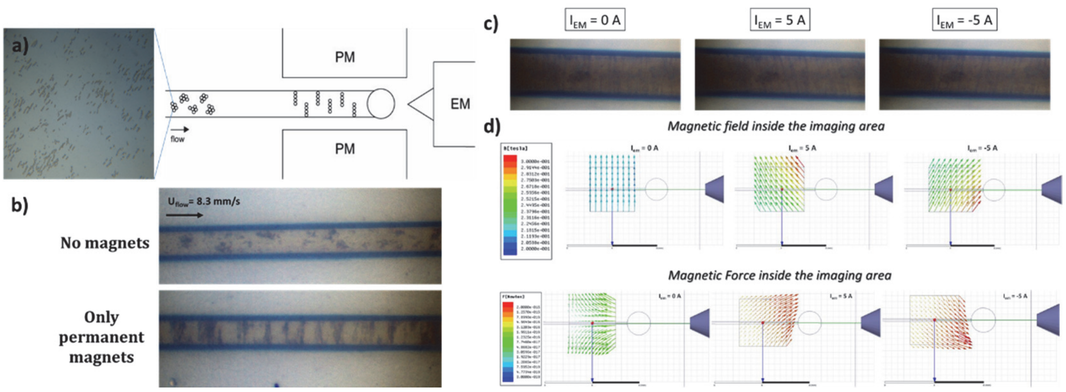

Figure 4: a) Schematic representation of the magnetic setup and the effect of the permanent magnets on the nanoparticles in the microchannel. b) Experimental verification of the effect of the permanent magnets. c) Static experiments (no fluid flow) for the study of the electromagnet's operation. d) Simulations of the magnetic fields and the magnetic forces applied on the magnetic nanoparticles inside a microfluidic chip. There is great convergence between simulations and experimental results.

The navigation capabilities of the iron oxide nanoparticles in a microfluidic channel were investigated by simulating the magnetic field and the magnetic force applied on the magnetic nanoparticles inside a microfluidic chip. The simulations have been performed using finite element method (ANSY'S software). The optimum setup (Figure 4) which intends to simulate the magnetic navigation of the nanoparticles, by the use of MRI-type fields, in the human circulatory system, consists of two parallel permanent magnets to produce a homogeneous magnetic field, in order to ensure the maximum magnetization of the magnetic nanoparticles, an electromagnet for the induction of the magnetic gradients and the creation of the magnetic force and a microfluidic setup so as to simulate the blood flow inside the human blood vessels.

The magnetization of the superparamagnetic nanoparticles and the consequent magnetic torque developed by the two permanent magnets, together with the mutual interactions between the magnetized nanoparticles lead to the creation of rhabdoid aggregates in the direction of the homogeneous field. Additionally, the magnetic gradients introduced by the operation of the electromagnet are capable for directing the aggregates, as a whole, in the desired direction (Figure 5). With the removal of the magnetic fields, the aggregates are disrupted, due to the super paramagnetic nature of the nanoparticles, avoiding thus the formation of undesired thrombosis.

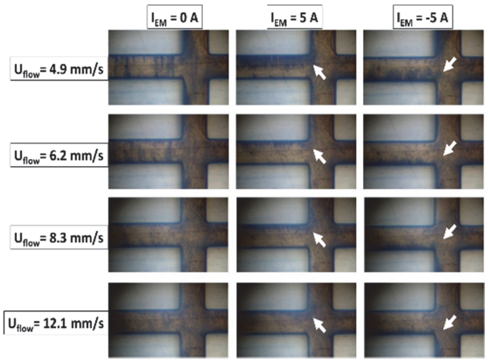

Figure 5: Snapshots from dynamic experiments for different fluid flows inside a cross shaped microfluidic channel for the study of the magnetic manipulation of the magnetite nanoparticles. Successful magnetic navigation of the nanoparticles in a microfluidic channel has been achieved, though the shape and size of the agglomerations is strongly influenced from the flow velocity.

Numerical simulations of drug release profiles

G. Kalosakas[1,2], **A. Hadjitheodorou**[3] **and D. Martini**[4]

[1]Materials Science Dept., University of Patras, Rio GR-26504, Greece
[2]CCQCN, Physics Dept., University of Crete, Heraklion GR-71003, Greece
[3]Bioengineering Dept., Stanford University, California, USA
[4]Pharmacy Dept., University of Patras, Rio GR-26504, Greece

E-mail: georgek@upatras.gr

We numerically calculate drug release profiles from simple [1] or composite [2] spherical devices, as well as from slabs [3], using Monte Carlo simulations [4], when diffusion is the dominant release mechanism [5]. The numerical results are compared with analytical solutions obtained from Fick's second law of diffusion [1-3].

Release curves are accurately described by the stretched exponential function (also known as Weibull function):

$$\frac{M_t}{M_\infty} = 1 - \exp\left[-(t/\tau)^b\right] \qquad (1)$$

where M_t is the amount of drug released at time t, M_∞ is the total amount of drug (released at very long time), and τ, b are parameters describing the analytical release profile given by Eq. (1) [1-4,6,7].

For example, in Figure 1 is shown the fractional release as a function of Monte Carlo time, from simple spheres of different radii R. Fitting of the computational release profiles with Eq. (1) provides the values of the stretched exponential parameters τ and b in each case [1-3]. It is found that release kinetics does not depend on the initial drug concentration.

The dependence of the two stretched exponential parameters, τ and b, on the device characteristics is investigated and simple analytical relations are provided.

Drug release form slabs with either flat, or irregular (non-planar), surfaces is considered. In the latter case the slabs are characterized by inhomogeneous thickness. The dependence of the release profiles on the degree of inhomogeneity and the corresponding variation of the stretched exponential parameters τ and b is presented [3].

We discuss in detail the numerical procedure followed in the Monte Carlo simulations. Particular emphasis is given in the techniques used to simulate regions of different drug diffusion coefficients when composite spheres are considered, as well as to construct slabs with irregular boundaries.

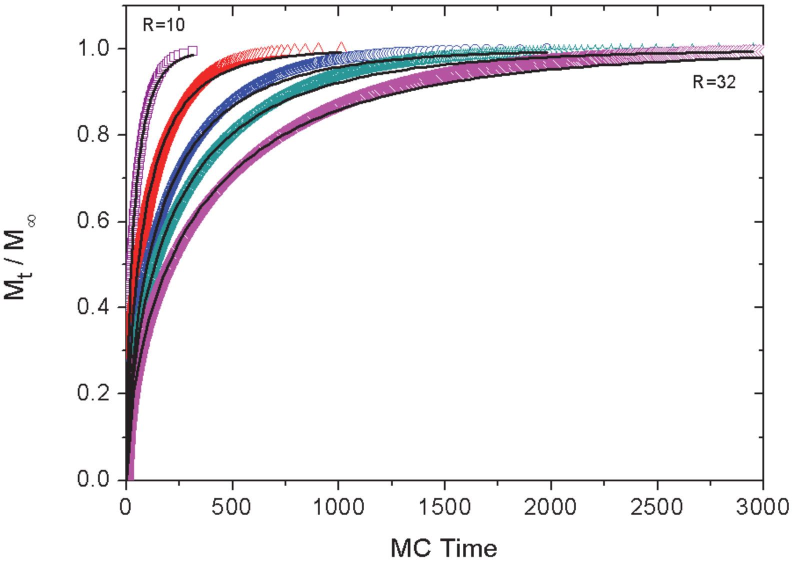

Figure 1: Release profiles, as obtained numerically by Monte Carlo simulations, for simple spheres of different radii R. Symbols represent the numerical results, while continuous lines show the corresponding fittings with Eq. (1). (From Ref. [1])

Acknowledgement: This work has been co-financed by the European Union (ESF) and Greek national funds (NSRF) through the THALES project MACOMSYS.

References

[1] A. Hadjitheodorou and G. Kalosakas, Mater. Sci. Eng. C 33 (2013) 763.
[2] A. Hadjitheodorou and G. Kalosakas, Mater. Sci. Eng. C 42 (2014) 681.
[3] G. Kalosakas and D. Martini, preprint (2015).
[4] K. Kosmidis, P. Argyrakis and P. Macheras, Pharm. Res. 20 (2003) 988.
[5] C.-C. Lin and A.T. Metters, Adv. Drug Deliv. Rev. 58 (2006) 1379.
[6] V. Papadopoulou, K. Kosmidis, M. Vlachou and P. Macheras, Int. J. Pharm. 309 (2006) 44.
[7] K. Kosmidis and P. Macheras, Int. J. Pharm. 343 (2007) 166.

THz oscillations in small B-DNA segments

K. Lambropoulos, K. Kaklamanis, G. Georgiadis, M. Theodorakou, M. Chatzieleftheriou, M. Tassi, A. Morphis, and C. Simserides

National and Kapodistrian University of Athens, Faculty of Physics, Department of Solid State Physics, Panepistimiopolis, GR-15784 Zografos, Athens, Greece

E-mail: csimseri@phys.uoa.gr

We call monomer a B-DNA base-pair and study charge transfer in small B-DNA segments e.g. monomers, dimers, trimers and other oligomers. We employ a tight binding (TB) approach (I) at the base-pair level using the on-site energies of the base-pairs and the hopping parameters between successive base-pairs and (II) at the single-base level using the on-site energies of the bases and the hopping parameters between bases. To this end, we solve a system of (I) N or (II) $2N$ coupled differential equations, to determine the spatial and temporal evolution of electrons or holes along a N base-pair DNA segment.

With approach (I) we predict carrier oscillations in dimers (0.25-100 THz) and in trimers (0.5-33 THz) i.e. in the mid- and far-infrared [1,2]. With approach (II) we predict carrier oscillations in monomers (50-550 THz), i.e. between the two bases constructing a base-pair. Approach (II) allows for higher detail, however, the results agree well with those of approach (I).

We also use a (III) Real-Time Time-Dependent Density Functional Theory (RT-TDDFT) approach for the adenine-thymine and the guanine-cytosine base-pair. Oscillations in smaller systems (p-nitroaniline, FTC chromophore, zinc porphyrin, green fluorescent protein chromophores and adenine-thymine base-pair) have been presented in the literature [3,4]. We compare the results of the RT-TDDFT approach (III) with the results of the TB approach (II).

Approaches (I) and (II) catch the key phenomena, while, we can easily treat dimers, trimers, and polymers. Approach (III) is time-demanding. Our results show that a non conventional source or receiver of THz and above THz electromagnetic radiation can be envisaged.

The TB methods can be applied to polymers, too [1, 5] allowing us to evaluate the extent at which a DNA segment can serve as an efficient medium for charge transfer.

References

[1] C. Simserides, Chem. Phys. 440 (2014) 31

[2] K. Lambropoulos, K. Kaklamanis, G. Georgiadis, and C. Simserides, Ann. Phys. (Berlin) 526 (2014) 249

[3] Y. Takimoto, F.D. Vila and J.J. Rehr, J. Chem. Phys. 127 (2007) 154114

[4] K. Lopata and N. Govind, J. Chem. Theory Comput. 7 (2011) 1344

[5] K. Lambropoulos, K. Kaklamanis, G. Georgiadis, M. Theodorakou, M. Chatzieleftheriou, M. Tassi, A. Morphis, and C. Simserides, in preparation.

Phase formation and stability in binary mixtures of cyanobiphenyl dimers

E. Ramou[1,2], Z. Ahmed[1], C. Welch[1], G. H. Mehl[1]
P. K. Karahaliou[2], A. G. Vanakaras[3] and D. J. Photinos[3]

[1]Department of Chemistry, University of Hull, HU6 7RX, UK
[2]Department of Physics, University of Patras, 26504 Patras, Greece
[3]Department of Materials Science, University of Patras, 26504 Patras, Greece

E-mail: eramou@upatras.gr

Liquid crystals (LCs) are a state of mater intermediate between that of a crystalline and an isotropic liquid. Such mesogenic materials exhibit a great variety of phases, which differ one from another by their structure and physical properties. The simplest mesophase is the uniaxial nematic in which the molecules exhibit a long range orientational order and no positional order. Single component LC systems which form more than one nematic phase are exceptional and bring new insights and challenges to our understanding of the “simplest of all LC phases”. A fascinating example is provided by certain types of symmetric cyanobiphenyl dimers with odd carbon-number alkyl spacers [1-6] exhibiting, in addition to the conventional uniaxial nematic phase, a low temperature nematic, termed as Nx. These, methylene linked dimesogens, show characteristic periodic stripe patterns and rope textures in thin films and an electro-optical response typically found in chiral systems, though the molecules are nonchiral.

Interestingly, a slight chemical modification of the flexible spacer that connects the mesogenic units of the dimer may suppress the nematic-nematic phase transition. For instance ether linked dimesogens form a single uniaxial nematic phase [7]. In this work we investigate the mesophase behaviour in binary mixtures of ether and methylene linked dimers [8,9]. The mixtures were characterized by their optical textures through polarizing optical microscopy, calorimetric studies and by X-ray investigations. We present temperature concentration phase diagrams which reveal the formation of a stable Nx phase for a surprisingly wide concentration range. A theoretical model is presented to shed light into the conformations adopted by the molecules of the two dimer constituents which differ only in the linking atom to the cyanobiphenyl mesogenic units.

References

[1] V. Borshch, Y.K. Kim, J. Xiang, M. Gao, A. Jakli, V.P. Panov, J.K. Vij, C.T. Imrie, M.G. Tamba, G.H. Mehl, O.D. Lavrentovich, Nat. Commun., 4 (2013) 26351-8

[2] D. Chen, J.H. Porada, J.B. Hooperc, A. Klittnick, Y. Shen, M.R. Tuchband, E. Korblova, D. Bedrov, D.M. Walba, M.A. Glaser, J.E. Maclennan, N.A. Clark, Proc. Natl. Acad. Sci., 110 (2013) 15931-6

[3] V.P. Panov, R. Balachandran, J.K. Vij, M.G. Tamba, A. Kohlmeier, G.H. Mehl, Appl. Phys. Lett., 101 (2012) 2341061-4

[4] L. Beguin, J.W. Emsley, M. Lelli, A. Lesage, G.R. Luckhurst, B.A. Timimi, H. Zimmermann, J. Phys. Chem. B, 116 (2012) 7940-7951

[5] A. Hoffmann, A.G. Vanakaras, A. Kohlmeier, G.H. Mehl, D.J. Photinos, Soft Matter, 11 (2015) 850-855

[6] E. Gorecka, M. Salamonczyk, A. Zep, D. Pociecha, C. Welch, Z. Ahmed, G.H. Mehl, Liq. Cryst., 42 (2015)1-7
[7] C. T. Imrie and P. A. Henderson, Chem. Soc. Rev., 36 (2007) 2096-2124
[8] C.S.P. Tripathi, P. Losada-Perez, J. Leys, A. Kohlmeier, M.G. Tamba, G.H. Mehl, C. Glorieux, Phys. Rev. E, 84 (2011) 0417071-7
[9] K. Adlem, M. Copic, G.R. Luckhurst, A. Mertelj, O. Parri, R.M. Richardson, B.D. Snow, B.A. Timimi, R.P. Tuffin, D. Wilkes, Phys Rev E, 88 (2013) 022503

SESSION TU3

INHOMOGENEOUS MATERIALS, COMPOSITE MATERIALS-1

Tuesday, 22 September 2015, 14^{30}-16^{30}

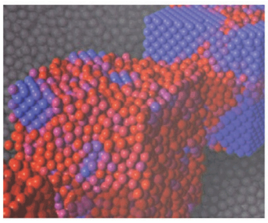

XXXI Panhellenic Conference on
SOLID STATE PHYSICS &
MATERIALS SCIENCE
Thessaloniki, 20-23 September 2015

Carbon based composite structures and advanced tools for mechanical behaviour assessment

C. Charitidis, E. Koumoulos, D. Dragatogiannis

Department of Materials Science and Engineering, School of Chemical Engineering
National Technical University
Iroon Polytechneiou 9, Zografou 157 80, Athens, Greece

E-mail: charitidis@chemeng.ntua.gr

Carbon based materials (such as carbon fibers (CFs) and carbon nanotubes (CNTs)) are under intense investigation, due to their unique properties and their future potential for enhancement of the mechanical properties of their composites. Their interaction with matrix through the interphase is not a simple concept, but a rather complex one, consisting of areas of imperfect bonding, mechanical stresses due to shrinkage, high stress gradients or even stress singularities due to the geometry of the inclusion, voids, microcracks etc. Despite the fact that the interactions between reinforcements and polymer at a molecular level is still not completely understood, it is clear that the interphase has a significant influence on the mechanical integrity of the composite as its distinct properties control the load transfer between matrix and fillers. Also, there is a major challenge in studying the local mechanical behaviour and mechanical properties in the small volume of interphase, since the conventional methods, e.g. tensile test and micro-hardness are not applicable. Instrumented indentation technique, widely known as depth-sensing indentation or nanoindentation, is a powerful and advanced tool to characterize the interphase region by local application of various loading protocols.

The effects of reinforcing fillers on the classical nanoindentation load-displacement curves of the composites and the deformation behaviour are investigated by the application of various loading protocols. Nanoscratching technique is applied so as to determine the frictional properties in the matrix, fiber and interphase regions and estimate the thickness of the interphase. Hardness and elastic modulus are evaluated, together with quantification of wear resistance, plastic deformation and the coefficient of friction of the composites. The surface topography of the indented and scratched regions is assessed using atomic force microscopy.

Molecular Simulation of Imidazolium-based Tricyanomethanide Ionic Liquids

N. Vergadou[1], **E. Androulaki**[1] **and I.G. Economou**[1,2]

[1]National Center for Scientific Research "Demokritos", Institute of Nanoscience and Nanotechnology, Molecular Thermodynamics and Modelling of Materials Laboratory, GR-153 10, Aghia Paraskevi Attikis, Greece
[2]Texas A&M University at Qatar, Chemical Engineering Program, Education City, PO Box 23874, Doha, Qatar

E-mail: n.vergadou@inn.demokritos.gr

Ionic liquids (ILs) are ionic compounds that are in the liquid state near room temperature and by convention below 100°C [1]. ILs exhibit a unique combination of properties such as extremely low vapor pressures, thermal stability, chemical tunability, good electrolytic and solvation properties, non-flammability and easy recycling. In combination with the aforementioned properties, several ILs exhibit also an unexpectedly large CO_2 absorption capacity and selectivity [2] and are, therefore, classified among the most attractive candidate sorbents for CO_2 capture and separation from post-combustion flue gases [3]. The chemical diversity in the molecular structure of the ions involved directly affects the physicochemical properties of the ILs, thus enabling the tuning of the properties of an IL by making moderate changes in ions' chemical formula and structure. Molecular simulation methods are proven to be extremely valuable in the direction of reliable property prediction and of revealing the underlying mechanisms that are responsible for the macroscopic behavior of ILs, aiming at the molecular design of materials with controlled properties.

The present work focuses on the molecular simulation of imidazolium-based [TCM^-] ionic liquids using an optimized classical atomistic force field. The force field in use has been validated against experimental data by performing molecular dynamics (MD) simulations of the [$C_n mim^+$][TCM^-], $n = 2, 4, 6, 8$ ionic liquid family at various temperatures and at atmospheric pressure. Very long molecular dynamics simulations of several tens of nanoseconds were performed in order to calculate the thermodynamic, structural and transport (self-diffusion coefficients and viscosities) properties of the pure ILs exploring, simultaneously, the intrinsic characteristics of the systems under study at the atomistic level [4-5].

The complex dynamic behaviour of the systems under study was thoroughly investigated and a wealth of microscopic information was extracted. The calculated radial distribution functions between the ions' centers of mass revealed that ILs retain organization at much longer distances compared to conventional liquids with the anion-cation interaction being stronger than the other two interactions (Figure 1a) at all temperatures. The effect of the alkyl tail length on these properties was also investigated and tail aggregation phenomena, which become more evident for the longer alkyl chain lengths, were detected (Figure 1b). The ions' translational motion was analyzed along specific axes in order to investigate anisotropy phenomena in the ions diffusion while the presence of heterogeneities in the dynamics was investigated by detecting deviations from the expected Gaussian behaviour.

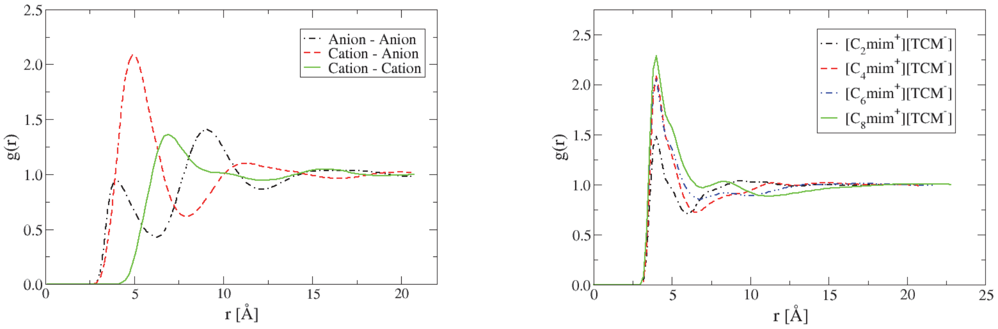

(a) (b)

Fig. 1: (a) Radial distribution function *g*(*r*) for the anion-anion (black), anion-cation (red) and cation-cation (green) center of mass of $[C_4mim^+][TCM^-]$ at 298.15 K and (b) Radial distribution function *g*(*r*) between the terminal carbon atoms in the cation's alkyl chain of $[C_2mim^+][TCM^-]$ (black), $[C_4mim^+][TCM^-]$ (red), $[C_6mim^+][TCM^-]$ (blue) and $[C_8mim^+][TCM^-]$ (green) at 298.15K.

Permeability and selectivity properties were estimated by calculating gas (CO_2, N_2, CH_4, Ar and O_2) diffusivity and solubility in $[C_nmim^+][TCM^-]$ ILs in a wide temperature range. Additional very long MD simulations were performed for the calculation of gas diffusion coefficients that were estimated one order of magnitude less than the ions' self-diffusivities gas solubilities were calculated in the Henry's law regime using the Widom test particle insertion method. All gases appear to have comparable diffusivities in each IL system studied and for that, the solubility is expected to control the selectivity properties of these ILs, a fact that is also supported by experimental results [6]. The agreement between available experimental data and molecular simulation is very good, rendering molecular simulation a reliable predictive tool.

References

[1] H. Weingärtner, Angewandte Chemie - International Edition 47 (2008) 654-670.

[2] P. Wasserscheid and T. Welton (eds), Ionic Liquids in Synthesis, Wiley-VCH: Weinheim, Germany (2003).

[3] S. Zhang, Y. Chen, F. Li, X. Lu, W. Dai, R. Mori, Catalysis Today,115 (2006) 61–69.

[4] E. Androulaki, N. Vergadou, J. Ramos and Economou I.G., Molecular Physics 110 (2012) 1139-1152.

[5] E. Androulaki, N. Vergadou and I.G. Economoux, Molecular Physics 112 (2014) 2694-2706.

[6] A. Finotello, J. E. Bara, D. Camper and R.D. Noble, Industrial & Engineering Chemistry Research 47 (2007) 3453-3459.

Molecular dynamics simulation of highly confined ionic liquids

G. Kritikos[1], **N. Vergadou**[1] **and I.G. Economou**[2]

[1] National Center for Scientific Research "Demokritos", Institute of Nanoscience and Nanotechnology, Molecular Thermodynamics and Modelling of Materials Laboratory, GR-153 10, Aghia Paraskevi Attikis, Greece

[2]Texas A&M University at Qatar, Chemical Engineering Program, Education City, PO Box 23874, Doha, Qatar

E-mail: g.kritikos@inn.demokritos.gr

Ionic Liquids (ILs) are salts that are in the liquid state at room temperature. In case they undergo glass transition, ILs exhibit dynamics of complex systems. As in many other glassy materials, high confinement may alters the diffusion mechanism, affecting glass transition temperature [1-3]. Upon confinement of ILs into pore channels (SILMs) with a size of ~1 nm, layers of different diffusivity and viscosity have been observed. For the alkyl-methyl-imidazolium tricyanomethanide ($[C_8mim^+][TCM^-]$), the experimentally measured diffusivity/permeability of CO_2 is enhanced [4]. Molecular simulation methods are proven to be an extremely valuable tool in the direction of unveiling the underlying microscopic mechanisms and predicting properties of such systems [5,6]. The present work focuses on the molecular dynamics simulation of imidazolium-based $[TCM^-]$ ionic liquids. Using an optimized and validated classical atomistic force field [7], the effect of confinement is studied in a comparative manner to the behavior of bulk ILs.

Long (over 100 ns) molecular dynamics simulations were performed in order to calculate structure and dynamic properties of the confined systems. In Fig. 1 the density profile of the $[C_8mim^+][TCM^-]$ is shown for two cases of confinement. The structure of the confined ILs reveals increased concentrations of cations (cation "tails") on the silica surface. The imidazolium ring plane close to silica has a tendency to become perpendicular to the surface. In the case of an inter-wall distance of 25 Å, the effect of the surface is present even in the middle layer and is reflected also in the shape anisotropy and the radius of gyration of the cation. Due to the wall potential we observe a suppression of the mobility in the z-axis and an enhancement of the diffusion in the xy-plane [3]. In all studied temperatures, the ions self-diffusion coefficient of the silica capped ILs was calculated slightly higher than the one of the bulk systems.

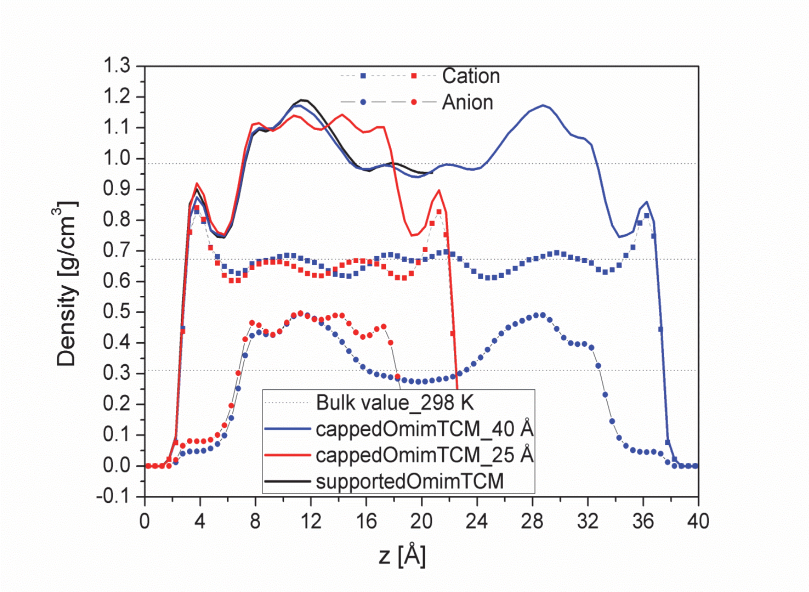

Fig. 1: Density profile of ILs confined between two silica surfaces (capped 25 and 40 Å) and one silica surface (supported) in equilibrium with the vacuum. Also we present the densities of each individual ion.

References

[1] M.E. Mackay, T.T. Dao, A. Tuteja, D.L. Ho, B. Van Horn, HC Kim, CJ Hawker, Nature Materials 2 (2003) 762-766.

[2] G. Kritikos, Polymer 55 (2014) 4658-4670.

[3] C. Pinilla, M.G. Del Pópolo, R.M. Lynden-Bell, J. Kohanoff, Physical Chemistry B 109 (2005) 17922-17927.[4] O. Tzialla, A. Labropoulos, A. Panou, M. Sanopoulou, E. Kouvelos, C. Athanasekou, K. Beltsios, V. Likodimos, P. Falaras, G. Romanos, Separation and Purification Technology 135 (2014) 22-34.

[5] E. Androulaki, N. Vergadou, J. Ramos, I.G. Economou, Mol. Phys. 110 (2012) 1139-1152.

[6] E. Androulaki, N. Vergadou, I.G. Economou, Mol. Phys. 112 (2014) 2694-2706.

[7] N. Vergadou, E. Androulaki, J.-R. Hill, I.G. Economou, submitted to PCCP.

TU3

O35

CoO octahedra with a Ferromagnetic Interface between two Antiferromagnets

Spasova M.[1], *Liébana-Viñas S.*[1,2], *N. Fontaíña-Troitiño*[2], *Zi-An Li*[1], *Salgueiriño V.*[2], *R. Pentcheva*[1], *Farle M.*[1]
[1] Fakultät fur Physik and CENIDE, Universität Duisburg-Essen, Duisburg, Germany
[2] Departamento de Física Aplicada, Universidade de Vigo, Vigo, Spain
marina.spasova@uni-due.de

Strain effects and chemical defects at artificial oxide interfaces like Perovskites have been shown to produce novel and unexpected physical properties ranging from superconductivity to ferro- or antiferromagnetic interactions [1] . Cobalt forms antiferromagnetic CoO and Co_3O_4 oxides with Neel temperatures of around 295 K and 40 K. Here, I will discuss novel types of geometrically near perfect octahedral Cobalt oxide nanoparticles which show a sizable ferromagnetic response above 295 K.

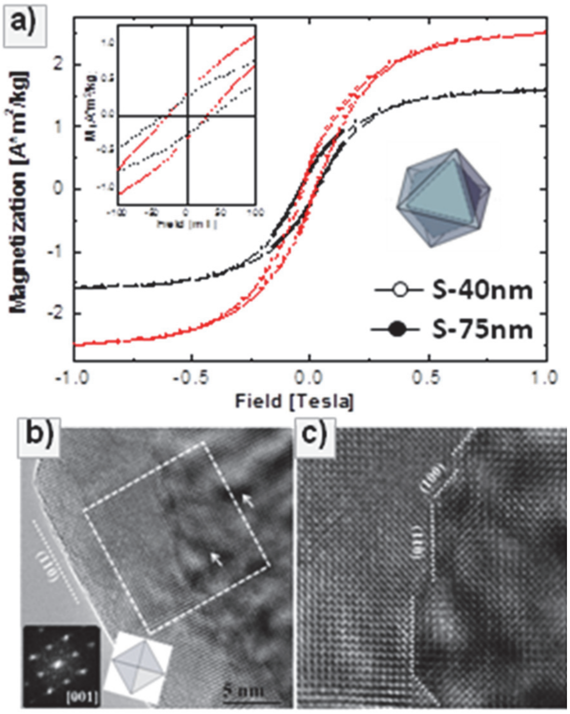

Fig. 1. a) Hysteresis loops of 40 and 75 nm samples recorded at 300 K. The insert shows the low-field parts of M(H). b) HRTEM image of the octahedron edge with c) an enlarged image of CoO/Co_3O_4 *interface.*

Octahedral nanoparticles with edge lengths of 40 and 75 nm were synthesized by thermal decomposition of cobalt acetate in trioctylamine. High Resolution Transmission Electron Microscopy (HRTEM) studies including 3D electron tomography show that the octahedron shaped nano-particles consist of a CoO core enclosed by eight {111} facets interfaced to a thin (~ 4 nm) surface layer of strained Co_3O_4 (Fig.1b, 1c). Nearly perfectly octahedral shaped particles with 40 and 75 nm edge length show a room-temperature ferromagnetic open hysteresis loop with a coercive field of 30 mT for both particle sizes (Fig.1a). Detailed X-ray Photoemission Spectroscopy and spatially resolved Electron Energy Loss Spectroscopy sudies allow to exclude the presence of metallic Co clusters as a possible reason for the observed ferromagnetic response. At low temperature the CoO/Co_3O_4 octahedral nanoparticles demonstrate the coexistence of antiferromagnetism below 290K (the Neel temperature of CoO) and ferromagnetism with a Curie temperature above 400K [3]. Below 50 K additional ferromagnetic contribution from AFM uncompensated spins is found [3]. Density functional theory calculations with an on-site Coulomb repulsion parameter identify the origin of the experimentally observed ferromagnetic phase as a charge transfer process (partial reduction) of Co^{3+} to Co^{2+} at the CoO/Co_3O_4 interface, with Co^{2+} being in the *low spin* state, unlike the high spin state of its counterpart in CoO. This finding may serve as a guideline for designing new functional nanomagnets based on oxidation resistant antiferromagnetic transition metal oxides [4].

[1] F. M. Granozio, G. Koster, and G. Rijnders, MRS Bulletin 38 (2013) 1017 ff
[3] S. Morup et al., J.Phys.:Condens. Matter **19** (2007) 213202 (Review Article). Et al..
[2] N. Fontaíña-Troitiño, S. Liébana-Viñas et al., *Nano Lett.*, **14** (2014) 640-647.
[4] Zi-An Li et al., Scientific Reports 5 (2015) 7997.

The impact of grain size/interface at Boron Carbide/epoxy composites: dielectric properties and molecular dynamics.

E.C. Senis[1] and G.C. Psarras[1,2]

[1]Interdepartmental Programme in Polymer Science and Technology, University of Patras, Patras 26504, Greece
[2]Department of Materials Science, University of Patras, Patras 26504, Greece

E-mail: ecsenis@upatras.gr

Recently composite systems consisting of epoxy resin and inorganic fillers have drawn the scientific interest because of their wide variety of applications and ease manufacturing. The incorporation of micro/nano-inclusions seems to have an impact at the properties of the composites, since the interactions between the matrix and the filler are changing with filler size [1,2]. Decreasing the particle's size the properties of surface/interfacial area dominate the properties of the overall material giving thus the opportunity to tailor its performance according to specific requirements [3].
The aim of this study was to investigate the influence of grain size on the properties of B_4C/epoxy composites. Two different filler types were used as inclusions and embedded in an epoxy resin. The first one has an average particle size of 30-60 nm, while the second one has mean particle diameter >10μm. Manufactured composites were characterized by means of BDS (Broadband Dielectric Spectroscopy), SEM (Scanning Electron Microscopy) and (Differential Scanning Calorimetry). BDS tests were conducted in a wide frequency (10^{-1}Hz – 10^{6}Hz) and temperature (30°C -160°C) range.
Experimental data reveal the impact of filler's size decrease on the properties of the composite systems as well as the influence of the employed volume fraction (Table 1).

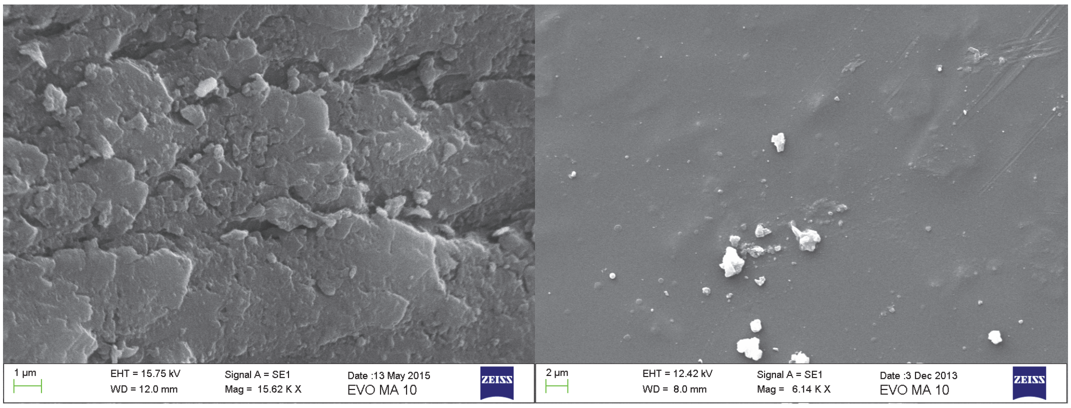

Figure 1: SEM images for the nanocomposite with 10 phr B_4C content (left) and for the microcomposite 10 phr B_4C content (right).

The type of interactions between the matrix and the filler exhibit size dependence and as a result the molecular dynamics and relaxation processes are affected. This is evident from the dielectric and thermal data.

Table 1: Volume fractions (%) and T_g temperatures for the manufactured composites with 5 and 10 phr nano- and micro-B_4C content.

Sample	Vol.% (nanocomp.)	Vol% (microcomp.)	T_g (ºC) (microcomp.)	T_g (ºC) (nanocomp)
5phr	3.39	1.45	56.8	57.3
10phr	6.94	3.94	55.7	57.6

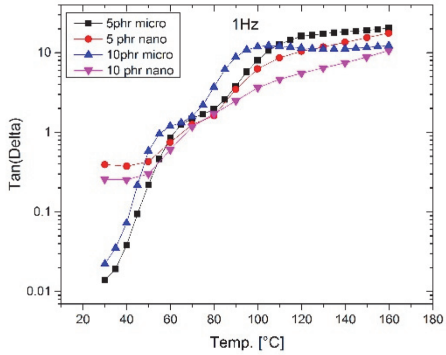

Figure 2: Loss tangent versus temperature for the specimens with 5 and 10 phr nano- and micro-B_4C content, at 1Hz.

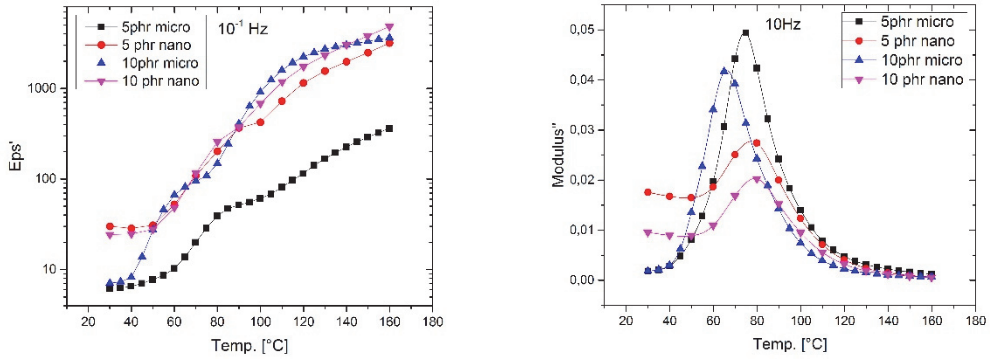

Figure 3: Real part of dielectric permittivity (ε΄) (left) and imaginary part of electric Modulus (right), versus temperature for the specimens with 5 and 10 phr nano- and micro-B_4C content at 0.1Hz and 10Hz.

Fittings according to the VFT (Vogel-Fulcher-Tammann) formalism were also conducted in order to investigate the dynamics of the α-relaxation mechanism and the influence of the filler's size on it.

References

[1] T. Hanemann and D.V. Szabo, Open Access Materials, 3, (2010), 3468-3517.

[2] P. Barber, S. Balasubramanian, et al., Open Access Materials, 2, (2009), 1697-1733.

[3] Schadler, L. S., Brinson, L. C., & Sawyer, W. G. (2007). Polymer nanocomposites: a small part of the story. *Jom*, *59*(3), 53-60.

[4] G. C. Psarras, Polymer nanocomposites: Physical properties and applications, ISBN: 978-1-84569-672-6, 31-69," 2010.

Structural properties of thermally treated chromium containing waste

S. Varitis, P. Kavouras, G. Kaimakamis, G. Vourlias, E. Pavlidou,
Ph. Komninou and Th. Karakostas

Department of Physics, Aristotle University of Thessaloniki, Thessaloniki 54124, Greece

E-mail: svaritis@physics.auth.gr

TU3

O37

We report on the structural properties of sintered and vitrified chromium containing end products produced from incinerated tannery sludge originated from the tannery industry in the area of Thessaloniki**.** The as-recovered sludge was incinerated at 500°C under anoxic conditions for 1,5h so as to retain the trivalent state of chromium and to remove as much of the organic content as possible [1]. Thermal treatment of the obtained ash was conducted following two different methods, sintering and vitrification, aiming to stabilize chromium into products that could be safely landfilled or used for the production of useful materials. All resulting products were characterized by X-Ray Diffraction (XRD), Electron Dispersive Spectrometry Differential Thermal Analysis (DTA), Scanning and Transmission Electron Microscopy (SEM and TEM) and microindentation. The structural properties of the materials produced by the two methods are compared.

For sintering the incinerated ash was mixed with recycled soda lime glass powder in different proportions, green state compacts were subsequently formed and thermally treated at four different temperatures at 600°C, 800°C, 1000°C and 1200°C **(Figure 1)**. The relative proportions of chromium ash over glass powder were 30/70, 40/60 and 50/50. The obtained opaque ceramic and glass ceramic products were composed of a variety of chromium and non-chromium containing crystal phases. The microhardness results indicated that they could be potentially used in building applications.

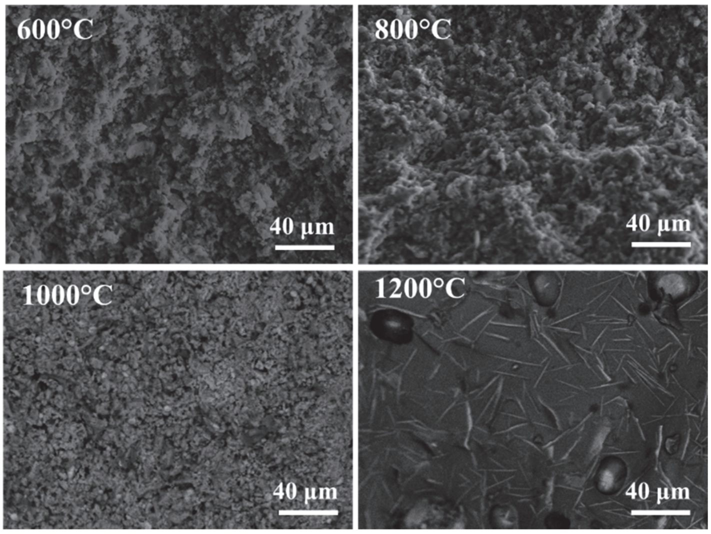

Figure 1: SEM images of the 40/60 products.

For vitrification the ash was mixed with glass forming oxides and melted together. The main glass-former used was SiO_2 while Na_2O and CaO were used as network modifiers. The glass-forming oxides were mixed with chromium ash in different proportions with decreasing Cr-ash content. The mixtures were melt at 1400°C and/or 1500°C for two hours and then casted on a refractory steel plate. The resulting as-vitrified products were amorphous with Cr_2O_3 crystals separated from the silicate matrix as it is depicted in **Figure 2**, except P4, that resulted to a totally X-Ray amorphous glass. At a second step the as-vitrified products were thermally treated at temperatures determined by the DTA analysis, in order to obtain the glass-ceramic products. The microhardness and the crack propagation of the as-vitrified and glass ceramic products were studied by microindentation.

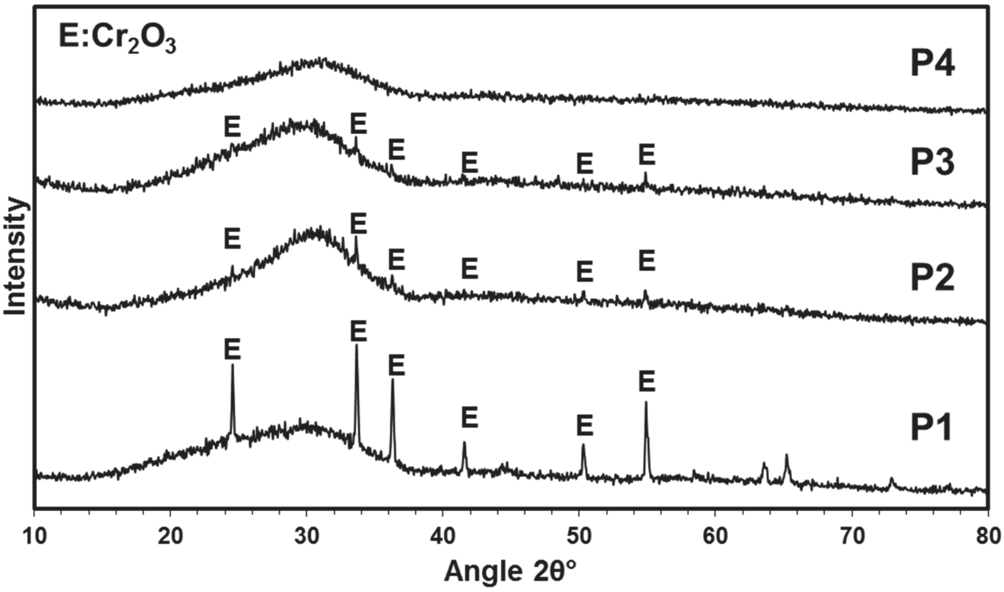

Figure 2: XRD graph of all the as-vitrified products

This research has been co-financed by the European Union (European Social Fund - ESF) and Greek national funds through the Operational Program "Education and Lifelong Learning" of the National Strategic Reference Framework (NSRF) - Research Funding Program: THALES: Reinforcement of the interdisciplinary and/or inter-institutional research and innovation.

References

[1] P. Kavouras et. al. J. Hazard. Mater. 283, (2015), 672-9.

Mesoscopic Simulations of the Viscoelastic Properties of Polymer Networks

Grigorios Megariotis, Georgios G. Vogiatzis and Doros N. Theodorou

School of Chemical Engineering, National Technical University of Athens, 9 Heroon Polytechniou,
Zografou Campus, Athens 15780, Greece

E-mail: gmegariotis@yahoo.gr

Multiscale modeling is a current trend in the field of molecular simulations, since the mixing of information from different levels of description provides a detailed picture for the system under consideration with reasonable computational cost. In the case of polymer systems, their long relaxation times constitute a severe restriction to molecular dynamics (MD) or Monte Carlo (MC) simulations at atomistic level. This may be alleviated by coarse-graining, which is the reduction in the number of degrees of freedom used to describe a given macromolecule. In this study we present a new methodology and the corresponding computational code in C++ for Brownian Dynamics simulations of rubbers and polymer melts. The polymer chains are modeled as sequences of beads, each bead encompassing a number of Kuhn (statistical) segments (e.g 5-10). In particular, a polymer network of cis-1,4-polyisoprene (PI) has been chosen as a model system. An initial configuration for the polymer melt is obtained by a field-theory inspired (MC) simulation of a coarse-grained model, wherein chains are represented as freely jointed sequences of Kuhn segments subject to a coarse-grained Helfand Hamiltonian which prevents the density from departing from its mean value anywhere in the system ([1],[2]). As far as the rubber configurations are concerned, they are created by random-crosslinking, i.e. a prescribed number of points (N_c) are selected at random in the simulation box and serve as the permanent links (crosslinks) of the polymer network. A visual representation of this coarse-graining procedure is provided in Figure 1. From a thermodynamic point of view, the system is fully described by a Helmholtz free energy containing three explicit terms: entropic springs, slip-springs and non-bonded interactions. The slip-springs are included to account for the entanglement effect. All beads execute Brownian motion in the high friction limit. The ends of slip-springs execute thermally activated hops between adjacent beads along chain backbones, which are tracked by a kinetic Monte Carlo simulation. In addition, creation/destruction processes are included for the slip-springs at chain ends, while their number remains constant during the simulations and the condition of microscopic reversibility is fulfilled. The free-energy density of non-bonded interactions is derived from the Sanchez-Lacombe equation of state and the isothermal compressibility of the polymer network is predicted correctly. The stress relaxation function ($G(t)$) plays a major role in the computation of rheological properties of polymer melts and networks. It is defined as the autocorrelation function of the non-diagonal elements of the stress tensor. Figure 2(a) depicts $G(t)$ for the entangled melt along with that of the unentagled melt (Rouse model) for comparison purposes. In the case of a crosslinked polymer network, the stress relaxation function is expected not to decay to zero, as is the case for a polymer melt. This is correctly predicted, as seen in figure 2(b). Moreover, this methodology was applied in the case of elongational deformations of polymer rubbers. Such deformations may be applied either under constant volume (Poisson ratio equal to 0.5) or under variable volume. This computational code was employed for the calculation of rheological properties from simulations of several microseconds at equilibrium or for the computation of stress-strain curves of crosslinked polymer networks under deformation.

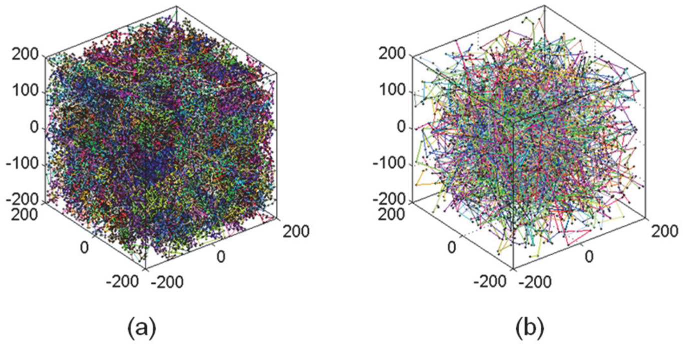

Figure 1: Graphical representations of a PI system. (a) macromolecules represented as freely jointed chains of Kuhn segments, (b) network represented in terms of beads (internal beads, end-beads and crosslinks). Lengths along the axes are in Å.

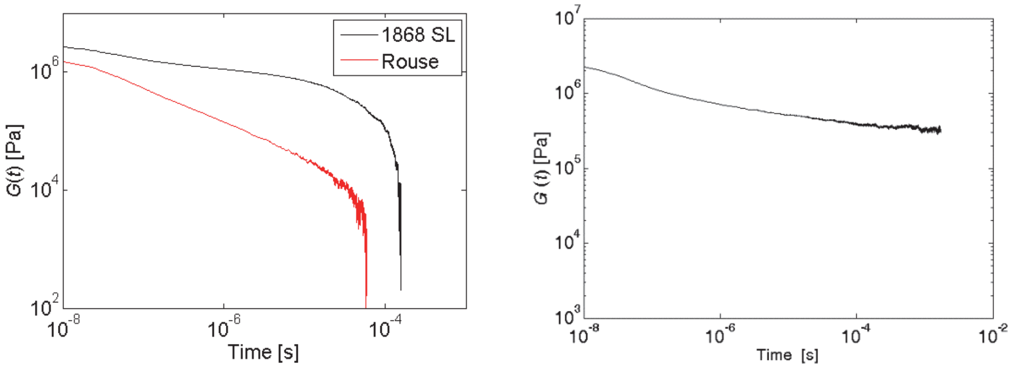

Figure 2: (a) Stress relaxation functions of a PI polymer melt (a) and a PI rubber (b).

Acknowledgments: This work was funded by Volkswagen Foundation and Limmat Foundation. Georgios G. Vogiatzis wants to thank the Alexander S. Onassis Public Benefit Foundation for a doctoral scholarship.

References

[1] G. G. Vogiatzis, E. Vogiatzis and D. N. Theodorou, Eur. Polym. J. 47 (2011) 699-712.
[2] G. G. Vogiatzis and D. N. Theodorou, Macromolecules 46 (2013) 4670-4683.

SESSION TU4

PHOTONICS & OPTOELECTRONICS-2

Tuesday, 22 September 2015, 17^{00}-18^{30}

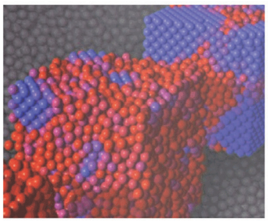

XXXI Panhellenic Conference on
SOLID STATE PHYSICS &
MATERIALS SCIENCE
Thessaloniki, 20-23 September 2015

Photonic materials and devices for sensors and solar cells

M. Sigalas[1]

[1]Department of Materials Science, University of Patras

E-mail: sigalas@upatras.gr

Results will be presented from a computational study of photonic materials and devices used for sensing in the micro- and nano-scale. Devices will include photonic crystal cavities and disk resonators. Similar type sensors will be also presented but with elastic waves as probing mechanism.

Also, results will be presented from computational studies of solar cells (both silicon and organic) with nanostructures or nanoparticles in their surface or in their interior. The purpose of those studies is to increase the absorption of light and consequently the efficiency of the solar cells.

TU4

O39

Enhancement of conversion efficiency of solar cells by down-conversion

S. Gardelis[1,2] **and A.G. Nassiopoulou**[1]

[1]NCSR Demokritos INN, Terma Patriarchou Grigoriou, Aghia Paraskevi, 15310 Athens, Greece
[2]Solid State Physics Section, Physics Department, National and Kapodistrian University of Athens, Panepistimioupolis, Zografos, 15784 Athens, Greece

E-mail: sgardelis@phys.uoa.gr

There has been an effort to increase the conversion efficiency of silicon- based solar cells beyond the Schockey-Queisser limit via various methods. The main idea of all these methods is to use more efficiently the photons of the solar spectrum with energies much higher than the energy band gap of the absorber which otherwise would be lost through thermal relaxation of the related carriers before their collection by the electrodes. One of these methods is to fabricate cells with different energy band gap materials in a tandem configuration. Another way to increase conversion efficiency is by down-conversion. Down-conversion is the conversion of photons with energies much higher than the energy band gap of the absorber to photons of energy near the energy band gap of the absorber. These photons can be converted more efficiently as thermal relaxation is reduced. As down-conversion material luminescent quantum dots with emission in suitable energies can be used. In this study we examine down-conversion provided by luminescent Cd-free $CuInS_2/ZnS$ quantum dots deposited on the active area of a silicon-based solar cell. $CuInS_2/ZnS$ quantum dots emit at 1.8 eV and show a broad photoluminescence (PL) spectrum (Figure 1a). Thus we would expect efficient conversion of the higher energy photons to lower ones that could be absorbed and converted into electricity more efficiently from the silicon absorber underneath. In this study, we report on the increase of up to 37.5% in conversion efficiency of a silicon-based solar cell after the deposition of the dots. We show that this effect is a combined effect of down-conversion and anti-reflection provided by the dots. We clearly distinguish the two effects and estimate that the enhancement due to the down-conversion is about 10.5% [1].

For this study we used a p-n silicon based solar cell which we fabricated by depositing nanocrystalline silicon on n-type crystalline silicon by Low Pressure Chemical Vapor Deposition (LPCVD). By aluminum-induced recrystallization and simultaneous p-type doping we fabricated a good quality p-n junction solar cell, which was used in this work [2]. The conversion efficiency of this cell was measured to be 8%. We used two different concentrations of the dots and examined their effect in down-conversion. Figure 1b shows the schematic of the cell with the different concentrations of the quantum dots on its active area. We observed that the effect of down-conversion increased considerably as the intensity of the PL signal from the quantum dot film deposited on the cell increased as a result of the increasing concentration of the quantum dots in the film. The conversion efficiency of the cell was increased from 8% to 11% as the concentration of the dots increased. To estimate the contribution of the antireflection property of the dots and the clear down-conversion effect we estimated the Internal Quantum Efficiency (IQE) of the cell before and after the deposition of the dots. The down-conversion effect was observed as an enhancement of IQE in the high energy spectral region where the dots absorbed the high energy photons and converted them into red light (Figure 1c).

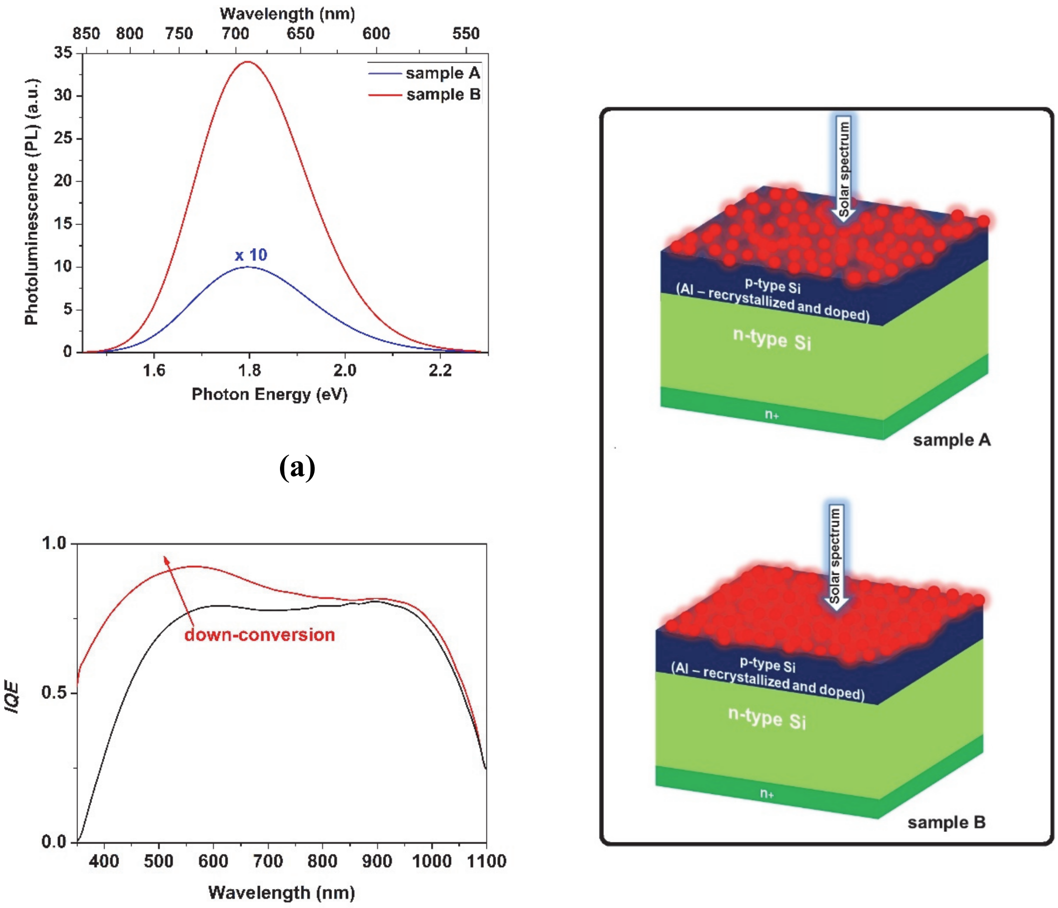

(a)

(b)

(c)

Figure 1: (a) PL spectrum of the low density (sample A) and high density (sample B) $CuInS_2/ZnS$ quantum dot films. **(b)** Schematic of the solar cell with the quantum dots. **(c)** IQE showing the down-conversion effect.

References

[1] S. Gardelis and A.G. Nassiopoulou, Appl. Phys. Lett. 104 (2014) 183902

[2] S. Gardelis, A.G. Nassiopoulou, P. Manousiadis, N. Vouroutzis, and N. Frangis, Appl. Phys. Lett. 103 (2013) 241114

Enhanced Light Emission in Extraordinary Optical Transmission Structures

Ch. .Mavidis[1,2], **M. Kafesaki**[1,2] , **E. Economou**[1,3] **and C. Soukoulis**[1,4]

[1]*Institute of Electronic Structure and Laser, FORTH, 71110 Heraklion, Crete, Greece*
[2] *Department of Materials Science and Technology, University of Crete, 71003 Heraklion, Crete, Greece*
[3] *Department of Physics, University of Crete, 71003 Heraklion, Crete, Greece*
[4] *Ames Laboratory and Department of Physics and Astronomy, Iowa State University, Ames, Iowa 50011, USA*

E-mail: mavidis@iesl.forth.gr

Photonic structures comprised of metallic materials, e.g. plasmonic structures, offer highly modified local density of electromagnetic states (compared to bulk materials) and thus they give the possibility to achieve high spontaneous emission rates [1] for emitters located in their neighborhood, a possibility which is extremely desirable in a variety of applications, especially in sensing and lightning.

In this work we examine the modified emission rate in metallic films perforated with a square array of subwavelength holes. In such systems the phenomenon of Extraordinary Optical Transmission (EOT) has been observed [2], which is attributed to Surface Plasmon Polaritons (SPPs) excited on the metal-air interfaces. We calculate numerically, by employing the Finite Difference Time Domain (FDTD) Method, the emission rate as a function of frequency for different emitter orientations and locations in a EOT system, as well as for systems of different hole sizes.

Very high emission rates, up to 200 compared to free space, for emitters placed near the holes have been found at the frequency where EOT occurs. The dependence of such emission rates on the system parameters is discussed and explained. The very high emission rates observed in our systems make those systems promising in the design of efficient light sources, sensing devices and surface enhanced Raman scattering systems.

References

[1] W. L. Barnes, J. Mod. Opt. 45 (1998) 661–699.
[2] T. Ebbesen, H. Lezec, H. Ghaemi, T. Thio, and P. Wolff, Nature 391 (1998) 667.

Energy level alignment of PCBM interfaces with low work function substrates

G. Skoulatakis[1], H. Zhang[2, 3], C. Brabec[2, 4], S. Kennou[1]

[1]Department of Chemical Engineering, University of Patras, 26504 Rion, Greece
[2]Institute of Materials for Electronics and Energy Technology (i-MEET), Friedrich-AlexanderUniversity Erlangen-Nuremberg, 91058 Germany
[3]Erlangen Graduate School in Advanced Optical Technologies (SAOT), 91052 Erlangen, Germany
[4]Bavarian Center for Applied Energy Research (ZAE Bayern), 91058 Erlangen, Germany

E-mail: skoulatakis@chemeng.upatras.gr

Organic photovoltaic (OPV) devices have attracted a lot of attention due to their interesting properties (mechanical flexibility, light weight and potentially low production cost). A lot of parameters can affect the conversion efficiency of these devices like structure arrangement, material processing etc. A number of interfaces are involved in such a device and the energy level alignment at organic/inorganic or organic/organic interfaces is important, because of their crucial role in charge separation and collection.

The aim of this work is the investigation of the chemical and the electronic structure of two series of interfaces. One with a spin coated DPP:PCBM film interfaced with aluminum doped zinc oxide (AZO) on ITO and a barium hydroxide ($Ba(OH)_2$) layer on top of AZO/ITO, and another one evaporated PCBM film on $Ba(OH)_2$/AZO/ITO in order to compare with the interface formed by a spin-coated PCBM film with the same substrate.

Figure 1 presents a comparison between the UP spectra of a spin coated and an evaporated PCBM film on $Ba(OH)_2$/AZO/ITO. Both interfaces exhibited similar electronic structures, the HOMO appears at 2.2±0.1 eV with the $HOMO_{Onset}$ at 1.5±0.1 eV and the work function of PCBM is equal to 4.5±0.1 eV which gives an Ionization Potential [$IP=(\Phi+HOMO_{Onset})$] of 6.0±0.1 eV.

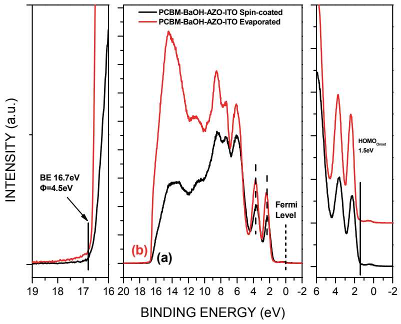

Figure 1 C1s XPS spectra of PCBM film on $Ba(OH)_2$/AZO/ITO.

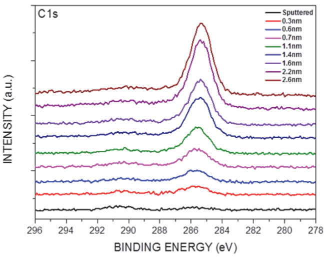

Figure 2 C1s XPS spectra of PCBM film on $Ba(OH)_2$/AZO/ITO.

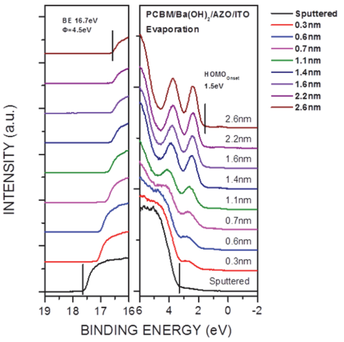

Figure 3 UPS spectra of evaporated PCBM film on $Ba(OH)_2$ /AZO/ITO.

In figure 2 the evolution of the C1s XPS peak during deposition of PCBM on cleaned $Ba(OH)_2$/AZO/ITO is presented. The intensity of C1s peak increases as the film of the PCBM is getting thicker. The peak appears at 285.2±0.1 eV binding energy and stays unchangeable which means no band bending is formed at the interface.

Figure 3 shows the evolution of the valence band during evaporation of PCBM on $Ba(OH)_2$/AZO/ITO. The HOMO level appears for PCBM thickness of 0.3 nm and remains stable. The high binding energy cutoff is shifted by 1.0±0.1 eV towards lower binding energy due to the deposition of the PCBM.

The Fermi level is pinned at 4.5±0.1 eV and an interfacial dipole of 1.0±0.1 eV is formed.

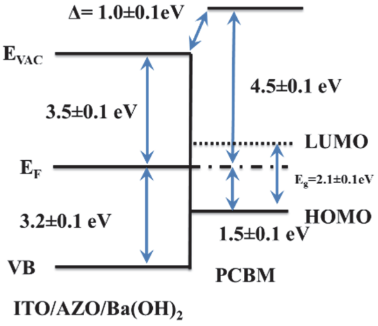

Figure 4 Energy diagram for PCBM/$Ba(OH)_2$/AZO/ITO.

In figure 5 the DPP:PCBM on AZO/ITO and DPP:PCBM on $Ba(OH)_2$/AZO/ITO UPS spectra are shown. The VBM of $Ba(OH)_2$ were determined at 3.2±0.1 eV and the work function is equal to 3.5±0.1 eV , while the VBM of AZO is at 3.2±0.1 eV and the work function is 4.0±0.1 eV. For DPP:PCBM on the two substrates the work function was estimated equal to 4.4eV, the $HOMO_{Onset}$ was determined at 0.4eVwhich gives an IP of 4.8±0.1 eV. As it is seen the valence band characteristics are similar in both substrates.

Considering all the experimental results we can draw schematically the energy diagram of the different interfaces (figure 6).

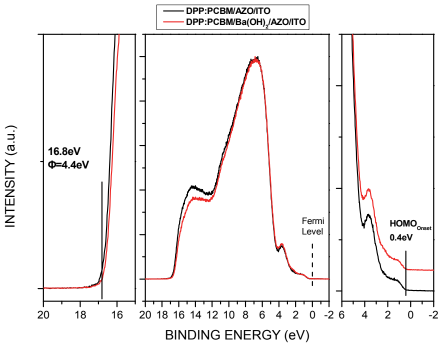

Figure 5 UPS spectra for (a) DPP:PCBM/AZO and (b) DPP:PCBM/BaOH

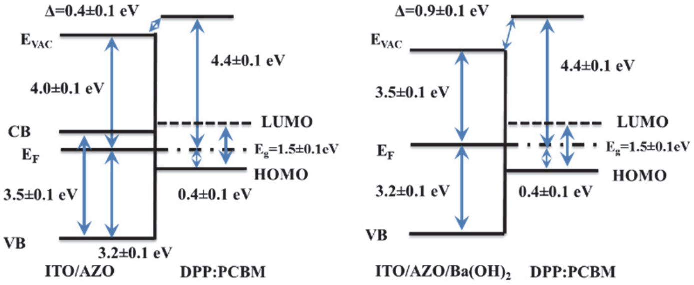

Figure 6 *Energy diagram for the interfaces.*

In both interfaces the Fermi level is pinned at 4.4±0.1 eV. The formed interfacial dipole of DPP:PCBM on AZO/ITO is equal to Δ=0.4±0.1 eV while the interfacial dipole for DPP:PCBM/$Ba(OH)_2$/AZO/ITO is double (Δ=0.9±0.1 eV) and equal to dipole of PCBM/$Ba(OH)_2$/AZO/ITO.

In all studied interfaces the results are in agreement with the Integer Charge Transfer (ICT) model which predicts that the Fermi level should be pinned to ECT^- when $\Phi_{Sub} < ECT^-$ [2] and the interface dipole is equal to $\Delta = ECT^- - \Phi_{Sub}$.

References

[1] Ning Li , Derya Baran , George D. Spyropoulos et al., *Adv. Energy Mater., 1400084*, Journal volume, 1-7 (**2014**).

[2] Z. Xu, L.-M. Chen, M. -H. Chen, G. Li and Y. Yang *Appl. Phys. Letters,* 95, 013301 (2009)

Frequency splitter based on the manipulation of surface modes in dielectric photonic crystals structures

A. C. Tasolamprou[1], L. Zhang[2], M. Kafesaki[1,3], T. Koschny[2] and C. M. Soukoulis[1,2]

[1] Institute of Electronic Structure and Laser, FORTH, 71110, Heraklion, Crete, Greece
[2] Ames Laboratory and Department of Physics and Astronomy, Iowa State University, Ames, Iowa 50011, USA
[3] Department of Materials Science and Technology, University of Crete, 71003, Heraklion, Crete, Greece

E-mail: atasolam@iesl.forth.gr

Contrary to the limitation imposed by the diffraction limit, highly directional emission has been found to occur in metallic and photonic crystal subwavelength apertures when the structure surrounding them features surface corrugations [1 2]. Like plasmonic waves that propagate bound to metallic/dielectric interfaces, properly designed photonic crystal configurations have been found to support the propagation of highly confined surface waves. The surface corrugations that surround these structures enable the coupling of the surface energy into outgoing radiation modes which allows the realization of minimized electromagnetic components and devices.
Here we present the design and the experimental validation of a dielectric photonic crystal structure that provides tunable directional emission and frequency splitting operation [3]. The device emission is controlled by the manipulation of the surface propagating waves. The schematic of the structure is presented in Figure 1(a). It consists of a bulk photonic crystal structure made of square alumina rods, a surface layer made of circular alumina rods and a grating layer made of square alumina rods same as in the bulk area. The line defect waveguide, formed in the bulk photonic crystal, feeds energy in the surface and grating layers. The key feature of the surface layer is the different shape and size dielectric rods that enable the propagation of surface waves and it is properly designed so as to support the highly confined surface modes within the bandgap of the bulk photonic crystal. As the surface waves propagate, they interact with the grating layer providing controllable emission. In particular the grating layers acts as an array of periodically aligned scatterers. The collective contribution of the scattered field in each grating rod, leads to the formation of a beam whose directionality depends on the frequency of operation and the periodicity of the grating layer. Subsequently, proper design of the grating layer can provide control over the emission angle. As presented in the schematic of our design, shown in Figure 1(a), we have selected a grating layer of asymmetric periodicity b_1 and b_2. Had the periodicity b_1 and b_2 been the same, the interference of the outgoing contributions would lead to the formation of on-axis emission. In our case, when the periodicities b_1 and b_2 are different, depending on the frequency, the interference of the outgoing waves leads to the formation of off-axis emission and enables the frequency spitting operation.

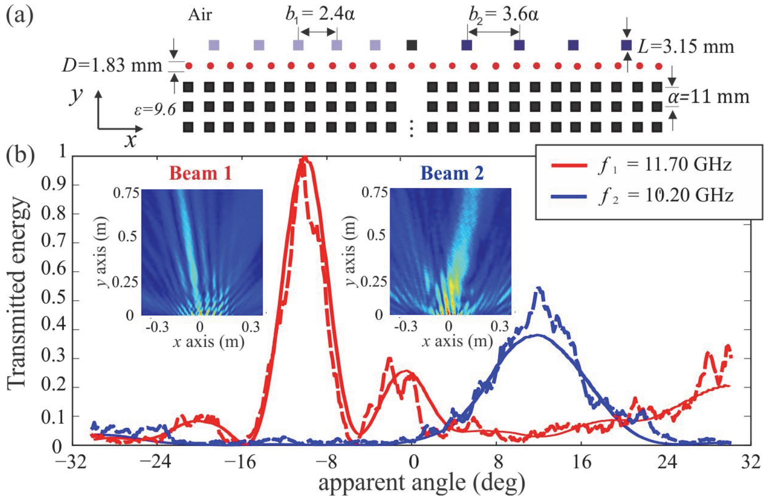

Fig. 1: Schematic of the bulk PC termination made of square and circular dielectric alumina rods in air. It consists of the PC waveguide and the output surface and grating bilayer. The grating layer is characterized by the asymmetric side periodicity b_1 and b_2. (b) Apparent angular distribution of beam 1 and 2 at propagation radius equal to 0.7 m. The emerging left going emission, beam 1 propagates along φ_1 = -11° apparent angular axis and the emerging right going emission, beam 2, along φ_2 =+13 ° apparent angular axis. Insets show the experimental 2D plot of the strength of the outgoing intermediate near field at frequency f_1 = 11.68 GHz and f_2 =10.20 GHz. Axis x is parallel to the grating layer and axis y perpendicular to the grating layer.

The evaluation of the structure as a frequency splitter and the experimental validation is presented in Figure 1(b). The device generates two Gaussian shaped beam, 1 and 2, at frequencies f_1 = 11.7 GHz and f_2 =10.2 GHz and angular directions φ_1 = -11° and φ_2 =+13°. The beams are characterized by Half Power Beamwidth $HPBW_1$ = 7° and $HPBW_2$ = 10°. The full 3dB bandwidth for the two beams is BW_1 = 200 MHz and BW_2 = 500 MHz correspondingly. The angular separation between the two beams is sufficiently larger than both the half $HPBW$ and their spectral separation is sufficiently larger than both the half BW. Cross-talk remains low for both high and low frequency beams in the corresponding beamwidth, that is XT_1< -23 dB in $HPBW_1$ and XT_2 < - 11 dB within $HPBW_2$. The return losses are low for both the frequencies, that is RL_1 = -7.8 dB and RL_2 = -10.5 dB. As a whole, the high spatial and spectral separation, the low cross-talk and the low return losses indicate that the emerging beams are well separated and that the structure may be used in frequency splitting applications. Moreover is has been found that the device can perform both in the intermediate near field region for short range application such as inter component coupling and in the far filed region for open space applications.

References

[1] P. Kramper, M. Agio, C.M. Soukoulis, A. Birner, F. Mueller, R. B. Wehrspohn, U. Goesele, and V. Sandoghdar, "Highly directional emission from photonic crystal waveguides of subwavelength width," Physical Review Letters 92 (2004) 113903.

[2] I. Bulu, H. Caglayan, and E. Ozbay, "Beaming of light and enhanced transmission via surface modes of photonic crystals," Optics Letters 30 (2005) 3078-3080.

[3] A. Tasolamprou, L. Zhang, M. Kafesaki, T. Koschny, and C. M. Soukoulis, "Frequency splitter based on the directional emission from surface modes in dielectric photonic crystal structures", Optics Express 23 (2015) 13972-13982.

POSTER SESSION II

Tuesday, 22 September 2015, 18^{30}-20^{00}

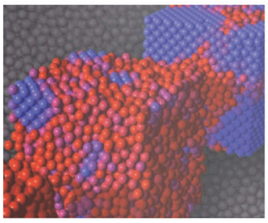

XXXI Panhellenic Conference on
SOLID STATE PHYSICS &
MATERIALS SCIENCE
Thessaloniki, 20-23 September 2015

TUP

P061

Development and Characterization of Epoxy Resin- Zinc Ferrite Nanocomposites

S.G. Stavropoulos[*], A. Sanida, E.C. Senis, O. Vryonis, G.C. Psarras

Department of Materials Science, University of Patras, Patras 26504, Greece

*e-mail: Stavropoulos@upatras.gr

Composite nanodielectrics belong to a new type of engineering materials suitable for improved performance as dielectrics and electrical insulators. The term nanodielectrics refers to dielectric materials which comprise entities at the nanoscale level. Polymer matrix—ceramic particles nanodielectrics especially those who demonstrate ferroelectric and ferromagnetic behaviour are considered as novel engineering materials due to their electrical and electronic properties with many potential applications as capacitors, electromagnetic shielding, switches and energy storage devices [1-3].

In the present study a set of specimens of epoxy resin and ceramic zinc ferrite ($ZnFe_2O_4$) nanoparticles with mean diameter less than 100 nanometers, has been developed varying the filler concentration. Ferrites are one of the most important classes of magnetic ceramic materials and are used extensively in electronic devices for the communications industry [4]. Zinc ferrite ($ZnFe_2O_4$) is of particular interest among ferrite spinels because of its transition from paramagnetic (bulk) to antiferromagnetic (nanopowder) state A possible ferroelectric to paraelectric phase transition in the same material has also been reported [5,6].

The dielectric response of the prepared samples was studied by means of Broadband Dielectric Spectroscopy (BDS) in the frequency range 10^{-1}-10^{7} Hz and temperature interval from 30°C to 150°C. BDS has been proved to be a powerful tool for the investigation of molecular mobility, phase changes, conductivity mechanisms and interfacial effects in nanocomposite systems [3].

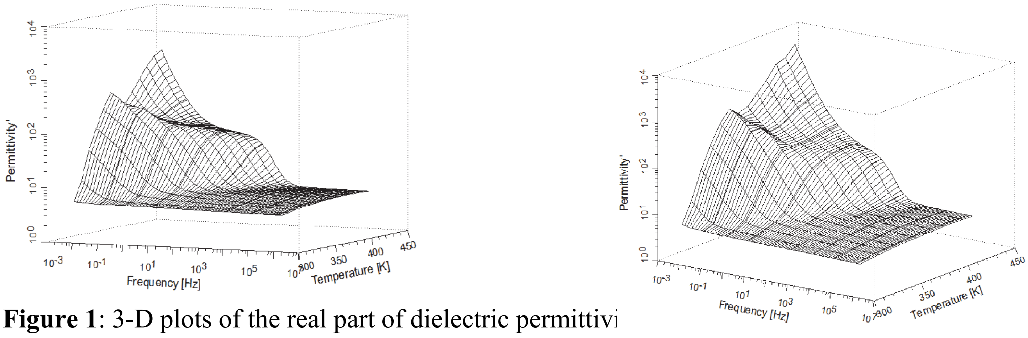

Figure 1: 3-D plots of the real part of dielectric permittivi 10 phr (right) zinc ferrite content as a function of frequency and temperature.

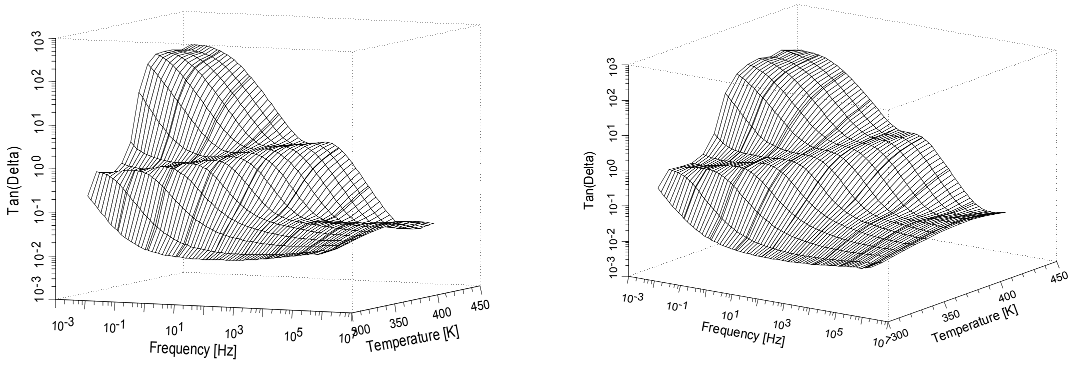

Figure 2: 3-D plots of loss tangent of the samples with 3 phr (left) and 10 phr (right) zinc ferrite content as a function of frequency and temperature.

Experimental results imply dielectric relaxations attributed to the polymer matrix and the interactions between host and reinforcing phase. Three distinct relaxation modes were recorded in the spectra. They were attributed to interfacial polarization (IP)-MWS-effect, glass to rubber transition (α-relaxation) and motion of small polar side groups (β-relaxation).

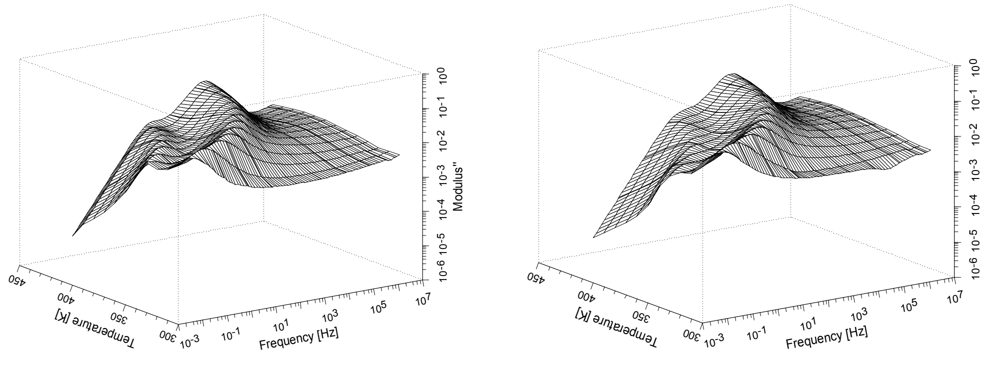

Figure 3: 3-D plots of the imaginary part of the electric modulus of the samples with 7 phr (left) and 15 phr (right) zinc ferrite content, as a function of frequency and temperature.

References:

[1] P. Barber, S. Balasubramanian, et al., Open Access Materials 2 (2009) 1697-1733.

[2] Frechette, Michel F., et al., International Conference on Solid Dielectrics, (2010) 1-29.

[3] G. C. Psarras, "Conductivity and dielectric characterization of polymer nanocomposites" in "Physical Properties and Applications of Polymer Nanocomposites", Ed. S,C Tjong and Y.W Mai, Woodhead Publishing in Materials (2010) 31-69.

[4] U. Hafeli, W. Schutt, J. Teller, M. Zborowski (Eds.), Scientific and Clinical Applications of Magnetic Carriers, Plenum Press, New York, (1997).

[5] K. Tanaka, M. Makita, Y. Shimizugawa, K. Hirao, N. Soga, J. Phys. Chem. Solids 59 (1998) 1611–1618.

[6] A. Mekap , P. R. Das , R. N. P. Choudhary, J Mater Sci: Mater Electron 24 (2013) 4757–4763.

Thermal and Dielectric Properties of Graphene/poly Cyclic Butylene Terephtalate (pCBT) Nanocomposites

S.G. Stavropoulos[1]*, J. Karger-Koscis[2], G.C. Psarras[1]

[1]Department of Materials Science, University of Patras, Patras 26504, Greece,
[2]Department of Polymer Engineering, Faculty of Mechanical Engineering, Budapest University of Technology and Economics, Budapest, Hungary

*e-mail: Stavropoulos@upatras.gr

TUP

P062

Carbon nanostructured/polymer nanocomposites are in the focus of scientific research for many years, because of their perspectives in the fields of mechanics, nanoelectronics and energy storage. The exfoliation of the graphene monolayer gave a new impetus in carbonaceous polymer composites [1-5]. In this study, the dielectric response of pCBT/graphene nanocomposites was studied via Broadband Dielectric Spectroscopy (BDS). Aiming to investigate further the structure-properties relationship specimens' morphology and thermal response was examined by means of Scanning Electron Microscopy (SEM) and Differential Scanning Calorimetry (DSC) respectively.

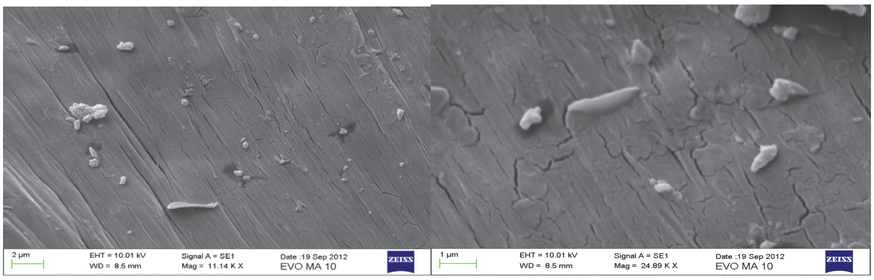

Figure 1: SEM images of the sample PCBT 97.5%/ Graphene 0.5%/PMDI 2%

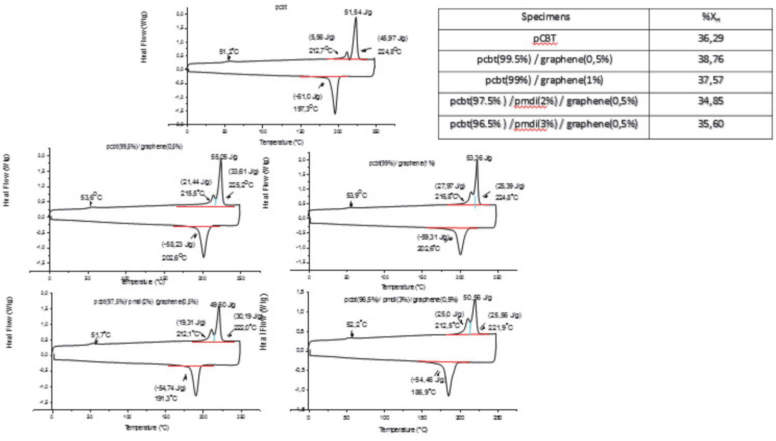

Specimens	%X_m
pCBT	36,29
pcbt(99.5%) / graphene(0,5%)	38,76
pcbt(99%) / graphene(1%)	37,57
pcbt(97.5%) /pmdi(2%) / graphene(0,5%)	34,85
pcbt(96.5%) /pmdi(3%) / graphene(0,5%)	35,60

Figure 2: DSC thermographs of the five samples and their crystallinity level (embedded table).

Broadband Dielectric Spectroscopy (BDS) has been proved to be a powerful tool for the investigation of molecular mobility, phase changes, conductivity mechanisms and interfacial effects in polymers and complex systems [5,6].

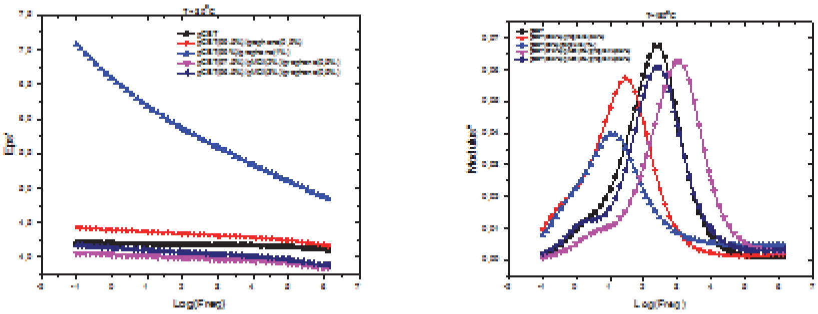

Figure 3: Variation, for all specimens, of the real part of dielectric permittivity at 30°C (left) and the imaginary part of the electric modulus at 180°C (right).

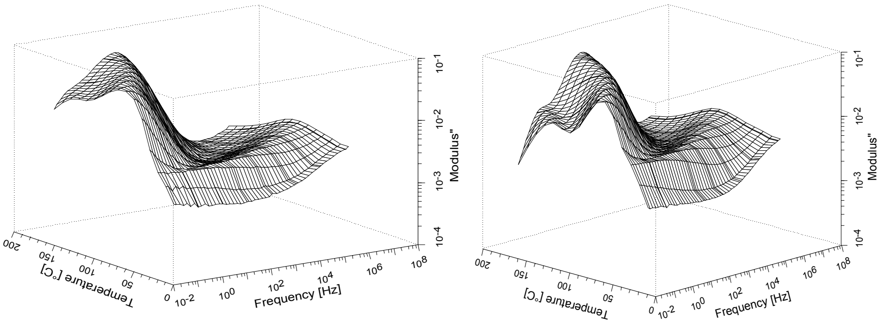

Figure 4: The imaginary part of the electric modulus of the PCBT 99.5%/graphene 0.5% (w/w) (left) and PCBT 96.5%/graphene 0.5%/PMD I3% (w/w) (right), samples as a function of frequency and temperature.

Three distinct relaxation modes were recorded in the spectra of all systems. They were attributed to interfacial polarization, glass to rubber transition (α–relaxation) and motion of polar side groups (β–relaxation). Concerning the thermal properties, all specimens exhibit double melting point, a behaviour associated with the pCBT matrix. DSC data clearly confirm the nucleating effect of graphene through the increase of the crystallization peak temperature with increasing graphene content.

References

[1] J. R. Potts , D. R. Dreyer, C. W. Bielawski, R. S. Ruoff, Polymer 52 (2011) 5–25.
[2] Bin Li, Wei-Hong Zhong, Journal of Materials Science 46 (2011) 5595–5614.
[3] R. K. Gupta, P. Mukhopadhyay, Plastics Engineering, SPE 32 (2011).
[4] G. C. Psarras, Express Polymer Letters 8 (2014) 73.
[5] A. C. Patsidis, K. Kalaitzidou, G. C. Psarras, Journal of Thermal Analysis and Calorimetry 116 (2014) 41–49.
[6] G. C. Psarras, Conductivity and dielectric characterization of polymer nanocomposites in Physical Properties and Applications of Polymer Nanocomposites , Ed. S,C Tjong and Y.W Mai, Woodhead Publishing in Materials, (2010) 31-69.

Dielectric and electrical properties of Fe_3O_4/CNT/PVDF Nanocomposites

C. Tsonos[1,2], E. Siores[2], A. Kanapitsas[1], G. C. Psarras[3], Th. Speliotis[4]

[1]Electronics Engineering Department, TEl of Stereas Elladas, 35100 Lamia, Greece
[2]Institute for Materials Research and Innovation, University of Bolton, BL3 5AB, UK
[3]Department of Materials Science, University of Patras, Patras, 26504, Greece
[4]Institute of Nanoscience and Nanotechnology, NCSR «Demokritos» Aghia Paraskevi, 15310 Athens, Greece

E-mail: tsonos@teilam.gr

TUP

P063

The production of multifunctional nanocomposites, which combine inexpensive material costs and easy of production processing in large scale, is of great challenge of the materials engineering. Polyvinylidene fluoride (PVDF) as a matrix, is a semi-crystalline polymer having remarkable thermal stability, good chemical resistance, extraordinary piezoelectric properties [1], which combined with its high elasticity, relative transparency and easy of processing, make this material suitable for various technological applications [2]. Among the nanosized fillers, iron oxides such as Fe_3O_4 have become of long standing interest, because of their diverse variety of applications in electronic, magnetic, optical, and mechanical devices [3].

The present work deals with a novel three-phase PVDF based system with carbon nanotubes (CNTs) and Fe_3O_4 as inclusions. In order to improve the dielectric and electrical characteristics of the composites, the CNTs content was kept constant at a value higher than the percolation threshold but lower than the one required reaching maximum values of electrical conductivity [4]. This system comprises a new type of multifunctional materials that combine the ferroelectric and piezoelectric properties of PVDF with the electrical properties of CNTs and the magnetic properties of Fe_3O_4. Data analysis, is focused, to compares the effect of Fe_3O_4 nanoparticles of various content in the CNT/PVDF matrix properties.

SEM measurements show a good dispersion of nanoinclusions in the PVDF matrix, and only at the used highest Fe_3O_4 particle concentration agglomerates containing three or more particles were observed. FTIR and XRD measurements provide clear evidence that mainly the presence of CNTs induces the formation of phase in nanocomposites. According to DSC measurements, the degree of crystallinity is practically unaffected by the addition of CNTs for the lowest concentration of Fe_3O_4 particles. For higher Fe_3O_4, content a decrease of the degree of crystallinity is observed. The incorporation of Fe_3O_4 in CNT/PVDF matrix gradually increases the values of both, dielectric permittivity and DC conductivity, when the content of Fe_3O_4 is up to 10% (Fig.1 and Fig. 2). At the higher magnetite content, the role of Fe_3O_4 as insulative barrier in the CNT/PVDF matrix is dominant. On the one hand, Fe_3O_4 nanoparticles increase the insulative gaps between CNTs which led to a reduction in the dielectric permittivity of nanocapacitors, as well as to the total dielectric permittivity. On the other hand, the barrier effect of Fe_3O_4 nanoparticles restricts the conductive network of CNTs and as a result reduces the DC conductivity.

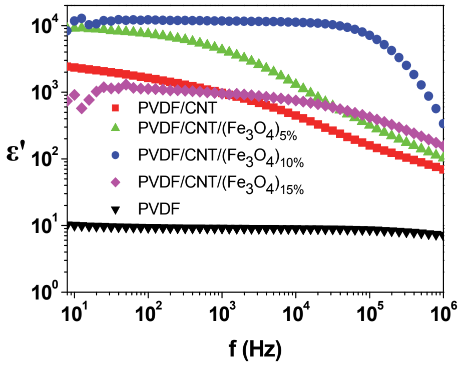

Figure 1. Real part of dielectric permittivity, as a function of frequency for PVDF system at room temperature.

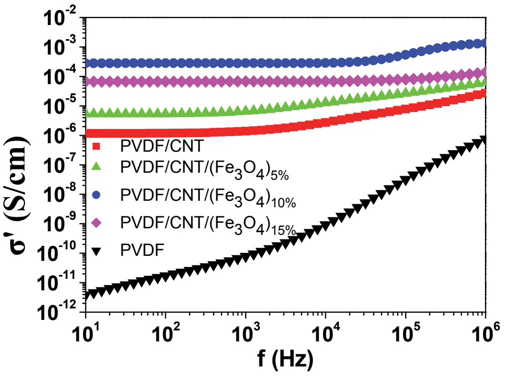

Figure 2. AC electrical conductivity as a function of frequency for PVDF system at room temperature.

Acknowledgments:

This research has been co-financed by the European Union (European Social Fund – ESF) and Greek national funds through the Operational Program "Education and Lifelong Learning" of the National Strategic Reference Framework (NSRF)-Research Funding Program: THALES. Investing in knowledge society through the European Social Fund, MIS 379346.

References

[1] V. Sencadas, V. M. Moreira, S. Lanceros-Mendez, A.S. Pouzada, R. Jr Gregorio, Materials Science Forum 514–516 (2006) 872–876.

[2] H. S. Nalwa, Ferroelectric Polymers: Chemistry, Physics and Applications. Marcel Dekker, New York (1995).

[3] G.A. Prinz, Science 282 (1998) 1660-1663.

[4] W. Bauhofer, J.Z. Kovacs, Composites Science and Technology 69 (2009) 1486–1498.

Stabilization of Cr-rich tannery waste in fly-ash based cementitious materials

A. D. Daniil[1], S. Varitis[1], E. Pantazopoulou[2], E. Pavlidou[1], G. Vourlias[1], G. Kaimakamis[1], Th. Karakostas[1], and G. P. Dimitrakopulos[1]

[1] Department of Physics, Aristotle University of Thessaloniki, Thessaloniki 54124, Greece
[2] Department of Chemistry, Aristotle University of Thessaloniki, Thessaloniki 54124, Greece

E-mail:gdim@ auth.gr

Solidification/Stabilization (S/S) using cementitious binders, is a promising method for the treatment of hazardous wastes that contain heavy metals. The method is advantageous due to the low energy consumption and the low cost of the raw materials.

In this study the combination of two wastes was investigated. Fly ash (FA) was used as the main binder to stabilize a Cr-rich ash obtained from tannery waste. Two types of fly ash were used. C-type FA was obtained from the lignite-fired power plants in Ptolemaida, and F-type FA originated from the Megalopolis power plant. The initial chromium-containing waste was recovered from the industrial zone of Thessaloniki in the form of tannery sludge. This sludge was incinerated at 500°C under anoxic conditions for 1.5 h in order to remove most of the organic content and to avoid oxidation of chromium [1]. The aim of this work was to fabricate cementitious materials that could be used either for safe disposal or for potential structural applications (e.g. in buildings, pavements etc.).

In order to fabricate stabilized cementitious materials, FA was used as the main binder, and calcium and sodium hydroxides, as well as sodium silicate, were used as activators. FA and Cr-ash were mixed in different proportions and homogenized in a ball mill. Then, the activators were added, and the mixtures were compressed in cylindrical samples. Finally the samples were immersed in a saturated water vapour atmosphere at 95^{o}C for 24h. The resulting products were characterized by X-Ray Diffraction (XRD), Scanning Electron Microscopy (SEM) and Energy Dispersive Spectroscopy (EDS). The elastic properties were measured with the Impulse Excitation Technique, and the chemical stability was studied by leaching tests.

XRD analysis showed no indication of any Cr-containing crystalline phase. Optimum concentrations for reducing calcite and ettringite formation were identified. SEM observations revealed the existence of the calcium silicate hydrate (C-S-H) gel in all products. EDS analysis indicated that chromium was homogeneously dispersed inside the amorphous cementitious matrix. As depicted in Figure 1, in the areas where chromium concentration was high, silicon and aluminum concentrations were lower, and vice versa. We postulate that chromium substitutes for aluminum in the -Si-O- chains, thereby reducing their length. This postulate is supported by the deterioration in sample stiffness with reducing the Si/(Al+Cr) ratio, as depicted in Figure 2. Leaching tests indicated that the leached chromium was below limits.

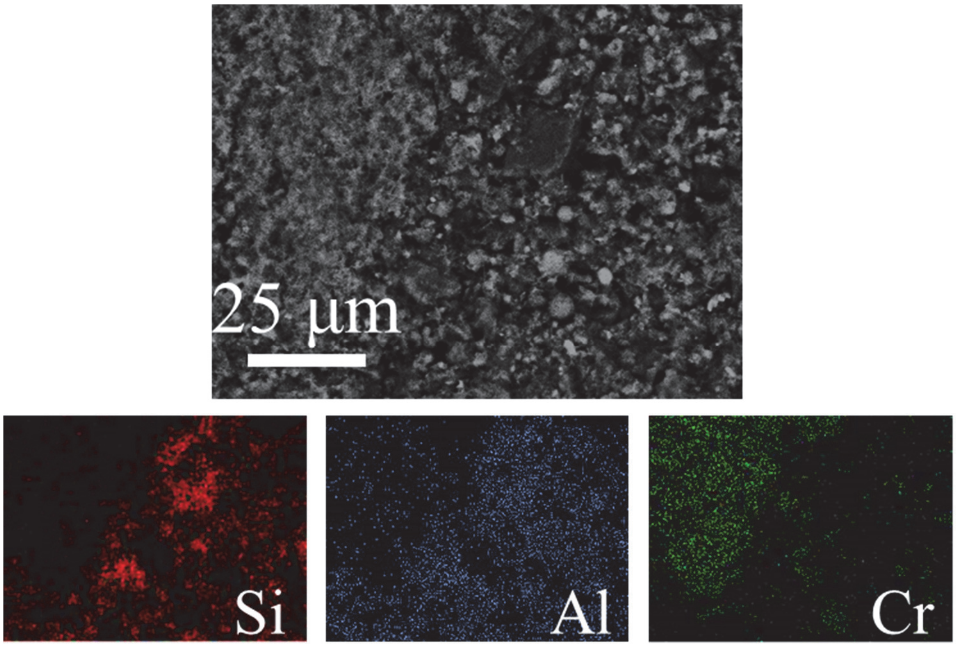

Figure 1: Elemental mapping of a sample containing 67 wt% C-type FA, 20 wt% Cr-ash and 13 wt% $Ca(OH)_2$.

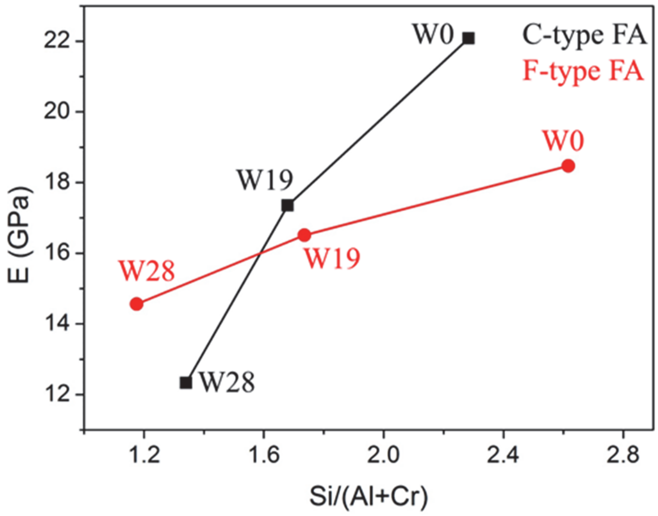

Figure 2: Young's modulus, E versus Si/(Al+Cr) for C- and F-type FA samples activated with $Ca(OH)_2$ and sodium silicate. FA is partially substituted by Cr-ash. W0, W19, W28 stands for the wt% of Cr-ash (Waste) in each sample.

Acknowledgements

Research co-financed by the EU (ESF) and Greek National Funds through the Operational Program "Education and Lifelong Learning" of the National Strategic Reference Framework (NSRF) – Research Funding Program: MIS380038 THALES. G. P. D. acknowledges support by the Research Committee of the Aristotle University of Thessaloniki (proj. 89318).

References

[1] P. Kavouras et. al. J. Hazard. Mater. 283, (2015), 672-9.

High pressure Raman study of L-phenylalanine crystals

A. Zerfiridou[1,2], **K. Filintoglou**[1], **A. M. Paschou**[1], **D. Christofilos**[3], **M. Katsikini**[1], **S. Ves**[1], **G. A. Kourouklis**[3] **and J. Arvanitidis**[1*]

[1]Physics Department, Aristotle University of Thessaloniki, 54124 Thessaloniki, Greece
[2]Food Technology Department, ATEI of Thessaloniki, 57400 Sindos, Greece
[3]Chemical Eng. Department, Aristotle University of Thessaloniki, 54124 Thessaloniki, Greece

*E-mail: jarvan@physics.auth.gr

Amino acids are biologically important organic compounds, constituting the building blocks of all proteins. All amino acids have a central C atom to which an amino group (NH_2), a carboxyl (-COOH) group and a side-chain, characteristic to each amino acid, are attached. In the solid state, amino acids form molecular crystals where the interplay between van der Waals interactions and hydrogen bonds determine their crystalline structure. Raman spectroscopy can provide valuable insight in the vibrational and structural properties of biomolecules and tissues. Moreover, the study of the structural stability and the possible structural modifications of amino acids under extreme pressure and/or temperature conditions, simulating interstellar or interplanetary conditions, is of great importance towards understanding the prebiotic organic synthesis and the chemical evolution forming the precursors of life [1,2]. Phenylalanine is an *essential* amino acid (provided solely by nutrition) that is hydrophobic, non-polar and aromatic. The L enantiomer of phenylalanine is a precursor of tyrosine, the skin pigment melanin and important neurotransmitter molecules like dopamine and epinephrine. Its crystal structure exhibits various polymorphs, all belonging to the monoclinic system [3]. In this work, L-phenylalanine crystals are subjected to hydrostatic pressure up to 5 GPa by means of a diamond anvil cell, using the 1:1 FC70-FC77 fluorinert mixture as pressure transmitting medium (PTM). Raman spectroscopy is used as a probe, providing crucial information on the vibrational properties and the structural stability of the system under pressure.

The Raman spectrum of the studied material is very rich, owing to the low symmetry of the phenylalanine molecule and the monoclinic crystal structure. Briefly, the intermolecular (lattice) modes appear in the low frequency region (<200 cm^{-1}), while the intermediate frequency region (600-1700 cm^{-1}) contains the backbone, aromatic and side-chain vibrational modes [4]. Finally, the high frequency region (2800-3300 cm^{-1}) is dominated by C-H and N-H stretching vibrations and combination modes [5]. Indicative Raman spectra of L-phenylalanine in the high frequency region recorded at various pressures are illustrated in Fig. 1(a). Pressure application causes the shift of all the observed Raman peaks to higher energies, their broadening (particularly, after the solidification of the PTM at ~1 GPa), as well as changes in their relative intensities. The pressure dependence of the frequencies of the Raman peaks in this region is depicted in Fig. 1(b). This dependence is quasi-linear up to ~2 GPa for all the studied peaks, with pressure slopes 1.6-16.2 $cm^{-1}GPa^{-1}$. However, above 2 GPa, significant changes occur with respect to the number of the Raman peaks, their frequencies and pressure slopes. Similar changes in the same pressure region are also observed in the low and the intermediate frequency regions (not shown), indicating that a structural phase transition of the crystalline L-phenylalanine takes place at ~2 GPa. Upon pressure application, amino acid crystals undergo molecular conformational changes and, in some cases, structural phase transitions even at relatively low pressures. For example this is the case for β-glycine, DL-alanine, L- and DL-leucine crystals [6].

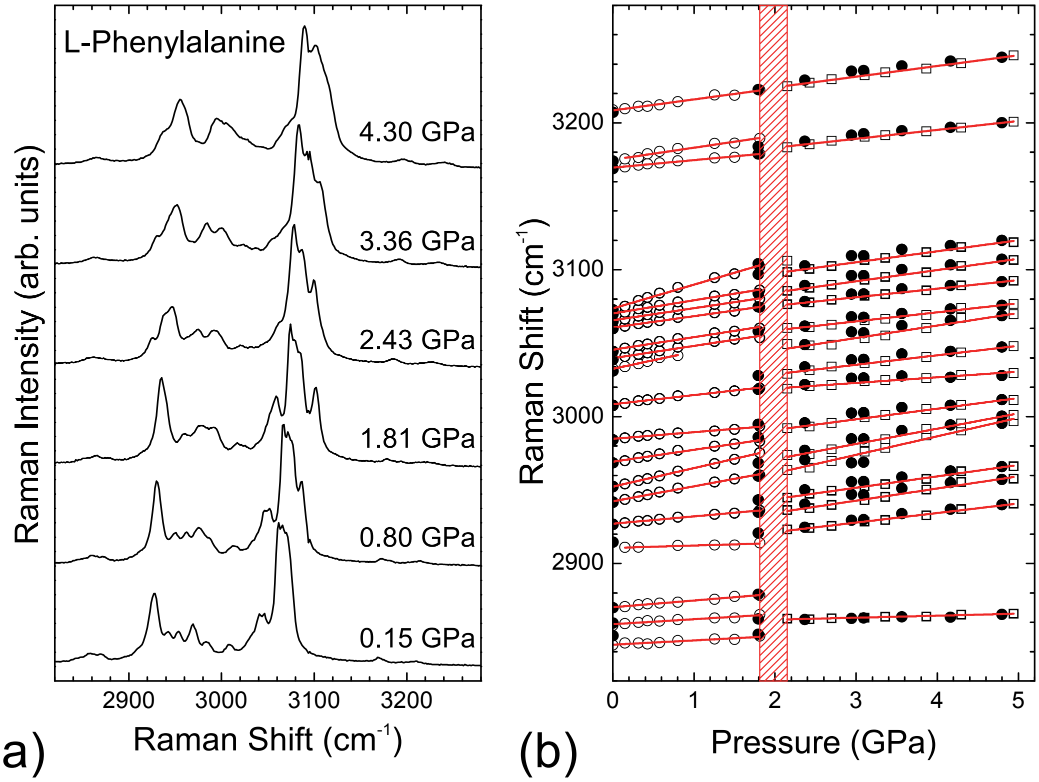

Figure 1 (a) Raman spectra of L-phenylalanine in the high frequency region recorded at various pressures. (b) Pressure dependence of the high frequency Raman peaks of L-phenylalanine. Open (solid) symbols denote data obtained upon pressure increase (decrease). Solid lines through data correspond to their linear fittings.

The new high pressure phase of L-phenylalanine is stable to pressure application up to 5 GPa. Nevertheless, the phase transition is reversible and the initial phase is recovered during the downstroke experiments below 2 GPa (solid symbols in Fig. 1).

References

[1] P.T.C. Freire in "High pressure crystallography", Eds.: E. Boldyreva and P. Dera (Springer 2010) 559-572.

[2] J. Chen, H. Cheng, X. Zhu, L. Jin and H. Zheng, Geochem. J. 41 (2007) 283-290.

[3] F.S. Ihlefeld, F.B. Pettersen, A. von Bonin, M. Zawadzka and C.H. Gorbitz, Angew. Chem. Int. Ed. 53 (2014) 13600-13604.

[4] B. Hernandez, F. Pfluger, A. Adenier, S.G. Kruglik and M. Ghomi J. Phys. Chem B 114 (2010) 15319-15330.

[5] J.L. Castro, M.R. Lopez Ramirez, J.F. Arenas and J.C. Otero, J. Molecular Struct. 744-747 (2005) 887-891.

[6] P.F. Facanha Filho, P.T.C. Freire, A.O. dos Santos and L.M. da Silva, Vibrational Spectr. 72 (2014) 15-19 and references therein.

Composition and Characterization of Silicate Glasses Containing ZnO and CuO prepared through the Sol-Gel Process

S.P. Petsi[1], G.S. Theodorou[1], E. Kontonasaki[2], N. Kantiranis[3], P. Koidis[2] and K. M. Paraskevopoulos[1]

[1]Department of Physics, [2] School of Dentistry, [3]School of Geology,
Aristotle University of Thessaloniki, 54124 Thessaloniki, Greece

E-mail: gtheodo@physics.auth.gr

Various sol-gel silicate glasses are promising candidate biomaterials for bone-tissue regeneration in orthopaedics and dentistry due to their ability to form on their surface a biologically hydroxyapatite layer when they get in contact with physiological or simulated body fluids (Simulated Body Fluid, SBF). This layer is then interconnected with the bone tissue collagen fibres and hydroxyapatite. As a result, a strong connection to the bone and/or soft tissues is created, which renders bioactive glasses significant biomaterials for tissue regeneration [1, 2]. Various studies report the beneficiary use of small amounts of Cu or Zn ions in a bioactive glass [3]. The effect of Mg ion addition stimulates new bone formation and increases bone cell adhesion and stability [4] whereas the addition of Zn ion shows anti-inflammatory effect and stimulates bone formation in vitro by the activation of protein synthesis in osteoblasts [5]. The aim of the present work was the introduction of Cu/Zn ions in a silicate based sol-gel derived bioactive glass, as well as the characterization of its apatite forming ability. In order to achieve that, six sol-gel systems, 9.5M0.5Zn (SiO_2 60, CaO 30, MgO 9.5, ZnO 0.5 in wt %), 9M1Zn (SiO_2 60, CaO 30, MgO 9, ZnO 1 in wt %), 8.5M1.5Zn (SiO_2 60, CaO 30, MgO 8.5, ZnO 1.5 in wt %), 1.5Zn1.5C (SiO_2 60, CaO 30, MgO 7, ZnO 1.5, CuO 1.5 in wt %), 1Zn3C (SiO_2 60, CaO 30, MgO 6, ZnO 1, CuO 3 in wt %), and 2Zn4C (SiO_2 60, CaO 30, MgO 4, ZnO 2, CuO 4 in wt %) were synthesized and their potential bioactive behavior was evaluated in inorganic environment (SBF solution) [6].

Sol-gel derived bioactive glasses were produced as described in literature [7]. The bioactivity test of glass-ceramics was conducted in SBF, with a ratio of 1.5 mg/mL for various immersion times (5, 10, 15, 20, 25 and 30days) [8]. FTIR and XRD were used for the characterization of the samples. FTIR transmittance spectra were obtained using a Perkin-Elmer Spectrometer Spectrum 1000 in MIR region (4000-400 cm^{-1}) with a resolution 4 cm^{-1}, respectively XRD measurements were carried out using a Philips (PW1710) diffractometer with Ni-filtered CuKa wave radiation. The counting statistics of the XRD study were: step size 0.02^o 2θ, start angle 5^o, end angle: 75^o and the time per step: 1.5 sec.

The six synthesized bioactive glasses revealed the characteristic FTIR bands of silicate glasses as shown in Figure 2 [9, 10]. The characteristic bands of silicate glasses presents the broad peak at 900-1200cm^{-1} assigned to the asymmetric stretching vibration of Si-O-Si and the peak at 496cm^{-1} assigned to the bending vibration of the Si-O-Si bonds respectively. FTIR spectra (Fig.1) and XRD patterns (Fig.2, here presented only patterns of Cu and Zn containing glasses) revealed that even after 10 days of immersion the onset of biological apatite formation did not occur. It seems that the addition of Zn in bioactive materials inhibits the ability of HCAp formation on the surface of the samples, as has been reported in previous studies for high amounts of ZnO.

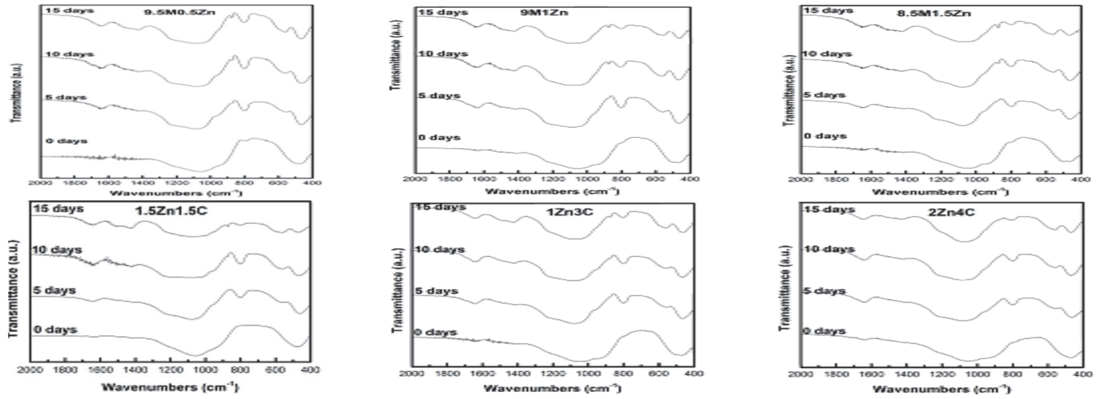

Figure 1: FTIR spectra of all synthesized glass ceramics before and after immersion in SBF solution for 15 days

The increase in Zn^{2+}/Mg^{2+} ratio decreases the chemical degradation of glasses as well as reduces their apatite forming ability [11]. FTIR analysis revealed the generation of a glass structure with higher network connectivity, which is associated to a lower dissolution process and the inhibition of the conversion from amorphous CaP to HA, as has been reported to other studies as well [12,13].

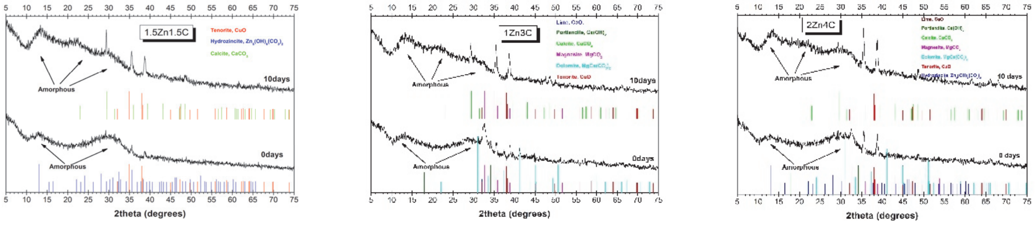

Figure 2: XRD patterns of Cu and Zn containing glasses before and after immersion in SBF solution for 10 days.

A number of Zn and Zn/Cu containing glass-ceramic materials were synthesized through the sol gel method. Their bioactive response was diminished probably due to the presence of Zn^{2+} ions which allowed the formation of a glass with higher network connectivity.

References

[1] W. Cao and L. L. Hench, Ceramics International, 22 (1996), 493–507.

[2] J.R. Jones, P. Sepulveda, and L.L. Hench, J Biomed Mater Res, 58 (2001), 720–726.

[3] A. Hoppe, N.S. Güldal, and A.R. Boccaccini Biomaterials 32 (2011), pp2757-2774

[4] H.Q. Xie and Y.J. Kang, Curr. Med. Chem., 16 (2009) 1304– 1314

[5] M. Yamaguchi, J Trace Elem Exp Med 11 (1998) 119-35.

[6] T. Kokubo, H. Kushitan, S. Sakka, T. Kitsugi, T. Yamamuro, J Biomed Mater Res 24 (1990) 721

[7] C. Wu and G. Chang, J Biomed Mater Res 83B (2006) 153-160.

[8] J. Zhong and D. C. Greenspan, J Biomed Mater Res, 53 (2000) 694–701.

[9] M.R. Filgueiras, G. LA Torre, and L.L. Hench, J. Biomed. Mater. Res. 27 (1993) 445

[10] E. Kontonasaki, T. Zorba, L. Papadopoulou, E. Pavlidou, X. Chatzistavrou, K. Paraskevopoulos, and P. Koidis, Cryst. Res. Technol. 37 (2002), 1165-1171

[11] A. Goel, S. Kapoor, A. Tilocca, R.R. Rajagopal, and JMF Ferreira, J Mater Chem B. 1 (2013) 3073-3082.

[12] S. Haimi, G. Gorianc, L. Moimas, B. Lindroos, H. Huhtala, S. Räty, H. Kuokkanen, GK Sándor, C. Schmid, S. Miettinen and R. Suuronen, Acta Biomater. 5 (2009) 3122-3131.

[13] M. Bini, S. Grandi, D. Capsoni, P. Mustarelli, E. Saino and L. Visai, J Phys. Chem. C 113 (2009) 8821–8828.

On the consolidation of Bi_2Te_3 pellets: Taguchi optimization analysis

K. Boutzi[1], **E.C. Stefanaki**[1], **P. Kyratsis**[2], **E. Hatzikraniotis**[1*],
K.M. Paraskevopoulos[1]

(1) Solid State Physics Section, Physics Department, Aristotle University of Thessaloniki, Greece
(2) Department of Mechanical Engineering and Industrial Design, TEI of Western Macedonia, Greece

(*) e-mail: evris@physics.auth.gr

Thermoelectric (TE) technology and solid-state devices based on the TE effect enable direct conversion between thermal and electrical energy and provide an alternative route for power generation and refrigeration. TE materials, which can either generate electricity from waste heat or be used as solid-state Peltier coolers [1], could play an important role in a global sustainable energy solution since they have a number of advantages, including no moving parts, and being reliable and scalable. Over the past ten years, they have attracted great attention with a view to industrial applications [2]. Bismuth telluride (Bi_2Te_3) and its alloys are widely used as materials for thermoelectric refrigeration and generators for 200-400 K [3], due to its high Seebeck coefficient, low electrical resistivity and relatively low thermal conductivity [4].

In this work, the Taguchi method [5], a powerful tool to design optimization for quality, is used to select properly the pressing parameters for Bi_2Te_3 pellets. Taguchi is a statistical method aiming to a robust design of experiments developed to a) minimize the amount of the experiments in a multi-parameter problem and b) investigate and analyze how different parameters affect the variance of a process performance. One of the common approaches employed by many engineers today in manufacturing companies is One-Variable-At-a-Time (OVAT), where we vary one variable at a time keeping all other variables in the experiment fixed. This approach depends upon guesswork, luck, experience and intuition for its success. Moreover, this type of experimentation requires large resources to obtain a limited amount of information about the process. OVAT experiments often are unreliable, inefficient, time consuming and may yield false optimum condition for the process [6]. Taguchi method tests pairs of combinations, and this allows for the collection of the necessary data to determine which factors mostly affect product quality with a minimum amount of experimentation, saving time and resources.

Powder of Bi_2Te_3 (250μm grain size) was pressed in a hydraulic press. The three parameters of the experiments are: Pressing time (t), Temperature (T) and pressure (P). Table I summarizes the combination of the parameters obtained by Taguchi method and the density & conductivity results. Density was determined by mass and volume measurements and conductivity by the van der Pauw method in room temperature. Taguchi analysis was performed by Minitab statistical software.

The morphology of the samples with the minimum and maximum density, namely #1 and #9 were examined with SEM. The pellet with the maximum density seems to be more compact and smooth. Furthermore, the grain's size in the two extreme cases was examined with SEM images, obtained from areas with roughness and apparent grain boundaries separation (Fig.1). Analysis peformed with Image J software on multiple images from each sample show that the grains tend to conglomerate as the pressing temperature increase.

Finally, our experimental results (density, conductivity) were analyzed applying the Taguchi method and the impact of each experimental parameter on the density and conductivity (Fig. 2) was determined. It seems that the pressing time and pressure have almost equal (the strongest) influence on the density of the pellet; while pressure affects the conductivity at the most. Careful control of the experimental planning should be taken under consideration to improve the microstructure and the properties of the pellet.

Table I. Pressing parameters (Pressure, Time & Temperature), density (d) and conductivity (σ).

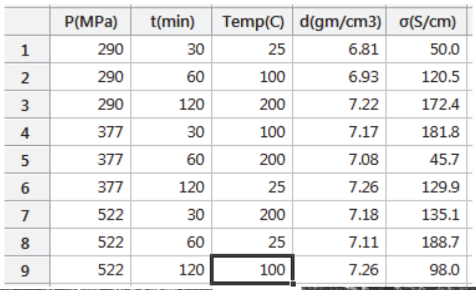

	P(MPa)	t(min)	Temp(C)	d(gm/cm3)	σ(S/cm)
1	290	30	25	6.81	50.0
2	290	60	100	6.93	120.5
3	290	120	200	7.22	172.4
4	377	30	100	7.17	181.8
5	377	60	200	7.08	45.7
6	377	120	25	7.26	129.9
7	522	30	200	7.18	135.1
8	522	60	25	7.11	188.7
9	522	120	100	7.26	98.0

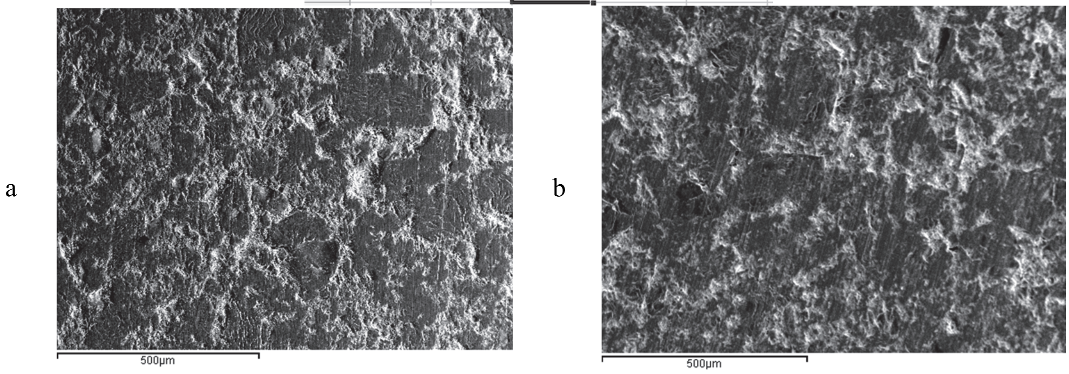

Figure 1 SEM images in backscattered mode for the samples with the minimum (#1, a) and maximum (#9, b) parameters (t, T, P) and density respectively.

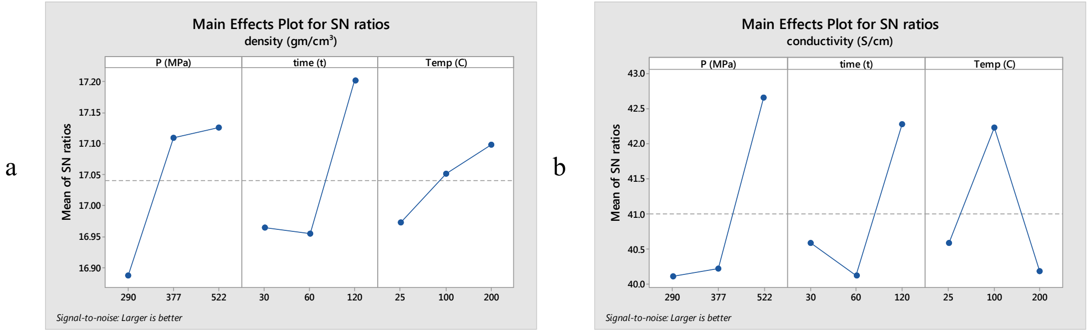

Figure 2 Density (a) and conductivity (b) signal to noise (SN) values for the three parameters

References

1. G.J. Snyder and E.S. Toberer, Nat. Mater. 7, 105-114 (2008).
2. J-F Li, W-S Liu, L-D Zhao and M. Zhou, NPG Asia Mater, 2, 152-158 (2010).
3. D.M. Rowe and C.M. Bhandari: Modern Thermoelectrics, Reston Publishing Company (1983).
4. G. Min and D. M. Rowe, Solid-State Electron. 43, 923-929 (1999).
5. C.F. Jeff Wu and M.S. Hamada, Experiments: Planning, Analysis, and Optimization, (2nd edition), Willey (2009).
6. J. Antony, Design of Experiments for Engineers and Scientists, Elsevier (2015).

Comparative study of natural fibre reinforced composite materials

D.A. Patsiaoura[1], **E. Pavlidou**[1], **G. Vourlias**[1], **D.N. Bikiaris**[2]. **K. Chrissafis**[1]

[1]Physics Department, Aristotle University of Thessaloniki, 54124, Thessaloniki, Greece
[2]Laboratory of Polymer Chemistry and Technology, Department of Chemistry, Aristotle University of Thessaloniki, 54124, Thessaloniki, Greece

E-mail: dpatsi@physics.auth.gr

Natural fiber reinforced polymer composites are used in many different contexts, since they offer improved mechanical properties over their non-reinforced counterparts. The extent to which this is achieved depends on several factors, including the fibers' dimensions, their chemical composition, their mechanical properties, their moisture content and the matrix-filler interactions. The current work is a comparative study between two series of HDPE unmodified polymer composites using kenaf and hemp as reinforcing materials. Composites containing 10, 20 and 30 wt% of filler were prepared by melt mixing in a twin screw extruder and were studied by means of TG, FTIR, XRD, DSC and SEM. Finally, tensile properties were evaluated and Izod Impact tests were conducted in both series of composites.

Figures 1 and 2 display the thermogravimetric behavior of composites. Mass loss curves of all the composites lie in the region between neat HDPE and the corresponding fiber, while a gradual shift of the total curves towards lower temperatures is displayed with increasing fiber content, influencing negatively their thermal stability. Nonetheless, hemp composites display a slightly more stable thermogravimetric behavior than kenaf based composites. Mass loss of neat HDPE occurs in a one step procedure, from 380ºC to about 550ºC due to the decomposition of C-C bonds in the main chain of HDPE [1]. Water loss is observed at around 100ºC for all composites, while further degradation takes place as a two-step process. The first degradation step appears between 240ºC and 400ºC which is attributed to the decomposition of lignocellulosic components [2], while the second degradation step between 430ºC and 550ºC is attributed to the matrix decomposition.

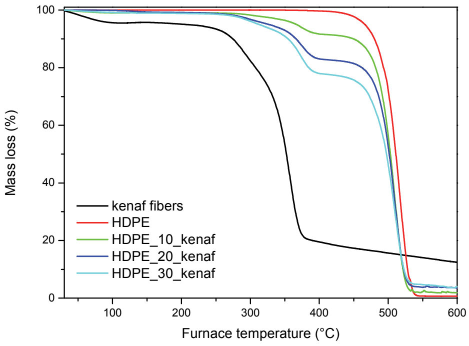

Figure 1: TG curves of kenaf based composites

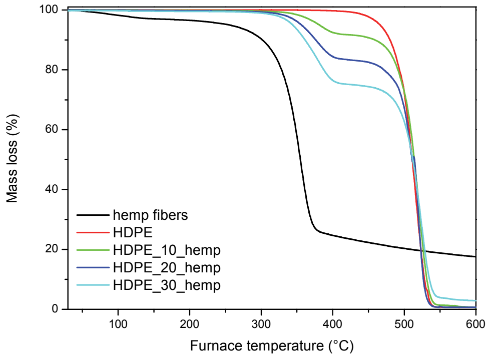

Figure 2: TG curves of hemp based composites

FTIR measurements were conducted in order to investigate any compatibility signs between hydrophilic fibers and hydrophobic HDPE, leading to a negative outcome, since no alteration or shift of any peak was observed. XRD was used in order to estimate the crystallinity of each fiber, since it defines their mechanical performance and their moisture content. Different methodologies were involved and they all inclined that hemp fibers are characterized by a larger crystallinity percentage than kenaf fibers. XRD measurements, also, displayed the reduction of composites' crystallinity upon increasing fiber content. DSC measurements were performed in order to study the effect of additives on the HDPE's thermal properties, as well as to estimate the composites' crystallinitiies, which were in accordance with XRD findings. SEM (Figures 3-8) was used to study the dispersion and interfacial adhesion of filler-matrix, while mechanical tests revealed that the incorporation of natural fibers radically changed the material's mechanical behavior.

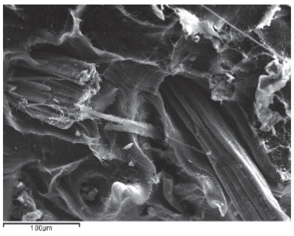

Figure 3:
HDPE_10_kenaf

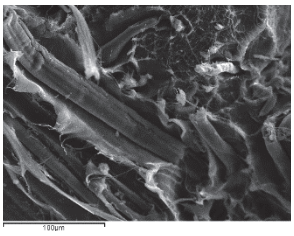

Figure 4:
HDPE_20_kenaf

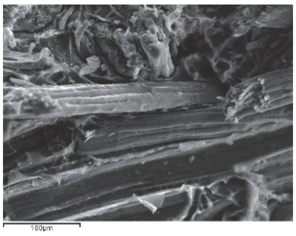

Figure 5:
HDPE_30_kenaf

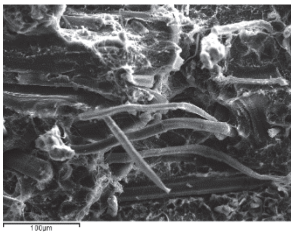

Figure 6:
HDPE_10_hemp

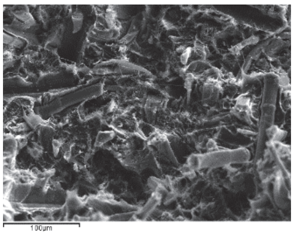

Figure 7:
HDPE_20_hemp

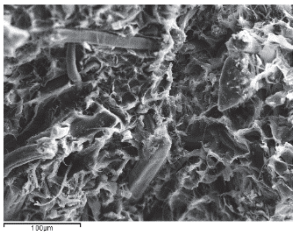

Figure 8:
HDPE_30_hemp

Concerning mechanical properties, incorporation of stiff fibers in the polymer matrix appeared to restrict the movements of macromolecular chains and thus any deformation of the matrix itself, while an increase of the stiffness of the composite materials was observed upon increasing additive content. Additionally, the low wettability of the fibers due to their incompatibility resulted in reduced mechanical performance. The behavior of both sets of materials, however, presented fundamental differences, as hemp composites exhibited superior mechanical performance than the kenaf based ones, probably due to the hemps fibers' higher crystallinity, their lower moisture content and their smaller intersection.

References

[1] A.N. Shebani, A.J. van Reenen, M. Meinchen, Thermochimica Acta 481(2009) 52-56

[2]M. Polleto, H.L. Ornaghi Jr, A. J. Zattera, Materials 7(2014) 6105-6119

Acknowledgement: This work was supported by the Greek General Secretariat of Research and Development (12CHN322)

Synthesis and Characterization of Silicate Glasses Containing SrO through the Sol-Gel Process

N.S. Dessou[1], <u>G.S. Theodorou</u>[1], E. Kontonasaki[2], L. Papadopoulou[3], N. Kantiranis[3], K. Chrissafis[1], P. Koidis[2], K. M. Paraskevopoulos[1]

[1]Department of Physics, [2] School of Dentistry, [3]School of Geology,
Aristotle University of Thessaloniki, 54124 Thessaloniki, Greece

E-mail: gtheodo@physics.auth.gr

Bioactive glasses are glass-ceramic biomaterials suitable for bone tissue engineering applications. Various studies have reported that Si-, Ca-, Mg- and Sr-containing glasses are highly bioactive and could be used for biomedical applications [1]. Specifically, Sr has been shown to have positive effects on bone cells and to enhance bone formation both in vitro and in vivo [2]. The aim of this work was the evaluation of the bioactive behaviour of two Sr-containing glass ceramic materials with similar composition, namely SiO_2 60, CaO 30, MgO 5 ,SrO 5 and SiO_2 60, CaO 30, MgO 5, SrO 10 in wt %, both thermally treated and untreated in inorganic environment (SBF solution)[3].

Sol-gel derived bioactive glasses were produced as described in literature [4]. The bioactivity test of glass-ceramics was conducted in SBF, with a ratio of 1.5 mg/mL for various immersion times (5, 10, 15, 20, 25 and 30days) [5]. FTIR, TG-DTA, XRD and SEM/EDS were used for the characterization of the samples. Differential thermal and thermogravimetric analysis were performed with a Setaram thermogravimetric-differential thermal analyzer SETSYS 16/18-TG-DTA (1400 °C rod), with heating and cooling rates 10 °C/min – in nitrogen atmosphere – and furnace cooling, respectively FTIR transmittance spectra, were obtained using a Perkin-Elmer Spectrometer Spectrum 1000 in MIR region (4000-400 cm^{-1}) with a resolution 4 cm^{-1}. XRD measurements were carried out using a Philips (PW1710) diffractometer with Ni-filtered CuKa wave radiation. The counting statistics of the XRD study were: step size 0.02° 2θ, start angle 5°, end angle: 75° and the time per step: 1.5 sec.

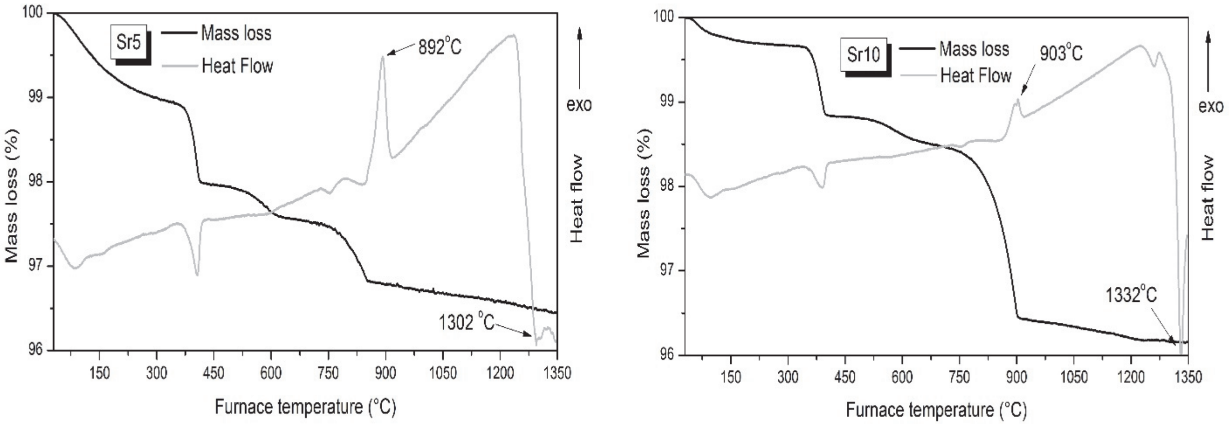

a b

Figure 1: Thermal measurements of **a) Sr5** and **b) Sr10** glasses

The thermal measurements (Fig.1) of the synthesized materials revealed crystallization peaks at 892ºC and 903ºC respectively. The melting point was found for Sr5 at 1302ºC and for Sr10 at 1332ºC. Both bioactive glasses are subject to mass loss up to approximately 900ºC due to release of H_2O, CO and CO_2 in the form of vapors. Nonetheless the mass loss of both materials was well under 5%.
FTIR spectroscopy revealed that all synthesized glass-ceramic materials presented the characteristic bands of silicate glasses, those being the broad peak at 900-1200cm^{-1} and the peak at 496cm^{-1}. These peaks are attributed to the asymmetric stretching vibration of Si-O-Si and the bending vibration of the Si-O-Si bonds respectively. After 5 days of immersion in SBF solution FTIR spectra revealed the formation of a double peak at 587cm^{-1} and 603cm^{-1} attributed to the vibrational bending of the $(PO_4)^{3-}$ group. SEM microphotographs of the synthesized materials (Fig. 2, 0 days) revealed a grain size under 40μm and a representative microphotograph after 5 days of immersion revealed altered surface morphology, indicating the formation of apatite on the grains' surface. The aforementioned results are confirmed by XRD patterns which are not presented here.

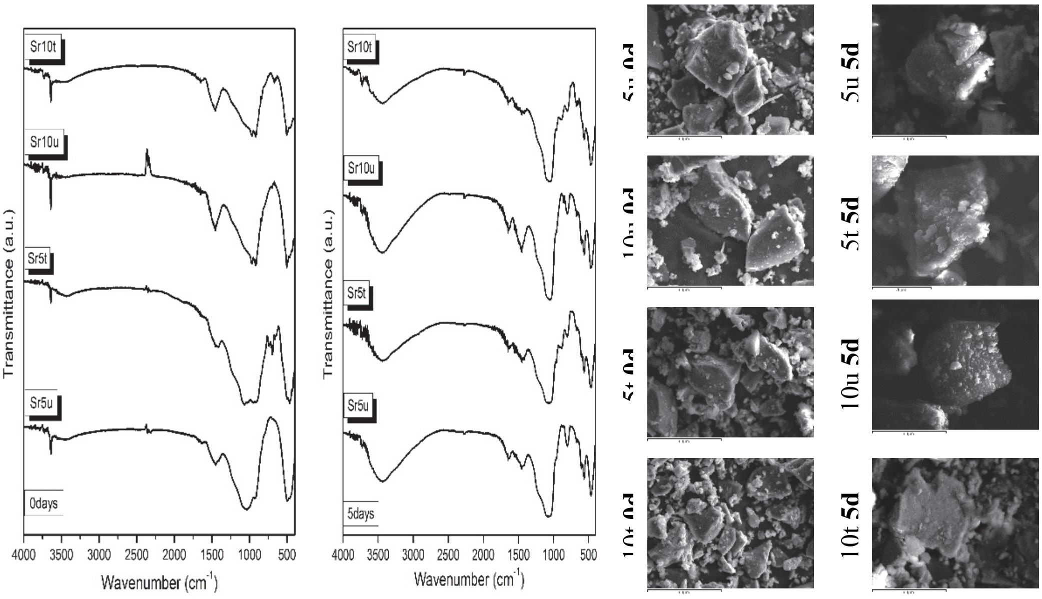

Fig. 2: FTIR spectra (left) and SEM microphotographs (right) of all synthesized glass ceramics (thermally treated and untreated) before immersion in SBF solution for days

In this work, two glass-ceramic bioactive materials were synthesized successfully. Thermal analysis of the synthesized glasses defined their crystallization and melting temperatures and the in vitro bioactivity test revealed the formation of apatite on the surface of all samples (both thermally treated and not treated) even after 5 days of immersion.

References

[1] A. Hoppe, N.S. Güldal and A.R. Boccaccini, Biomaterials 32 (2011) 2757-2774.
[2] P.J. Marie, P. Ammann P, G. Boivin and C. Rey, Calcif Tissue Int 69 (2001) 121-129.
[3] T. Kokubo, H. Kushitan, S. Sakka, T. Kitsugi and T. Yamamuro, J Biomed Mater Res 24 (1990) 721-734 .
[4] J. Zhong and D.C. Greenspan, J Biomed Mater Res 53 (2000) 694–70.
[5] C. Wu and G. Chang, J Biomed Mater Res 83B (2006) 153-160 .

Strontium doped Mg-based ceramic: Characterization and bioactivity evaluation

G.S. Theodorou[1], E. Kontonasaki[2], L. Papadopoulou[3], K. Chrissafis[1], P. Koidis[2], K.M. Paraskevopoulos[1]

[1]Department of Physics, [2]School of Dentistry [3]School of Geology,
Aristotle University of Thessaloniki, 54124 Thessaloniki, Greece

E-mail: gtheodo@physics.auth.gr

Bioactive glasses are widely used in orthopaedic and dental restorative applications, due to their ability to bond with surrounding tissues [1]. A variety of studies report the biological effect of various metallic ions when incorporated in a glass-ceramic material [2]. The addition of Sr^{2+} is found to enhance bone formation both in vitro and in vivo (through the up-regulation of osteoblasts and down-regulation of osteoclasts) [1,2], so it constitutes a potential doping-ion for biomaterials targeted to bone tissue regeneration. The present work elaborates on the synthesis, characterization and the *in vitro* bioactivity test of a Sr-doped glass-ceramic system before and after sintering aimed to be used for the construction of 3D scaffolds for bone applications.

Sol-gel derived bioactive glasses (with composition in wt%: $60SiO_2$, 30CaO, 7.5MgO, 2.5SrO) were produced as described by J. Zhong and D.C. Greenspan [3], while the sintering temperature of the material was determined after its thermal characterization. In order to evaluate the bioactive response of the synthesized glass-ceramic the in vitro test was conducted in SBF solution, with a ratio of 1.5 mg/mL for various immersion times (5, 10, 15 and 25 days) [4]. Fourier Transform InfraRed spectroscopy (FTIR), Differential thermal and thermogravimetric analysis (TG-DTA) and SEM/EDS were used for the characterization of the samples. TG-DTA were performed with a Setaram thermogravimetric-differential thermal analyzer SETSYS 16/18-TG-DTA (1400 °C rod), with heating and cooling rates 10 °C/min – in nitrogen atmosphere – and furnace cooling, respectively. FTIR transmittance spectra were obtained using a Perkin-Elmer Spectrometer Spectrum 1000 in MIR region (4000-400 cm^{-1}) with a resolution 4 cm^{-1}.

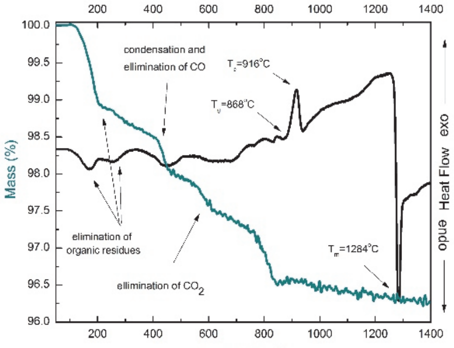

Figure 1: Thermal measurements of the bioactive glass

Thermal measurements (Fig.1) of the synthesized material revealed that under 650°C the elimination of organic residues CO and CO_2 takes place, followed by the expected mass loss. A crystallization peak is observed at 916°C by an exotherm reaction- which determined the final sintering temperature- while the endotherm reaction at 1264°C indicates the melting point of the glass ceramic. Nonetheless the mass loss of the sample was under 5%.

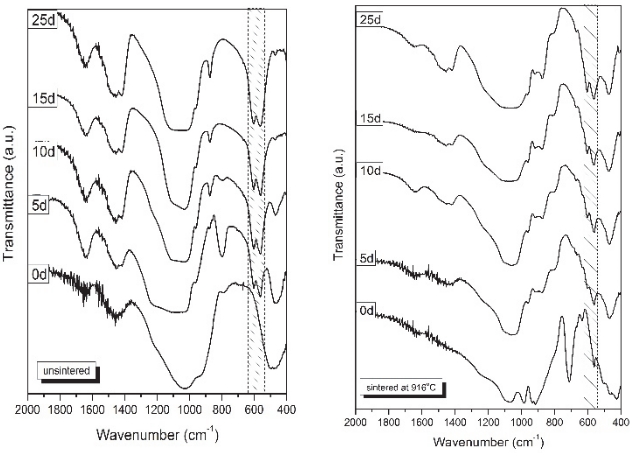

Figure 2: FTIR spectra of as produced (left) and sintered (right) bioactive glass before and after immersion in SBF solution.

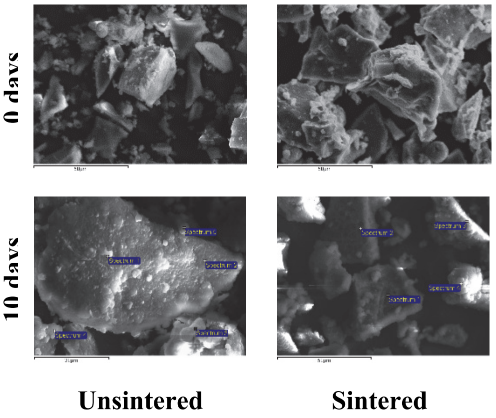

Figure 3: SEM microphotographs of synthesized glass ceramics (thermally treated and untreated) before and after immersion in SBF solution for 10 days.

FTIR spectra of both sintered and unsintered glass-ceramic (Fig. 2) presented the characteristic peaks of the silicate glass network, namely, the broad peak at 900-1200cm^{-1} and the peak at 470cm^{-1}. The onset of apatite formation is observed after 5 days of immersion in SBF on the surface of both sintered and unsintered samples, indicated by the formation of a double peak at 587 cm^{-1} and 603 cm^{-1} and the shift of the broad peak at 900-1200cm^{-1} to higher wavenumbers. After 15 days of immersion, of the unsintered samples, the silica network peaks were not visible on the spectra indicating the thickening of the apatite layer on the samples. On the other hand, the aforementioned peaks of the silica network were still present in the spectra of sintered samples, even after 25 days of immersion, indicating that the formation of apatite is delayed. The presence of a single peak at 796 cm^{-1}, attributed to the symmetric stretch of the Si-O-Si bond, indicates the presence of non-bridging oxygen, resulting to the delay of apatite crystallization. These findings are in accordance with SEM microphotographs (Fig.3) of the samples and EDS analysis, which revealed a mean molar Ca/P ratio of approximately 1.61 and 1.53 for unsintered and sintered samples respectively after 10 days of immersion in SBF.

The formation of apatite on the surface of sintered samples was delayed probably due to the persistent presence of non-bridging oxygen on their surface, indicated in the respective FTIR spectra by the peak at 796 cm^{-1}. Due to its apatite forming ability, the synthesized glass-ceramic may be suitable for bone regeneration. Further work is being carried out in order to determine its applicability for the construction of 3D scaffolds with potential use in bone tissue applications.

References

[1] M.D. O'Donnell, P.L. Candarlioglu, C.A. Miller, E. Gentlemanc, M.M. Stevens, J. Mater. Chem. 20 (2010) 8934–8941.

[2] A. Hoppe, N.S. Güldal and A.R. Boccaccini, Biomaterials 32 (2011) 2757-2774.

[3] J. Zhong and D.C. Greenspan J Biomed Mater Res 53 (2000) 694–70.

[4] C. Wu and G. Chang, J Biomed Mater Res 83B (2006) 153-160

Effect of synthesis through foam replica technique method on the porosity and mechanical strength of Cu containing scaffolds

M. Venetikidou[1], G.S. Theodorou[1], E. Kontonasaki[2], L. Papadopoulou[3], N. Kantiranis[3], P. Koidis[2], K. M.Paraskevopoulos[1]

[1]Department of Physics, [2]School of Dentistry [3]School of Geology,
Aristotle University of Thessaloniki, 54124 Thessaloniki, Greece

E-mail: gtheodo@physics.auth.gr

Bioactive glass based scaffolds are commonly used in Tissue Engineering in order to create proper conditions for 3D cell attachment, differentiation and proliferation [1]. Porosity and pore interconnectivity of scaffolds play a critical role in 3D bone ingrowth [2]. Moreover it is prerequisite that scaffolds exhibit mechanical properties similar to that of the host bone [2]. Sol-gel derived bioceramic scaffolds have been proposed as promising materials for bone tissue regeneration due to their increased surface area and apatite forming ability. One of their major advantages is that they can be fabricated with versatile properties, such as enhanced mechanical strength and porosity, by tailoring their synthesis methodology. The aim of this study was to determine in which way the number of sol-gel layered coatings affects porosity and mechanical strength of copper containing scaffolds.

The scaffolds were fabricated using the foam replica technique [3], varying the number of bioceramic slurry layers. Archimedes method was applied to measure the porosity of samples [4] and the mechanical strength of the scaffolds was studied under compression load. FTIR transmittance spectra and SEM microphotographs, for the characterization of the produced scaffolds, were obtained using Perkin-Elmer Spectrometer Spectrum in MIR region 4000-400 cm^{-1} with resolution $4cm^{-1}$ and a JEOL JMS840A Oxford ISIS 300 Detector, respectively.

Table 1: **Average strength of scaffolds under compression load**

Coatings	Compressive load (MPa)
5	0.00589±0.00231
5+1	0,00656±0.00124
8	0,01100±0.00331
8+1	0,01050±0.00233

Mechanical strength (Table 1) evaluation of all scaffolds revealed, as expected, slightly higher bearing load when more ceramic layers were added. Porosity measurements (Table 2) indicated that the average porosity of scaffolds was decreasing as more layers were deposited, while all scaffold groups exhibited average porosity over 70%. Fourier Transform Infrared Spectroscopy (Fig.1) revealed that all produced scaffolds presented the characteristic bands of silicate glasses (broad peak at $900\text{-}1200cm^{-1}$ and a peak at $496cm^{-1}$ attributed to the asymmetric stretching vibration of Si-O-Si and the bending vibration of the Si-O-Si bonds respectively).

Table 2: **Average porosity measurements of scaffolds**

Coatings	Average Porosity (%)

5	85.212±5.795
5+1	80.706±7.320
8	82.910±8.081
8+1	74.060±5.799

Additionally the FTIR spectra and XRD patterns of scaffolds with 5 and 5+1 coatings verified the presence of Wollastonite ($CaSiO_3$). These findings were confirmed by XRD patterns which are not presented here. Representative scanning Electron Microscopy microphotographs (Fig.1) showed a pore size of about 200-500 mm with good interconnectivity.

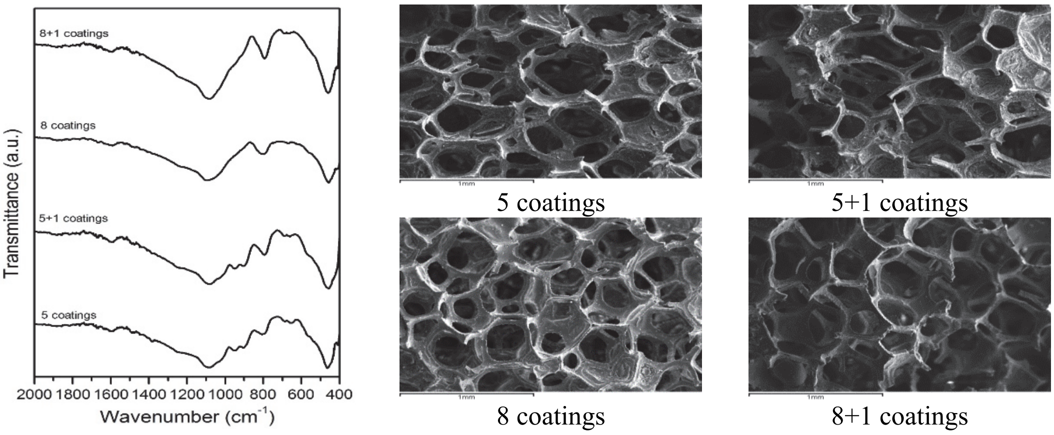

5 coatings 5+1 coatings

8 coatings 8+1 coatings

Fig.1: FTIR spectra (left) and SEM microphotographs (right) of produced scaffolds

Bioceramic scaffolds with different number of ceramic slurry layers were produced through the foam replica technique. FTIR spectra showed that all scaffolds present the characteristic bands of silicate glasses. SEM microphotographs revealed very good pore size and pore interconnectivity and Archimedes method revealed high porosity for all scaffolds. Although mechanical strength was not dramatically increased after adding more layers, variations in porosity could probably affect cells' attachment and proliferation. In vitro bioactivity tests, as well as cell biocompatibility experiments should be conducted in order to determine the bioactive response and cell proliferation rates of the synthesized scaffolds respectively, in relation to the number of applied layers, in order to reveal the optimum conditions of bioceramic scaffolds synthesis for bone tissue regeneration.

References

[1] O.M. Goudouri, E. Theodosoglou, E. Kontonasaki, J. Will, K. Chrissafis, P. Koidis, K.M. Paraskevopoulos and A.R. Boccaccini Mat. Res. Bulletin 49 (2014) 399–404

[2] J. R Jones, S Lin1, S Yue, P.D Lee, J. V Hanna, M. E Smith, and R. J Newport Bioactive glass scaffolds for bone regeneration and their hierarchical characterization (2010) 1374

[3] D.Desimone, W. Li, J.A. Roether, D.W. Schubert, M.C. Crovace, A.C.M. Rodrigues, E.D. Zanotto, and A.R. Boccaccini Sc. Techn. Adv. Mat. 14 (2013) 045008

[4] M. B Berger, The Southern Afr. Inst. of Mining and Metallurgy Refract.Conference (2010) 101-116

Development and Characterization of Epoxy Resin- Barium Tungstate Composites

S. Termine*, **S. G. Stavropoulos, E. C. Senis, O. Vryonis, G. C. Psarras**

Department of Materials Science, University of Patras, Patras 26504, Greece

*e-mail: msci1248@upnet.gr

Web: http://smatlab.upatras.gr/

Dielectrics can be used in energy storage applications due to their ability to be polarized under the influence of an external electric field. The need for energy storage systems with high energy density led to the development of polymer composite systems that combine the ease of manufacture and breakdown strength of polymers with the high dielectric constant of ceramic fillers. Polymer matrix-ceramic particles composites can be exploited in potential applications such as filters, oscillators, self-current regulators, and dielectric resonators [1,2].

In the present study 7 samples of epoxy resin and ceramic Barium Tungstate ($BaWO_4$) were developed varying the filler concentration. Filler content varied between 0 and 50 phr (parts per hundred resin per weight). Barium Tungstate, which has a scheelite structure (tetragonal phase), is an important material in the electro-optical industry with wide applications in solid-state Raman laser and laser host materials. Tungstates have good dielectric properties at microwave frequencies and low sintering temperatures, which make $BaWO_4$ a good candidate for dielectric research [2,3].

The dielectric response of the prepared samples was studied by means of Broadband Dielectric Spectroscopy (BDS) in the frequency range of 10^{-1}-10^{6} Hz and temperature interval from 30°C to 150°C. BDS has been proved to be a powerful tool for the investigation of molecular mobility, phase changes, conductivity mechanisms and interfacial effects in nanocomposite systems [4].

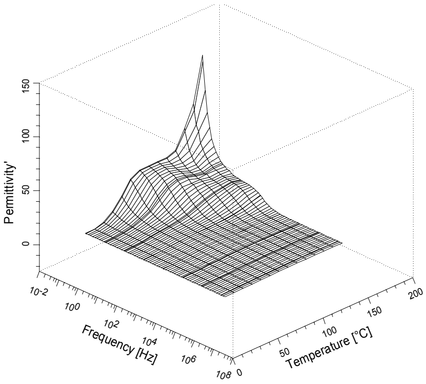

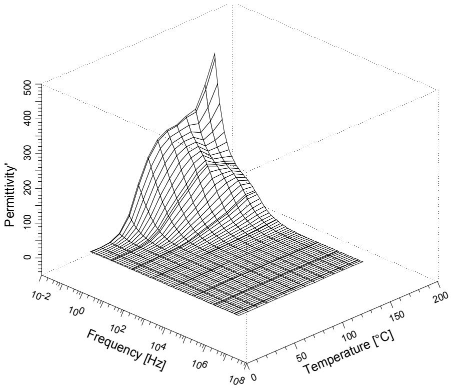

Figure 1: 3-D plots of the real part of dielectric permittivity (ε′) of the samples with 10 phr (left) and 50phr (right) Barium Tungstate content as a function of frequency and temperature.

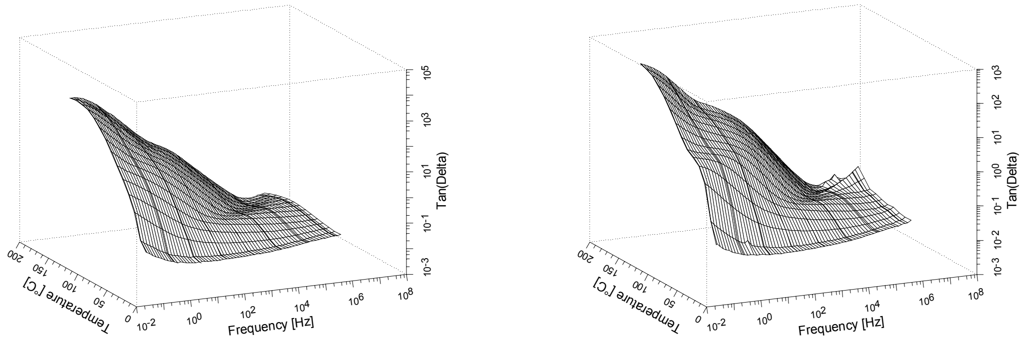

Figure 2: 3-D plots of loss tangent (tanδ) of the samples with 10 phr (left) and 50phr (right) Barium Tungstate content as a function of frequency and temperature.

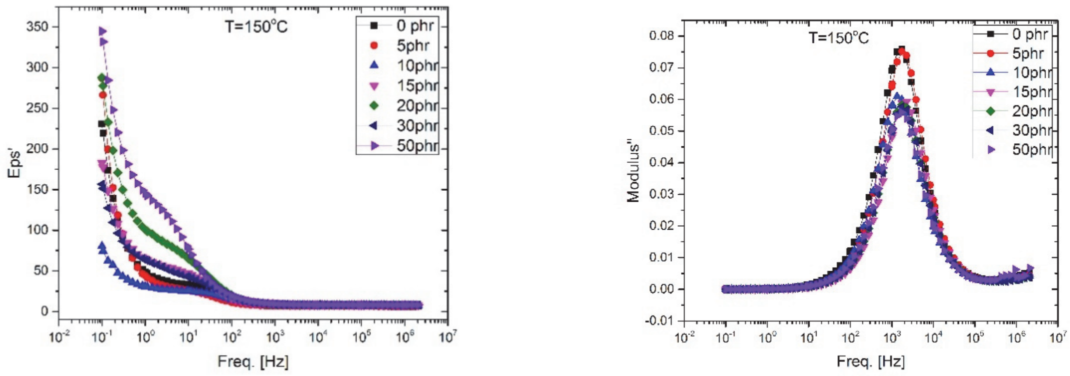

Figure 3: Comparative plots of the real part of dielectric permittivity (left) and imaginary part of the electric modulus (right) at constant temperature, T=150°C, for all studied samples.

Three distinct relaxation processes were recorded in the spectra. Experimental results imply dielectric relaxations attributed to the polymer matrix and the interactions between matrix and reinforcing phase. They were attributed to glass to rubber transition (α-relaxation), reorientation of small polar side groups (β-relaxation) and MWS-effect, also known as Interfacial Polarization (IP).

REFERENCES:

[1] Peter Barber, Shiva Balasubramanian et al., Open Access Materials 2 (2009) 1697-1733
[2] Cailan Tian, Zhenxing Yue, et al., Journal of Solid State Chemistry 197 (2013) 242–247
[3] Bo Xie, Yue Wu,et al., Journal of Crystal Growth 235 (2002) 283–286
[4] G. C. Psarras, “Conductivity and dielectric characterization of polymer nanocomposites” in “Physical Properties and Applications of Polymer Nanocomposites”, Ed. S,C Tjong and Y.W Mai, Woodhead Publishing in Materials (2010) 31-69

Synthesis, characterization and applications of copper based nanoparticles.

C. Gkanatsiou[1], O. Antonoglou[1], A. Dafnomili[1], F. Noli[1], U. Menkissoglu-Spiroudi[2]
and C. Dendrinou-Samara[1]

[1] Department of Chemistry, Aristotle University of Thessaloniki, GR-54124 Thessaloniki, Greece
[2] School of Agriculture, Laboratory of Pesticide Science, Aristotle University of Thessaloniki, Thessaloniki 54124, Greece

E-mail: christigz@chem.auth.gr

Copper based nanoparticles have attracted attention from diverse disciplines spanning from electronics, optics, sensors, catalysts, to medical applications. However, nanoscale synthesis of stable and low polydispersity Cu-based NPs remains an interesting task mainly because of the rapid air oxidation of metallic copper to Cu^{2+} ions and/or Cu_xO oxides (x = 1 or 2) and hydroxides in addition with the unique properties of the nanosizes.

We have undertaken a study on hydrothermal synthesis of Cu-based NPs in an attempt to model various properties in terms of size and composition relationships as antimicrobials and for environmental applications. In so, the antimicrobial properties of Cu-based NPs have been tested against a range of plant pathogenic bacteria (Gram+, Gram-) while they have been evaluated as nematicidals. The NPs were found with high nematicidal activity for concentrations up to 50 μg/mL. Additionally, metallic Cu and copper nitrate hydroxide nanoparticles have been prepared and characterized while their ability to adsorb radioactive elements from drinking water have been tested. The NPs were found with high uranium adsorption capacity from water while metallic Cu appears to combine redox processes with adsorption phenomena and in case of copper nitrate hydroxide nanoparticles adsorption and ion exchange phenomena can be stated.

Acknowledgement: This research has been co-financed by the European Union (European Social Fund–ESF) and Greek national funds through the Operational Program "Education and Lifelong Learning" of the National Strategic Reference Framework (NSRF)-Research Funding Program: THALES. Investing in knowledge society through the European Social Fund.

Corrosion behaviour of dissimilar metal/metal joints including reinforcing additives

I.A Kartsonakis, D. A. Dragatogiannis, E. P. Koumoulos, A. Karantonis, C.A. Charitidis*
National Technical University of Athens, School of Chemical Engineering, "Research Unit of Advanced, Composite, Nano Materials & Nanotechnology", 9 Heroon, Polytechneiou st., Zografos,
*e-mail: charitidis@chemeng.ntua.gr

The evaluation of the corrosion behavior of dissimilar metal/metal joints and a comparison with the parent metal alloys is demonstrated in the present study. The metal/matrix joints reinforced with nanoparticles are produced via friction stir welding (FSW). Friction stir welding is a solid-state joining process that uses a third body tool to join two facing surfaces and has been employed in aerospace, rail, automotive and marine industries. In the present work, dissimilar friction stir welds were produced in plates of AA 6082-T6 and AA 5083-H111 aluminum alloys using cerium molybdate (CeMo) nanocontainers, titanium-carbon (TiC) nanoparticles and carbon nanotubes (CNTs) additives as reinforcing materials (table 1). The process parameters were optimized in order to achieve non-defective welds with and without the addition of reinforcing materials. Radical polymerization as well as the sol-gel method were used for the synthesis of CeMo nanocontainers. The produced CeMo nanocontainers were then loaded with the corrosion inhibitor 2-mercaptobenzothiazole (MBT). The use of the loaded CeMo nanocontainers as additives was accomplished via their incorporation into hybrid organic-inorganic coatings that were applied on the joining faces of the aluminium plates prior to the welding process. In order to incorporate the reinforcing fillers, half volume grooves were machined at the joining faces of the plates. The morphology of the produced nanocontainers, nanoparticles and nanotubes was determined by scanning electron microscopy (SEM) and transmission electron microscopy (TEM); their elemental analysis was accomplished via energy dispersive x-ray spectroscopy (EDS). The produced TiC nanoparticles had an average size of 150-200 nm (Fig. 1a), the diameter of the synthesized CeMo nanocontainers was 230 ± 20 nm (Fig. 1b) and the external diameter of the fabricated CNTs ranged between 60 nm and 100 nm while their length was roughly 5 μm (Fig. 1c). Figure 2 demonstrates the SEM images of the cross-section of the Stir Welded metal/metal joints reinforced with CNTs (SW-CNTs) and with TiC (SW-TiC) at the welded nugget (WN), where the dark areas are attributed to the incorporation of the additives due to the presence of carbon element. The corrosion resistance of the samples (with and without additives) was studied by electrochemical impedance spectroscopy (EIS), linear polarization resistance (LPR) and linear sweep voltammetry (LSV). Corrosion test process includes the exposure of the panels to a 5 mM NaCl solution prepared with distilled water. The Bode plots of the EIS spectra obtained for samples after 24 hours of exposure to corrosive environment are demonstrated in Fig. 3; as presented, the Stir Welded metal/metal joint including CeMo (SW-CeMo) has the highest absolute total impedance value compared to the samples with TiC and CNTs or without additives. Regarding the presence of TiC and CNTs into the composite, it is observed that they do not impart additional corrosion protection to the final product compared with the SW-blank sample, as their absolute total impedance values are almost similar. Thua, this result clearly denotes that the incorporation of CeMo loaded nanocontainers during the FSW process enhances the anticorrosive properties of the final product.

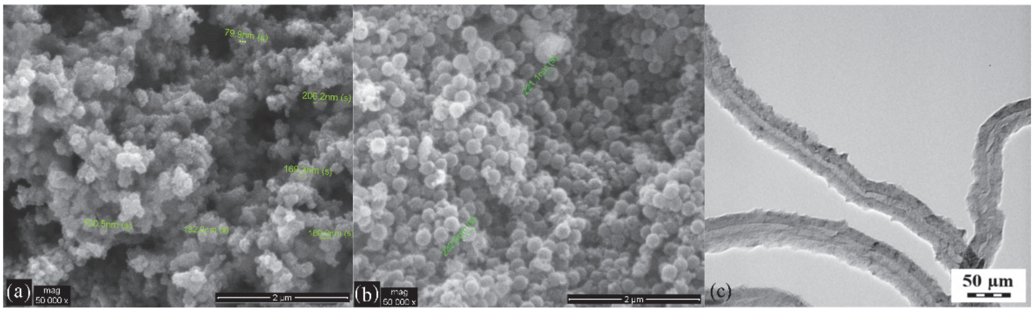

Figure 1: SEM images of TiC nanoparticles (a), CeMo nanocontainers (b); TEM image of carbon nanotubes (c).

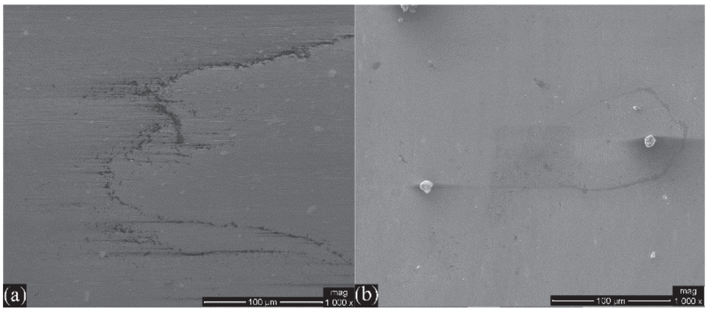

Figure 2: SEM images of the cross-section of SW-CNTs and SW-TiC at the welded nugget.

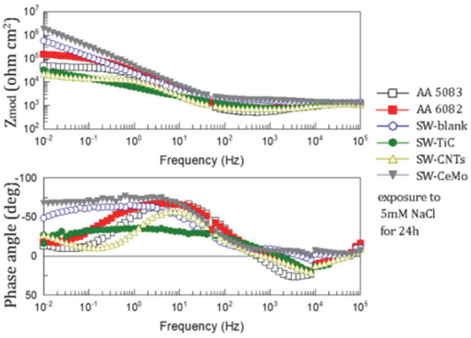

Figure 3: The Bode plots of the EIS spectra obtained for samples after 24 hours of exposure to corrosive environment.

Acknowledgement

This work was supported by the project: «SELF-HEALING NANOMATERIALS FOR PROTECTION OF METAL ALLOYS», CODE 3456& ACRONYM: "SHELL" for the National Action "ARISTEIA II" of the Operational Programme "Education and Lifelong Learning", by the European Union - European Social Fund (ESF) and National Funds through the Operational Program "Education and Lifelong Learning" (ELL), and by FP7 Collaborative project "SAFEJOINT". The abbreviation "SAFEJOINT" stands for "Enhancing structural efficiency through novel dissimilar material joining techniques" (Grant agreement no.: 310498).

TUP

P075

Study of keratin tissues by means of Small Angle X – Ray Scattering (SAXS)

C. Kamaraki[1], M. Katsikini[1], F. Pinakidou[1], E. C. Paloura[1], K. Manika[2] and D. Papakosta[2]

[1]Aristotle University of Thessaloniki, School of Physics, 54124 Thessaloniki, Greece
[2] Pulmonary Department, Arisotle University of Thessaloniki, G. Papanicolaou Hospital, Exochi 57010, Thessaloniki, Greece.

e-mail: katsiki@auth.gr

The potential applications of Small Angle X-Ray Scattering (SAXS) from biological tissue samples, like hair and nails, as a diagnostic tool of diseases such as cancer, are extensively investigated. More specifically, the X-ray scattering patterns recorded far behind the investigated sample provide information on the internal structure of the scattering particles, and especially, the structure of keratin fibrils of nails and hair. It has been proposed that the existence of specific characteristics in the scattering patterns could be associated with the donor's disease [1]. In this work, we report a SAXS study of nail samples from humans and companion animals. The scattering patterns were acquired at the I911 – SAXS beamline of the MAX-IV storage ring of Max Lab Laboratory.

The scattering patterns of the studied samples were classified according to their characteristics and quantitative analysis was applied in the intensity distributions which were extracted from the scattering patterns. Representative scattering patterns of two samples are shown in Fig. 1. The characteristic ring at q=~1.3 nm^{-1} that is evident in the scattering pattern of sample SP1946A1, indicates random orientation of the keratin fibrils. In this study, this ring appeared in the patterns of 4 of the 7 samples of cancer patients. The same ring was also found in 4 out of the 13 samples of healthy donors and cannot yet be used as a cancer indicator.

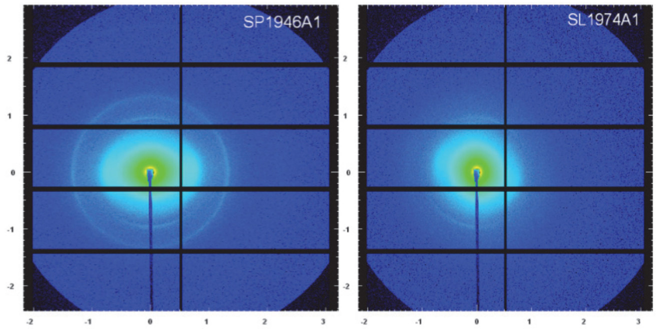

Fig. 1: Scattering patterns from the samples SP1946A1 and SL1974A1 that belong to donors affected by lung cancer. The characteristic ring is obvious only in the SP1946A1 scattering pattern.

The preliminary quantitative analysis was performed on the data from 14 selected samples. Characteristic distances between the keratin fibrils were determined from the maxima of intensity distributions along the equatorial, meridional and radial directions. Representative intensity distributions along the horizontal and vertical directions are shown in Fig. 2. From the q-values of the intensity maxima, and using the equation $d=q/2\pi$, the distance along the horizontal dimension, which represents the diameter of a keratin intermediate filament, was found approximately equal to d_{Hor}= 8-10 nm. The characteristic distance along the vertical dimension was found equal to $d_{Vert.}$=6-6.5 nm, which represents the distance between the tetramers consisting one keratin intermediate filament.

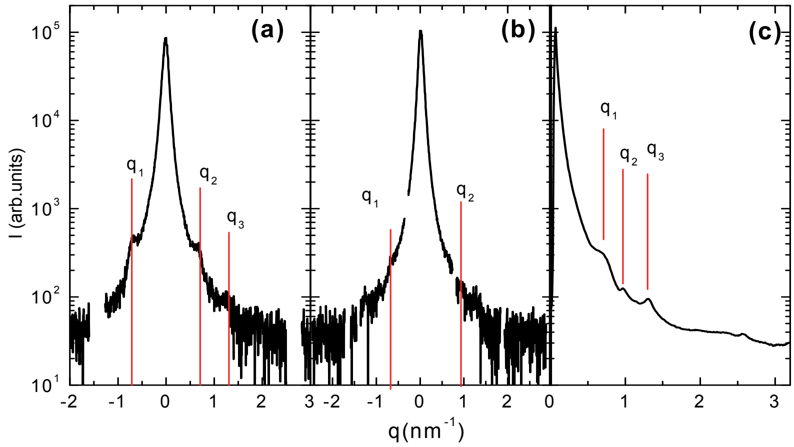

Fig. 2: Intensity distributions *vs.* q along the (a) horizontal and (b) vertical dimensions and (c) radial average for the KAL1942A sample. The maxima are denoted with q_i (i=1-3).

The size of the scattering particle, assuming of a cylindrical shape with radius R and length L, was determined using the Guinier approximation, which involves plotting lnI(q) *vs* q^2. The dimensions of the cylindrical particle were found approximately equal to R=10-12±0.3 nm and L=35-50±2 nm. Moreover, information about the “fractal” dimension of the scattering particles was deduced by the Porod approximation. This approximation involves plotting logI(q) *vs* logq with the plot’s slope providing information on the complexity of the particles. Representative Porod plots for the equatorial intensity distribution of three different samples are shown in Fig. 3. The slope was found to range between -3 and -2 corresponding to “mass fractals”, such as branched systems or networks, thus confirming the complex structure of the keratin filaments.

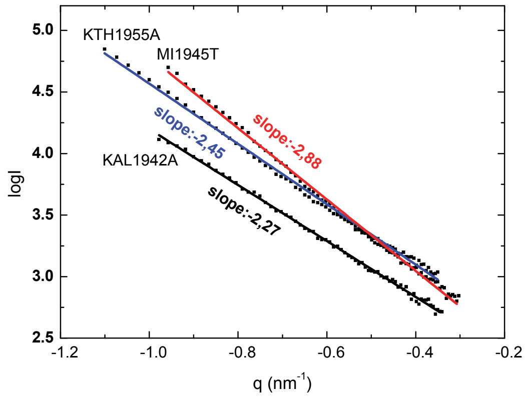

Fig. 3: Porod plots for the samples KAL1942A, MI1945T and KTH1940A. The slope’s increase is related to an increase of the structure’s complexity.

References

[1] V. James, International Journal of Cancer, **125**, 133 (2009).

Acknowledgments: The research leading to these results has received funding from the European Community's Seventh Framework Programme (FP7/2007-2013) under BioStruct-X (grant agreement N°283570).

TUP

P076

Linear and Nonlinear Optical Properties of CdTe/ZnO Core/Shell Quantum Dots

I. Chatzopoulos[1,2], Z. Zeng[1], S. Baskoutas[1] and E. Paspalakis[1]

[1]Materials Science Department, University of Patras, Patras 265 04, Greece
[2]Department of Physics and Astronomy, University of Southampton, Southampton SO17 1BJ, UK

E-mail: paspalak@upatras.gr

In this work we present new theoretical results on the linear and nonlinear optical properties of CdTe/ZnO core/shell quantum dots [1]. The quantum dot structure is shown in Fig. 1. A CdTe core is combined with a ZnO shell. The shell contains several ZnO monolayers. We first calculate the electronic structure of the quantum dot system numerically using the potential morphing method. We then use the acquired results for the energies and the electric dipole matrix elements for the calculation of the linear susceptibility $\chi^{(1)}$ [2] and the third-order nonlinear (Kerr-type) susceptibility $\chi^{(3)}$ [2] for a different number of ZnO monolayers. We also present the total intensity-dependent susceptibility χ_{tot} [2] for different intensities of the applied electromagnetic field as well as for a different number of ZnO monolayers. Typical results for $\chi^{(1)}$ and $\chi^{(3)}$ are shown in Fig. 2.

Acknowledgements: This research has been co-financed by the European Union (European Social Fund—ESF) and Greek national funds through the Operational Program “Education and Lifelong Learning” of the National Strategic Reference Framework (NSRF)—Research Funding Program: Thales, investing in knowledge society through the European Social Fund.

Fig.1: The quantum dot structure under study contains a CdTe core and several monolayers of ZnO shell.

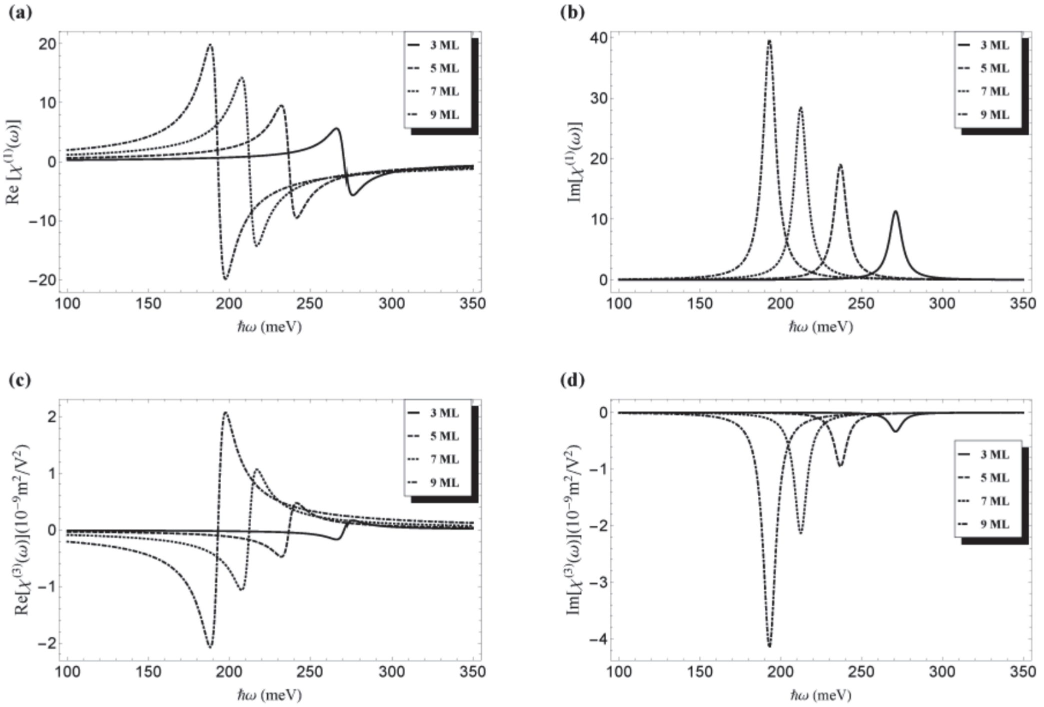

Fig. 2: The real (a) and imaginary part (b) of $\chi^{(1)}$ as well as the real (c) and imaginary (d) part of $\chi^{(3)}$ for a different number of ZnO monolayers in a CdTe/ZnO core/shell quantum dot.

References

[1] Z. Yuan, Q. Ma, A. Zhang, Y.Q. Cao, J. Yang and P. Yang, J. Mater. Sci. 47 (2012) 3770-3776.

[2] Z. Zeng, E. Paspalakis, C.S. Garoufalis, A.F. Terzis, and S. Baskoutas, J. Appl. Phys. 113 (2013) 054303.

TUP

P077

Optimization of out of plane optical coupling between optical/optoelectronic components and optical waveguides

T. Vezyrtzis[1], K. Vyrsokinos[1] and S. Ves[1]

[1]Solid State Physics Department, School of Physics, Aristotle University of Thessaloniki, 54124, Thessaloniki, Greece

E-mail: kv@auth.gr

Efficient out of plane coupling is a key technology for enhanced flexibility in the design and fabrication of 3D integrated systems targeting information transfer by optical means. The light beam coming out of an optical source should be steered and reoriented in a different plane that will enable the connection between optical components lying in different layers. In this paper it is investigated the coupling from a Vertical Cavity Surface Emitting Laser (VCSEL) and a Si Grating Coupler (GC) to an optical waveguide embedded in a Printed Circuit Board (PCB) framing a 90^0 and a 82^0 relative angle, respectively. Both sources are assumed to be flip chip bonded on top of a Through Silicon Vias (TSV) formed on a Si interposer that is assembled on top of the PCB. The light steering is achieved through a glass lens shaped at the bottom side of the TSV and either a 45^0 reflector or a curved reflector embedded in the PCB. Vertical light redirection has been implemented so far only for absolute 90^0 angle, addressing coupling from VCSELs to waveguides by the exploitation of the 45^0 Total Internal Reflection Mirrors (TIRMs). Various methods have been proposed for the patterning of the TIRMs in PCBs such as laser cutting [1], mold imprint [2] and dicing with a 45^0 dicing blade [3] with 60%, 65% and 66% coupling efficiency, respectively. In the present paper it is demonstrated through simulations that losses can be nearly minimized to less than 8% for both optical setups with the optimization of the coupling system parameters.

The initial setup under investigation is the straightforward setup of coupling light between a Single Mode (SM) VCSEL and a SM optical waveguide that is illustrated in Fig. 1(a). The laser source is emitting at 1550nm wavelength with a 3.5μm mode diameter, 11.2^0 divergence angle and a homogeneous beam profile. The SM waveguide is emulated by a photodetector with a 10x10μm^2 cross section. The VCSEL is mounted on top of the 100μm thick Si interposer at 30μm height and is emitting downwards to the TSV of 50μm diameter. Simulations have revealed that any TSV diameter above 30μm does not impose loss of signal through reflections in TSV's inner sidewalls. The beam is then propagating through a combination of an orthogonal and a spherical lens with refractive index of n=1.44 and Abbe number V=67.8 that parallelize the rays. The light is reoriented horizontally through an 80x80μm^2 45^0 mirror embedded in the PCB. With the simulation software the two parameters of lens thickness and curvature radius were scanned and the results are presented in Fig. 1(b). Maximum coupling efficiency of 97.3% is obtained for thickness and radius of 70μm and 61μm respectively.

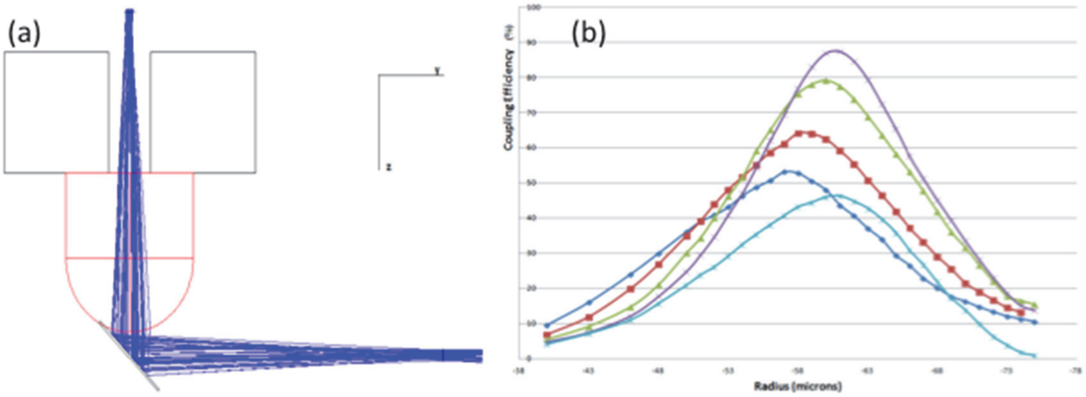

Fig. 1: (a) Side view of optical setup for VCSEL to waveguide coupling at maximum efficiency, (b) Coupling efficiency for different combinations of lens thickness and radius; blue, red green, magenta and light blue lines correspond to lens thickness of 0μm, 20μm, 45μm, 70μm and 90μm respectively.

Subsequently are presented the results by the replacement of the VCSEL with a Si GC in the optical setup. The side view of the system is depicted in Fig. 2(a). The beam is propagating now under 8^0 relative to the vertical axis forming an 82^0 angle with the optical waveguide and is propagating again through the same TSV of 100μm thickness and 50μm diameter. At the bottom side is attached a spherical lens of variable radius with n=1.44 and V=67.8. Embeded in the PCB there is a curved reflector with variable radius and slope. The efficiency is again calculated by measuring the power collected by a $10x10\mu m^2$ photodetector. Scanning of the three parameters reveals that maximum efficienty of 92.3% (Fig. 2(b) is obtained for lens radius of 56μm and reflector curvature and slope of 830μm and 47.9^0, respectively.

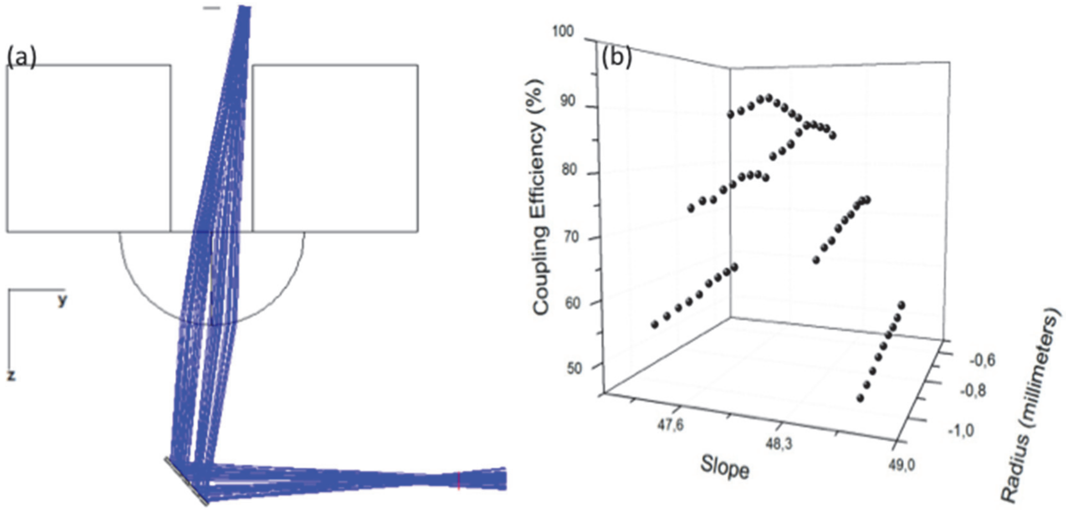

Fig. 2: (a) Side view of optical setup for GC to waveguide coupling at maximum efficiency, (b) Coupling efficiency for various reflector parameters and fixed lens radius of 56μm.

References

[1] T. G. Lim et. al., IEEE Trans. Advanc. Packag. 32 (2009) 509-516.
[2] X. Lin et. al., OSA Opt. Exp. 21 (2015) 4736–4750.
[3] M. Tokunari et. al., IEEE/OSA J. Lightw. Technol. 32, (2013) 1207-1712.

Natural Dose Evaluation using Thermoluminescence and component resolved Optically Stimullated Luminescence analysis.

TUP

P078

M. Karampiperi[1], **I. K. Sfampa**[1], **N. Kazakis**[2], **N. C. Tsirliganis**[2] **and G.Kitis**[1]

[1] *Aristotle University of Thessaloniki, Nuclear Physics Laboratory, 54124-Thessaloniki, Greece*
[2]*Laboratory of Radiation Applications and Archaeological Dating, Department of Archaeometry and Physicochemical Measurements, 'Athena' - Research and Innovation Center in Information, Communication and Knowledge Technologies, Kimmeria University Campus, 67100, Xanthi, Greece.*

E-mail: makaramp@physics.auth.gr

Introduction: Fired ceramics are used to make everyday objects like tiles, bricks and plates. They were also used in ancient world as vessels, amphorae and cookware, because of the development of pottery art. Luminescence techniques are frequently applied in archaeological science for absolute dating studies [1] or for the characterization of materials of archaeological interest.

In the present study, an integrated approach towards the comparison between the different types of luminescence dating is attempted. Namely, are compared results from thermoluminescence (TL) and optically stimulated luminescence (OSL). Specifically, the comparative study includes the Single Aliquot Regeneration Method (SAR) [3], the multiple aliquot additive dose method (MAAD) and the very deep traps (VDT) method [2].

Experimental Procedure: Measurements were carried out using a Risö TL/OSL reader (model TL/OSL (DA-15)), equipped with a ^{90}Sr/^{90}Y beta particle source, delivering a nominal dose rate of 0.075 Gy/s. A 9635QA photomultiplier tube is used for light detection. All measurements were performed in a nitrogen atmosphere with a low constant heating rate of 2^0C/s, in order to avoid significant temperature lag.

Aliquots were prepared under the fine grain technique [4]. Concerning the OSL measurements two types were used: Linear Modulated – OSL (LM – OSL) and Continuous Wave – OSL (CW – OSL). Each data point reported in this paper was the average of two measurements carried out on two different aliquots/disks.

Generally speaking, both protocols, SAR and MAAD have advantages and disadvantages. SAR protocol includes measurements with a single aliquot. In this case, a correction for samples with sensitization is necessary. On the other hand, MAAD protocol requires measurements on different samples (more than 10 samples were used). This procedure erases the problem with the sensitization but initiates a new one concerning the mass reproducibility.

In the following table are presented the protocols that were applied during the experimental procedure.

Results and Discussion: Following are presented several of the experimental results. There are the glowcurves (TL) of the MAAD protocol presenting the sample’s dose response (Figure 1, left). Finally, there are presented the CW-OSL curves of the SAR protocol (Figure 1, right).

Table I: Summary table of the protocols.

Steps	**SAR**	**MAAD- TL, VDT**	**MAAD- OSL, VDT**
1	Dose Di	Dose Di on NTL (NTL + Di)	Dose Di on NTL (NTL + Di)
2	Preheat at 220°C for 10 sec	TL (up to 500°C)	Preheat at 280 °C for 10 sec
3	CW OSL at 125 °C for 100 sec	CW OSL at 180°C for 500 sec	LM OSL at 125 °C for 500 sec
4	TestDose = 5Gy	RTL (up to 500°C)	RTL (up to 500°C)
5	Heat up to 160 °C	Repeat for new Di (Di= 10,15,25 Gy)	CW OSL at 180°C for 500 sec
6	CW OSL at 125 °C for 100 sec		RTL (up to 500°C)
7	Repeat for new Di (Di=10,15,25,0,10Gy)		Repeat for new Di and fresh aliquot (Di =10,15,25 Gy)

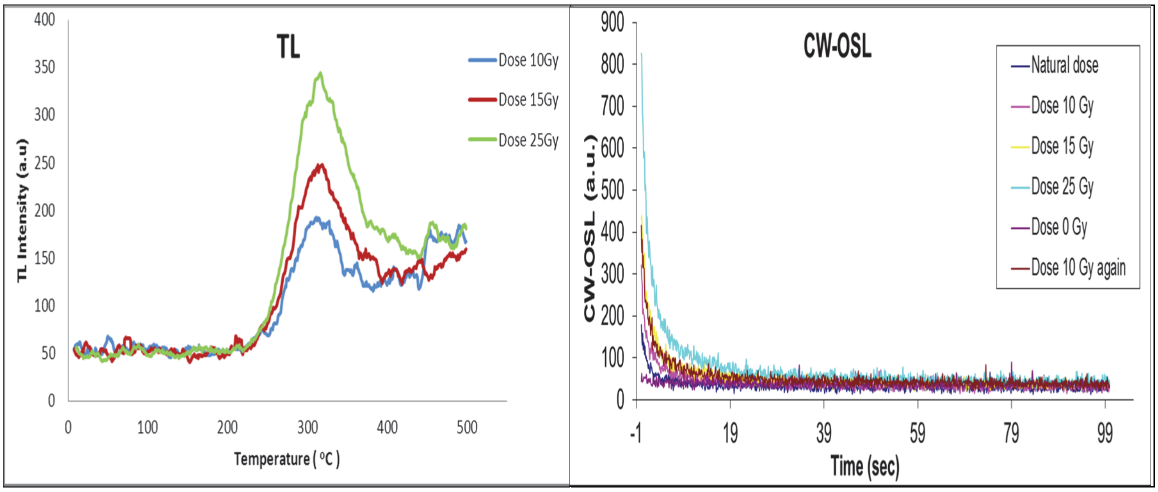

Fig. 1: (Left) Glowcurves showing the sample's Dose Response, (Right) CW-OSL measurements from the SAR protocol.

The experimental procedure is followed by a component resolved Optically Stimulated Luminescence analysis in order to explain the physical meaning of the results.

References

[1] Aitken, M.J., London, Academic Press (1985).
[2] G.S. Polymeris, V. Giannoulatou, I.K. Sfampa, N.C. Tsirliganis, G. Kitis, J. of Luminescence 153(2014)245-251.
[3] A.S. Murray, A. G. Wintle, Radiation Measurements (2000)57–73.
[4] Zimmerman, D. W. Archaeometry(1971), 13(1), 29-56.

Polysterene on 101 nm Nitride on Si

A. Sotiropoulos[1] , **Th. Speliotis**[1], **E. Spyratou**[1], **I. Raptis**[3], **E. Lidorikis**[2],
K. Misiakos[1] **and D. Niarchos**[1]

[1] Institute of Nanoscience and Nanotechnology, NCSR Demokritos, Aghia Paraskevi 15310, Attiki,Greece
[2] University of Ioannina, Department of Materials Science and Engineering, 45110 Ioannina, Greece
[3] ThetaMetrisis S.A., Polydefkous 14, 12243, Aigaleo, Greece

E-mail: a.sotiropoulos@inn.demokritos.gr

Fischer and Zingsheim [1] are the first to report, in 1981, the formation of an ordered polysterene (PS) monolayer on a glass plate. They simply deposited a suspension of colloidal PS spheres with a diameter of 312 nm and allowed it to evaporate. They obtained small area particle monolayers. The term of “naturally” assembled PS latex nano-spheres (NS) was then introduced. However, the focus of their work was the replication of submicroscopic patterns using visible light and not fabrication of lithographic colloidal masks. A year later, Deckman and Dunsmuir [2] extended the scope of the approach of Fischer showing that a monolayer of nano-spheres can be used both as a 'deposit material’ and as a lithographic mask.

In this work, 1.5mm×1.5 mm silicon wafers with thermally grown Nitride (101 nm) were used as substrates. Colloidal dispersion is prepared as follows: Triton X-100 is diluted with methanol by 0.1 ml : 40 ml. Triton is used to make the substrate hydrophilic and bond the particles with the substrate. This solution is then mixed with an equal volume (~0.08 ml) of polystyrene beads with mean diameter 600 or 460 nm as described in literature [3]. The final polystyrene bead solution is then spin-coated on PMMA plates in order to form close-packed monolayer polystyrene nano-spheres using a two stage spinning protocol [4]. The first step is a slow one (~800 rpm) with low acceleration, in order to coat the whole sample uniformly. The second step is faster (1000 rpm or 1300 rpm) in order to remove the excess bead solution. We applied experimental design to spin coating, to evaluate the efficiency of this method to extract and model the relationships between the experimental parameters and the degree of ordering in the particles monolayers.

The reflectance measurements were conducted by a FR-basic tuned to operate in the 400-1000 nm spectral regime equipped with an integrating sphere with a 50 mm port diameter. Also, the total reflectance of PS NS structures with 300, 500 and 600 nm in diameter was simulated by FDTD analysis on a Si substrate with perfectly hexagonal close packed PS nano-spheres. For the reference measurements a standard Si wafer was used.

Results indicate that the PS NS colloidal solution has a relatively good dispersion and the nano-spheres have a uniform size and almost smooth surface and also indicate that the spin-coating method is a simple, cost-effective and high volume method to assemble monolayer and close-packed PS nano-spheres arrays. Scanning electron microscopy and Reflectance measurements was used to observe the morphological and optical properties of the PS NS array for each diameter as shown in Fig1. A relatively good result can be easily obtained by a spinning speed (second step) of : 1000 rpm for

~25 sec (600 nm diameter) or 40 sec (460 nm diameter) and 1300 rpm for ~15 or 20 sec (460 nm diameter), when each solution concentration is around 10 wt.%.

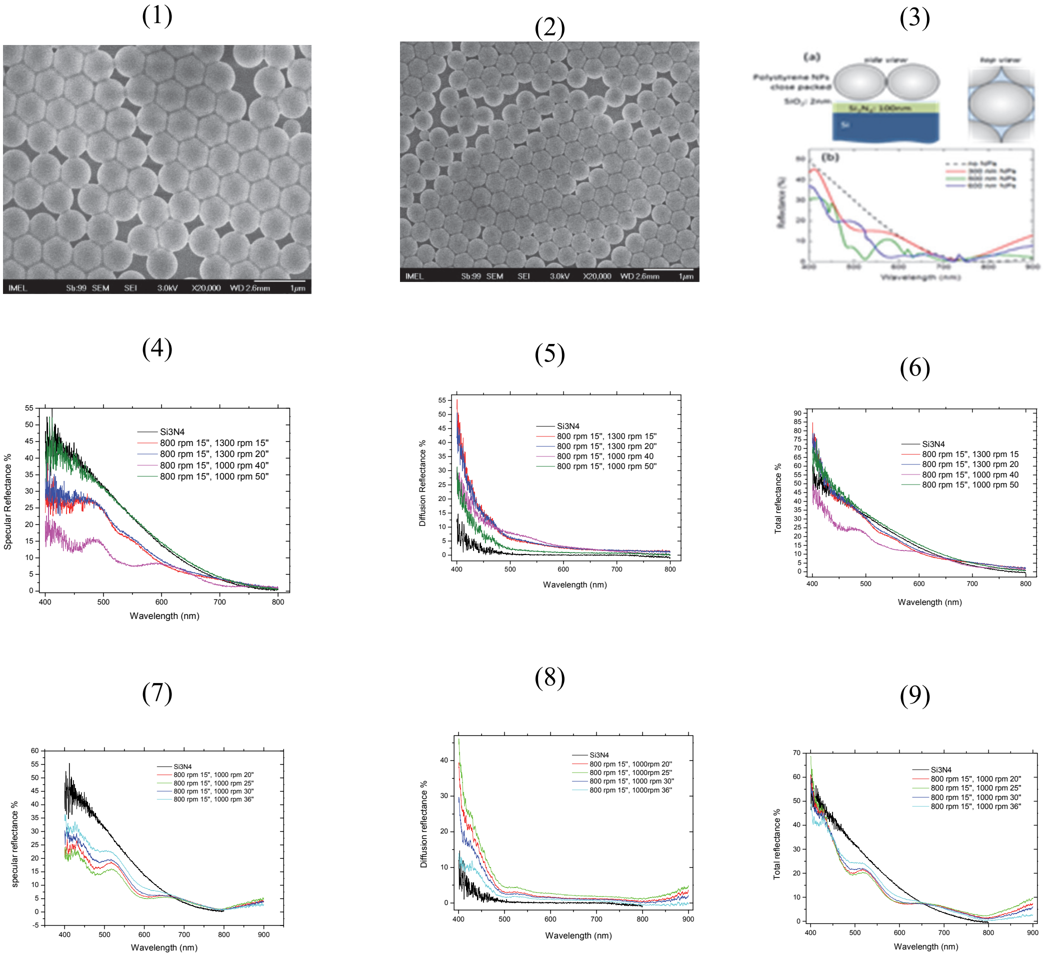
(1) (2) (3) (4) (5) (6) (7) (8) (9)

Fig.1. PS NS with mean diameter 600 nm and 460 nm on 101 nm Nitride on silicon substrate of SEM & reflectance measurements photos with magnification of : (1) SEM: x20000, diameter 600 nm:, (2) SEM: x20000, diameter 460 nm, (3) (a) perfectly hexagonal close packed PS NS, (b) Simulated Reflectance curves by FDTD analysis for 300, 500 and 600 nm PS NS in diameter, (4)–(9): Measured specular, diffusion and total reflectance spectra at normal incident for the PS nano-particles with mean diameter 460 nm ((4)-(6)) and 600 nm ((7)-(9)), respectively.

References

[1] U. Fischer and H. Zingsheim, J. Vac. Sci. Technol.. 19(4) (1981) 881-885.
[2]H. Deckman and J. Dunsmuir, Appl.Phys.Lett. 41(4) (1982) 377-379.
[3] J. Hulteen, R. Vanduyne, J. Vac. Sci. Technol. A 13 (1995) 1553–1558.
[4] C. Cheung, R. Nikolic, C. Reinhardt, T. Wang, Nanotechnology 17 (2006) 1339–1343.

Influence of nonlocality on fluorescence from a dipolar emitter coupled to a metallic nanoshell

C. Tserkezis[1], **M. Wubs**[2,3], **N. A. Mortensen**[2,3] **and N. Stefanou**[4]

[1]Donostia International Physics Center and Centro de Física de Materiales CSIC-UPV/EHU,
Paseo Manuel de Lardizabal 4, Donostia-San Sebastián, 20018, Spain
[2]Department of Photonics Engineering, Technical University of Denmark,
DK-2800 Kgs. Lyngby, Denmark
[3]Center for Nanostructured Graphene (CNG), Technical University of Denmark,
DK-2800 Kgs. Lyngby, Denmark
[4]Department of Solid State Physics, National and Kapodistrian University of Athens,
University Campus, 15784 Athens, Greece

E-mail: christos_tserkezis001@ehu.es

It is has long been known that emission from classical or quantum emitters depends not only on their intrinsic properties but also on their environment [1]. Experiments on fluorescent molecules or quantum dots in the vicinity of planar metallic surfaces [2] or photonic crystal cavities [3] have shown that, under certain conditions, large enhancement of fluorescence and spontaneous emission rates can be achieved. A particularly promising template for engineering the emitter environment is provided by metallic nanoparticles (NPs). The optical response of these NPs is dominated by localized surface plasmon (LSP) modes, which modify drastically the local density of electromagnetic (EM) states and focus EM fields in regions below the diffraction limit, opening new possibilities to control light-matter interactions.

In the past both fluorescence enhancement and quenching were observed experimentally for emitters close to plasmonic NPs. It is now understood that the final result depends on the interplay between emitter excitation, which is enhanced due to the plasmonic environment, and emission into two decay channels: radiation in the environment and ohmic losses in the metal [4]. An optimum emitter-NP distance, for which the two mechanisms lead to a maximum fluorescence enhancement, can then be obtained. This is shown Fig. 1(a) for an emitter, described here as a classical dipo-le of dipole moment **p** parallel to the external electric field **E**, placed at a distance d from the surface of a spherical gold NP with radius $R = 40$ nm. The dipole is excited at wavelength $\lambda = 532$ nm and emits at $\lambda = 560$ nm, values which are appropriate for Rhodamine 6G, and R is selected so that the plasmon resonance lies close to these wavelengths (516 nm). It can be seen that fluorescence, η, is enhanced by about 2.5 times if the dipole is 20 nm away from the NP surface. This value could be significantly enhanced if absorptive losses in the metal were reduced, by choosing for example a different NP material. Silver is a good plasmonic material characterized by low absorptive losses. However, for a silver sphere of similar size, the main LSP peak is at much shorter wavelengths (about 360 nm). In order to bring the LSP reso-nance within the wavelength region of interest, we take advantage of the tunability provided by hybridization of the plasmonic modes excited at the inner and outer sur-faces of a metallic nanoshell [5]. To this end, in Fig. 1(b) we consider a complex NP consisting of a SiO_2 core of radius $R_1 = 32.7$ nm, covered by a silver shell of thick-ness 7.3 nm, parameters which were chosen so that the total radius R and LSP wavel-ength remain the same as in Fig. 1(a). Reduction of ohmic losses in the metallic mate-rial leads then to much stronger fluorescence enhancement, of more than an order of magnitude, and this holds for a much larger range of emitter-NP distances [6].

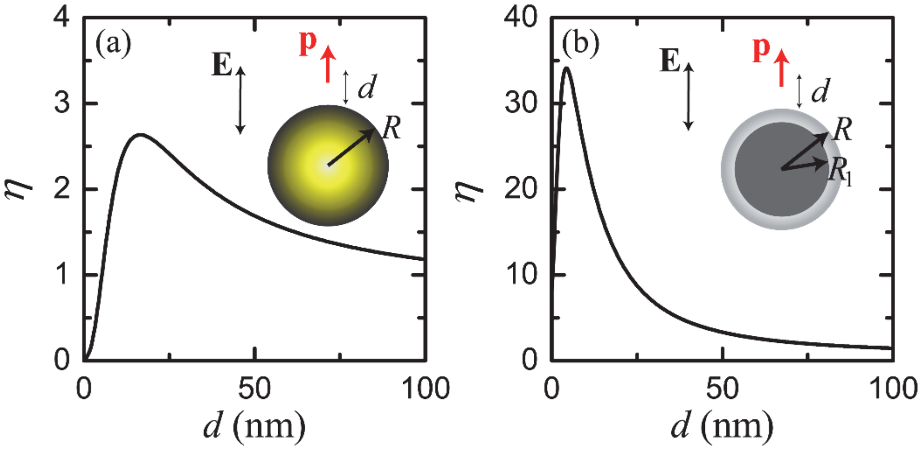

Figure 6: (a) Dependence of fluorescence enhancement, η, for an emitter with dipole moment **p**, polarized parallel to the external electric field **E**, on distance d from a gold nanosphere of radius R = 40 nm. (b) Same as (a), for a silver nanoshell consisting of a SiO_2 core of radius R_1 = 32.7 nm and a silver shell of thickness 7.3 nm, so that the total NP radius is R = 40 nm.

An important issue that arises when such emitters are placed close to plasmonic NPs, or when the metallic shell of the NP is very thin, is that the nonlocal character of the dielectric function of the metal becomes relevant. For example, it was recently shown, through theoretical studies with a simple hydrodynamic model, that emission rates for a classical dipole in the vicinity of a metallic NP can be significantly redu-ced because of nonlocality [7]. Within the same model, it has also been shown that strong shifts of the plasmonic modes are also expected [8]. Here we will explore the-se issues in a systematic way, and study the effect of nonlocality for different NP si-zes, shell thicknesses, and emitter distances, by use of both the hydrodynamic model and the recently proposed Generalized Nonlocal Optical Response theory [9]. Our re-sults are expected to shed light on the importance of a description of the optical response of plasmon-emitter hybrids that goes beyond classical electrodynamics and facilitate the design of novel architectures for controlling light-matter interactions.

References

[1] E. M. Purcell, Phys. Rev. 69 (1946) 681.
[2] R. R. Chance, A. Prock and R. Silbey, Adv. Chem. Phys. 37 (1978) 1-65.
[3] P. Lodahl, A. F. van Driel, I. S. Nikolaev, A. Irman, K. Overgaag, D. Vanmaekelbergh and W. L. Vos, Nature 430 (2004) 654-657.
[4] P. Anger, P. Bharadwaj and L. Novotny, Phys. Rev. Lett. 96, (2006) 113002.
[5] E. Prodan, C. Radloff, N. J. Halas and P. Nordlander, Science 302 (2003) 419-422.
[6] C. Tserkezis, *Light emission and propagation in nanostructured plasmonic metamaterials*, PhD Thesis, National and Kapodistrian University of Athens (2012).
[7] R. Filter, C. Bösel, G. Toscano, F. Lederer and C. Rockstuhl, Opt. Lett. 39 (2014) 6118-6121.
[8] C. Tserkezis, G. Gantzounis and N. Stefanou, J. Phys.: Condens. Matter 20 (2008) 075232.
[9] N.A. Mortensen, S. Raza, M. Wubs, T.Søndergaard and S. I. Bozhevolnyi, Nature Commun. 5 (2014) 3809.

Growth and optical characterization of GaAs-InGaAs core-shell piezoelectric nanowires on silicon substrates

K. Moratis[1], S. Germanis[1,2], C. Katsidis[1], M. Androulidaki[2], K. Tsagaraki[2], Z. Hatzopoulos[1,3] and N.T. Pelekanos[1,2]

[1]Department of Materials Science and Technology, University of Crete, P.O. Box 2208, 71003 Heraklion, Greece.
[2]Microelectronics Research Group, IESL-FORTH P.O. Box 1385, 71110 Heraklion, Greece.
[3]Department of Physics, University of Crete, P.O. Box 2208, 71003 Heraklion, Greece

E-mail: moratisk@materials.uoc.gr

Semiconductor nanowires are currently under extensive study, due to the inherent quantum phenomena related to the nanowire (NW) configuration, leading to the development of novel optoelectronic devices and applications, such as for instance cost-effective and high efficiency photovoltaic devices. In this work, we present the growth and optical characterization of core-shell GaAs/InGaAs NWs grown on silicon substrates. Our goal is to exploit the large piezoelectric fields, emerging from the significant lattice-mismatch strain between core and shell materials in this NW heterostructure, in order to increase carrier recombination lifetimes and enhance the overall carrier collection efficiency in future photovoltaic applications.

The samples are grown on n+ Si (111) substrates by molecular beam epitaxy (MBE) via the Ga-assisted vapor-liquid-solid (VLS) mechanism. After an initial annealing of the substrates at 650^{o}C for 10min in the MBE chamber, the substrate temperature is set to 600^{o}C, and Ga is pre-deposited for 20s, to form droplets on the substrate. Next, the GaAs core is VLS-grown for 30min, leading to GaAs NWs with an average diameter of 63nm, length of 3 μm and a density of $2\cdot10^{8}$ cm^{-2}. Once the core part is grown, the Ga droplet on the NW tip is removed by exposing the sample to As flux for several minutes. Then, in order to grow the InGaAs shell, the V/III flux ratio is adjusted for two-dimensional growth and the substrate temperature is lowered to 500^{o}C. Several samples, having identical GaAs core, but different InGaAs shell thicknesses between 1 and 50nm and compositions between 5-10%, are grown. Reference samples having only GaAs core NWs are grown as well.

In Figure 1, SEM top-view and cross-section images are shown from a typical GaAs/In$_{0.10}$Ga$_{0.90}$As core-shell NW sample, for which the shell growth time is 40min. While the average NW length and density remain similar to those of the reference GaAs NWs, the NW diameter is increased significantly giving an average value <d> of 165 nm, indicating a shell thickness of ≈50nm. The In incorporation in the InGaAs shell is independently confirmed by micro-Raman measurements to be ≈10%. From photoluminescence (PL) studies on ensembles of NWs the following conclusions can be drawn: (i) the band-edge exciton emission peak from the GaAs core, redshifts with increasing shell thickness, in agreement with the tensile stress applied to the core by the shell layer. However, the observed redshifts are smaller than those expected based on the In composition obtained from micro-Raman, which possibly suggests either inhomogeneous distribution of In in the shell, or plastic relaxation reducing the average strain in the NW. (ii) There is a broad emission band between 880-980 nm directly related to the InGaAs shell, which redshifts with increasing shell thickness, as shown on the left-hand side of Figure 2. Furthermore, as confirmed by micro-PL experiments on single NWs, this broad band consists of sharp lines, attributed to recombination in In-rich enclosures in the shell. Ongoing transmission microscopy experiments will shed light on the structural details of this interesting NW heterostructure and will allow enhanced understanding of its optical properties.

This work is supported by the European Social Fund and National resources through the THALES program "NANOPHOS", the ARISTEIA II program "NILES", and the PROENYL research project, Action KRIPIS, project MIS-448305 funded by the General Secretariat for Research and Technology, Ministry of Education, Greece and the European Regional Development Fund (Sectoral Operational Programme: Competitiveness and Entrepreneurship, NSRF 2007-2013)/European Commission.

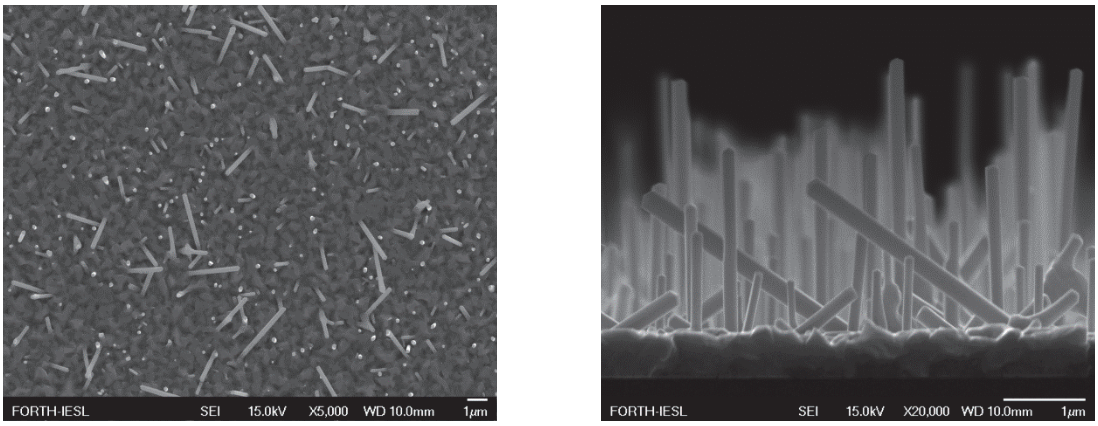

Figure 1: SEM images from GaAs/InGaAs core-shell nanowires. *Left:* top-view. *Right:* cross-section.

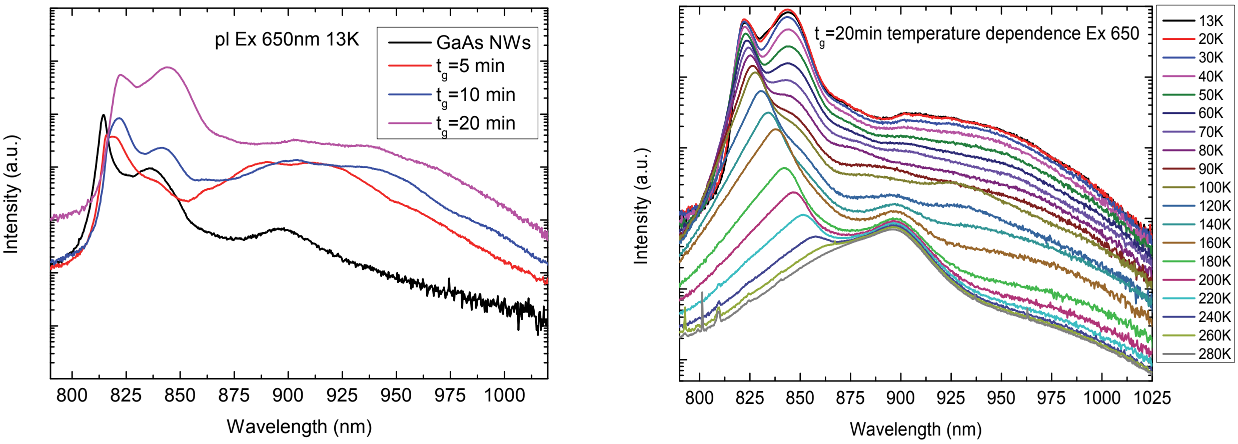

Figure 2: *Left:* PL spectra from ensembles of GaAs/InGaAs core-shell NWs with different shell growth time and thickness. *Right:* temperature-dependent PL spectra for the core-shell NWs with 20 min shell growth time.

The Role of Intentional and Unintentional Nitridation of Si (111) in the Growth of GaN Nanowire by Plasma Assisted Molecular Beam Epitaxy

S. Eftychis[1], **J. Kruse**[1,2], **A. Adikimenakis**[2], **K. Tsagaraki**[2] , **M. Androulidaki**[2], **T. Koukoula**[3], **Th. Kehagias**[3], **Ph. Komninou**[3], **E. Iliopoulos**[1,2], **Z. Hatzopoulos**[1] **and A. Georgakilas**[1,2]

[1]Physics Department, University of Crete, P.O. Box 2208, 71003 Heraklion, Greece
[2] Microelectronics Research Group, IESL/FORTH, P.O. Box 1385, 71110 Heraklion, Greece
[3] Physics Department, Aristotle University of Thessaloniki, GR-54124 Thessaloniki, Greece

E-mail: eftychis@physics.uoc.gr

When GaN is deposited on a Si (111) substrate by Plasma Assisted Molecular Beam Epitaxy (PA-MBE) under N-rich conditions and at high temperatures, GaN nanowires (NWs) are formed. An amorphous SiN layer is also formed at the interface between GaN NWs and Si(111).

In this work, we study the role of the Si (111) substrate nitridation, and the effect it has on the nucleation and the properties of the NWs. Two samples were grown by PA-MBE. In sample A, GaN was deposited directly on a bare Si (111) surface and in sample B, an intentional nitridation of the Si (111) surface preceded the GaN deposition.

The samples are analysed by field-effect scanning electron microscopy (FE-SEM) to find their morphological characteristics. X-ray diffraction measurements reveal the alignment of the NWs and their crystallographic orientation with respect to the Si (111) substrate. KOH etching tests are performed to identify the polarity of the GaN NWs and photoluminescence measurements (PL) are made to evaluate their optoelectronic properties. High resolution transmission electron microscopy (HRTEM) is used to study the interface between the NWs and the substrate and to identify the epitaxial relationship between the GaN and the Si (111) surface.

We observe an improvement in the alignment of the NWs in the intentionally nitridated sample B compared to sample A, as indicated by FE-SEM images, and from the FWHM of the (0002) GaN XRD rocking curves (5.6° in sample A compared to 3.4° in sample B). Measurement of the diameter of the NWs reveal a smaller diameter in sample A (25nm) compared to that of sample B (40nm). HRTEM analysis of the interfacial layer show that in the case of sample A, some regions have a crystalline interface while some others have a amorphous SiN layer. On the other hand, sample B has a continuous amorphous interfacial layer on which GaN NWs grow. PL spectra taken at 20K reveal relaxed GaN NWs in both samples, with the Donor-Bound exciton located at 3.470eV.

This work contributes to a better understanding of the nucleation mechanism of the GaN NWs. The role of the amorphous SiN in the growth and the properties of the NWs are revealed through a comparison between intentional and unintentional nitridation of the Si (111) substrate.

Acknowledgments: this research has been co-financed by the European Union (European Social Fund – ESF) and Greek national funds through the Operational Program "Education and Lifelong Learning" of the National Strategic Reference

Framework (NSRF) - Research Funding Program: THALES.

Optical Point spread function as a method for testing dynamic operation of CCDs

V.E. Gavriil[1], A. C. Cefalas[1], Z. Kollia[1] and E. Sarantopoulou[1]

[1]National Hellenic Research Foundation, Theoretical and Physical Chemistry Institute, 48 Vassileos Constantinou Avenue, Athens 11635 Greece

E-mail: vgavriil@eie.gr

TUP

P083

Point spread function (PSF) is the response of an optical system to a point light source. The convolution of the PSF, which is the function that describes an optical projection system, with the function of the light source (input function), is a measure of the resolution of an optical and the image analysis systems, such as an iris/lens optical system and a CCD-CMOS sensor. In this work, a theoretical calculation of exit functions accounts for both diffraction and aberration parameters (comma, astigmatism, etc). Theoretical results were used to evaluate experimentally the efficiency and the operational limits of a CCD-CMOS sensor and the minimum spot size of a lithographic projection system of a ps second harmonic Nd-YAG laser at 532 nm. For this type of laser, a minimum spot size of 10μm taken with a simple iris/lens optical system is well within the resolution limits of 6μm of the CMOS-sensor.

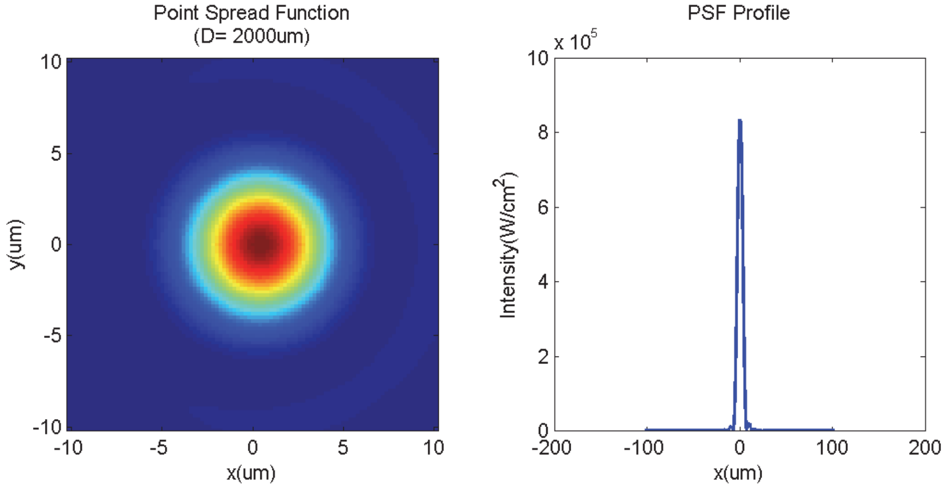

Figure 1 Calculated Point Spread Function of a lithographic projection system (focal length f=22.5mm and entrance pupil D=2mm)

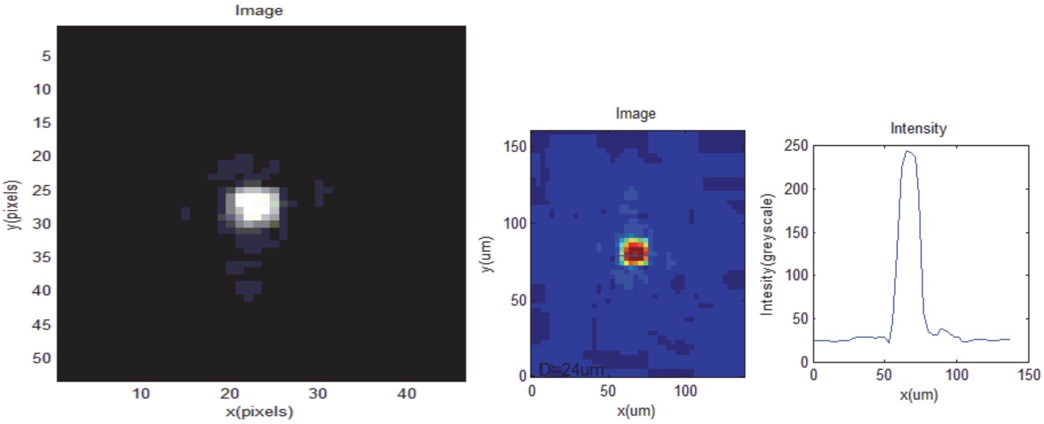

Figure 2 Exit function as recorded in a CCD-CMOS sensor of a lithographic projection system (focal length f=22.5mm and entrance pupil D=2mm) of a ps second harmonic Nd-YAG laser at 532 nm.

Catalyst-free growth of GaN NWs on Si (111) and *r*- plane sapphire

**T. Koukoula[1], T. Kehagias[1], A. Lotsari[1], G.P. Dimitrakopulos[1], J. Kioseoglou[1],
Th. Karakostas[1], S. Eftychis[2], A. Adikimenakis[2], J. Kruse[2],
A. Georgakilas[2], Ph. Komninou[1]**

[1]Physics Department, Aristotle University of Thessaloniki, GR-54124 Thessaloniki, Greece
[2] Microelectronics Research Group, IESL, FORTH, P.O. Box 1385, GR-71110 Heraklion, and
Physics Department, University of Crete, P.O. Box 2208, GR-71003 Heraklion, Greece

E-mail: tkouk@auth.gr

High quality III-N nanowires (NWs) are promising nanostructures for a variety of technological applications, as opto-, micro-electronics, solar cells and chemical sensors. Important properties emerge from their high surface/volume ratio, stress-free state, absence of structural defects and minimization of the polarization effect which is the main drawback for optoelectonics in the commonly used polar growth (along *c*-axis) of thin films and nitride multilayered nanostructures. For non-catalytic growth molecular beam epitaxy (MBE) is the most reliable technique that results in high uniformity of NWs. The substrate surface treatment is a key parameter for GaN NWs growth which delineates their morphological features and crystal quality. Silicon substrate is used due to its excellent physical properties and low cost and sapphire is desirable due its optical transparency.

In this work, we present a transmission electron microscopy (TEM) investigation accomplished to elucidate the spontaneous nucleation, the morphology and the interfacial structure of GaN NWs grown on (111) Si and *r*-plane sapphire, by plasma-assisted MBE. Regarding Si substrates, AlN nucleation layers (NLs) of varying thickness were deposited and GaN NWs were subsequently grown either on the as-grown or on high temperature annealed NLs under nitrogen flux. In the case of *r*-plane sapphire substrates, different nitridation processes were investigated.

It was found that when a 0.5-1.5 nm thick nitridated or as-grown AlN NL was deposited prior to GaN NWs growth, the formation of amorphous Si_xN_y layer was eliminated from the interfacial area and improved alignment and crystal quality of the GaN NWs was achieved. For thinner NLs, a thin Si_xN_y layer was formed, while for thick AlN layers GaN NWs growth was suppressed. The overall NWs morphology is shown in the XTEM micrographs of Fig. 1, for GaN NWs grown on (a) a 1.5 nm nitridated AlN NL and (b) a 1.5 nm as grown AlN NL. GaN islands along with GaN NWs are observed in the first case while a very thick rough GaN base layer grown along with the NWs in the latter. We concluded that, in the initial stages of AlN NL growth, and under the condition that the NL thickness does not surpass the critical thickness of AlN growth on Si (111), AlN forms strained 3D islands that act as nuclei for the spontaneous growth of GaN NWs. Subsequent annealing transforms the AlN NL into a partially-relaxed compact 2D layer that favors the formation of GaN faceted domains.

In the case of *r*-plane sapphire substrate, the NWs were grown along the *c*-axis forming a ~61° with respect to the substrate normal. The nitridation process introduced a periodical step array morphology. These steps acted as nucleation points where two variants of inclined NWs were grown as shown in Fig. 2(a). Moreover, the density and size of the NWs depended on the nitridation duration, the power of and the III/V flux ratio. It was revealed that the NWs were grown either directly on sapphire surface protrusions or on small semipolar GaN nanocrystals, as shown in Fig. 2(b). Between the NWs a thin nonpolar *a*-plane GaN film was also grown. The orientation relationship and the misfit accommodation mechanism between the nonpolar GaN film and the NWs were also studied. It was found that the two materials exhibit a rotation of 90° about $<\bar{1}2\bar{1}0>$ axis and the grain boundary (GB) formed is an energetically favored one. Combing the cross-sectional, plan view and Selected Area Electron Diffraction (SAED) observations, the construction of a 3D NW model was possible, taking into account the facet and orientation changes inside and outside the nonpolar GaN film [1].

[1] A. Adikimenakis, A. Lotsari, G.P. Dimitrakopulos, Th. Kehagias, K.E. Aretouli, K. Tsagaraki, M. Androulidaki, Ph. Komninou and A. Georgakilas, J. Appl. Phys. **117**, 244302 (2015).

Acknowledgment: Research co-financed by the European Union (ESF) and Greek national funds through the Operational Program "Education and Lifelong Learning" of the National Strategic Reference Framework (NSRF) - Research Funding Program: THALES, project “NanoWire”.

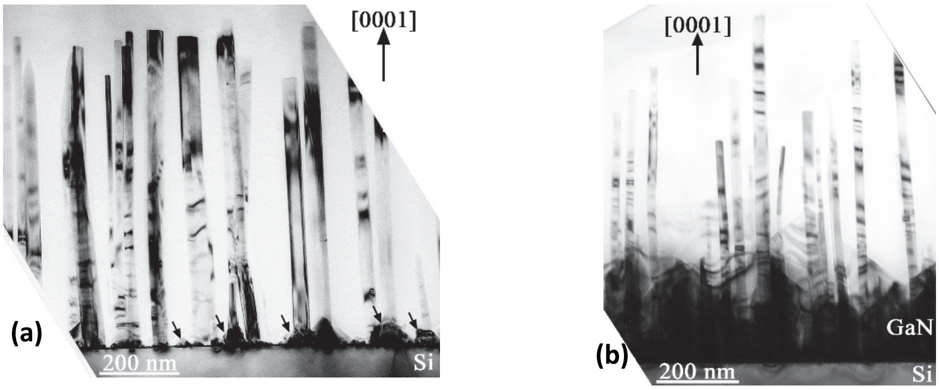

Figure 1: Cross-sectional TEM images showing the overall morphology of GaN NWs grown on (a) 1.5 nm nitridated AlN NL, and (b) 1.5 nm AlN NL as-grown

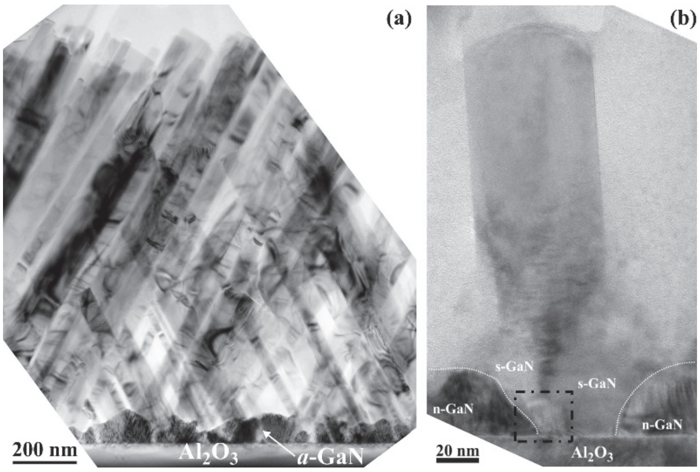

Figure 2: (a) XTEM image of the inclined NWs along $[0001]_{a\text{-GaN}}$ // $[1\bar{1}0\bar{1}]_{sap.}$. The NWs are grown in two crystallographically equivalent variants subjecting 61° with respect to the sapphire substrate. **b)** XTEM of a NW along $[1\bar{1}00]_{a-GaN}$ // $[11\bar{2}0]_{sap.}$ which is grown between two *a*-GaN nanocrystals. In the NW base, a small semipolar GaN nanocrystal is identified (dashed rectangle).

Cobalt Ferrite Magnetic Nanoparticles as Anti-Inflammatory Drug Carriers

V. Georgiadou[1], G. Makris[2], D. Papagiannopoulou[2] and C. Dendrinou-Samara[1]

[1] *Inorganic Chemistry Lab, Chemistry Department, Aristotle University of Thessaloniki, Greece, 54124 Thessaloniki, Greece*
[2] *Department of Medicinal Chemistry, School of Pharmacy, Aristotle University of Thessaloniki, 54124 Thessaloniki, Greece*

E-mail: vgeorgia@chem.auth.gr

TUP
P085

Currently, most drugs for clinical applications have limitations such as being nonselective, toxic, offer poor targeting, and cause damage to normal cells, resulting in significant side effects to normal tissues and reduced drug efficacy.[1-2] Therefore, it is critical to improve the efficiency and reduce the side effects of drugs. Magnetic nanoparticle drug carriers are proposed as an effective solution. Especially, cobalt ferrite magnetic nanoparticles ($CoFe_2O_4$ MNPs) can be found in a range of applications in biotechnology such as in targeted drug delivery, hyperthermia and magnetic resonance imaging. However, to our knowledge the combination of MNPs with non steroidal antiflammatory drugs (NSAIDs) is not yet reported. NSAIDs are used as analgesic, anti-inflammatory and antipyretic agents and show antitumorigenic activity by reducing the number of carcinogen–induced colon tumors. To attenuate the side effects of NSAIDs, MNPs carriers of NSAIDs that control the drug release can be proposed. For this kind of bioapplications, MNPs should have optimized magnetic, morphological and surface properties. Regulation of these features depends basically on synthesis.

Based on our previous results[3], we chose to use octadecylamine as a surfactant due to its ability, under specific synthetic conditions, to offer free NH_2 groups on the surface of the MNPs that can serve for biofunctionalization. For that reason, $CoFe_2O_4$ MNPs were solvothermally synthesized[4] via the decomposition of different ratios (Fe:Co) of acetylacetonate precursors ($Fe(acac)_3$, $Co(acac)_2$ and $Co(acac)_3$) in the presence solely of octadecylamine. Structural characterization (XRD, TEM) showed that the MNPs were of small sizes ~7 nm (by TEM) and moderate saturation magnetization ~60 emu g^{-1} (by VSM and SQUID). FT-IR and ^1H-NMR spectroscopy and TGA analysis have been used to verify the organic coating.

Ninhydrin colorimetric assay certified the presence of free NH_2 groups on the MNPs. The MNPs were functionalized with carboxylate NSAIDs such as naproxen and ibuprofen by direct and indirect ways: i) direct coupling through amide formation between the NH_2 group and the carboxylate group; ii) indirect coupling by grafting the NSAIDs molecules on an intermediate linker (PEI) and/or on PEG-ylated MNPs. DLS, FT-IR, ^{1}H-NMR and UV-Vis data were used to investigate the addition of the NSAIDs on $CoFe_2O_4$ MNPs. The radiolabeling and biodistribution properties are being exploited. The *in vivo* fate of MNPs@NSAIDs carriers is in direct relation with the functionalization pathway that is followed in each case.

Acknowledgements

This research has been co-financed by the European Union, European Social Fund (ESF) and by the Greek National Strategic Reference Framework (NSRF) (Operational Program "Education and Lifelong Learning" of the Research Funding Program "Thales").

References

[1] D. Leveque, A. Delpeuch, B. Gourieux, Anticancer Res. 34 (2014) 1573-1578

[2] E. Cukierman, D. R. Khan, Biochem. Pharmacol. 80 (2010) 762-770

[3] V. Georgiadou, C. Dendrinou-Samara, Eur. J. Inorg. Chem. (2014) 3645-3656

[4] V. Georgiadou, C. Kokotidou, B. Le Droumaguet, B. Carbonnier, T. Choli-Papadopoulou, C. Dendrinou-Samara, Dalton Trans. 43 (2014) 6377-6388; Z. Iatridi, V. Georgiadou, M. Menelaou, C. Dendrinou-Samara, Georgios Bokias, Dalton Trans. 43 (2014) 8633-8643

Embedded Atom Method potentials for the simulation of Pt-Ni nanostructures fitted upon DFT calculations.

E. Symianakis[1], A. Kucerna[1]

[1]Department of Chemistry, Imperial College London, South Kensington, London SW7 2AZ, UK.

E-mail: e.symianakis@imperial.ac.uk

TUP

P086

In 1937 Murnaghan [1] introduced the Equation of States (EOS) which allowed the correlation of experimentally measurable properties of a material to the equation of states (EOS). In the early 80's Rose et. al. [2-4] obtained the universal EOS which permitted the development of several empirical many body potential methods for the atomistic simulation of metals and metal alloys. In 1984 Daw and Baskes [5, 6] introduced the embedded atom method (EAM) potentials suitable for pure metals and their work was soon expanded to alloys by Foiles [7-9] and Johnson [10, 11].

EAM potentials for cubic monoatomic metals and alloys are currently fitted upon the experimental values of the equilibrium lattice parameter a_0, the cohesive energy E_0, the three elastic constants, and the vacancy formation energy E_v^f. This basic set of properties is often complemented with low-index surface energies, phonon frequencies, etc. [12]. The later introduction of semi-empirical potentials [13-17], where the individual metal potentials are fitted empirically, but the cross-interaction term is fitted upon density functional theory calculations of the alloyed systems has improved the reliability of computer simulation studies on binary systems. The unavailability of experimental information on properties, especially of binary and ternary systems, accompanied by the fact that most experimental properties represent very small regions of configuration space near or at equilibrium, limits the availability and the transferability of those potentials [12].

One such limiting case of interest is the study of small, ~2-5 nm, metallic binary nanoparticles which are known to exhibit properties considerably different to those of the macroscopic materials [18] and are used for catalytic functions such as the Oxygen Reduction Reaction (ORR). The small number of atoms in those nanoparticles results in quantized valence states instead of valence bands and also to an alteration of the outer electronic orbitals themselves.

The ability of interatomic potentials, fitted upon bulk and planar surfaces properties at equilibrium, to provide information on the properties of small alloyed nanoparticles is therefore questionable and the most popular approach for the study of their properties is the employment of self-consistent Density Functional Theory (DFT) calculations which takes into account the electronic interactions of the atoms but their high computational cost limits the size of the studied systems to ~1.0 nm.

In this study, EAM potentials has been fitted for Ni, Pt and Ni-Pt binary systems completely upon DFT predictions on the EOS of bulk and nano sized slabs at equilibrium and out of equilibrium. The agreement of the total energy calculations of the fitted potentials to the DFT predictions for each class of structures is achieved within ±1 meV for the bulk EOS of the pure metals and within ±3 meV for the EOS for the stable alloys while the three elastic constants, the vacancies formation energies and the surface energies of the surfaces with orientations 100, 110, 111 are calculated by DFT and are reproduced within ±10 meV by the EAM potentials, Table1.

Furthermore, total energy calculations on binary nano-slabs with the surface orientations of 100, 110 and 111 and thicknesses between 2-5nm of core shell and interface configurations obtained by DFT has been included in the fitting database and are reproduced within ±20 meV while the lattice relaxations are reproduced within 0.1 Å providing the one dimension description of a core shell nanoparticle.

In summary, the information on the precision and scattering of the total energy calculations of the fitted potentials to the DFT predictions for each class of structures provides a guide on the transferability and reliability of the obtained potentials. The physical properties that are normally included to empirical and semi empirical fitting have been calculated by DFT and reproduced by the EAM potentials while the shear moduli and C' values of the stable Pt-Ni alloys are reported for the first time.

Method	Units	Ni	Pt	Ni1Pt3	Ni2Pt2	Ni3Pt1
DFT	α(Å)	3.524	3.977	3.885	a=3.852 c=3.634	3.661
EAM	α(Å)	3.525	3.978	3.885	a=3.884 c=3.575	3.661
Exper.	α(Å)	3.525	3.922	3.885	3.794	3.607
DFT	B(Gpa)	196	251	235	219	206
EAM		194	254	241	227	212
Exper.		180	230-270	223-227	209-214	202
DFT	C44(Gpa)	129	61	99	119	121
EAM		69	34	38	46	50
Exper.		132-123	76-78			
DFT	Shear C' (Gpa)	51	41	59	154	53
EAM		16	10	11	16	13
Exper.		54-49.6	52			

Table1: DFT and EAM calculations on properties and experimentally reported values. α: lattice parameter, B : Bulk modulus, C44 and C' shear modulus.

References

[1] F.D. Murnaghan, American Journal of Mathematics (1937) Vol. 59, No. 52.
[2] J.H. Rose, J. Ferrante and J.R. Smith., Physical Review Letters 47 (1981) 675-678.
[3] P. Vinet, J.R. Smith, J. Ferrante and J.H. Rose., Physical Review B 35 (1987) 1945-1953.
[4] J.H. Rose, J.R. Smith, F. Guinea and J. Ferrante. Physical Review B 29 (1984) 2963-2969.
[5] M.S. Daw and M.I. Baskes., Physical Review B 29 (1984) 6443-6453.
[6] M.S. Daw and M.I. Baskes., Physical Review Letters 50 (1983) 1285-1288.
[7] S.M. Foiles, M.I. Baskes and M.S. Daw., Physical Review B 33 (1986) 7983-7991.
[8] G.F. Wang, M.A. Van Hove, P.N. Ross and M.I. Baskes., Journal of Chemical Physics 122 (2005).
[9] S.S. Pohlong and P.N. Rama., Journal of Materials Research 13 (1998) 1919-1927.
[10] R.A. Johnson., Physical Review B 39 (1989) 12554-12559.
[11] R.A. Johnson and D.J. Oh., Journal of Materials Research 4 (1989) 1195-1201.
[12] M. Y. Handbook of Materials Modeling ed S Yip The Netherlands: Springer, 2005. pp. pp 459–478 chapter 452.
[13] M.I. Baskes., Physical Review Letters 59 (1987) 2666-2669.
[14] M.I. Baskes, J.S. Nelson and A.F. Wright., Physical Review B 40 (1989) 6085-6100.
[15] M.I. Baskes., Physical Review B 46 (1992) 2727-2742.
[16] M.I. Baskes and R.A. Johnson., Model. and Simul. in Mater. Scie. and Engin. 2 (1994) 147-163.
[17] B.J. Lee, J.H. Shim and M.I. Baskes., Physical Review B 68 (2003).
[18] K. M.T.M. Fuel Cell Catalysis A surface science Approach John Wiley& Sons,Inc, 2009. pp. pp 507-556 chapter 515.

Phase investigation of PbTe +25%$PbSnS_2$ thermoelectric composite by electron crystallography

C. Ioannidou[1], N. Frangis[1], C.B. Lioutas[1], and M.G. Kanatzidis[2]

[1]Solid State Physics Section, Department of Physics, Aristotle University of Thessaloniki
GR-54124, Thessaloniki, Greece
[2]Dept. of Chemistry, Northwestern University, 2145 Sheridan Road, Evanston,
IL 60208-3113, Illinois, USA

E-mail: xrysaioannidou@hotmail.com

Recent increase in world energy demand has focused research attention on alternative energy sources, of which thermoelectric materials are among the most important candidates due to their low cost and environmentally friendly heat-to-power generation. Thermoelectric materials are suitable for applications in thermoelectric generators and refrigerators. Their wide-scale utilization is limited because of their low efficiency; however, nanoscale inclusions can improve it by suppressing the lattice thermal conductivity [1,2].

Here we report results of the structural characterization of thermoelectric composite of PbTe +25%$PbSnS_2$. PbTe is a well known thermoelectric material with good electrical transport properties. It has a cubic rock salt structure that belongs to the Fm3m (225) space group [1],[2]. $PbSnS_2$ has a structure with cell dimensions 4.047 × 4.286 × 11.34 Å and belongs to the orthorhombic space group Pmcn (62) [1,2].

We provide extensive structural characterization of this system and investigate phases with nano-dimensions based on the current electron crystallography data. Electron Diffraction and High-resolution images are examined in detail (Figures 2 and 1, respectively).

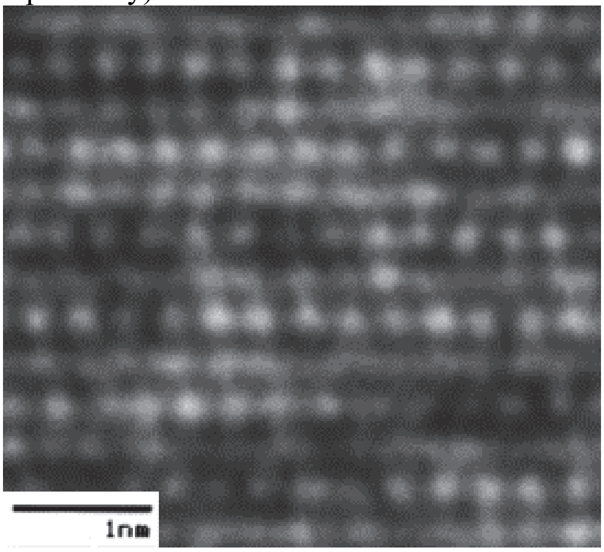

Figure 7: a) HTEM lattice image along the [110] $PbSnS_2$ direction.

Sample rotation experiments were carried out for observing consecutive sections of the reciprocal lattice and Precession Electron Diffraction (PED) was used for clear nanocrystal structure determinations due to the elimination of dynamical diffraction contributions and its ability to solve complex structures in the nanometric scale.

From electron diffraction and high-resolution transmission electron microscopy images, it is obvious that the PbTe +25%$PbSnS_2$ system appears to be nanostructured. $PbSnS_2$ appears as the dominant phase in nanocrystals form, endotaxially grown in the PbTe matrix (Figure 2a). In $PbSnS_2$ a superstructure ordering of the metal atoms is observed [1-3]. At least the presence of one more phase is determined. The interplanar distances calculated from the ED suggest the growth of $Pb_{0.9}Sn_{0.1}S$ or PbS phase (Figure 2b).

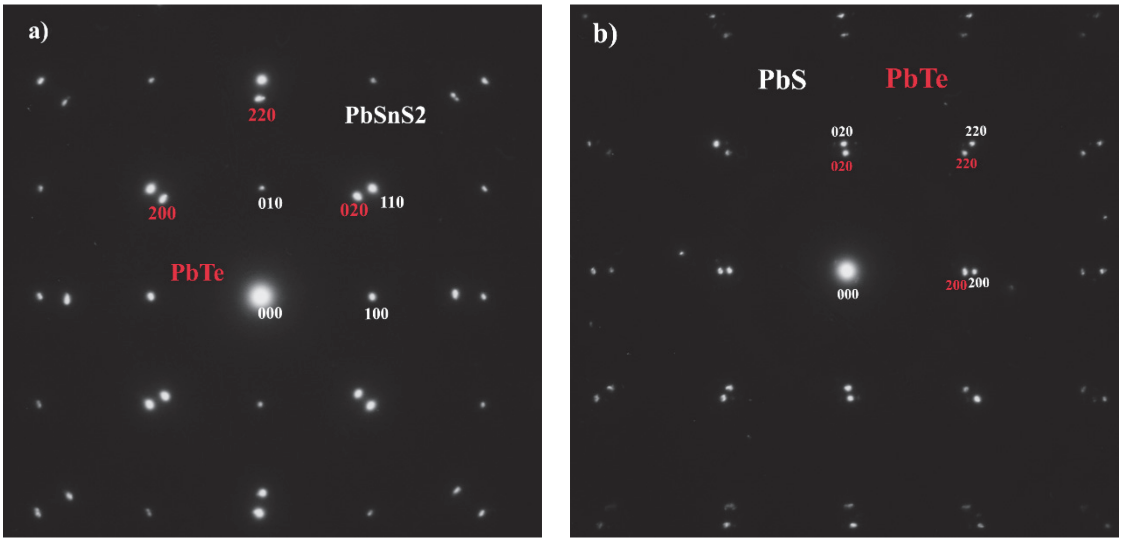

Figure 8: PED in TEM images along the $[001]_{PbTe}$ direction of the a) PbTe-$PbSnS_2$ system and b) PbTe-PbS system

References

[1] Jiaqing He, Steven N. Girard, Jin Cheng Zheng, Lidong Zhao, Mercouri G. Kanatzidis and Vinayak P. Dravid, Advanced Materials 24 (2012) 4440-4444.

[2] Steven N. Girard, Thomas C. Chasapis, Jiaqing He, Xiaoyuan Zhou, Euripides Hatikraniotis, Ctirad Uher, K. M. Praskeuopoulos, Vinayak P. Dravid and Mercouri G. Kanatzidis, Energy and Environmental Science 5 (2012) 8716.

[3] Alexander Lebedev, Irina Sluchinskaya and Ian Munro, Journal of Synchrotron Radiation 8 (2001) 800–802.

Monte Carlo study of the exchange bias effect in ferromagnetic/antiferromagnetic hybrid nanoparticles

V. Dimitriadis[1], A. Tzavellas[1], D. Kechrakos[1], N. Moutis[1], E. Sideris[1], V. Tzitzios[2], I. Panagiotopoulos[3], D. Niarchos[2] and G. Hadjipanayis[4]

[1]School of Pedagogical and Technological Education, Athens 14121, Greece
[2]Institute of Nanoscience and Nanotechnology, NCSR Demokritos, Athens 15310, Greece
[3]Department of Materials Science and Engineering, University of Ioannina, Ioannina 45110, Greece
[4]Department of Physics and Astronomy, University of Delaware, Newark DE-19716, USA

E-mail: dkehrakos@aspete.gr

Solution chemistry methods provide a versatile bottom-up approach for the growth of nanoparticles with tailor-made size, shape and material combinations. In the present work solution chemistry methods have been used to grow γ-Fe_2O_3/CoO hybrid nanoparticles with both the direct (FM grown on AF) and the inverted (AF grown on FM) morphology and various sizes. A combination of imaging techniques (TEM) and magnetometry (SQUID) has been used to study their magnetic properties [1].

In the present work, computer simulations are implemented in order to understand the factors controlling the exchange bias effect in these hybrid nanoparticles and to suggest optimum geometrical aspects (size, shape) for maximizing the exchange bias effect. To this end, we model the morphology of the hybrid nanoparticles by two partially overlapping spherical particles of FM and AF material. The magnetic structure is modeled by a classical Heisenberg Hamiltonian with uniaxial anisotropy. Parameters for the exchange and anisotropy strength are chosen to fit bulk properties (critical temperature, etc) of the constituent materials and their surface properties (anisotropy etc). We use the Metropolis Monte Carlo algorithm with local spin updates to study the isothermal magnetic hysteresis after field-cooling in a weak field to obtain the exchange bias effect. We study the dependence of the exchange bias effect on the different geometrical lengths characterizing the hybrid nanostructure (particle diameters, center-to-center distance) and the nanostructure parameters (exchange and anisotropy energy, easy axes symmetry). Our simulations demonstrate that the exchange bias field shows a non-monotonous dependence on the degree of overlap between the spherical particles and suggest an optimum overlap fraction for maximizing the exchange bias effect. The role of surface anisotropy of the seed and the decorating particle are discussed in view of their contribution to the exchange bias effect. Similarities and differences with respect to the core-shell morphology are presented. Finally, our simulations support the experimental findings for the γ-Fe_2O_3/CoO system.

Acknowledgment. Research co-financed by the European Social Fund and Greek national funds through the Research Funding Program *ARCHIMEDES-III*.

References

[1] I. Panagiotopoulos, G. Basina, V. Alexandrakis, E. Devlin, G. Hadjipanayis, L. Colak, D. Niarchos and V. Tzitzios, J. Phys. Chem. 113 (2009) 14609.

DNA hybridization on ultrasmall gold nanoparticles

I. Michelakaki[1], G. Tsekenis[2], M. Chatzipetrou[1], D. Tsoukalas[1]

[1] *National Technical University of Athens, Physics Department, Heroon Polytechneiou 9, 15780 Zografou-Athens, Greece*
[2]*Biomedical Research Foundation of the Academy of Athens, Soranou Ephessiou 4, 11527 Athens, Greece*

E-mail: michelakaki.irini@gmail.com

The interaction between DNA and metal nanoparticles has attracted much interest because a detailed understanding can contribute to the further development of DNA biosensor development and nanoparticle functionalization. One of the most studied metal is gold because it resists oxidation and interacts with thiolated DNA. Most of the previous work has been performed with planar gold surface and with nanoparticles which exhibit diameter above 10nm [1]. In this work we study the hybridization efficiency of thiolated DNA strands on ultrasmall gold nanoparticles with mean diameter between 1-2.5nm.

The Au nanoparticles were produced in a magnetron sputtering, gas condensation nanoparticles beam source. A vapor of Au atoms is produced by dc magnetron sputtering of an Au target, in a high pressure Ar atmosphere. The high pressure leads to aggregation of the atoms into nanoparticles. The nanoparticles are forced due to a pressure difference to enter a deposition chamber, where they land on the SiO_2 substrate. The size and density of the Au nanoparticles was characterized by AFM and TEM. The optimum conditions for the hybridization of the oligomer probes to their complementary targets have been tested with the use of Confocal Fluorescence microscope [2].

The Confocal Fluorescence Microscope results reveal that oligomer hybridization depends both on Au nanoparticles size and density [3]. Optimum conditions for maximum oligos hybridization efficiency could be determined.

References

[1] H. Hill, J. Millstone, M. Banholzer, C. Mirkin, ACS Nano. 3(2) (2009) 418-424.

[2] L. Demers, C. Mirkin, R. Mucic, R. Reynolds, R. Letsinger, R. Elghanian, G. Viswanadham, Analytical Chemistry 72 (2000) 5535-5541.

[3] A. Peterson, R. Heaton, R. Georgiadis, Nucleic Acids Research 29 (2001) 5163-5168.

TUP

P090

Fabrication and characterization of free-standing porous silicon and alumina membranes

<u>M. Dimitropoulos</u>, P. Kontou, M. Savranakis, A. Christoulaki, N. Spiliopoulos, D. L. Anastassopoulos, A. A. Vradis

Solid State Laboratory, Department of Physics, University of Patras, GR 26504, Greece
E-mail: phy4904@upnet.gr

The purpose of this study is to fabricate free-standing porous alumina and silicon membranes in order to use them in various applications such as matrix for nanowires, fluid flow experiments and optoelectronic devices. Porous materials are of scientific and technological importance due to the presence of controllable dimension voids at the nanometer scale. Research efforts in this field have been driven by the rapidly emerging applications such as biosensors, drug delivery, gas separation, energy storage and fuel cell technology. The research in this field offers exciting new opportunities for developing new strategies and techniques for the synthesis and applications of these materials.

<u>Porous Alumina (PA)</u>: Anodization of an aluminum foil is carried out in sulfuric acid 0.3M and oxalic/phosphoric acid 0.3M under applied voltages of 20V and 100V-180V respectively in a two-step anodization process [1].The process takes place into an electrochemical cell (fig.1). Subsequently, the membranes' barrier layer is dissolved in a solution of phosphoric acid 5%wt. in a double tank cell in order to obtain a free-standing membrane [2].

<u>Porous Silicon (PSi)</u>: Anodization of a silicon wafer is carried out in various concentrations of $HF:H_2O:CH_3CH_2OH$ electrolyte solution [3]. The procedure takes place inside a double tank electrochemical cell (Fig.2). Electrical contact is achieved with an electrolytic backside contact [4].

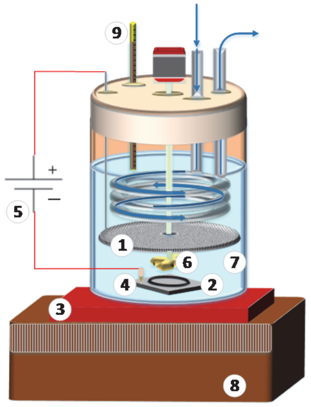

Fig. 9: *Electrochemical cell for PA anodization. (1) Ni cathode electrode, (2) aluminum foil, (3) Cu plate, (4) spring loaded electric contact, (5) Power supply, (6) stirrer, (7) electrolyte, (8) Cold Plate, (9) mercury thermometer*

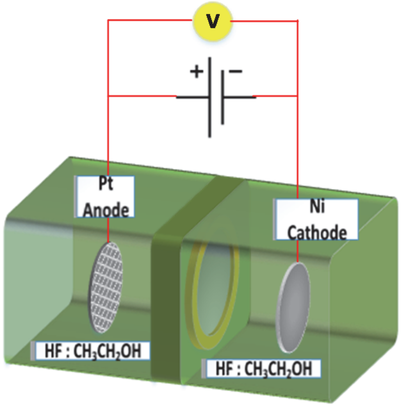

Fig. 2: *Double tank cell for PSi electrochemical etching.*

The membrane thickness, pore density and pore diameter is measured with Scanning Electron Microscopy (SEM).

Figure 3 shows the electrical current as a function of time during aluminum anodization in potentiostatic mode for constant applied voltage of 20 V. In this figure we can observe three characteristic stages of PA formation. During the first step a layer of dense aluminum oxide is created and therefore the current is decreased. In the next step the creation of the first pores starts and an increase in the current is observed. The current reaches a steady state value in the third step indicating the development of the pores with a steady growing rate.

Figure 4 presents the anodizing voltage as a function of time during silicon anodization in galvanostatic mode under constant current density of 20 mA/cm^2. During first seconds of the process the voltage is increasing until the pore creation is initiated. The peak in voltage corresponds to the pore opening.

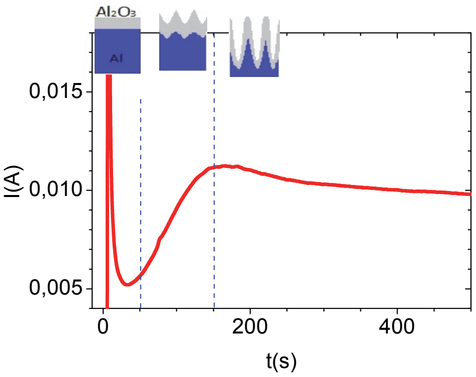

Fig. 3: *Anodization current as a function of time for constant voltage of 20 V.*

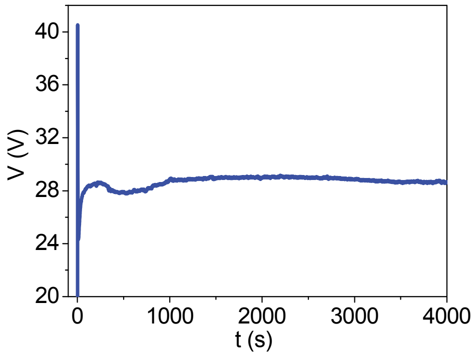

Fig. 4: *Anodization voltage as a function of time for constant current density of 20mA/cm^2*

The membranes are analyzed by SEM (Fig. 5, 6, 7) for the characterization of the structure.

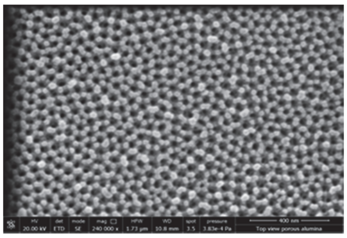

Fig. 5: *Top View of PA*

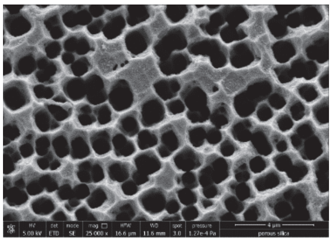

Fig. 6: *Top View of PSi (square pores)*

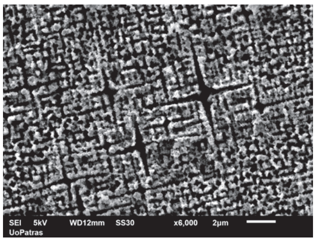

Fig. 7: *Top View of PSi (branched pore*

REFERENCES

[1] A.Christoulaki et al., *J.Appl.Electrochem* (2014) 44, 701-707.
[2] M. Lillo et al., *Journal of Membrane Science* (2009) 327, 11-17.
[3] Michael J. Sailor, *Porous Silicon in Practice: Preparation, Characterization and Applications* (2012) 4, 119-122
[4] Leigh Canham, *Properties of Porous Silicon (1997) 1.2 , 12-14*

TUP

P091

Raman spectroscopy indications of the Verwey transition in epitaxial Fe_3O_4(111) films on Pt(111) and Ru(0001)

N. Michalak[1], M. Lewandowski[1,2*], B. Scheibe[2], Th. Vasileiadis[3,4], Z. Miłosz[1], R. Ranecki[1], S. Mielcarek[5], T. Luciński[1], S. Jurga[2]

[1]Institute of Molecular Physics, Polish Academy of Sciences, M. Smoluchowskiego 17, 60-179 Poznań, Poland
[2]NanoBioMedical Centre, Adam Mickiewicz University, Umultowska 85, 61-614 Poznań, Poland
[3]Foundation for Research and Technology Hellas—Institute of Chemical Engineering Sciences (FORTH/ICE-HT), P.O. Box 1414, GR-26504 Rio-Patras, Greece
[4]Department of Materials Science, University of Patras, GR-26504 Rio-Patras, Greece
[5]Faculty of Physics, Adam Mickiewicz University, Umultowska 85, 61-614 Poznań, Poland

E-mail: lewandowski@amu.edu.pl

Magnetite (Fe_3O_4) crystallizes in an inverse spinel structure. In a bulk form, it is a ferrimagnet and a semiconductor. One of the most interesting properties of magnetite is the phase transition which occurs at ~120 K – the so called Verwey transition [1]. During the transition, the crystallographic structure of Fe_3O_4 changes from cubic to monoclinic which is accompanied by significant changes in crystal's electric and magnetic properties. For low-dimensional forms of magnetite, such as nanoparticles or thin films, the temperature at which the Verwey transition occurs and the character of the changes may differ.

We grew few-nanometers-thick epitaxial Fe_3O_4(111) films on Pt(111) and Ru(0001) single crystal supports by repeated cycles of iron deposition and oxidation in an ultra-high vacuum chamber [2,3]. We performed Raman spectroscopy measurements in temperatures ranging from 300 to 80 K, trying to find indications of the Verwey transition in the prepared films. The evolution of the magnetite's A_{1g} Raman peak, corresponding to symmetric stretching of oxygen atoms along Fe–O bonds, gave indications for the presence of the Verwey transition-characteristic structural changes in Fe_3O_4 films on both supports [4].

This work was financially supported by the National Science Centre of Poland (SONATA program, 2013–2016, grant No. 2012/05/D/ST3/02855 — Pt(111) part) and by the Polish Ministry of Science and Higher Education (Iuventus Plus program, 2012–2015, grant No. IP2011 030071 — Ru(0001) part). S.J. acknowledges the support of the National Centre for Research and Development (PBS program, 2012–2015, grant No. PBS1/A9/13/2012). M.L. would like to thank the Foundation for Polish Science for the START scholarship.

References

[1] E. J. Verwey, Nature 144 (1939) 327.
[2] W. Weiss et al., Phys. Rev. B 59 (1999) 5201.
[3] G. Ketteller et al., J. Phys. Chem. B 107 (2003) 4320.
[4] M. Lewandowski et al., Surf. Coat. Technol. 271 (2015) 87.

Room temperature/ambient conditions study of the magnetic properties of few-nanometers-thick epitaxial Fe_3O_4(111) films on Pt(111) and Ru(0001)

Z. Miłosz[1], **M. Lewandowski**[1,2], **N. Michalak**[1], **R. Ranecki**[1], **I. Sveklo**[3], **Z. Kurant**[3], **A. Maziewski**[3], **S. Mielcarek**[4], **T. Luciński**[1], **S. Jurga**[2]

[1]NanoBioMedical Centre, Adam Mickiewicz University, Umultowska 85, 61-614 Poznań, Poland
[2]Institute of Molecular Physics, Polish Academy of Sciences, M. Smoluchowskiego 17, 60-179 Poznań, Poland
[3]Faculty of Physics, University of Białystok, Lipowa 41, 15-424 Białystok, Poland
[4]Faculty of Physics, Adam Mickiewicz University,Umultowska 85, 61-614 Poznań, Poland

E-mail: lewandowski@amu.edu.pl

Magnetite (Fe_3O_4) is a ferrimagnet with a Curie temperature of 858 K. It has been proved to exhibit high spin polarization of electrons in the (111) crystallographic direction [1]. Due to this, few-nanometers-thick (111)-oriented magnetite films with bulk-like magnetic properties could potentially act as "building blocks" for nanoelectronic and spintronic devices. Low-dimensional magnetite forms often preserve the properties of bulk magnetite, however, these always have to be the subject of case studies.

e used magneto-optical Kerr effect and magnetic force microscopy to study the magnetic properties of few-nanometers-thick epitaxial Fe_3O_4(111) films on Pt(111) and Ru(0001) single crystal supports. The films were grown by sequential iron deposition and oxidation in an ultra-high vacuum chamber [2,3]. Low energy electron diffraction and x-ray photoelectron spectroscopy were used to confirm the presence of magnetite iron oxide phase. The studies of magnetic properties were carried out at room temperature and in ambient conditions. The Kerr measurements confirmed the presence of magnetic ordering in both films and indicated in-plane orientation of magnetization. The latter was supported by the lack of magnetic contrast in magnetic force microscopy images [4]. The magnetic properties of magnetite on Pt(111) and Ru(0001) slightly differed which was tentatively attributed to the influence of epitaxial strain.

This work was financially supported by the National Science Centre of Poland (SONATA program, 2013–2016, grant No. 2012/05/D/ST3/02855 — Pt(111) part) and by the Polish Ministry of Science and Higher Education (Iuventus Plus program, 2012–2015, grant No. IP2011 030071 — Ru(0001) part). S.J. acknowledges the support of the National Centre for Research and Development (PBS program, 2012–2015, grant No. PBS1/A9/13/2012). M.L. would like to thank the Foundation for Polish Science for the START scholarship.

References

[1] M. Fonin et al., Lect. Notes Phys. 678 (2005), 289.
[2] W. Weiss et al., Phys. Rev. B 59 (1999), 5201.
[3] G. Ketteller et al., J. Phys. Chem. B 107 (2003), 4320.
[4] M. Lewandowski et al., Thin Solid Films (2015), in press.

Plasmon sensors based on metallic bilayers

K. Kondili, P. Athanasiadis, G. Tassis, A. Christoulaki, N. Spiliopoulos, D. Anastassopoulos, A. Vradis and E. Mytilineou

Department of Physics, Universty of Patras, GR – 26504, Patras, Greece

E-mail: phy5307@upnet.gr

Metal bilayers for plasmonic sensors are synthesized by means of RF sputtering and thermal evaporation on microscope glass slides. The layers consist of an adhesion layer and a plasmonic layer with optimum thicknesses for the excitation of surface plasmons. The samples are annealed in different temperatures in order to enhance the adhesion properties. In advance the impact of the annealing effect on the SPR reflectivity curve and on the film's surface is studied. The samples are characterized by SPR, AFM and SEM. The presented results can be implemented in the fabrication of a metal/porous medium plasmon sensor with enhanced sensitivity.

Surface Plasmon Resonance-based sensors (SPR sensors) constitute a well-defined technology for detection and characterization analysis in a wide spectrum of fields [1]. Gold metal films consists an ideal choice for SPR sensors, due to gold's high chemical stability. However gold films present a low adhesive strength to the glass substrate and thus, the stability of the sensor is affected.

In this study we synthesize a bilayer film which consists of a very thin adhesion layer of Ti (3nm), the plasmonic layer of Au (99.999%) deposited at the optimum thickness for the SPR response and a very thin layer of Ti (3nm) on top. Deltalab microscope slides, BK-7 type, are used as substrate for the deposition. The top layer of Ti provides a decent adhesion in order to have the capability to deposit on this, a layer of Al. Moreover the Ti as an intermediate layer acts as a diffusion barrier.

Furthermore the samples undergo thermal treatment at various temperatures in order to increase the mechanical strength of the gold layer. Afterwards the samples are characterized at SPR to evaluate the impact of the annealing process on the SPR reflectivity curve. The experimental investigation of the reflectivity spectrum is performed under the Kretchmann configuration. We use a BK-7 prism (Edmund optics) and the glass substrate is in optical contact to it via a matching liquid of the same refractive index (n=1.515). The incident beam is originated from a He-Ne laser (λ=632.8nm) (Figure 1). The aim of the study is the fabrication of an SPR sensor with nanoporous alumina (p- Al_2O_3) layer on the top [2, 3]. The nanoporous alumina layer is a result of aluminum anodization, while the morphology of p- Al_2O_3 permits the adsorption of small

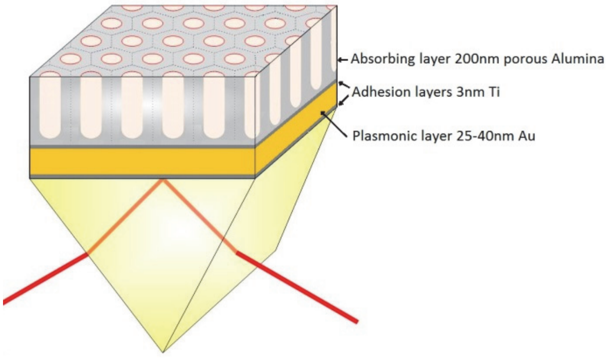

Fig. 1: Kretchmann configuration

molecules or polymers inside the pores. In Figure 2 we present the theoretical dependence of the SPR curve on the Au film thickness of the system Ti (3nm) / Au / Ti (3nm) / p- Al_2O_3.

We study the angular reflectivity of the final system and during the stages of the fabrication procedure in order to determine the optimal treatment conditions. The thermal treatment affects the characteristics of the sensor's SPR curve, so it's important to specify the critical annealing temperature that enhances the sensor's adhesion and preserves the SPR signal.

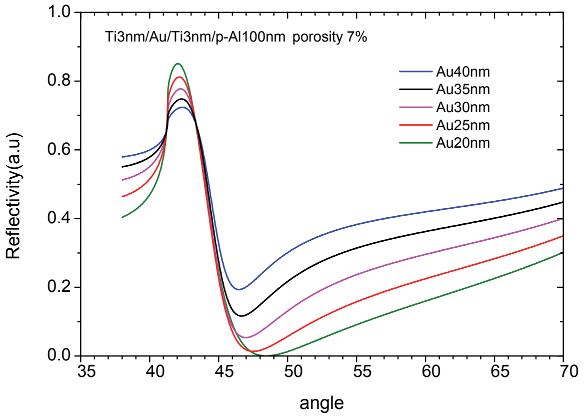

Fig. 2: optimization of gold Thickness in the system Ti/Au/Ti/ p- Al_2O_3

In Figure 3 we demonstrate the SPR response of the Ti/Au system as sputtered and under different annealing temperatures. We see that annealing treatment doesn't affect the characteristics of the SPR curve. The results are stimulated with fitting algorithms and an indicative diagram of fitting stimulation is presented in Figure 4.

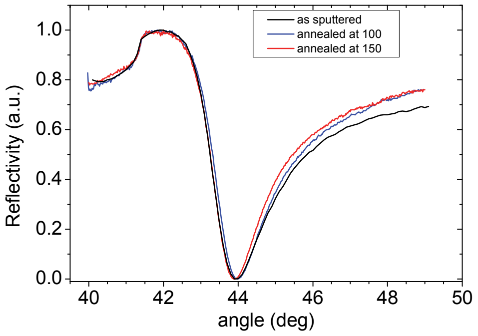

Fig. 3: SPR response of the Ti/Au system as sputtered and under different annealing temperatures

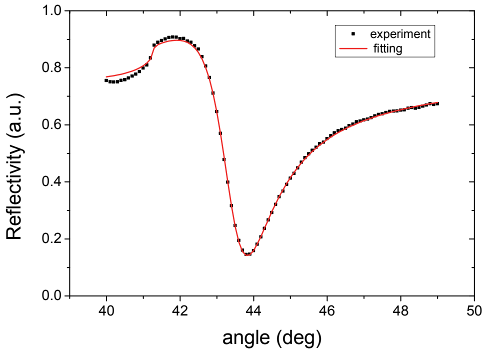

Fig. 4: An indicative diagram of fitting results

References

[1] A. Koutsioubas, N. Spiliopoulos, D. Anastassopoulos, A. Vradis and G. Priftis, Surf. Interface Anal. 41, (2009) 897.

[2] A. Koutsioubas, N. Spiliopoulos, D. Anastassopoulos, A. Vradis and G. Priftis, J. Appl. Phys. 103, (2008) 094521.

[3] A. Koutsioubas, N. Spiliopoulos, D. Anastassopoulos, A. Vradis and G. Priftis, Materials Science and Engineering B 165, (2009) 270.

Nanoparticle Production and Surface Micromachining Through Femtosecond Laser Ablation

Harry Georgiou[1], Amedee Lacraza[2], Loukas Koutsokeras[1], Kyriacos Kallis[2], Georgios Constantinides[1]

[1]Research Unit for Nanostructured Materials Systems, Department of Mechanical Engineering and Materials Science and Engineering, Cyprus University of Technology, Limassol, Cyprus
[2]Nanophotonics Research Laboratory, Department of Electrical Engineering, Computer Engineering and Informatics, Cyprus University of Technology, Limassol, Cyprus

E-mail: g.constantinides@cut.ac.cy

TUP

P094

Femtosecond (fs) lasers have recently evolved into an innovative tool for high-resolution inscription and micromachining in a variety of materials. The ability to fabricate complex microstructures on the surface of non-transparent materials, or within the bulk volume of optically transparent materials, has been the main driver in employing this innovation into applications in medicine for implant production (e.g., stents), photonics for the development of micro-devices and sensors, and in the production of plasmonic nanoparticles. In contrast to picosecond and nanosecond lasers, femtosecond lasers can ablate material using a nonlinear process called optical breakdown which relates to a highly confined ionization event rather than a diffuse thermally driven one. This relatively athermal process significantly reduces the heat affected zone (HAZ) of the micromachined part and creates smooth surfaces without the need for additional post-processing steps. In this work we report on fs laser–metal interactions with the purpose of processing and modifying the metal surfaces, whilst simultaneously producing nanoparticles and nanostructures that result from the ablation process. We particularly studied the fs-laser processing capabilities of silver (Ag), niobium (Nb) and hafnium (Hf), while the metals were submerged in water and an aqueous solution of Sodium dodecyl sulphate surfactant (SDS), an anionic surfactant that modifies the water's surface tension. The inscription was performed using a fs-laser system (HighQ laser femtoREGEN) operating at 1035nm, with a 300-fs pulse duration and variable 1-100 kHz repetition rate. The metal samples were machined using pulse energies between 0.1-10μJ/pulse at a repetition rate of 1 or 100 kHz, and at scanning speeds of 100μm/s to 2000μm/s, whereas the laser beam focal point varied to below, at and above the sample surface. The metal targets and the solutions were characterized using SEM, AFM, profilometry, and uv/vis optical spectroscopy. Analysis of the results showed the existence of nanoparticles in the aqueous solution and dependence of the particle size to a number of parameters, namely the SDS concentration and laser focal depth. At the same time the laser-exposed metal surfaces were significantly altered and interesting nano-scale and micro-scale features were produced.

Aknowledgements

The authors would like to acknowledge the financial support from the Strategic Infrastructure Project NEW INFRASTRUCTURE/STRATE/0308/04 of DESMI 2008, which is co-financed by the European Regional Development Fund, the European Social Fund, the Cohesion Fund, and the Research Promotion Foundation of the Republic of Cyprus.

Quantitative analysis of interfaces in multilayer structures grown on SiC

A. Gkanatsiou, Ch. B. Lioutas, N. Frangis

Solid State Physics Section, Department of Physics, Aristotle University of Thessaloniki,
GR-54124 Thessaloniki, Greece

E-mail: alexgkan@auth.gr

Wide band gap semiconductors, such as SiC and GaN, exhibit many attractive properties: a unique combination of the wide band gap, high breakdown field, high saturation velocity and the ability to form high quality AlGaN/GaN heterostructures with good transport properties make them ideal candidates for high power and high frequency applications. Hexagonal silicon carbide materials (SiC) are considered to be promising candidates for electronic devices as the third generation key materials for transistors. A typical example of a high performance device is the $Al_xGa_{1-x}N$/GaN heterostructure used as a high electron mobility transistor (HEMT) [1-2].

As 6-inch SiC wafers are being introduced into the market, a decrease of the substrate off-cut for SiC heteroepitaxy is desirable to reduce the manufacturing costs [3-4]. Therefore, multilayer (5 layers) and multicomponent structures (based on GaN and related materials) were grown on 6H-SiC (with a misorientation of 1 deg. off from the (0001) plane) substrates using the MOVPE method, for high power applications. The layers were grown epitaxially, as it was confirmed from the corresponding electron diffraction patterns. Several types of interfaces were observed between the layers that either ran parallel to the interface or formed V-shaped defects (e.g. the SiC/AlN, GaN/AlN, GaN/AlGaN interfaces etc.). Moreover, High Resolution TEM (HRTEM) images showed the existence of steps in the 6H-SiC/AlN interface. A typical HRTEM image where an atomic scale step is observed is shown in Fig. 1.

In this study, quantitative analysis of the 6H-SiC/AlN interface is presented based on experimental HRTEM micrographs, showing and proving the steps sites, the layers' sequence and any strain relaxation situation existing. A structural model based on this analysis is proposed and simulated HRTEM images are also obtained. The corresponding atomic models proposed are found to describe well the 6H-SiC/AlN interface, with the corresponding computer simulation images coinciding with the experimental HRTEM images. An example is shown in Fig. 2, illustrating the monolayer step observed in the 6H-SiC/AlN interface. In Fig. 3, a characteristic plot shows the phase shift of the fitting of the intensity's distribution along a line that corresponds to the projection of a close-packing layer revealing the stacking sequence and therefore the starting position of the AlN epilayer. Moreover, the comparison of the sequence clearly shows the height of the step and any alteration on the stacking sequence between the two parts of the image.

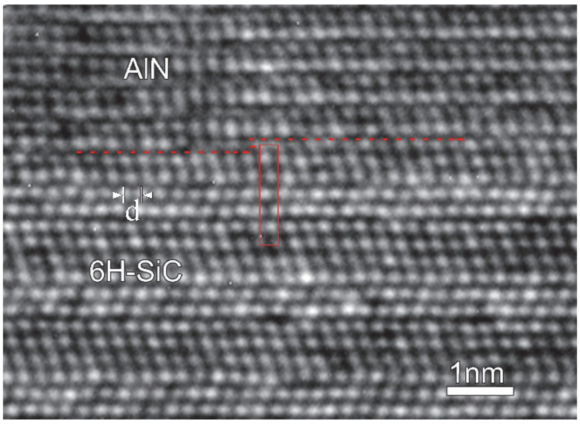

Figure 1. HRTEM image showing an atomic scale step in the 6H-SiC/AlN interface.

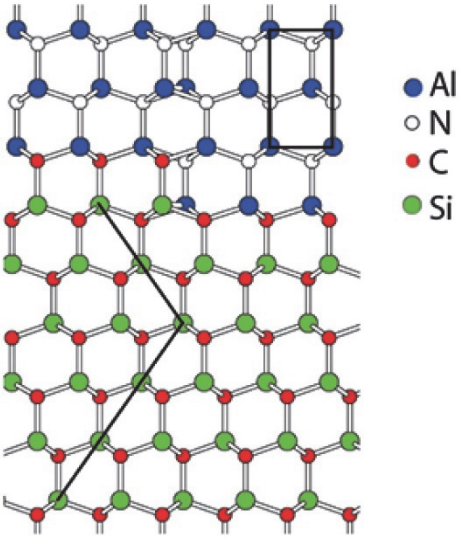

Figure 2. Atomic model describing the one atomic scale step in the 6H-SiC/AlN interface.

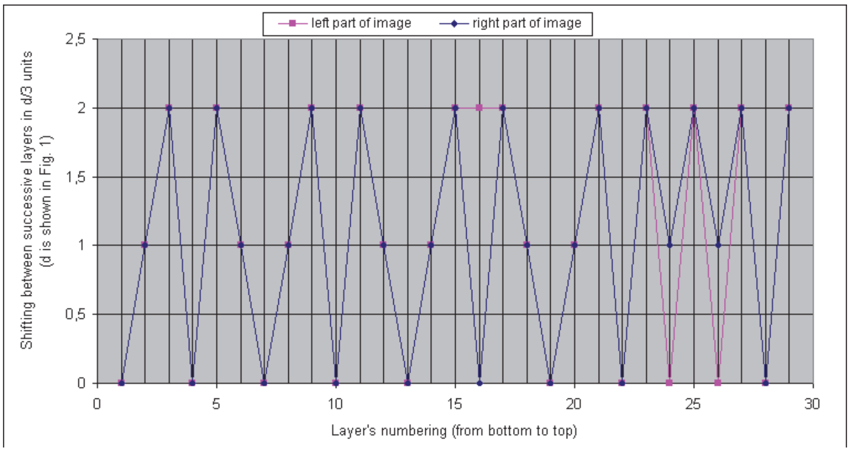

Figure 3. Characteristic plot of the alteration of the phase shift across the stacking layers, revealing the position of the step. The layer's numbering begins from the bottom of the image.

Supported by IKY Fellowships of Excellence for Postgraduate Studies in Greece-Siemens Program, the JU ENIAC Project Last Power Grant agreement no. 120218 and the Greek G.S.R.T., contract SAE 013/8 - 2009SE 01380012.

References

[1] F. A. Ponce, C. G. Van de Walle, and J. E. Northrup, Physical Review B 53 (1996) 7473.

[2] J.A. del Alamo, J. Joh , Microelectronics Reliability 49 (2009) 1200.

[3] Leszczynski Mike, Prystawko Pawel, Kruszewski Piotr, Sarzynski Marcin, Plesiewicz Jerzy, Domagala Jarek, Gkanatsiou Alexandra, Lioutas Christos, Frangis Nicolaos, Polychroniadis Efstathios, Materials Science Forum 806 (2015) 73.

Structural models of defects in an Al-doped Si emitter of a p-n junction solar cell

I. Katrantzis, N. Vouroutzis and N. Frangis

Solid State Physics Section, Department of Physics, Aristotle University of Thessaloniki,
GR-54124 Thessaloniki, Greece

E-mail: ikatrant@physics.auth.gr

The process of aluminum-induced crystallization (AIC) of amorphous silicon [1] was used for the fabrication of a silicon-wafer based p-n junction solar cell. The emitter was originally nanocrystalline, grown on n-type crystalline Si and covered with a thin Al layer. Annealing in nitrogen ambient at 430^{o}C resulted in the simultaneous Al-induced recrystallization and doping of the emitter, which was converted to a p-doped poly-Si layer [2]. Although this process had beneficial impacts on the structural, electrical and photovoltaic properties of the p-n junction, some structural defects were detected and are analyzed in the present work. Structural models and possible preferential sites of Al atoms in defects of the emitter are proposed. The defects were observed by transmission electron microscopy (TEM), using a JEOL 2011 microscope. Computer simulations of the high resolution TEM (HRTEM) images of the defects were implemented with the JEMS software.

Figure 1 shows a HRTEM image of a defected area in the emitter. The first attempt focuses on the characterization of the {112} Σ3 grain boundary (blue dashed line), which is perpendicular to and sandwiched between two {111} Σ3 grain boundaries (Figure 2(a) in larger magnification). The quality of the image was improved by processing with the ImageJ software. The resulting image is shown in Figure 2(b). Past works presented that a rigid body-translation (RBT) occurs in most of the cases of such boundaries and the symmetric structure, i.e. without a RBT, is a meta-stable structure [3]. In our case only the symmetric structure is identified. There are two reasons which may result to this: a) the small length of the detected defect or b) the preferential concentration of Al atoms on the defected region. An atomic model is proposed, as shown in Figure 2(e). Figure 2(c) shows the simulated with JEMS image of this model and Figure 2(d) superimposes the configuration of Si atoms (brown spheres) on the later. Probably, the source of the mentioned meta-stability is the existence of coordination defects in the symmetric structure: 5-fold and 3-fold coordinated atoms are labeled in Figure 2(e) as “5” and “3”, respectively. Simulations based on models involving Al atoms show similar results with the one of Figure 2(c), which is based on the pure Si model of Figure 2(e). Since however, the positioning of Al atoms in sites “3” reduces the number of coordination defects and consequently is expected also to reduce the total energy, the presence of Al atoms at these sites is highly probable.

The second defect to be characterized is shown in Figure 3(a). It runs parallel to an {111} plane (yellow dashed line in Figure 1). The three central layers of dots in Figure 3(a) seem to be aligned along $[1\bar{1}\bar{1}]$, with the dots of the central layer being weaker. This configuration is consistent neither with a twin plane nor with a stacking fault. Figure 3(e) depicts the proposed atomic model. Along $[1\bar{1}\bar{1}]$, layers of atoms are labeled with numbers 1-6. The structure below layer 2 and above layer 5 is periodical

(…AaBbCc…). Layers 1 and 5 can be labeled as “a”, while layers 2 and 6 can be labeled as “B”. Layers 3 and 4 could be labeled as “a” and “B” respectively, but both with a displacement of 0.192 nm along [$01\bar{1}$], in order to construct a fourth covalent bond (blue color). Therefore, the inter-atomic distances in Figure 3(e) drawn with blue color are wider (0.260 nm) than the normal inter-atomic distances in Si (0.235 nm) and consequently distorted tetrahedra are formed. All these indicate a possible positioning of Al atoms in the defected area. Figure 3(b) and 3(c) show simulated images produced with JEMS, based on two versions of the model of Figure 3(e). While in Figure 3(b) no Al atoms were included, in Figure 3(c) Al atoms (purple spheres) on layers 3 and 4 were considered. Only the later is able to reproduce the experimental HRTEM image. Thus, the correct atomic model is the one in Figure 3(e), where Al atoms are purple spheres and Si atoms are brown spheres. Figure 3(d) superimposes the configuration of Si (brown spheres) and Al atoms (purple spheres) on the simulated with JEMS correct image.

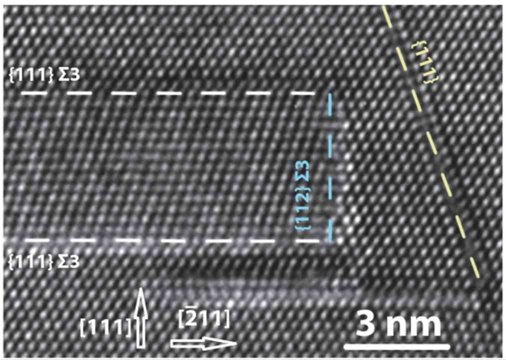

Figure 1: HRTEM image of a defected area in the emitter.

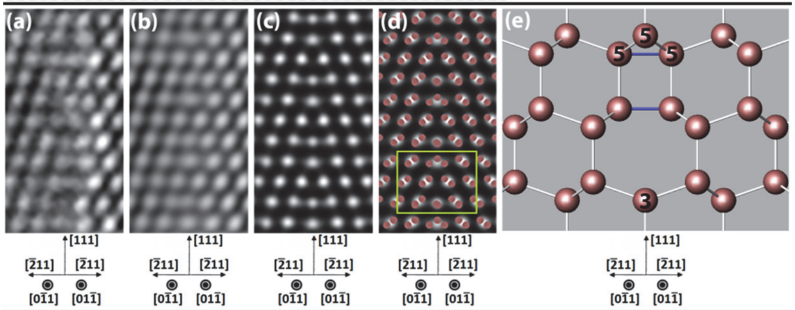

Figure 2: For details, see paragraph 2 (text above). Blue bonds are smaller (0.223nm). The trace of {112} Σ3 grain boundary is along [111] direction.

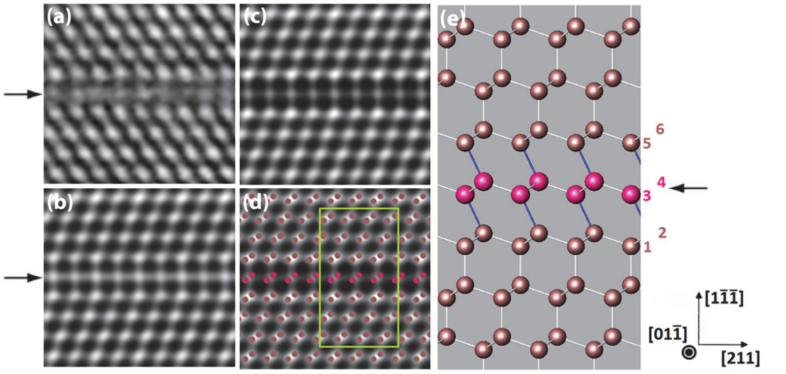

Figure 3: For details, see paragraph 3 (text above). The arrows indicate the {111} plane. Blue bonds are wider (0.260nm).

In both Figures (d), yellow frames show the atomic model on the right.

References

[1] O. Nast, *et al.*, Solar Energy Materials & Solar Cells 65 (2001) 385-392

[2] S. Gardelis, *et al.*, Applied Physics Letters 103 (2013) 241114

[3] N. Sakaguchi, H. Ichinose and S. Watanabe, Materials Transactions 48 (2007) 2585-2589

Formation of Zn-Mg and Zn-Al alloyed coatings by hot dip galvanizing

V. Syropoulos[1], D. Chaliampalias[1], E. Pavlidou[1], G. Vourlias[1]

[1]Physics Department, Aristotle University of Thessaloniki, 54124 Thessaloniki, Greece

E-mail: vspirop@physics.auth.gr

For the protection of steel from corrosion various techniques have been developed, of which the most common and most effective and applied in industrial scale is hot-dip galvanizing [1]. In conventional galvanizing, steel protection is achieved by immersing the sample in a melt of pure zinc which results to the formation of a thick coating, which provides the required protection. The technique of hot-dip galvanizing is based on the cathodic protection of the ferrous substrate [2]. Essentially, the technique consists in converting the object that needs protection, in this case steel, in cathode of a galvanic element. The result is that oxidation reactions do not occur on the metal substrate, and thus it can be protected [3]. Several efforts have been made in order to improve the properties and to extend the lifetime of Zn coatings by alloying them with other metallic compounds [4]. Mg or Al alloyed zinc coatings have been reported as promising candidates because they form compounds and solid solutions with superior durability. Moreover, their reaction with oxygen results to the formation of chemically stable oxides. In the present work Zn-Mg and Zn-Al coatings formed with hot-dip galvanizing, are examined while the effect of dipping time was also investigated. The whole deposition setup was in a controlled Ar purged atmosphere in order to prevent the reaction of the molten metal bath with oxygen. The experimental data were acquired from Scanning Electron Microscopy (SEM) and X-Ray analysis (XRD).

References

[1] N. Katiforis, G. Papadimitriou, Surf. Coat. Technol. 78 (1996) 185.

[2] N. Pistofidis, G. Vourlias, S. Konidaris, E. Pavlidou, A. Stergiou, G. Stergioudis, Mater. Lett. 60 (2006) 786–789.

[3] X.G. Zhang, Corrosion and Electrochemistry of Zinc, Plenum Press, New York, 1996.

[4] E. Pavlidou, N. Pistofidis, G. Vourlias, G. Stergioudis, Mater. Lett. 59 (2005) 1619.

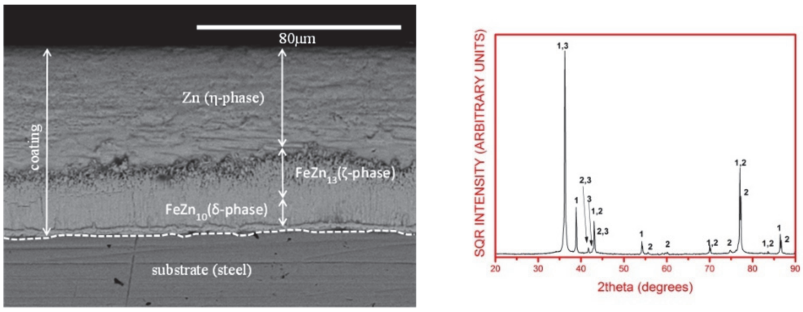

Figure 1: Cross sectional SEM micrograph of the Zn coated steel with hot-dip galvanizing and the corresponding XRD diffraction pattern (Pdf cards 1-Zn: #65-3358, 2-FeZn$_{13}$: #65-1238, 3-FeZn$_{10}$: #45-1184, PC Powder Diffraction Files, JCPDS-ICDD, 2005).

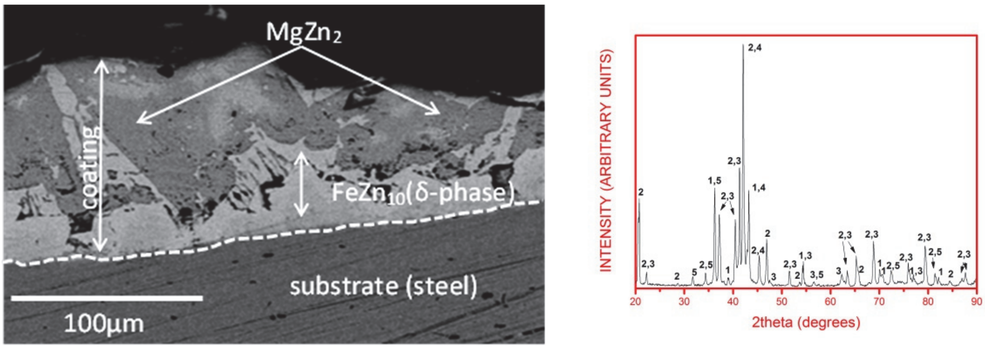

Figure 2: Cross sectional SEM micrograph of the Zn-Mg coated steel with hot-dip galvanizing and the corresponding XRD diffraction pattern (Pdf cards 1-Zn: #65-3358, 2-$MgZn_2$: #65-0120, 3-$FeZn_{13}$: #65-1238, 4-$FeZn_{10}$: #45-1184, 5-ZnO: #36-1451)

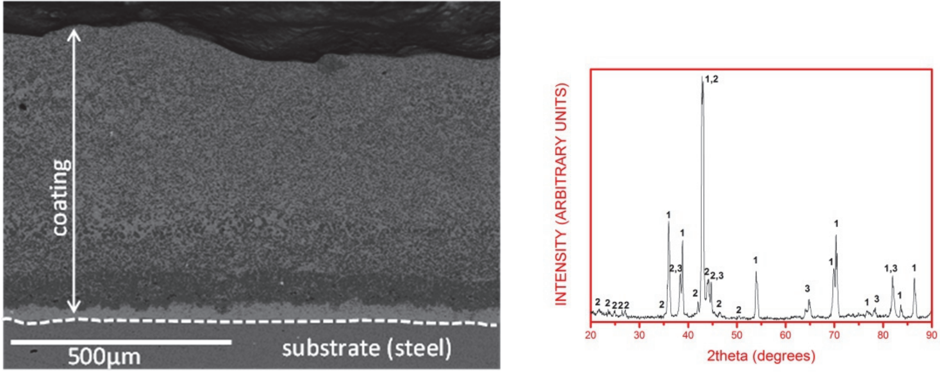

Figure 3: Cross sectional SEM micrograph of the Zn-Al coated steel with hot-dip galvanizing and the corresponding XRD diffraction pattern (Pdf cards 1-Zn: #65-3358, 2-$Al_{13}Fe_4$: #50-0797, 3-Al: #04-0787)

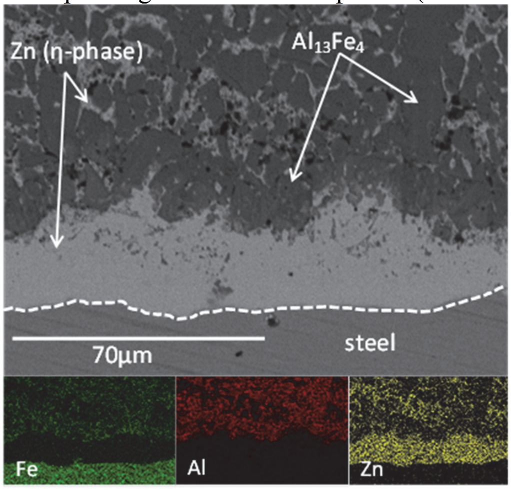

Figure 4: Cross sectional SEM micrograph of the Zn-Al coated steel with hot-dip galvanizing and chemical mapping analysis.

Ab initio calculations of ionization and excitation energies of biologically important heterocyclic planar molecules

A. Morphis, M. Mantela, M. Tassi, and C. Simserides

National and Kapodistrian University of Athens, Faculty of Physics, Department of Solid State
Physics, Panepistimiopolis, GR-15784 Zografos, Athens, Greece

E-mail: csimseri@phys.uoa.gr

We calculate [1] the lowest ionization and excitation energies in a variety of biologically important molecules, i.e. π-conjugated systems like DNA and RNA bases and isomers plus related heterocyclic molecules. These electronic transitions are mainly but not exclusively of π and π-π* character, respectively. We perform symmetry-constrained Density Functional Theory (DFT) [2,3] geometry optimization at the B3LYP/6-311++G** level of theory. With the ground-state geometries obtained from DFT, we calculate vertical excitation energies with the Completely Renormalized Equation of Motion Coupled Cluster with Singles, Doubles, and non-iterative Triples (CR-EOMCCSD(T)) method [4] and vertical ionization energies with the Ionization Potential Coupled Cluster with Singles and Doubles (IP-CCSD) method [5]. We, also, provide π-π* excitation and π ionization energies with a semi-empirical Hückel-type model [6] with novel parametrization. Our CC results are in very good agreement with experimental results. The Hückel-type model predictions generally follow the trends with some deviation. Computationally, CC methods are much more demanding both in CPU cycles and memory.

References

[1] A. Morphis, M. Mantela, M. Tassi, and C. Simserides, in preparation
[2] P. Hohenberg and W. Kohn, Phys. Rev. 136 (1964) B864
[3] W. Kohn and L.J. Sham, Phys. Rev. 140 (1965) A1133
[4] K. Kowalski and P. Piecuch, J. Chem. Phys. 120 (2004) 1715
[5] S. Hirata, M. Nooijen, and R.J. Bartlett, Chem. Phys. Lett. 328 (2000) 459
[6] L.G.D. Hawke, G. Kalosakas, and C. Simserides, Mol. Phys. 107 (2009) 1755

L-glutamine on Cu-Fe surfaces by Density Functional Theory Calculations

M. G. Bouri[1] **and Ch.E. Lekka**[1]

[1]Department of Materials Science & Engineering, University of Ioannina, Greece

E-mail: chlekka@cc.uoi.gr

The design of metallic coatings with enhanced corrosion resistance is very important since it may prevent environmental pollution and provide low cost opportunities to manufacturers and industry [1,2]. To this end, organic non-toxic molecules like amino acids were investigated as corrosion inhibitors on metallic surfaces [3,4]. In this work, density functional theory calculations were used to identify the adsorption properties of the L-glutamine amino acid on Cu-Fe surfaces. Starting from the Cu(111) surface, the L-glutamine was softly deposited according to seven possible configurations as presented in Figure 1.

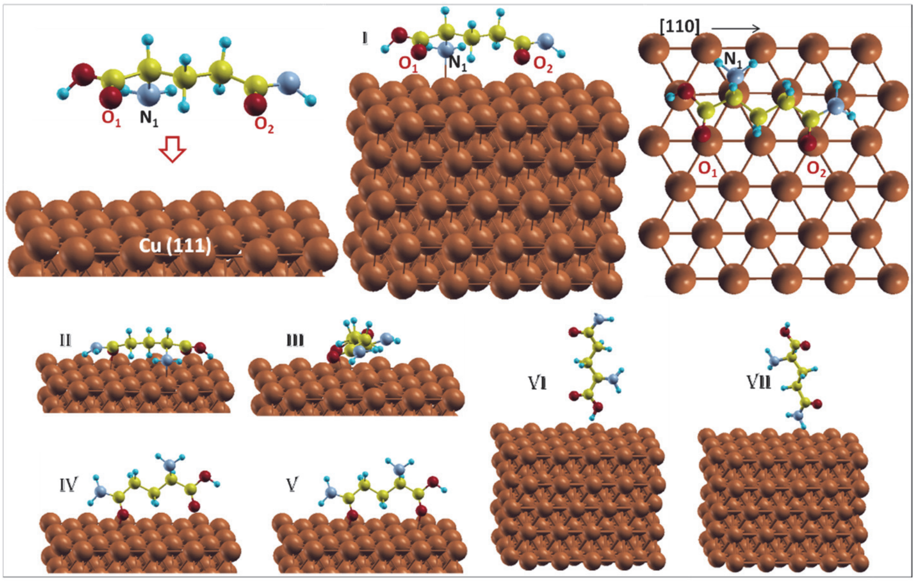

Figure 1. L-glutamine on Cu(111) surface: Schematic representation of the several adsorption sites. Grey, yellow, red, blue and orange balls stand for the N, C, O, H and Cu atoms, respectively.

The energetically favoured site (I) is the one where the L-glutamine's C zig-zag chain is aligned parallel to the [110] surface direction, having the nitrogen atoms and the oxo-group oxygen atoms (labeled O_1 and O_2) laying almost on-top of Cu surface atoms. The orientation preference of C atoms parallel to the [110] direction is in line with previously reported data for the graphene's zig zag edge alignment on Cu surfaces [5]. In addition, the C atoms of L-glutamine relax outwards compared to the O or N atoms on the Cu substrate while close to the Fermi level the system's wavefunction is mainly distributed on Cu revealing weak C-Cu or H-Cu hybridizations. The I configuration is followed by II (total energy difference DE=0.003eV) slightly shifted along [110], IV (1.78eV) and V (1.80eV) which are vertically oriented having only the oxo-group's oxygen atoms (O_1 and O_2) close to the surface and III (2.05eV) where the C chain is aligned along the [112] direction. Finally, the normal to the surface L-glutamine's deposition are energetically unfavoured (VI, 2.8eV and VII, 2.7eV) denoting the preference of the amino acid to form 2d coating on the Cu surfaces and therefore to act as corrosion inhibitor. The adsorption of L-Glutamine on Fe and Fe-Cu surfaces will be also evaluated in order to reveal the differences due to the Fe presence. These results could be used for the design of environmental friendly corrosion resist coatings.

Acknowledgments: This work was supported by the SELECTA (No. 642642) H2020-MSCA-ITN-2014 project

References

[1] Atmospheric corrosion of metals in industrial city environment, Elzbieta Kusmierek, Ewa Chrzescijanska, Data in Brief Volume 3, June 2015, Pages 149–154

[2] Corrosion: Understanding the Basics, The Effects and Economic Impact of Corrosion, 2000 ASM International. All Rights Reserved.

[3] Using Molecular Dynamics Simulations and Genetic Function Approximation to Model Corrosion Inhibition of Iron in Chloride Solutions K.F. Khaled1,2,* and A.M. El-Sherik3 , Int. J. Electrochem. Sci., 8 (2013) 10022 - 10043

[4] Electrochemical and molecular simulation studies on the corrosion inhibition of L-glutamine monolayers on an iron surface, ZHE ZHANG, SHENHAO CHEN, YUANYUAN FENG, YUNQIAO DING, JUANJUAN ZHOU, HENGLEI JIA, Journal of Serb. Chem. Soc. 74 (4) 407–415 (2009)

[5] Controlling the Orientation, Edge Geometry, and Thickness of Chemical Vapor Deposition Graphene, Adrian T. Murdock, Antal Koos, T. Ben Britton, Lothar Houben, Tim Batten, Tong Zhang,Angus J. Wilkinson, Rafal E. Dunin-Borkowski, Christina E. Lekka, and Nicole Grobert, ACS Nano, 2013, 7 (2), 1351–1359

Density Functional Theory Calculations of H_2O Adsorption on Cu(111)

Manos Zegkos[1] **and Ch.E.Lekka**[1]

[1]Department of Materials Science and Engineering University of Ioannina, Ioannina 45110 Greece

E-mail: chlekka@cc.uoi.gr

TUP

P100

The hydrophilicity or the hydrophobicity as well as the related antifouling capability of the metallic surfaces have various technological applications. Ab inition calculations on two prototype metallic (Pt and Au) surfaces revealed that Pt is hydrophilic while Au is hydrophobic and correlated their preference with the number of valence *d*–electrons [1,2]. In this work, the adsorption of H_2O molecules on Cu(111) surface was studied by means of density functional theory calculations. A H_2O molecule was initially deposited on the Cu(111) surface at the adsorption sites presented in Figure 1.

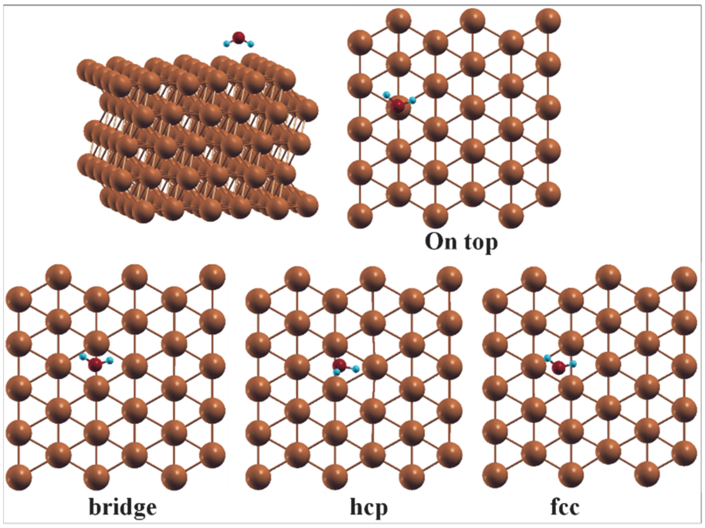

Figure 1. Schematic representation of selected H_2O molecule's adsorption sites on Cu(111) surface. Grey, yellow, red, blue and orange balls stand for the N, C, O, H and Cu atoms, respectively

The energetically favoured H_2O site was found to be the *On top* where the oxygen atom lays over a Cu surface atom in line with previous calculations [1,2]. The second favoured relax site was the *bridge* one, followed by the hcp and the fcc positions with total energy differences up to 0.2eV. The cases of H_2O dimmer, trimmer and hexamer along with the H_2O monolayer are in progress in order to reveal the 2d or 3d preference of molecule adsorption which can be related with the hydrophilic or hydrophobic character of the Cu surfaces.

Acknowledgments: This work was supported by the SELECTA (No. 642642) H2020-MSCA-ITN-2014 project

References

[1] Sheng Meng, E.G. Wang, Shiwu Gao, Journal of Chemical Physics **119**(2003) 7617-7620
[2] Sheng Meng, E. G. Wang, Shiwu Gao, PHYSICAL REVIEW B 69 (2004) 195404

Interaction of CVD graphene with femtosecond laser

N. Chourdakis[1], S. Katsiaounis[1], E. Michael[2], M. Fakis[2], I. Polyzos[1], J. Parthenios[1], C. Galiotis[1,3] and K. Papagelis[1,4]

[1]Foundation of Research and Technology Hellas, Institute of Chemical Engineering Sciences, P.O. Box 1414, GR-26504 Patras (Greece)
[2]Department of Physics, University of Patras, GR-26504 Patras (Greece)
[3]Department of Chemical Engineering, University of Patras, GR-26504 Patras (Greece)
[4]Department of Materials Science, University of Patras, GR-26504 Patras (Greece)
E-mail: kpapag@upatras.gr

Nowadays, there is a frantic activity worldwide to exploit the unique optical properties of graphene and other 2D crystal materials in photonic applications ranging from solar cells and light-emitting devices to touch screens, photodetectors and ultrafast lasers [1]. On the other hand, it has been recently shown experimentally that two-photon absorption in graphene is an extremely intense phenomenon [2]. Moreover, graphene is an ideal memory material because of its transparency, conduction properties and solution processability [3]. In this line, a novel technique for 3D optical data storage is proposed. Defects induced in graphene upon pulsed laser illumination will be used as the recording mechanism in the proposed 3D optical memory.

In a first step, we examine the generation of defects on CVD graphene deposited on the top of Si/SiO_2 substrate, at normal conditions. The graphene lattice is illuminated using 80 fs pulses centered at 820 nm and a repetition rate of 80 MHz (laser spot ~1 μm) with different experimental parameters such as laser power and exposure time in order to create defects having the appropriate size to provide clear detection and high storage density. The illuminated samples are characterized by SEM imaging as well as Raman spectroscopy using the laser excitation of 514 nm and a x100 objective yielding 1 μm laser spot size.

Detailed Raman mapping of graphene took place before and after the laser illumination. The Raman spectrum of pristine graphene consists of two distinctive features, known as G and 2D peaks which are located at around 1580 and 2680 cm^{-1}, respectively. The presence of defects gives rise to other two features at around 1350 cm^{-1} (D peak) and 1615 cm^{-1} (D` peak). The Raman spectra identify the different types of damage on graphene from femtosecond laser interaction. Two different types of damage can be found on graphene from femtosecond laser interaction: (a) material degradation involving oxidation and/or formation of disordered carbon or carbon species, and (b) complete or partial ablation [4,5]. The defected areas exhibit much higher I(D)/I(G) ratio compared to the non-defected ones indicating successful generation of defects (**Figure 1a**).

Electron microscopy and optical spectroscopy gave similar results concerning the size and shape of the defected areas. The defected regions can be easily identified by SEM images (**Figure 1b**). Increased laser power (ranging from 1 to 12 mW) leads to simultaneously increased defect size for a given exposure time of 20 sec. Laser power is not the only parameter that affects the size of the defected areas; by varying the exposure time (from 1 up to 100 sec) at the relatively low laser power level of 2 mW defected regions of different size can also be obtained. The higher the exposure time the higher the characteristic length of the defected areas. In any case, the laser fingerprint on graphene is nearly elliptic.

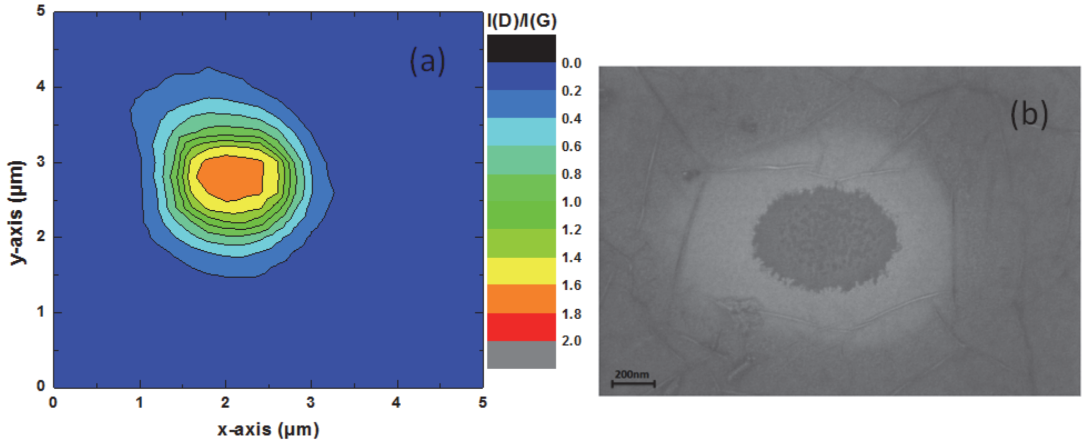

Figure 1. (a) Raman map of I(D)/I(G) measured with 0.2 μm step of CVD graphene after illumination with 3 mW laser power for 20 sec and (b) Corresponding SEM image.

Finally, we have measured by means of time-resolved pump-probe anti-Stokes Raman spectroscopy the relaxation rate of the G-mode of CVD graphene sample. The pump beam for excitation of the sample had an 816 nm central wavelength and it was supplied by an 85 MHz repetition rate with pulse duration of ~100 fs. The probe beam at 408 nm obtained by frequency doubling of the pump beam had almost the same pulse duration. A G-mode lifetime of 1.2 ps at 300 K was measured (**Figure 2**). The results will be discussed in terms of possible decay channels of the G-band into phonons of other branches due to phonon-phonon interactions [6].

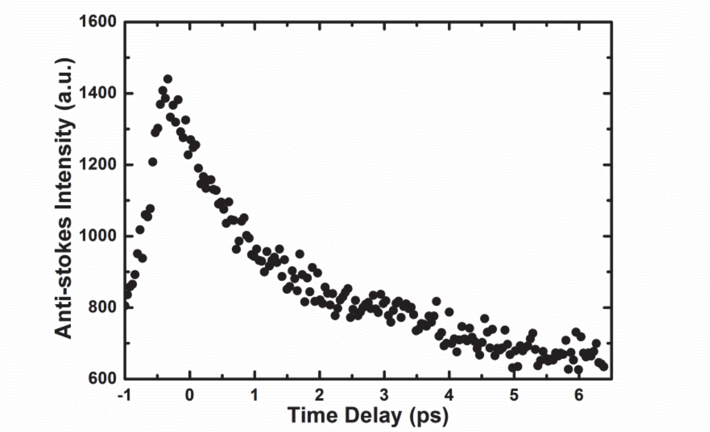

Figure 2. Anti-Stokes Raman signal for CVD monolayer graphene. The G-band signal is plotted as a function of the delay time between pump and probe beam.

References

[1] F. Bonaccorso et al, Nature Photonics 4 (2010) 611
[2] H. Yang et al, Nano Letters 11 (2011) 2622
[3] D.I. Son et al, Nano Letters 10 (2010) 2441
[4] M. Currie et al, Applied Physics Letters 99 (2011) 211909
[5] R. Sahin et al, Applied Physics Letters 104 (2014) 053118
[6] S. Wu et al, Nano Letters 12 (2012) 5495
[7] This research is supported by the programme "Aristeia II: Graphene physics in the time domain and application to 3D optical memories" implemented in the frame of the Operational Program "Education and Lifelong Learning" and is co-financed by the European Union and Greek national funds.

The effect of confinement and coupling with the substrate in the electron-phonon coupling constant of magic Gold nanoclusters studied with ultrafast electron diffraction

Thomas Vasileiadis[1], Lutz Waldecker[1], Roman Bertoni[1], Dawn Wells[2], Richard Palmer[2] and Ralph Ernstorfer[1],

[1]Physical Chemistry Department , Fritz Haber Institute, Faradayweg 4-6, 14195 Berlin, Germany.
[2]Nanoscale Physics Research Laboratory,
University of Birmingham
Edgbaston Birmingham
B15 2TT.

E-mail: vasileiadis@fhi-berlin.mpg.de

In this poster presentation we will inform you about our recent results regarding the effect of confinement in the electron-phonon coupling constant. Our approach consists of studying size-selected “magic” Gold nanoclusters [1]. Using ultrafast diffraction we observe directly the response of the lattice to electronic excitations, created by femtosecond laser pulses, with time resolution in the order of 100 fs [2]. The lattice temperature is probed by the decrease of intensity of the diffraction peaks due to the Debye-Waller effect. A strong enhancement of the dynamics of heat transfer from the electrons to the lattice is observed which indicates an enhancement of electron-phonon interaction in confined systems, possibly because of the presence of non-thermal electrons in longer than usual time delays (~1 ps). From the position of diffraction peaks, ultrafast expansion of the nanoclusters is probed with subpicometer resolution. Coupling of the nanoclusters with the substrate also has important effects like charge transfer and heat exchange through phonon-phonon interaction.

References

[1] Pekka Pyykkö, Nature Nanotechnology 2, 273 - 274 (2007).
[2] L. Waldecker, R. Bertoni, R. Ernstorfer, J. Appl. Phys. 117, 044903 (2015)

Morphology, Structure, and Strain properties of Quantum Nanostructures

N. Florini[1], J. Kioseoglou[1], G. P. Dimitrakopulos[1], Th. Pavloudis[1], Ph. Komninou[1], T.Walther[2], S. Germanis[3], K. Moratis[3], Z. Hatzopoulos[3], N. T. Pelekanos[3] and Th. Kehagias[1]

[1] Physics Department, Aristotle University of Thessaloniki, 54124 Thessaloniki, Greece
[2] Department of Electronic and Electrical Engineering, University of Sheffield, Mappin St, Sheffield S1 3JD, UK
[3] Materials Science & Technology and Physics Departments, University of Crete and IESL/FORTH, GR-71003 Heraklion, Greece

E-mail: nflori@physics.auth.gr

Quantum nanostructures exhibit significant electrical and optical properties, suitable for advanced applications in sensors, photonics and photovoltaics. The field of low-dimensional studied systems include quantum dots (QDs) and nanowires (NWs) grown on GaAs and Si substrates, respectively. In order to elucidate the morphology, the structural characteristics and the strain properties of quantum nanostructures, transmission electron microscopy (TEM) techniques were employed.

In the first case, piezoelectric InAs quantum dots (QDs) were grown either on the surface, or embedded in (211)B GaAs layers, by molecular beam epitaxy (MBE) via the Stranski-Krastanow mechanism. Combined plan-view and cross-sectional TEM/HRTEM observations showed that surface QDs were either large asymmetric agglomerates with diameters up to 250 nm, or individual InAs QDs with a pyramidal anisotropic shape with diameter 40-70 nm and height 5-15 nm, elongated along the [-111] direction [Fig. 1(a)]. The base-aspect-ratio ranges from 1.2 to 1.4 for the uncapped QDs. Embedded InAs QDs are also elongated along the same direction with a 6-10 nm length, while their height is of the order of 2 nm to 4 nm [Fig. 1(b)]. The strain properties of the nanostructure were studied by the geometric phase analysis method (GPA), applicable to images of high resolution TEM (HRTEM), Surface QDs were almost strain-free due to the introduction of a misfit dislocation network at the InAs/GaAS interface [Fig. 2(a)]. On the other hand, buried QDs are fully strained and optically active [Fig. 2(b)]. Moreover, assuming a plane stress state, an estimation of the chemical composition of the embedded QDs by quantitative GPA analysis showed a gradual increase of the In content from the base of the QDs to the apex region, suggesting possible Ga segregation in the initial stages of QD growth.

In the second case, GaAs NWs and GaAs/AlGaAs core-shell NWs were grown on Si(111) substrate by MBE via the vapor-liquid-solid (VLS) mechanism, using Ga droplets as a catalyst. Although the principal crystallographic structure of the NWs is zinc-blende (ZB), wurtzite (WZ) segments were sporadically observed within the ZB structure through the insertion of stacking faults (SFs). In addition, GaAs NWs grow along the <111> direction and emerge directly from the Si surface despite the presence of the thin amorphous native oxide [Fig. 3(a)]. Growth of NWs is actually promoted by the consecutive formation of mirror twins along the growth direction for several microns. The core-shell structure was confirmed by TEM and annular dark –field (ADF) STEM imaging, showing that the AlGaAs shell occupies at least one half of the projected diameter of the NWs [Fig. 3(b)]. Furthermore, the energy dispersive X-ray (EDX) analysis reveals that the Al content of the shell is ~35%. Finally, molecular dynamics simulations of hexagonal plan-view nanowire slices were applied to calculate the variation of the energy, the strain and stress related characteristics of the core-shell configuration.

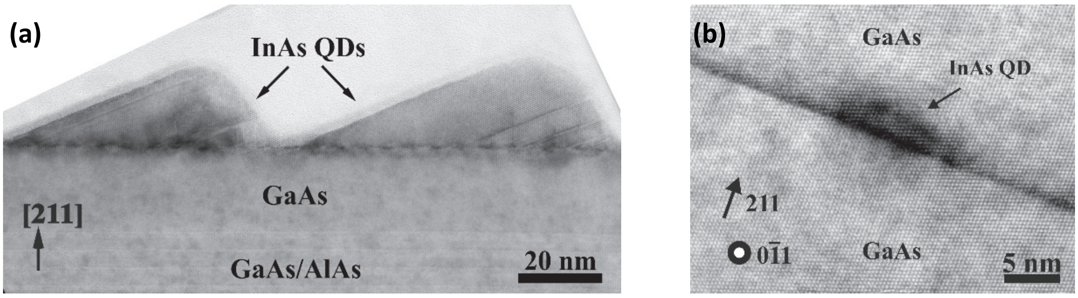

Fig.1 Cross-sectional HRTEM images, along the [0-11] zone axis, showing (a) two surface InAs QDs on top of the GaAs layer and (b) an individual buried InAs QDs inside the GaAs layer.

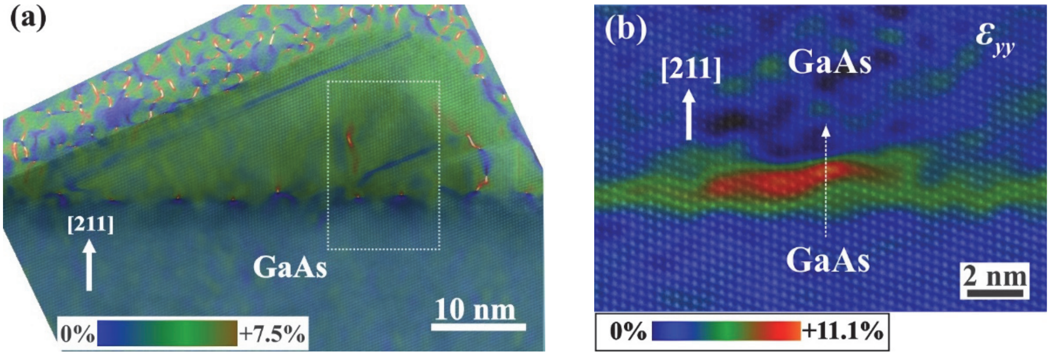

Fig.2 (a) Cross-sectional HRTEM images of (a) an uncapped InAs QD superimposed with the corresponding in-plane GPA strain map and (b) an embedded InAs QD superimposed with the corresponding GPA strain map along the growth (ε_{yy}) direction. Line profiles of the average strain have been obtained from the marked areas in images.

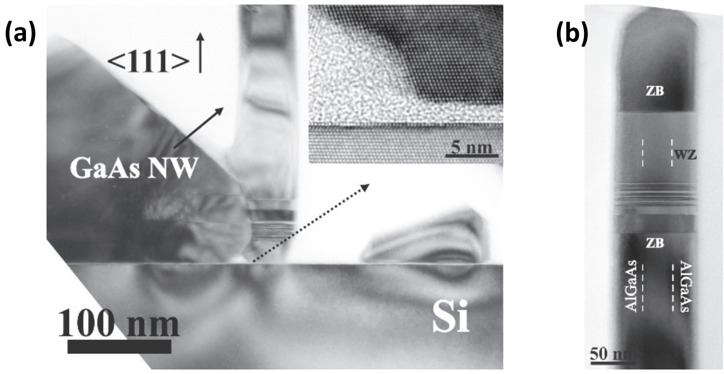

Fig.3 (a) TEM image of a NW emanate directly from the Si surface despite the presence of the amorphous native oxide (inset). (b) Diffraction contrast TEM image revealing the GaAs/AlGaAs core-shell configuration.

Acknowledgments Research co-financed by the EU (ESF) and Greek national funds - Research Funding Programs: THALES, project NANOPHOS and ARISTEIA II, project NILES

Hydrogenated Zinc and Titanium Oxide Cathode Interfacial Layers For Efficient and Stable Inverted Organic Solar Cells

E. Polydorou[1,2], **V. Papamakarios**[1], **A. Soultati**[1,3], **P. Argitis**[1], **L. C. Palilis**[2] **and M. Vasilopoulou**[1]

[1]NCSR “Demokritos”, Institute of Nanoscience and Nanotechnology (INN), POB 60228,
15310 Agia Paraskevi Attiki, Greece
[2]Department of Physics, University of Patras, 26500, Patras, Greece
[3]Department of Chemical Engineering, National Technical University of Athens,
15780 Athens, Greece

E-mail: e.polydorou@inn.demokritos.gr

Solution-processed bulk heterojunction organic photovoltaic cells (OPVs), composed of an interpenetrating network of a conjugated polymer as absorbing and electron donating material combined with an electron accepting fullerene derivative sandwiched between a transparent metal oxide anode and a metallic cathode, have been extensively investigated in the past decade as an alternative low cost renewable energy technology for light weight, flexible solar cells [1]. To optimize device performance in terms of efficiency and stability, many research advancements have been made particularly regarding the modification of electrode interfaces with wide band-gap modified transparent metal oxides as charge selective/transport layers and the implementation of inverted architectures. In this regard, zinc oxide (ZnO) and titanium oxide (TiO_x) are two of the most widely investigated cathode interfacial (i.e. electron selective) layers with diverse and tunable physical, chemical, optical and electronic properties that strongly depend on the deposition method and environment as well as on post-deposition treatment. One of the key issues is the presence of oxide surface defects in the form of either oxygen vacancies, surface hydroxyl groups or interstitials that may act as charge trapping/exciton quenching centers enhancing interfacial charge recombination/exciton dissociation or as charge donor/acceptor intra-gap states that could either reduce charge selectivity or facilitate charge extraction/transport.

To circumvent interfacial recombination or excitonic losses, research has geared towards different surface modifications such as post-deposition hydrogenation or plasma treatment as effective methods to passivate surface defects. Both ZnO and TiO_x are known to consist of two luminescence spectral regions: a short-wavelength (UV) band, located near the absorption edge of the oxide, that is attributed to emission from the excitonic band gap transition and a broader band usually centered in the visible arising from defects’ emission [1,2]. For example, it has been observed that hydrogenation can lead to a strong suppression of the defects’ emission and an enhancement of the excitonic emission, thus indicating that incorporation of hydrogen into the oxide may effectively passivate or “deactivate” surface defects [3].

Herein, we report on highly efficient and stable inverted bulk-heterojunction [based on a blend of regioregular poly(3-hexylthiophene) and (6,6)-phenyl C71 butyric acid methyl ester] organic solar cells with nanostructured ZnO and TiO_x films, as electron selective layers, that were subjected to varying treatments and molybdenum suboxide (MoO_x) as the hole selective layer. Significantly enhanced solar cell efficiency was achieved for hydrogen treated oxide layers. We investigate the effects of plasma treatment and hydrogenation as well as annealing of both oxides at various temperatures with regard to their optical and electronic properties. In particular, photoluminescence measurements verified the effective passivation of surface oxide traps after hydrogen annealing. We have, thus, demonstrated that post-deposition thermal annealing in hydrogen ambient introduces a reliable, low-cost and non-destructive surface passivation technique allowing the modification of different oxide materials incorporated to solution-processed inverted solar cells, enhancing both their efficiency and their stability.

Acknowledgements

The project "Implementing advanced interfacial engineering strategies for highly efficient hybrid solar cells" (Acronym: IMAGINE-HYSOL) is implemented under the "ARISTEIA II" Action of the "OPERATIONAL PROGRAMME EDUCATION AND LIFELONG LEARNING" and is co-funded by the European Social Fund (ESF) and National Resources.

References

[1] B. R. Lee, E. D. Jung, J. S. Park, Y. S. Nam, S. H. Min, B. –S. Kim, K. –M. Lee, J. –R. Jeong, R. H. Friend, J. –S. Kim, S. O. Kim and M. H. Song, Nature Communications DOI: 10.1038/ncomms5840.

[2] A. Sharma, J. B. Franklin, B. Singh, G. G. Andersson, D. A. Lewis, Organic Electronics 24 (2015) 131-136.

[3] H. L. Gao, X. W. Zhang, J. H. Meng, Z. G. Yin, L. Q. Zhang, J. L. Wu, X. Liu, Journal of Materials Chemistry A DOI: 10.1039/c4ta05541a.

Tailoring Molybdenum Oxide Electronic Properties and Stoichiometry For Application as an Anode Interfacial Layer in Efficient and Stable Organic Solar Cells

A. Soultati[1,2], A. M. Douvas[1], E. Polydorou[1,3], L. C. Palilis[3], P. Argitis[1] and M. Vasilopoulou[1]

[1]NCSR "Demokritos", Institute of Nanoscience and Nanotechnology (INN), POB 60228,
15310 Agia Paraskevi Attiki, Greece
[2]Department of Chemical Engineering, National Technical University of Athens,
15780 Athens, Greece
[3]Department of Physics, University of Patras, 26500, Patras, Greece

E-mail: a.soultati@inn.demokritos.gr

Transition metal oxides (TMOs) have been widely used as charge transport interlayers in organic optoelectronic devices due to their ability to exchange charges with several organic semiconductors, a process that requires interfacial energy-level alignment for barrier-free charge transport [1]. In particular, under-stoichiometric metal oxides with high work function such as molybdenum (MoO_x), tungsten (WO_x) and vanadium (V_2O_x) oxide that also show an enhanced density of mid-gap states have been used as anode interfacial layers as it has been demonstrated that these states could facilitate charge transfer from the highest occupied molecular orbital (HOMO) of an organic molecule in a more effective manner relative to their stoichiometric form. Moreover, under-stoichiometry and the formation of gap states near the Fermi level improves the oxide n-type conductivity, thus facilitating its implementation as a charge extraction layer in organic solar cells (OSCs) [2].

Herein, under-stoichiometric MoO_x films with tunable stoichiometry, work function and conductivity that have subjected to varying treatments, are used as anode interfacial layers in OSCs. Thermal and microwave annealing of the oxide films as well as hydrogenation are employed in an effort to tailor MoO_x electronic properties and stoichiometry and establish oxide treatment-electronic structure correlations. We demonstrate that when under-stoichiometric MoO_x films with controlled stoichiometry and work function are used as anode interfacial layers in OSCs based on a poly(3-hexythiophene):[6,6]-phenyl-C71 butyric acid methyl ester (P3HT:PC71BM) blend, solar cell performance is optimized as a result of excellent interfacial energy-level alignment and enhanced crystallinity/morphology of the photoactive blend (as revealed from X-ray diffraction and Atomic Force Microscopy measurements). This results in increased charge extraction and generation efficiency and a high power conversion efficiency of up to 4.34% that is demonstrated for a hydrogenated under-stoichiometric MoO_x anode interfacial layer [3].

Acknowledgements

The project "Implementing advanced interfacial engineering strategies for highly efficient hybrid solar cells" (Acronym: IMAGINE-HYSOL) is implemented under the "ARISTEIA II" Action of the "OPERATIONAL PROGRAMME EDUCATION AND LIFELONG LEARNING" and is co-funded by the European Social Fund (ESF) and National Resources.

References

[1] J. Meyer, S. Hamwi, M. Kröger, W. Kowalsky, T. Riedl, A. Kahn, Advanced Materials 24 (2012) 5408-5427.
[2] M. T. Greiner, M. G. Helander, W. -M. Tang, Z. -B. Wang, J. Qiu, Z. -H. Lu, Nature Materials 11 (2012) 76.
[3] M. Vasilopoulou, A. M. Douvas, D. G. Georgiadou, L. C. Palilis, S. Kennou, L. Sygellou, A. Soultati, I. Kostis, G. Papadimitropoulos, D. Davazoglou, P. Argitis, Journal of the American Chemical Society 134 (2012) 16178-16187.

TUP

P106

Stress-Strain Relation in (211)B-oriented InAs/GaAs Quantum Dot Superlattice

T. Koukoula[1], N. Florini[1], J. Kioseoglou[1], T. Kehagias[1], N. Pelekanos[2], Th. Karakostas[1]

[1]Physics Department, Aristotle University of Thessaloniki, GR-54124 Thessaloniki, Greece
[2]Microelectronics Research Group, IESL, FORTH, P.O. Box 1385, GR-71110 Heraklion, and Materials Science & Technology Department, University of Crete, P.O. Box 2208, GR-71003 Heraklion, Greece

E-mail: kehagias@auth.gr

The strong piezoelectric effect of InAs quantum dots (QDs) grown on high index GaAs surfaces, makes them suitable candidates for single photon sources operating at room temperature. Our study concerns the growth of fully strained InAs QDs buried on (211)B-oriented GaAs and the detection of potential Ga segregation in the InAs QDs to form $In_xGa_{1-x}As$ ternary alloys. For an accurate a posteriori determination of the chemical composition of the $In_xGa_{1-x}As$ QDs, its relation with the strained lattice parameters of the different alloys is required.

At first, an efficient route to modify strain fields in (211)-oriented InAs QDs system and determine their elastic characteristics is needed. Thus, the initial step was the transformation of the stiffness tensor of the (001)-oriented zinc-blende system to a stiffness tensor suitable for a (211)-oriented system, using a rotation matrix which transforms vectors and tensors from one coordinate system to another [1,2]. In (001)-oriented crystals, there are only three independent stiffness constants: C_{11}, C_{12}, and C_{44}. The stiffness tensor $C_{ij}(211)$ is shown in Fig. 1, where the equations of the new stiffness constants $C'_{11}, C'_{12}, C'_{13}, ...$ are a combination of the C_{11}, C_{12}, and C_{44} ones.

Subsequently, in the framework of continuum elasticity theory, we calculated the excess energy and the out-of-plane strained lattice *d*-spacing of the {422} lattice planes in buried (211)-oriented $In_xGa_{1-x}As$ QDs. Initially, two primary types of stress states were independently considered, namely the biaxial and the hydrostatic. Taking into account the experimentally determined very small dimensions of the $In_xGa_{1-x}As$ QDs, a combined stress mode comprising an "elastic" hydrostatic stress component accompanied by a biaxial elastic infinitesimal one was also considered [3]. The calculated excess energies for each model versus the Indium content of the QDs are depicted in the graph of Fig. 2, showing that the combined biaxial/hydrostatic stress mode for QDs exhibited the lowest excess energy and therefore is energetically favorable. In Fig. 3 a graph of the GPA strain along the growth direction is depicted, calculated from the strained out-of-plane lattice spacing deriving from the abovementioned methodology, as a function of the QDs' In content for each case, along with the corresponding calculated GPA strain from Vegard's law. It is evident that if the combined stress mode is active, a higher In content is incorporated in less strained QDs, compared to the pure plane-stress mode. Hence, measuring the experimental out-of-plane lattice spacing from HRTEM and/or GPA, these graphs can be utilized to determine the chemical composition of the $In_xGa_{1-x}As$ QDs.

[1] J. F. Nye, Physical Properties of Crystals: Their Representation by Tensor and Matrices (Oxford University Press, New York, 1985).

[2] S. Schultz, M.A. Caro, E.P. O'Reilly, and O. Marquardt, Phys. Rev. B 84, 125312 (2011)

[3] F. Birch, Phys. Rev. 71, 809 (1947)

$$C_{ij}(211)=\begin{bmatrix} c'_{11} & c'_{12} & c'_{13} & c'_{14} & 0 & 0 \\ c'_{12} & c'_{22} & c'_{12} & 0 & 0 & 0 \\ c'_{13} & c'_{12} & c'_{11} & -c'_{14} & 0 & 0 \\ c'_{14} & 0 & -c'_{14} & c'_{44} & 0 & 0 \\ 0 & 0 & 0 & 0 & c'_{55} & c'_{14} \\ 0 & 0 & 0 & 0 & c'_{14} & c'_{44} \end{bmatrix}$$

Figure 1: The stiffness tensor of (211)-oriented zinc-blende systems

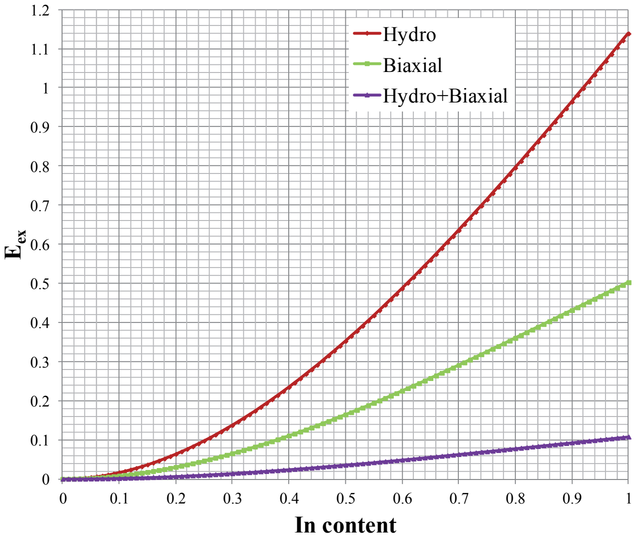

Figure 2: The calculated excess energy, E_{ex}, as a function of the QDs' Indium content.

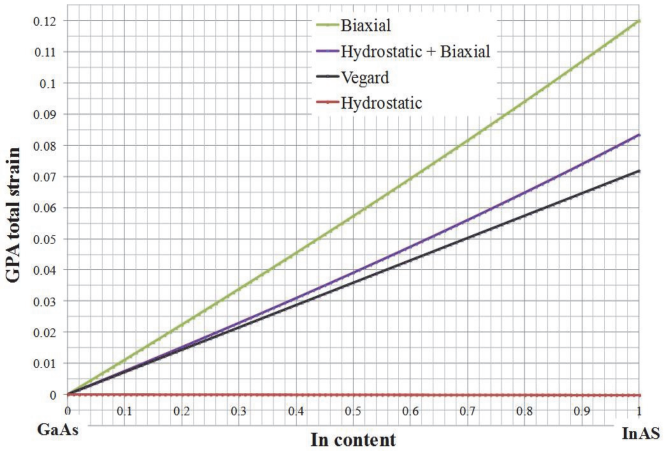

Figure 3: The calculated GPA strain as a function of the QDs' Indium content.

Acknowledgment: Research co-financed by the European Union (ESF) and Greek national funds through the Operational Program "Education and Lifelong Learning" of the National Strategic Reference Framework (NSRF) - Research Funding Program: THALES, project "NanoPhos".

Structural reconstructions, band gaps and bowing parameters of the ternary nitride alloys

Th. Pavloudis[1], Ph. Komninou[1], Th. Kehagias[1], G. Dimitrakopulos[1], Th. Karakostas[1] and J. Kioseoglou[1]

[1]Physics Department, Aristotle University of Thessaloniki, GR-54124 Thessaloniki, Greece

E-mail: corresponding-sifisl@auth.gr

The USPEX structure prediction code in combination with *ab initio* calculations is implemented in order to reveal energetically favourable reconstructions of the ternary nitride alloys. Sixteen 2x2x2 supercells (32 atom) are used to explore the entire range of concentrations (x=0÷1). Total energy calculations are accomplished under the Heyd-Scuseria-Ernzerhof hybrid functional, Local Density Approximation and the Perdew-Burke-Ernzerhof derivation of the Generalized Gradient Approximation using Projector Augmented Wave pseudopotentials. The formation energies, and band gaps are examined. The formation energy plots show local minima at specific concentrations. The valance band maximums, conduction band minimums and the band gaps are plotted and the composition-independent bowing parameters for the quadratic Vegard's equation are extracted. The band gap deviations from Vegard's law show total maxima at specific concentrations. The band gaps cannot be accurately described by single composition-independent bowing parameters, however they are sufficiently described by region dependent bowing parameters (Figure 1). The *ab initio* results are verified by molecular dynamics calculations. The molecular dynamics calculations are realized using a bond-order interatomic potential. Supercells of ~10^4 atoms are used. The obtained local minima of the formation energy for the specific alloy compositions concur with those predicted by *ab initio* calculations, proving the results are not influenced by the supercell size. The predicted InxGa1-xN atomic reconstructions, corresponding to the local minima of the relative formation energies, present structural ordering in a 2x2x2 supercell configuration. This could be experimentally identified using selected area electron diffraction due to the anticipated appearance of superllatice reflections as it is revealed from the simulated electron diffraction patterns.

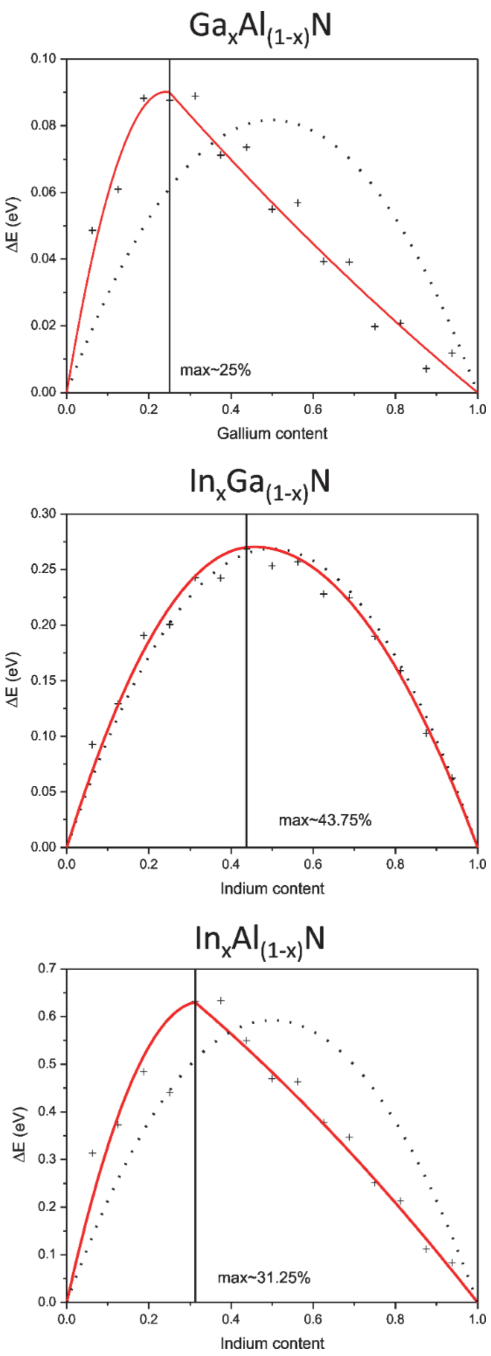

Figure 1. Band gap deviations for the GaxAl(1-x)N, InxGa(1-x)N and InxAl(1-x)N alloys. The dotted line represent Eq. (5) where the composition independent bowing parameters is considered, while the solid lines correspond to composition dependent bowing parameters, before and after the deviation maxima.

Acknowledgements

Research co-financed by the European Union (ESF) and Greek national funds through the Operational Program "Education and Lifelong Learning" of the NSRF - Research Funding Program: THALES, project “NitPhoto”. This work was supported by the LinkSCEEM-2 project, funded by the European Commission under the 7th Framework Program through Capacities Research Infrastructure, INFRA-2010-1.2.3 Virtual Research Communities, Combination of Collaborative Project and Coordination and Support Actions (CP-CSA) under grant agreement no RI-261600.

Strain and elastic constants in GaN and InN: a first principles study

M.M. Soumelidou[1], J. Kioseoglou[1], Ph. Komninou[1], and Th. Karakostas[1]

[1]Physics Department, Aristotle University of Thessaloniki, GR-54124 Thessaloniki, Greece

E-mail: corresponding-karakost@auth.gr

Group III-nitrides and their alloys have attracted researchers' interest because of their optoelectronic properties. The band gap tuning of their ternary alloys (InGaN, AlInN, AlGaN) in the visible spectrum makes them suitable for a vast variety of applications, such as laser diodes, light-emitting diodes, photovoltaics. The lack of understanding the effect of strain on the electronic properties yields to further investigations. Intentionally or unintentionally the strain embedded in the structures modifies the electronic band structure. A recent study revealed that the deformation potentials of AlN, GaN, and InN can be used to explain the effect of strain on the electronic band structure [1]. Previous results on the elastic properties of AlN, GaN and InN were presented by A.F. Wright [2] where the elastic constants for small strains were calculated by DFT within the local density approximation (LDA). Theoretical DFT calculations using local density approximation (LDA) and generalized gradient approximation (GGA) in group III-nitrides cannot yet overcome the band gap problem which is influenced by discrepancies in the values of the lattice constants [3,4]. This problem is essential in studying the structural and electronic properties of InAlN, InGaN and AlGaN alloys because of the composition fluctuations as well as the deviation from Vegard's law. Great effort is made to comprehend the band gap bowing of these alloys taken into account the internal local strain of the structures. No previous results have been presented in order to define the linearity or not of the whole region of elastic deformation in III-nitrides.

In this work, density functional theory (DFT) implemented in ABINIT code will be used for studying the structural, electronic and elastic properties of group III-nitrides and their ternary alloys under very small (<1%) and very large (>3%) strain (Fig.1,2). The exchange and correlation were treated using the LDA under modified, norm conserving Troullier-Martins pseudopotentials (MPP-LDA), which result in a band gap value of 3.40 eV and 0.75 eV for bulk GaN and InN respectively thus overcoming the band gap underestimation problem. The values of the elastic constants of GaN and InN for $\delta \pm 0.02$ are in accordance to Wright's [2] results. However, different effects are observed in the three areas of strain ($\delta \pm 0.02$, $\delta \pm 0.01$, $\delta \pm 0.1$). There is an open question as to how the heterostructures, such as GaN/InN structures or InN monolayers grow under large strains. Intense deformation is observed in InN quantum dots on GaN due to the large mismatch between the two materials (~10%). It is also known that when the growth temperature is below the half of the melting point the critical thickness for plastic relaxation is enormously large, and consequently the elastic relaxation mechanism become dominant even for large strains.

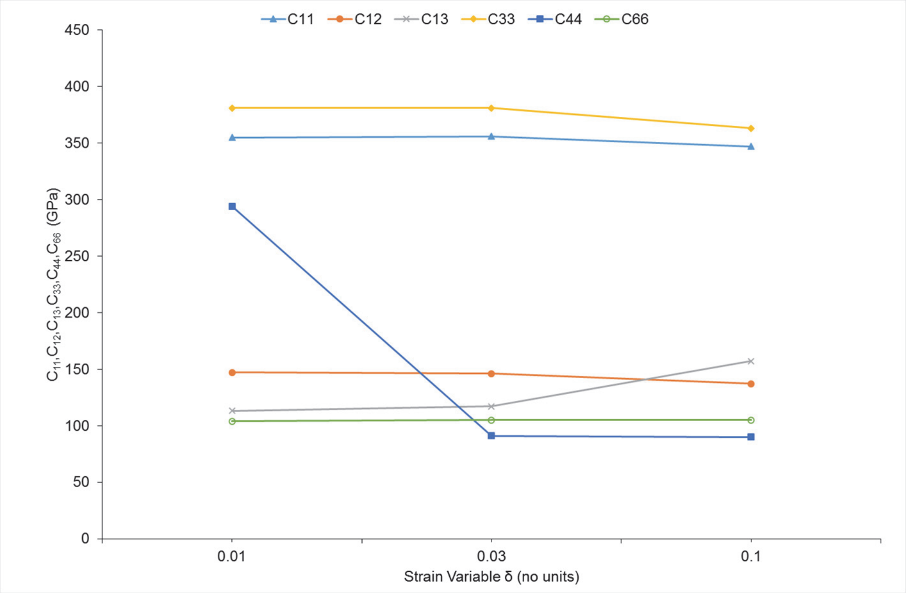

Figure 1 Calculated Elastic Constants in wurtzite GaN for Strain variable δ =±0.01, δ =±0.03 and δ= ±0.1.

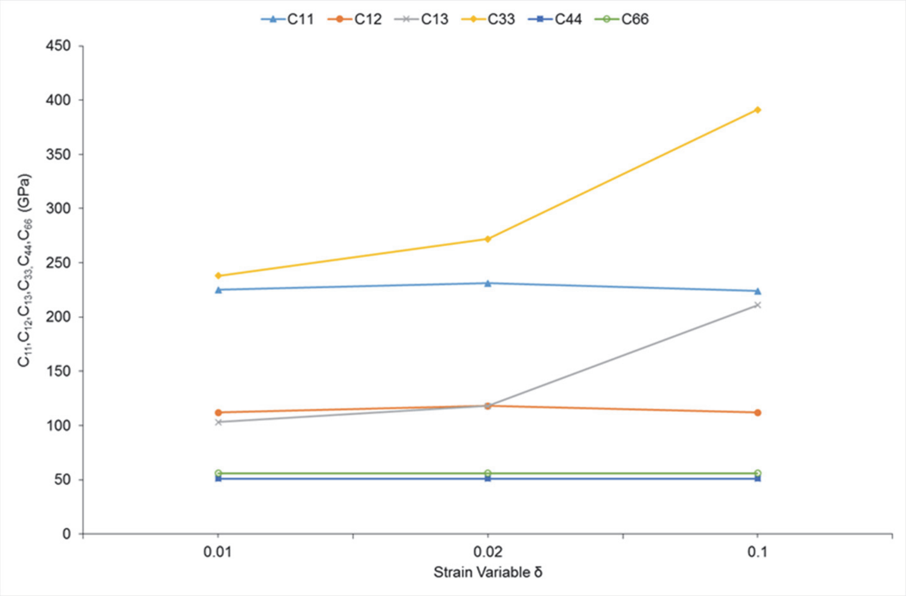

Figure 2 Calculated Elastic Constants in wurtzite InN for Strain variable δ =±0.01, δ =±0.02 and δ= ±0.1.

Acknowledgements: Research co-financed by the European Union (ESF) and Greek national funds through the Operational Program "Education and Lifelong Learning" of the National Strategic Reference Framework (NSRF) - Research Funding Program: THALES, project “NanoWire”.

References

[1] Q.Yan, P. Rinke, M. Scheffler, and C. G. Van de Walle Appl. Phys. Lett. 95 (2009) 121111.
[2] A. F. Wright, J. Appl. Phys., Vol. 82, No. 6 (1997).
[3] C. Stampfl and C. G. Van de Walle, Phys.Rev. B, Vol.59, No. 8 (1999).
[4] M. Fuchs, J. L. F. Da Silva, C. Stampfl, J. Neugebauer, and M. Scheffler, Phys. Rev. B, Vol. 65, (2002) 245212.

TUP

P109

Improved Hg^0 Removal from Flue Gases by Mn(IV) Feroxyhyte

E. Kokkinos[1]*, I. Kellartzis[1], G. Stavropoulos[1], G. Vourlias[2] and M. Mitrakas[1]

[1]Department of Chemical Engineering, Aristotle University of Thessaloniki, 54124, Thessaloniki, Greece
[2]Department of Physics, Aristotle University of Thessaloniki, 54124 Thessaloniki, Greece

E-mail: kokkinosevgenios@yahoo.gr

Mercury is recognized as a global contaminant because it can undergo long range transport in the atmosphere, be persistent in the environment, be accumulated in the food chain and pose severe adverse effects on the human and ecosystem health. Development of new technologies to remove mercury from flue gases and also drinking water has attracted the attention of researchers for quite a long time now and remains an extremely active field. The conventional mercury treat is by air pollution control devices, like electrostatic precipitators and scrubbers. However these technologies were not developed for this use and therefore their efficiency is limited.

A more specific solution can be an adsorbent injection inside the flue gas. The material must adsorb effectively metallic mercury, which is the metal's speciation at high temperatures. Iron manganese oxy-hydroxides have already proved to exhibit enhanced performance in the removal of mercury from water which is attributed to the high negative surface charge density and specific surface area [1]. Oxy-hydroxide evaluation of mercury removal was carried out using a down flow packed bed reactor inside a tubular furnace under 150°C. The elemental inflow mercury was controlled at 400 μg/m^3 by adjusting the N_2 flow rate passing through the mercury saturator and a cold vapor atomic absorption spectrometer (CVAAS) recorded the effluent concentration.

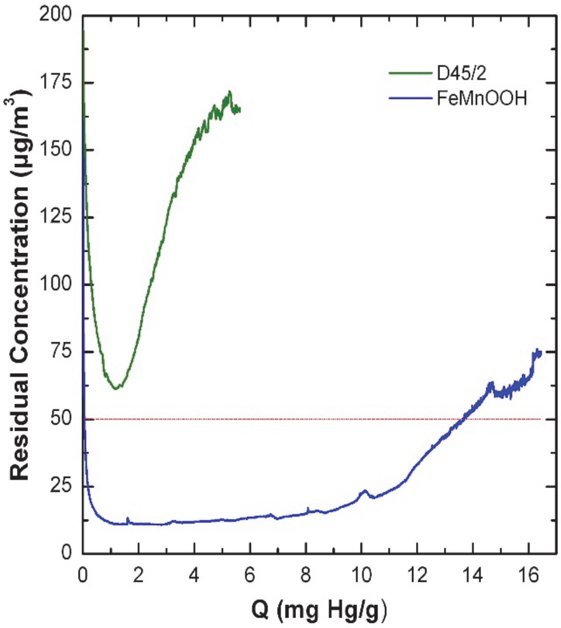

Figure 1. Breakthrough curves under N_2 atmosphere.

Breakthrough curves of tested binary oxyhydroxide (Fig. 1) and a commercial carbon (D45/2), which used as a reference material, show that only FeMnOOH has the ability to reduce the residual mercury concentration below regulation limit (50 μg/m^3). Carbon's ability to remove mercury depends on their surface area (1230 m^2/g) and as a result does not show high capacity. This kind of adsorbents has no efficiency at low concentrations, such as regulation limit. Instead, tetravalent manganese feroxyhyte, beside surface area, can achieve an order of magnitude higher capacity due to negative surface charge (1.75 mmol H^+/g). Additional attributes low residual concentrations as mercury binds strongly with the material's active sides.

The proof that the surface charge is a key feature reinforces the possible adsorption mechanism from binary oxy-hydroxides that follows. Also, it is assumed the existence of tetravalent manganese in almost constant rate for this kind of materials (~ 12%) and that mercury is oxidized after the end of the process. The information obtained through the spectra of X-ray spectroscopy (XPS), where peaks at 100.5 eV and 104.5 eV are observed, indicates the presence of bivalent mercury (Fig. 2).

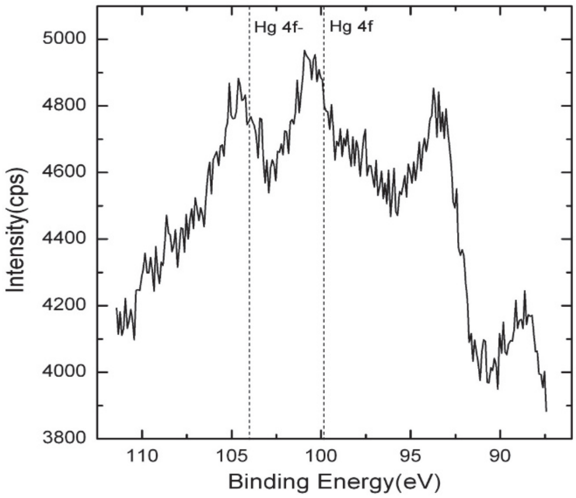

Figure 2. XPS diagram, detail spectrum of mercury 4f.

The possible mechanism is:

$$\equiv \quad + \mathrm{Hg}^0 \rightarrow \equiv \quad \text{-}\mathrm{Hg}^0$$
$$\equiv \quad \text{-}\mathrm{Hg}^0 + \equiv\mathrm{Mn}^{4+} \rightarrow \equiv\mathrm{Mn}^{2+}\mathrm{Hg}^{2+}$$
$$\equiv\mathrm{Mn}^{2+}\mathrm{Hg}^{2+} + 2\ \equiv\mathrm{O}^{-} \rightarrow \equiv\mathrm{Mn}^{2+} + \equiv\mathrm{O}^{-}{}_{2}\mathrm{Hg}^{2+}$$

In the first step, mercury is absorbed and reaches the surface. Then the process of oxidation from the tetravalent manganese takes place, resulting in a change valence from +4 to +2. This information however is not confirmed by XPS spectra as the percentage of divalent manganese is not enough to shift the tetravalent's peaks. On the other hand, the oxidation caused by ferric iron is minimal to zero, since respective materials without manganese have significantly low uptake compared with binaries [1]. Finally, since mercury is converted to the bivalent form will form bonds with two oxygens that carry the negative charge.

Acknowledgements

The financial support through the co - Financed by the European Union and the Greek State Program EPAN-II (OPC-II)/ESPA (NSRF): 'SYNERGASIA II', Project (MERCAP) - "Advanced Materials for Mercury Capture (11SYN-8-206), is gratefully appreciated.

References

[1] E. Kokkinos et al., Desalination and Water Treatment J., 54 (2015) 2082-2090.

Vitrification as a tool for sustainable solid waste management

P. Kavouras, S. Varitis, G. Kaimakamis, Ph. Komninou and Th. Karakostas

Department of Physics, Aristotle University of Thessaloniki, Thessaloniki 54124, Greece

E-mail: pkavo@physics.auth.gr

TUP

P110

The increasing economic, scientific and social pressure towards more sustainable solid waste management practices is transforming the available solidification and stabilization strategies from a linear to a circular approach. According to this trend, after the application of the urban mining concept in municipal and industrial waste streams [1], the residues should be placed in geological repositories, closing in such a way the material cycle [2]. The whole process can be visualized in the schematic of Figure 1. Such a termination of the waste treatment process sets high demands on the properties of the end product, in terms of long-term chemical stability and mechanical performance.

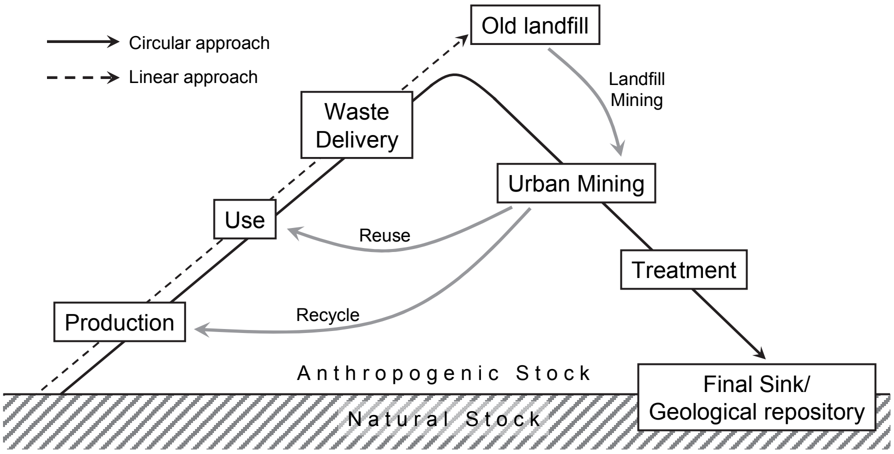

Figure 1: Comparison between the linear (traditional) and circular (novel) approach of stabilization and solidification strategies.

The research for a remediation technology appropriate for nuclear technology by-products has concluded to the vitrification method. Its place has been crucial since early 1960's, when it started being applied as the method for immobilization of high-level radioactive wastes [3]. Despite vitrification's end products evident advantages in terms of high chemical stability, endurance in time, superior mechanical properties, versatility, reduced volume and lack of organic content [4,5], it has not been extensively applied for the solidification and stabilization of solid industrial or municipal wastes.

The main cause is that application of vitrification is more expensive, compared to alternative methods of solidification and stabilization. This shortcoming is nevertheless being dwarfed by the increasing demands of the circular approach strategy, described above. It is plausible that vitrification will again become one of the focal points of scientific research on sustainable solid waste management.

In the present work an overview of the application of vitrification method is being made for three case studies, i.e. for solidification and stabilization of three different industrial solid wastes. These wastes come from the oil distillery and storage [6], steel recycling [7] and leather industry [8] sectors. In those cases the vitreous products stand at the crossroad of the vitrification method, as they are the starting materials for the production of glass-ceramic or glass-based end products. The adaptability of the vitrification method is based on the many “degrees of freedom” coming from the diversity of the potential vitrifying agents, vitrification and devitrification conditions and the vitreous nature of the end products.

Scope of this work is to present the versatility and effectiveness of vitrification method, in order to illustrate its potential leading role on the solid waste management field, as it is being progressively diverted towards the circular approach strategy.

This research has been co-financed by the European Union (European Social Fund - ESF) and Greek national funds through the Operational Program "Education and Lifelong Learning" of the National Strategic Reference Framework (NSRF) - Research Funding Program: THALES: Reinforcement of the interdisciplinary and/or inter-institutional research and innovation.

References

[1] P. Baccini, P.H. Brunner, Metabolism of the Anthroposphere – Analysis, Evaluation, Design. The MIT press, Massachusetts Institute of Technology, Cambridge, 2012.
[2] R. Cossu, Waste Manag. 33 (2013) 497-498.
[3] M.I. Ojovan, W.E. Lee, An Introduction to Nuclear Waste Immobilization, Elsevier, Oxford (2nd Edition), 2014.
[4] P. Colombo, G. Brusatin, E. Bernardo, G. Scarinci, Cur. Opin. Sol. Stat. Mater. Sci. 7 (2003) 225-239.
[5] E. Bernardo, G. Scarinci, P. Colombo, Vitrification of waste and reuse of waste-derived glass, in: Meyers, R.A. (Ed.), Encyclopedia of Sustainability Science and Technology. Springer, Berlin, 2012, pp. 11581-11613.
[6] P. Kavouras, G. Kaimakamis, Th.A. Ioannidis, Th. Kehagias, Ph. Komninou, S. Kokkou, E. Pavlidou, I. Antonopoulos, M. Sofoniou, A.I. Zouboulis, C.P. Hadjiantoniou, A. Prakouras, Th. Karakostas, Waste Manag. 23 (2003) 361-371.
[7] P. Kavouras, Th.A. Ioannidis, G. Kaimakamis, I. Tsilika, K. Chrissafis, Th. Kehagias, A.I. Zouboulis, Ph. Komninou, Th. Karakostas, J. Europ. Ceram. Soc. 27 (2007) 2317-2323.
[8] S. Varitis, E. Pavlidou, P. Kavouras , G. Vourlias, K. Chrissafis, A. Xenidis, Th. Karakostas, J. Therm. Anal. Calorim. DOI 10.1007/s10973-015-4539-7 (2015) article in press.

TUP

P111

Color fastness of green pigments in egg tempera technique under accelerated aging and weathering tests

E. Lykartsi[1], L. Malletzidou[1], T. Zorba[1], G. Vourlias[1], T.G. Stamkopoulos[2],
N. Nikolaidis[3] and K.M. Paraskevopoulos[1]

[1]Physics Department, Aristotle University of Thessaloniki, GR-54124, Thessaloniki, Greece
[2]University Ecclesiastical Academy of Thessaloniki, GR-54250 Thessaloniki, Greece
[3]Chemistry Department, Aristotle University of Thessaloniki, GR-54124, Thessaloniki, Greece

*elykarts@gmail.com

Egg tempera is a painting technique that was used by great artists through the centuries as it gives great plasticity and color brilliance to whichever artwork is used. Pigments can be natural or synthetic, inorganic and organic, grounded into fine powders. The green pigments, to which this study is focused, are used since ancient times but are very problematic and unstable colors [1]. Determining the degradation mechanisms of these materials helps a conservator to plan the methods of preventive and interventive conservation of works of art, which has aesthetic aims and also leads to prolonging life expectancy as well as better exhibition and storage conditions in the future [2].

The present analysis is a part of a comprehensive study of the artificial aging of art materials in different painting techniques and focuses on different green pigments (malachite, verdigris, viridian, green earths etc.) mixed with egg yolk as a medium. The samples were aged artificially in different conditions in order to isolate the factors that influence them. Firstly, the samples were kept for 45 days at 60ºC in a drying oven and then, for 24 hours, at 120°C lacking humidity in another oven. In a second experiment, thin layers of the samples were exposed to UV light for 700 hours in a controlled environment chamber at 40 % relative humidity and 50ºC temperature [3]. Another color palette with green pigments and egg yolk including 20% TiO_2 was prepared and exposed to the latest conditions. Titanium dioxide white is the leading white color since the beginning of the 20th century and used by many artists to produce the desired color tone and make the final color last more in time [4]. Measurements were taken periodically using Fourier Transform Infrared Spectroscopy (FTIR) and X-ray diffraction (XRD) in order to identify the possible changes in the chemical composition of the samples. Changes in the physical properties were observed even without the use of optical augmentation. The samples were also measured by a reflective spectrophotometer so as the color coordinates L, a, b, E, H to be determined [5].

The surface mechanical and chemical properties of the pigments were also observed after four experimental circles according to ISO B06 - concerning color fastness to artificial daylight including humidity adjustments - inside a weathering chamber, where the samples were exposed to alternating cycles of UV light and moisture at controlled and elevated temperature. The photodegradation that occurred was a reproduction of the damage that would have occurred naturally over months or years outdoors [6].

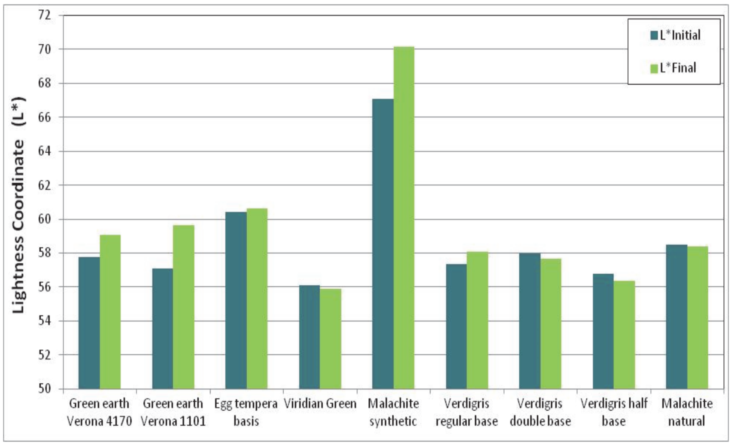

Figure 1. Lightness coordinate diagram of samples before and after the accelerated aging

The experimental results showed that heat alone does not chemically affect the samples and does not contribute to their aging process. As far as the physical properties are concerned, a change in the color of the samples was observed and the surface of some of them was crackled. However, regar-ding the influence of UV radiation combined with temperature, changes were observed in the FTIR spectra mainly to the sample of the pure binder, as well as cracking, yellowing and discoloration [6]. Color change, gloss loss, cracking and embrittlement was also observed due to aging in the weathering chamber. The modifications in the chemical composition under the conditions of weathering experiment, as well as the results concerning the interaction of organic binders with inorganic pigments in general and the overall observation on the light fastness of the colors, were very interesting and will be investigated extensively in future work.

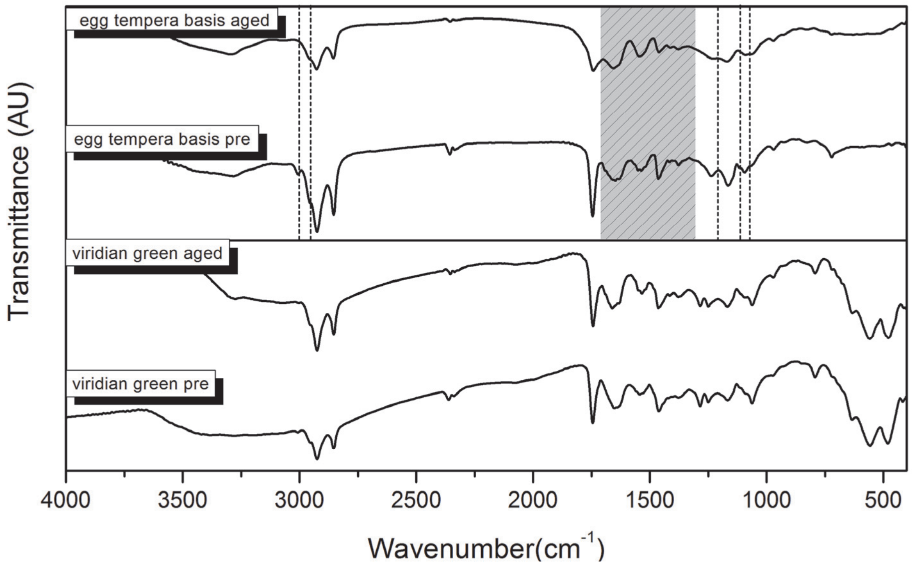

Figure 2. FTIR spectra of indicative samples before and after the accelerated aging

References

[1] N. Eastaugh, V. Walsh, T. Chaplin, R. Siddall, Pigment Compendium, Butterworth-Heinemann (2004) 248 and 385

[2] P. Dellaportas, E. Papageorgiou, G. Panagiaris, Heritage Science 2 (2014) 2

[3] D. Saunders, J. Kirby, National Gallery Technical Bulletin 15 (1994) 79 - 97

[4] Z. E. Papliaka, N. Wendland, E. A. Varella, e-PS 7 (2010) 48-54

[5] L. Samain, G. Silversmit, J. Sanyova, B. Vekemans, H. Salomon, B. Gilbert, F. Grandjean, G. J. Long, R.P. Hermann, L. Vincze, D. Strivay, J.Anal. At. Spectrom. 26 (2011) 930 - 994

[6] M. San Andres, J.M de la Roja, V.G. Baonza and N. Sancho, J.Raman Spectrosc. 41 (2010) 1468 - 1476

[7] J.M. Powers, P.L. Fan, C.N. Raptis, J. Dent Res 59 (1980), 2071-4

Saint Demetrios Monastery of Stomion: Comparative analysis of plasters via TG-DSC and FTIR

L. Malletzidou[1], D.A. Patsiaoura[1], T. Zorba[1], P. Beinas[2], K. Chrissafis[1] and K.M. Paraskevopoulos[1]

[1]Solid State Physics Department, Aristotle Univ. of Thessaloniki, GR-54124, Thessaloniki, Greece
[2]Painting Conservator, "Esaeitexnon" Artwork Conservation Laboratory, GR-60100, Katerini, Greece

e-mail: labrinim@auth.gr

Introduction

Plasters from St. Demetrios Monastery of Stomion near Larisa town, Greece, were studied in order to achieve a full characterization of the materials as well as the techniques that were employed for the completion of the pictorial decoration. The samples came from the partial existing wall paintings in the side chapels of the monastery's Catholicon and date back to at least mid-18th century. These were extensively studied by means of Thermogravimetry and Differential Scanning Calorimetry (TG-DSC) and Fourier Transform Infrared Spectroscopy (FTIR) [1].

Materials and methods

Numerous wall painting samples were collected during the works of restoration and certainly after the stabilization of the painting and plaster layers because of the poor preservation state of the Catholicon. The plaster samples were extracted from the wall painting samples with the use of a micro-scalpel in granular form. For the FTIR measurements, the plaster samples were mixed with potassium bromide powder in a mass ratio of 1:100 in order to prepare pellets. The spectra were obtained in transmittance mode, in the region of mid-IR (4000-400 cm^{-1}) using a Spectrum 1000 Perkin Elmer and 32 scans with 4 cm^{-1} resolution. Thermal analysis measurements were performed with a Setaram TG-DSC SETSYS 16/18 system. Samples of 5-8 mg in powder form were placed in alumina crucibles and were measured in dynamic conditions, in the temperature range from 25 to 1000°C with a heating rate of 20°C/min and in N_2 atmosphere.

Results and discussion

FTIR analysis revealed that the main constitution of the plasters was calcite by the clear and dominating presence of the characteristic bands at 1445, 866 and 712 cm^{-1} in all of the samples' spectra (Fig. 1) [2]. The characteristic bands of gypsum at 3550 and 3406 cm^{-1} were scarcely present only in a small number of the spectra while the peaks at 1146, 668 and 602 cm^{-1} were absent or overlapped by the dominating bands of calcite, while the presence of kaolinite was indicative and organic traces were only suggested. Thermal analysis (Fig. 2) confirmed the main contribution of calcite by the wide endothermic peak at 798°C in all of the thermal curves, which was accompanied by significant mass loss and is well attributed to the calcite decarboxylation [1]. The contribution of gypsum was confirmed only in the minority of the plasters and it was detected by the small endothermic peak along with mass loss due to dehydration of chemical bound water between 130-160°C. The use of kaolinite could be dismissed because of the absence of the endothermic peak between 530-590°C regarding dehydroxylation and the exothermic peak between 900-1000°C regarding crystalline transformation [3]. The wide endothermic peak at 570°C, which is not accompanied by mass loss, can be attributed to the transformation of quartz from a-SiO_2 to β- SiO_2

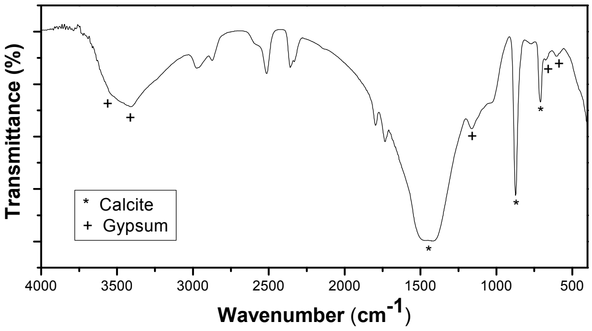

Figure 1. FTIR transmittance spectrum of sample St13 with the characteristic bands of calcite and gypsum

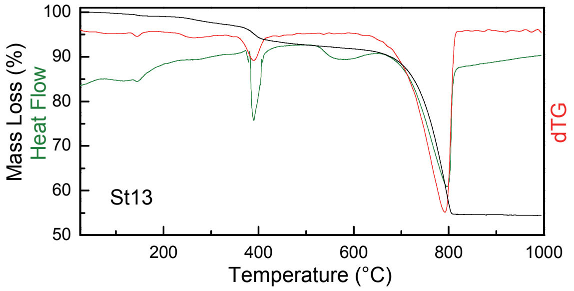

Figure 2. Thermal curves of sample St13

although with great uncertainty [4]. The endothermic peak at 390°C can be attributed to organic traces and was also present in some of the samples.

The samples can be separated in two main categories, regarding their gypsum component, by the comparative study of the applied techniques. The use of kaolinite in a small quantity cannot be completely excluded although its absence was supposed by TG-DSC. The presence of quartz cannot be supported by the thermogravimetric analysis because of the low enthalpy attributed to the corresponding heat flow peak, probably due to its low concentration in the specific sample. The occasional presence of organic traces can be attributed to the application of restoration materials and not to the presence of some kind of binder because of its occurrence in some of the samples.

Conclusions

The thermal analysis of plasters was in agreement with the FTIR spectroscopy, confirming the same results. The comparative evaluation of thermal and spectroscopic analysis showed that fresco technique was most likely applied to the examined wall paintings because of the absence of organic binders. The small and unclear participation of gypsum in some of the samples cannot be attributed solely to the usage of two different plaster recipes or/and two different artistic workshops but to the state of the wall paintings during the sampling.

References

[1] M. Anastasiou, Th. Hasapis, T. Zorba, E. Pavlidou, K. Chrissafis and K.M. Paraskevopoulos, J. Therm. Anal. Cal., 84 (2006) 27-32.

[2] V.C. Farmer, The Infrared Spectra of Minerals, Mineralogical Society, Bartholomew Press, Surrey, 1974, 227.

[3] M. Földvári, Handbook of thermogravimetric system of minerals and its use in geological practice, Geological Institute of Hungary Budapest, 1974.

[4] J.I. Alvarez, I. Navarro, Thermochimica Acta 365 (2000) 177-187.

Comparative study of contemporary restoration mortars

D. Papazoglou[1], **L. Malletzidou**[1], **T. Zorba**[1], **E. Pavlidou**[1] **and K.M. Paraskevopoulos**[1]

[1] Physics Department, Solid State Physics Section,
Aristotle University of Thessaloniki, GR- 541 24, Thessaloniki, Greece

*depapazo@physics.auth.gr

TUP

P113

Introduction

In the Museum of Byzantine Culture, in Thessaloniki, Greece, there is a need for knowledge of the correct mortar to be used in restoration procedures. The subject of our study is the characterization of five modern mortars which are used in restoration of wall paintings and floor mosaics and the determination of their mechanical properties in order to specify the optimum one for restoration use. The good mechanical tolerance of such mortars is of high importance because it ensures the conservation of these categories of works of art and cultural heritage through time.

Materials and methods

A large number of samples of five categories of modern mortars were provided by the Museum of Byzantine Culture. In order to specify the differences of their composition, the samples were analyzed by means of Fourier Transform Infrared Spectroscopy (FTIR) and Scanning Electron Microscopy with Energy Dispersive Spectroscopy (SEM-EDS)

Cubic test pieces from the samples originated from floor mosaics and from wall paintings mortar, with volume $1cm^3$ and $0.5cm^3$ respectively, were used to study their mechanical properties (compressive strength test) using in an Instron machine [1].

Results and Discussion

The results from the analysis of the FTIR spectra are presented in TABLE 1. The combination with the elemental analysis, obtained by EDS, reveals qualitative and quantitative differences. Specifically, in sample BY_11, the amount of gypsum was greater than in sample 6 and, additionally, the samples BY_6 and BY_11 included less calcite than sample BY_18. The sample BY_18 also includes a small amount of quartz, without many impurities. The mural mortars C_12 and D_21 consisted of calcite and kaolinite but in different amounts˙ C_12 contained more calcite and less kaolinite while D_21 had exactly the opposite content.

TABLE 1. FTIR results

Sample	Origin	Calcite	Gypsum	Quartz	Kaolinite
BY_6	Floor mosaic	✓	✓	-	-
BY_11	Floor mosaic	✓	✓	-	-
BY_18	Floor mosaic	✓	✓	✓	-
C_12	Mural	✓	-	-	✓
D_21	Mural	✓	-	-	✓

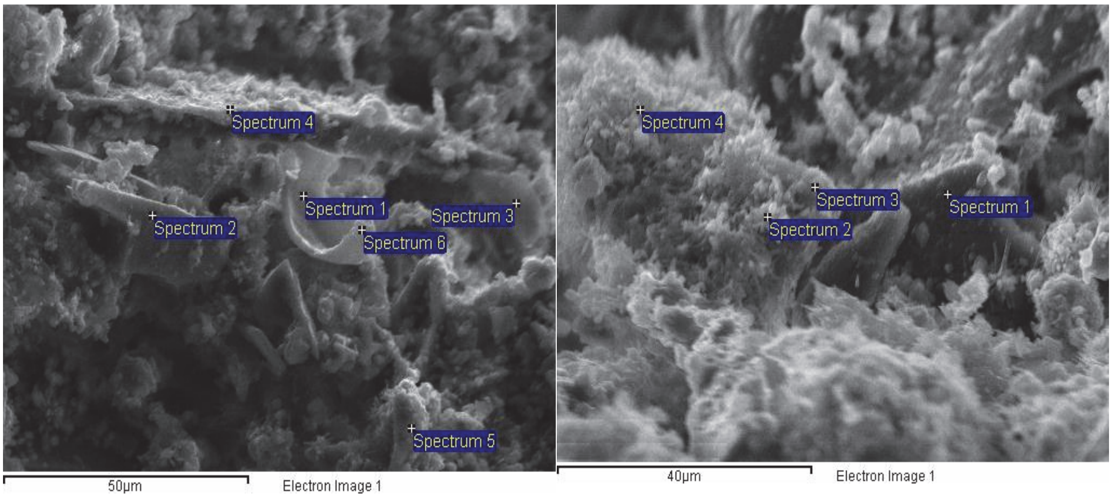

Fig 1. SEM microphotographs of sample BY_11

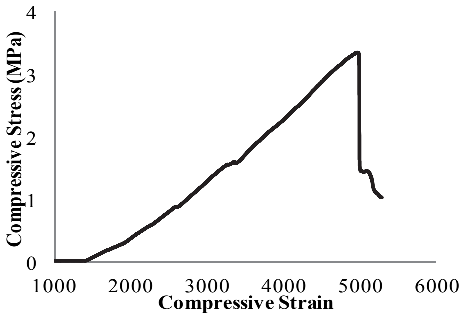

Fig 2. Stress-strain curve of sample BY_6

TABLE 2. Compressive Strength results

Samples	BY_6	BY_11	BY_18	C_12	D_21
Fracture point (average)	3.187	0.709	1.407	1.304	1.536
Deviation	±0.727	±0.338	±0.660	±0.163	±0.291

The results of compressive strength test are presented in TABLE 2. Mean values of compressive strength were calculated from the maximum value at the peak of the stress-strain curves. Descriptive statistics revealed low standard deviation, less than 1. The mosaic sample BY_6 has the greatest strength of all the investigated samples.

Conclusion

In accordance to the experimental results, the examined mortars show great differences concerning their chemical composition. The most common chemical components were calcite, kaolinite, gypsum and various silicates like quartz. The mechanical tolerance of the mortars is of high importance as well as their durability over time, as they are usually exposed to extreme weather conditions as temperature, humidity and UV radiation.

References

[1] S. Andrejkovicova, A.L. Velosa and F. Rocha, Construction and Building materials 44 (2013) 133-141

TUP

P114

Authenticity study of two German expressionism paintings using spectroscopic techniques

K. Karatzia[1,2], **E. Kampasakali**[1], **G. Heydenreich**[2] **and G. Kourouklis**[3]

[1] Interdepartmental Post Graduate Program on Protection, Conservation and Restoration of Cultural Monuments, Aristotle University of Thessaloniki, 54124 Thessaloniki, Greece
[2] Department of Conservation and Restoration, University of Applied Sciences of Cologne, 50678 Cologne, Germany
[3] Department of Chemical Engineering, Aristotle University of Thessaloniki, 54124 Thessaloniki, Greece

E-mail: katerina_karatzia@hotmail.gr

In recent decades a number of forged artworks appeared in the international art market. As traditional stylistic analysis and provenance research failed in a several of cases to identify the forgeries, art technological research and scientific material analysis gained further importance and may serve to date paintings and to contribute to their authentication. However, analysis of modern painting materials remains a challenge. This case study uses spectroscopic techniques to identify pigments and binding media of two forged works.

Samples of two paintings attributed to the German expressionists, Johannes Molzahn (1892 – 1965) and Heinrich Nauen (1880 – 1940), were collected. The paintings were suspected as forgeries as their texture was similar to those of acrylic paints. Artists' acrylic emulsion paints were introduced after 1950 [1].

Figure 1: Paintings attributed (a) to J. Molzahn and (b) H. Nauen. The numbers indicate the sampling areas.

Pigments were identified both with Raman and FTIR spectroscopy, while the binding medium was better identified with FTIR spectroscopy. Scientific analysis identified the binding medium as drying oil and not as acrylic resin proving the importance of scientific analysis alongside visual examination in order to verify the authenticity of an artwork. The inauthenticity of both paintings was actually demonstrated by the pigments present in the paintings and not by the binding medium. More specifically, titanium white was identified in the painting attributed to Johannes Molzahn (date in signature is 1920). However, its use started in Europe after 1945 [2]. The synthetic pigments phthalocyanine blue (PB15) and dioxazine purple (PV23) were identified in the painting attributed to Heinrich Nauen (date in signature is 1911), even though synthetic pigments appeared after 1950 [3-4], long after artist's death.

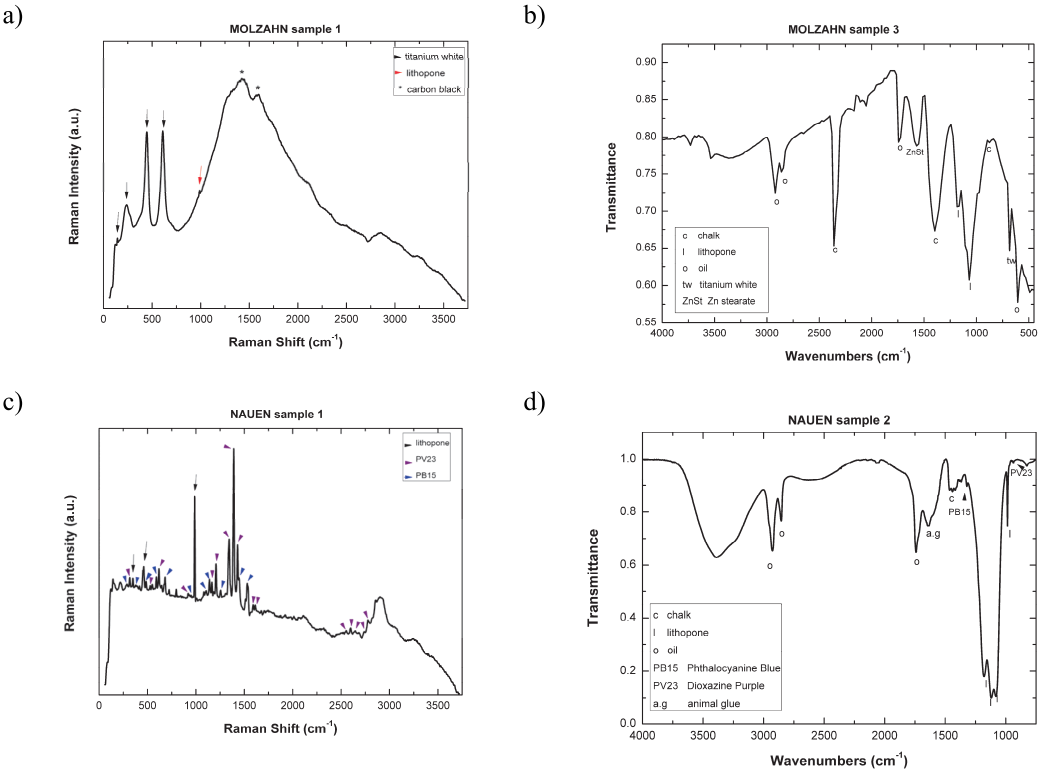

Figure 2: Representative Raman (a and c) [532 nm, 5mW] and FTIR spectra (b and d) of the samples collected from the paintings of J. Molzahn and H. Nauen.

Table 1: Identification of binding medium and pigments by Raman and FTIR spectroscopy.

ARTWORK	SAMPLE	BINDING MEDIUM	PIGMENTS IDENTIFIED
Painting attributed to Johannes Molzahn	1	Drying Oil	Titanium White, Lithopone, Chalk, Carbon Black
	2	Drying Oil	Titanium White, Lithopone, Chalk, Carbon Black
	3	Drying Oil	Titanium White, Lithopone, Chalk, Carbon Black
	4	Drying Oil	Titanium White, Lithopone, Chalk, Carbon Black
Painting attributed to Heinrich Nauen	1	Drying Oil	PB15, PV23, Lithopone, Chalk
	2	Drying Oil	PB15, PV23, Lithopone, Chalk

References

[1] T. Learner, Analysis of modern paints (2004), Getty Publications.

[2] E.W. FitzHugh, Artists' Pigments: A handbook of their History and Characteristics Volume III (1997), New York: Oxford University Press.

[3] C. Defey and D. Strivay, PV15 as 20th and 21st artists' pigments: Conservation Concerns, e-Preservation Science 11 (2014) 6-14.

[4] T. D. Chaplin, R. J. Clark and B. W. Singer, Early 20th C Russian painting? Raman identification of modern pigments on a pastel supposedly painted by the renowned artist Natalia Goncharova, Journal of Raman Spectroscopy, 45 (2014) 1322-1325.

Investigation of stiffness in micromagnetic simulations of spinvalve sensors with OOMMF

S. Mitropoulos[1], **V. Tsiantos**[2], **K. Ovaliadis**[2], **D. Kehrakos**[3] **and M. Dpnahue**[2]

[1]Department of Computer and Informatics Engineering, TEI of Eastern Macedonia and Thrace, Kavala, Greece
[2]Department of Electrical Engineerig, TEI of Eastern Macedonia and Thrace, Kavala, Greece
[3]Department of Education, ASPETE, Heraklion, Athens, Greece
[4]Applied and Comput. Mathematics Division, NIST, Gaithersburg, MD,USA

E-mail: tsianto@teikav.edu.gr

There are many micromagnetic codes that simulate magnetic materials. Some of the codes are freeware, such as magpar [1], OOMMF [2], NMag [3], some are used for scientific purposes FastMag [4], and some are commercial products, such as LLG [5], MicroMagus [6], etc. These codes use different ODE solvers, either explicit or implicit methods. Explicit methods are suitable for non stiff problems, whereas implicit methods are suitable for stiff problems. Stiffness is an important issue in the solution of ODEs and much attention has been paid into this subject. A rigorous definition of stiffness is not yet acceptable by all authors. However, there are various proposed definitions and criteria about stiffness [7]. One case is to consider that an ordinary differential equation problem is stiff if the solution being sought is varying slowly, but there are nearby solutions that vary rapidly, so the numerical method must take small steps to obtain satisfactory results. If the computation time was not a concern of us perhaps we wouldn't be concerned about stiffness [8]. Nonstiff methods can solve stiff problems; they just take a long time to do it. In the context of micromagnetics, stiffness has been studied by Della Torre and co-workers [9], and then by Tsiantos [10]. According to Della Torre in many magnetic structures appears strong exchange, which leads to numerical problem stiffness. The stiffness manifests itself in that the time step becomes very small and the linear solver part of implicit time integration methods becomes slowly convergent. Therefore, there are codes, such as FastMag, that use implicit schemes including the backward differentiation formula (BDF) [11]. The BDF method requires the evaluation of the numerical system Jacobian to enhance the time integration. FastMag implements a technique that allows evaluating the product of the numerical system Jacobian with the magnetization vector exactly without a need to create any matrices and it does it at the speed of the conventional effective field evaluation. The ability to execute this task allows using the BDF without a need for a linear solver preconditioner, which is important for allowing using GPUs with low memory [4].

In this work we used 3D OOMMF (Object-Oriented MicroMagnetic Framework) [2] for the spinvalve hysteresis simulations. The calculations are based on using the Landau-Lifshitz (LL) equation, where the effective field includes the anisotropy, applied, exchange, and self magnetostatic fields. With regards to the ODE solver we used RKF54 and we also incorporated into OOMMF the CVODE code from the SUNDIALS package for the analysis of stiffness [12]. Spin valve is a device, which consists of two or more conducting magnetic materials, whose electrical resistance can change between two values that depends on the relative alignment of the magnetization in the layers. The magnetic layers of the device align either "up" or "down", and this depends on the existence of an external magnetic field. In a simple case, a spin valve consists of a non-magnetic material sandwiched between two ferromagnets, one of which is fixed (pinned) by an antiferromagnet, that works in order to raise its magnetic coercivity and behaves as a "hard" layer, while the other is free (unpinned) and behaves as a "soft" layer [13]. Due to the difference in coercivity, the soft layer changes polarity at lower applied magnetic field strength than the hard one. Upon application of a magnetic field of appropriate strength, the soft layer switches polarity, producing two distinct states: a parallel, low-resistance state, and an antiparallel, high-resistance state.

In the simulations, the exchange field was computed using the six nearest neighbors. Parameters for Co (free and pinned layer) were used, such as, exchange coupling constant of $A=30.0\times10^{-12}$ J/m, saturation magnetization $Ms=1400\times10^{3}$ A/m, and crystalline anisotropy $K=0$. The damping constant alpha was set to 0.5. The particle was 400×200×9 nm, and the cell size was 5 nm × 5 nm × 3 nm in x, y, and z-directions. The simulations showed that for the spinvalve case (Ferromagnetic) the number of functions evaluations (NFEs), which is the first criterion for the comparison of different methods for the speed of the simulations ([11]), taken by the RKF54 are almost double the number of the iterations taken by CVODE, $2.968913e^{6}$ and 1.66961e6 respectively, for the same simulation time $5.83160e^{-7}$ secs. On the other hand, for the spinvalve case with antiferromagnetic coupling the NFEs are $3.296803e^{6}$ for the RKF54 and $1.98188e^{6}$ for the CVODE case, for the same simulation time $6.46313e^{-7}$ secs. So, considering NFEs as a measure of stiffness we conclude that spinvalve simulations are stiff problems and implicit methods, such as BDF should be employed. The same applies for the spinvalve with antiferromagnetic coupling between layers, that is, this case is also a stiff case. Moreover, the maximum spin angle was within the accepted limits, that is, less than 30 degrees.

References

[1] W. Scholz *et al.*, Computational Material Sciences 28 (2003) 366-383.

[2] M. J. Donahue and D. G. Porter, OOMMF User's Guide, Version 1.0, Interagency Report NISTIR 6376, NIST, Gaithersburg, MD, Sept 1999.

[3] T. Fischbacher *et al.*, IEEE Trans on Magnetics, 43 (2007) 2896-2898.

[4] R. Chang *et al.*, J. Appl. Phys. 109 (2011).

[5] M. R. Scheinfein and E. A. Price, LLG Micromagnetics Simulator, LLG User Manual v2.50, 2003.

[6] http://www.micromagus.de/home.html

[8] M. N. Spijker, Journal of Computational and Applied Mathematics, 72 (1996) 393-406.

[9] C. Moler, Stiff Differential Equations, http://www.mathworks.com/company/newsletters /articles/stiff-differential-equations.html

[11] E. Della Torre, IEEE Trans on Magn. 29 (1993) 2371.

[12] V. Tsiantos, Numerical methods for ordinary differential equations in micromagnetic simulations, PhD thesis, University of Manchester, Manchester, UK, 2000.

[13] C.F. Curtiss and J. O. Hirschfelder, Proc. Nat. Acad. Sci. 38 (1952) 235-243.

[14] A. C. Hindmarsh, P. N. Brown, K. E. Grant, S. L. Lee, R. Serban, D. E. Shumaker, and C. S. Woodward, ACM Transactions on Mathematical Software, 31 (2005) 363-396.

[15] http://en.wikipedia.org/wiki/Spin_valve

Anomalous fading in Durango apatite: comparison between grain sizes in the micro and the nano scale

M. Niora[1], I.K. Sfampa [1] and G. Kitis[1]

[1] *Aristotle University of Thessaloniki, Nuclear Physics Laboratory, 54124-Thessaloniki, Greece*

E-mail: mniora@physics.auth.gr

TUP

P116

Introduction: In some inorganic materials a rapid fading of the luminescence signals is observed experimentally within short times after irradiation, instead of within the long lifetimes predicted by standard kinetic models. This rapid fading process has been termed anomalous fading (AF), and is one of the most serious problems in TL and OSL dating. In the present work was investigated the grain size dependence of anomalous fading in a specific material that is known to exhibit strong AF, the Durango apatite [1].

Currently, the widely accepted explanations of AF are based on quantum mechanical tunneling from the ground state or from the excited state of the trap [2]. Since the donor-acceptor distance affects the phenomena, there is also a possibility of being affected by the sample's grain size too. The experimental method to study that possibility is based on the comparison between grain sizes in the micro and the nano-meters scale.

Experimental Procedure: The sample used in these experiments was a natural crystal of Durango apatite. The grains were divided into two different sizes: (a) coarse grains 80-140μm and (b) fine grains at the nanoscale. In order to achieve the nano grains, ball milling method was applied on the sample for a period up to 48 hours. In the case of coarse grains, aliquots with the same mass of 5 mg were attached to stainless steel disks. In the other case, the aliquots were pellets with the same mass of 35 mg. Each data point reported in this paper was the average of two measurements carried out on two different aliquots/disks.

All samples were firstly annealed up to 700^0C for 1 hour, irradiated for a test dose of 26Gy and then stored under dark room conditions for different storage times. TL measurements were carried out using a Harshaw 3500 TLD-Reader. The irradiations were applied through a ^{90}Sr/^{90}Y beta particle source. All measurements were performed in a nitrogen atmosphere with a low constant heating rate of 2^oC/s, in order to avoid significant temperature lag, and the samples were heated up to the maximum temperature of 400^0C.

Results and Discussion: Experimental results indicate that anomalous fading is weakly affected by the grain size. In Fig. 1 presented glowcurves show the AF phenomenon in cases of nano-grains and grains between 80-140μm.

Finally, the normalized integrals enhance the hypothesis that the AF affects the glowcurves almost in the same manner (Fig. 2).

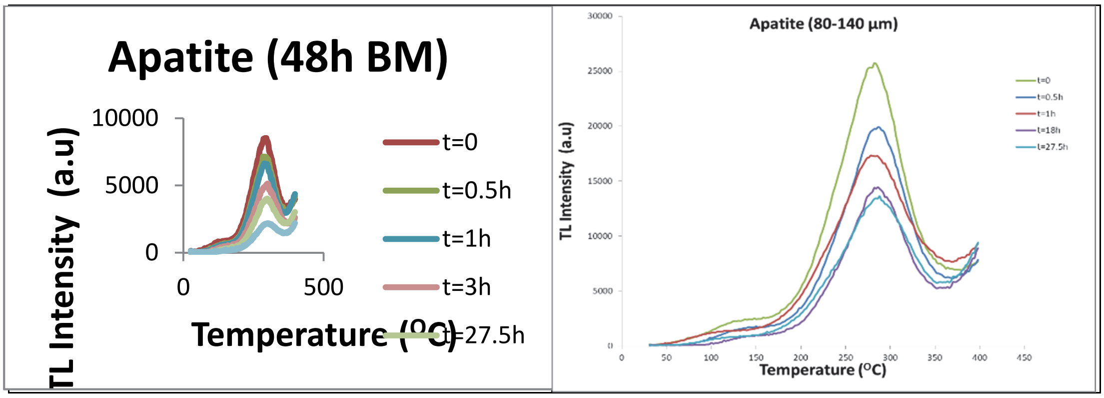

Fig. 1: Glowcurves for different storage times showing the AF: (left) fine grains after 48h of ball milling, (right) coarse grains between 80-140μm.

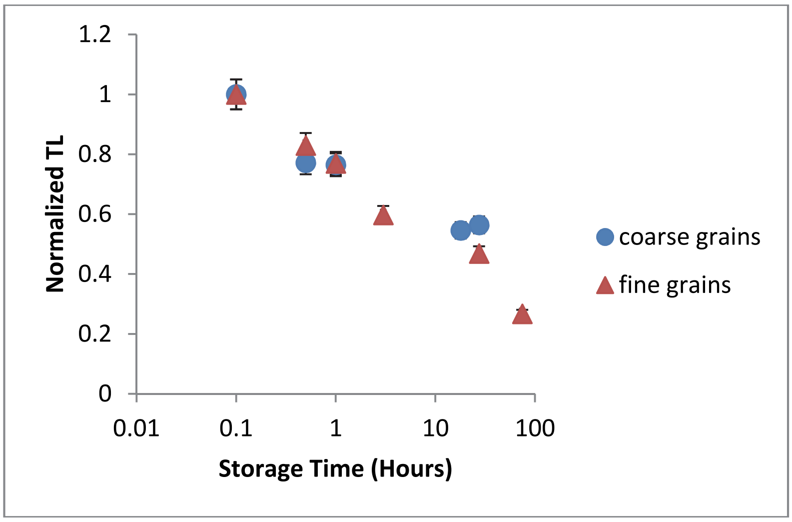

Fig. 2: Normalized TL integrals versus storage times in both cases.

Further investigation is required in order to establish the above results. AF seems to be independent of the grain size in the case of apatite Durango. Future work on other materials that exhibit strong AF is about to take place.

References

[1] G. Kitis, G.S. Polymeris, V. Pagonis, N.C. Tsirliganis, Phys. Stat. Sol. (a) 203 (2006) 3816
[2] I.K. Sfampa, G.S. Polymeris, N.C. Tsirliganis, V. Pagonis, G. Kitis, NIM in Phys. Res. B 320 (2014) 57–63

Research on anomalous fading of feldspars billion years old using thermoluminescence signal

Z. Papari[1], I.K Sfampa [1] and G. Kitis[1]

[1] *Aristotle University of Thessaloniki, Nuclear Physics Laboratory, 54124-Thessaloniki, Greece*

zpapari@physics.auth.gr

Introduction: Luminescence stands among the basic research tools in the fields of ionizing radiation dosimetry, geo-archaeological dating and retrospective dosimetry. In some inorganic materials a rapid fading of the luminescence signals is observed experimentally within short times after irradiation, instead of within the long lifetimes predicted by standard kinetic models [1]. This rapid fading process has been termed as anomalous fading (AF), and is one of the most serious problems in TL (Thermoluminescence) and OSL (Optically Stimulated Luminescence) dating [2]. The aim of the present work is to investigate anomalous fading on materials, like the feldspars. Specifically, the feldspars used are estimated to be billion years old. Those igneous rocks exist everywhere around us especially in archaeological monuments.

Experimental Procedure: The rock was divided into white, black and green grains. Aliquots with the same mass were attached to aluminum discs (mass reproducibility for all aliquots was kept within ±5%). TL measurements were carried out using a Harshaw 3500 TLD-Reader. The irradiations were applied through a ^{90}Sr/^{90}Y beta particle source. All measurements were performed in a nitrogen atmosphere with a low constant heating rate of 2^{o}C/s, in order to avoid significant temperature lag, and the samples were heated up to the maximum temperature of 400^{0}C. The following protocol was applied for all feldspars:

Step 0: Record zero dose TL signal (ZDTL)
Step 1: Test Dose (TD) of 26Gy, immediately record TL sensitivity S_0
Step 2: TD, set aside for storage time t_i, protected from light and high temperature.
Step 3: Record fading after storage time (TL sensitivity S_1)
Step 4: TD, immediately record TL sensitivity S_f
Where t_i= 0min, 30min, 1h, 2h, 3h, 1day, 3d, 5d, 10d, 15d, 30d.

Results-Discussion: Following are presented the results for all the feldspars. The left parts of Figures 1, 2 and 3 show the glowcurves after each storage time, while the right ones show the normalized integrals concerning the deep traps. First of all was measured the "black feldspar".

Second sample was the "white feldspar".

For both samples the only part of the glowcurve that is affected by the AF is the first peak which is widely reported as the "110^{o}C peak of quartz". That peak corresponds to a shallow trap and this is the reason for not using it for dating purposes. On the other hand is obvious that the rest glowcurve is almost stable and no AF is recorded.

Finally, there is the "green feldspar":

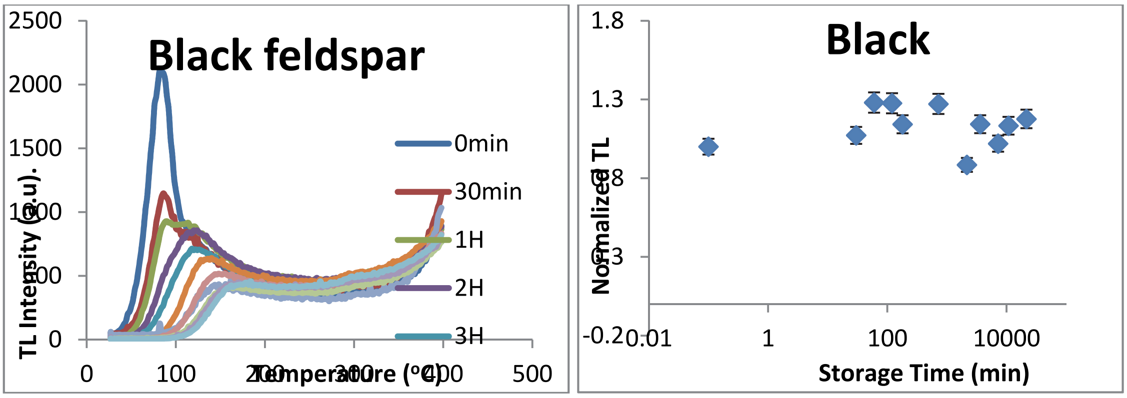

Fig. 1. Black feldspar. (Left) glowcurves after storage times, (Right) Normalized TL Integrals of high temperature peaks.

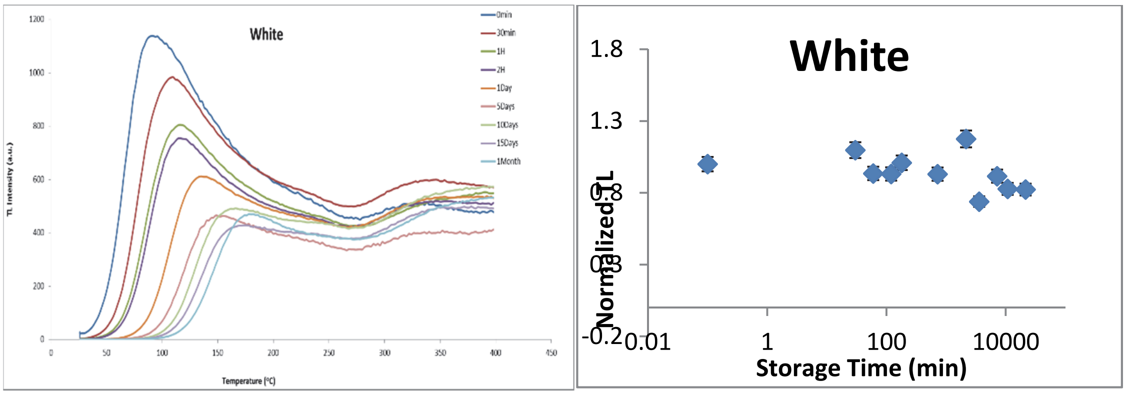

Fig. 2. White feldspar. (Left) glowcurves after storage times,(Right) Normalized TL Integrals of high temperature peaks.

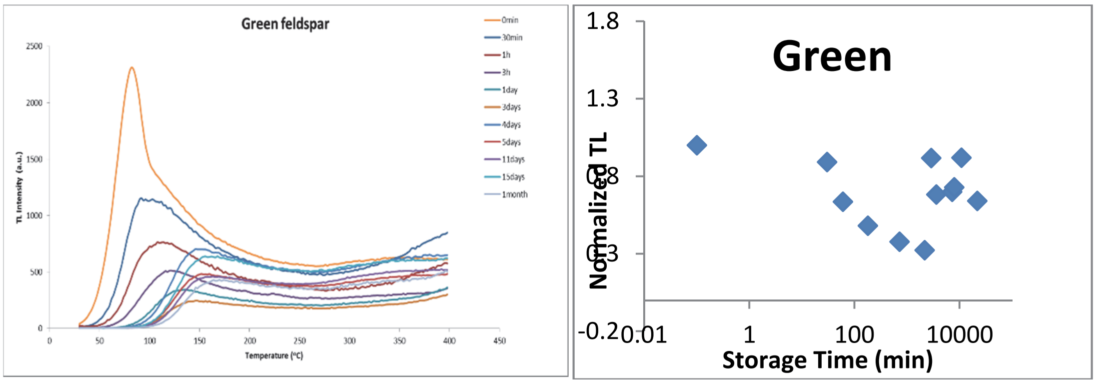

Fig. 3. Green feldspar. (Left) glowcurves after storage times, (Right) Normalized TL Integrals of high temperature peaks.

In the case of the green feldspar further investigation has to take place since the results are rather unexpected. For storage time between 0-5days a strong AF is reported, while after that period the signal is raising again.

References

[1] R. Chen, S.W.S. McKeever, Theory of Thermoluminescence and Related Phenomena, World Scientific, Singapore, 1997.

[2] G. Kitis, G.S. Polymeris, V. Pagonis, N.C. Tsirliganis, Phys. Stat. Sol. (a) 203 (2006) 3816

Characterization of fossil remains using XRF, XPS and XAFS spectroscopies

I. M. Zougrou[1], M. Katsikini[1], F. Pinakidou[1], M. Brzhezinskaya[2], L. Papadopoulou[3], E. Vlachos[3], E. Tsoukala[3], and E. C. Paloura[1]

[1]Aristotle University of Thessaloniki, School of Physics, 54124 Thessaloniki, Greece
[2]Institute for Nanometre Optics and Technology, Helmholtz Zentrum Berlin, 12489 Berlin, Germany
[3]Aristotle University of Thessaloniki, School of Geology, 54124 Thessaloniki, Greece

E-mail: katsiki@auth.gr

TUP

P118

Synchrotron radiation spectroscopies XAFS, XPS and XRF are used for the study of fossils. A Pliocene costal plate of the gigantic terrestrial turtle *Cheirogaster bacharidisi* from the Michaniona (Greece) excavation site and a Late Pleistocene fossilized coprolite of the cave spotted hyena *Crocuta crocuta spelaea* from the cave of Agios Georgios (Kilkis, Greece) are studied. XRF maps were recorded at the KMC-II beamline whereas the Ca-L-edge XANES and Ca2p XPS spectra were recorded at the PM4 beamline (using the SURICAT end-station) of the BESSY-II storage ring of the Helmholtz Zentrum Berlin. Fe-K-edge XAFS spectra were recorded at the beamline C of HASYLAB-DORIS storage ring.

Soft X-ray XANES and XPS spectroscopy were used to investigate the chemical composition of the gigantic turtle cortex and cancellous bone. Representative Ca-L-edge XANES spectra are shown in Fig. 1. The energy split of the a_1 and a_2 peaks is used for the identification of the Ca-containing minerals. The external cortex consists of hydroxylapatite while in the cancellous bone 65% hydroxylapatite and 35% calcite were identified. High resolution XPS spectra at the Ca2p electronic levels, shown in Fig. 2, were also used to evaluate the chemical state and chemical environment of Ca in the cancellous bone. In agreement with the Ca-L-edge XANES findings, the chemical state of Ca was identified as ionic Ca^{2+} and the percentage of hydroxylapatite over calcite was found equal to 64% and 36% respectively.

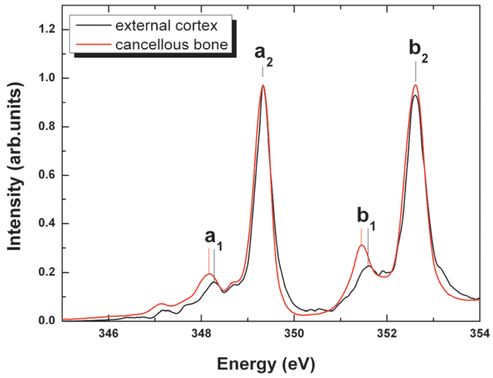

Figure 1: Ca-L-edge XANES spectra of compact and cancellous bone from the gigantic turtle sample.

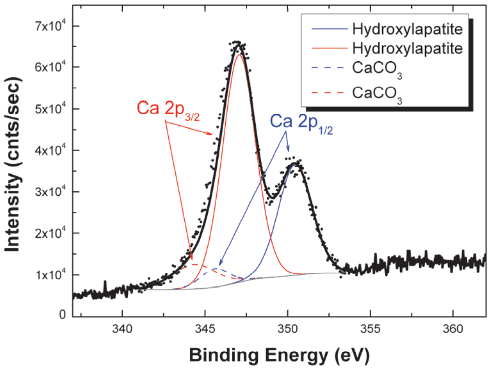

Figure 2: Ca 2p XPS spectra of cancellous bone from the gigantic turtle sample.

The hyena coprolite matrix consists of a non-apatitic mineral, where the Ca/P atomic ratio as determined by SEM ranges between 1.54-1.57, with inclusions of well-preserved as well as digested bone remains. Organic phases and small mineral inclusions of monocline, quartz and grossular garnet were also identified using transmitted light and secondary electron microscopies. The latter-inclusions are related to minerals introduced from the deposition environment. XRF recorded in the cross section of the coprolite are shown in Fig. 3. The maps show the distribution of P, Ca, Mn and Fe. Fe-rich inclusions originating from the deposition environment are present along with apatite contributions evidenced from the Ca and P distribution. The Fe-K-edge XANES spectrum recorded in the cross section of the coprolite shows that iron is in the trivalent state. The Fe-K-edge macro EXAFS spectrum is shown in Fig. 4. Fitting of the spectrum revealed that Fe participated in the formation of the akaganeite mineral.

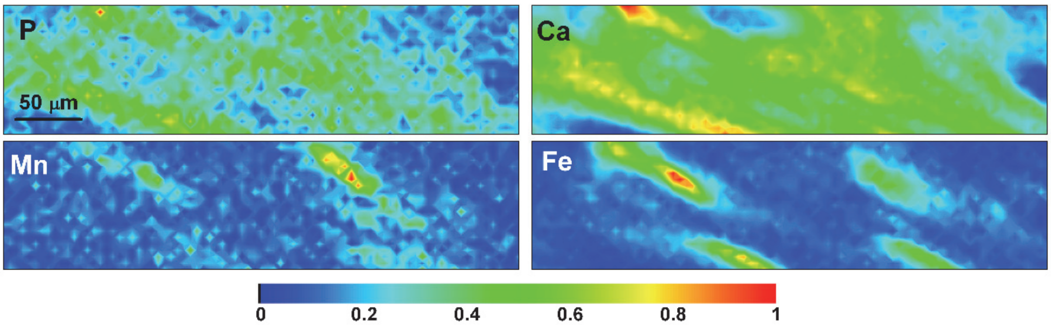

Figure 3: SR-XRF maps of the hyena coprolite.

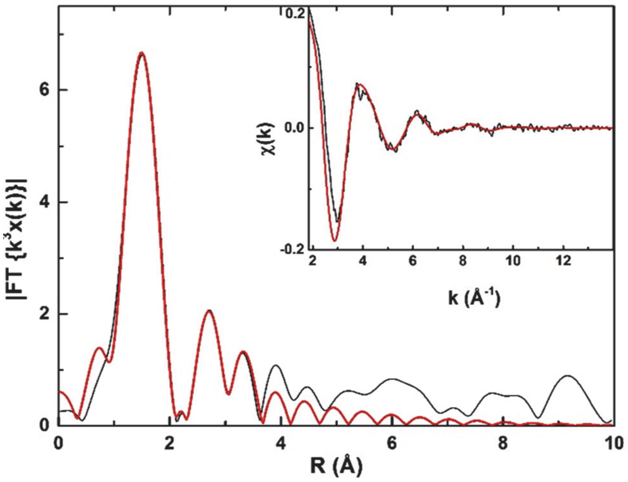

Figure4: Fourier Transform of the Fe-K-edge χ(k) spectrum of the hyena coprolite spectrum. The χ(k) spectrum is shown in the inset. The experimental and fitting curves are shown in black and red lines, respectively.

Acknowledgements:

Part of the research leading to these results has received funding from the European Community's Seventh Framework Programme (FP7/2007-2013) under grant agreement n.°312284.

Study of archaeological and contemporary ceramic artifacts with physical-chemical techniques

T. Kazakou[1], K. Chrissafis[1], E. Pavlidou[1] and G. Vourlias[1]

[1]Section of Solid State Physics, Department of Physics, Aristotle University of Thessaloniki, 541 24, Thessaloniki, Greece

E-mail: tkazakou@yahoo.com

The subject of the present work is the thorough study of different ceramic artifacts with the use of various physical-chemical techniques, in order to derive information about their main components and manufacturing conditions (heating temperature and atmosphere). Ceramics are very complicated regarding their mineralogical composition. Usually, they consist of a large number of minerals, including mixtures of different clay minerals as well as clastic grains, such as quartz, feldspars, calcite and several other accessory minerals. Moreover, they undergo physical and chemical alterations during heating, which depend not only on their original composition, but also on the highest temperature, the duration and the conditions of heating. For this reason, the use of just one analytical technique is not sufficient for their study. In this work, the supplementary techniques of Scanning Electron Microscopy – Energy Dispersive Spectroscopy (SEM-EDS), X-Ray Diffraction (XRD), Fourier Transform Infrared Spectroscopy (FTIR) and Thermogravimetric Analysis (TGA) are complementary used for the study of ceramics.

With the use of the above techniques, two archaeological ceramic vessels from Cyprus where thoroughly examined. Firstly, they were observed under the stereoscopic microscope, so that an estimation could be made about the type and the manufacturing technology of each ceramic. This was followed by a more detailed morphological and elemental analysis of the ceramic paste with the help of the Scanning Electron Microscope and Energy Dispersive Spectroscopy respectively. For the mineralogical characterization of the ceramics and the determination of their composition, X-ray Diffractometry was applied. This was assisted by the use of FTIR Spectroscopy. In order to thoroughly examine each ceramic and estimate its firing temperature, the technique of Thermogravimetric Analysis was used. Therefore, the samples were heated up to 1000^o C, with a rate of 10^o C/min, in an N_2 atmosphere. For the better determination of the ceramics' composition and manufacturing conditions, the spectroscopic techniques of X-ray Diffractometry and FTIR Spectroscopy where applied again on the samples after Thermal Analysis. By complementary processing all data, an estimation of both the composition and the highest heating temperature of the ceramics was made. In order to evaluate the results of the above study, the same procedure was applied on two ceramic artifacts of present time, manufactured in Thessaloniki and the island of Naxos respectively, for which there is information about the type of the ceramic paste used and the heating temperature. As far as the contemporary ceramics are concerned, the resulting conclusions were in good agreement with the information provided by the manufacturers.

The two archaeological ceramic vessels are porous and friable. They were manufactured by heating at relatively low temperatures, lower than 850^o C and higher than 700^o C, and made of calcareous clay, rich in Fe. With the help of all the applied techniques, inclusions of quartz, calcite and hematite have been detected in both ceramics, while there are indications for the occurrence of amphiboles, micas/illite, plagioclase feldspars (anorthite), pyroxenes (diopside) and gehlenite. The concentrations of the quartz and calcite inclusions are high. The results of Thermogravimetric Analysis led to the conclusion that the minimum concentration of $CaCO_3$ in the original ceramic paste must have been 15,2 % and 17,5 % for each ceramic respectively.

The two contemporary ceramics belong to the earthenware type, have lower porosity, and are quite hard and less brittle. They were heated at high temperatures, around 1000^o C, in an oxidizing atmosphere, and made of earthen clay, rich in Fe and having a minor or zero concentration of Ca. By the use of all the applied techniques, high concentrations of quartz inclusions have been detected in both ceramics, but not any calcite. Moreover, there are indications for the occurrence of hematite, plagioclase feldspars (albite/anorthite) and alkali feldspars (microcline).

The presence of quartz in the form of natural inclusions, or its addition as an admixture, reduces the plasticity of clay and thus reduces shrinkage and cracking during heating. For this reason, it has been used as much in antiquity as in modern times. The finer the raw clay used, the higher is the percentage of quartz in the ceramic paste.

Calcium carbonate has the same thermal expansion properties as the average clays used in pottery. Therefore, calcite inclusions prevent cracking and fracture induced by thermal shock after rapid heating or cooling of vessels, during cooking for example. Furthermore, potters used calcite in order to attain heating at low temperatures, because at these temperatures it decomposes into CaO, which acts as a flux, causing ceramic sintering at a low temperature. However, at the high heating temperatures used at present times, the decarboxylation of calcium carbonate into hygroscopic CaO constitutes a problem, since the following formation of $Ca(OH)_2$ is accompanied by expansion, which raises stresses in the surrounding ceramic matrix that induce cracking.

Study and characterization of a late 17th century portable icon

N. Kyriakou[1*], L. Malletzidou[1], T. Zorba[1], V. Ganitis[2], C. Tananaki[3], E. Pavlidou[1], K.M. Paraskevopoulos[1]

[1]Physics Department, [3]School of Agriculture, Laboratory of Apiculture – Sericulture,
Aristotle University of Thessaloniki, 54124, Thessaloniki, Greece
[2] Museum of Byzantine Culture of Thessaloniki, Leoforos Stratou St 2, 54640 Thessaloniki, Greece

*nkiria@physics.auth.gr

Introduction: The purpose of this study is the characterization of a portable late 17th century panel painting icon (Fig. 1). The icon dates from around 1670 to 1690, and belongs to the personal collection of the Charisis family from the village Kaksos (Pogoni region) near Ioannina city in Greece. The icon was found inside the priest's house in the above village that they bought which is located in the same building as the village priest's residence.

In the center of the icon is Virgin Mary that holds in her hands the Christ. Right and left praying are two Saints: although there is lack of inscriptions about their identity, through comparison with orthodox iconography of the same period, the depicted hierarch on the left side is probably St. Nicholas and on the right side is most likely St. Charalambos. The hypothesis about the left saint relies on the fact that the main temple of the village is dedicated to St. Nicholas, who was fairly widespread in the further region. The icon was in very poor condition and its varnish had been blackened too much by time. There is no inscription on the icon indicative of the name of the painter, or the artistic workshop, but the expressive style of the icon is in no case islandic, Ionian, or Cretan; it is clear that it resembles the style of Northern Greek folk art, very likely to have been ordered from a Kastoria city workshop.

Fig. 1. The icon after the restoration procedures

Experimental: A total number of twenty samples, which included a sample of the wooden substrate and also fibers from the textile support, were collected before the restoration procedures. The samples were firstly examined by means of optical microscopy ZEISS STEMI DV4. All of the samples, except the one of the wooden substrate, were analyzed by micro Fourier Transform Infrared Spectroscopy (micro-FTIR) and Scanning Electron Microscopy with Energy Dispersive Spectroscopy (SEM-EDS), in order to identify the used pigments and binders. A small amount of each layer was placed on a KBr pellet for the micro-FTIR analysis using an i-Series Perkin-Elmer FTIR microscope, in transmission mode and in the spectral region between 4000 to 550 cm^{-1} [1]. For the elemental analysis with SEM-EDS, a JEOL model JMS-840A instrument with an Oxford ISIS 300 detector was employed, and parts of the samples were embedded in resin in order to examine the cross sections.

Results and Discussion: The combined analysis with micro-FTIR (Fig.2) and SEM-EDS (Figs 3, 4) revealed the following:

Ground layer: The use of gypsum was clearly confirmed with indication of kaolinite. The organic binder has animal origin and most probably rabbit glue has been used. Textile support: The fabric used for the paint layer's support was identified as pure cotton, because the microphotographs obtained by SEM showed that the fibers have the form of a slightly twisted flat ribbon (Fig. 3). Gilding: A high gold content alloy has been used for the background of the icon. Pigments: For the red pigments the presence of the Fe is an indication of the use of ochre, while the presence of Hg guides us to conclude the use of cinnabar (HgS). For the sample of black dye the presence of P, attributed to hydroxyapatite, confirms the presence of bone black. The combination of the two above characterization methods did not succeed in identifying the green and the blue pigments. Egg yolk was confirmed as binding media. Varnish: Although the icon's surface had extended damage, there were signs of varnish existence that were confirmed by optical observation. It is suspected that the resin used for varnish is mastic. Pollen grains: During the life of the icon, contamination of samples with some pollen grains is observed. The first grain (Fig. 4) is pollen pinus type (pollen from some kind of pine), while the other, common to several plants, is tricolporate type.

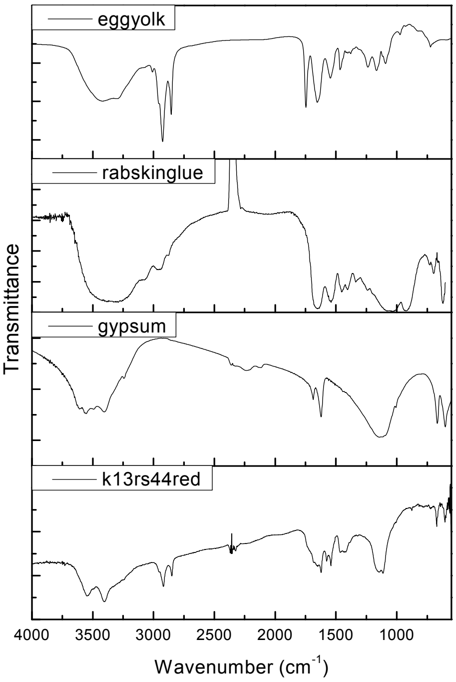

Fig.2. micro-FTIR spectra

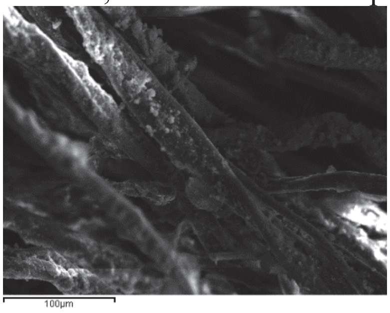

Fig. 3. SEM image from the fabric fibers

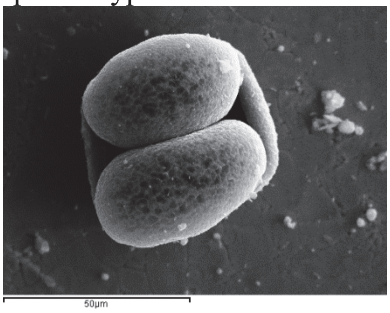

Fig. 4. SEM image from pollen pinus type

Conclusions: There is not wide range of colors and thus we could describe the painter's palette as "poor". From the above - mentioned, we conclude that although it is a folk art icon and has relatively few colors, it is also an icon of high quality. This assumption is indicated by the high quality wooden panel, the extensive use of the valuable pigment of cinnabar, as well as from the gold gilding. Furthermore, the good quality is evidenced by the presence of cloth on which the icon was made. Future plans include the study of the wooden panel so as to identify the species of the tree that it came from.

References

[1] E. Pavlidou, M. Arapi, T. Zorba, M. Anastasiou, N. Civici, F. Stamati, K.M. Paraskevopoulos, Applied Physics A 83 (2006) 709

[2] B. Smith, Infrared Spectral Interpretation, CRC Press, USA (1999)

Micro and conventional XAFS study of incinerated Cr-rich tannery wastes.

F. Pinakidou,[1] **M. Katsikini,**[2] **S. Varitis,**[2] **P. Kavouras, E. C. Paloura**[2]

[1]Aristotle University of Thessaloniki, School of Chemical Engineering, Analytical Chemistry Laboratory, 54124, Thessaloniki, Greece
[2]Aristotle University of Thessaloniki, School of Physics, Department of Solid State Physics, 54124, Thessaloniki, Greece,

E-mail: fpina@physics.auth.gr

TUP
P121

The common practice of land-based disposal of tannery wastes, where trivalent chromium [Cr(III)] is the dominant species, is responsible for the contamination of soils. The presence of naturally occurring minerals (e.g. Mn oxides) can promote the oxidation of Cr(III) to the more toxic Cr(VI), thus water pollution with Cr(VI) can also be related to the current disposal criteria for tannery wastes.[1] Chrome tanning produces two types of sludge, hair-burn and chrome: the former is produced during the mechanically scrapping and soaking of salt-cured hides and is mainly organic, while the latter is a chrome sludge, produced after sequentially cleansing and soaking of hair in a NaCl-H_2SO_4 solution, bathed for several hours in a basic $Cr(SO_4)_3$ solution and neutralized with $NaHCO_3$.[2] Incineration of the Cr-sludge at extremely high temperatures is a process that minimizes the need for additional land disposal; during incineration, the toxic components are converted to harmless or less harmful compounds whereas the volume of waste is significantly reduced. Stabilization via vitrification of incinerated tannery waste is a promising and cost effective method that leads to the formation of glass and vitroceramic products, capable of immobilizing the Cr(III) and Cr(VI) species (glass forming role of Cr(VI) and network modifying role of Cr(III)).[3]

The tannery sludge originates from the industrial zone of Thessaloniki in northern Greece and was incinerated for 1.5 h at 500 ^{o}C in an oxygen-starved atmosphere under anoxic conditions. The chemical composition of the studied glass is 10 wt% ash, 20 wt% CaO and a SiO_2/Na_2O ratio equal to 3.66. In an effort to produce vitroceramic products by controlled crystallization of the initial vitreous products, thermal treatment is applied at 880^{o}C. The XAFS measurements were conducted at the KMC2 beamline at BESSY in Berlin. The beamline is equipped with capillary optics that allow the reduction of the beam diameter down to 4.8μm. A representative 300 μm^2 2D-map of the studied thermally treated glass depicting the varying distribution of Cr is shown in Fig. 1. It is characteristic that in the Cr-rich regions, the Cr-content is 5 to 10 times higher compared to the Cr-depleted regions.

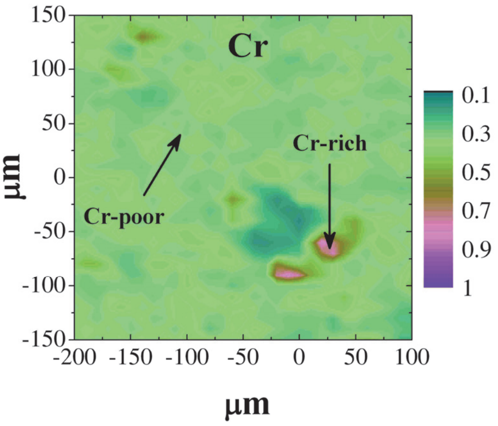

Figure 1: 2D μ-XRF scans of the annealed glass showing the inhomogeneous distribution of Cr.

In an effort to correlate modifications in the oxidation state and the bonding environment of Cr as a result of its inhomogeneous distribution, Cr-*K*-μ-XANES spectra were recorded from spots high- and low-Cr concentration. Similar to all 3d-trasistion metals, a pre-edge absorption occurs in the XANES spectra from both regions (shown in fig. 2) which is a measure of the proportion of Cr(VI) in mixed valence samples: a prominent pre-edge peak occurs for Cr(VI) species and though forbidden for octahedral Cr(III), a small pre-edge peak is present. As shown in fig. 2, both the intensity and energy position of the pre-edge peak, is not significantly altered, however, the structure above the absorption edge (E_{abs}) is modified between the two regions. The same conclusion can be drawn for the XANES spectra of the glassy and annealed sample. Thus linear combination fitting (LCF) was applied in order to evaluate the changes in the Cr(III)/Cr(VI) ratio as a function of both Cr-concentration and annealing process. During LCF, the experimental spectra of Cr_2O_3, CrO_3 and $Cr(OH)_3$ were used and the fitting is shown as dotted lines in fig. 2. In both Cr_2O_3 and $Cr(OH)_3$, Cr is trivalent, however. the $Cr(III)O_6$ octahedra link in different modes: in the former case they share one face, two edges and three corners while in the latter case, two Cr-octahedra share two edges and link to four adjacent polyhedra. Thus, the LCF results indicate the modification in the polymerization of the Cr-O-Cr chains while Cr(VI) species are always detected: the same amount of Cr(VI) exists in both the Cr-depleted and Cr-rich regions while upon annealing, no change in the percentage of Cr(VI) is detected. However, Cr(III) belongs only to Cr_2O_3 inclusions in the Cr-rich region. In the Cr-depleted region, half of the Cr(III) ions connect in a network similar to the structure of Cr_2O_3 while 28.5 % of $Cr(III)O_6$ follow the polymeric structure of $Cr(OH)_3$. In the glassy sample, the Cr-octahedra connect as in $Cr(OH)_3$, while upon annealing the polymerization of the Cr-O-Cr chains changes completely. Thus, it is concluded that the Cr(VI) concentration is not affected by the varying distribution of Cr in the annealed sample, however changes in the type of linkage among the Cr-octahedra are induced. Upon thermal treatment, no reduction of Cr(VI) occurs while the Cr(III)-groups change their polymerization.

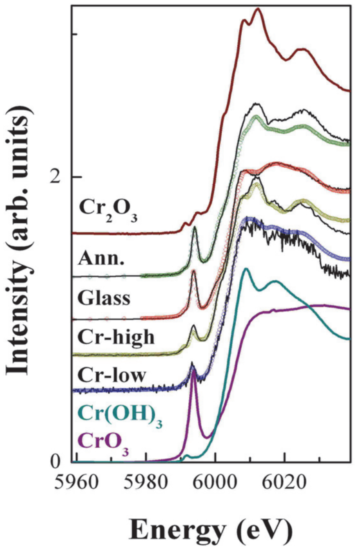

Figure 2: Cr-*K*-μ-XANES spectra recorded from the Cr-rich and Cr-porr regions and Cr-*K*-XANES spectra of the glassy and annealed sample. The LCF results are shown in colored circles.

Table 1. μ- & conventional-Cr-*K*-XANES results.

	CrO_3 (%)	Cr_2O_3 (%)	$Cr(OH)_3$ (%)
Cr-high	11.2	88.8	-
Cr-low	17.4	53.1	29.5
Glass	49.4	-	51.6
Annealed	37.9	49.5	17.6

References

F.Y. Saleh et al., Sci. Tot. Env. 86 (1989) 25
S.J. Driess S J, Ground Water 24 (1986) 312
T. Basegio et al., J. Hazard. Mater. 165 (2009) 604

PLENARY SESSION

T. MOUSTAKAS
(BOSTON UNIVERSITY, USA)
NITRIDE SEMICONDUCTORS: PHYSICS AND APPLICATIONS

Tuesday, 22 September 2015, 20^{00}-21^{00}

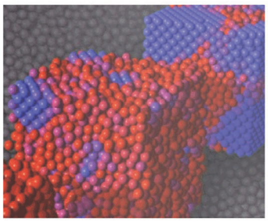

XXXI Panhellenic Conference on
SOLID STATE PHYSICS &
MATERIALS SCIENCE
Thessaloniki, 20-23 September 2015

Nitride Semiconductors: Physics and Applications

Theodore D. Moustakas

Department of Electrical and Computer Engineering, Department of Physics,
Materials Science and Engineering Division, Photonics Center, Boston University, USA

The family of Nitride semiconductors, consisting of the three binary compounds (InN, GaN, AlN) and their alloys, has been the subject of intense investigation over the past 25 years, because of their unique physical properties and their potential applications to a broad range of optoelectronic and electronic devices. Due to unavailability of native substrates these materials are generally grown heteroepitaxially on foreign substrates such as sapphire, silicon carbide and silicon, and as a result they have a high concentration of extended defects. Such include, for example, threading dislocations, stacking faults and band structure potential fluctuations due to phase separation and various forms of partial alloy ordering. Paradoxically, the performance of optoelectronic devices, such as LEDs and lasers, based on Nitride semiconductors is insensitive to this high concentration of defects, while the performance of similar devices based on traditional III-V requires orders of magnitude smaller concentration of defects. In this presentation I will argue that the difference in these two families of materials is related to their crystal structure, low growth temperature, chemical bonding, and various forms of band structure potential fluctuations.

A. Crystal structure: The equilibrium crystal structure of Nitride semiconductors is the wurtzite; however, they can also exist in the metastable zincblende structure, and the enthalpy of formation of these two allotropic forms differs by only a few meV [1]. Since these materials are grown at temperatures higher than 1000 K, the conversion between the two phases occurs easily by the formation of stacking faults along the closed packed (0001) and (111) planes [2]. As a result basal plane stacking faults are abundant in all nitride semiconductors. Since a basal plane stacking fault can be viewed as a monolayer of a cubic domain embedded into a wurtzite matrix and since the cubic GaN has a smaller energy gap by 0.1 to 0.2 eV compared to wurtzite GaN [3], one expects that basal plane stacking faults introduce band structure potential fluctuations. Evidence will be presented that such potential fluctuations are beneficial for devices such as LEDs, since they induce exciton localization leading to efficient radiative recombination [2]. This is to be contrasted with the traditional III-V compounds whose equilibrium structure is cubic and a basal plane stacking fault is the equivalent of a monolayer of a wurtzite structure embedded into a cubic matrix. Since the wurtzite structure has a larger energy gap, the stacking faults in III-V compounds introduce band structure potential fluctuations, which, however, are not favoring exciton localization.

B. Low growth temperature: Another important difference in these two families of materials is the origin of threading defects. Heteroepitaxial growth always proceeds via the nucleation and coalescence of islands. In both families threading defects occur at the boundaries of the domains due to incomplete coalescence of the islands. However, while in traditional III-V compounds the domains are also decorated with dislocations if their thickness exceeds the Mathews critical thickness, in Nitride semiconductors the islands are coherent to the substrate for significantly larger thickness than the Mathews critical thickness, since their growth temperatures is much lower than the half of their melting temperature, where the brittle to ductile transition occurs [2].

C. Chemical Bonding: The traditional III-V compounds are mostly covalent materials. Thus, the intrinsic surface states due to dangling bonds occur in a narrow half-filled band near the center of the energy gap and are potent non-radiative recombination centers. Also, these surface states pin the Fermi level close to the middle of the gap and thus, the barrier height of metallic contacts is independent of the work function of the metal. Similarly, dangling bonds in edge dislocations contribute also states close to the middle of the gap, and this accounts for the poor performance of minority type devices such as LEDs and lasers at high concentration of edge dislocations.

On the contrary the chemical bonding in Nitride semiconductors is mostly ionic, which results in the bunching of the intrinsic surface states due to dangling bonds near the band edges, where they act as traps rather than recombination centers [4, 5, 6]. Such states have been observed in clean (0001) GaN surfaces by angle resolved photoemission studies to occur near the valence band maximum and were identified as surface states, since they have spz character (dangling bonds) and are removed upon hydrogenation [7]. Similarly, dangling bonds in edge dislocations, which are the majority of threading dislocations in these materials, are not expected to be non-radiative recombination centers but traps. This then can account for the insensitivity of the performance of GaN based LEDs to high concentration of edge dislocations. Evidence will be presented that screw dislocations, whose density is orders of magnitude smaller than edge dislocations are the non-radiative recombination centers in Nitride semiconductors [8]. It should be stressed that the intrinsic surface states due to dangling bonds should be distinguished from extrinsic surface states, whose origin is surface reconstruction associated with excess Ga during growth by MBE or surface contamination [9, 10].

D. Band Structure Potential fluctuations: Besides the band structure potential fluctuations due to stacking faults, which are present in both Nitride compounds and alloys, there are other potential fluctuations in Nitride alloys due phase separation, partial alloy ordering and compositional fluctuations induced by specific growth modes. These potential fluctuations lead to exciton localization, which prevents them from diffusing and recombining non-radiatively in extended and point defects.

The influence of these unique physical and chemical properties of Nitride semiconductors to optoelectronic and electronic applications will be discussed.

REFERENCES:

[1] S-Y Yeh, Z.W. Lu, S. Froyen and A. Zunger, PRB 46, 10086 (1992).
[2] T. D. Moustakas, Phys. Status Solidi A 210, pp. 169-174 (2013).
[3] T.Lei, T. D. Moustakas, R. J. Graham, Y. He and S. J. Berkowitz, J. Appl. Phys., 71, 4933 (1992).
[4] W. Shockley, Phys. Rev. 56, 317 (1939).
[5] S. Kurtin, T C McGill, and C. A. Mead, Phys. Rev. Lett. 22, 1433 (1969).
[6] J. Foresi and T. D. Moustakas, Appl. Phys. Lett. 62, 2861 (1993).
[7] S. S. Dhesi, C. B. Stagarescu, K. Smith, D. Doppalapudi, R. Singh and T. D. Moustakas, Phys. Review B 56, 10271 (1997).
[8] J. Abell and T. D. Moustakas, Appl. Phys. Lett. 92, 091901 (2008).
[9] M. Kočan, A. Rizzi, H. Lüth, S. Keller, and U. K. Mishra, Phys. Status Solidi B, 234, 773 (2002).
[10] Chris G. Van de Walle and David Segev, J. Appl. Phys. 101, 081704 (2007).

SESSION WE1

NANOSCALE, SURFACE AND INTERFACE SCIENCE-2

Wednesday, 23 September 2015, 9^{30}-11^{00}

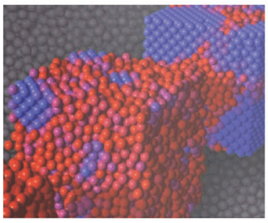

XXXI Panhellenic Conference on
SOLID STATE PHYSICS &
MATERIALS SCIENCE
Thessaloniki, 20-23 September 2015

Electrochemical Characterization and Quantified Surface Termination Obtained by LEIS and XPS of Orthorhombic and Rhombohedral $LaMnO_3$ Powders

E. Symianakis[1], *D. Malko*[1], *E. Ahma*[1,2], *A.-S. Mamede*[3], *J.-F. Paul*[3], *N. Harrison*[1,2], *A. Kucernak*[1]

[1]Department of Chemistry, Imperial College London, South Kensington, London SW7 2AZ, UK.
[2]Thomas Young Centre, Imperial College London, South Kensington, London SW7 2AZ, UK.
[3]Unité de Catalyse et de Chimie du Solide, UMR CNRS 8181, Université Lille 1, Cité Scientifique, Bâtiment C3, 59655 Villeneuve d'Ascq Cedex, France.

E-mail: e.symianakis@imperial.ac.uk

$LaMnO_3$ is an ABO_3 perovskite with known catalytically active surface and applications in solid oxide (SOFCs) [1], and alkaline fuel cells (AFCs) [2]. With the use of electron paramagnetic resonance it has been possible to correlate the influence of oxygen stoichiometry to the catalytic activity of $LaMnO_3$ [3] while density functional theory (DFT) calculations suggest that the active site of the oxygen reduction reaction(ORR) is the on-top position of the surface Mn ions[4],[5],[6],[7]. Based on this hypothesis Suntivich et al. [8] provided an explanation on the higher electrochemical activity of the rhombohedral structure observed, compared to the orthorhombic, by correlating the ORR activity for oxide catalysts to the s*-orbital (e_g) occupation and the covalency of the B-site transition-metal–oxygen interaction.

This type of ORR activity identifiers obtainable by DFT calculations can enhance the predictive ability of theoretical calculations for the engineering of new non-precious ORR catalysts. However it is the characterization of the first atomic layer of the samples as synthesized that will allow the reliable correlation of such theoretical predictions to the observed electrocatalytic activities.

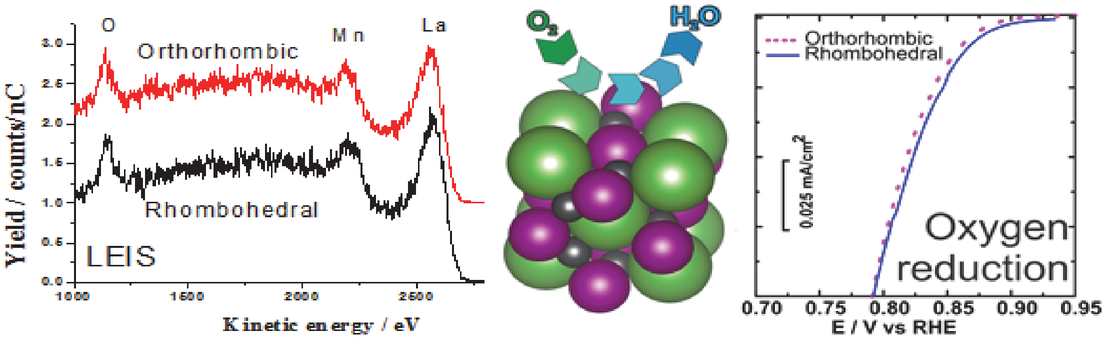

Fig. 1, Right: LEIS spectra, He^+ ions with kinetic energy 3KeV and pass energy 3KeV obtained from the rhombohedral and orthorhombic $LaMnO_3$ powders. Left: RDE Cyclic voltammetry from the same batches with 1600 rpm in O_2-saturated 0.1M NaOH. Scan Rate: 10 mV/s, Loading: 250 $\mu g_{oxide}/cm^2$, 50 $\mu g_{carbon}/cm^2$, 50 $\mu g_{Nafion}/cm^2$. Current normalised to specific surface area of the perovskite.

In this study we present the first quantified characterization of the surface termination of $LaMnO_3$ powders synthesized via glycerin combustion with the rhombohedral and orthorhombic structure by Low Energy Ion Scattering (LEIS) and X-ray

Photoelectron spectroscopy (XPS) while electrochemical characterization is performed by the Rotating Disk Electrode (RDE) method.

The X-Ray diffraction (XRD) and XPS techniques suggest that the $LaMnO_3$ powders as synthesized are consistent to samples discussed in the literature. Characterization by LEIS suggests that the two phases have the same La/Mn atomic ratio within experimental error, 1.5 and 1.7 ± 0.3 for the rhombohedral and orthorhombic respectively, Fig.1-Right, while comparison of the La/Mn surface atomic ratio of the orthorhombic phase to the predictions of its crystallite morphology from a Wulff construction model that is based on surface energies calculated from Density Functional Theory (DFT) calculations, $La/Mn_{(model)}=1.4\text{-}1.8$, suggest that the orthorhombic phase as synthesized is near thermodynamic equilibrium.

The oxygen reduction reaction (ORR) activity of the materials was assessed with the rotating disk electrode (RDE) method. Electrochemical characterisations were conducted in a 3 compartment electrochemical glass cell while a glassy carbon rod was used as counter. The catalyst ink was prepared by mixture of $LaMnO_3$ to carbon with Ketjen Black EC600 (Akzo Nobel) and Na^+ exchanged Nafion solution as per literature[9] while the electrode is prepared by drop casting of ink onto a glassy carbon disk electrode [9]. The RDE measurements suggest that the ORR activity of the $LaMnO_3$ with two structures is the same within the experimental error. Fig1-Left. The performed measurements do not allow the observation of a significantly higher activity of the rhombohedral or oxygen rich phase as previously reported [8].

In summary the surface termination of the first atomic layer of $LaMnO_3$ powder synthesized by glycine combustion with the rhombohedral and orthorhombic structures, as confirmed by XRD and XPS, has been characterized by LEIS for the first time suggesting that the La/Mn atomic ratio is the same for the prepared samples. Furthermore the La/Mn surface termination of the orthorhombic phase is in good agreement with the theoretical predictions of a Wulff construction model that is based on DFT surface energy calculations. The ORR activity of the synthesized powders measured with the RDE method is found to be the same within the experimental error. This indicates that the preparation method and the resulting surface termination might play a crucial role for the activity of perovskite catalysts since our catalyst was prepared by the glycine combustion method as opposed to the coprecipitation method used [8].

References

[1] S. Tao, J.T.S. Irvine and J.A. Kilner, Advanced Materials 17 (2005) 1734-.
[2] M. Hayashi, H. Uemura, K. Shimanoe, N. Miura and N. Yamazoe, Journal of the Electrochemical Society 151 (2004) A158-A163.
[3] L.F. C. Oliva, Catalysis Communications (2000) 5-8.
[4] Y. Wang and H.-P. Cheng, Journal of Physical Chemistry C 117 (2013) 2106-2112.
[5] G. Pilania and R. Ramprasad, Surface Science 604 (2010) 1889-1893.
[6] E.A. Kotomin, Y.A. Mastrikov and E. Heifetsa, J. Maier, Physical Chemistry Chemical Physics 10 (2008) 4644-4649.
[7] E.A. Ahmad, G. Mallia, D. Kramer, A.R. Kucernak and N.M. Harrison, Journal of Materials Chemistry A 1 (2013) 11152-11162.
[8] J. Suntivich, H.A. Gasteiger, N. Yabuuchi, H. Nakanishi, J.B. Goodenough and Y. Shao-Horn, Nature Chemistry 3 (2011) 546-550.
[9] J. Suntivich, H.A. Gasteiger, N. Yabuuchi and Y. Shao-Horn, Journal of the Electrochemical Society 157 (2010) B1263-B1268.

Raman study of graphene irradiated with 350 eV N^+ ions

K. Filintoglou[1], **J. Sommerfeld**[2], **J. Arvanitidis**[1], **D. Christofilos**[3], **M. Katsikini**[1], **S. Ves**[1], **G.A. Kourouklis**[3], **E. Wendler**[2], **J. Parthenios**[4] **and K. Papagelis**[4]

[1]Physics Department, Aristotle University of Thessaloniki, 54124 Thessaloniki, Greece
[2]Institute für Festkörperphysik, Friedrich-Schiller Universität Jena, 07743 Jena, Germany
[3]Chemical Eng. Department, Aristotle University of Thessaloniki, 54124 Thessaloniki, Greece
[4]Institute of Chemical Engineering Sciences, FORTH/ICE-HT, 26504 Rio Patras, Greece

E-mail: kfilinto@physics.auth.gr

Owing to its fascinating properties, graphene provides a broad field for many nanotechnology applications [1]. Although ion irradiation induces defects, it may provide an alternative method to dope graphene after appropriate annealing [2]. Raman spectroscopy is a non-destructive technique that due to its sensitivity to defects is widely used to study graphene by recording the changes of the D, G and 2D characteristic Raman bands [3]. Here, we present our Raman study (λ_{exc}= 514.6 nm) of pristine graphene on Cu/Si and of that transferred on SiO_2/Si as well as of implanted graphene/SiO_2/Si after irradiation by 350 eV N^+ ions at fluences of 10^{12}, 10^{13}, 10^{14}, 10^{15} and 10^{16} cm^{-2}. Typical Raman spectra from graphene on Cu/Si and on SiO_2/Si are shown in Fig. 1. The frequencies, lineshapes and I_{2D}/I_G intensity ratios of the G and 2D bands in the studied samples, along with the absence of the disorder-induced D band in graphene/Cu/Si or its low intensity in graphene/SiO_2/Si, are indicative of the high quality of the graphene layers. Moreover, the spectral profiles for spectra a and b are indicative of single layer graphene (SLG), while those for c and d are characteristic of bilayer graphene (BLG).

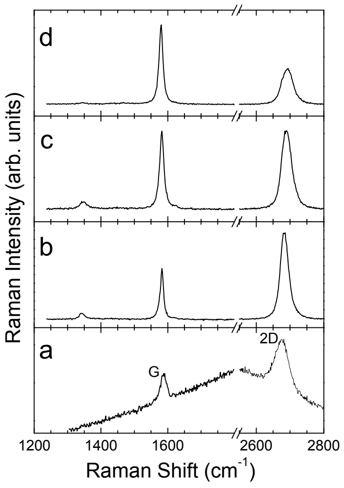

Fig. 1. Raman spectra of (a) graphene/Cu/Si and (b-d) different sites of graphene/SiO_2/Si.

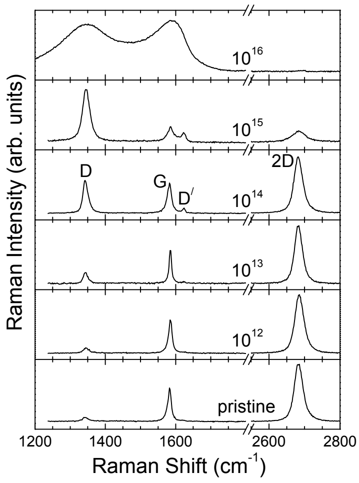

Fig. 2. Raman spectra of graphene/SiO_2/Si for various 350 eV N^+ fluences.

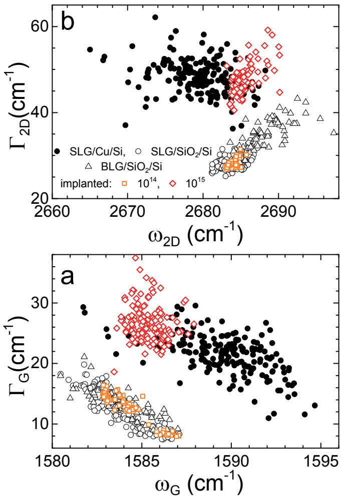

Fig. 3. Linewidth *vs.* frequency for (a) G and (b) 2D band.

As it can be inferred from Fig. 2, N^+ implantation causes the gradual intensity enhancement of the D band, the appearance of the also disorder-induced D′ band at fluences 10^{14} and 10^{15} cm^{-2}, the abrupt intensity decrease and broadening of the G and the 2D bands at 10^{15} cm^{-2} (see also Fig. 3), and the huge broadening of the D and G bands at 10^{16} cm^{-2}. Taking into account these spectral modifications and the existing literature [3], we conclude that at the N^+ fluence of 10^{15} cm^{-2} graphene becomes nanocrystalline (damage stage 1), while at 10^{16} cm^{-2} nanocrystalline graphene tranforms to low sp^3 amorphous carbon (damage stage 2).

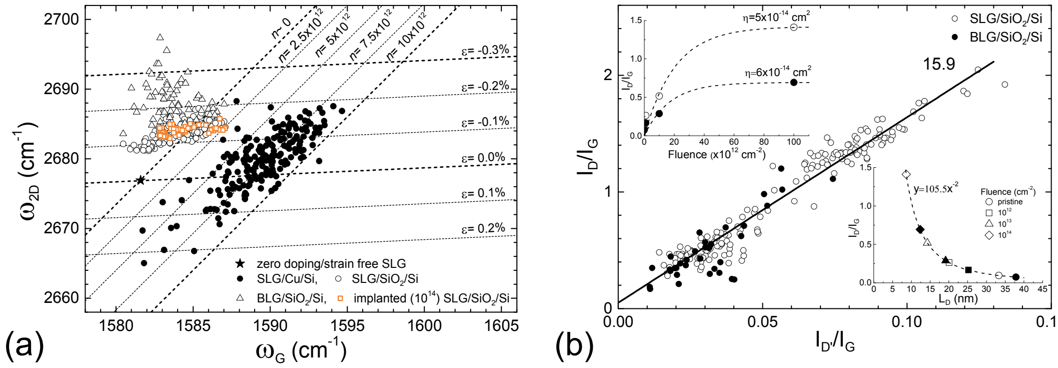

Fig. 4. (a) ω_G-ω_{2D} correlation plot. (b) Correlation plot between I_D/I_G and $I_{D'}/I_G$ intensity ratios for fluences up to 10^{14} cm^{-2}. Top inset: I_D/I_G *vs.* fluence. Bottom inset: I_D/I_G *vs.* mean distance between defects, L_D.

The correlation plot between the G and 2D peak frequencies, allowing for the evaluation of the local strain and doping state of SLG [4], is illustrated in Fig. 4(a). As it can be seen, although the pristine SLG layer on Cu/Si exhibits a rather inhomogeneous local strain and a carrier density of 5-10x10^{12} cm^{-2}, its transfer onto SiO_2/Si leads to the loss of the free carriers and to the homogeneity of the local strain (compressive). Noticeably, N^+ implantation up to the fluence of 10^{14} cm^{-2} does not alter the doping and the strain state of the SLG layer. Moreover, the BLG/SiO_2/Si data lie outside the strain/doping grid, which should be interpreted as a consequence of the interlayer interaction.

The I_D/I_G *vs.* $I_{D'}/I_G$ correlation plot is depicted in Fig. 4(b). Linear fitting of the data yields a slope of ~16 for both SLG and BLG and, according to the analysis of Eckmann et al. [5], we deduce that the N^+ ions are on top of graphene layer, forming sp^3 bonds with the C atoms. The dashed lines in the top inset correspond to fitting of the I_D/I_G *vs.* fluence (φ) data using the formula $I_D/I_G= (I_D/I_G)_{saturated} \times (1-e^{-\eta\varphi})$, where η is the efficiency in the production of disorder [6]. We found that both SLG and BLG have similar disorder efficiency. Finally, from the I_D/I_G *vs.* L_D plot (bottom inset), where the values for the mean distance between defects (L_D, that is a measure of the amount of disorder) have been obtained using the appropriate formula of Ref. 7, we conclude that for the same ion fluence BLG is less vulnerable to N^+ irradiation than SLG.

References

[1] K. S. Novoselov, A. K. Geim, S. V. Morozov et al., Science 306 (2004) 666-669.

[2] B. Guo, Q. Liu, E. Chen et al., Nano Lett. 10 (2010) 4975-4980.

[3] L. G. Cancado, A. Jorio, E. H. Martins Ferreira et al., Nano Lett. 11 (2011) 3190-3196.

[4] J. E. Lee, G. Ahn, J. Shim et al., Nat. Commun. 3 (2012) 1024.1-8.

[5] A. Eckmann, A. Felten, A. Mishchenko et al., Nano Lett. 12 (2012) 3925-3930.

[6] G. Compagnini, F. Giannazzo, S. Sonde et al., Carbon 47 (2009) 3201-3207.

[7] M.M. Lucchese, F. Stavale, E.H. Martins Ferreira et al., Carbon 48 (2010) 1592-1597.

Multiscale approach to field-dependent energy barrier calculation of exchange biased nanoparticles

P. Nieves[1], D. Kechrakos[2] and O. Chubykalo-Fesenko[1]

[1]Instituto de Ciencia de Materiales de Madrid, CSIC, Cantoblanco, Madrid 28049, Spain
[2]School of Pedagogical and Technological Education, Athens 14121, Greece

E-mail: dkehrakos@aspete.gr

The exchange bias phenomenon is widely used in magnetic recording information technology, for example, to pin the magnetization of the pinned layer in magnetic recording heads. Also, thermal stability of a bit of information is of critical importance particularly as bits are made smaller and media are made thinner. In 2003 Skumryiev *et al* [1] demonstrated an impressive increase of the blocking temperature of Co nanoparticles embedded in a CoO matrix and suggested to "beat the superparamagnetic limit" using the exchange bias phenomenon. Evans *et al* [2] demonstrated that at remanence the exchange bias indeed *increases* the energy barrier for forward reversal of the magnetization, but at the same time it *reduces* the barrier for backward reversal. Since both barriers are crucial for the desired thermal stability of magnetic storage media, the same authors [2] suggested that under conditions of large interfacial exchange, which renders the FM core unconditionally stable, an external heating source acting in synergy to the applied field is required in order to reverse the AF shell and restore the required barrier for the backward reversal of the FM moment. This idea paved the way to utilization of core-shell nanoparticles in heat-assisted magnetic recording (HAMR) applications. Evans *et al* [2] also calculated the energy barriers at remanence (H=0), while in actual recording applications what matters is the values of the energy barriers under an applied field (head field).

In the present work, we perform atomistic multi-spin magnetization dynamics of FM core – AF shell nanoparticles to obtain the magnetic hysteresis and constrained magnetization dynamics to obtain the dependence of forward and backward energy barriers under an externally applied field for different values of the interface exchange coupling strength (J_{int}). We show that the applied field and the interface exchange strength have opposite effects on the values of the energy barriers. In particular, the forward (backward) energy barrier increases (decrease) linearly with the strength of the interface exchange coupling and it decreases (increases) almost quadratically with the applied magnetic field (H_z). Our results from atomistic simulations are fitted to the well-known Meiklejohn-Bean model of exchange bias and we discuss the limits of applicability of the macrospin approach to the study of field-dependent energy barriers in core-shell Co/CoO magnetic nanoparticles.

Acknowledgment: Research co-financed by the European Social Fund and Greek national funds through the Research Funding Program *ARCHIMEDES-III*.

References

[1] R. F. L. Evans, R. Yanes, O. Mryasov, R. W. Chantrell and O. Chubykalo-Fesenko, EPL 99 (2009) 57004.

[2] V. Skumryev, V. Skumryev, S. Stoyanov, Y. Zhang, G. Hadjipanayis, D. Givord, and J. Nogués, Nature, 423 (2003) 19.

Theoretical study on hydrogen evolution edge-site activity of MoS2 and hybrid MoS_2/Graphene structures

Aristea E. Maniadaki[1], **Georgios Kopidakis**[1]

[1]Department of Materials Science and Technology,
University of Crete, Heraklion, Crete, Greece

E-mail: maniadaki@materials.uoc.gr

Recent studies have shown that transition metal dichalcogenides (TMDs) are rising candidates in the replacement of Pt as catalysts in the water splitting process. In this study we focus on the hydrogen evolution reaction (HER) part of this process and how hydrogen (H) interacts with the TMDs, specifically MoS_2, as a free standing nanostructure or when positioned on a graphene substrate. Our results are obtained through Density Functional Theory (DFT) calculations.

First we show the stability of MoS_2 structures. We examine various nanostructures, from a 2D infinite MoS_2 monolayer to the quasi-1D MoS_2 ribbons and the quasi-0D MoS_2 flakes. We calculate the adsorption of H on various sites of the TMD, including the Mo and S edges. We also evalute the activity of each site.

Futhermore, the stability of the MoS_2/Graphene hybrid system is investigated. Additional calculations of the adsorption of H in the MoS_2/Graphene hybrid structure indicate that the effect of graphene in the adsorption process of H on MoS_2 nanostructures is quite significant.

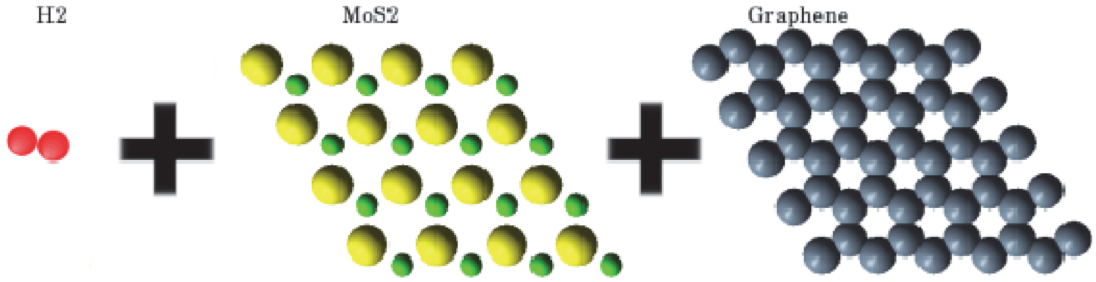

Fig. 1: Illustration of an H_2 molecule (left), an MoS_2 single layer structure (center) and a graphene sheet (right)

This research has been co-financed by the European Union (European Social Fund – ESF) and Greek national funds through the Operational Program "Education and Lifelong Learning" of the National Strategic Reference Framework (NSRF) – Research Funding Program: Heracleitus II. Investing in knowledge society through European Social Fund.

Adsorption of water on a cesium covered $SrTiO_3$ (100) surface

D. Vlachos, M. Kamaratos, E. Giotopoulou and S.D. Foulias

Department of Physics, University of Ioannina, Ioannina 45110, Epirus, Greece
E-mail: dvlachos@cc.uoi.gr

We describe the adsorption of water on a cesium covered strontium titanate $SrTiO_3$ (100) surface, by means of AES, TDS and work function measurements. The results show that water neither dissociates nor reacts with the predeposited cesium on the surface. In contrast when simultaneous adsorption of water and cesium takes place on the surface, interaction between the co-adsorbates occurs, resulting in water dissociation and cesium oxide formation.

During the last decades the adsorption of water at surfaces has been a widely studied subject and has been presented by several excellent overviews [1,2,3]. The interest on water-surface interaction originates not only from fundamental scientific reasons, namely to understand better wetting and corrosion phenomena, but also from environmental concerns underlining the increasing importance of hydrogen as a fuel for green energy production. Despite the scientific effort, our knowledge of water adsorption with additives on surfaces remains incomplete. Thus here, we investigate experimentally the role of cesium as a promoter for water adsorption on the strontium titanate surface, $SrTiO_3$ (STO). STO is a perovskite with outstanding catalytic properties in photoelectrolysis of water [4]. The motivation of this work is the well known enhancement of the catalytic properties of metal oxides by the addition of alkali species.

The experiments were performed in an ultra high vacuum system (UHV) at base pressure of 10^{-10} Torr. The system was equipped with Auger electron spectroscopy (AES), a quadrupole mass spectrometer (QMS) for the thermal desorption spectroscopy (TDS) measurements and a diode for work function measurements (WF). The sample was a $SrTiO_3$(100) single crystal. Cesium deposition was carried out by means of a commercial evaporation SAES Getters source, while H_2O adsorption on the surface took place by supplying vapors of distilled water, into the experimental chamber through a leak valve. The water exposure was counted in Langmuirs (L), where $1L=1\times10^{-6}$ Torr.s.

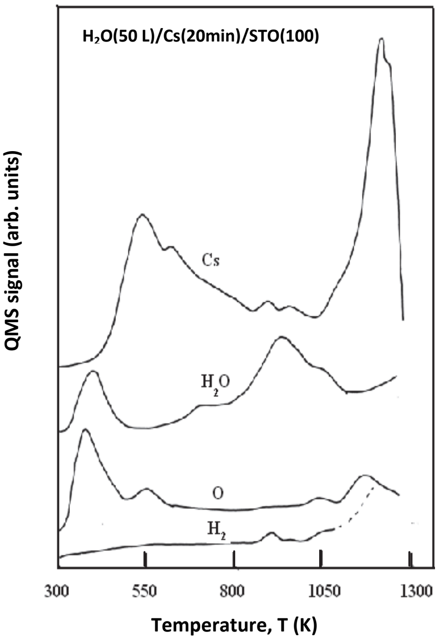

Fig. 1 *The QMS signal of Cs, H_2O, O and H_2, after H_2O exposure on the cesiated Cs(20 min)/STO(100).*

For reference purpose we firstly performed measurements of Cs adsorption on the clean STO(100) surface. The combination of AES and WF results, indicate that Cs forms a single layer on the surface, showing the same behavior as that of Cs on metallic substrates [5], but different to that on semiconducting [6,7] and insulating surfaces [8].

The next step was to adsorb H_2O on

different cesiated STO(100) surfaces. TDS spectra of Cs after H_2O adsorption on the Cs(1ML)/STO(100) surface, showed that the metallic TD peak shifts to higher temperatures as the water exposure increases. This means that the presence of water on STO increases the binding energy of Cs on the surface. In addition, the presence of Cs on the surface increases the sticking coefficient of water. For Cs coverages above 0.5 ML, water desorption gives characteristic TD peaks at several temperatures. However, the main question is whether the water dissociates in the presence of Cs on the surface. In that case presumably Cs interacts on the surface forming cesium oxide. To test this question, we performed TDS spectra for Cs, H_2O, O and H_2, after H_2O exposure on cesiated Cs(20 min)/STO(100) as Fig. 1 shows. The Cs desorption does not coincide with those of H_2O, O and H_2. Analogous results have been reported for water adsorption on potassium covered Si(100) surface [9]. This implies that the H_2O does not interact strongly with Cs, nor does it form any Cs-H_2O compound, concluding that the water does not adsorb dissociatively on the cesiated STO surface. On the other hand, previous experiments of H_2O, show partial dissociation of water and oxidation of the substrate [10], while rapid dissociation of water has also been observed on cesium covered MgO(100) surface [11].

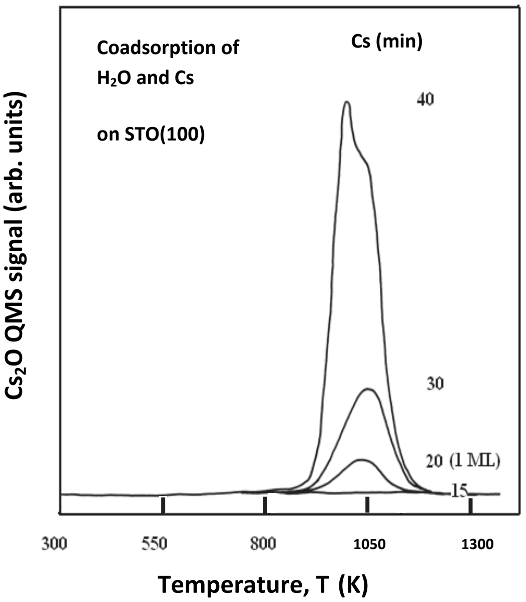

Fig. 2 *The QMS signal of Cs_2O after H_2O and Cs simultaneous adsorption on the STO(100) surface.*

We also tried simultaneous deposition of Cs with H_2O on the STO(100) surface. Those experiments resulted in the detection of Cs_2O in QMS signal as Fig.2 shows. It is important to note that the oxidation of cesium is observed only if the corresponding Cs coverage is equivalent or larger than 1 ML. In that sense a prerequisite minimum amount of Cs is necessary in order to react with H_2O and form cesium oxide. From the above, we conclude that codeposition of Cs with water can dissociate the molecule of H_2O on the STO(100) surface, resulting in the oxidation of Cs.

References

[1] P.A. Thiel and T.E. Madey, *Surf. Sci. Rep.* **7** (1987) 211.
[2] M.A. Henderson, *Surf. Sci. Rep.* **46** (2002) 5.
[3] A. Hodgson and S. Haq, *Surf. Sci. Rep.* **64** (2009) 381.
[4] M.S. Wrighton, A.B. Ellis, P.T. Wolczanski, D.L. Morse, H.B. Abrahamson and D.S. Ginley, *J. Am. Chem. Soc.* **98** (1976) 2774.
[5] C.A. Papageorgopoulos, *Phys. Rev. B* **25** (1982) 3740.
[6] C.A. Papageorgopoulos, *Surf. Sci.* **75** (1978) 17.
[7] S. Kennou, S. Ladas and C. Papageorgopoulos, *Surf. Sci.* **152/153** (1985) 1213.
[8] S. Kennou, M. Kamaratos and C. Papageorgopoulos, *Surf. Sci.* **25**, 312 (1991).
[9] S. Hongo, S. Tanigushi, K. Ojima, T. Urano and T. Kanaji, *Appl. Surf. Sci.* **82/83** (1992) 437.
[10] S. Ferrer and G.A. Somorjai, *Surf. Sci.* **97** (1980) L304.
[11] M.A. Karolewski and R.G. Cavell, *Surf. Sci.* **271** (1992) 128.

Effects of Macromolecular Architecture and Size on Polymer/Graphene Nanocomposites:Insight from Molecular Dynamics Simulations

K. Karatasos and Roza-Eleftheria Roussou

Laboratory of Physical Chemistry, Department of Chemical Engineering,
Aristotle University of Thessaloniki,
54124 Thessaloniki, Greece

E-mail: karatas@eng.auth.gr

Fully atomistic molecular dynamics simulations were employed to study nanocomposites comprised by graphene and two different families of polymeric materials, namely hyperbranched polyesters and poly(ethylene glycol), in a wide temperature range. Static, dynamic and thermodynamic properties of the polymeric components and of the mixtures are examined in order to assess the effects of the presence of graphene in the polymer's behavior, as well as to monitor the effects of size, of polymeric architecture and of temperature in the structural rearrangement of the graphene nanosheets in the composites. Results from the present study can be exploited toward a better understanding of the response of polymer/graphene nanocomposites in different thermal conditions and thus toward the fabrication of graphene-based nanocomposites with optimized properties.

Acknowledgements: This research has been co-financed by the European Union (European Social Fund – ESF) and Greek national funds through the Operational Program "Education and Lifelong Learning" of the National Strategic Reference Framework (NSRF) - Research Funding Program: Thales. Investing in knowledge society through the European Social Fund (MIS 377278).

References

[1] Karatasos, K., Macromolecules 47 (2014) 8833-8845.
[2] Roza-Eleftheria Roussou and K. Karatasos, (2015) in preparation

SESSION WE2

ELECTRONIC TRANSPORT PHOTONICS AND INTERFACE SCIENCE-2

Wednesday, 23 September 2015, 11^{30}-13^{15}

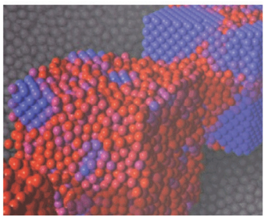

Low-Dimensional Charge-Transport Phenomena in Solution-Processed Metal Oxide Materials and Devices

Professor Thomas D. Anthopoulos

Department of Physics and Centre for Plastic Electronics, Blackett Laboratory
Imperial College London, London, UK
E-mail: t.anthopoulos@ic.ac.uk

Semiconducting materials that combine enhanced charge transporting characteristics with processing versatility are currently in great demand due to their potential for application in the emerging field of printed electronics. Semiconducting metal oxides represent one such family of materials that promise to revolutionise the area of thin-film transistors for applications spanning from next generation ultra-high-definition large-area displays to ubiquitous transparent opto/electronics. In this presentation I will discuss the development of solution-processable metal oxides and their application in low-dimensional semiconducting structures and devices. In particular, I will describe how ultra-thin layers of different oxides can be grown from solution-phase at low temperatures and how these layers can be combined to form complex superlattice structures with controlled dimensionality and spatially-varying conduction band characteristics. The application of these simple to implement oxide systems in high-electron mobility thin-film transistors that can be processed directly onto temperature-sensitive substrate materials such as plastic, will also be discussed. I will show that in contrast to conventional single metal oxide-based devices, the performance level oxide superlattice transistors is not limited by the carrier mobility of the individual semiconductors involved but instead is determined by the physical properties of the oxide heterointerfaces. Finally, the development of other quantum-effect devices such as double-barrier resonant tunnelling diodes that exploit the energy quantization effect in these solution-grown oxide structures will be presented.

WE2

O49

Tungsten and tungsten-based alloy thin films as copper substitutes for microelectronics interconnects

A. Kaidatzis[1], V. Psycharis[1], K. Mergia[2] and D. Niarchos[1]

[1] Institute of Nanoscience and Nanotechnology, NCSR Demokritos, Aghia Paraskevi, 15310, Greece
[2] Institute of Nuclear & Radiological Sciences and Technology, Energy & Safety, NCSR Demokritos, Aghia Paraskevi, 15310, Greece

E-mail: a.kaidatzis@inn.demokritos.gr

Metallic W thin films are considered as candidate substitutes of Cu interconnects in microelectronics applications [1] and as current-line metallization in magnetic memories applications [2]. The resistivity of W, in the form of very thin films, becomes comparable to that of Cu, due to the low electron mean free path. Moreover, W suffers lower thermal degradation than Cu, due to its much higher melting point. In this respect, we study sputtered thin films of W and W alloys with Cu, Al, and Ag, having thicknesses in the range between 1.5 to 100 nm and the effect of vacuum annealing on their structure and resistivity.

All thin films were deposited using an ultra-high vacuum magnetron sputtering setup in diode configuration. The source materials were metallic targets and the working gas was high purity Ar. Single-side polished Si (100) wafers with a 500 nm thick thermal oxide were used as substrates.

Films with thickness between 1.5 and 100 nm were deposited and annealed in the temperature range between 200 and 800^{o}C for 30 min, using a resistive heater mounted inside a high vacuum chamber. X-ray diffraction and reflectivity measurements were used to assess the crystalline structure and the structural properties (thickness, density, roughness) of the film versus depth. Atomic force microscopy was employed to obtain the film surface morphology. Electrical resistivity was obtained by Van der Pau measurements.

We show that the films are highly resistive and primarily have the β-W phase in the as-deposited state and after annealing at 200^{o}C (Fig. 1). After annealing at 300^{o}C there is a steep resistivity drop with a corresponding phase transition from the β-phase to the α-phase (Fig. 2). Resistivity continues to decrease as annealing temperature increases. However, even for the thicker film (100 nm) and after annealing at 800^{o}C for 30 min, the film resistivity is 17.0 μΩcm, much higher than the bulk 5.3 μΩcm value. This is attributed to the very low deposition rate (0.016 nm/s) which promotes the incorporation of oxygen into the films, resulting in the persistence of β-phase. This indicates that for obtaining low resistivity sputtered W films, besides an ultra-high vacuum environment, high deposition rate is also needed.
Taking into account the industrial scalability of the sputtering film deposition method, our work demonstrates the feasibility of using W-based microelectronics interconnects, provided that much higher deposition rates and ultrahigh vacuum environment would be employed.

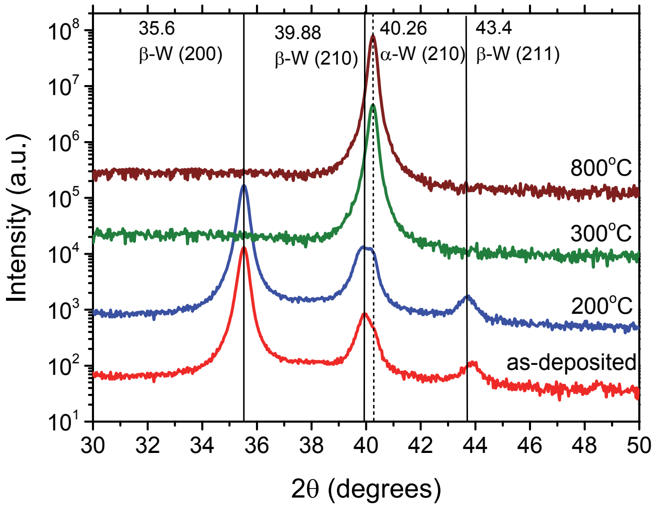

Figure 1. XRD spectra of 100 nm thick W films before and after annealing. The β-W phase prevails even after annealing at 200°C.

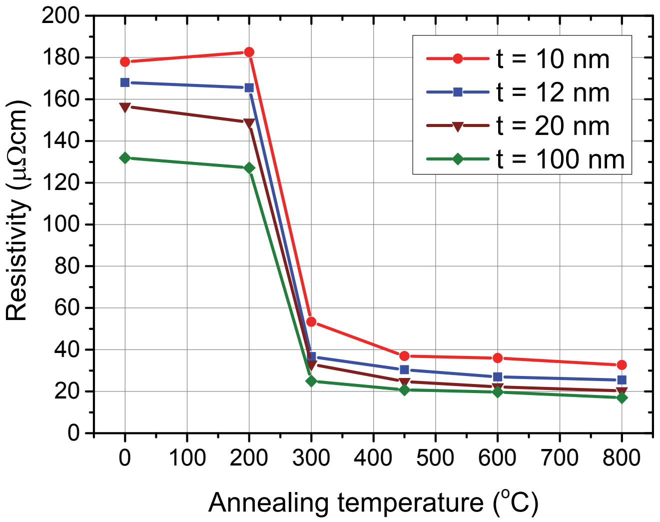

Figure 2. Resistivity measurements of W films before and after annealing. The steep resistivity drop corresponds to a β-W to α-W phase transition.

Acknowledgements

Funding from the E.C. through a FP7-ICT project (Grant No. 318144) is acknowledged.

References

[1] D. Choi, B. Wang, S. Chung, X. Liu, A. Darbal, A. Wise, N.T. Nuhfer, K. Barmak, A.P. Warren, K.R. Coffey, M.F. Toney, J. Vac. Sci. Technol. A 29 (2011) 051512.

[2] A. Kaidatzis, V. Psycharis, J. M. Garcia-Martin, C. Bran, M. Vazquez, and D. Niarchos, MRS Proceedings 1729 (2015) doi:10.1557/opl.2015.191.

Nanocrystalline TiO_2 Films Synthesized through a Simple Procedure for Dye-sensitized Solar Cells' Photoanodes

D. Sygkridou[1, 2], **E. Stathatos**[1] **and E. Vitoratos**[2]

[1] Nanotechnology and Advanced Materials Laboratory, Dept. of Electrical Engineering,
Technological-Educational Institute of Western Greece, Patras 26334, Greece
[2] Dept. of Physics, University of Patras, Patras 26500, Greece

E-mails: dim.sigridou@gmail.com; estathatos@teiwest.gr

Dye-sensitized solar cells (DSSCs) have attracted substantial interest since their first report as they are thought to be a promising alternative for harnessing the solar energy. This is mainly due to the fact that they are based on earth abundant nanocomposite materials, their manufacture requires simple chemical processes, which are more or less benign, and have low fabrication cost. DSSCs' components are being extensively investigated by researchers trying to ameliorate them in order to further increase the cells' efficiency, which has recently reached 13%. A large volume of recent studies on DSSC's is devoted to the study of structural properties of the inorganic semiconductor as a negative electrode, which in most cases is titanium dioxide (TiO_2). There are various ways that can influence the photoanode film fabrication and as a result the DSSCs' performance, such as the surfactant or the TiO_2 precursor used, the morphology of the TiO_2 particles, the preparation method of choice, whether the photoanode will be pure TiO_2 or TiO_2 doped with another material and so on.

In this work nanocrystalline Titanium dioxide films were synthesized through a simple procedure in order to be used as photoanodes for dye-sensitized solar cells. Dioctyl sulfosuccinate sodium salt (AOT) was used in the precursor TiO_2 solution as a surfactant to prepare reverse micelles. The formation of the TiO_2 with the reverse micellar method was carried out through the hydrolysis of Titanium(IV) isopropoxide and the end product of the polycondensation reaction is an inorganic–O-Ti-O-Ti-network. Specifically, the films are composed by dipping conductive glasses to the TiO_2 solution leaving them to dry in air for a couple of minutes. Afterwards, the glasses are rinsed with distilled water to remove the AOT and as soon as they're dried, a film of amorphous TiO_2 is apparent. Films are annealed at 500^oC to obtain crystalline TiO_2. This procedure is repeated a few times to increase the final film thickness. The films fabricated are characterized structurally (Fig. 1), while the performance of the dye-sensitized solar cells is studied through photocurrent-voltage measurements (Fig. 2) and electrochemical impedance spectroscopy (EIS).

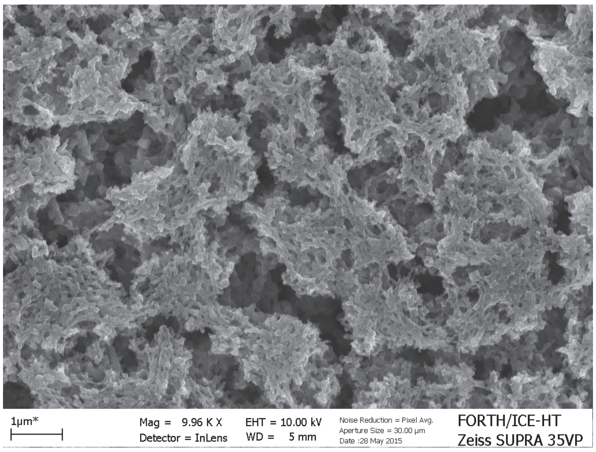

Figure 1: SEM image of TiO_2 film, using AOT as a surfactant, annealed at 500°C.

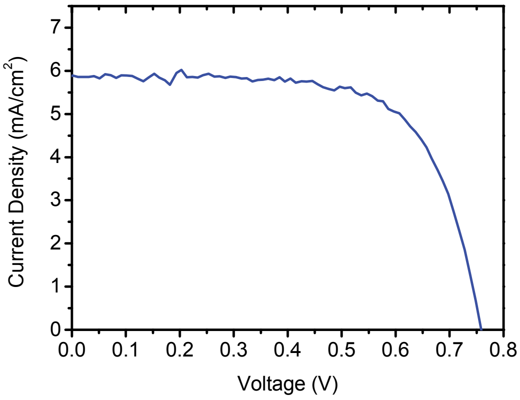

Figure 2: Photocurrent-voltage curve of DSSC with TiO_2 nanocrystalline film using AOT as a surfactant.

Acknowledgements

This research has been co-financed by the European Union (European Social Fund - ESF) and Greek national funds through the Operational Program "Education and Lifelong Learning" of the National Strategic Reference Framework (NSRF) - Research Funding Program: ARCHIMEDES III, Investing in knowledge society through the European Social Fund.

References

[1] E. Stathatos, H. Choi and D. D. Dionysiou, Environmental Engineering Science 24 (2007) 13-20.

TiO_2 transport layer made with Pluronic P123 as template for efficient perovskite solar cells.

D. Karageorgopoulos[1,2], **A. Rapsomanikis**[2] **and E. Stathatos**[2]

[1]Physics Department, University of Patras, 26500 Patras, Greece
[2]Electrical Engineering Department, Technological-Educational Institute of Western Greece, 26334 Patras, Greece

E-mail: dkarageorgop@upatras.gr; rapsosan@gmail.com; estathatos@teiwest.gr

Hybrid organic-inorganic halide perovskite based solar cells have recently emerged as one of the most promising approach for high efficiency solar cells. The general formula that describes a perovskite structure is ABX_3 where A and B are cations and X is the anion. Although perovskite structure was known for many years the first time that it was incorporated for the fabrication of a perovskite based solar cell was in 2009 by Miyasaka et al.[1] achieving a solar energy conversion efficiency of 3.8%. Since then, high power conversion efficiencies of more than 20% have been reported from various independent researchers. This unprecedented rapid rise of perovskites in solar photovoltaic research, where usually takes decades for efficiencies to rise up, compared with other photovoltaic technologies is a challenging perspective as a research field. Some very attractive characteristics of these perovskite based solar cells include the ease of fabrication, high solar absorption and low carrier recombination, tuneable band gap and long carrier diffusion lengths. On the other hand, negative aspect of perovskites cells is the fact that some toxic materials are used such us lead, raising toxicity issues during device fabrication, deployment and disposal. Perovskites are also extremely sensitive to environmental conditions such as moisture and ultraviolet radiation therefore efficient shielding techniques and appropriate filters are required to prevent rapid degradation of the device.

Even higher device efficiencies can be achieved with optimizations and better control over all processing parameters. A number of materials have been studied so far as alternatives electron transport layers to TiO_2 for perovskite solar cells such as ZnO PCBM etc. Despite all this research, TiO_2 remains on top of these materials therefore it is important to further investigate its potentials. In this study we are focusing on improving the electron transport layer as it is widely accepted the importance of the interface between the perovskite and this layer. Moreover our aim is to propose a simple synthetic procedure for preparing efficient TiO_2 films that could boost device efficiency further. According to this novel proposed method, we fabricated TiO_2 electron transport layers using Titanium (IV) butoxide as a precursor of Titanium oxide and Pluronic 123 as an organic template. Extensive studies on the structural and morphological properties of the prepared transport layers were conducted using various characterization techniques. The deposition technique that we followed is the one-step process where mixed metal halide is mixed with methylammonium iodide and the as-synthesized $CH_3NH_3PbI_{(3-x)}Cl_x$ perovskite is spin-coated on the top of the prepared substrates. The hole-transporting material (HTM) was deposited by spin coating a solution of doped P3HT on the perovskite layer. Finally, 100 nm gold was deposited as bottom electrode by thermal evaporator under pressure of 1×10^{-6} Torr to form an FTO/TiO_2/ $CH_3NH_3PbI_{(3-x)}Cl_x$ /P3HT/Au architecture as described in Figure 1.

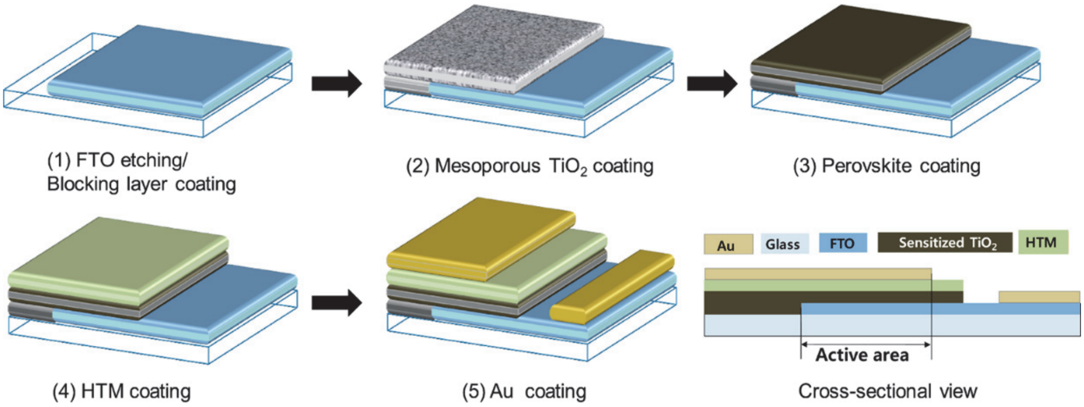

Figure 1. Device architecture

A number of devices were assembled to ensure the reproducibility and consistency of the measurements. In order to evaluate the benefits of our proposed approach, we compared the electrical characteristics of the prepared devices versus transport layers based on TiO_2 paste. Results show that the proposed modification outmatches our base. Overall energy conversion efficiencies of up to 12.8% for the best cell and 10% the average cell were measured and can be attributed to the better filling of perovskite due to bigger pore size.

References

[1] A. Kojima, K. Teshima, Y. Shirai and T. Miyasaka, J. Am. Chem. Soc. 131 (2009) 6050-6051.

Sponsors

A.U.TH RESEARCH COMMITTEE

ANELIS
ANALYTICAL ENVIRONMENTAL
LIFE INDUSTRIAL SCIENCES

KLOTHAKIS ELEFTHERIOS
2, Plastira Sq, 11635 Athens-Greece
Τηλ: +30 210 7524444 Fax: +30 210 7560849
E-mail: eklot@tee.gr Website: www.anelis.gr

SPECS™ Rigaku RENISHAW
apply innovation™

ITC
International Technology Corporation

VECTOR
TECHNOLOGIES

ASTERIADIS

ΑΝΑΛΥΤΙΚΕΣ ΣΥΣΚΕΥΕΣ Α.Ε.
Δρ Κ.Ι. ΒΑΜΒΑΚΑΣ - ΕΠΙΣΤΗΜΟΝΙΚΟΣ ΕΞΟΠΛΙΣΜΟΣ